SCIENTIFIC SOCIETY
OF MECHANICAL ENGINEERS

SECTION OF TECHNICAL SCIENCES,
HUNGARIAN ACADEMY OF SCIENCES

PROCEEDINGS OF THE SEVENTH CONFERENCE ON FLUID MACHINERY

Volume 2

AKADÉMIAI KIADÓ, BUDAPEST 1983

Conferences on fluid machinery have been arranged regularly by the Section of Technical Sciences of the Hungarian Academy of Sciences and the Hungarian Scientific Society of Mechanical Engineers.

These two volumes contain the texts of 108 lectures delivered at the seventh Conference held in Budapest in the autumn of 1983. The authors are recognized as eminent scientists in their respective fields. They represent 21 countries of four continents. The papers deal with topics related to design, testing, and operation of fluid machinery, presented as follows: Ideal and real flow through passages, boundary layers, flows around bodies, flow through cascades; Two-phase flow, mixing; Cavitation, erosion, noise, surge; Positive displacement pumps; Water turbines; Axial fans, compressors; Centrifugal fans, pumps, compressors; Seals; Branching networks and distribution systems; Turbocompressors; Nozzles, jet pumps; Flow measurements, orifice flows; Fluid couplings; Stresses in rotors.

Beyond the discussion of these topics, the papers also forecast the further development of this important field.

ISBN 963 05 3462 2 vols 1–2

ISBN 963 05 3464 9 vol. 2

PROCEEDINGS
OF THE SEVENTH CONFERENCE
ON FLUID MACHINERY

SCIENTIFIC SOCIETY
OF MECHANICAL ENGINEERS

SECTION OF TECHNICAL SCIENCES,
HUNGARIAN ACADEMY OF SCIENCES

PROCEEDINGS OF THE SEVENTH CONFERENCE ON FLUID MACHINERY

Volume 2

AKADÉMIAI KIADÓ, BUDAPEST 1983

Editors:

L. Kisbocskói and Á. Szabó

ORGANIZING COMMITTEE
OF THE SEVENTH CONFERENCE
ON FLUID MACHINERY

Chairman:

Professor Dr h. c. Dr J. J. Varga

Vice-Chairman:

L. Kisbocskói

Secretary:

Á. Szabó

Members:

Prof. Dr T. Czibere, Dr Á. Fáy, Dr Cs. Fáy, Prof. Dr O. Fűzy, Mrs. E. Hajós, Dr Z. Hankó, Prof. Dr M. Kozák, Dr L. Mátay, Prof. Dr A. Nyíri, Prof. Dr L. Pápai, D. Pattantyús-Á., L. Pázmány, Mrs. É. Pesti, Dr Gy. Sebestyén, Dr Sz. Szabó, Prof. Dr T. Szentmártony, Dr. D. Szüle, Prof. Dr Z. Terplán, E. Trenka, Dr Z. Vajna, Dr A. Verba, Miss M. Wagner

ISBN 963 05 3462 2 Vols 1—2
ISBN 963 05 3464 9 Vol. 2

Printed in Hungary

CONTENTS TO VOLUME 2

A SIMPLIFIED METHOD FOR DIMENSIONING OF CROSS FLOW FANS

T.Lajos - F.Szlivka

SUMMARY

On the basis of theoretical considerations and experimental results a simple method is proposed for calculation of the flow field in cross flow fans of given performance. Knowing the flow pattern the main design parameters can be determined.

INTRODUCTION

Cross flow fans invented by Mortier in 1892 have numerous advantages such as the relatively large capacity compared to their dimensions, the advantageous shape of casing as well as inlet and outlet cross section and the relatively high efficiency for small Reynolds' number. Some disadvantages delay the spread of this type of fan: e.g. the performance, even the stability of operation depends greatly on geometrical parameters of impeller and casing and there is no method available for dimensioning of fans of given performance. Many experiences have been reported in the literature about relations of fan performance and geometrical characteristics, but the success of development of a cross flow fan for a given application is rather doubtful for lack of calculative method of dimensioning.

The flow field in fan has been investigated by several authors [1] - [8] contributing to understanding the relatively complicated flow processes and numerous models have been elaborated for calculation the flow field in the cross flow fan [1] , [2] , [5] , [6] , [8] - [15] . On the basis of theoretical considerations and experimental results a simplified method for calculation of flow field and so the design parameters of cross flow fans can be proposed.

CHARACTERISTICS OF FLOW FIELD

The cross flow fan has a drum type impeller closed at both ends. The forward-curved blades of impeller are usually circular arcs manufactured from thin sheets. The chord of blades is relatively short, the diameter ratio is great: $\nu = 0.75 - 0.85$ /Fig. 1./.

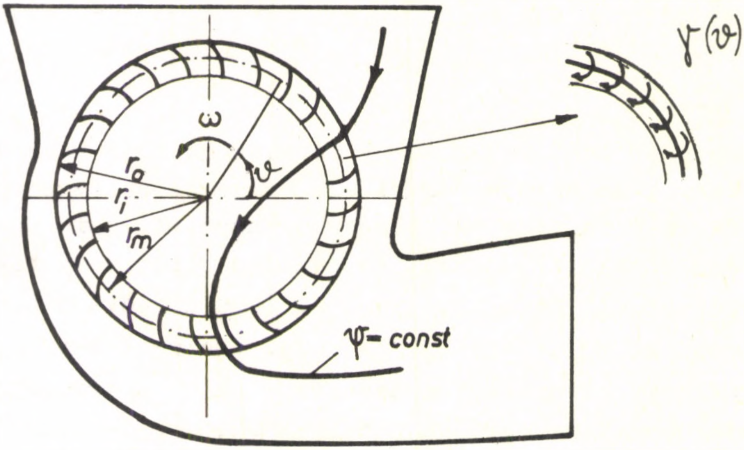

Fig. 1.

Neglecting the effect of end walls the flow field in cross flow fan is two-dimensional. The flow is unsteady both in absolute and in relative /corotating/ coordinate systems. That is why the blade circulation changes around the periphery of the impeller. As a consequence of change of blade circulation vortices are shed at the trailing edges of blades making the flow rotational in the impeller and in discharge side [5] , [12] . /The Euler head changes along the cascade, so the total pressure belonging to various streamlines is different i.e. the flow passing the impeller blades is rotational./ According to the proposal of the author [5] , [12] , [14] the eccentric vortex dominating the flow pattern in the impeller, characteristic of cross flow fan is produced by shedded vortices.

Experimental observations suppose this assumption: a relation was found between the change of blade circulation and the vorticity of flow field [5] , [13] ; reducing the change of blade circulation by application of swinging blades the vortex can be ceased [4] ; the significant function of vortex shedding in formation process of vortex has been observed by means of moire method [6] .

The evaluation of measurements of our own [5] as well as the measurements of Porter [3] , method of which has been presented in [13] , shows that the vorticity is relatively large in the recirculatory area /i.e. in the vortex/ and moderate outside of it. This conclusion is supported by measurements of total pressure distribution, too [5] , [7] . Nevertheless the error due to neglect of rotation in the calculation of flow field in impeller can be significant [15] . This calculation has been carried out by solving the

$$\Delta\psi = - f\,/\psi/ \qquad /1/$$

differential equation containing the assumption that the vorticity is constant along a streamline in the impeller. This assumption has been verified by experiments [13] , [14] .

The extension of solving the differential equation /1/ to the whole flow field of cross flow fan in order to develop a method for dimensioning seems to be disadvantageous:

- the most important design parameter, the shape of casing being a boundary condition has to be given previously;
- the shear stresses in real fluid exert a great influence on the vorticity distribution in the recirculatory area and on the decay of vorticity along streamlines in discharge side of the fan.

That is why a simplified method has been chosen which is making use of experimental results in calculation of flow field.

EXPERIMENTAL RESULTS

Let us substitute the blading of impeller with a line vortex distribution $\gamma/\vartheta/$ around the circle of radius $r_m = (r_i + r_o)/2$ /Fig. 1./. Each streamline $/\psi =$ const. curve/ intersects this circle twice i.e. two γ values belong to a ψ value. A very useful diagram can be constructed by plotting the line vortex distribution against the stream function /Fig. 2./

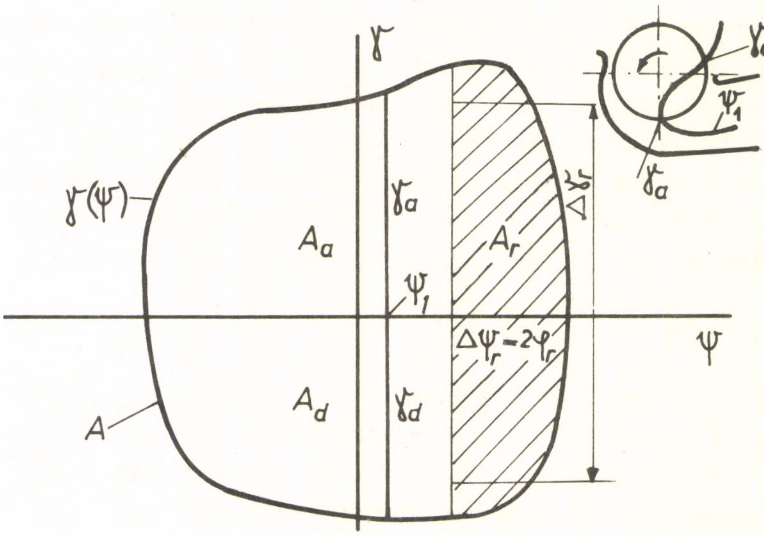

Fig. 2.

The extent of area /A/ surrounded by $\gamma/\psi/$ curve is proportional to the power coefficient [14] :

$$A = \frac{2}{1+\nu} \lambda \, r_o \, u_o^2 \qquad /2/$$

The horizontal and vertical dimensions of this area are proportional to the flow rate delivered by impeller and the ideal total pressure rise of fan respectively. The change of vorticity across the cascade as a consequence of shedded vortices /i.e. the change of blade circulation/ is proportional to the rise of γ /ψ/ curve.

However the sign of blade circulation changes in two points of impeller periphery usually one recirculatory area can be observed in the fan. The recirculatory area surrounds the blades changing the sign of their circulation, being nearer to discharge side. The "centre" of area is in the vicinity of inner radius of cascade at fan types allowing the moving of "vortex" [3] .

A part of flow rate recirculates. The evaluation of Porter's results [3] shows that the flow coefficient relating to recirculating flow is $\varphi_r \approx 0.3 \sim 0.4$, i.e. the quotient of the recirculating flow rate and that delivered by the impeller is between 0.3 and 0.5 in the vicinity of the best efficiency point. So

$$\varphi_{impeller} \approx (1.3 \sim 1.5) \times \varphi_{fan} \qquad /3/$$

The extent of area of Fig. 2. belonging to recirculating flow /A_r/ is proportional to the power input in recirculatory area. The evaluation of Porter's results [3] shows that 20∼50 % /in the vicinity of best efficiency point 25 %/ of power input is required to maintain the recirculation and a close relation exists between the power input in recirculatory area and the circulation around it [14] .

Assuming that there is no significant power transfer between recirculating and throughflowing air /evidence of which can be found in [3] , [8] / the efficiency of impeller blading and the outlet diffuser can be estimated as quotient of power output of fan and the power input reduced by that maintaining the recirculatory area. The maximum values of blade efficiency for two types of cross flow fans investigated by Porter were 0.64 and 0.77. The abscissa divides the area A surrounded by the curve γ /ψ/ into two parts A_d and A_a ratio of which shows the distribution of power input between inlet /decelerating/ and outlet /accelerating/

parts of cascade. The evaluation of Porter's measurements shows that the value of A_d/A_a increases from o.7 to 1.4 at decreasing flow rate, but in operating conditions about the best efficiency $A_d/A_a \approx 1$. A correlation has been found between the change of blade circulation in the recirculatory area $\Delta\gamma_r$ /Fig. 2./ and the circulation Γ_r around the recirculatory area [14] :

$$\Gamma_r = 6 \cdot r_o \, u_o \left(\frac{\Delta \gamma_r}{u_o} \right)^{0.28} \qquad /4/$$

CALCULATION OF FLOW FIELD

The flow field in a cross flow fan can be determined by superposition of flow field around a corner, the flow field induced by line vortex distribution $\gamma /\vartheta/$ substituting the cascade, and the flow field induced by a vortex substituting the recirculatory area. It is expedient to choose constant intensity of line vortex distribution along the inlet and outlet arcs of cascade, because so - except for the place of sudden change of blade circulation - no vortices are shed, i.e. the flow passing the cascade remains potential.

In this case the area surrounded by curve $\gamma/\psi/$become oblong /Fig.3./

At beginning of the dimensioning process the flow coefficient φ_{fan} and pressure coefficient ψ to be realised are given. On the basis of experiences the diameter ratio ν, the efficiency η of fan have to be chosen /e.g. $\nu = 0.8$, $\eta =$ $= 0.4$/.

Determining the power coefficient $\lambda = \varphi\psi/\eta$ and using /2/ the extent of area A surrounded by curve $\gamma/\psi/$/Fig.3./ can be determined. Using /3/ the width and height of oblong-shaped area A can be calculated:

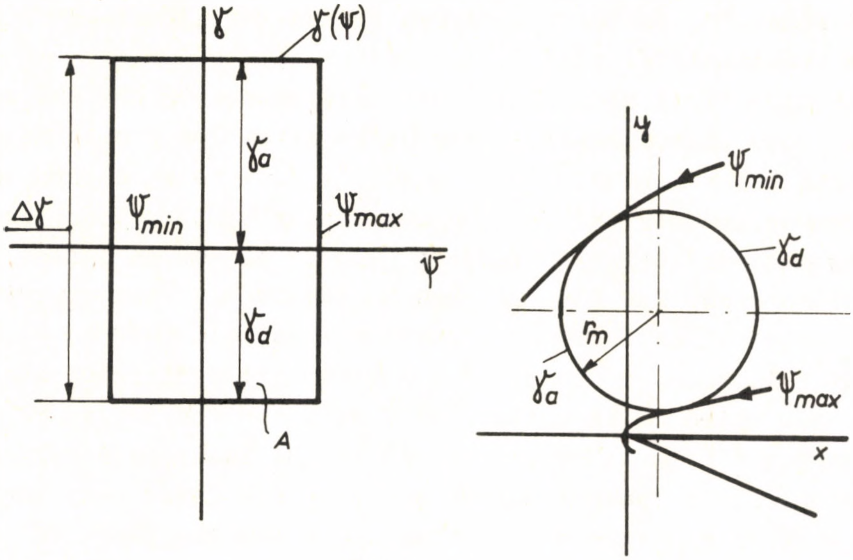

Fig. 3.

$$\frac{1}{r_o\, u_o}\left(\psi_{max} - \psi_{min}\right) = 2\,\varphi_{impeller} = (2.6\sim3)\,\varphi_{fan} \qquad /5/$$

$$\Delta\gamma = A \;/\; \left(\psi_{max} - \psi_{min}\right) \qquad /6/$$

Choosing the value of A_d/A_e /i.e. distributing the power input between decelerating and accelerating blades/ the line vortex distribution substituting the cascade can be determined:

$$|\gamma_d| = \Delta\gamma / \left(1 + A_e/A_d\right) \quad , |\gamma_a| = \Delta\gamma - |\gamma_d| \qquad /7/$$

Using /4/ the circulation Γ_r around the potential vortex substituting the vorticity in the recirculatory area can be calculated.

An undisturbed flow is to be selected being suitable for determination of the flow direction farther from impeller. The flow around a corner can be such an undisturbed flow. Three parameters have to be chosen for the calculation: the angle of corner, the location of centre of impeller in relation to the corner /Fig.3./ and the intensity of undisturbed flow. The latter can be determined taking into account the relation /5/.

In the first step of the calculation the inflow and outflow arcs of the impeller periphery /i.e. the positions of points belonging to Ψ_{max} and Ψ_{min}/ have to be determined considering only the undisturbed flow /Fig.3./. The line vortex distributions γ_d and γ_a can be placed on inflow and outflow arcs. The flow induced by the line vortex distribution alters the inflow and outflow arcs, so repeated calculation is required to place the line vortex distribution.

As a third component of the flow field the vortex of strength Γ_r is to be positioned on the inner periphery of the cascade between the inflow and outflow arcs near the corner. The flow induced by vortex can alter the place of opposite boundary of inflow and outflow arcs, this is why a modification of line vortex distribution can be necessary.

Calculating the flow pattern the streamline bounding the recirculatory area and that representing the casing of fan can be selected. The flow rate between these streamlines does not equal to that prescribed by φ_{fan}, so the intensity of the undisturbed flow has to be altered.

The result of calculation is a flow pattern giving information about the shape of casing. Knowing the flow field components, the velocity distribution around the inner and outer periphery of cascade can be calculated. The knowledge of velocity-distribution helps the proper selection of blade angles.

SYMBOLS

A [m^3/s] area
r [m] radius
$u = r\omega$ [m/s] peripheral velocity
γ [m/s] line vortex distribution
Γ [m^2/s] circulation
η [-] efficiency
ϑ [rad] angle
$\lambda = \varphi\psi/\eta$ [-] power coefficient
$\nu = r_i/r_o$ [-] diameter ratio
φ [-] flow coefficient
ψ [-] pressure coefficient
Ψ [m^2/s] stream function
ω [1/s] angular velocity

Subscripts

o outer
a accelerating
d decelarating
i inner
m middle
max maximum
min minimum
r recirculatory

REFERENCES

[1] Coester, R.: Theoretische und experimentelle Untersuchungen an Querstromgebläsen. Diss. ETH Zürich /1959/

[2] Ilberg,H. - Sadeh,W.: Flow theory and performance of tangential fan. Proc. of Inst. of Mechanical Engineers 18o /1965-66/ 19. 481-496.

[3] Porter,A.M.: A study of the tangential fan. Ph.D.Theses Queen's University Belfast /1969/

[4] Torii,O. - Ide,M. - Tojo,C.: A Study of Cross Flow Fan with Swinging Vanes. Bull. of the Osaka University, Engineering and Natural Sciences 19 /197o/ 1. 1-15.

[5] Lajos,T. - Preszler,L.: Zur Theorie des Querstromgebläses Teil 1., 2. Zeitschrift für Heizung Lüftung Klimatechnik, Haustechnik 24 /1973/ 5. 134-14o., 6. 189-196. Translated by NEL: On the Theory of the Reactive Fan. NEL TT 2597

[6] Yamafuji,K.: Studies on the Flow of Cross-Flow Impellers /1st and 2nd Report/ Bull. of the JSME 18 /1979/ 123. 1o18-1o25; 126. 1425-1431.

[7] Murata,S. - Nishihara,K.: An Experimental Study of Cross Flow Fan /1st and 2nd Report/ Bull. of the JSME 19 /1976/ 314-321; 321-329.

[8] Murata,S. - Ogawa,T. - Shimizu,I. - Nishihara,K.- Kiroshita„K.: A study of Cross Flow Fan with Inner Guide Apparatus. Bull. of the JSME 21 /1978/ 154. 681-688.

[9] Fratzscher,W.: Zur Berechnung von Querstromgebläsen. Diss. T.H. Otto von Guericke, Magdeburg /1965/

[1o] Ikegami,H. - Murata,S.: A study of cross flow fan. Part 1. Theoretical Analysis. Technical Reports of Osaka University 16 /1966/ 557-578.

[11] Turbin,V.G. - Szücsugov,N.P.: K analizu rabotü diametralnovo ventilatora. Zapiszki Leningradszkovo Szelszkohozjajsztvennovo Insztituta 1o8 /1966/ 97-1o6.

[12] Lajos,T. - Preszler,L.: Calculative method for sizing the tangential flow fan. Proc. of the Fourth Conference on Fluid Machinery, Budapest /1972/ 731-742.

[13] Lajos,T.: Investigation of the flow characteristics in the impeller of the tangential fan. Proc. of the Fifth Conference on Fluid Machinery, Budapest /1975/ 567-577.

[14] Lajos,T.: Az áramlás sajátosságai a keresztáramu ventilátorban. Kandidátusi értekezés, Budapest /1976/

[15] Hoffmann,A. - Lajos,T. - Szlivka,F.: Mathematical interpretation of flow pattern in the impeller of the tangential fan. Proc. of the Sixth Conference on Fluid Machinery, Budapest /1979/ 485-492.

Lajos,Tamás Dr.Techn. Cand. of techn.Sc. associated professor

Szlivka,Ferenc, Dr. Techn. assistant

Department of Fluid Mechanics, Technical University Budapest, Bertalan Lajos u. 4-6. H-1111 Budapest.

TRANSONIC INVISCID FLOW CALCULATIONS FOR FLOW PAST SWEPT-BACK PLANE TURBINE CASCADES

F r i t z   L e h t h a u s

DFVLR - Institute for Experimental Fluid Mechanics, Goettingen, FRG

SUMMARY

Some results of two-dimensional and three-dimensional calculations on swept-back plane turbine cascades are presented. The method used is a time-marching finite-volume technique applied to the Euler equations. The 2D calculations are based on two different flow models, i.e., projection and section methods. By comparison of these 2D results with a corresponding 3D result, it is seen that the section method may be used only as a very first step for midspan calculations of swept-back plane turbine cascades of moderate aspect ratios. For details and for other blade sections 3D calculations are necessary.

SYMBOLS

XA,YA,ZA	- Axial coordinate system	β_σ	- Flow angle in $X\sigma$,$Y\sigma$-plane
$X\sigma$,$Y\sigma$=YA	- Swept coordinate system	M	- Mach number
M,N,L	- Computational grid system	p	- Static pressure
t	- Pitch length	p_0	- Total pressure
l	- Chord length		
LA	- Axial width of the cascade	Indices	
HA	- Height of blades	A	- Flow in XA,YA-plane
β_s	- Stagger angle	σ	- Flow in $X\sigma$,$Y\sigma$-plane
σ	- Sweep angle, flow angle in XA,ZA-plane	1	- Homogeneous inlet flow
		2	- Homogeneous outlet flow
β	- Flow angle in XA,YA-plane	is	- Isentropic

1. INTRODUCTION

For design and development of axial flow turbomachinery bladings theoretical and experimental investigations of corresponding rectilinear cascades are the traditional first steps. The two-dimensional cascade flow model is exactly valid only for coaxial cylindrical stream surfaces which may exist in incompressible flow machines of free vortex design. But this flow model has turned out to be also very useful when the flow does not meet these conditions exactly, as for example when the compressibility effects of the flow are no longer negligible but are of a moderate magnitude. Due to several reasons, transonic flow regimes exist in modern axial turbines, i.e., the flow is accelerated in the blade passages from subsonic to supersonic velocities. Such high expansion of the flow calls for a corresponding increase of the annular flow cross-section. Therefore, even neglecting secondary flow effects, induced by viscous boundary layers, a three-dimensional, complicated, more or less conical flow exists. In these cases the use of 2D cascade characteristics as input data for design is questionable. This paper presents some investigations on swept-back plane turbine cascades using 2D and 3D time-marching finite-volume calculations of the Euler equations, to determine whether the simplifying assumption of coaxial stream surfaces is helpful.

2. TIME MARCHING FINITE VOLUME METHOD

Starting from the isentropic time-marching finite-volume method of P.W. McDonald, (1), some years ago a computational method and a corresponding computer program, F. Lehthaus (2), was developed at DFVLR in order to calculate the 2D inviscid transonic turbine cascade flow. The basic equations, i.e., the time-dependent conservation laws in integral form for mass, momentum and energy were discretised, elaborating and using an extended version of the damping surface technique, which was suggested by J.J. Smolderen et al., (3). The lower part of FIGURE 1 shows the typical 2D computational domain for a hub section cascade. Starting from an assumed distribution of local flow values at the nodes of the computational grid ,the solution for stationary flow is found by iteration with respect to time. Using this iteration, prescribed values of total temperature, total pressure and flow angle are kept constant in the inlet plane, as well as the static pressure in the outlet plane. To improve the solution obtained in this coarse computational grid, this grid is refined up to three times successively always using the solution of the coarser grid as the starting condition for the next grid.

For some examples it was shown in (2) that the computed pressure distributions on the blade contours agree very well with the corresponding experimental results provided that the real flow does not separate from the profile before reaching the trailing edge. The comparison between calculated and measured homogeneous upstream Mach numbers is quite perfect.

The homogeneous downstream flow conditions are calculated from the inhomogeneous distributions of the computed flow values in the outlet plane of the computational domain by integration, using the conservation laws of mass, momentum and energy. The deviation between computed and experimentally derived downstream flow angle is found to be less than one degree. The total pressure losses show good agreement at least in their behaviour.

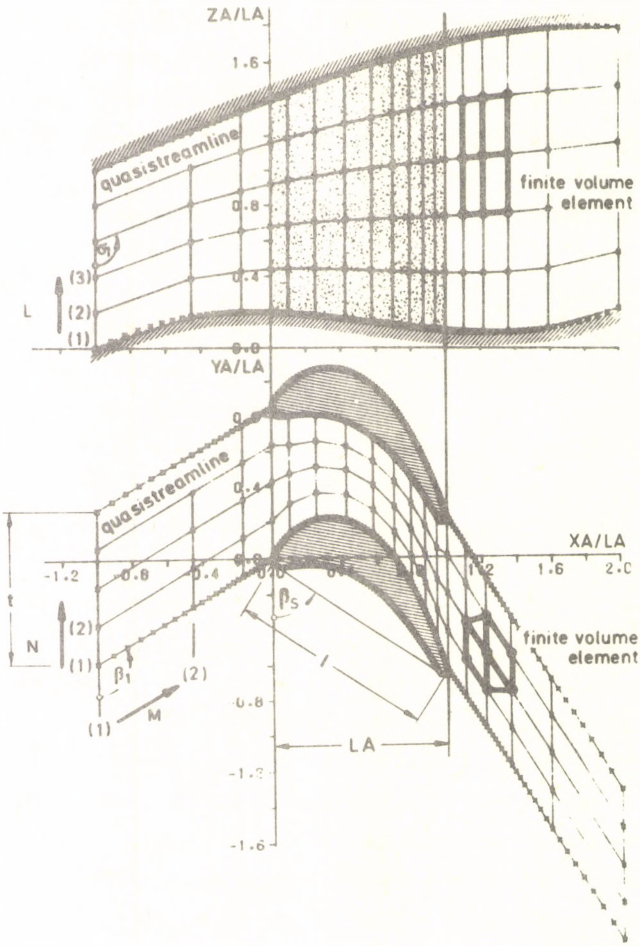

FIGURE 1

A detailed discussion of the method as well as the important advances in time-marching finite-volume techniques during the last few years, for example J.D. Denton, (4,5), is beyond the scope of this paper.

3. SWEPT BACK PLANE TURBINE CASCADES OF INFINITELY HIGH AND OF INFINITELY LOW ASPECT RATIO

There are two possibilities for looking at the flow through swept- back plane turbine cascades by the application of 2D calculation methods, as shown for incompressible flow by U. Stark and H. Gotthardt, (6).

Corresponding to the flow model for an infinitely long swept-back wing a swept-back plane turbine cascade of infinitely high aspect ratio may be assumed. Following this concept termed projection method the usual 2D calculation is done in the XA,YA-plane, FIGURE 2, for a given inlet angle β_1 and a given ratio of back pressure p_2 to inlet total pressure p_{01A} of the flow component in the XA,YA-plane. In order to get the prescribed sweep angle of the inlet flow σ_1, the Mach number component M_{1ZA} along the ZA-axis has to be superimposed on the inlet Mach number component M_{1A} calculated in the XA,YA-plane. In this superposition the inlet angle $\beta_{1\sigma}$ and the Mach number $M_{1\sigma}$ are derived by simple trigonometrical relations. Now the ratio of back pressure to inlet total pressure $p_2/p_{01\sigma}$ can be computed. By superposition of the velocity component corresponding to the Mach number M_{1ZA} in ZA-direction to the whole flow field in the XA,YA-plane all other flow quantities are determined.

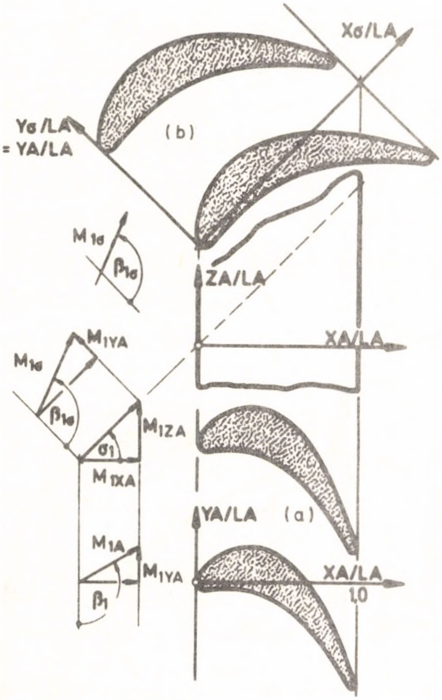

FIGURE 2

Assuming a swept-back plane turbine cascade of infinitely low aspect ratio another 2D flow model for calculation is evident. In this section method the swept Xσ,Yσ-plane which contains the prescribed inlet flow direction has to be chosen as the 2D computational plane. In order to calculate for comparable flow conditions, the transformed inlet angle $\beta_{1\sigma}$ and the ratio of back pressure p_2 to inlet total pressure $p_{01\sigma}$ as derived in the projection method has to be used.

3. SWEPT-BACK PLANE TURBINE CASCADES OF FINITE ASPECT RATIO

In order to calculate the 3D inviscid transonic flow past swept-back plane turbine cascade configurations of finite aspect ratios the above 2D method was extented straightforwardly to the third dimension of the Cartesian coordinate system as shown schematically in the upper part of fig. 1.

In FIGURE 3 the profile pressure distributions on the lower end wall, the mid section and the upper end wall are shown for the hub section cascade with $\sigma=30^{\circ}$ sweep angle at two different outlet Mach numbers. In both the cases the pressure level on the pressure side is higher for the lower wall than for the upper wall. The same result is found for the suction side in the subsonic case up to 60% and in the transonic case up to 80% of the axial width of the cascade, after which the curves intersect. From the lower end wall to the upper end wall the loading strongly increases at the profile leading edge and decreases at the trailing edge. In the transonic regime, the flow on the lower surface follows the limit loading condition while on the upper surface the flow is characterized by shock reflection in the rear part of the suction side. Therefore, a curved shock surface is formed in part of the blade passage.

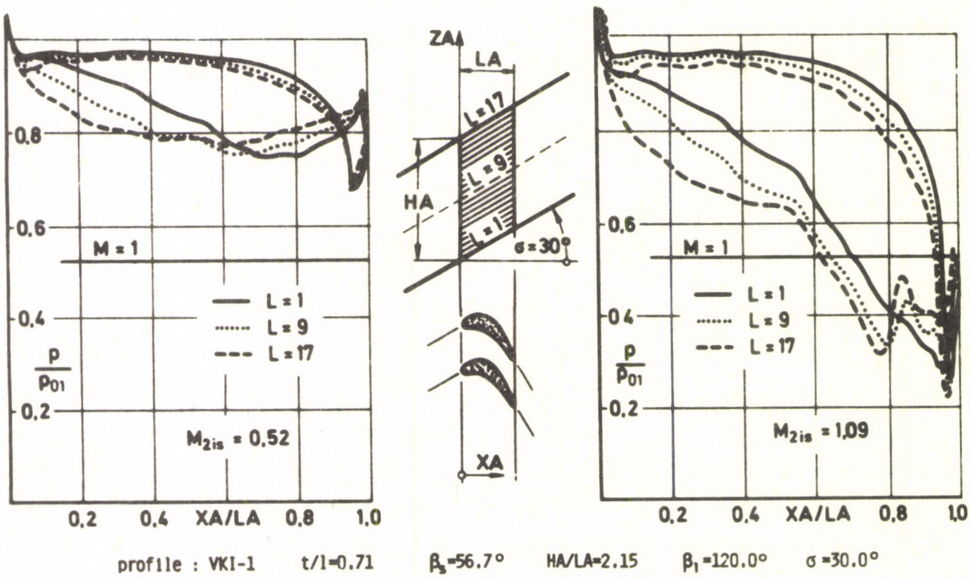

FIGURE 3

A comparison of the 3D pressure distributions, computed for a swept-back plane turbine cascade and measured for a corresponding rotating conical cascade, is shown in FIGURE 4. Both cascades have the same geometry only at the midsection. Therefore, some geometrical differences exist which add to the influences due to rotation of the test wheel, and this comparison can only show qualitative agreement.

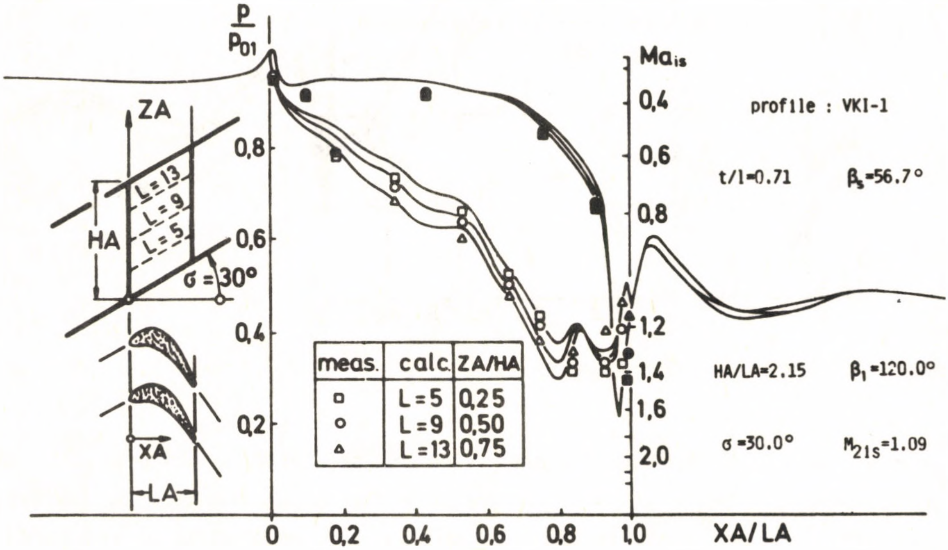

FIGURE 4

The differences between the pressure distributions on the lower and the upper walls increase with sweep angle as is evident from FIGURE 5 for $\sigma=45^{\circ}$ compared with the right hand side of fig. 3 for $\sigma=30^{\circ}$.

Concerning this sample calculation the spatially curved streamlines are computed from the time-marching solution beginning at the nodes in the inlet plane, M=1, of the computational grid, FIGURE 6. The traces of the streamlines starting on the lower end wall, L=1, at 50% of the channel height, L=9, and on the upper end wall, L=17, are plotted in the XA,YA-plane. Correspondingly in the XA,ZA-plane the traces of those streamlines are shown, which start from three different pitchwise positions in the inlet plane. These are streamlines passing the blade passage close to the suction side of the profiles, N=2, at midchannel, N=9, and close to the pressure side, N=16. On the lower surface the streamlines

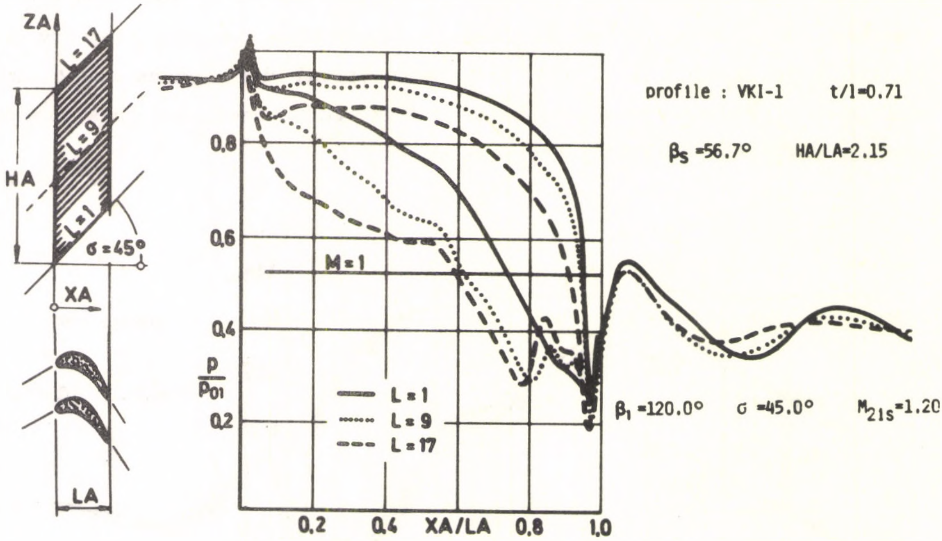

FIGURE 5

are shifted towards the pressure side of the profile when passing the blade passage, L=1. The whole flow in front of the cascade is deflected towards the upper wall, in this way decreasing the loading at the profile leading edge region at the lower wall and increasing it at the upper wall as already determined from the pressure distributions. The streamline shift towards the upper end wall continues up to the cascade outlet plane for all those streamlines which are passing the blade channel close to pressure side, N=16. Some streamlines are found forming a stagnation streamline parallel to the ZA-axis at the profile nose. According to this flow behaviour at the pressure side, the streamlines on the upper end wall are shifted towards the suction side when passing the blade channel, L=17, and those close to the suction side in the rear part of the blade passage are deflected towards the lower end wall, N=2.

5. COMPARISON OF RESULTS OBTAINED BY PROJECTION, SECTION AND 3D METHODS

In the left part of FIGURE 7 the pressure distribution on the profile contour computed by the three methods are compared for the case of the hub section cascade with $\sigma_1=45^{\circ}$ sweep angle of the inlet flow. The back pressure is chosen corresponding to an isentropic outlet Mach number $M_{2is}=1.2$.

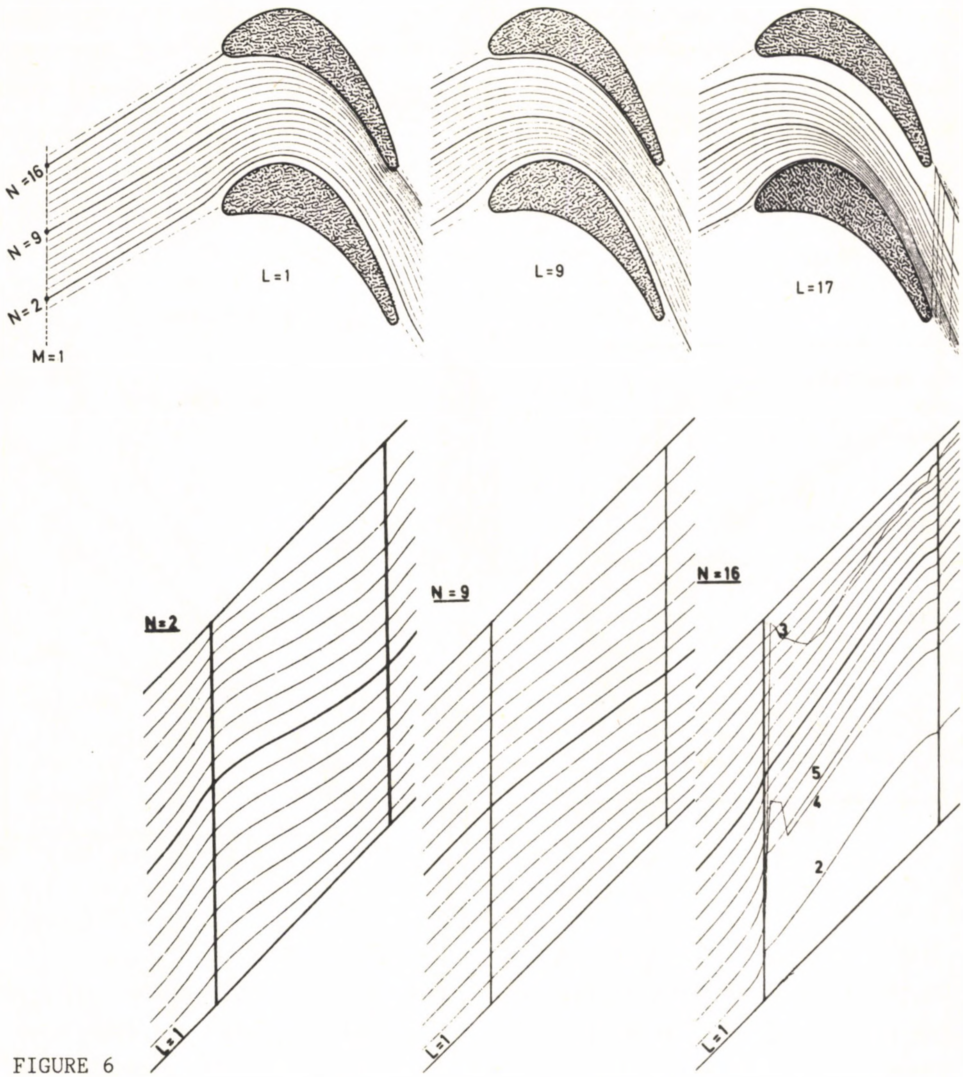

FIGURE 6

The projection method gives a higher pressure level than the section method for most of the pressure side while on the suction surface up to 85% of the axial width the projection method gives lower pressures. On the rear part of the suction side the calculation using the section method results in a higher expansion than the projection method. As a result the two curves intersect and the reflection of the right running shock, which is starting from the confluence of the suction and pressure side flows behind the trailing edge of the adjacent blade, is shifted more downstream in the section method. Summarizing all the above differences in the calculated pressure distributions the projection method predicts a higher blade loading than the section method. The left part of fig. 7 shows a good agreement of the pressure distributions on the pressure side calculated by the section method with the midspan result, L=9, of the 3D method while on the suction side there is a better agreement between the distributions predicted by the projection and the 3D method.

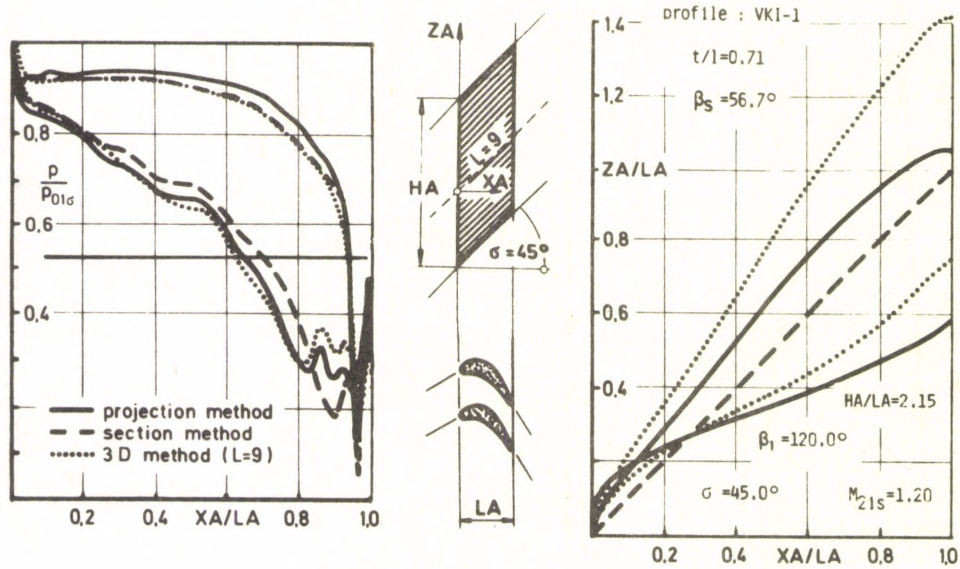

FIGURE 7

On the right hand side of fig. 7 the traces of the streamlines close to the profile contour are compared. For the section method all the streamlines lie in the computational plane, so the sweep angle is constant $\sigma=45^{\circ}$ and in the XA,YA-plane only one common trace exists for all streamlines. The projection method results in different shifts of the streamlines close to suction and pressure sides, thus predicting twisted stream surfaces in the blade passages. Additionally the sweep angle changes from the homogeneous $\sigma_1=45^{\circ}$ inlet to the homogeneous $\sigma_2=28^{\circ}$ outlet flow, i.e., a strong deflection of the flow towards the axial direction occurs when passing through the blade row.

The 3D method predicts at midspan a difference in the streamline shifts between pressure and suction side of the same order as the projection method. But due to the influence of the end walls the mean sweep angle of the flow remains $\sigma=45^{o}$. This is the reason why the homogeneous outlet flow values calculated from the inhomogeneous outlet conditions of the 3D time-marching results are comparable to those obtained from the section method, while the projection method predicts a distinctly different outlet flow behaviour.

6. CONCLUDING REMARKS

It may be concluded that at least for comparable aspect ratios, as in the described sample calculations, the section method may be applied to swept-back plane turbine cascades as the very first step to calculate the overall flow behaviour at midspan. Correspondingly a conical stream surface may be helpful for a midspan calculation for actual stator and rotor bladings. In order to look at the flow details or at other blade sections simplifying 2D assumptions are too restrictive and 3D considerations are necessary.

7. REFERENCES

(1) McDonald P. W.
The Computation of Transonic Flow through Two-dimensional Gas Turbine Cascades.
ASME Paper 71-GT-89
New York, American Society of Mechanical Engineers, 1971

(2) Lehthaus F.
Berechnung der transsonischen Stroemung durch ebene Turbinengitter nach dem Zeit-Schritt-Verfahren
In: VDI-Forschungsheft 586
Duesseldorf, Verein Deutscher Ingenieure, 1978

(3) Couston M., McDonald P. W., Smolderen J. J.
The Damping Surface Technique for Time-Dependent Solutions to Fluid Dynamics Problems
VKI-Technical Note 109
Rhode-Saint-Genese/Belgium, Von Karman Institute, 1975

(4) Denton J. D., Singh U. K.
Time Marching Methods for Turbomachinery Flow Calculation
VKI-Lecture Series on Transonic Flows for Turbomachinery
Rhode-Saint-Genese/Belgium, Von Karman Institute, 1979

(5) Denton J. D.
An Improved Time Marching Method for Turbomachinery Flow Calculation
ASME-paper 82-GT-239
New York, American Society of Mechanical Engineers, 1982

(6) Stark U., Gotthardt H.
Theoretische und experimentelle Untersuchungen an konischen Turbinengittern
Teil 1: Potential-theoretische Untersuchungen an gepfeilten Verdichter- und konischen Turbinengittern
Bericht 78/2
Braunschweig, Techn. Univ., Inst. f. Stroemungsmechanik, 1978

SIMULTANEOUS ANALYSIS OF BOUNDARY LAYER AND POTENTIAL FLOWS

by

R. I. Lewis

Summary

A numerical cellular boundary layer method is presented aimed at the simultaneous analysis of thick boundary layer growth on curved boundaries. The method is first compared with classical solutions for laminar boundary layers with accelerating main stream flows. Initial work on the application of this to the flow of a thick shear layer over a curved wall is covered, including comparisons with the traditional approach of modifying the wall contour in potential flow by addition of the displacement thickness. The method represents the first stages of an extension of the well established Martensen method towards a full viscous/potential model of real flows.

INTRODUCTION

The author recently[1] extended Martensen's method to deal with separated flows by allowing the surface vorticity to be shed continuously from separation points. Subsequently Porthouse[2] developed a viscous diffusion model based on Brownian motion which was applied by Lewis and Porthouse[3] to separated flows past bluff bodies and stalling aerofoils and cascades. In the final numerical model[3] vorticity is created, shed and diffused from each discrete element of the body surface during every time step, resulting in a generalised method for stalled or unstalled flows past two-dimensional bodies of arbitrary shape. The viscous diffusion model resembles that of Chorin[4], in parallel with whom quite reasonable simulations of laminar boundary layers have been obtained. Typical sample results are shown in figure (1).

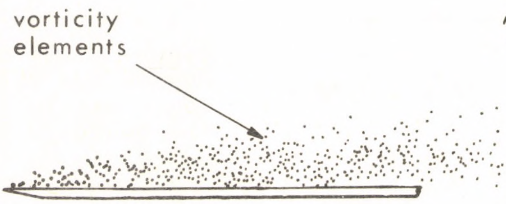

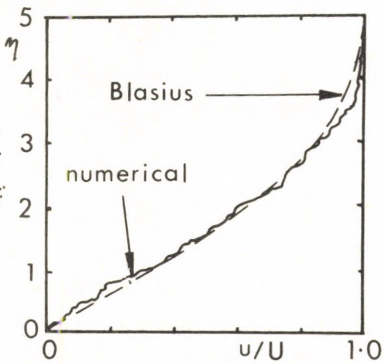

Figure 1. Numerical simulation of a flat plate boundary layer.

The main disadvantages of this method lie in (a) inaccuracy without excessively large numbers of vorticity elements in the field and (b) the consequent outrageous computing requirements. Consequently cellular methods are being explored to deal with the near body flow. This paper contains two contributions to this end. Firstly a cellular technique for two-dimensional plane walled boundary layers is briefly described. This method was formulated to permit later extension to viscous flow past curved surfaces. Although not yet accomplished for viscous flow, the paper concludes with a preliminary extension of Martensens method to deal with a thick inviscid shear layer adjacent to a curved wall.

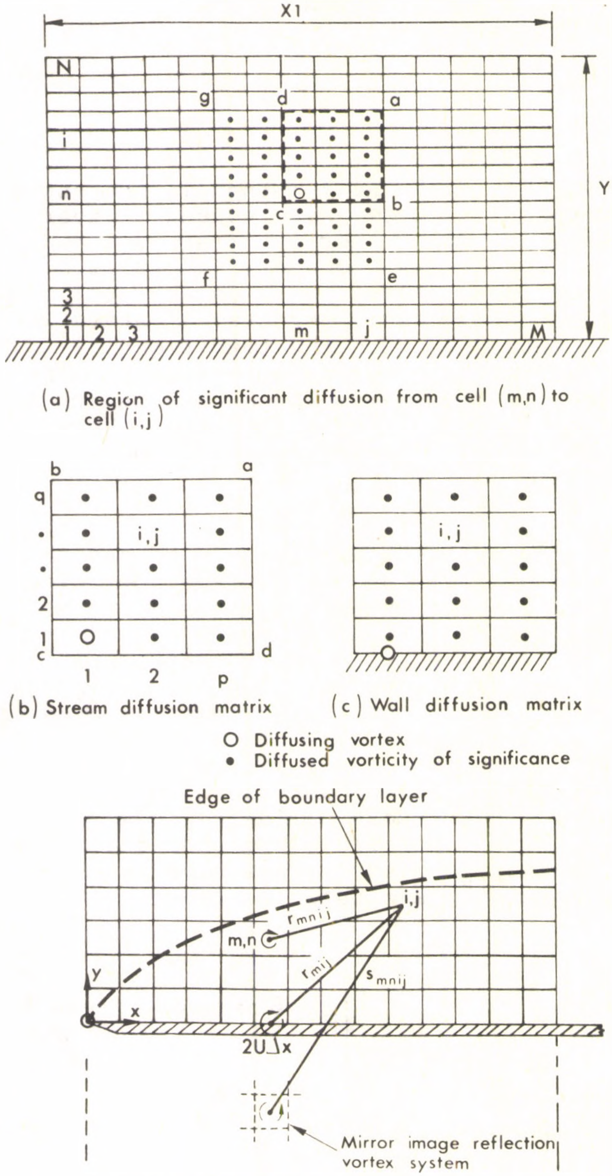

Figure 2. Grid system and diffusion matrices for boundary layer method.

CELLULAR METHOD FOR LAMINAR BOUNDARY LAYERS

In order (a) to limit the number of vorticity elements and (b) to speed up the diffusion calculation, a cellular control volume or grid may be defined to cover the region of a boundary layer, figure (2). For the grid depicted here, a fixed number of elements MN will apply for all time. Furthermore over the prescribed time step Δt the diffusion of a typical vorticity element mn at 0, will result in the redistribution of vorticity of significant magnitude to only the limited region aefg. By symmetry diffusion coefficients need only be calculated for the region abcd, and may be evaluated at the beginning of the calculation once and for all for a so-called "diffusion matrix". Computation is reduced by an order of magnitude through this technique and sufficient for the author to complete all of the remaining solutions in this paper by means of an 8 bit micro-computer.

The motion of a diffusing vortex of initial strength Γ centred on the origin of the (r,θ) plane is described by the vorticity diffusion equation[5]

$$\frac{\partial\omega}{\partial t} = \nu\left\{\frac{\partial^2\omega}{\partial r^2} + \frac{1}{r}\frac{\partial\omega}{\partial r}\right\} \tag{1}$$

from which we may obtain the well known solution for the subsequent vorticity distribution

$$\omega(r,t) = \frac{\Gamma}{4\pi\nu t}\, e^{\{-r^2/4\nu t\}} \tag{2}$$

Since equation (1) is linear, solutions for multiple distributions of vortices in close proximity may be superimposed. Equation (2) may thus be applied to the vorticity within each grid element at time t to evaluate the amount diffused during time Δt into all other cells. Thus the vorticity in cell (i,j) will be the sum of vorticity contributions which have diffused from all MN cells in the field during time Δt, namely

$$\omega(i,j)_{t+\Delta t} = \frac{1}{4\pi\nu\Delta t}\sum_{m=1}^{M}\sum_{n=1}^{N}\omega(m,n)\left\{e^{\{-\frac{r^2_{mnij}}{4\nu\Delta t}\}} + e^{\{-\frac{s^2_{mnij}}{4\nu\Delta t}\}}\right\} \tag{3}$$

where r_{mnij} and s_{mnij} are defined in figure (2). In this particular model a reflection system is introduced to accomplish the wall boundary condition.

In most cases, particularly flows with a non-uniform mainstream velocity U(x), vorticity $\gamma(x)$ is continuously created at the wall itself for which a second diffusion equation is required, namely

$$\omega(i,j)_{\substack{t+\Delta t\\ \text{wall}}} = \left\{\frac{\gamma(x)\Delta x}{4\pi\nu\Delta t}\right\}\sum_{m=1}^{M} e^{\{-r^2_{mij}/4\nu\Delta t\}} \tag{4}$$

As illustrated in figure (2) and discussed above, the coefficients of equations (3) and (4) may be evaluated once and for all and deposited into the stream and wall diffusion matrices. The range MN of the summations may also be reduced to the significant range pq.

Diffusing Vortex Sheet

This solution was first applied to the case of a diffusing vortex sheet located on the x axis. To compensate for leakage at the ends of the cellular region, the total vorticity strength at each x location was conserved by application of the condition

$$\int_0^\infty \omega(y)dy = U \tag{5}$$

where U is the velocity at $y = \infty$. This condition was enforced after time step Δt by the scaling formula

$$\omega(i,n) := \left\{ \frac{U}{\sum_{n=1}^{N} \omega(i,n)\Delta y} \right\} \omega(i,n) \tag{6}$$

As shown below in Table I, for a grid aspect ratio $\Delta x/\Delta y = 1.0$ and a single time step $\Delta t = 0.005$, the numerical form delivers the exact solution precisely. For extreme aspect ratios of 10.0 suitable for boundary layer calculations, equal accuracy is retained provided the vorticity conservation condition equation (6) is enforced.

TABLE I

Diffusion of a vorticity sheet according to equations (4) & (6)

$\Delta t = 0.005$, $\nu = 1.0$, $\gamma = 2.0$

y	x = 0.05	0.15	0.25	Exact Solution
0.05	7.041307	7.041307	7.041309	7.041309
0.15	2.590351	2.590352	2.590352	2.590352
0.25	0.350566	0.350566	0.350566	0.350566
0.35	0.017453	0.017453	0.017453	0.017454
0.45	0.000320	0.000320	0.000320	0.000320
0.55	0.000002	0.000002	0.000002	0.000002

As illustrated by figure (3), over 20 time steps the diffusion of a vorticity sheet is predicted with acceptable precision compared with the exact solution[5], namely

$$\omega(y,t) = \frac{U}{\sqrt{\pi \nu t}} e^{\{-y^2/4\nu t\}} \tag{7}$$

Boundary layer solutions

The aim of this method is to simulate the growth over a period of time of an ultimately steady state laminar boundary layer under the influence of a mainstream veocity U(x) which varies with x. This is achieved by the following time stepping procedure.

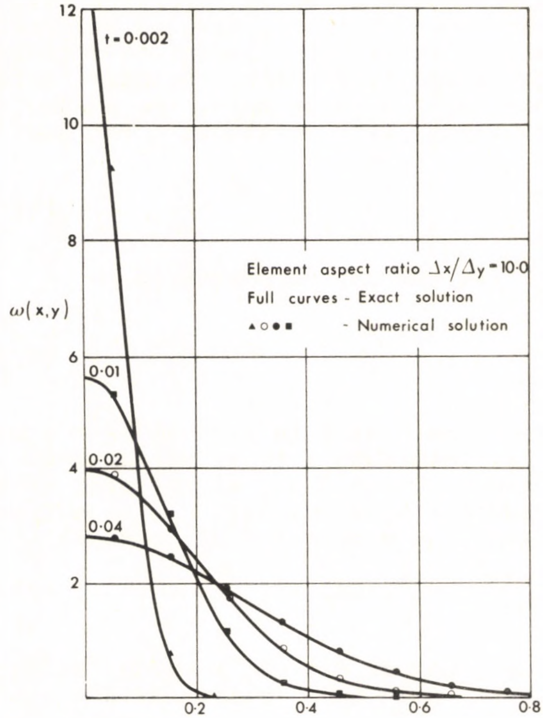

Figure 3. Diffusion of a vortex sheet.

t = 0

(i) Wall vorticity sheet $\gamma(x) = 2U(x)$ is diffused over first time step Δt

(ii) Cellular vorticity is diffused

(iii) Cellular vorticity is convected

(iv) New wall vorticity is diffused

(v) Time advanced by Δt

No mention has yet been made of the convection process (iii) fuller details of which are given in reference (6). Although for accuracy this would normally involve evaluation of u(i,j) and v(i,j) at the centre of each element to define the vorticity drift path, for simplicity laminar boundary layers may be treated by assuming v(i,j) to be zero, the assumption underlying the normal boundary layer equations. For the definition of vorticity

$$\omega = \frac{\partial u}{\partial y} \tag{8}$$

u(i,j) follows directly and may be expressed in numerical form as

$$u(i,j) = \sum_{n=1}^{j} \omega(i,n)\Delta y \tag{9}$$

Following convection, there will in general be too much or too little vorticity at locations i to bridge between $u(i,j) = 0$ at the wall and $u(i,j) = U(x_i)$ at the edge of the boundary layer. The resultant slip velocity can be expressed as a new vorticity created at the wall and of strength

$$\gamma(x_i) = U(x_i) - \sum_{n=1}^{N} \omega(i,n)\Delta y \tag{10}$$

For accelerating, constant or extremely mildly diffusing mainstream flows, this results in the creation of new positive vorticity which must be diffused over the grid during stage (iv). For stronger diffusing mainstream flows, negative wall vorticity is created which leads to reverse flow and boundary layer separation.

Blasius solution - U(x) = constant. The well known Blasius[6] solution for constant mainstream velocity is compared with the cellular method in figure (4) for the following input parameters:

$M = 10$, $N = 13$, $X_1 = 25.0$, $Y_1 = 1.0$, $\Delta x = 2.5$, $\Delta y = 0.076923$,

$\nu = 0.05$, $\Delta t = 0.05$, $U = 50.0$.

Both profile and vorticity distributions were predicted with accuracy which is remarkable bearing in mind the coarseness of the grid. As shown in Table II, displacement and momentum thicknesses and wall shear stress were all predicted extremely well over most of the plate length.

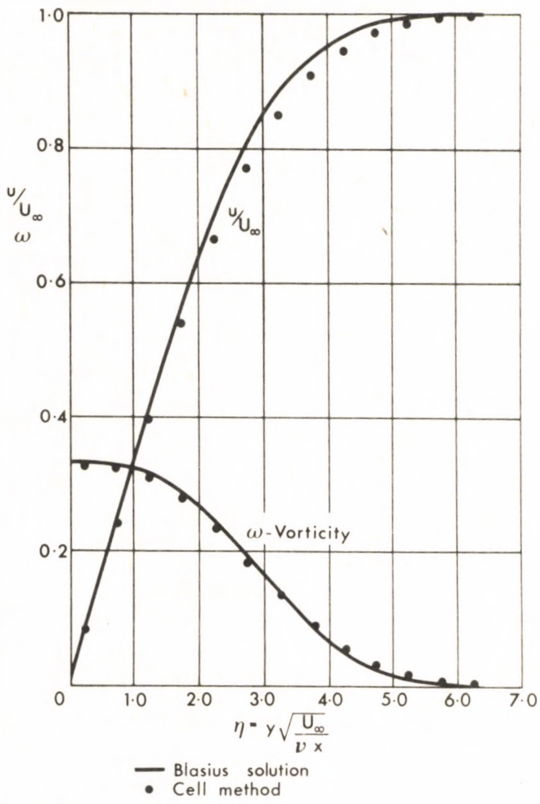

Figure 4. Flat plate Blasius boundary layer.

TABLE II

Flat Plate Boundary Layer

For $\nu = 0.05$, $U = 50.0$, $M = 10$, $N = 13$, $X_1 = 25.0$, $Y_1 = 1.0$

x	δ^*		θ		$\tau_0/\rho U^2$	
	numerical	Blasius	numerical	Blasius	numerical	Blasius
1.25	.059021	.06116	.025959	.023474	.012239	.009390
3.75	.103037	.10594	.042603	.040661	.006346	.005422
6.25	.134965	.13677	.054600	.052494	.004546	.004200
8.75	.161050	.16183	.064584	.062113	.003721	.003549
11.25	.183520	.18349	.073208	.070426	.003231	.003130
13.75	.203433	.20286	.080832	.077861	.002897	.002831
16.25	.221355	.22053	.087650	.084643	.002652	.002604
18.75	.237590	.23689	.093770	.090992	.002463	.002425
21.25	.252285	.25219	.099252	.096794	.002315	.002278
23.75	.265480	.26661	.104137	.102329	.002198	.002154

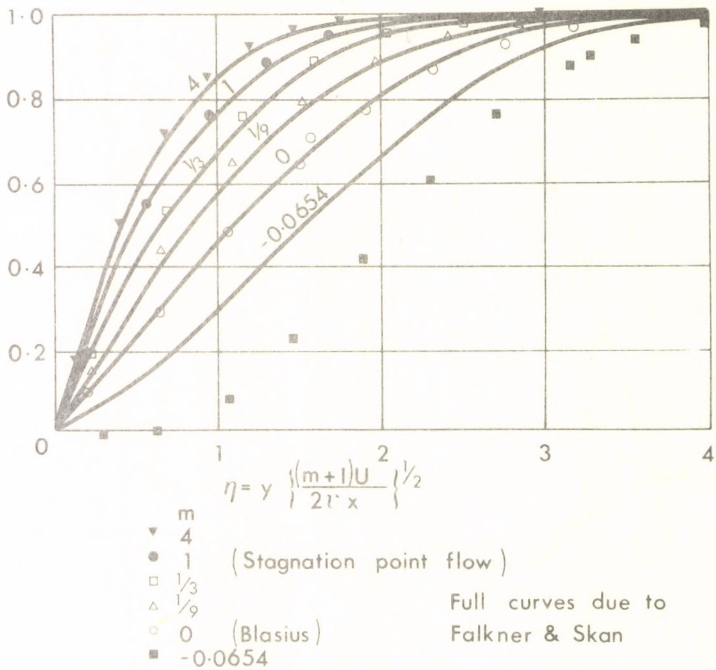

Figure 5. Similarity boundary layer solutions.

Similarity Solutions. Shown in figure (5) are comparisons with the similarity solutions of Falkner and Skan(7)-(9) derived for mainstream velocities of the form

$$U(x) = U_1(x/x_1)^m \tag{11}$$

The dimensionless velocity profiles (u/U) have a unique form when plotted versus the dimensionless coordinate $\eta=y\{(\frac{m+1}{2})(\frac{U}{\nu x})\}^{\frac{1}{2}}$ and solutions are compared here for values of m equal to 0, 1/9, 1/3, 1.0 and 4.0. Results shown here were taken from location x = 16.25 although equally reasonable predictions were obtained over the range $8.0<x<25$. Also shown in figure (6) is a prediction for mild diffusion, namely m = -0.0654. As anticipated for this case, inaccuracies due to the importance of v velocities tend to invalidate both numerical and classical theories leading to poor agreement.

Further details of this method and in particular the selection of grid dimensions, time step and diffusion matrix size for optimum computation, may be found in reference (10).

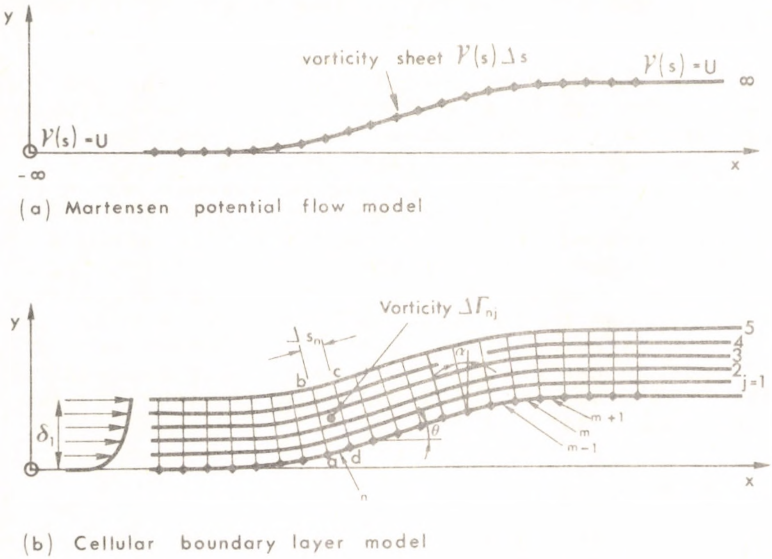

Figure 6. Shear flow past a curved wall

THICK SHEAR LAYER FLOWING PAST A CURVED WALL

Model 1

Two models for simulation of an inviscid shear flow past a sinusoidal shaped wall are illustrated in figure (6).The first model follows the standard Martensen potential flow for an infinitely thin vorticity sheet $\gamma(s)$ sandwiched between the wall and the outer irrotational flow. 20 vorticity elements were used here to simulate the wall vorticity, coupled to semi-infinite sheets of strength $\gamma(s) = U$ upstream and downstream of the curved section of the wall. The resulting pressure distribution is shown in figure (7) where C_p is defined

$$C_p = (p - p_\infty)/\tfrac{1}{2}\rho U^2 \qquad (12)$$

Model 2

An improved flow model based upon a flexible cellular grid is also depicted in figure (6), having the same number of elements M along the contour and N elements normal to the wall. This is achieved by raising normals at the element ends of initial height δ_1 equal to that of the approaching shear layer. The calculation proceeds in steps to convergence by allowing the local shear layer thickness δ to change to accommodate accelerations or decelerations of the outer flow while conserving both mass flow and vorticity. At the conclusion of a computation the cellular grid is thus aligned with the streamlines (preserving mass flow) and the vorticity ω remains constant along each streamline (preserving vorticity). The analytical and computation details are too elaborate for the present paper but are covered to some extent by references (11) and (12).

As shown in references (1),(2),(3),(11) and (12), the Martensen method can be adapted to include the influence of drifting vorticity in the outer flow. All that has been done here with the improved shear flow model is to lift the vorticity from the surface into the mainstream where it would in nature be. Martensen's method then handles the potential flow interactions of the curved wall with the uniform stream and the shear layer vorticity with little difficulty. However, unless the shear layer has a form which retains sufficient dynamic head close to the wall, a reverse flow will occur which is similar to a free surface flow and therefore inappropriate - and difficult to handle with this particular cellular grid. To avoid this the example of figure (7) was calculated for a non-separating shear layer of the form

$$\left(\frac{u}{U_1}\right) = \left(\frac{y + \varepsilon}{\delta_1 + \varepsilon}\right)^{1/7} \tag{13}$$

which is similar to a 1/7th power law profile but in this case with a velocity of 0.3U at the wall upstream of the curved section.

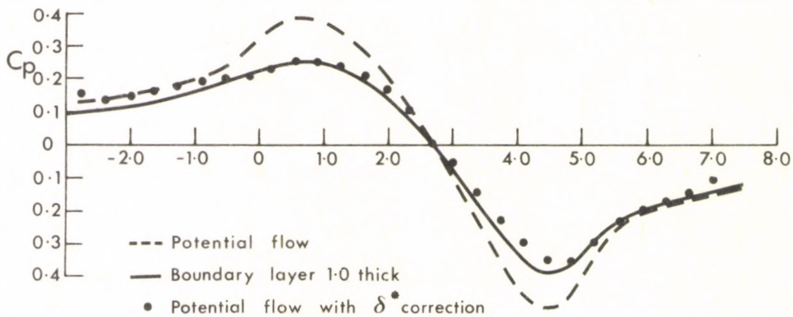

Figure 7. Predicted pressure distribution past a curved wall with a thick shear layer.

For comparison with the predicted surface pressure, a second calculation was done adopting the established practice in the aerodynamic field of computing the potential flow (model 1) past a contour adjusted in shape to include the displacement thickness (as calculated by model 2). The excellent agreement is encouraging in that the new method is confirmed by established practice and vice versa, for a shear layer that is equal in thickness to the height change of the contour.

RECOMMENDATIONS

The foundations are laid through the above studies for the development of a new numerical technique for computation of the flow of a thick viscous shear layer past two-dimensional contours of any shape. A good deal of work will be involved in bringing the above two methods together and especially in seeking means for extension of the work to turbulent flow, but a generalised method would now seem to be within reach for simultaneous boundary layer/potential flow calculations.

REFERENCES

1. LEWIS,R.I.: Surface vorticity modelling of separated flows from two-dimensional bluff bodies of arbitrary shape. Jn.Mech.Eng.Sci., Vol.23,No.1, Feb.1981.
2. PORTHOUSE,D.T.C.,LEWIS,R.I.: Simulation of viscous diffusion for extension of the surface vorticity method to boundary layer and separated flows. Jn.Mech.Eng.Sci., Vol.23,No.3, June 1981.
3. LEWIS,R.I.,PORTHOUSE,D.T.C.: A generalised numerical method for bluff body and stalling aerofoil flow. ASME Gas Turbine Conf, 1982, Paper No.82-GT-70.
4. CHORIN,A.J.: Vortex sheet approximation of boundary layers. J.Comp.Phys., 1978, 27, 428-442.
5. BATCHELOR,G.K.; An introduction to fluid dynamics. Cambridge University Press 1967.
6. BLASIUS,H.: Z.Math.Phys. 56, 1908.
7. SCHLICHTING,H.: Boundary layer theory.Pergamon Press 1955.
8. FALKNER,V.M.,SKAN,S.W.: Some approximate solutions of the boundary layer equations. Phil.Mag.12,865 (1931); ARC R.& M.No.1314, (1930).
9. HARTREE,D.: On an equation occurring in Falkner and Skan's approximate treatment of the boundary layer. Proc.Camb.Phil.Soc., 33, Part II,223, (1937).
10. LEWIS,R.I.: A cellular method for unsteady boundary layer calculations. Dept.of Mech.Eng.University of Newcastle Upon Tyne, Internal Report No.Tb.57, 1982.
11. LEWIS,R.I.: A method for calculating the flow of a boundary layer over a two-dimensional hill or contour. Dept.of Mech.Eng.,University of Newcastle Upon Tyne, Internal Report No.Tb.59, 1982.
12. LEWIS,R.I.,PORTHOUSE,D.T.C.: Recent advances in the theoretical simulation of real fluid flows.Dept.of Mech. Eng.,University of Newcastle Upon Tyne, Internal Report No.Tb.60, 1983.

AERODYNAMIC INVESTIGATIONS OF A KORT NOZZLE DUCTED PROPELLER

by

R. I. Lewis and V. Balabaskaran

SUMMARY

The performance characteristics of a Wind Tunnel operated Kort Nozzle ducted propeller have been established. Suitability of such tests for marine ducted propeller investigations has been confirmed by the comparison of these results with those obtained from the conventional open water tests. Measured duct surface pressure distributions for a wide range of advance coefficients have been presented. The validity of axisymmetric Surface Vorticity Theory for the analysis of marine ducted propellers has been established by comparing the predicted results with the above measured test values.

INTRODUCTION

Kort Nozzle ducted propellers have been used for many years in tug boats and trawlers and more recently their effectiveness in improving the propulsive performance of large supertankers and bulk carriers has been successfully demonstrated (1). In the last ten years a number of non-linear theoretical methods have been published for the analysis of a complete ducted propeller system in zero incidence flow (2, 3, 4). However published experimental data on marine ducted propellers are generally scarce. In particular, little information is available on the measured pressure distributions over the duct surfaces at different operating points of the ducted propeller. The lack of experimental data in this area creates difficulties for the validation of theoretical developments for ducted propeller performance prediction.

Experimental investigations of marine ducted propellers are generally carried out in towing tanks or cavitation tunnels which require expensive capital investments and high operating costs. Moreover measurement of duct surface pressure distributions in these test rigs is more difficult. On the contrary experimental research on wind tunnel operated ducted propeller models offers greater flexibility and scope. Wind tunnel tests are less expensive and allow easy and direct access to more detailed flow studies with reduced power input.

This paper presents the results obtained from such experimental studies conducted on the Newcastle (UK) wind tunnel model of a Kort Nozzle ducted propeller. The suitability of aerodynamic tests for marine ducted propellers is discussed by comparing these tests with the published open water test results. The duct surface pressure distributions for different advance coefficients have been predicted using a recently published theoretical method based on surface vorticity distribution and actuator disc theories. These predicted values are compared with the measured values from the present aerodynamic tests and the validity of the above theoretical method for the analysis of Kort Nozzle ducted propellers is established.

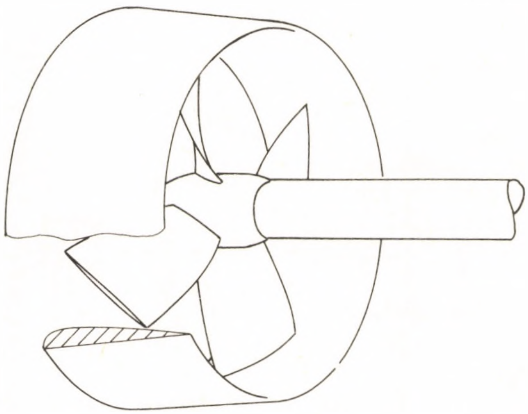

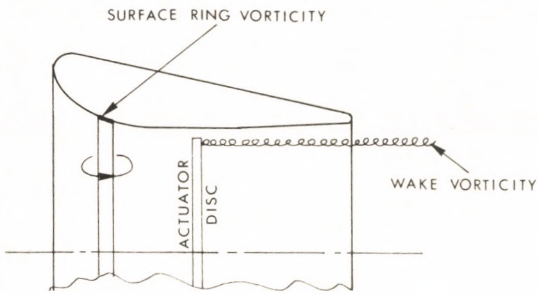

Figure 1. Ducted propeller and fluid dynamic model.

THEORETICAL METHOD

The Gibson-Lewis (4) fluid dynamic model (Fig.1) has been adopted for the present theoretical analysis. The duct and centre-body are modelled by continuous distribution of ring vorticity $\gamma(s)$ and the propeller is represented by a constant load actuator disc. The helical vortex sheets leaving the propeller blades are thus replaced by circumferentially spread helical vorticity of same total strength. With the application of the Dirichlet boundary condition to the interior surfaces of the duct and centre-body, the problem reduces to the solution of the following Fredholm Integral equation of the second kind,

$$-\frac{\gamma(s_m)}{2} + \oint \gamma(s_n) K_{m,n} ds_n + W_\infty x'_m + (V_{wx} x'_m + V_{wy} y'_m) = 0 \qquad (1)$$

where $K_{m,n}$ is a coupling coefficient which relates the strength of the ring vorticity at n to its induced velocity at m. V_{wx} and V_{wy} are axial and radial components of the propeller induced velocity V_w.

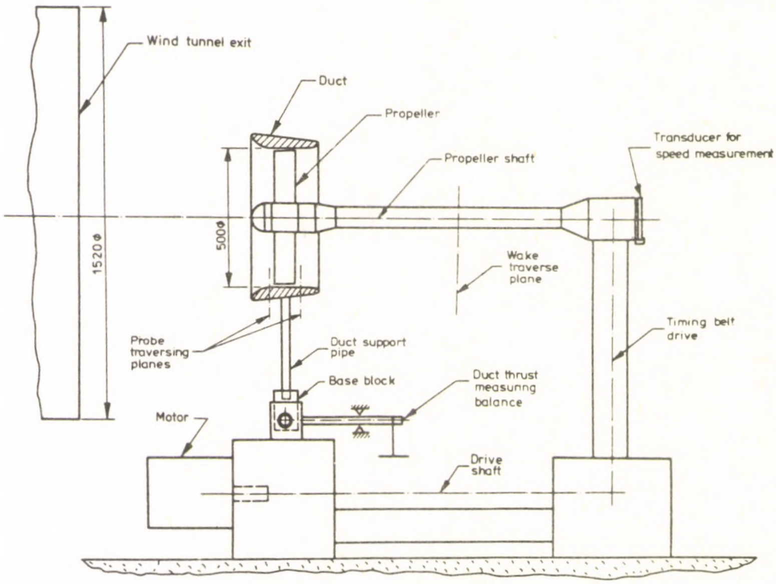

Fig.2. Test stand

EXPERIMENTS

Experimental investigations were carried out using the 5 ft. open jet wind tunnel facility available at the University of Newcastle Upon Tyne. The test stand (Fig.2) consists of an NSMB Ka 4.55 propeller operating within a 19A duct. Thirty two surface pressure tappings were provided at suitable locations around the duct profile. The total thrust of the system was determined by wake velocity surveys behind the duct. The forward duct thrust was measured directly by balancing the duct to its neutral position. The propeller thrust was thus calculated as a difference between total and duct thrusts. The experiments were carried out at a constant propeller speed of 2000 rpm and the duct surface pressure distributions were measured by suitable electronic micromanometers. Different velocities of advance were obtained by varying the wind tunnel velocity. More details about the test rig and instrumentation are reported in reference 5.

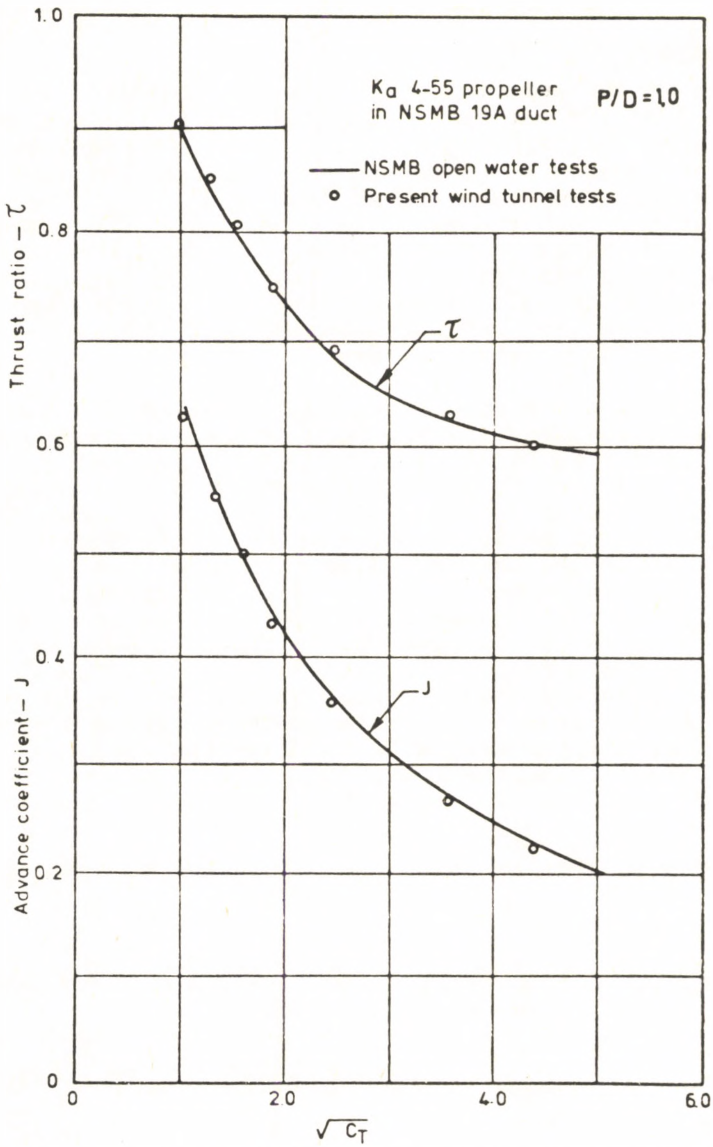

Fig.3. Comparison of open water and wind tunnel test results.

DISCUSSION OF RESULTS

The measured performance characteristics of the present aerodynamic model of the Kort Nozzle ducted propeller has been presented in Fig.3. The relationship between total thrust, thrust ratio and velocity of advance has been presented in the form of two non-dimensional characteristic curves

$$\tau = f_1\ (C_T) \tag{2}$$

$$J = f_2\ (C_T, \tau) \tag{3}$$

The above characteristics are compared with the results derived from the published open water test results of the Netherlands Ship Model Basin (6). The comparison shows an excellent agreement between the wind tunnel and open water test results. The results given in Fig.3 are for the design pitch ratio 1.0 of the propeller. The above experiments were repeated for two more pitch ratios and the agreement between open water and wind tunnel results in these cases too have been uniformly good. These studies thus confirm the suitability of the less expensive aerodynamic tests for marine ducted propeller investigations.

The pressure distributions on the inner and outer surfaces of the duct for a number of advance coefficients have been presented in Figs.4,5 and 6. These measured values are also compared with the computed pressure distributions obtained on the application of a computer program DUCTPROP (5) developed on the basis of the theoretical method described earlier. With the actuator disc representation of the propeller one would expect a steep predicted pressure rise at the propeller plane. However by suitably increasing the numerical tip clearance employed in the computer program more gradual pressure rise can be obtained as shown in these figures. It may be observed that generally good agreement is then obtained between the inviscid theory and experiment. Duct thrust coefficients were obtained from the predicted pressure distributions using the expression

$$K_{Td} = \frac{\pi J^2}{D^2} \oint r_n\ C_{pn}\ dr_n \tag{4}$$

The predicted duct thrusts have been compared with the directly measured duct thrusts in Table I.

Table I

Comparison of predicted and measured duct thrusts
(Wind Tunnel Model)

S.No.	J	C_T	K_{Td} (Predicted)	K_{Td} (Measured)
(1)	0.224	19.289	0.1332	0.1500
(2)	0.265	12.998	0.1198	0.1310
(3)	0.312	8.758	0.1074	0.1080
(4)	0.360	6.133	0.0903	0.0950
(5)	0.433	3.684	0.0689	0.0680
(6)	0.499	2.474	0.0552	0.0470
(7)	0.551	1.844	0.0457	0.0320

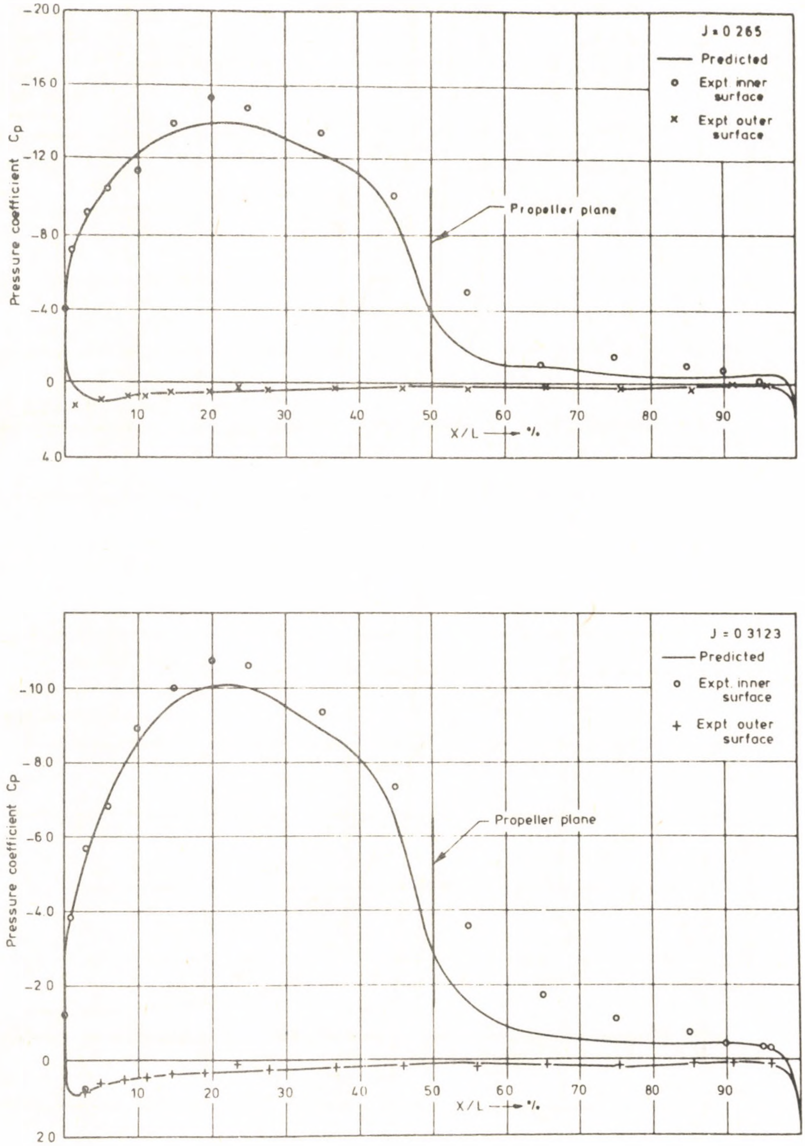

Figure 4. Pressure distribution over NSMB 19A duct.

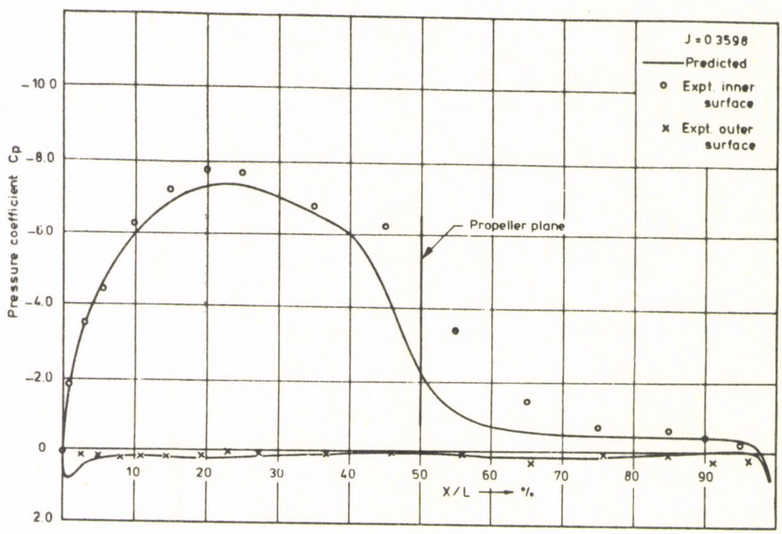

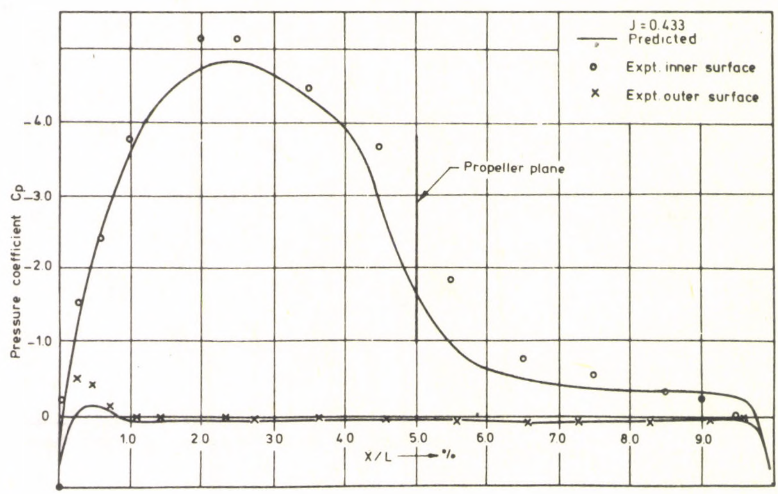

Figure 5. Pressure distribution over NSMB 19A duct.

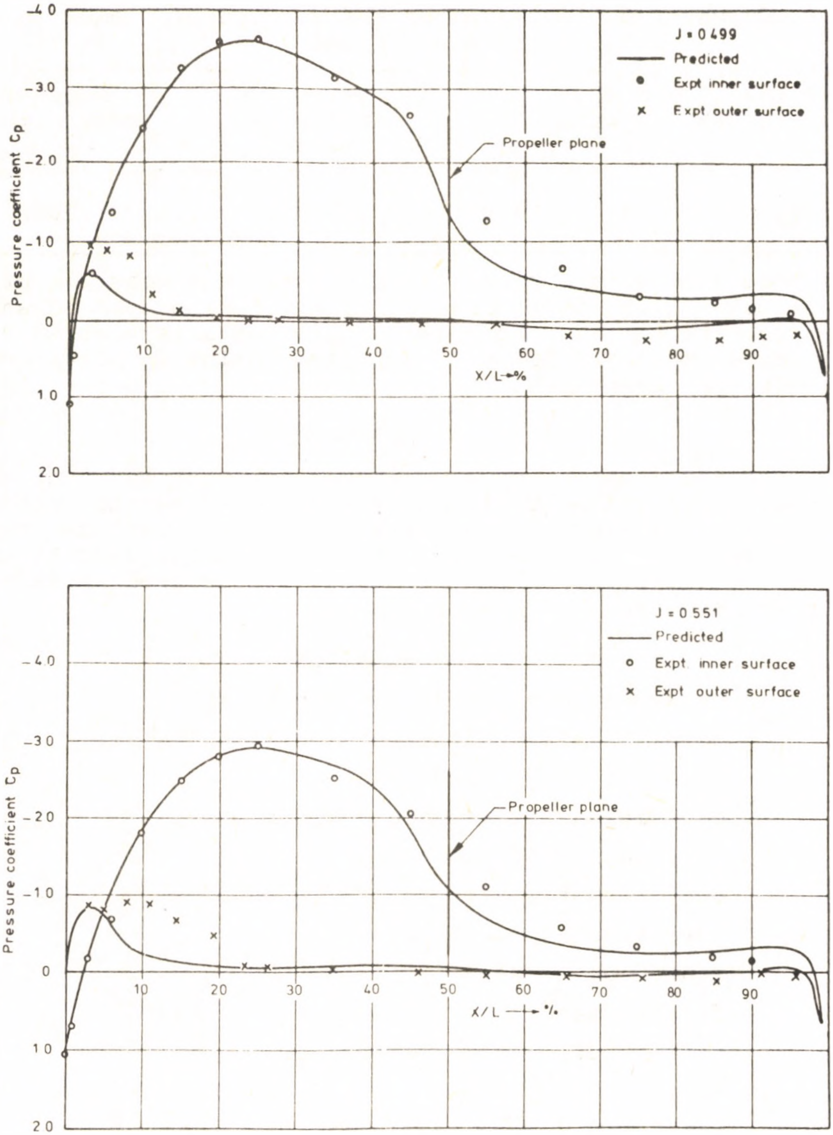

Figure 6. Pressure distribution over NSMB 19A duct.

Table II compares the presently predicted and measured duct thrusts with the published open water test results.

TABLE II

Comparison of open water and wind tunnel model (Measured duct thrusts)

Duct Thrust Coefficient	NSMB open water tests	Present aerodynamic tests	Present prediction
K_{Td}	0.0652	0.0680	0.0689

The good agreement between the predicted and measured pressure distributions and duct thrusts for a wide range of advance coefficients confirm the acceptability of axisymmetric surface vorticity modelling for the duct flow, using an actuator disc to model the propeller.

CONCLUSIONS

For the results reported it can be concluded that aerodynamic tests can be confidently applied to marine ducted propeller investigations and that non-linear surface vorticity theory for the duct combined with the actuator disc theory for the propeller produces results which are in good agreement with the experimental results.

NOMENCLATURE

C_p	pressure coefficient $= (p - p_\infty)/\frac{1}{2}\rho W_\infty^2$
C_T	total thrust coefficient $= T/(\frac{1}{2}\rho V_a^2 \pi D^2/4)$
D	diameter of the propeller
J	coefficient of advance $= V_a/nD$
$K_{m,n}$	coupling coefficient
K_{Td}	duct thrust coefficient $= T_d/\rho n^2 D^4$
n	rotational speed in r.p.s.
p	static pressure
p_∞	free stream static pressure
P/D	pitch, ratio of the propeller
r	radius
T, T_d	total and duct thrust
V_a	velocity of advance
W_∞	free stream velocity
$\gamma(s)$	vortex strength per unit length of perimeter
τ	thrust ratio = propeller thrust/total thrust

REFERENCES

1. ANDERSON,O.,TANI,M.: Experience with S.S.Golar Michu. R.I.N.A.Symp.on Ducted Propellers,Paper No.12, London (1973).

2. WEETMAN,R.J.,CROMACK,D.E.: Calculation of Inlet Flows by means of a closed Vorticity Distribution applied to Ducted Propellers. Report No.UM-71-11, School of Engineering,University of Massachussets,Amherst, U.S.A. (1972).

3. RYAN,P.G.,GLOVER,E.J.: A Ducted Propeller Design Method: A New Approach using Surface Vorticity Distribution Techniques and Lifting Line Theory. Trans.RINA, Vol.144 (1972).

4. GIBSON,I.S.,LEWIS,R.I.: Ducted Propeller Analysis by Surface Vorticity and Actuator Disc Theory. RINA Symp. on Ducted Propellers, Paper No.1, (1973).

5. BALABASKARAN,V.: Aerodynamic Investigations of a Ducted Propeller. Ph.D.Thesis, Dept.of Mech.Eng.Indian Institute of Technology, Madras, India (July 1982).

6. OOSTERVELD,M.W.C.: Wake adapted Ducted Propeller. Publication No.345, Netherlands Ship Model Basin, Wageningen (June 1970).

ON THE SEPARATION BUBBLE OVER BLUNT THIN BLADES

E. Litvai

SUMMARY

The k^2/ε turbulence model for the case of the assymmetric flow around blunt flat plates with sharp and trimmed edges respectively is solved numerically, using Schwartz-Cristoffel type transformation. Experimental results are presented and compared.

INTRODUCTION

One of the unresolved problems in the turbomachinery is the predection of the separation and reattachement on blunt sheat metal blades. The related phenomenon on aerofoils seems to be more throughly investigated /see e.g. the literature in [1] , and the effectiveness of Navier-Stokes and B.L. type solutions respectively are compared [2] , [3] .
For blunt wedges the symmetric laminar case /Fig. 1.a./ has been treated theoretically [4] and the turbulent case experimentally [5] . From the point of view of the turbomachinery the assymmetric case i.e. the flow with an angle of attack . around the sharp edge or a trimmed blunt edge /Fig. 1.b. and c./ is of importance, the symmetric one beeing the exceptional operating condition.

In both cases the separation bubble may be transitional since the separating laminar flow generally is hydrodinamically unstable.
It is clear, that boundary layer-type solutions - which may be helpfull in the somewhat "smoother" case of aerofoils - will be less effective in the predection of separating bubbles on blunt blades.

On the following pages the author proposes a method of predection, which assumes potential flow to the calculation of the boundary conditions far from the blade only, the flow itself being deseribed by the k^2/ε turbulence model [6] , i.e. by the transport equations of the vorticity, of the turbulence kinetic energy, and of the dissipation respec-

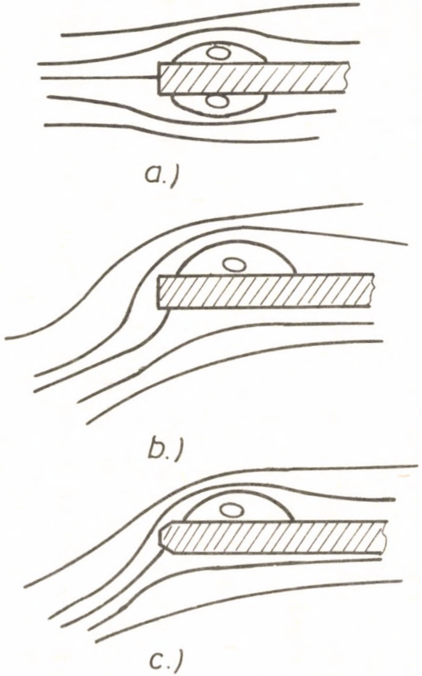

FIG. 1

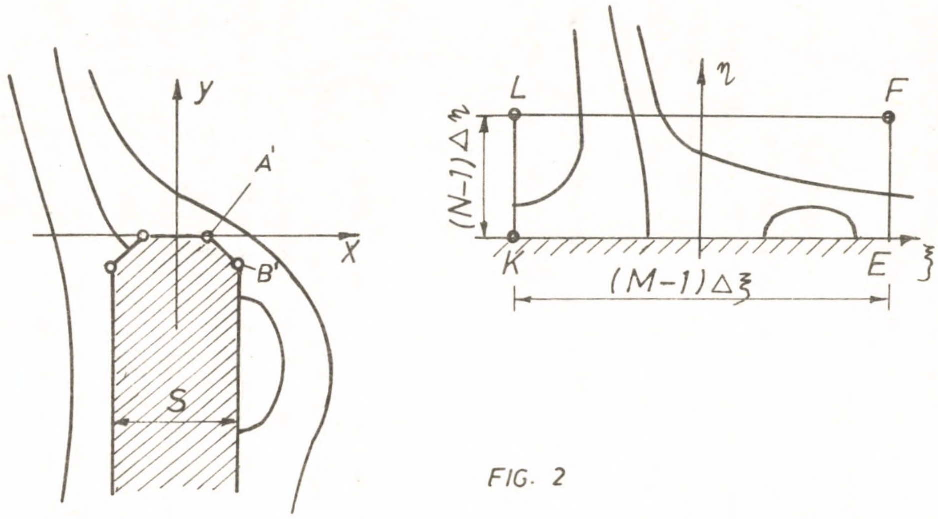

FIG. 2

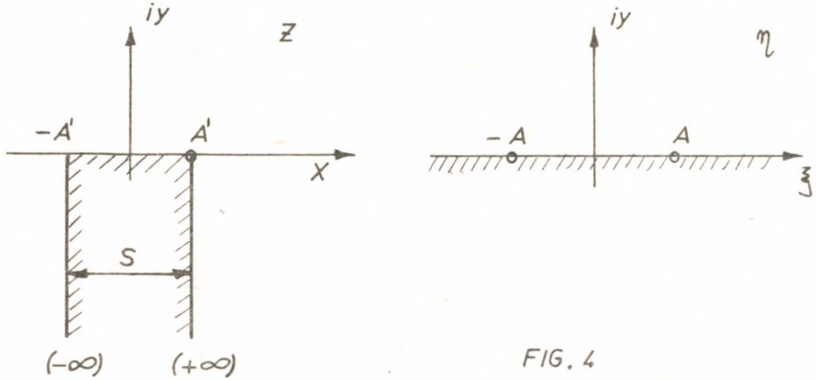

FIG. 4

tively, and by Poissons equation. The effect of the viscous sublayer will be taken into consideration by the formulas published recently by Kuei Yuan Chien [7] .

To solve the above equations the numerical method of finite differences has been used in a transformed system of coordinates ξ , η rather than in that of the original coordinates x, y /Fig.2./ the transformation beeing of Schwartz-Cristoffel type according to the cases shown in Fig. 1.b. and 1.c. respectively.

So, the field of the numerical solution characterised by the points E, K, L and F /Fig. 2./ is a rectangular one independently of the blade shape.

IDEAL FLOW BOUNDARY VALUES

Let us restrict ourselves to the case of a single flat blade and assume, that the distance E F /Fig.2./ is long enough for the flow along the line L F be identical with the ideal flow characterized by zero viscosity and zero vorticity. So the values of the stream function $\psi/\xi,\eta/$ along L F can be calculated by complex potentials and conformal mapping. Really by assumming, that the thickness S of the blade /Fig. 2./ is negligibly small as compared to its length in the y direction, the series of conformal mappings, shown in Fig. 3. transforms the potential flow on the plane of the complex variable $\zeta = \xi + iy$ into the flow around a circle of the radius equal to unity on the plane $z_2 = x_2 + iy_2$ and vice versa. The blade replaced by an infinitely thin flat plate is represented on the plane z_0. The complex potential w of the flow on the plane z_2 is

$$w = v_\infty /z_2 e^{-i\alpha} + e^{i\alpha} /z_2/ + i\varepsilon\Gamma/2\pi \ln z_2 \qquad /1/$$

with the usual value of the circulation Γ

$$\Gamma = 4\pi v_\infty \sin\alpha \qquad /2/$$

and with the coefficient ε allowing for different values of Γ too.

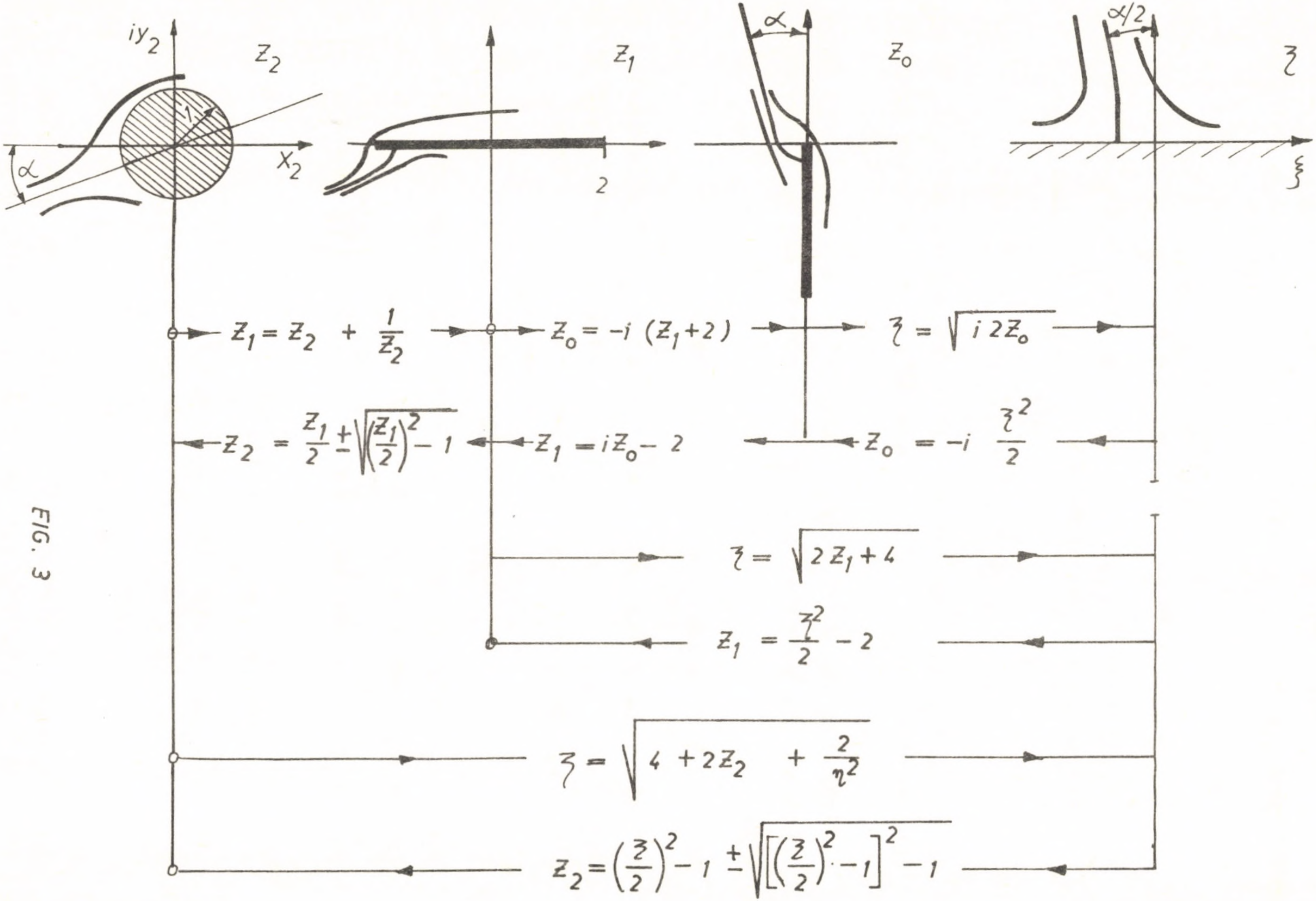
iy_2
Z_2
X_2
α
1
Z_1
2
α
Z_0
$\alpha/2$
ζ
ξ
$Z_1 = Z_2 + \frac{1}{Z_2}$
$Z_0 = -i\,(Z_1 + 2)$
$\zeta = \sqrt{i\,2Z_0}$
$Z_2 = \frac{Z_1}{2} \pm \sqrt{\left(\frac{Z_1}{2}\right)^2 - 1}$
$Z_1 = iZ_0 - 2$
$Z_0 = -i\,\frac{\zeta^2}{2}$
$\zeta = \sqrt{2Z_1 + 4}$
$Z_1 = \frac{\zeta^2}{2} - 2$
$\zeta = \sqrt{4 + 2Z_2 + \frac{2}{\eta^2}}$
$Z_2 = \left(\frac{\zeta}{2}\right)^2 - 1 \pm \sqrt{\left[\left(\frac{\zeta}{2}\right)^2 - 1\right]^2 - 1}$

FIG. 3

So we get for the stream function as

$$\psi/x_2,y_2/ = v_\infty\left[\varepsilon \ln\left(x_2^2 + y_2^2\right) + x_2\left(\frac{1}{x_2^2 + y_2^2} - 1\right)\right]\sin\alpha +$$

$$+ v_\infty\left(1 - \frac{1}{x_2^2 + y_2^2}\right) y_2 \cos\alpha \qquad /3/$$

By substituting the complex vectors $\zeta = \xi + i\eta$ of the line L F /Fig.2./ into the formula

$$z_2 = \left(\frac{\xi}{2}\right)^2 - 1 \pm \sqrt{\left[\left(\frac{\xi}{2}\right)^2 - 1\right]^2 - 1} \qquad /4/$$

taken from Fig.3. we can select those values of $z_2 = x_2 + iy_2$, for which abs$/z_2/ - 1$, and then $\psi/\xi,\eta/$ follows from Eq /3/.

Starting values for the relaxation proceedure have been taken on the same way in the node points of the numerical mesh.

CONFORMAL MAPPING OF THE BLADE CONTOURS

It can be easily seen, that in order to transform the real axis ξ of Fig.4. into the curve $/-\infty/$, $-A'$, A', $/+\infty/$ on the plane z, the appropriate formula must have the form

$$\frac{dz}{d\xi} = -i\sqrt{\xi^2 - A^2} \qquad /5/$$

where A is a real number corresponding to the edge A'. Eq /5/ can be integratéd in closed form giving

$$z = -i\left[\frac{A + /\xi - A/}{2}\sqrt{\xi^2 - A^2} - A^2 \ln\left(\sqrt{\xi - A} + \sqrt{\xi + A}\right)\right] +$$

$$+ \frac{A^2}{2}\left[\frac{\pi}{2} - i \ln\left(2A\right)\right] \qquad /6/$$

for the sharp-edged blade contour.

By substituting $z = A$ and $z = -A$ respectively, we get

$$S = \frac{\pi}{2} A^2 \qquad /7/$$

for the thickness of the blade, and for the selection of the value of A. Fig.5. gives the ξ = const. and η = const.curves

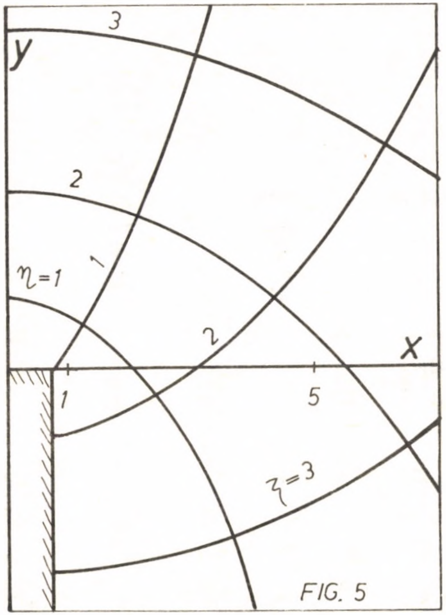

FIG. 5

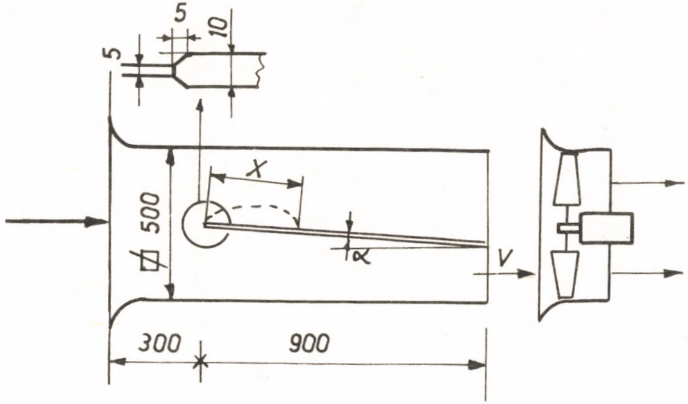

FIG. 6.

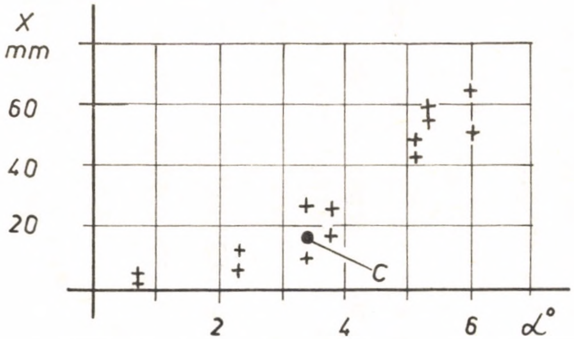

FIG. 7

on the x, y plane, the value of A being unity.
It is interesting to note, that for A = 0, Eq /5/ gives $dz/d\xi = -i\xi$, or integrated, $z = -i\xi^2/2$ in agreement to the formula $z_0 = -i\xi^2/2$ in Fig.3.

For the trimmed blade contour, shown in the Fig.2., the appropriate mapping formula is

$$\frac{dz}{d\xi} = -i\sqrt[4]{\xi^2-B^2} \cdot \sqrt[4]{\xi^2-A^2} \qquad /8/$$

where now a second real number B arises corresponding to the two abrupt changes of the contour.

Since the author did not suceed in integrating Eq /8/ in closed form numerical treatment was necessary.

TRANSFORMATION OF THE SYSTEM OF EQUATIONS

The transformed equations for the determination of the flow are

$$\frac{1}{h^2}\frac{D\omega}{Dt} = (\nu+\nu_t)\left(\frac{\partial^2\omega}{\partial\xi^2}+\frac{\partial^2\omega}{\partial\eta^2}\right) \qquad /9/$$

$$\frac{1}{h^2}\frac{Dk}{Dt} = (\nu+\nu_t)\left(\frac{\partial^2 k}{\partial\xi^2}+\frac{\partial^2 k}{\partial\eta^2}\right) + P_t - \varepsilon - \frac{2\nu k}{\eta^2} \qquad /1o/$$

$$\frac{1}{h^2}\frac{D\varepsilon}{Dt} = \left(\nu+\frac{\nu_t}{1.3}\right)\left(\frac{\partial^2\varepsilon}{\partial\xi^2}+\frac{\partial^2\varepsilon}{\partial\eta^2}\right) + 1.35\frac{\varepsilon}{k}P_t - \frac{\varepsilon}{k}D_1+D_2 \qquad /11/$$

where according to Kuei Yuan Chien [7]

$$D_1 = 1.83 \cdot \varepsilon\left(1-o.22\exp(-k^2/6\nu\varepsilon)^2\right) \qquad /12/$$

$$D_2 = 2\nu k \exp\left(-o,5\eta\sqrt{\tau_o/\varrho/\nu}\right)/\eta^2 \qquad /13/$$

and

$$\nu_t = o.o9\, k^2/\varepsilon\left(1-\exp\left(-o.o115\eta\sqrt{\tau_o/\varrho}/\nu\right)\right) \qquad /14/$$

and finally

$$\frac{\partial^2\psi}{\partial\xi^2}+\frac{\partial^2\psi}{\partial\eta^2} = -\omega h^2 \qquad /15/$$

with

$$h = |\, dz/d\mathfrak{z}\,| \qquad /16/$$

defined by /5/ and /8/ respectively and

$$P_t = \nu_t \left[4\,(\partial^2\psi/\partial\xi/\partial\eta)^2 + (|\,\partial^2\psi/\partial\xi^2| + \right.$$
$$\left. + |\,\partial^2\psi/\partial\eta^2|)^2 \right] / h^2 \qquad /17/$$

Initial conditions were $k = k_o$: the turbulence kinetic energy corresponding to the outer degree of turbulence and $\varepsilon = (k_o)^{3/2}/\eta$. These values served as boundary conditions along L F /Fig.2./. Along the wall /η=0/ k = 0 and ε = 0 have been taken [7]. Along the lines E F and L K boundary condition of second kind /linearly varying values in ξ direction/ were assumed.

The weighted upstream method as described by Rheinländer [8] was used to resolve the above system of equations.

EXPERIMENTS

The setup shown in Fig.6. served to measure the length x of the separation bubble at different angles of attack α, the flat plate having a trimmed blunt edge. The reattachment point was determined by injection of smoke. Results are shown in Fig.7. The scatter is caused by the relatively low flow velocity /v = 1 ÷ 3 m/s/ and the high degree of turbulence /2 ÷ 15 %/ respectively. The result of a preliminary computer run is also indicated by C.

LITERATURE

[1] Pletcher, R.H.: Prediction of Incompressible Turbulent Separating Flow. J. Fluids Eng. /1978/ <u>1oo</u>. 427-433.

[2] Briley, W.R. - McDonald, H.: Numerical Prediction of Incompressible Separation Bubbles. J. Fluid Mech. /1975/ <u>69</u>. 631-656.

[3] Crimi, P. - Reeves, B.L.: Analysis of Leading-Edge Separation Bubbles on Airfoils. AIAA Journal /1976/ <u>14.</u> 1548-1555.

[4] Ghia,V. - Davis,R.T.: Navier-Stokes Solution for Flow Past a Class of Two-Dimensional Semi-Infinite Bodies. AIAA Journal /1974/ 12. 1659-1665.

[5] Ota, T. - Itasaka, M.: A Separated and Reattached Flow on a Blunt Flat Plate. J. Fluids Eng. /1976/ 98. 79-86.

[6] Launder, B.E. - Spalding, D.B.: The Numerical Computation of Turbulent Flow. Computer Methods Appl. Mech. Eng. /1974/ 3. 269-289.

[7] Kuei Yuan Chien: Predictions of Channel and Boundary Layer Flows with a Low-Reynolds-Number Turbulence Model. AIAA Journal /1982/ 20. 33-38.

[8] Rheinländer,J.: Numerische Berechnung von vorwiegend durch die Schwerkraft angetriebenen Raumströmungen. Fortschr.-Ber. VDI Z. 7. 60 /1981/

SYMBOLS NOT INTERPRETED IN THE TEXT

k	kinetic energy of turbulence
t	time
ε	dissipation
ν	laminar viscosity
ω	$\partial v_\eta/\partial\xi - \partial v_\xi/\partial\eta$
ψ	stream function
ρ	density
τ_0	wall shear stress

LITVAI ELEMÉR, Dr. techn.
Reader
Techn. Univ. Budapest
H-1521 Budapest

REGULATION OF IMPELLER PUMPS BY MEANS OF PREROTATION INDUCED WITH A BY-PASS JET

A.Łojek

SUMMARY

The report presents the conception of prerotational - by-pass jet regulation by means of liquid swirl before its inlet into the impeller with simultaneous driving the part of liquid from delivery pipe into the suction side of a pump. An arrangement giving the possibility of utilizing a by-pass jet energy for liquid prerotation inducing has been described. There are presented the results of tests and observations of performance parameters, of cavitation phenomenon, of liquid flow in the suction region and vibrations of the diagonal pump /n_{sQ}=102/ controlled by this arrangement. The efficiency and "quality" of the prerotation - by-pass jet device operation have been compared with other known methods of pumps regulation. The application possibilities of prerotational - by-pass jet regulation of highspeed impeller pumps have been estimated.

INTRODUCTION

The prerotation control, which consists in alterations of the liquid swirl by means of the guide vanes placed before the pump impeller, can be improved by suitable design of the prerotational guide wheel /selection of proper dimensions, shape and number of vanes and the distance of the inlet guide vanes from the impeller/ to ensure it most effective adaptation to the pump type and anticipated operational conditions.

It seems to be expedient to search such "suplementary means" for the prerotational control system which could extend the range of pump regulation with small power losses and good cavitation properties by possibly most simple guide vanes construction, and searching the methods of prerotation inducing others than by prerotational guide wheel too.

In this paper there have been presented the effects of arrangement tests in which a prerotation has been induced by-pass jet.

PREROTATIONAL - BY-PASS JET DEVICE

It is the spiral casing /Fig.1/ fixed to the pump suction nozzle and connected to the delivery pipe /Fig.2/ by the by-pass piping provided with a control gate valve. The by-pass jet fed to the spiral casing flows from it by eight slots perpendicular and tangential to the main stream out. Regulation of the pump is effected by driving the part of liquid from the delivery piping to the suction side with simultaneous forcing the alterations of the liquid swirl before the impeller. The presented device is much simpler than a prerotational guide wheel; the prerotational guide vanes are "replaced" by the by-pass jet and control is arranged by opening or closing the gate valve in the by-pass piping.

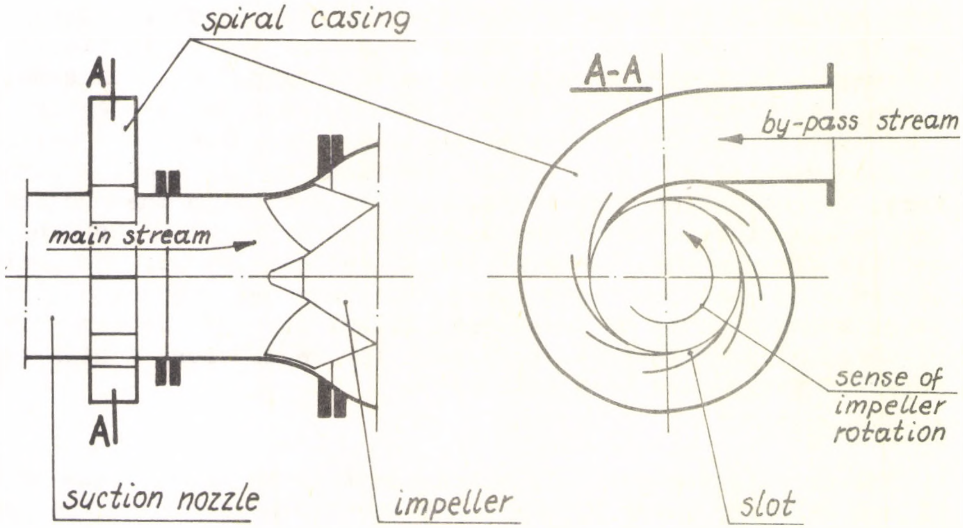

Fig.1 Prerotational - by-pass jet device

The device has been fitted in the diagonal pump of impeller dia D =314 mm and specific speed n_{sQ}=102. The tests had been performed by the Institute of Fluid-Flow Machinery of Polish Academy of Sciences at the test stand for hydraulic machines testing /Fig.2/.

RESULTS OF TESTS

The parameters of pump operation were successively altered by increasing the liquid flow rate from full closing to full opening of the gate valves in the delivery piping. The suction pressure during tests was not kept stable and dropped suitably to growth of the flow rate.

The head/discharge curve H=f/Q/ of the diagonal pump, shown in Fig.3, can be divided in a stipulated way into three zones.

The head/discharge curve in zone III, at flow rates from 0 to ca. 0.4 Q_n/Q_n- flow rate at maximum efficiency/ visibly breaks. The alterations of the velocity components of flow, shown in Fig.4, indicate that strong free prerotation forced by the impeller takes place in the suction side and backflows appear.

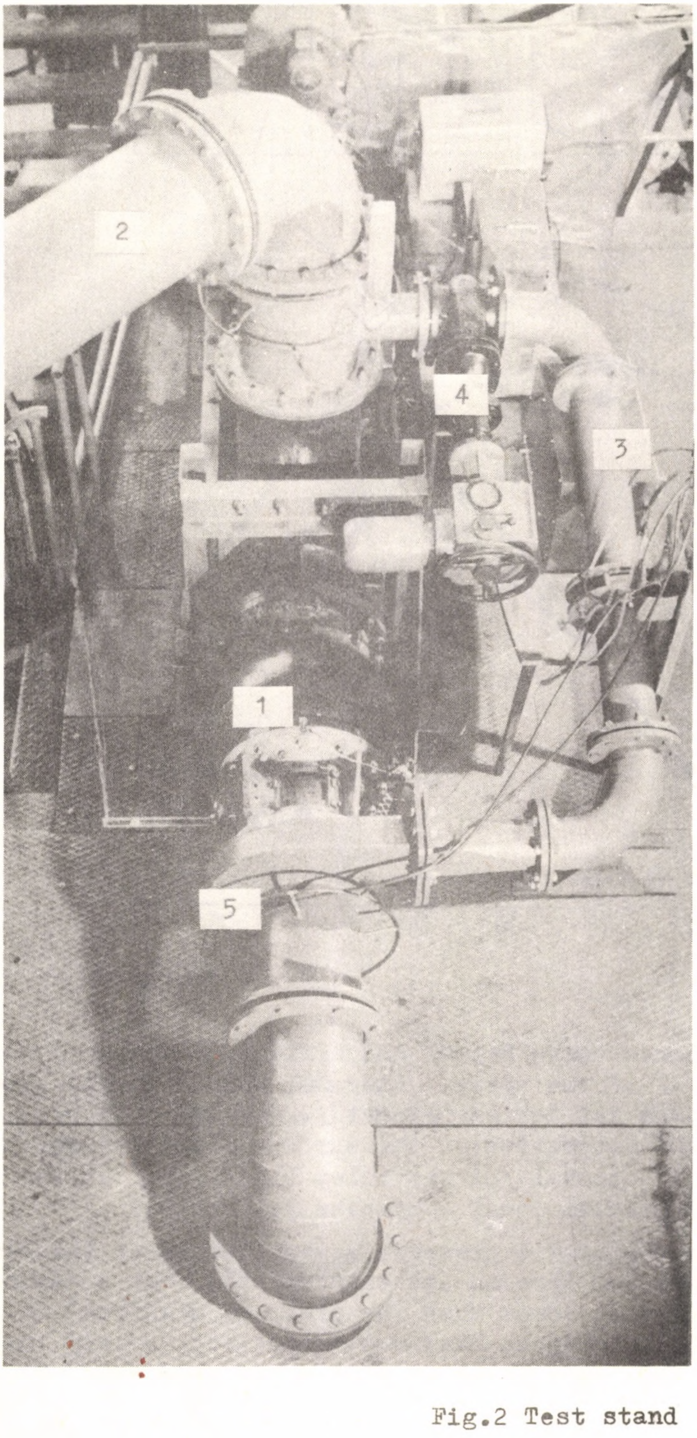

1 diagonal pump
2 delivery piping
3 by-pass piping
4 control gate valve
5 prerotational - by-pass jet device

Fig.2 Test stand

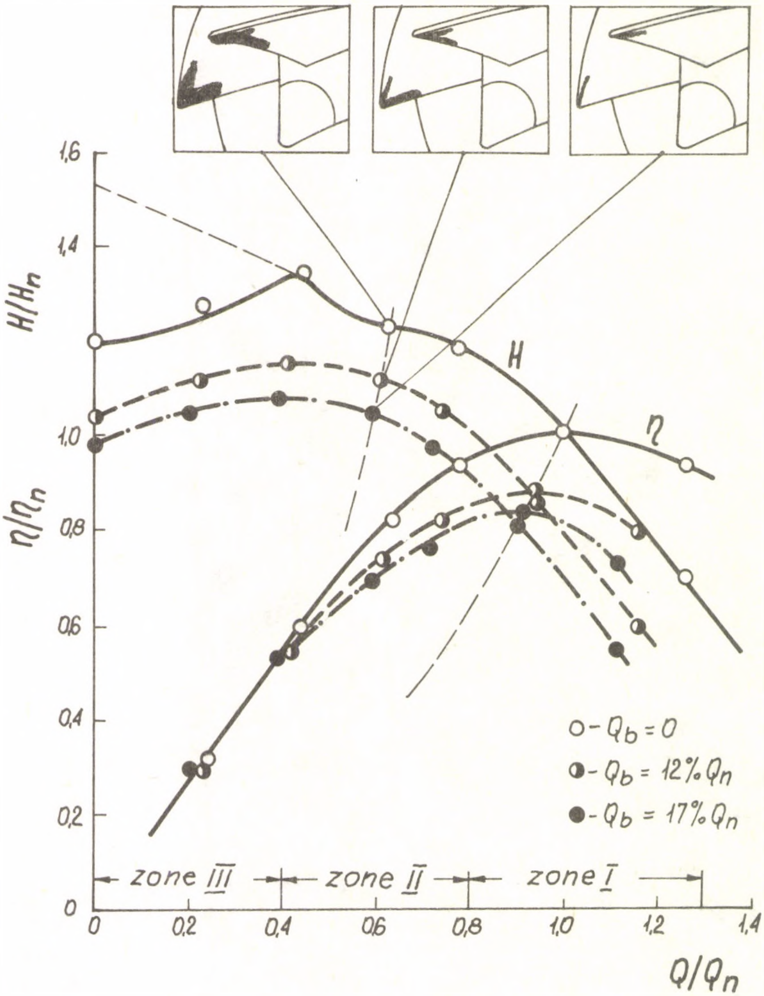

Fig.3 Head/discharge curve H=f/Q/ and efficiency characteristics η =f/Q/ of the system: diagonal pump - prerotational - by-pass jet device without /Q_b=0/ and with by-pass jet and alteration of the surface cloud /on the vane/ and rotational /on the inlet blade edge/ as the results of prerotational - by-pass jet control

In these conditions the static pressure against walls of the suction pipe is much greater than in its axis and the mean pressure in the measure section is lower than the pressure measured 1/ in the suction pipe circumference. The pump efficiency is very low. The pump works unstably especially at flow rates near zero. No cavitation occurs.

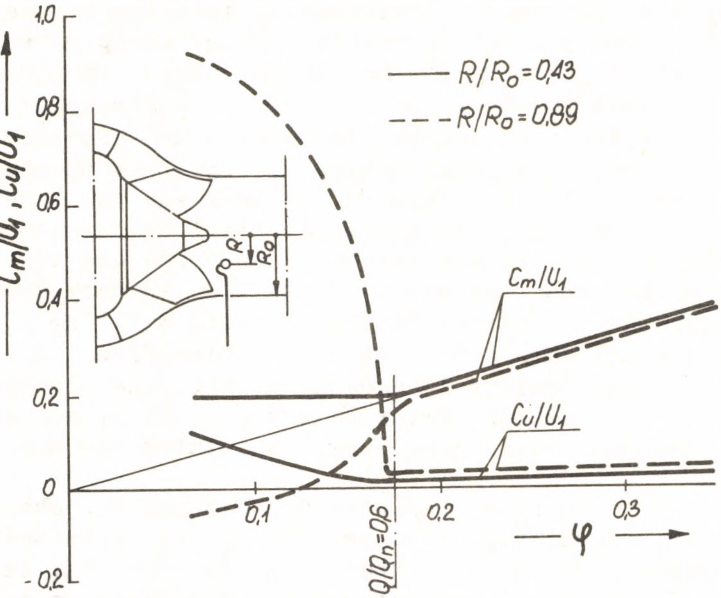

Fig.4 Alterations of meridian /C_m/ and circumferential /C_u/ components of the flow velocity as the result of changes of the flow rate through the pump caused by throttling the flow with the valve on discharge piping;
φ - capacity coefficient,
U_1 - peripheral velocity of blades edges on inlet.

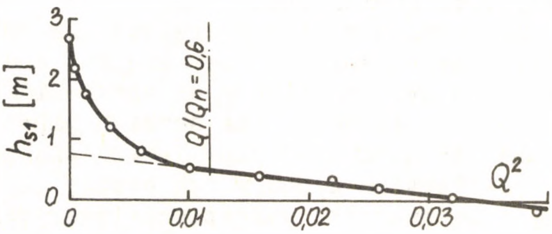

Fig.5 Pressure in the suction region as function of the capacity: $h_{s1} = f/Q^2/$

1/ Assuming that the drop of pressure at growth of flow rate in a given measure section is proportional to the increase of Q^2 /Fig.5/, the measured value of pressure h_{s1} /the measure section before spiral casing/ should be corrected, and the course of the head/discharge curve in zone III after correction should be such as it has been drawn in Fig.3 with thin broken line.

Feed of by-pass jet causes considerable lowering of the total head at small alteration of the capacity /very steep pipe-line characteristics/. Efficiency of the system changes insignificantly. The by-pass jet fed in accordance with the direction of free positive prerotation, changes velocities and pressure distributions. The circumferential motion of liquid at the suction pipe wall is braked. The pressure on the wall and the range of the back flow are reduced. The circumferential component of velocity and the pressure in the middle of the pipe are increasing. The pressure pulsations indicate that the flow is very chaotic being the result of two stream mixing - strong whirling of main stream /free prerotation/ and by-pass jet which flows to it tangentially and perpendiculary in accordance with the direction of rotation of the main stream. Nevertheless the vibrations are decreasing and the pump works more easy. Cavitation was not observed.

The curve $H=f/Q/$ in zone II $/Q=0.4\div0.8\ Q_n/$ has the characteristic deepening for highspeed pumps. Strong free prerotation begins to develop at capacites lower than $Q/Q_n=0.6$ what is seen in Figs 4 and 5. The meridional components distribution of flow velocities and static pressures at $Q/Q_n>0.6$ in the suction pipe section is rather uniform and prerotation of the liquid is low. However, in these conditions very high pressure pulsations and vibrations of the pump housing take place /Fig.6/. Moreover, small cavitation cloud on the impeller blades has been observed. Though the pump efficiency reaches the values about maximum, the pump operation in this zone is unsatisfying because of intense vibrations and possible danger of cavitation.

The by-pass jet fed to the suction region increases the swirl before the impeller /similarly as in zone I - see Fig.8a/ and causes the "compression" of main stream /growth of the meridional component in the middle and its lowering at the suction pipe wall/. The static pressure in the middle of pipe lowers and by the wall alters little. The cavitation cloud which occurs in these conditions is very small. The pressure pulsations lower very visibly /ca. 40%/ and accordingly vibrations /Fig.6/. The efficiency of the system lowers more and more at increasing flow rates of both the by-pass jet and the main stream.

The pump reaches the highest efficiency in zone I $/Q=0.8\div1.3Q_n/$. Free prerotation takes place also in this zone. The distribution of meridional velocities and static pressures in the cross section of suction pipe is rather uniform. The flow separation and cavitation were not observed. The pressure pulsations are smaller than in zones II and III and the pump vibrations get lower with the increase of the pump capacity.

The by-pass jet increases the prerotation /see Fig.8a/ and causes lowering of the suction pressure. It has been stated that the cavitation cloud does not appear in the impeller region. The pressure pulsations and vibrations become lower, however power losses increase and efficiency of the system visibly decreases.

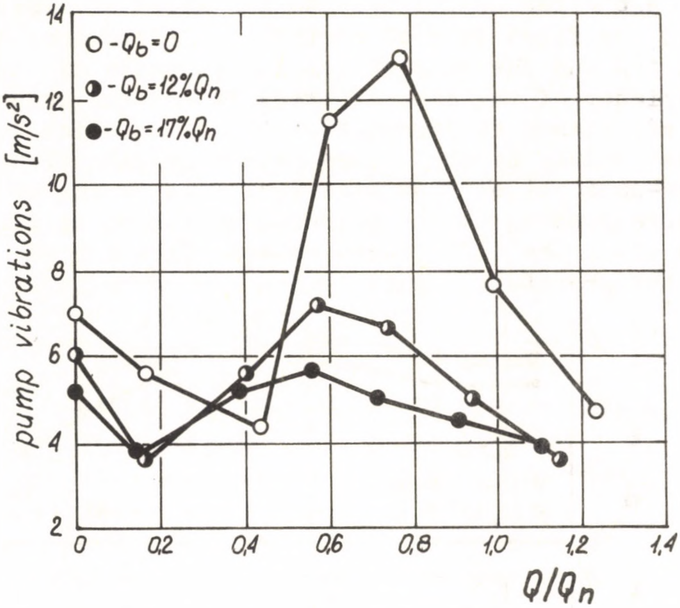

Fig.6 Vertical vibrations of the pump housing without /Q_b=0/ and with by-pass jet

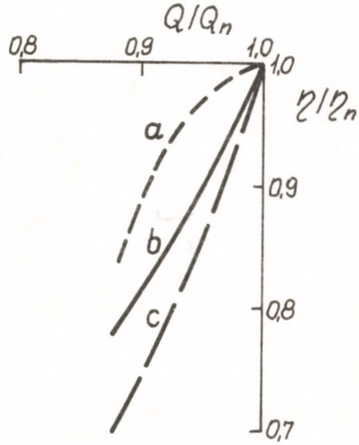

Fig.7 Efficiency of the system: pump - control arrangement during prerotational control /a/, prerotational - by-pass jet control /b/ and by-pass regulation /c/

Regulation of the pump by the prerotation induced with by-pass jet is less effective /taking into account efficiency of the whole system/ than that forced by the guide vanes /Fig.7/. For example: If there occurs the necessity for the ΔQ=10% alteration of capacity in a pump - control arrangement system with the uniform pipe-line characteristics, the by-pass jet in the prerotational - by-pass jet device should be equal Q_b=17% Q_n and the blade angle of the prerotation guide wheel α= +40°/the positive prerotation accordingly to the sense of impeller rotation/. At the first type of control the efficiency of system lowers ca. 12% and the pump efficiency 2% while at the second one the efficiency of the system lowers 7% and the pump efficiency 5%. The efficiency of prerotational - by-pass jet regulation is determined mainly by the losses in the by-pass flow.

The by-pass jet of flow rate Q_b=17% Q_n causes small prerotation, corresponding to the prerotation forced by guide vanes at angle α= +10°. The differences between flow forced by the by-pass jet and the prerotation guide vanes are shown in Fig.8.

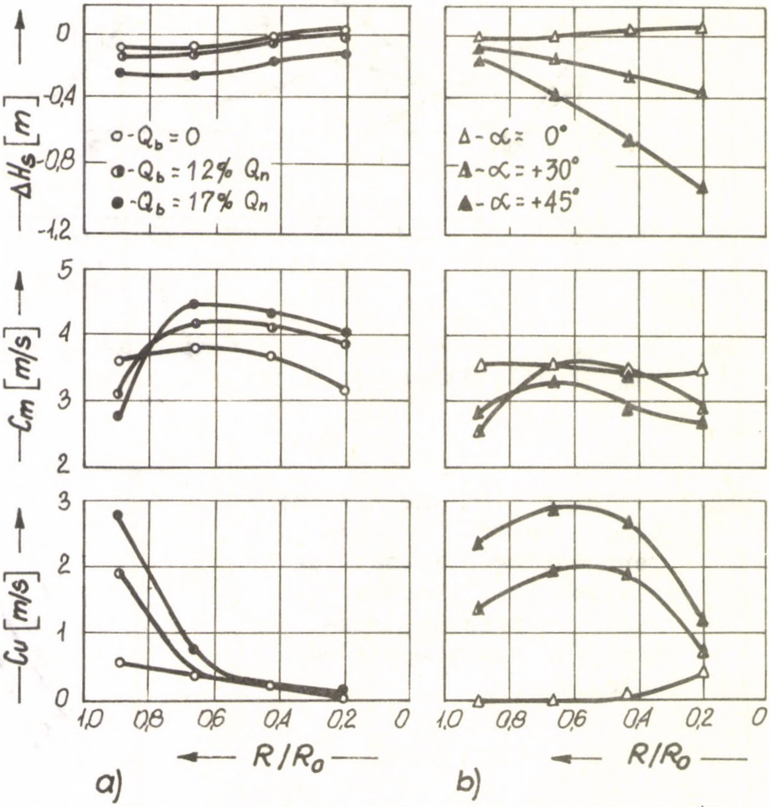

Fig.8 Alterations of flow velocities and pressures /ΔH_s-pressure differences between measure point on the suction pipe circumference and in the flow/ in the regions of pump suction as the result of prerotation forced by:
a/ by-pass jet,
b/ guide vanes.

It must be emphasized that by the same parameters of the system /uniform pipe-line characteristics/ the pump works at different operating conditions[2]. They are more adventageous for the pump, which can be seen in higher pump efficiency /see the example above/ by prerotational - by-pass jet regulation.

The tests of cavitation carried out at stable flow rate through the pump do not indicate significant differences of cavitation cloud in the impeller. But the structure of liquid as well as vibrations and noise accompanying cavitation were different. The "hard"[3] cavitation caused by the by-pass jet has been changed into "soft"[4] one but performance effects of cavitation with regard to the flow of free prerotation or prerotation forced by by-pass jet were similar /the head difference seen in Fig.9 is caused by regulation/. By forcing the positive prerotation with guide vanes /Fig.10, $\alpha = +30°$/, the worsening of cavitation properties was not observed. However, the pressure differences in the flow at increasing blade angle of prerotation guide wheel become visibly greater /Fig.8/ and one had to expect worsening of the cavitational properties of the pump in wide range of regulation, similarly as at negative prerotation /Fig.10, $\alpha = -30°$/.

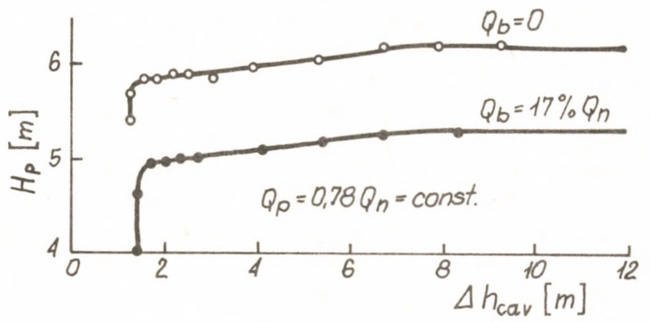

Fig.9 Cavitation characteristics of pumps:
Q_b=0 - flow with free prerotation,
Q_b=17% Q_n- flow with prerotation forced by by-pass jet.

2/ The flow rate through the pump during prerotational control is equal to the system capacity while at prerotational - by-pass jet control with the system capacity the flow rate through the pump is different being the sum of the system capacity and flow rate in the by-pass piping.

3/ Fine air bubbles were in the water; "dry" clicks and intensive vibrations accompanied the cavitation.

4/ Larger air bubbles were in the water. It can be supposed that water supplied with the by-pass jet was self aerated. The vibrations became visibly smaller and "clicks" were much weaker.

Fig.10 Net positive suction head suited to the break of head/discharge curve of pump:

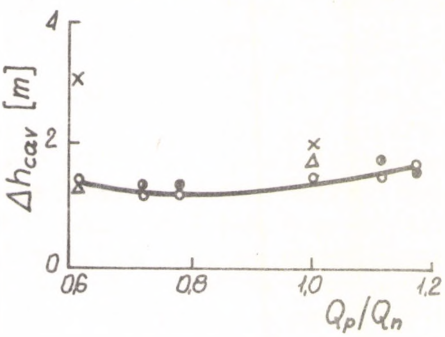

o - $Q_b=0$, flow with free prerotation,

◐ - $Q_b=12\%\ Q_n$ and

● - $Q_b=17\%\ Q_n$, flow with positive prerotation forced with by-pass jet,

Δ - $\alpha = +30°$, flow with positive prerotation forced by guide vanes,

x - $\alpha = -30°$, flow with negative prerotation forced by guide vanes.

The positive prerotation caused as well by the by-pass jet as by the vanes of a prerotation guide wheel cause lowering of the pump vibrations while at the throttling the pump vibrations increase.

SUMMARY

Generally, the prerotational - by-pass jet device adventageously affects the pump operation and the accompanied phenomenon. It is especially adventageous at "partial loading" of the pump, i.e. when the pump has to work for a long time in zone II /placed near the nominal one/ where the most intense vibrations and pressure pulsations occur and also cavitation can take place, while the changes of the pump operation conditions by means of the prerotational - by-pass jet device should adventageously affect its durability and reliability. The device described above is very effective in operation /e.g. the by-pass jet $Q_b=21\%\ Q_n$ gives the same effects as prerotational control with the guide vanes $\alpha = 0...+45°$ or by-pass flow $Q_b=33\%\ Q_n$ at by-pass regulation/. However the efficiency of the pump provided with prerot.-by-pass jet device /efficiency of the system/ has been proved lower than with the prerotational guide vanes. But the prerotational - by-pass jet control is surely more effective than by-pass and throttling controls. Great advantage of this arrangement is its very simple construction and principle of operation. When then not efficiency of the system but the conditions of pump operation and reliability of the arrangement operation should decide about selection of a regulation system, so the application of the prerotational - by-pass jet device in place of prerotational guide vanes can be acknowledged as most effective.

ŁOJEK, Andrzej M.Sc.Eng.
Institute of Fluid-Flow Machinery Pol.Ac.Sci.
80-952 Gdańsk, ul.Fiszera 14
POLAND

SOME DETAILS OF FLOW IN THE END WALL REGION OF AEROFOIL CASCADES WITH TIP CLEARANCES

Krzysztof Majka and S.Soundranayagam

Introduction

Flow conditions in the tip clearance region can have a dominating effect on the performance of axial compressors and blowers and that influence can be felt deep into the annulus and is not confined to the tip region alone. Methods of calculating the annulus wall boundary layer have been developed [1][2] and are of use in estimating flow blockage effects and the variation of machine efficiency. The successful application and further development of these calculation methods need information about the variation of blade force in the boundary layer and its modification by the presence of tip clearance etc. Experimental investigations in rotating rigs [3][4] and stationary cascades [5] have been carried out to obtain qualitative estimates of these effects. This paper discusses some results of a detailed study of tip clearance flows in a large scale cascade of compressor blades [6].

Experimental Details

The experiments were conducted in a low speed cascade wind tunnel of test section 300 mm x 750 mm. The cascade blade were of 10c430c50 profile having circular arc mean lines of 30^{o}camber. They had a chord of 300 mm and were placed at a stagger of 36^{o}at a space to chord ratio of 0.633. The central blade was equipped with a large number of pressure taps to enable the chord wise pressure distribution to be measured at a series of stations along the span placed particularly close in the tip region. The cascade had an arrangement by which the tip clearance could be varied. The side wall opposite to the blade tips was also equipped with static pressure taps on the surface to measure the wall pressure distribution. Flow visualisation tests were carried out with a surface film technique and also using dye traces in a water flow rig. Velocities were measured using pitot and hot wire probes. Wall shear stresses were measured using hot film gauges and Preston tubes. All the tests were run at a Reynolds number of 6.8×10^5 based on inlet velocity and chord.

Experimental results

Visualisation tests in water showed a complex flow pattern. Fig.1 is a sketch based on photographs of the pattern of dye traces introduced upstream of the blades with no tip clearance. The upstream traces were actually touching the end wall. The flow separates well upstream of the blade leading edges leaving a clear horseshoe shaped region where the surface flow does not penetrate. The upstream surface flow is swept on to a fairly narrow portion of the blade suction surface where it rolls up into a vortex having the same sense as the conventional passage secondary flow. Small dye crystals introduced in regions B and A showed that the flow immediately next to the wall went over the horse shoe shaped "separation" line and attached itself to the clear regions A and B and flowed in a generally forward direction and being swept on to the suction surface to join the vortex in the suction surface corner. These streamlines are shown dotten in region C.

When the dye traces were introduced about 2 mm above the wall surface, the streamlines approached the blade leading edges closely. Just upstream of the leading edges they coiled downwards to form leading edge vortices that wrapped themselves around the individual leading edges. The suction side leg touches the suction surface of the blade and merges with the strong rolled up vortex already there. The sense of the leading edge vortex on the suction side is opposite to that of the existing rolled up vortex in the suction side corner. The pressure side leg of the leading

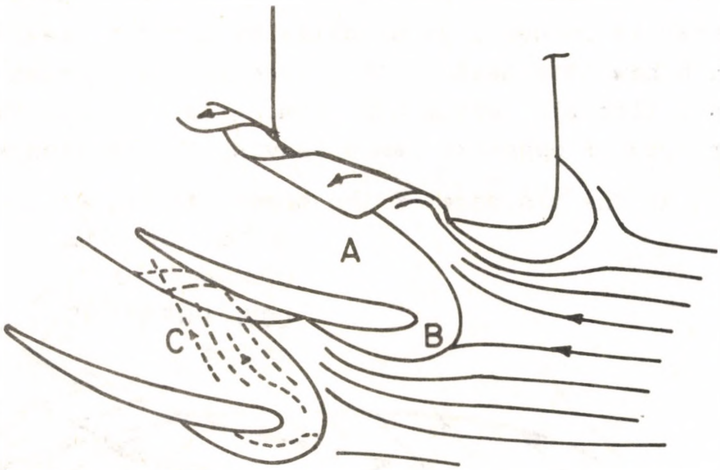

Fig.1. Flow pattern at end wall.

edge vortex has the same sense of the passage rolled up vortex and is swept a little away from the blade pressure surface. The entire flow pattern is dominated by the strong rolled up vortex in the suction surface corner. A very narrow region of reverse flow is present immediately next to the nose of the blades associated with the curling up of the leading edge vortex.

When tip clearance is increased the horse shoe shaped separation region is much reduced with the demarcation line approaching the blade leading edges. The separation line is also blurred and diffused by the higher speed flow streaming towards the clearance gap. Instead of the pattern shown by the dotten lines of Fig.1 the wall streamlines nearer the pressure surface in region C now flow under the blade and emerge at the suction side. There is a strong flow through the tip clearance from the pressure side to the suction side which rolls up immediately on emerging at the suction side corner to form a strong vortex in the opposite sense to the existing rolled up passage vortex already there. The passage vortex is pushed away slightly by the tip clearance vortex which now sits next to the blade in the suction surface corner The entire flow pattern is dominated by these two rolled up vortices of opposite sense leaving the suction surface corner.

At the tip edge of the blade itself, Fig.2, the flow

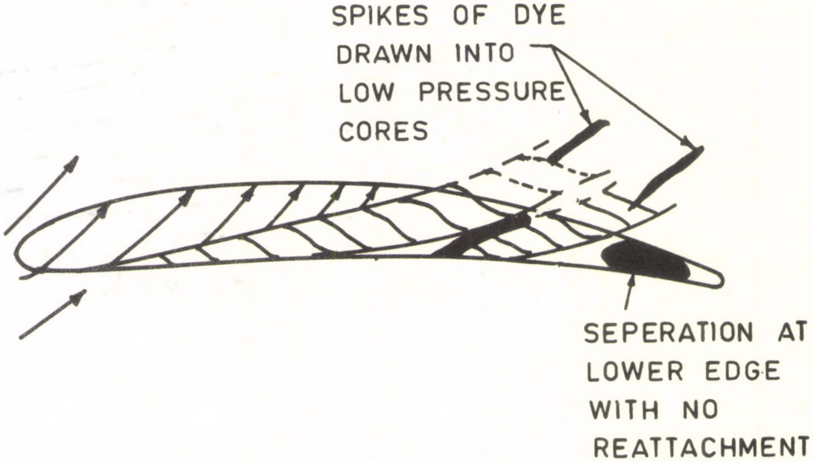

Fig.2.Rope-like seperation bubbles at blade edge.

separates at the sharp pressure surface edge to form a rope like separation bubble that rolls up as a vortex. The vortex is swept towards the suction surface near the trailing edge. As it is swept from the blade tip another separation bubble immediately forms and is rolled up and swept away towards the suction surface. The sense of rotation of these two rope like vortices is the same as that of the clearance vortex. In the water flow experiments dye from the main stream was sucked into the low pressure cores of the two ropes as they emerged at the suction side corner forming two clear distinct spikes. These low pressure regions are associated with a movement of the blade suction peaks towards the trailing edge near the tips.

CONTOUR No	1	2	3	4	5	6	7	8	9	10	11	12	13	14	15
$C_{P_{st}}$	-1·2	-1·1	-1·0	-0·9	-0·8	-0·7	-0·6	-0·5	-0·15	-0·4	-0·3	-0·2	-0·1	-0·05	-0·00

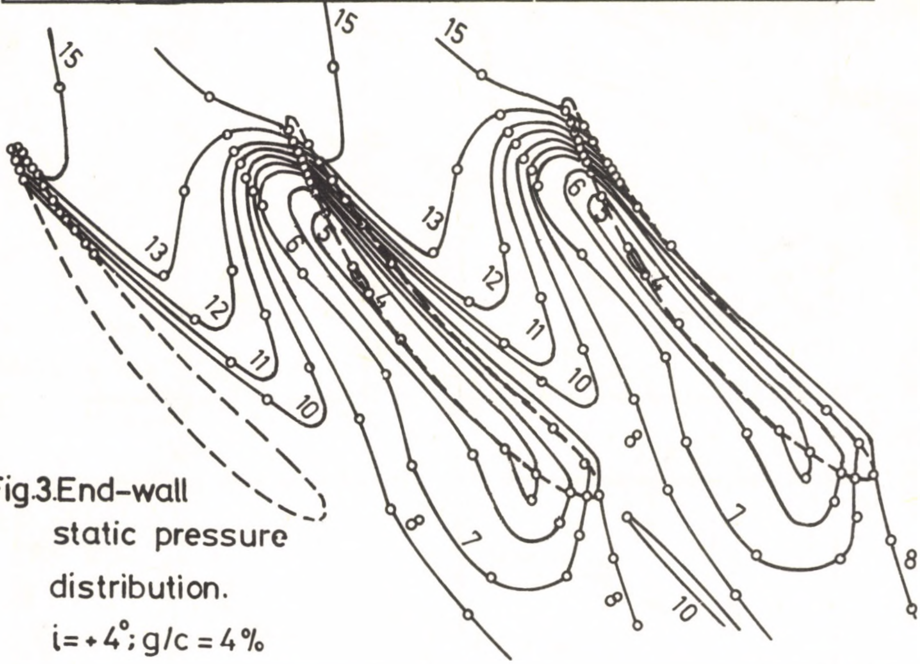

Fig.3.End-wall static pressure distribution.
$i = +4^{\circ}$; $g/c = 4\%$

CONTOUR No	1	2	3	4	5	6	7	8	9	10	11	12	13	14	15
$C_{P_{st}}$	-1·2	-1·1	-1·0	-0·9	-0·8	-0·7	-0·6	-0·5	-0·45	-0·40	-0·3	-0·2	-0·1	-0·05	-0·00

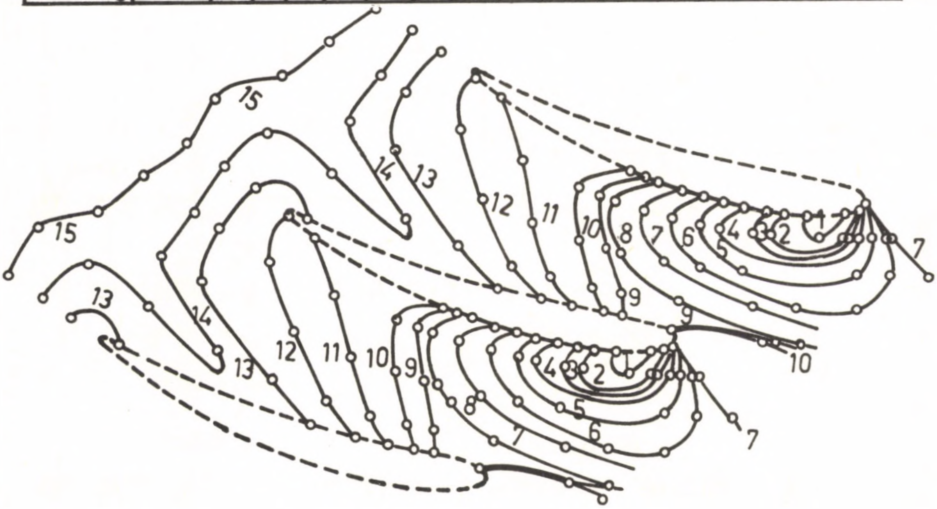

Fig.4.End-wall static pressure distribution $i = +4^{\circ}$; $g/c = 0\%$

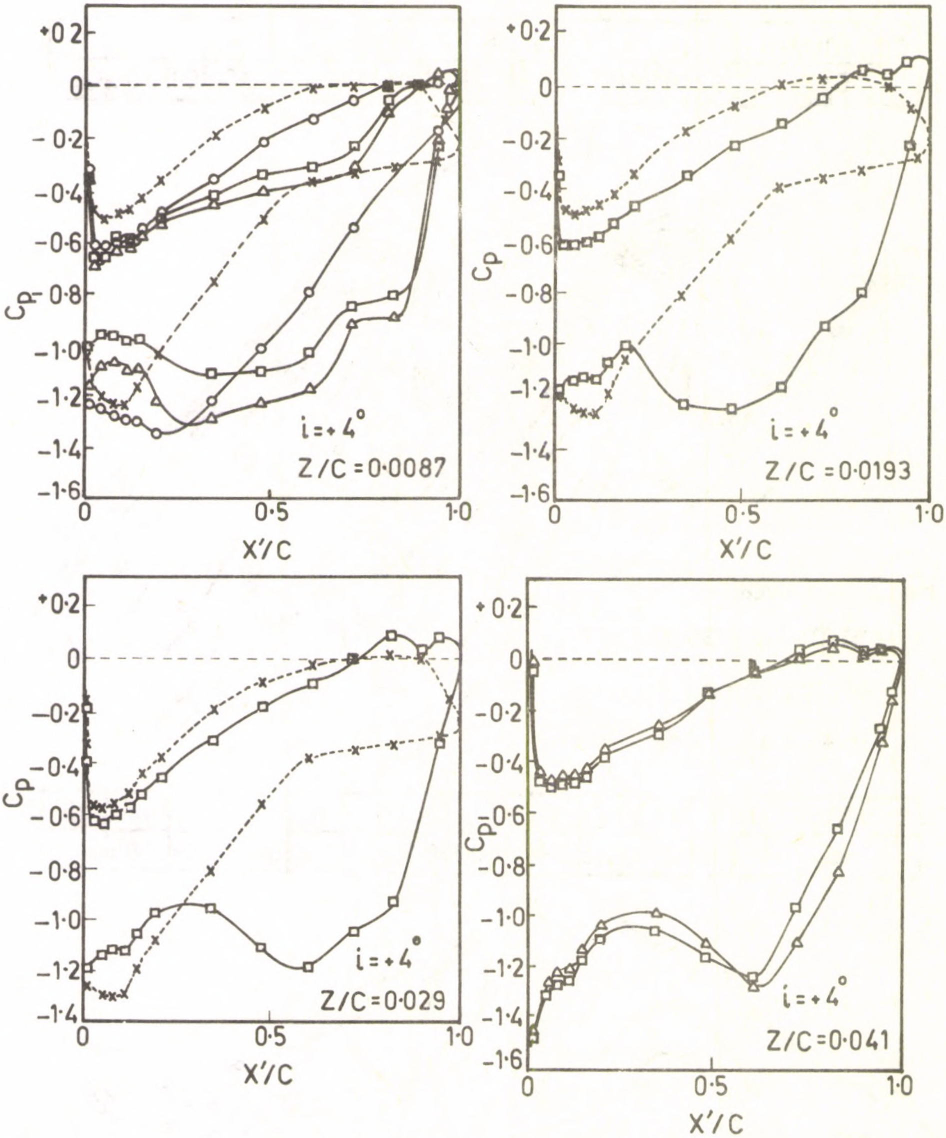

X–X–X TIP CLEARANCE g/c = 0 %

O–O–O " " g/c = 2 %

□–□–□ " " g/c = 4 %

△–△–△ " " g/c = 5 %

Fig. 5. Blade pressure distribution in the tip region.

In the casing boundary layer calculating methods it is assumed that the blade lift falls to zero at the tip. The present experimental results clearly show that this is not so. The blade lift is retained across the gap. This is clearly seen in Figures 3 and 4 for the case of zero tip clearance and for a gap of 4 percent chord. The existence of the gap changes the shape of the static pressure contours with the low pressure regions being pushed towards the trailing edge. The vortex action in the tip region has a pronounced effect on the blade pressure distribution. Not only is the blade lift non zero at the tip but it rises above the value at centre span. Fig.5 shows the blade pressure distribution at a few spanwise positions very near the tip for various clearance gaps. When there is no clearance gap the suction peak is near the leading edge and there is separation on the suction surface from about 60 percent chord. The effect of tip clearance is to push the suction peak towards the trailing edge and completely eliminate the separation on the suction surface. The effect is a big rise in the area of the pressure distribution curve indicating an increase in the blade lift.

The lift distribution along the span was obtained by integrating the pressure distributions. In the absence of tip clearance the lift falls steadily from about 30 percent span from the wall to a value at the wall of about 50 percent of mid span lift. When there is tip clearance the lift variation along the span is much more uniform with about a 10 percent increase in lift near the tip compared to centre span. The lift retained at the wall is of the order of 40 percent that at centre span and is influenced by the size of the tip gap. The lift variation can be integrated to obtain blade force defect coefficients that are needed for the annulus boundary layer calculation methods. With no tip clearance though there is a decrease in blade lift towards the tip the direction of the blade force vector hardly changes along the span. With the introduction of tip clearance the blade force vector rotates backwards towards the blade trailing edge but the

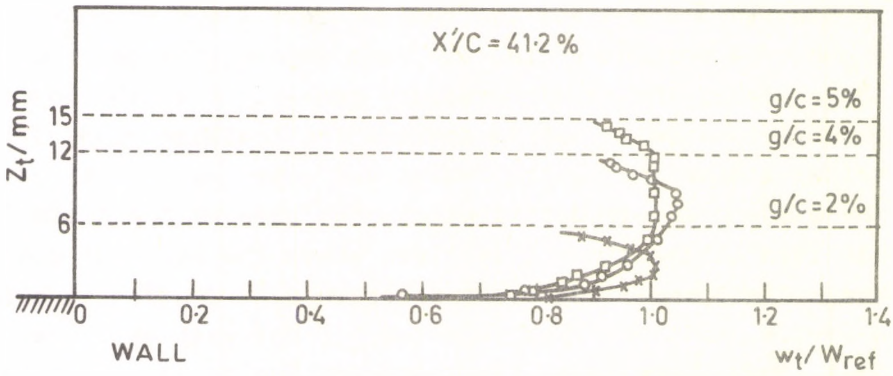

Fig.6.Velocity distributions within the tip clearance.

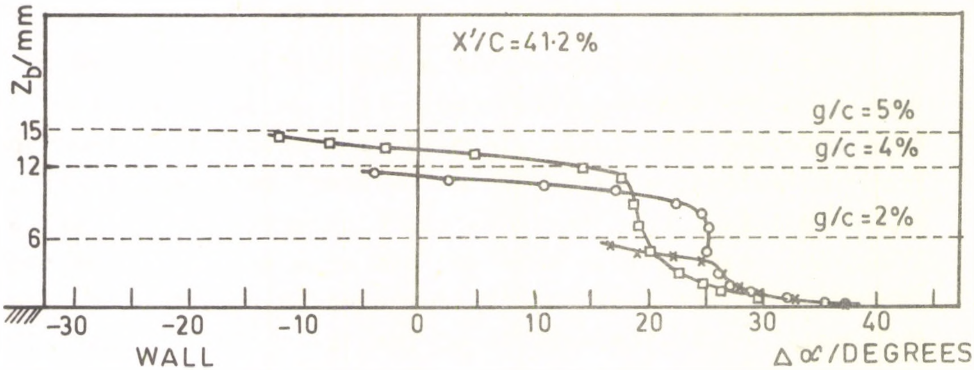

Fig.7. Flow direction within the tip clearance.

maximum difference in angle from centre span to the tip is of the order of 10 degrees. The swing of the force vector does not seem to be directly related to the strong skewing of the boundary layer.

Velocity measurements were also made within the clearance gap to estimate the magnitude of the mass and energy flux through the clearance gap. Velocity and angle measurements in the clearance gap at a chordwise position of approximately 40 percent are shown in Figures 6 and 7. Such plots were used to estimate the mass and kinetic energy flux as shown in Figs 8 and 9. It will be seen that the maximum flux of these quantities is towards the trailing edge and not near the leading edge as may be suggested from considerations of centre span pressure distributions.

The magnitudes of the leakage flow is given in the tables below.

g/c %	Flow rate = $\frac{\text{leakage flow}}{\text{flow through cascade}}$		
	$i = +4^\circ$	$i = +1^\circ$	$i = -2^\circ$
2	.03	.02	.02
4	.06	.04	.03
5	.07	.05	.03

g/c %	$\frac{\text{K.E. leakage flow}}{\text{K.E. flow through cascade}}$		
	$i = +4^\circ$	$i = +1^\circ$	$i = -2^\circ$
2	.05	.03	.03
4	.10	.06	.05
5	.12	.09	.06

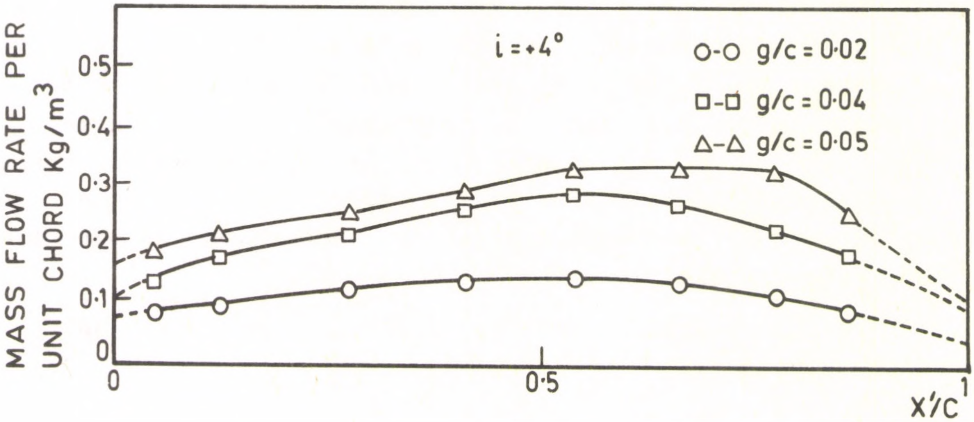

Fig. 8. Leakage flow within tip clearance.

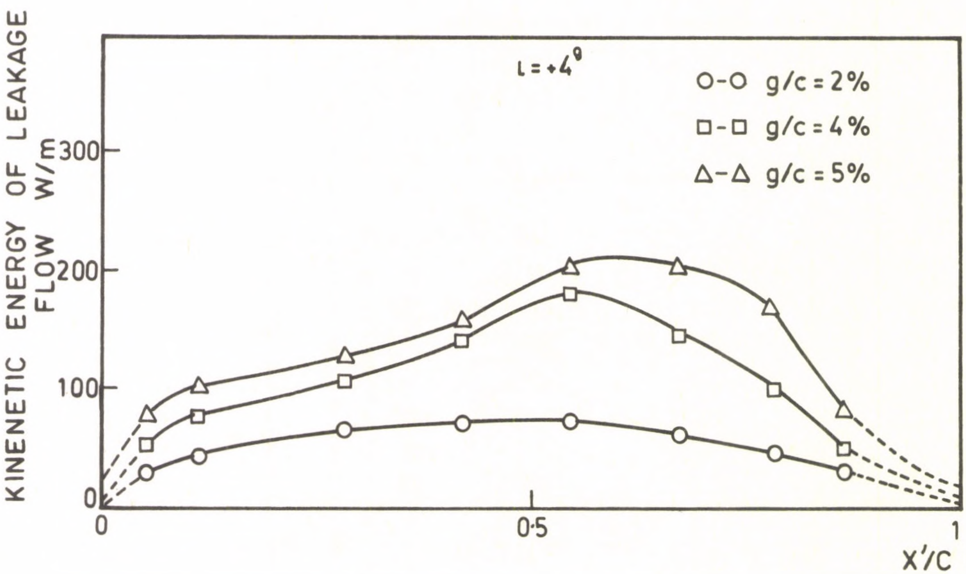

Fig.9. Distribution of leakage flow kinetic energy along blade chord.

Nomenclature

c	chord
C_{p_1}	pressure coefficient based on inlet velocity
i	incidence
W_{ref}	reference velocity
X'	distance along chord
z	distance from side wall
λ	stagger angle between chord and axial direction

References

[1] Mellor G.C. and Wood G.M. An axial compressor end wall boundary layer theory. Jnl. Basic Engg. 1971.

[2] Horlock JH and Perkins H.J. Annulus wall boundary layers in turbomachines. AGARDOGRAPH AG-185 1974.

[3] Bhowmik S.K. Hub boundary layer development in axial impellers. Ph.D.thesis. Indian Institute of Science 1980.

[4] Prasad CRK. Casing boundary layer development in axial impellers with clearance. Ph.D.thesis. Indian Institute of Science 1981.

[5] Papaillon K.Flot.R & Mathien J. Secondary flow in compressor blading. Jnl. Engg for Power 1977.

Krzysztof Majka
Research Scholar
Indian Institute of Science
Bangalore 560012
India

S.Soundranayagam
Professor
Indian Institute of Science
Bangalore 560012
India

DESIGN OF FIX COMPONENT OF HYDRAULIC TURBINE BY HODOGRAPH METHOD

F. Martelli, G. Bidini

Istituto di Energetica - Università di Firenze

Abstract

The paper presents the extension to the mixed turbomachines of the classical hodograph method developed by Fowler for axial turbine.

The basic equations are transformed to be solved by the hodograph procedure and the hypothesis of the calculation are discussed. The computer code has been developed and some applications to design the inlet vanes of Francis turbines, are shown.

Further developments to moving blades or pumps components are discussed.

Symbols

b	stream surface thickness
m	meridional coordinate
u, v	velocity components
x	axial coordinate
y	tangential coordinate
w	velocity modulus
$z = x + iy$	physical complex plane
R	radius
$W = \phi + i\psi$	complex potential, relative velocity vector
Z	axial coordinate (Fig. 2)
θ	flow direction, tangential coordinate
ω	angular velocity
ϕ	potential velocity
ψ	stream function
$\zeta = \ell nw - i\theta$	logarithmic hodograph plane
γ	farflow field angles
Subscripts	
1	upstream
2	downstream
m	meridional component
t	tangential component

INTRODUCTION

The hodograph method has shown to be a simple and quick tool to design, in incompressible flow, the blades of axial turbine[1,2,3]. The technique proposed many years ago by Fowler has widely shown flexibility and reliability and has been employed for many years by various steam turbine manifactures. The most significant features of the method are the computational speed, that allows a conversational use, the small number of parameters which define the velocity distribution along the blade, and the quasi-analitical approach to the solution that gives very accurate results, the error closure can be easily less than 10^{-5}.

All these features have suggested its application to hydraulic mixed-type turbomachinery.

The philosophy of this approach is the looking for a suitable formulation of the basic equations of flow along a general stream surface blade-to-blade in order to be formally identical to the starting or axial hodograph equations. This procedure must lead to the use of the axial code (the computer program developed for axial turbine) without any modification, and to the development of a compact algorithm to transform those output in a form suitable for design mixed or radial turbine.

The calculation could be extended to pumps by suitable consideration.

HODOGRAPH EQUATIONS

The incompressible irrotational planar flow is governed, in the physical plane, by the continuity and the irrotational equations:

$$\frac{\partial u}{\partial y} - \frac{\partial v}{\partial x} = 0 \qquad\qquad \frac{\partial u}{\partial x} + \frac{\partial v}{\partial y} = 0 \tag{1}$$

In the logarithmic hodograph plane those equations lead to the complex equation (Fig. 1):

$$dW = e^{\zeta}\, dz \tag{2}$$

The flow through axial cascades can be built by a complex potential of source-vortex type:

$$2\pi \cdot W = w_1 t\, e^{-i\gamma_1}\, \ell n(\zeta - \zeta_1) - w_2 t\, e^{-i\gamma_2} \cdot \ell n(\zeta - \zeta_2)$$

where ζ_1, ζ_2 are the images of the far flow field upstream and downstream.

Once the ζ is prescribed as a function of W, then the equation (2) can be integrated and gives the physical profile of a blade that has the velocity distribution assigned. In his approach

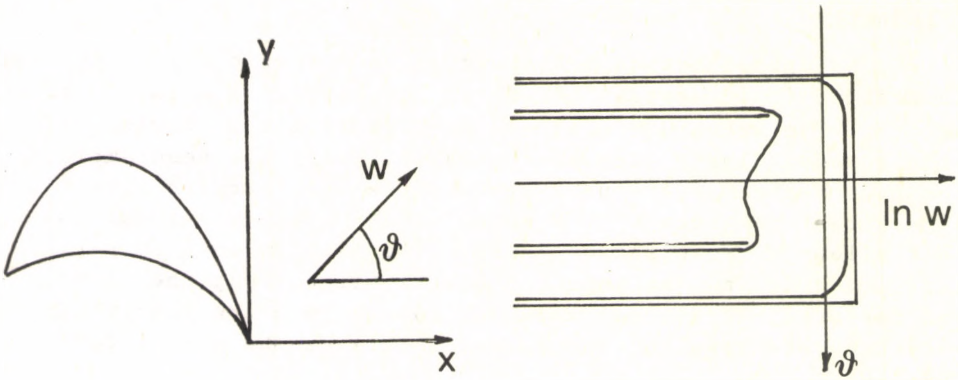

FIG.1

physical plane hodograph plane

Fowler proposed a simple structure (only 6 parameters) of the relation between W and ζ, taking into account the usual velocity distributions wished for blades turbine.

FLOW IN MIXED MACHINES

The incompressible irrotational flow along a revolution stream surface (Fig. 2) is governed by equations similar to eqs. (1); in the reference frame rotating with the rotor they are:

$$\frac{\partial W_m}{\partial \theta} - \frac{\partial R W_t}{\partial m} = \frac{\partial \omega R^2}{\partial m} \; ; \qquad \frac{\partial b W_t}{\partial \theta} + \frac{\partial b R W_t}{\partial m} = 0 \qquad (3)$$

These equations can be written again by the substitutions:

$$dx = \frac{dm}{R} \; ; \qquad dy = d\theta$$
$$u = R W_m \; ; \qquad v = R W_t \qquad (4)$$

Then eqs. 3 turn out:

$$\frac{\partial u}{\partial y} - \frac{\partial v}{\partial x} = + \, 2\omega \sin\alpha \; R^2$$
$$\frac{\partial u}{\partial x} + \frac{\partial v}{\partial y} = - \, u \, \frac{d \ell n b}{dx} \qquad (5)$$

These equations are formally equal to eqs. 1 if RHS is zero. It is possible to define also in this case a stream function ψ and a velocity potential ϕ; then eq. 2 is still valid and the Fowler approach can be performed.

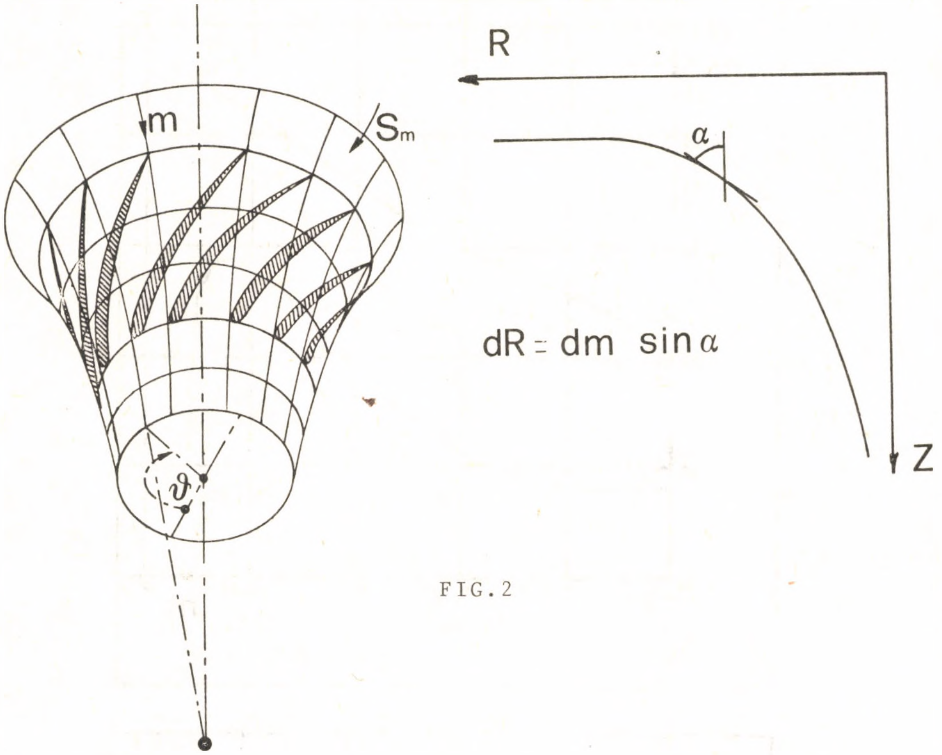

FIG.2

DESIGN PROCEDURE

The design procedure can be exactly applied only for fix blades ($\omega = 0$) and with constant width.

Starting from an assigned meridional curve R(Z) and then R(m), Z(m), and the flow conditions it is possible to compute the x = x(m) and the upstream and downstream singularity $(RW)_1$, $(RW)_2$ from mass flow and flow turning considerations.

After choosing the hodograph parameters the procedure leads to a blade shape in the x, y plane that has to come back to the m, θ coordinates system. The results are dimensionless, but in this case the pitch-chord ratio that is a typical hodograph output has no meaning. Then to fix the pitch it is usefull to choose the blades number; the whole blade configuration is then defined.

It has to be pointed out that variation in the blades number not only influences the blade length but leads to a substantial modification of the blade shape and of the velocity profile because of the different radius along the blade.

The blades designed by this method has wedged trailing and leading edge, various procedures have been proposed to get manifacturing blades for the axial code[4]; the same procedures

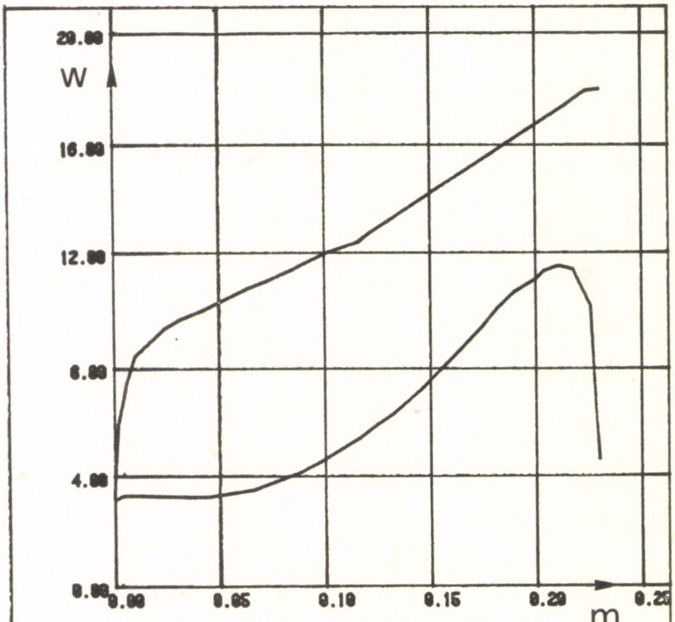

FIG.3 Velocity profile
(15 blades)

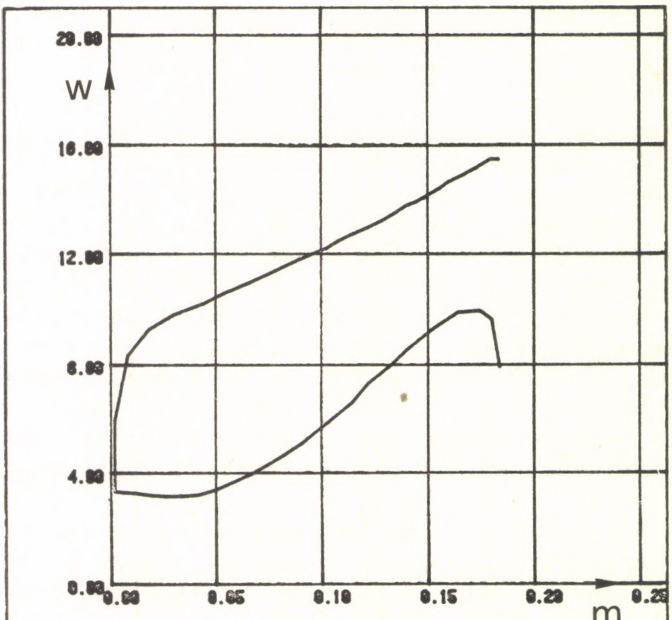

FIG.4 Velocity profile
(20 blades)

can be applied here.

APPLICATION OF THE METHOD

The procedure has been satisfactory tested for several configurations of the curves R(Z) under the numerical point of view. Then the method has been applied to design the inlet guide vanes of a Francis turbine. We have chosen the curve in the meridional plane (Fig. 2) and the inlet and outlet contition from the turbine design data.

In fig. 3-4 are shown the velocity profile for two different blades number. To get results with physical meaning the inlet radius has been fixed, then the m, W are dimensional. The velocity distributions appear to be good in both cases. The tangential blade thickness in the two configurations, is shown in fig. 5-6; in fig. 7-8 the blade shapes in the polar coordinates are presented. From these pictures it can be notice that, by the blades number, it is possible to change the meridional length, and the blade shape. This feature gives a further degree of freedom to the designer who has to optimize the blade shape taking into account the various technological and mechanical needs. The fluiddynamic aspects are automatically felt by the method itself. These calculations have shown a good affidability and high computation speed that suggests the chance of its conversational use.

CONCLUSIONS

The method has demonstrated to be simple, fast and usefull in the design of fix component of radial machinery. It has been applied only to turbines which the scheme of the velocity distribution along the blade was though for; but its extention to the pump ducts is mathematically possible, problems can arise for the unusual blade shapes and velocity distributions. Testes in that direction will be done for diffusers. The influence of the width can not be taken into account by this method, but it can be investigated by running an analysis code[6] on the designed blade with the prescribed width or by the curves provided in literature[5].

The approach to design rotating blades can be carried out theoretically but the starting scheme has to be modified; attemps to use the formulation proposed have been done but the need to work in the fix reference frame leads to a shape in this frame that has no meaning in the rotating system. The simplest chance consists to design impeller blades neglecting the rotational effects by our approach and then to test, by an analysis code, the goodness of the shape.

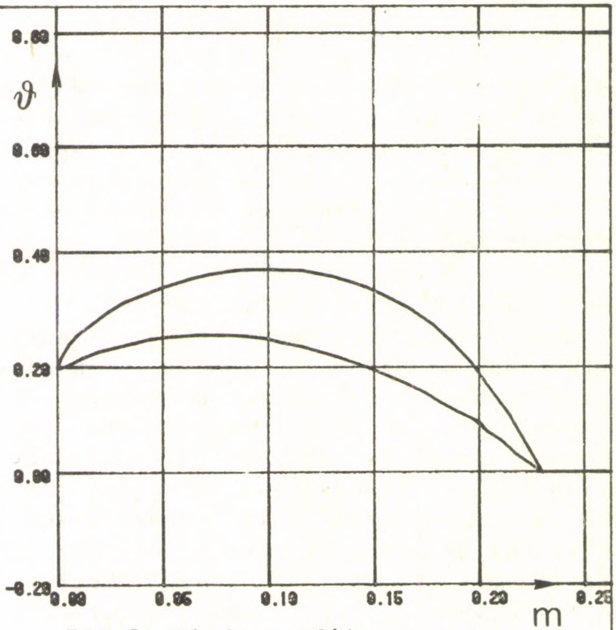

FIG.5 Blade profile — m-θ coordinates (15 blades)

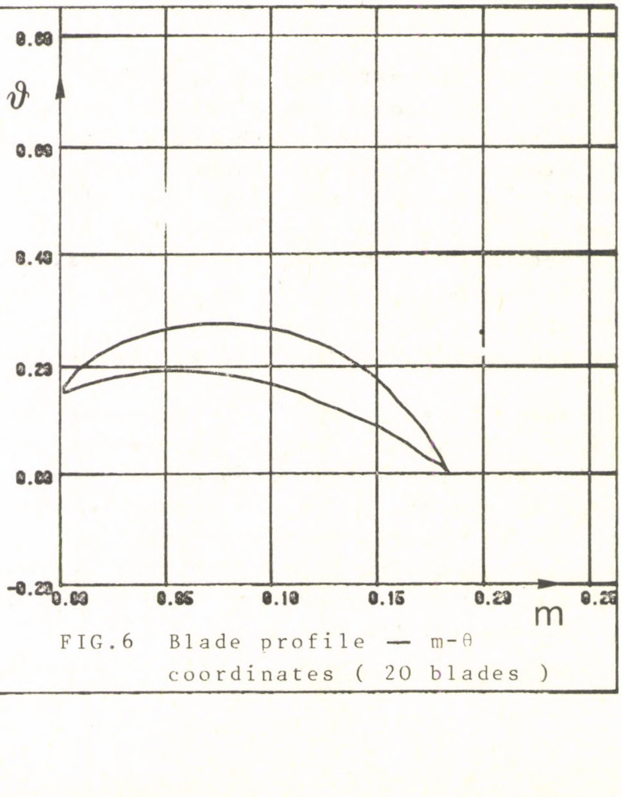

FIG.6 Blade profile — m-θ coordinates (20 blades)

REFERENCES

[1] CANTRELL, H.N., FOWLER, J.E.: "The Aerodynamic Design of Two-Dimensional Turbine Cascades for Incompressible Flow with a High Speed Computer", Trans. ASME, vol. 81, Series D, 1959, pp. 349-361.

[2] MARTELLI, F.:"Progetto di palettature con il metodo odografo", Internal Report, 1978, Istituto di Energetica.

[3] MARTELLI, F., BIDINI, G.: "Progetto di profili di palettature: alcuni sviluppi del metodo odografo", XXXVI Congresso Nazionale ATI, settembre 1981.

[4] BIDINI, G.: "Sintesi di tesi di Laurea", Bollettino degli Ingegneri, n° 7-8, 1981.

[5] MURATA, S., OGAWA, T., GOTON, N.: On the flow in a centrifugal impeller", Bullettin of the JSME, vol 21, n° 151 (1978).

[6] MARTELLI, F., MANFRIDA, G.: "Flow Calculation in Pump Impellers by Finite Elements", 7th Conference on Fluid Machinery, Budapest, 1983.

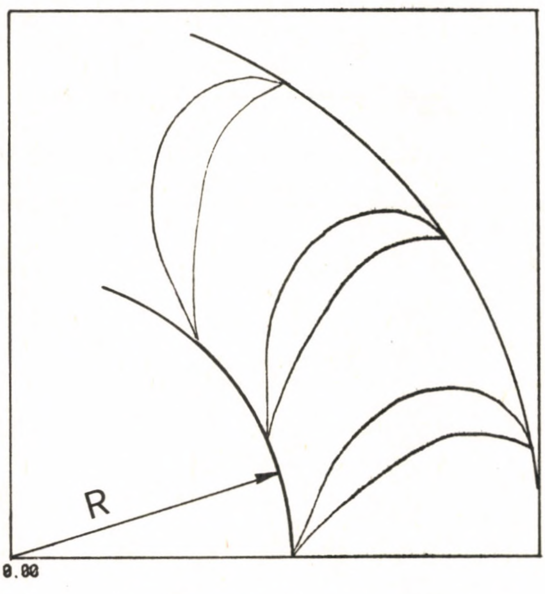

FIG.7 Blades profile — polar coordinates (15 blades)

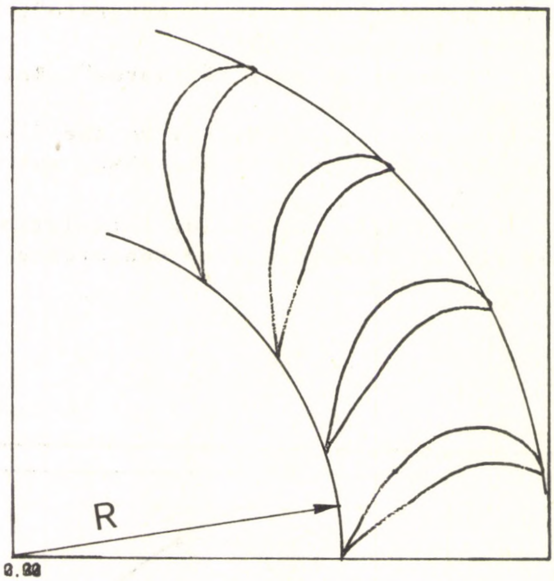

FIG.8 Blades profile — polar coordinates (20 blades)

FLOW CALCULATION IN PUMP IMPELLERS BY FINITE ELEMENTS

by F. Martelli, G. Manfrida

Istituto di Energetica - University of Florence

Via S. Marta 3 - 50139 FIRENZE

INTRODUCTION

It is common practice to study the flow in turbomachines by means of two-dimensional inviscid numerical calculations. Three-dimensional or viscous models, even if available, are still prohibitively expensive for most designers. On the other hand, a coupling of the two-dimensional calculation on the meridional (S2) flow surface with a set of calculations on blade-to-blade surfaces (S1) can provide the designer with the most significant informations on the local flow behaviour and on the full machine performance [1]. An extension to off-design conditions can also be cheaply obtained, as long as large separations are not expectable (in this case, anyway, also viscous three-dimensional codes would fail).

The flow model on the S1 surface is of particular importance, as it provides information on the velocity and pressure field inside the blade-to-blade channel, which are needed for boundary layer calculations on the blade surface, and still for qualitative analysis of the blade design. Further the blade-to-blade code is able, when a suitable closure condition on the trailing edge is imposed, to predict the discharge angle of the impeller, which is a phenomenon typically affected by the properties of the fluid, and, in mixed-flow or centrifugal geometries, by the rotationality of the flow in the discharge section. From the numerical point of view, the S1 calculation presents some difficulties, such as an intrinsic non-linearity of the flow equations on non-axial geometries and the need of dealing with periodic boundaries ahead and after the blade; needless to say, the computer code has to be fast and of easy implementation, as a certain number of S1 surfaces need to be examined (from a minimum of 3 to 5-7) to get, by the interaction with the S2-code, a picture of the quasi-three dimensional flow. Complex geometries are also commonly encountered which can present difficulties to a finite difference discretization.

To overcome such difficulties, a Finite Element discretization has been implemented, together with a formulation of the flow equations in the m-θ domain (Fig. 1)(m = meridional abscissa, θ = angular tangential abscissa) thus allowing the treatment of any geometry ranging from axial to centrifugal without discontinuities, as are encountered in many approaches [2,3]. An original treatment of the trailing edge closure condition allows to predict the impeller discharge angle.

BASIC EQUATIONS

The flow equations on a mixed-flow S1 surface can be derived in the relative reference frame from the momentum equation:

$$\bar{W} \times (\bar{\nabla} \times \bar{W}) + 2\bar{W} \times \bar{\omega} = \bar{\nabla} I - T\,\bar{\nabla} s - \bar{D} \qquad (1)$$

where $\bar{W}$ is the relative velocity, $\bar{\omega}$ the rotational speed, I rothalpy, T temperature, s entropy and D is the flow-adverse force simulating viscous effects, acting opposite to the flow direction [2].

Projecting Eq. 1 in the direction η locally orthogonal to the flow vector, the flow-adverse force $\bar{D}$ vanishes; by furtherly introducing the hypothesis of axial simmetry of the S1 surface, one gets:

$$W \left(\frac{1}{r}\frac{\partial Wm}{d\theta} - \frac{\partial W\theta}{\partial m}\right) = \frac{dI}{d\eta} - T\frac{\partial s}{\partial \eta} + \sin\alpha \left(2\omega + \frac{W\theta}{r}\right) W \qquad (2)$$

where r is the local radius of the S1 surface and α its angle with respect to the axial direction.[Fig. 1].

The satisfaction of the continuity equation implies the existence of a stream function ψ, defined by:

$$\frac{\partial \psi}{\partial m} = - b\,\rho\,W_\theta/\dot{m} \qquad (3)$$

$$\frac{\partial \psi}{\partial \theta} = r\,b\,\rho\,W_m/\dot{m} \qquad (4)$$

where $\dot{m}$ is the mass flow rate, ρ is density and b is the streamtube local thickness in the direction orthogonal to the S1 surface. By Eqs. 3-4 and Eq. 2 the inviscid incompressible flow equation on the S1 surface is:

$$\frac{\partial}{\partial \theta}\left(\frac{1}{r^2}\frac{\partial \psi}{\partial \theta}\frac{1}{b}\right) + \frac{\partial}{\partial m}\left(\frac{\partial \psi}{\partial m}\frac{1}{b}\right) = \rho\frac{\sin\alpha}{\dot{m}}\left(\frac{W\theta}{r} + 2\omega\right) + \frac{\rho}{\dot{m}W}\frac{dI}{d\eta} + - \frac{\rho T}{\dot{m}W}\frac{\partial s}{\partial \eta} \qquad (5)$$

Eq. 5 is typically non-linear due to the presence of W_θ, W at the right-hand side. The problem is closed by the energy equation $\frac{dI}{dt} = 0$ along the streamline, the eventual empirical correlation to compute entropy gradients, and by the associated boundary conditions which are collected in Fig. 2, where a sketch of the computational domain is shown. Sides 5A, 5B represent the periodic boundaries, while the condition on the discharge section 3 can be replaced by the closure condition at the trailing edge, which actually determines $W_{\theta 3}$.

In order to apply the Finite Element discretization, one needs to reformulate Eq. 6 in a variational form. This can be done if the right-hand side is considered known as a function of m, θ, and leads to:

$$\pi = \int_{\Omega} \frac{1}{2}\left[\frac{1}{br^2}\left(\frac{\partial\psi}{\partial\theta}\right)^2 + \frac{1}{b}\left(\frac{\partial\psi}{\partial m}\right)^2\right] + \psi\left[\rho\frac{\sin\alpha}{\dot{m}}\left(\frac{W\theta}{r} + 2\omega\right) + \frac{\rho}{\dot{m}W}\frac{\partial I}{\partial\eta} - \frac{\rho T}{\dot{m}W}\frac{\partial s}{\partial\eta}\right] d\Omega + \int_{\Gamma} \rho\frac{Wt}{\dot{m}}\psi d\Gamma \tag{6}$$

The minimum of functional π corresponds to Eq. 5. By the Finite Element discretization [4], which in this case consists in three-node triangular elements, any variable inside an element can be expressed by

$$A = \Sigma_i N_i(\theta,m) A_i \qquad i = 1,2,3 \tag{7}$$

where N_i are the shape functions and A_i the nodal values of variable A. The minimum of functional π is then equivalent to the solution of the linear system:

$$\left[k_{ij}\right]\{\psi_i\} = \{g_i\} \qquad \begin{matrix} i = 1,\dots, p \\ j = 1,\dots, p \end{matrix} \tag{8}$$

where p is the total number of nodes and

$$k_{ij} = \Sigma^e \int_{\Omega_e} \left(\frac{\partial N_i}{\partial\theta}\frac{\partial N_j}{\partial\theta}\frac{1}{br^2} + \frac{\partial N_i}{\partial m}\frac{\partial N_i}{\partial m}\frac{1}{b}\right) d\Omega_e \tag{9}$$

$$g_i = g'_i + g''_i + g'''_i \tag{10}$$

$$\begin{aligned} g'_i = &- \Sigma_e \int_{\Omega_e} W_\theta \frac{\rho}{\dot{m}} \sin\alpha \sum_{ij}^{3}\left(\frac{1}{r_j} N_j\right) N_i \, d\Omega_e \\ &- \Sigma_e \int_{\Omega_e} \frac{2\omega\rho\sin\alpha}{\dot{m}} N_i d\Omega_e - \Sigma_e \int_{\Omega_e} \frac{\rho}{\dot{m}W}\frac{dI}{d\eta} N_i d\Omega_e \\ &\Sigma_e \int_{\Omega} \frac{\rho T}{\dot{m}W}\frac{\partial s}{\partial\eta} N_i d\Omega_e \end{aligned} \tag{11}$$

$$g''_i = {}^1g''_i + {}^2g''_i$$

$$
\begin{aligned}
{}^1g''_i &= -\frac{\rho}{\dot{m}} \Sigma_e \int_{\Gamma_1} W_t \, N_i \, d\Gamma \\
{}^2g''_i &= -\frac{\rho}{\dot{m}} \Sigma_e \int_{\Gamma_3} W_t \, N_i \, d\Gamma \\
g'''_i &= -\frac{\rho}{\dot{m}} \Sigma_e \int_{\Gamma_5} W_t \, N_i \, d\Gamma
\end{aligned}
\qquad (12)
$$

where Ω_e is the m-θ surface of the generic element e, W_t the velocity component tangent to a boundary segment, and Σ_e represents a summation over all elements in the domain. ${}^1g''_i$ and ${}^2g''_i$ represent the contributions of inlet-outlet boundaries; the inlet term is known from the problem data, the outlet term ${}^2g''_i$ can be imposed or computed as a suitable closure is applied. g'''_i represents the contributions to the right-hand side of the periodic boundary terms. On these boundaries, W_t is a priori unknown; anyway, a manipulation of the solution matrix [5] leads to the elimination of g'''_i from the right-hand side, obviously at the price of some numerical work which goes to increase the CPU time. The final linear system is:

$$\left[k'_{ij}\right] \{\psi_i\} = \{g'_i\} + \{g''_i\} \qquad \begin{array}{l} i = 1,\ldots,p \\ j = 1,\ldots,p \end{array} \qquad (13)$$

which can be solved by a SOR method, which allows an easy treatment of periodic boundaries.

In Eq. 13, $\{g'\}$ is supposed known each time the solution algorythm is called; actually, there is in $\{g'\}$ a contribution of non-linear terms, involving W_θ, W, which is zero only in the case of axial-flow impellers ($\sin\alpha = 0$ everywhere). The final solution is then obtained by an iteration of the described procedure, using the ψ field at each iteration to calculate the right-hand side for the next one, until convergence.

CLOSURE CONDITION AT THE BLADE TRAILING EDGE

Physical arguments suggest that the wake will develop from two points respectively on the blade suction side and pressure side. In first approximation one is allowed to say that in such points the velocities are equal in modulus and obviously tangent to the blade surface (Fig. 3). Actually these two points should be close to the trailing edge for well-designed blades, but can be far ahead of it if separation on one side of the blade occurs at an early stage. Arguments on similar machines can help the designer to situate these two points on the blade surface. Once these points are determined, then the circulation around the airfoil is imposed, i.e., the discharge angle is fixed and the inviscid flow solution is equivalent from this point of view to the physical solution, in which only one discharge angle exists.

By this approach the term W_t, i.e. the outlet angle, that appears in ${}^2g''$ is unknown and will be a result of calculation.

Eq. 13 is then transformed to take into account the new nodeless variable W_t:

$$\left[\overline{k'_{ij}}\right] \{\overline{\psi_i}\} = \{g'\} + \{{}^1g''_i\}, \quad \left[\overline{k'_{ij}}\right] = \left[k'_{ij}, \overline{g_i}\right] \tag{14}$$

where $\psi_i = < \psi_1, \ldots \psi_i, \ldots \psi_p, W_t >^{T'}$ includes this new unknown W_t and the new matrix has a further column

$$\overline{g_i} = - \frac{\Sigma e \rho}{\dot{m}} \int_{\Gamma_3} N_i d\Gamma_e$$

The system is now rectangular px(p+1) and the further equation, needed to get a single solution, is supplied by the condition of equal velocity at the prescribed T.E. points.(Fig. 3) This corresponds to an equation which links the inner nodes of the two elements,of the type

$$A\ \psi_J = B\ \psi_{Jp} + C \qquad \text{or} \qquad <AB_i> \{\psi_i\} = \{C\} \tag{15}$$

where A, B, C are coefficients depending on the blade surface angle β in the m-θ surface, on the local radius r and on the local discretization.

Finally the new square matrix is:

$$\left[k^*\right] = \left[\begin{array}{c|c} k'_{ij} & \overline{g_i} \\ \hline \multicolumn{2}{c}{AB_i} \end{array}\right], \quad \left[k^*\right] \{\overline{\psi_i}\} = \{g'_i\} + \{{}^1g''_i\} + \{C\} \tag{16}$$

In principle system (16) could be solved by the S.O.R. technique used for the system (13) where the outlet angle was imposed but numerical problems arise because the matrix k^*, resulting from the conjunction of $\overline{k'_{ij}}$ with the coefficient of eq. 15, has a zero on the diagonal and manipulations to avoid this configuration would lead to a big increase in the complication of the solution algorithm and then in the cpu time and storage requirements, without appreciable results on the stability of the procedure. The situation is more complicated, as the outlet flow boundary is distant from the trailing edge, due to the presence of a segment of periodic boundary, and many iterations are required in order that the nodeless variable feels the variation of the nodes value of eq. 15.

Better results have been achieved looking for the zero, by a chord technique, of eq. 15 as an equation in W_t, $f(W_t) = 0$, through system (14).

The whole procedure is now the following:

- Solution of system (14) with W_t of first guess
- Evaluation of the residual of eq. 15
- Solution of system (14) with a new value of W_t
- Calculation of a new W_t by the chord method from residual of eq. 15
- Solution of system (14)

This procedure goes on till the solution of eq. 15 is achieved with the required accuracy.
After the first step the other solutions of system (14) require few iterations and the whole iterations number needed in this case is only 30% greater then the iterations number needed in the case of imposed outlet angle.

The proposed scheme is quite simple and besides, by suitable tricks, further reductions of computer time can be achieved;this calculation method appears suitable for analysis or design problems because of its flexibility,fastness, and compactness.

Particular attention has to be paid to the selection of the accuracy in the calculation of system (14),in fact there is a strict dependence of its value on the accuracy on the outlet flow angle: $\Delta\beta_3 = f(\Delta\psi)$
where $\Delta\psi$ represents the maximum difference between two iterations at the convergence.

ANALYSIS OF THE RESULTS

The results of the numerical calculation have been thoroughly tested for several geometries under design or off-design operating conditions.

A check against experimental measurements is possible for the test rig examined by Watanabe [6] , on which some numerical calculations by other Authors are also available for various flow coefficients. The results of this comparison are collected in figs. 4-5-6, respectively for ϕ_2 = 0.4, 0.3 and 0.5. the calculations here presented have been performed by a direct application of the blade-to-blade code, without any previous through-flow analysis; their agreement should then be considered extremely good, especially with respect to other numerical calculations (which were not able to calculate the flow in the impeller inducer as well as in the radial part of the blade); the calculated values tend to predict a higher pressure ratio for this impeller: this should be ascribed to viscous effect as well as to the meridional shape of the S2 surface in the connecting part from the axial inducer to the radial blade, which causes a steep pressure gradient on the blade suction side.

Fig. 7 shows the convergence history of the closure condition for the three flow coefficients. It is also possible to compare the absolute outlet flow velocity with the measured values: the values predictable by the application of a Busemann slip factor correlation are also shown in Fig. 8.

Calculations for other geometries of industrial pumps are reported in refs. [5,7].

LIST OF REFERENCES

[1] Wu, C.H., "A General Theory of the Two-Dimensional Flow in Subsonic and Supersonic Turbomachines of Axial, Radial and Mixed-Flow Type", NACA TN 2604.

[2] Bosman, C., Marsh, H.: "An Improved Method for Calculating the Flow in Turbo-Machines, Including a Consistent Loss Model",Journ.Mech.Eng.Science, Vol. 16, n°1, 1974.

[3] Adler, D., Krimerman, Y., "Calculation of the Blade-to-Blade Compressible Flow Field in Turbo Impellers Using Finite Element Method", Journ.Mech.Eng.Science, Vol. 19, n°3, 1977.

[4] Zienkiewicz,O.C., "The Finite Element Method", Mc Graw-Hill, 1975.

[5] Martelli, F., Manfrida, G., "Studio del flusso interpalare in pompe assoradiali con il metodo degli Elementi Finiti", Proceedings of the 37th ATI Congress, Padova, Italy, 1982.

[6] Mizuki, S., Ariga, I., Watanabe, I., "Investigation Concerning the Blade Loading of Centrifugal Impellers", ASME Paper n. 74-GT-143.

[7] Martelli, F., Manfrida, G., "Calcul aux éléments finis de l'écoulement aube à aube dans les pompes", 121éme Session du Comité Technique de la Societé Hydraulique de France, Paris, 1982.

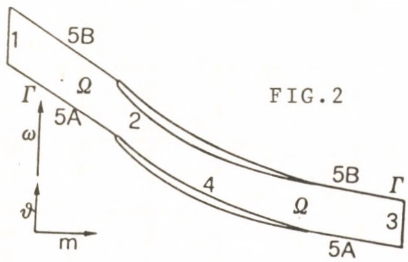

FIG.2

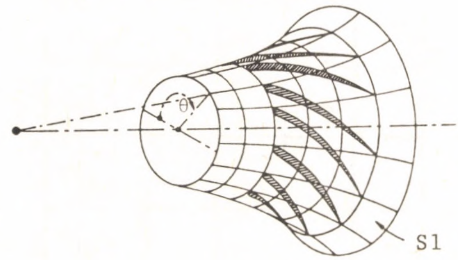

FIG.1

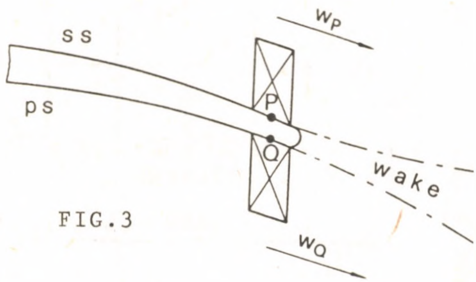

FIG.3

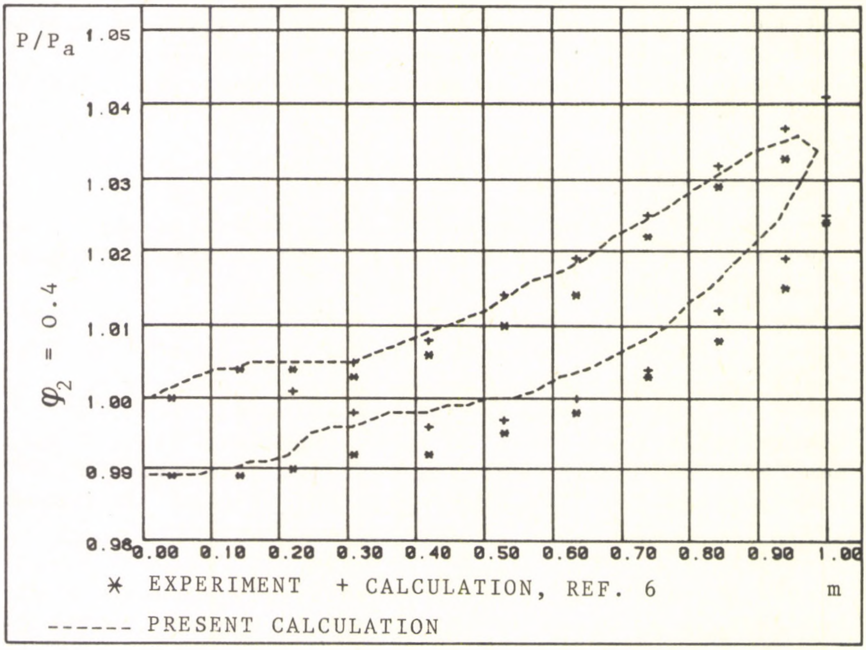
P/Pa
1.05
1.04
1.03
1.02
1.01
1.00
0.99
0.98
φ_2 = 0.4
0.00 0.10 0.20 0.30 0.40 0.50 0.60 0.70 0.80 0.90 1.00
m
* EXPERIMENT + CALCULATION, REF. 6
------ PRESENT CALCULATION

FIG.4

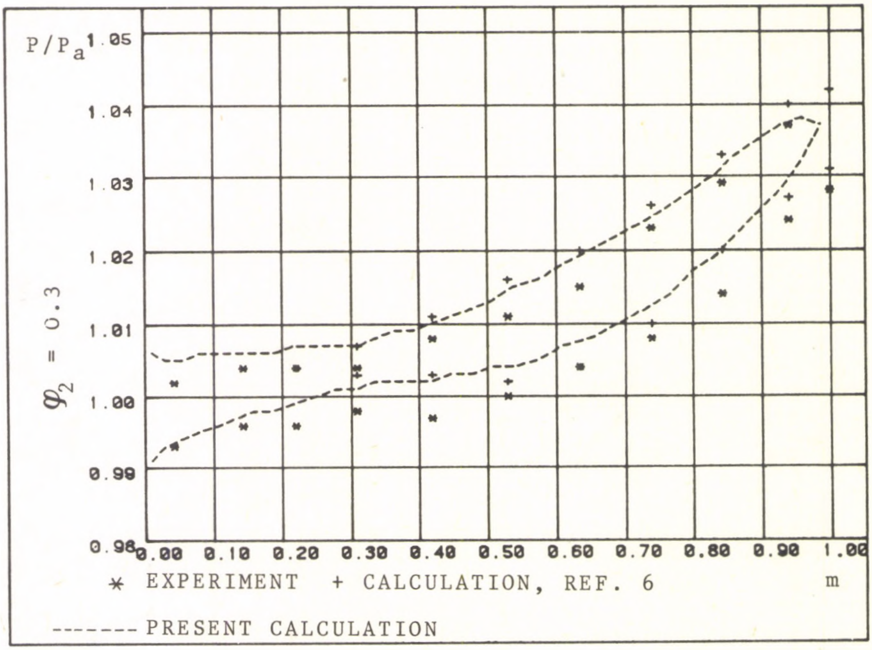
P/Pa
1.05
1.04
1.03
1.02
1.01
1.00
0.99
0.98
φ_2 = 0.3
0.00 0.10 0.20 0.30 0.40 0.50 0.60 0.70 0.80 0.90 1.00
m
* EXPERIMENT + CALCULATION, REF. 6
------- PRESENT CALCULATION

FIG.5

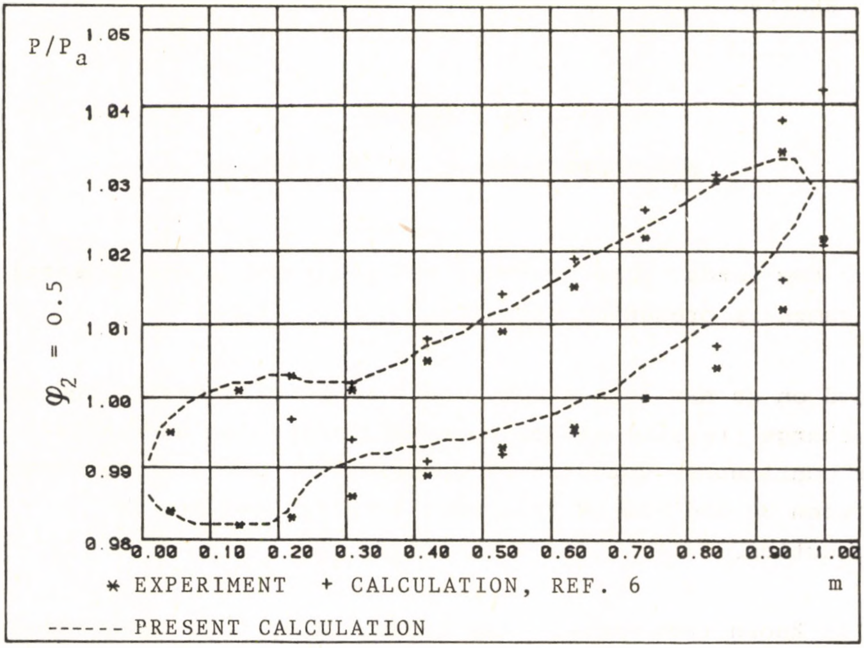

FIG.6

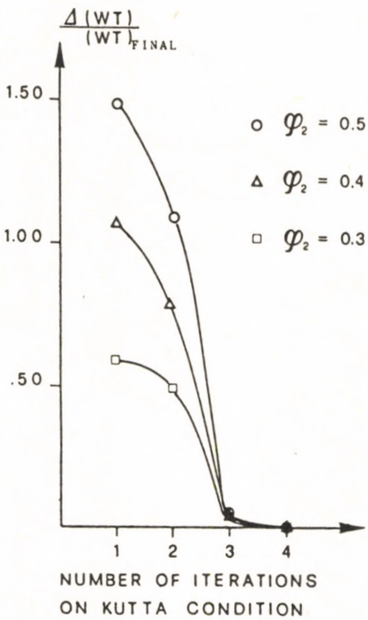

FIG.7

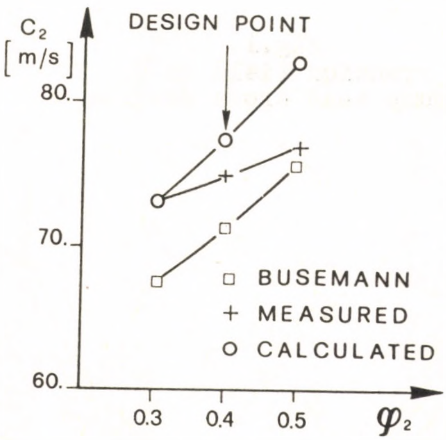

FIG.8

RECIPROCATING PUMPS FOR HIGH PRESSURE WATER JETTING

B. Missmahl

WOMA-Apparatebau, F. R. Germany

With few words, some drawings and diagrams, a new generation of pumps is presented herewith.

Based on an new idea and by means of a solid design concept discharge pressure ranges up to 2000 bars can be realized for continuous duty. Pumps covering the performance range between 30 and 400 kW have been supplied and are in production.

It is known that normal pump heads suffer from zones sensitive to cracking. These cracks are caused by tension peaks within the material that occur at the T-borings according to

Fig.1
Tension field in a pump head cross section

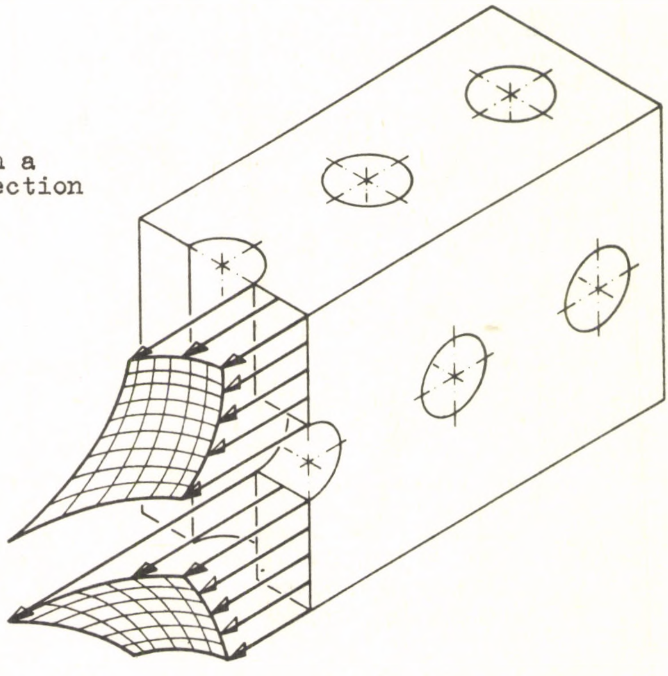

fig. 1. At first the peaks depend on the geometry of the pump head (i. e. bore sizes and outer dimensions) and on the profile of the pressure line.

We have performed experimental investigations and calculations to define the peaks existing within a pump head. The result cannot be compressed in a simple, closed formula. Peak tensions may reach several times of the fluid pressure.

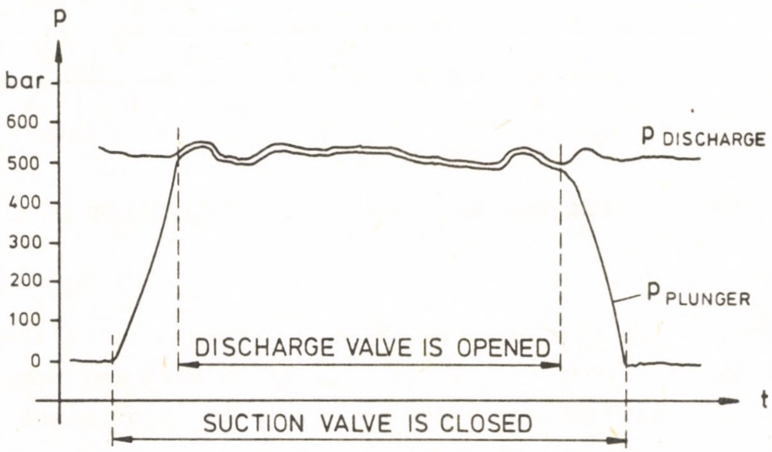

Fig.2 Pressure/time correlation inside a pump head

Fig. 2 shows measured fluid pressure inside the pump head. Two pressure/time correlations are indicated. The lower p_{PL}-line shows pressure/time curve inside the plunger working space, the upper one p_D gives pressure curve inside discharge space where a quasi-static pressure with superposed small pulsation is existing. The plunger working space however shows a fluctuating pressure between zero and maximum without a static component. In accordance to that pressure - but several times higher - the material stresses are fluctuating at the crack-sensitive areas.

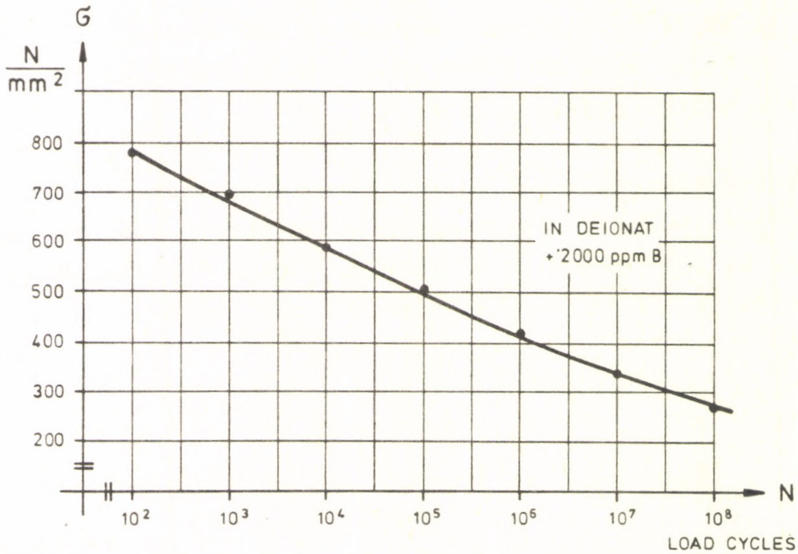

Fig.3 Fatigue diagram of the material X5CrNi134 in a liquid

For example fig. 3 shows the fatigue-diagram of the material X 5 Cr Ni 13.4 (No. 1.4313) that is often used for pump heads. Tensile strength is about 900 N/mm², yield point about 650 N/mm². These figures would trace back to an operating time of approximately 333 hours at a crankshaft rotating speed of n=500/min. How is it possible to get another curve tendency with increased fatigue strength values?

The new design concept now enables us to replace the dynamic stressing of a pump head by a (quasi-) static one. This is performed by inserting solid bushes dynamically stressed by their inner hydraulic load and pressed also externally by the "static" discharge pressure of the pump.

Fig. 4 shows all relevant details of the "hydrostatic armed" pump head. Only the bushes are stressed by the fluctuating plunger working pressure. Tightness of these simply exchanged parts is given by O-rings.

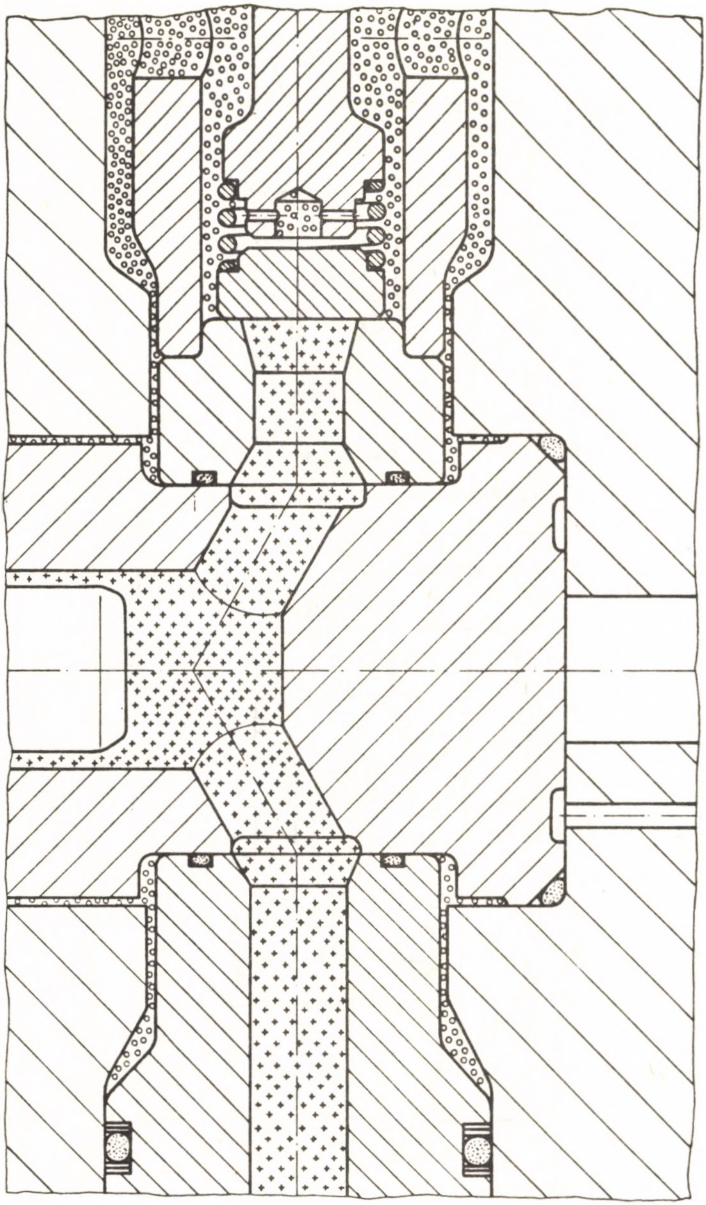

Fig.4 Hydrostatic armed pump head

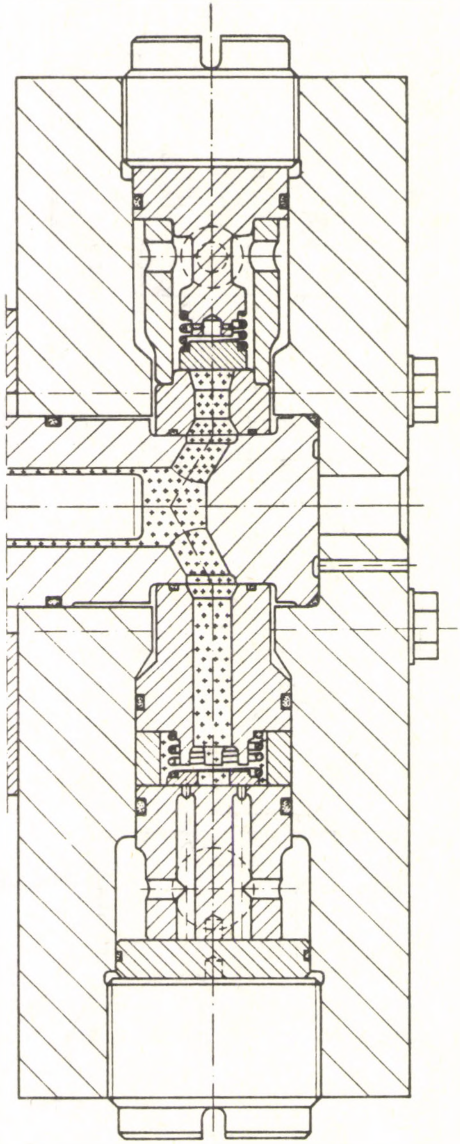

Fig.5 Pump head with suction and discharge valves

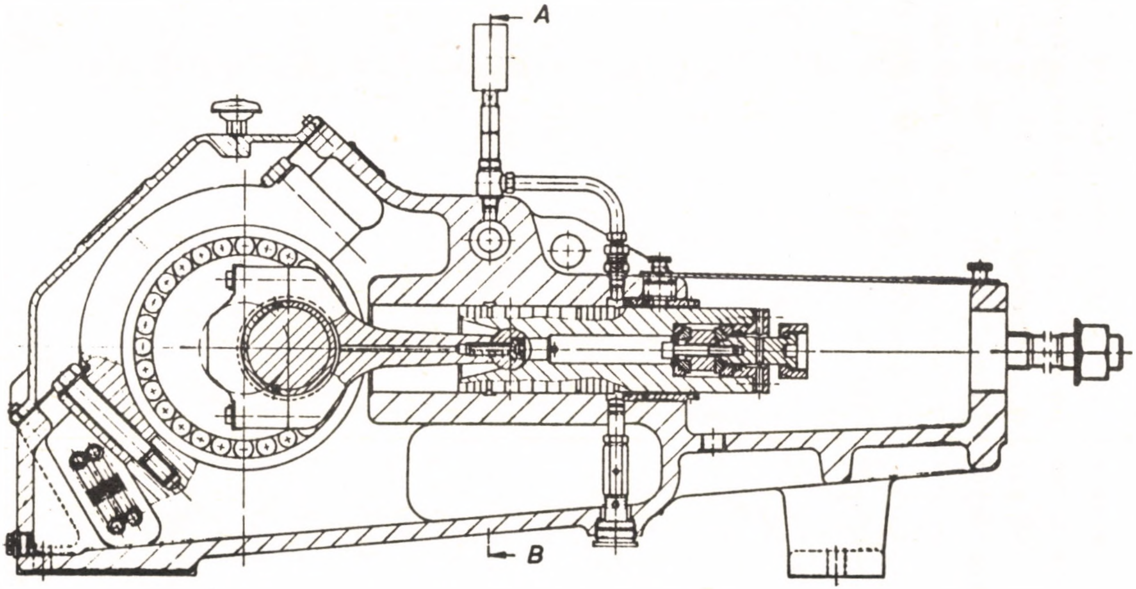

Fig.6 Power end of a three plunger pump

To complete the information fig. 5 shows a cross-section of the entire pump head. At the bottom is the double-charging, spring-guided valve, in the centre the head of the plunger and above the simply beaming, spring-guided discharge valve.

Fig. 6 gives a cross-section of the power end of the pump consisting of cast pump housing, roller-beared crankshaft, conrod, cross-head piston with integrated lubrication pump and spharic joint plunger connection. The heat exchanger for oil-cooling can also be seen. Not seen - but nevertheless existing - is a drive shaft powering the crankshaft by means of a one speed gear.

EXPERIMENTAL RESEARCH ON REVERSE-FLOW CHARACTERISTICS OF HIGH SPECIFIC SPEED PUMP AND ITS GENERATION MECHANISM

H. MURAI* and S. TEZUKA**

SUMMARY

Through the results of experiment conducted with an axial-flow pump, a working mechanism of impeller blades and its relation to flow patterns around a flow channel between blades at partial discharges smaller than one of maximum head were clarified. And the materials for predicting a head-discharge characteristics rising with decreasing discharge were presented, and it was deduced that a sufficient condition of generating the characteristics is the generation of a delivery-side reverse flow growing with decreasing discharge.

INTRODUCTION

Although improvements of a performance of turbomachinery at partial discharge have been being required for long time, the demand is considered to be even growing in accordance with the recent trend of enlargement of the capacity, followed by the enhancement of specific speed and the expansion of operating discharge range of them. As for the interrelation between a head-discharge characteristics and a flow in a turbomachine of high specific speed at partial discharge, the following items have been clarified by the many studies(1)(2) conducted mostly by early in 1970's: in case areas of stall near blade tips are expanded radially inwards with decreasing discharge, a head-discharge characteristics becomes to behave falling with decreasing discharge(3), in which case small-scale reverse flows to suction side are generated in forms of vortices or a vortex extending to the suction side from vicinities of leading edge/s(4)(5), and propagates to the succeeding channel between blades(6). With the further decrease of discharge, the reverse flow grows to be large-scaled and stable, in which stage the head-discharge characteristics becomes to behave rising(6) (the reverse-flow characteristics(7)). It was pointed out qualitatively(2)(4) that the change of characteristics from falling to rising could be considered to have some relation to a reverse flow from the delivery side. However, the generation mechanism of the reverse-flow characteristics, and the part which the reverse flow from the delivery side plays in the mechanism have not yet been clarified, as far as the authors are aware.

In the present research, experiments on an axial-flow pump were conducted, by using air as working fluid, for the purpose of clarifying a working mechanism of impeller blades of a high specific speed pump at a partial discharge smaller than one of maximum head, and offering materials for predicting a so-called reverse-flow characteristics and conditions for the pump to change its characteristics from falling to rising at the discharge of minimum head. Pressure distributions on the impeller blades and on the casing as well as velocity and pressure distributions in the stream before and behind the impeller were measured and compared with oil-flow patterns on the impeller blades, hub and casing to investigate the correlation between the impeller work and the flow pattern.

---

*Professor, Institute of High Speed Mechanics, Tōhoku University, Sendai, Japan

**Formerly, Post Graduate Student of Tōhoku University, Currently Dengyosha Machine Works Ltd., Mishima, Japan

EXPERIMENTAL EQUIPMENT AND METHODS OF MEASUREMENT

Pump and Impellers

An axial-flow pump with 430mm diameter was installed in the pipe line open to atmospheric air as shown in Fig.1. This pump is the one used in the experimental research published previously by one of the authors [8]. In the present experiment, two impellers were used, one having five blades without sweep angle (impeller A) and the other having ten blades swept back by π/4 towards the hub (impeller B). The design items and principal dimensions are shown in Table 1.

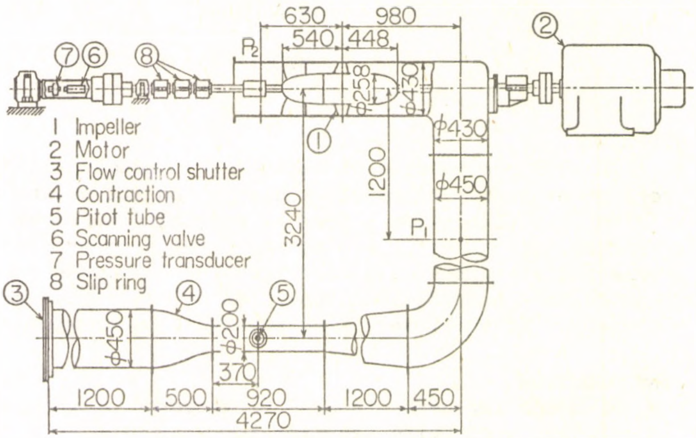

Fig. 1 Experimental apparatus

Table 1 Design items of pump

Specific speed	1520
Head (m)	3.5
Rate of flow (m^3/min)	29
Angular speed (rpm)	720
External diameter (mm)	430
Hub-to-tip ratio	0.6

Table 2 Principal data of impellers

Symbol		A	B
Swept-back angle (rad)		0	0.785
Number of blades		5	10
Chord length (mm)	tip	171	
	mean	158	
	hub	142	
Blade angle (rad)	tip	0.370	0.406
	mean	0.473	0.534
	hub	0.741	0.886
Lift coefficient	tip	0.367	0.183
	mean	0.479	0.239
	hub	0.728	0.364

Measurement of Head-Discharge Characteristics of Pump

The arrangement of the experimental apparatus is outlined in Fig.1. The air comes in through the flow control shutter ③ attached to the entrance of the suction pipe of 450mm diameter, enters into the pump through the nozzle ④ for measuring the discharge and then is exhausted to the open air. The volumetric discharge rate flowing through the nozzle was calibrated by the Prandtl type Pitot tube installed at the location ⑤. The Pitot tube was installed at the centre of the pipe at the same location and was used for the measurement of discharge during the experiments. The static pressures on the suction and delivery sides of the pump were calculated as the averages of the values measured at the pressure taps provided at each four points around the peripheries at the locations P_1 and P_2, respectively. The number of revolution of the pump was fixed at 1,200 r.p.m., measured by using the pick-up of photo-electric type and the frequency counter.

Measurement of Pressure on Surface of Blade

The measurement of the pressure on the surface of blade was made through the pressure taps of 0.3mm diameter provided on the surfaces of blades along the circles with radii of 20, 40, 60, 75, 85 and 96% of the blade height from the hub, 14 points on the suction surface and 12 points on the pressure surface along each height, and 156 points all together.

Each pressure tap was connected by copper pipe of 1mm inner diameter to the scanning valve ⑥ in Fig.1 through the hollow shaft, and the static pressure was detected on the static strainmeter connected, through the slip rings ⑧ , to the pressure transducer ⑦ .

Measurement of Pressure and Velocity Distributions at Up- and Downstreams of Impeller

The measurement of the time averaged flow at the suction and delivery sides of the impeller was made by using the yawmeter of arrow type with five holes. The positions of measurement were set at 50mm and 130mm upstream and 57mm and 137mm downstream the impeller A and 75mm and 152mm upstream and 72 mm and 152mm downstream the impeller B, measured from the centres of impeller blades (40% chord of blade tip).

The static pressure on the inner surface of the casing was measured through the pressure taps provided at four points upstream and five points downstream at intervals of 25mm starting from the point facing to the leading edge of the blade tip of the impeller A.

EXPERIMENTAL RESULTS AND DISCUSSION

Head-Discharge Characteristics

The measured head-discharge characteristics are shown in Fig.2 in comparison with those of the same pump using water as working fluid(8). In spite of the difference in the Reynolds number, both results showed good coincidences with each other over the discharge ranges smaller than the discharges at the maximum heads. Considering those facts, the results of the present experiments were examined referring to the oil flow patterns obtained in the experiments with water as working fluid.

Pressure Distribution on Blade Surfaces and Velocity and Pressure Fields around Impeller

For the convenience of investigating the working condition of impeller blades and its relation to the flow around the impeller, the pressure distributions on blade surfaces were represented in the map of isobars (full lines) on each surface in comparison with the oil-flow pattern (broken lines) at each flow coefficient and are shown in Fig.3(a)∿(f) for the impeller A and Fig.5(a)∿(c) for the impeller B. Also, the measured results of the radial distributions of velocity and pressure at each two points up- and downstream the impeller are shown in Fig.4(a)∿(f) for the impeller A and Fig.6(a)∿(c) for the impeller B, at corresponding flow coefficients to the isobars maps. In the figures, thin full lines express stream lines at an interval of the same flow rate calculated by using c_m, and one and two dotted chain lines correspond to a half and a quarter flow rate respectively.

Impeller A.- At ϕ=0.194 near $\phi_{\psi max}$, the flow coefficient of maximum head, isobars on the suction and pressure surfaces indicate a normal working condition of the blade at a discharge smaller than one of maximum efficiency, except in the vicinity of blade tip on the suction surface, where the negative peak pressure just behind the leading edge is

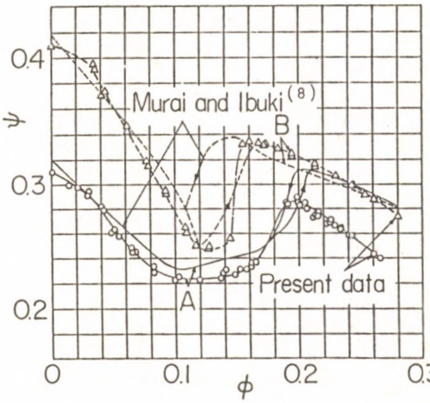

Fig. 2 Characteristics of pump

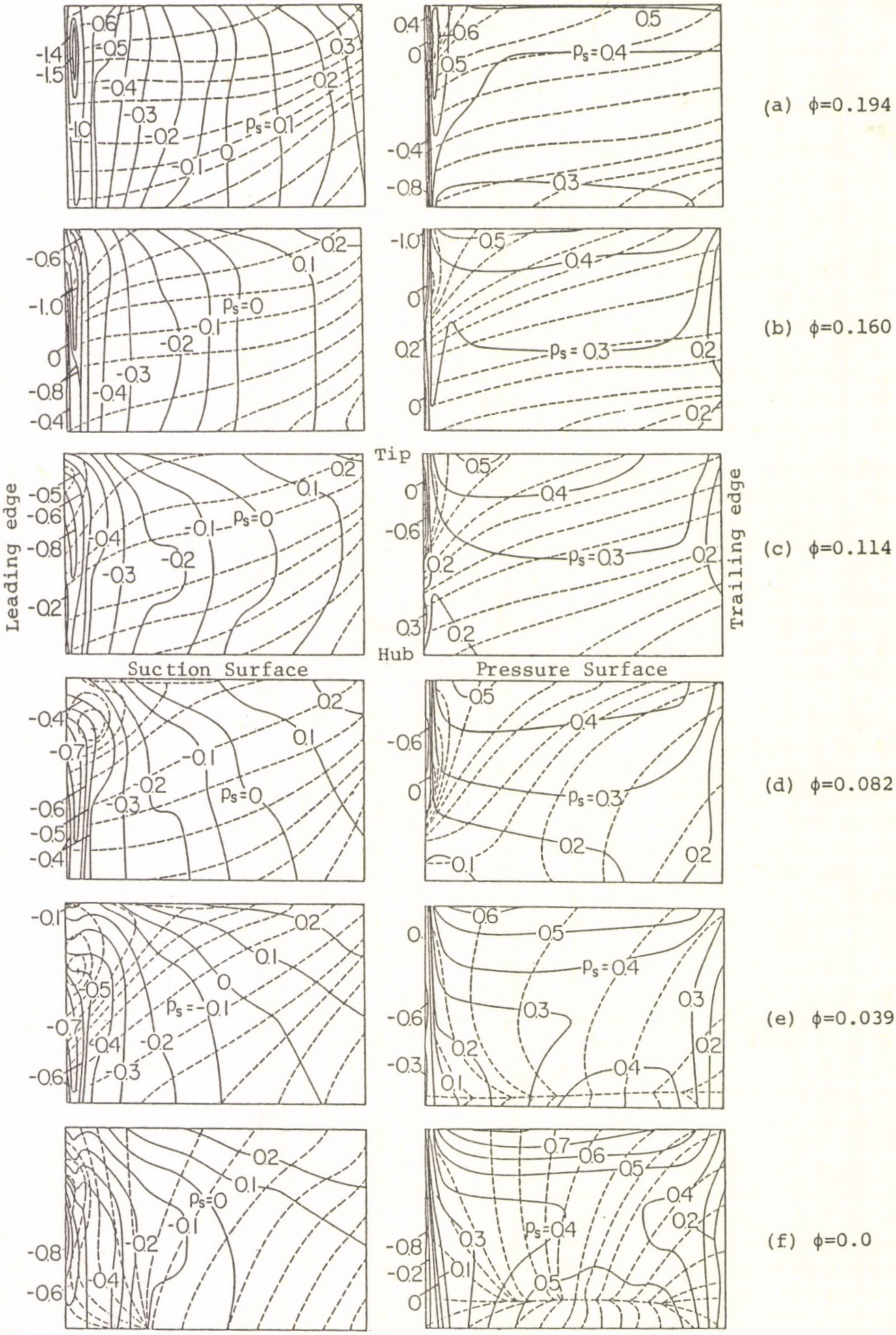

Fig. 3 Pressure distribution and oil-flow patterns on blade surfaces, A

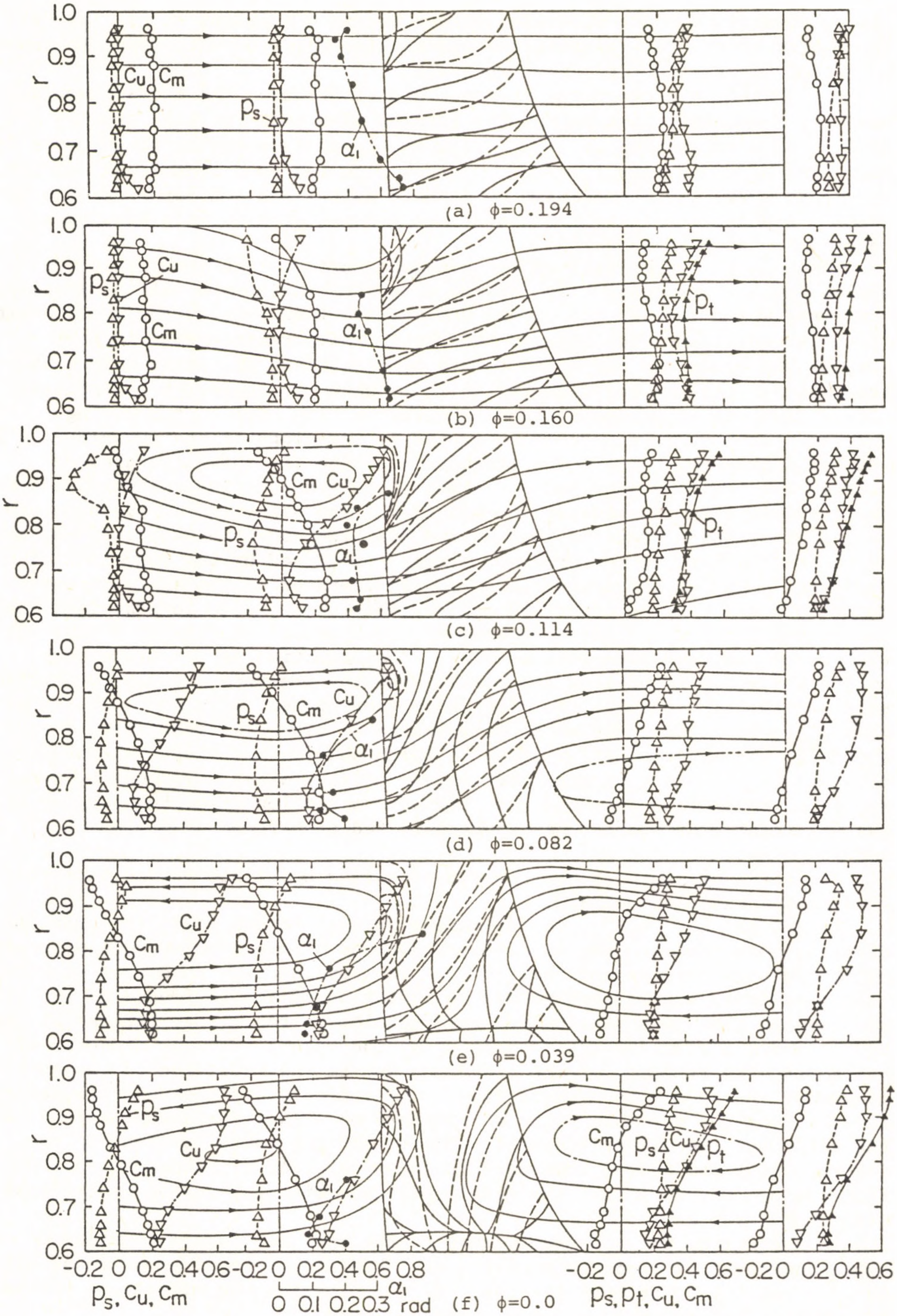

Fig. 4 Distributions of velocity and pressure, and stream lines, A

rising upwards, and the chordwise rising pressure gradient is the larger, the nearer to the tip, so that isobars incline forwards with upwards, showing a loss of circulation due to a tip stall.

At ϕ=0.160, the chordwise pressure distribution on the suction surface has lost a negative peak behind the leading edge near the tip, showing a leading edge separation of flow. Into the separation region fluid comes from the lower side and gets a little pressure rise due to a centrifugal effect of the blade work, as is expressed by isobars being inclined forwards with upwards. And a part of the fluid near the leading edge is made flow back towards the suction side.

While on the upper half of the pressure surface, the isobars in the narrow region just behind the leading edge show the upward falling pressure gradient, which induces the upward and reverse flow towards the suction side [9]. The adjoining flow outside the suction-side reverse flow is bent towards the blade tip and bumps to the inner surface of casing before it reaches the trailing edge, during which passage it receives a centrifugal effect from the blade and a stagnant effect of its bump to the casing. However, the latter is reduced chordwise as the slope of the outward flow is reduced chordwise, to give the pressure near the tip a falling gradient towards the trailing edge and a maximum in a fore position, which divide the reverse flow from the passing through flow. The reduction of the absolute values of pressure near the leading and trailing edges on both surfaces and on the middle part of the pressure surface is caused by the reduction of the incidence angle of the approaching flow accelerated in the axial direction owing to a loss of the effective area by the suction-side reverse flow and the reduction of the static pressure of the approaching flow by a pressure loss in the suction-side reverse flow. The reduction of the blade work except the vicinity of tip, associated with the pressure loss in the suction-side reverse flow results the steep reduction of head with the decrease of ϕ from $\phi_{\psi max}$ to 0.160. The working mechanism of blades written above corresponds to the experimental result[10] which showed that when the approaching flow was kept to have no pre-rotation and uniform axial component by separating from the suction-side reverse flow with a suction ring, the pumping head was not reduced at the discharge where it had been reduced without the suction ring.

The total pressure at the rearest measuring point has become inclined to increase radially outwards.

At ϕ=0.114 near $\phi_{\psi min}$, the discharge at the minimum head, the pressure distributions indicate the downward extentions of the leading edge separation on the suction surface and the suction-side reverse flow on either surface, which, however, are suppressed by the reduction of the incidence of the approaching flow just outside the reverse flow to the blade, because it has been given a circumferential component by the reverse flow in a degree of overcoming the increase of the incidence due to the reduction of the axial component caused by the reverse flow. The reduction of incidence causes the reduction of the absolute value of pressure on either surface near the leading edge, but the circumferential velocity and the total pressure on the delivery side are rather increased in the upper half of blade due to the increase of prerotation in the middle part associated with the centrifugal effect near the tip.

In the bottom part, caused mainly by the radially inward increase of the axial component of approaching flow, the absolute value of pressure on either surface and the blade work are reduced, which causes the reductions of the circumferential velocity and the total pressure.

The increase in the upper half and the decrease in the lower half of the blade work with decreasing discharge are almost canceled with each other in this discharge range. But the gradient of total pressure at the delivery side rising upwards increases with decreasing discharge, and generates the the reverse flow from the delivery side towards the blade[11]. A small rise of pressure near the hub and trailing corner on the pressure surface is considered to owe to the reverse flow.

At $\phi=0.082$, where the head-discharge characteristics has become rising, the pressure distribution on the pressure surface is changed rather markedly. The region of suction-side reverse flow extends downwards suddenly for the decrease of the discharge from $\phi=0.114$ to 0.082, and the stagnant region at the blade tip is pushed forwards by the passing through flow, which is bent upwards so strongly by the delivery-side reverse flow that even the flow approaching the blade through the nearest part to the hub bumps to the inner surface of casing before it reaches the trailing edge. And the whole of passing through flow receives the enough energy by the centrifugal effect of blade work to be delivered against the head.

While on the suction surface, the downward extension of the leading edge separation and the reduction of the absolute value of negative pressure near the leading edge in the middle and bottom parts of the blade progress further, and most of the isobars become to incline forwards with upwards in the whole surface.

The foregoing changes of the pressure distribution on either surface and the average flow pattern around the blade progress with the decrease of discharge beyond $\phi_{\psi min}$ to the shut-off state.

Impeller B.- At $\phi=0.152$ near $\phi_{\psi max}$, the isobars on the suction surface are almost parallel to the swept-back leading edge, and there exists the pressure gradient falling radially downwards, which is apt to induce a secondary flow radially downwards against the centrifugal force acting on the boundary layer. Accordingly the accumulation of the boundary layer to the blade tip near the trailing edge is suppressed so that a tip stall hardly occurs until ϕ is reduced to less than $\phi_{\psi max}$ of the impeller A.

At $\phi=0.121$ near $\phi_{\psi min}$, the pressure distributions change much from those at $\phi=0.152$. On the top part of the suction surface, the leading edge separation extends fairly downwards, and the maximum pressure near the tip and trailing corner is reduced but is still higher than that on the impeller A at $\phi=\phi_{\psi min}$. On the lower half of the suction surface, the absolute value of negative pressure near the leading edge is reduced and the chordwise rising pressure gradient is also reduced, which indicate the reduction of the blade work on the lower half, similarly to the impeller A.

On the pressure side, the isobars become inclined forwards with upwards, and the inclination is the smaller, the upper. The pressure rise towards the tip is generated similarly to the impeller A, but as the inclination of the passing through flow is relatively large and remains as it is owing to the chordwise breadth of the suction-side reverse flow and the sweep of the blade, the pressure near the tip is kept high until the trailing edge and a loose maximum exists at rearer position, dissimilarly to the impeller A, which causes the large-scale reverse flow towards the suction side. The increase and decrease of the blade work on the top and bottom parts, repectively bring the upward rising gradient of total pressure in the delivery side of the impeller, which causes the delivery-side reverse flow though it has not reached the trailing edge yet. The reduction of the blade work in the whole height causes the reduction of ψ.

At $\phi=0.097$, in the discharge range of the rising characteristics, the delivery-side reverse flow has reached the trailing edge. But its effects can be recognized only near the bottom and trailing corner on either surface, and hardly come up to the upper half of the blade. In the case of the impeller B, the growth and approach of the delivery-side reverse flow to the

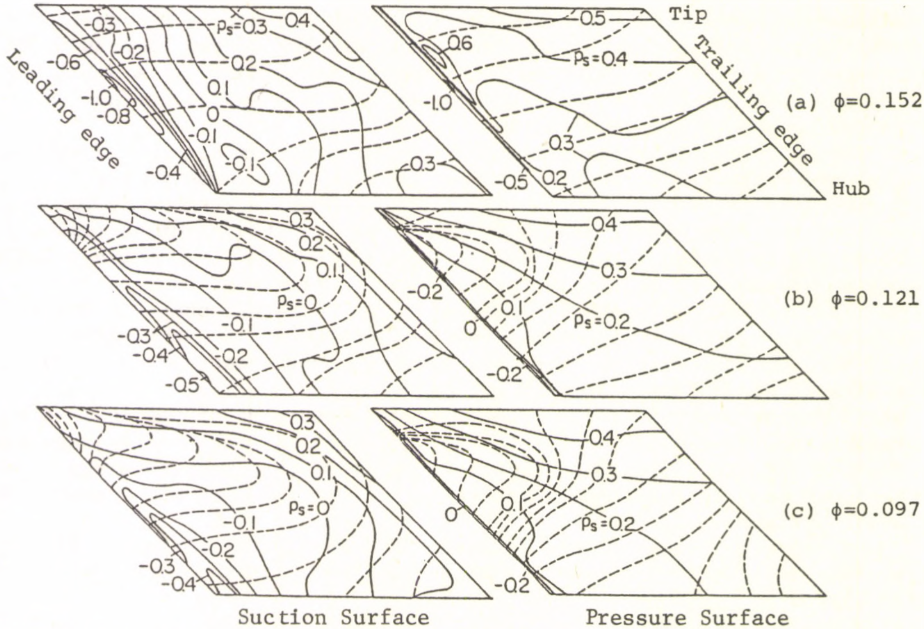

Fig. 5 Pressure distribution and oil-flow patterns on blade surfaces, B

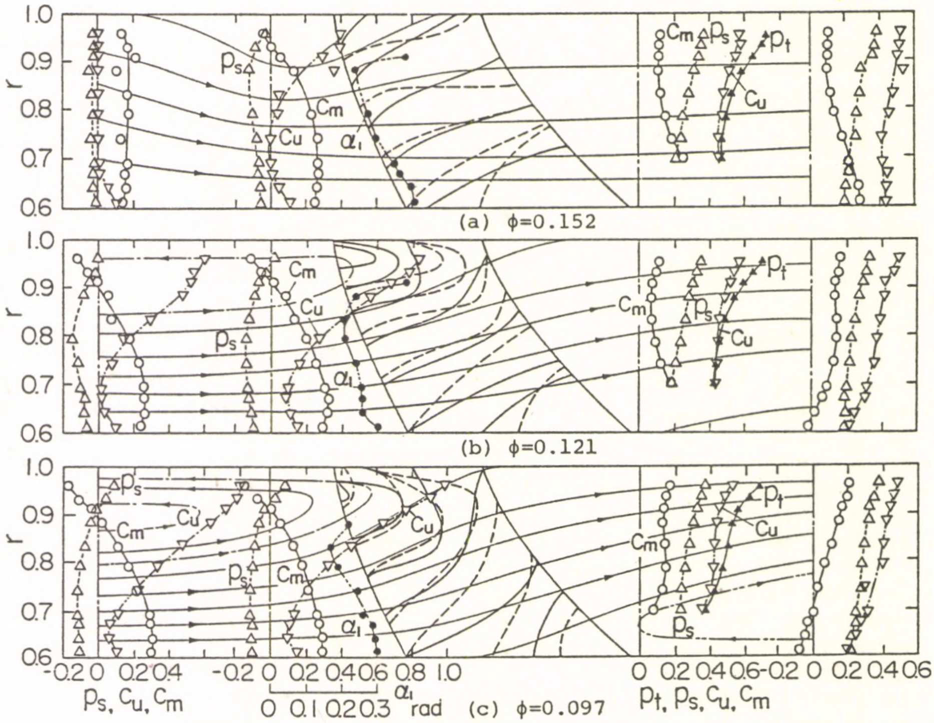

Fig. 6 Distributions of velocity and pressure, and stream lienes, B

blade with decreasing discharge cause only the growth of the suction-side reverse flow and hardly change the flow pattern of the passing through flow directly in the vicinity of blade near $\phi_{\psi min}$.

Generation Mechanism of Reverse-Flow Characteristics

Through the foregoing investigations, a flow pattern around a flow channel between blades in the discharge range where a head-discharge characteristics behaves rising with decreasing discharge is considered as follows; fluid enters a flow channel through the middle and bottom parts near the suction surface of a blade and then the bottom part near the pressure surface of the succeeding blade, and, though partly flows back towards the suction side, mostly bumps to the delivery-side reverse flow which is covering the area connecting the upper part near the trailing edge on the pressure surface of the preceding blade to the lower and rear part of the pressure surface of the succeeding blade through the vicinity of the inner surface of casing near the delivery side of the preceding blade and underneath the delivered passing through flow near the succeeding blade. And the part of fluid having entered through the vicinity of the suction surface of the preceding blade is pushed back towards the suction side through the top and fore part of the flow channel together with the reverse flow from the vicinity of the leading edge of the pressure surface of the succeeding blade, because it has not been given enough energy by the blade to break through the delivery-side reverse flow towards the delivery side. The rest part of fluid having entered the flow channel through the vicinity of the bottom part of the pressure surface of the succeeding blade is given enough energy by the blade work to pass towards the delivery side through the top and rear part of the flow channel together with the delivery-side reverse flow, and only the former is delivered.

Accordingly, it is necessary for a head to increase with decreasing discharge the radially outward component of the passing through flow, which is caused by either the suction-side reverse flow, or the delivery-side reverse flow, or both, is enlarged with decreasing discharge. A suction-side reverse flow promotes a blade work in the upper half but reduces it in the lower half, and can never realize a rise of head by itself, unless a delivery-side reverse flow is associated. Then it can be concluded that a growth with decreasing discharge and a generation of a delivery-side reverse flow are the sufficient conditions for a generation and a beginning of a reverse-flow characteristics, respectively.

CONCLUDING REMARKS

An experimental research on an axial-flow pump was conducted, and pressure distributions on the impeller blades and on the casing as well as velocity and pressure distributions in the stream before and behind the impeller were measured and compared with oil-flow patterns on the impeller blades, the inner surface of casing and the hub. Through the experimental results a working mechanism of impeller blades and its relation to flow patterns around a flow channel between blades at partial discharges smaller than one of maximum head were clarified. The main items deduced from the present research can be summerized as follows:

(i) Blade works, velocity and pressure fields around blades and their correlation in the discharge range smaller than one of maximum head were presented.

(ii) A suction-side reverse flow reduces a head by itself, but increases a head when associated with a delivery-side reverse flow.

(iii) A sufficient condition of generating a head-discharge characteristics rising with decreasing discharge is the generation of a delivery-side reverse flow growing with decreasing discharge.

NOMENCLATURE

c_m = (axial velocity)/U_a $\quad$ c_u = (circumferental velocity)/U_a

P_1, P_2 : static pressure at measuring point P_1, P_2 in Fig.1,

P_s : static pressure, $\quad$ P_t : total pressure,

$p_s = (P_s - P_1)/\frac{\rho}{2}U_a^2$ $\quad$ $p_t = (P_t - P_1)/\frac{\rho}{2}U_a^2$

$r = R/R_a$ (R: radius, R_a: radius of impeller at blade tip),

U_a : rotation velocity of impeller blade at tip,

α_1 : incidence angle of approaching flow to blade,

ρ : density of working fluid,

ϕ : flow coefficient,

ψ : head coefficient.

REFERENCES

(1) "A Report of Research on the Performance in Partial Flow Region of Turbomachinery", Jour. Japan Soc. of Mech. Engrs., 69-568 (1966), 566.

(2) "Report of Researches on the Improvement of Performance in Partial Flow Region of Turbomachinery., ibid., 72-604 (1969), 631.

(3) Toyokura, T., "Studies on the Characteristics of Axial-Flow Pumps (Part 1, General Tendencies of the Characteristics of Pumps)", Trans. Japan Soc. Mech. Engrs., 26-168 (1960), 1069.

(4) Murai, H., "Oil Film Patterns and Their Relation to Characteristics of an Axial-Flow Pump at Low Flow Rate., Jour. Japan Soc. Mech. Engrs., 70-578 (1967), 359.

(5) Hironaka, K., "Flow in the Deria Pumpturbine", Proc. 2nd Int. Japan Soc. Mech. Engrs. Symp., 1 (1972), 139.

(6) Murai, H. and Takeuchi, H., "Observations of Cavitations and Their Application for Analysis of Flow Patterns in an Axial-Flow Pump at Partial Discharge", ASME Paper, 73-FE-11 (1973).

(7) Toyokura, T., "Reverse Flow Characteristics of Axial-Flow Pumps", Jour. Japan Soc. Mech. Engrs., 64-507 (1961), 602.

(8) Murai, H. and Ibuki, S., "Research on Axial-Flow Turbomachinery with Blades Having Swept-back or Swept-forward Angles/Report 2. Experimental Research on Axial-Flow Pump With Swept-forward Blades". Mem. Inst. High Speed Mech., Tohoku Univ., Japan, 47-415 (1981) 143.

(9) Toyokura, T. and Kubota, N., "Studies on Back-Flow Mechanism of Turbomachines (Part 1, Back-Flow Mechanism to the Suction Side of Axial-Flow Impeller Blades)", Bulletin of JSME, 11-43 (1968), 147.

(10) Murai, H. and Narasaka, T., "Working Mechanism of Suction Ring and Effects on Its Geometry", Journal of Fluids Engineering, Trans. ASME, Ser. I, 95-4 (1973), 505.

(11) Pfleiderer, C., "Die Kreisel Pumpen", 4th Aufl. (1955), 131, Springer, and Ishihara, T. and Tahara, H., "On Characteristics of Axial Flow Pump", Trans. Japan Soc. Mech. Engrs., 18-66 (1952), 131.

STANDARDIZATION OF FIELD TESTING

OF

INDUCED DRAFT COOLING TOWER FAN

K. S. MURTHY, S. J. BASU, SUBIR KAR.

ABSTRACT :

The aim of this paper is to suggest a standard for field testing of cooling tower fans so as to improve the standards in fan industry. The paper also enumerates the suggestions for the standardization of field testing of cooling tower fans. The test procedure outlined in this paper protects the installation owners against any improper operation of the fan.

1. INTRODUCTION :

The industrial growth of a country depends mainly on the power generation capability. In India, with increasing demand of power, a large number of power stations are being built using a recirculating type of cooling system with induced draft cooling towers to carry away the heat from the condenser. The induced draft cooling towers essentially have axial flow fans of large sizes of the order of 5 meter dia. and above. The fertilizer plants, process industries and captive power plants make use of induced draft cooling towers in which large diameter axial flow fans are installed. The energy crisis all over the world has made demand on the fan industry to produce more efficient fans.

In a typical 210 MW thermal power station, 36 Nos. of 7.315 mtr. dia. fans, each consuming 40 KW power are operated continuously. All these fans typically handle humid air and have a normal operating capacity of the order of 2 x 10^5 NM^3/Hr. of air at pressure drop values of the order of 6 to 10 mm WG. These fans operate continuously for 8760 hours per year. In India, the authorities inviting bids for tenders of cooling towers levy a penalty of about 1500 U.S. Dollars for each excess KW consumed by each fan, for the purpose of tender evaluation. Hence the cooling tower designers and fan manufacturers are trying to economically optimize their designs. The authorities have to make a judicious selection of the cooling tower fan manufacturer. The available standards viz. IS:3588 1966 (Ref.1) or BS:848: Part 1: 1963 (Ref.2) - suggest the test codes for either laboratory evaluation of performance or field testing of mine fans which are not cooling tower fans. As such, there is no standard available for the cooling tower fans.

The purpose of conducting a field test on fan system installation generally falls into one of the following categories :

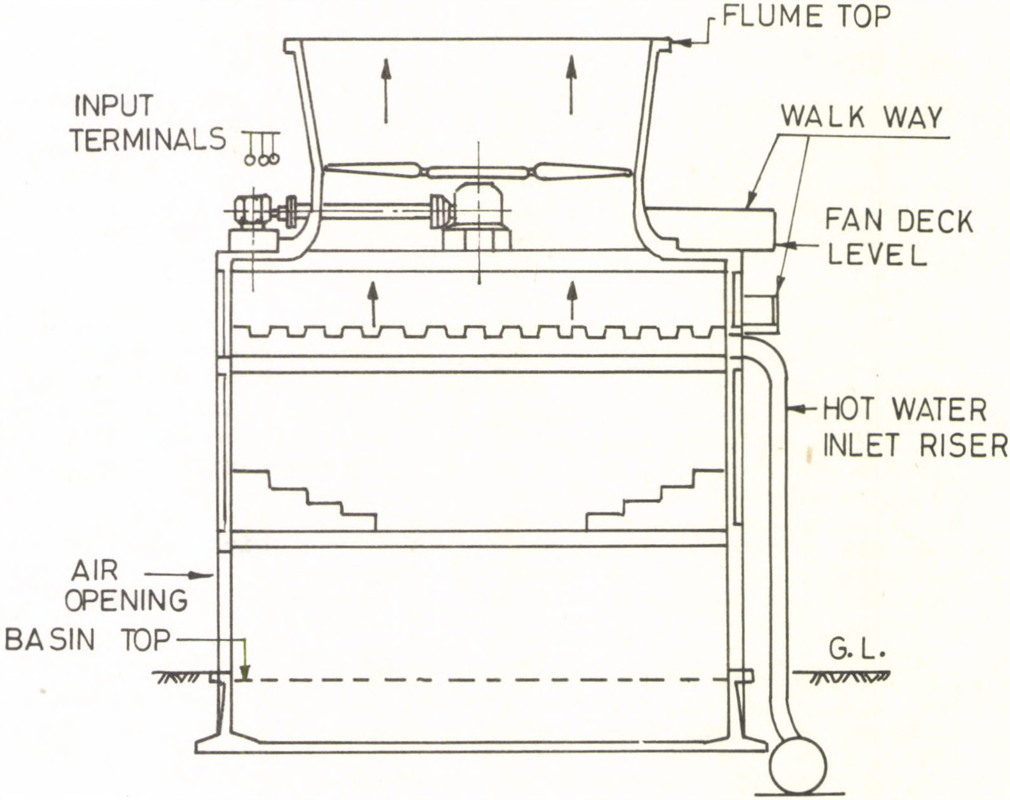

FIG. 1. CROSS SECTION OF A CELL OF A TYPICAL INDUCED DRAFT COOLING TOWER

1) The field test is conducted as a part of sales agreement between the owner and the manufacturer for the purpose of verifying the guaranteed or quoted performance. This can be called Acceptance Test .

2) The field test is conducted sometimes as a proof of performance, when the installation owner feels that the fan is not operating at the specified performance.

When field tests are to be conducted for any of the above mentioned purposes, it has become difficult to set a test procedure in the absence of any standard. Hence, there is a need for a simple, accurate and practical method of evaluating the fan performance. This paper attempts to provide a guideline for a testing procedure, including suggested instrumentation under field conditions based on the experience of the authors. The authors have drawn up the procedure based on the ASME Power test codes (Ref.3) and cooling tower institute, USA,(Ref.4) test bulletins in formulating the proposed test procedure.

2. FAN PERFORMANCE :

The fan performance is a statement of fan flow rate, fan total or static pressure and fan power input at a stated fan speed and air density. The fan air density is the density at the fan inlet. The fan flow rate is the volume flow rate at this density.

3. PRELIMINARY OBSERVATIONS :

Before the actual test is conducted, some simple checks are to be made on the fan: the anti-camber face of the blade has to be on the leaving air side. The direction of rotation of fan should be as suggested by the manufacturer. The fan tip clearance should be checked to satisfy the manufacturer's recommendation. The clearances, if excessive, would adversely affect the fan performance. The barometric pressure has to be found from the local power plant which is quite accurate. Otherwise, the temperature compensated aneroid barometer can also be used.

The fan speed is generally very difficult to measure due to the size of the fan and actual physical limitation to use stroboscopes. The motor shaft speed can be measured with a tachometer having an accuracy better than 1% . Then by using the gear ratio of the gear box, the fan speed can be calculated. The fan blade angle can be measured at the point of the blade recommended by the manufacturer using a bevel protractor alongwith spirit level and a straight edge. The tracking of the blades should be checked for consistency in the fan blade angles.

4. PERFORMANCE PARAMENTERS AND INSTRUMENTS :

The air flow rate, the static pressure, the power input, the air density and the wind conditions are the various parameters

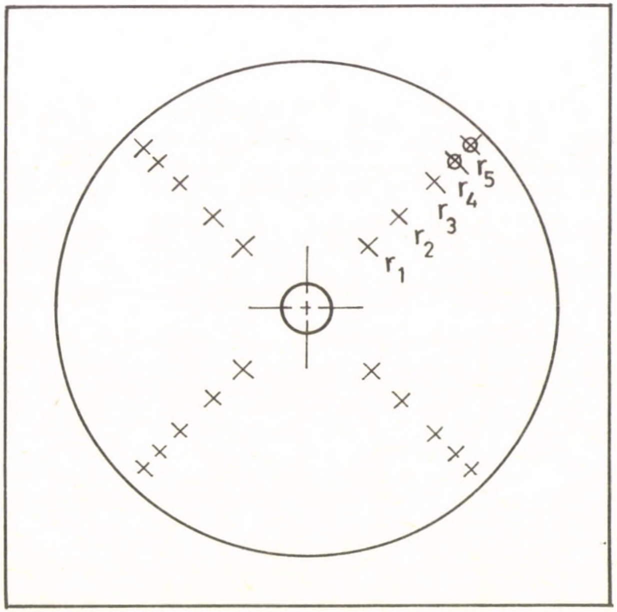

$r_1 = 0{\cdot}316\,R$; $r_2 = 0{\cdot}548\,R$; $r_3 = 0{\cdot}707R$; $r_4 = 0{\cdot}837R$

$r_5 = 0{\cdot}948\,R$

FIG. 2 .LOCATIONS FOR VELOMETER READINGS

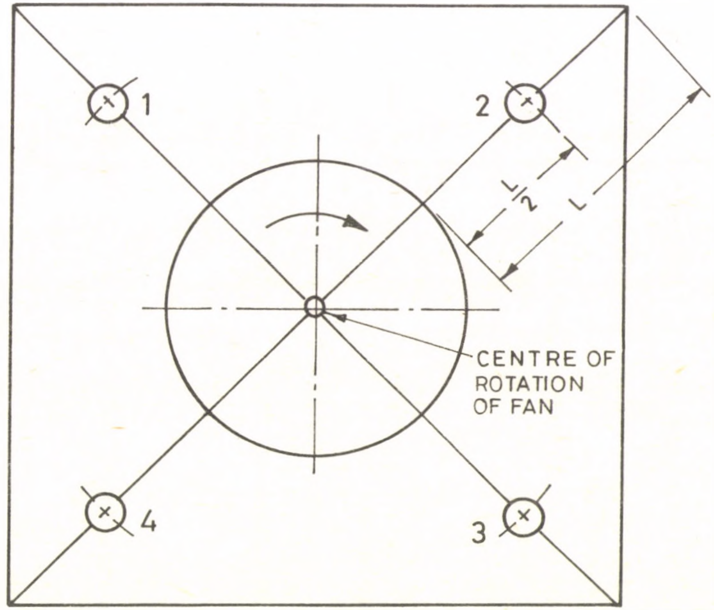

FIG. 3 .STATIC PRESSURE MEASUREMENT LOCATIONS

required to be measured for the fan performance testing. Each parameter needs a different type of instrument.

4.1 Flow Rate :

The pitot tube is generally used for velocity measurement but is very sensitive to yaw angle. The air flow can be measured conveniently with a photoelectric air flow meter which is essentially a rotating-vane type anemometer with a pointer display on a meter connected to the anemometer with a long wire. This anemometer is also known as velometer. The instrument is quite accurate at velocities from 1.5 - 15 meter per second which cover the range required in cooling towers. The anemometer is negligibly affected by the changes in yaw angle and/or densities - other than calibrated. The Table -1 shows the corrections for anemometer yaw angles and the tolerance of changes in density.

Table - 1.

a)

YAW ANGLE (Degrees)	5	10	15	20	25	30
CORRECTION (Per cent)	-0.10	-0.50	-1.10	-2.00	-3.00	-4.00

b) Anemometer Tolerance of changes in Air Density

Velocity (m/sec)	1.50	3.0	6.0	9.0	d = test density
d/dc,(Max. for 1% error)	1.05	1.10	1.21	1.32	dc = calibration density.

An extension rod at the end of which the anemometer is clamped is required to traverse the anemometer on discharge side of the fan. The traverse location and test procedure are outlined in Section 5. The anemometer should be calibrated in a windtunnel against a pitot - tube for velocity measurement and the calibration chart should be used alongwith the anemometer to correct the readings.

4.2 Static Pressure :

The static pressure readings are very low and are generally 15 mm WG or less. The inclined tube manometer is best suited for the measurement of static pressure. The static pressure of the fan is the pressure developed by the fan to overcome the system resistance. The fan has to deliver the air flow against the system resistance by producing an equal amount of static pressure. The static pressures are measured beneath the fan and so are negative (lower than atmospheric) and in most cases are all that need to be taken. The inclined tube manometer should have a zero adjustment, a built in spirit level and a slope of atleast 10:1 to measure 0.1 mm WG. The manometric fluid may be kerosene and the graduations of the manometer may be made to give pressure readings directly in mm water guage. The U - tube manometer is not recommended, as an error of 1 mm on a 10 mm measurement is a 10% and cannot be tolerated. A probe will be required alongwith a manometer to insert it beneath the fan through the deck of the tower. A 6 mm dia. polythene tubing of about 10 mtr. length will enable to leave the inclined tube at one point while the probe is inserted in various locations. The suggested locations for pressure measurement are given in Section 5. The inclined tube manometer is a primary instrument and hence does not need any calibration.

4.3 Power Input :

The Cooling Tower fan assemblies are usually driven by an electric motor through a propeller shaft and a gear box as shown in Fig.1. The power input to the fan can be found out by knowing the individual efficiencies of the motor and the gear box and measuring the power input to the motor. The power input to the motor can be measured either by a three phase wattmeter or two single phase wattmeters. If neither of these is available, a voltmeter, ammeter and power factor meter must be used. All these meters should be calibrated and should have an accuracy of 1% full scale reading or better.

4.4 Air Density :

The discharge air density of fan can be calculated by knowing the atmospheric pressure, the wet and dry bulb temperatures of the fan discharge. The psychrometer can be conveniently used for this purpose. The scale divisions of no greater than 0.5 C should be used. It is quite difficult to measure the dry bulb temperature quite accurately as the fan discharge has free water droplets (due to drift loss) in the fan air stream. However, the percentage error in air density for a 1^{o}c error in dry bulb reading is extermely small (approximately 0.2%) and need not cause any concern.

4.5 Wind Velocity :

The wind has the greatest external influence on a test and the field test should not be attempted under high wind or gusty conditions. The field tests should preferably be conducted in the early morning or late afternoon when the wind velocity is low and reasonably steady. The wind velocity should not exceed 4.5 meters per second. If the wind velocity is greater than 75% of the fan average outlet velocity, the test should be avoided (Ref.4).

5. FIELD TEST PROCEDURE :

The various parameters that affect the fan performance are measured with the instruments specified in section 4. The method of testing will now be dealt with in detail in this section.

5.1 Air Flow Rate :

The volume of air (m^3/Hr.) delivered by the fan will be given by the product of the outlet velocity as measured by the anemometer and the area of discharge. The cooling tower fans essentially have a recovery stack (diffuser section) at the outlet. The large fans of 5.75 mtr. diameter and above have a recovery stack height of more than half of the diameter. Hence the entire area of the stack above the plane of the blades could be used as the discharge area. At a point 1.5 mtr. above the fan blade level, the discharge area may be divided into five equal areas. The radii of the centers of each area can then be found out. Two stack diameters at right angles to each other are to be chosen. The radii of the five equal areas would then be : $r1 = 0.316\ R$, $r2 = 0.548\ R$, $r3 = 0.707\ R$, $r4 = 0.837\ R$, $r5 = 0.948\ R$, as shown in Fig.2. The discharge from the fan has varying amounts of rotational component and so is not truly axial. The fan stream tends to loose some of this rotational component at a point farther away from the fan blade level. Hence, a distance of 1.5 mtr. above fan blade level is chosen as the location of anemometer traverse. The inside diameter of the stack is measured for atleast two points 90^o apart at 1.5 mtr. above the blade level. Using the average diameter (D), the discharge area (A) can be calculated. The radii r1, r2, r3 can be calculated knowing average diameter D and hence, average radius R . After the anemometer is traversed at 10 points on each of the two diameters chosen, the reading noted should be corrected for calibration, if any. Since these 20 corrected readings are taken at centers of areas of five equal areas, the average of these readings (m/sec.) multiplied by the fan discharge area in m^2 will give the volume of flow of air (m^3/sec) delivered by the fan. This value multiplied by 3600 gives air flow rate in m^3/Hr.

5.2 Static Pressure :

The static pressure measurements should be taken in the plenum chamber beneath the fan deck area which is as quiet as possible and in plane which is 15 to 30 cms. below the fan stack entry. The 6 mm tubing will have to be inserted through holes drilled at the fan deck level (Fig.1) of cooling tower at four points approximately midway between the base of the fan cylinder and the corner of the cell on the two diagonals of the cell as shown in Fig.3. The inclined tube manometer should be levelled with spirit level and shielded from strong air currents. The readings should be taken at each of the four locations at the beginning and the end of the air flow rate test. The average of these eight readings will be the fan static pressure, if there are no obstructions on the fan discharge.

5.3 Fan Input Power :

The motor input horse power can be calculated by knowing power factor, amperes and voltage in the three phase electrical connection.

$$\text{Motor Power (Input)} = \frac{(\sqrt{3})(\text{Volts})(\text{Amperes})(\text{Power Factor})}{1000} \text{ KW}$$

The impeller power of the fan can be calculated by knowing motor and gear box-efficiencies from manufacturers.

$\therefore$ Impeller Power = (motor power)(gear box Effy)(motor Effy)

The motor efficiency curves are not reliable when operating voltage varies greater than $\pm$ 10% of that specified on motor name plate (Ref.5).

5.4 Fan Air Density :

To measure wet and dry bulb temperatures, the psychrometer can be used at four different points at the fan discharge near the outlet of the stack. These four readings are averaged to get the fan density. By knowing the wet bulb and dry bulb temperatures and barometric pressure, standard tables and psychnometric charts can be used to find out the fan air density.

6. FAN PERFORMANCE EVALUATION :

The fan manufacturer usually submits a fan performance curve for the particular size of fan. The fan performance curve is usually based on standard air density of 1.205 kg/m^3. The field performance test values of air flow, static pressure and impeller power are at the density conditions existing at the fan outlet and so are not at standard density. In order to relate these values to those of the curve, they are to be converted to standard air with a density of 1.205 kg/m^3. The air flow does not need any conversion since the fan is a constant volume machine and the volume handled does not vary with density. Hence, Standard Air Flow (M^3/Hr) = Test Air Flow (M^3/Hr.).

$$\text{Static Pressure (Std.Air)} = \text{Static Pressure} \times \frac{1.205}{\text{Test Density}}$$

$$\text{Impeller Power (Std.Air)} = \text{Impeller Power} \times \frac{1.205}{\text{Test Density}}$$

In order to calculate static efficiency of fan, Air power will be calculated.

$$\text{Air Power} = 2.723 \times 10^{-3} \times \times Q \times Ps \quad \text{KW}$$

Q - Air flow rate (m^3/Hr)

Ps - Static pressure (mm of WG)

$$\therefore \text{Static efficiency} = \frac{\text{Air Power}}{\text{Impeller Power}}$$

In order to calculate the total efficiency of the fan the dynamic or velocity head which is commonly called as Velocity pressure (VP) has to be calculated and added to the static pressure. By knowing the area of traverse,

$$VP = \left[\frac{(Flow)}{(Traverse\ area\ x\ 4.03)} \right]^2 \text{ mm Water}$$

The velocity pressure and the negative static pressure are added arithmetically without considering the sign :

$\therefore$ Fan total Pressure(TP) = Static Pressure + Velocity Pressure.

The total efficiency can be found from the formula with all the factors in standard air :

$$\text{Fan Total efficiency} = \frac{\text{Air Flow X Total Pressure X } 2.723 \text{ X } 10^{-3}}{\text{Impeller Power}}$$

7. DISCUSSION :

The values of air flow rate and static pressure can be used to plot the point on the fan curve which is submitted by the fan manufacturer. This point of intersection of flow and pressure on the curve when extended upwards cuts the impeller power curves of the fan at a particular blade setting angle. This field test operating point can be compared with the guaranteed duty point of the fan manufacturer. The field test operating point generally falls within $\pm$ 5% of the fan curve. These field test values are anyway a far cry from the laboratory tests. However, it should be remembered that the laboratory tests in wind tunnel have a more or less streamlined entry into the test chamber whereas the flow situation in the field is quite opposite. Moreover, the laboratory tests have a controlled tip clearance, whereas in the field, the installations do not have uniform tip clearance and therefore performance is affected to some extent. This also clearly explains the reason for the discrepancy between the guaranteed fan curve point and the field test point.

8. RECOMMENDATIONS :

The suggested instruments, performance test procedure and evaluation of fan performance in the field tests discussed in this paper would help the cooling tower installation authorities in protecting the equipment from malfunctioning as well as the fan manufacturer in proving his claim of the fan performance. It is hoped that this paper forms as a basis for drawing up a ISO standard on field testing of cooling tower fans.

9. CONCLUSIONS :

1. The field testing of cooling tower fans is a new area in which ISO standard has to be drafted.

2. A compliance to this proposed standard by the cooling tower installation authorities and fan manufacturers would go a long way in improving the standards of Fan Industry.

3. The cooling tower installation authorities would benefit to a large extent as the proposed standard would help to test the fan in site and take a corrective measure to improve the cooling tower performance.

4. The proposed standard gives a simple and practical method of field testing of cooling tower fans and protects the cooling tower installation against any improper operation of the fans.

5. The test procedure described in this paper would facilitate the testing of large induced draft cooling tower fans either for performance evaluation or for acceptance tests.

10. ACKNOWLEDGEMENT :

The authors gratefully acknowledge the cooperation and enthusiasm of Mr. M.L. Shishoo, Technical Director, Maharashtra State Electricity Board, Bombay, in conducting various tests on the field in the cooling towers of Nasik Thermal Power Station, Nasik, India for fan performance evaluation. The authors gratefully acknowledge the kind permission given by the Board of Directors of M/s. Recondo Limited, Bombay, India, to publish this paper.

11. REFERENCES :

1. IS : 3588 - 1966 Specification for electrical axial flow fans ISI, New Delhi, India.

2. BS : 848 : (Part II) - 1963 Methods of testing fans for general purpose, including mine fans. BSI, U.K.

3. ASME - PTC - 23 : American Society of Mechanical Engineers, Power Test Codes, U.S.A.

4. CTI Bulletin TPR - 122 : 1962 Fieldtests of fan performance on induced draft cooling tower, CTI, Texas, U.S.A.

5. CTI Bulletin TPR - 127 Cooling Tower fan motors - applications and performance characteristics CTI, Texas, U.S.A.

K. S. MURTHY
Research Scholar,
Mechanical Engineering Department,
Indian Institute of Technology,
Powai, Bombay 400 076, INDIA.

S. J. BASU
Vice President(Development)
Recondo Limited
Sir P. M. Road, Fort,
Bombay 400 001, INDIA.

Prof. Dr. SUBIR KAR,
Mechanical Engineering Department,
Indian Institute of Technology,
Powai, Bombay 400 076. INDIA.

A NOTE ON THE BLOCKAGE OF CYLINDRICAL PROBES

C. K. Ng, and T. B. Ferguson

SUMMARY

An experimental investigation into the effect of projected area and insertion depth on the performance of cylindrical type combination probes.

INTRODUCTION

The standards relating to the measurement of fluid flow in pipes [1,2] give corrections to be used for the blockage effect of the stem of a Pitot-static tube. However neither they nor Bryer and Pankhurst appear to treat this matter for combination probes such as the three hole Pitot-cylinder or the wedge probe which are frequently used in research on turbo-machines. In this type of application the restricted size of the flow passages and the aerodynamic forces acting on the stem may necessitate the use of probes where the blockage effect may be significant.

This present investigation owed its inception to the work of Horsley [4] and in particular that of Jolleys [5]. Jolleys used a 2.8 mm stem diameter wedge probe to traverse the 127 mm diameter inlet section of a multi-Venturi test rig by varying the depth of insertion of the probe from one wall and obtained an apparent velocity profile which was eccentric. After ensuring that the eccentricity of the profile was not a true effect it became apparent that the apparent eccentricity was due to the flow round the probe and it was finally eliminated by the use of a constant blockage probe spanning the whole diameter.

It seemed then that an experimental programme should be carried out on the blockage effects of cylindrical and wedge probes. This study was originally reported by Ng [6] and so far has been mainly concerned with the variation of the pressure, yaw (θ) characteristic of a cylindrical probe as the size and Reynolds number of the probe was varied so that some idea could be obtained of the errors in dynamic pressure measurement in three hole probes when they occupy a significant proportion of the flow cross sectional area. A short excursion was made into the relative blockage effects of cylindrical probes and those with wedge shaped heads.

EXPERIMENTAL EQUIPMENT

The experiments were carried out in a low speed wind tunnel (air speeds up to 60 m/s) with a perspex working section 127 mm square and 457 mm long. The area ratio of the contraction is 20:1.

Two types of cylindrical probe were used, cantilevered probes which could be used at various depths of insertion into the airstream and constant blockage probes which completely traversed the working section.

Each cantilevered probe had a 0.50 mm diameter static pressure tapping drilled normal to its axis at least two probe diameters from the free end which was square. The static pressure tapping in each constant blockage probe was also 0.50 mm diameter and located midway along its length. The cantilever probes could be yawed through $\pm$ 180^{o} and the constant blockage probes through $\pm 90^{\circ}$.

Both sets of probes covered a range of ratios probe diameter to wind tunnel working section side width of 0.025 to 0.15. In addition 30° and 60° wedge probes were used to compare the blockage effect of cylindrical and wedge probes. These probes had a wedge base height and stem diameter of 6.35 mm.

EXPERIMENTAL INVESTIGATION

The wind tunnel was first calibrated. A yaw survey was made and traverses were carried out at working section inlet with each of the test probes in situ to ensure that the probe being tested was not interfering grossly with the tunnel calibration. These traverses showed a maximum variation of 1% of the dynamic pressure from that obtained in the tunnel calibration.

The main part of the work comprised an investigation into how probe circumferential pressure distribution varied with probe diameter and depth of insertion.

The cantilevered probes were each tested when inserted at three different depths. For four of the probes these depths were 38.1 mm, 63.5 mm and 92.55 mm. The largest diameter probe was not inserted less than 49.5 mm into the airstream because of the greater distance of the pressure tapping from the free end of the probe. At each depth the probe tapping was first aligned to the flow before yawing to obtain the probe circumferential pressure distribution. The tests on the constant blockage probes were carried out with the tapping in the centre of the working section.

The relative blockage of the wedge and cylindrical probes was ascertained by a row of static pressure tappings in the tunnel wall upstream from the probe position.

EXPERIMENTAL RESULTS

The constant blockage probes exhibited a blockage effect due to the projected area of the probe and its wake as is seen in Fig. 1. In the region where the static pressure tapping of a combination probe would be placed (about 40°) the static pressure coefficients fall progressively with probe diameter due to the increased acceleration at the same upstream air speed as the probe diameter was increased. In this region of the yaw characteristic the Reynolds number effect was small over the range of probe Reynolds numbers covered by the test (Re_d 6.1×10^3 to 3.7×10^4).

As far as the cantilevered probes are concerned the flow was more complex and the blockage comprises two effects (Figs. 2a and 2b). One is that due to the variation of three dimensional flow over the end of the probe as the insertion was changed. The general result being a depression of the pressure coefficient as both the insertion and the blockage was increased. This effect is reported by Bryer and Pankhurst [3] as having been noticed by Becker [7]. It is a result of considerable practical import and hence worthy of repetition.

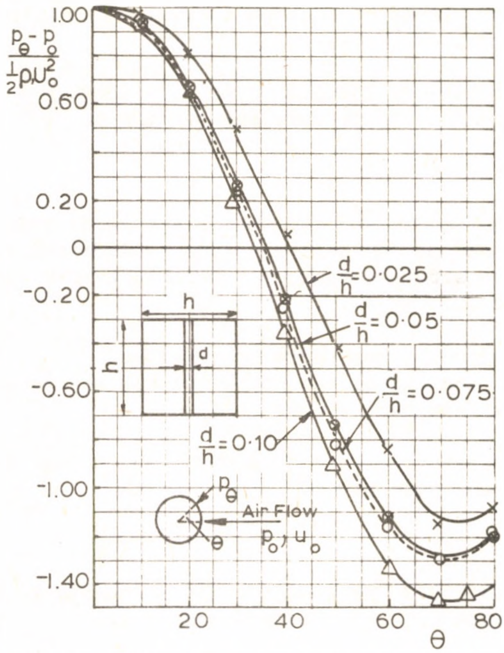

FIG.1. Pressure Distributions for Constant Blockage Probes.
(U_o = 33 m/s) $6.1 \times 10^3 \leq Re_d \leq 3.7 \times 10^4$

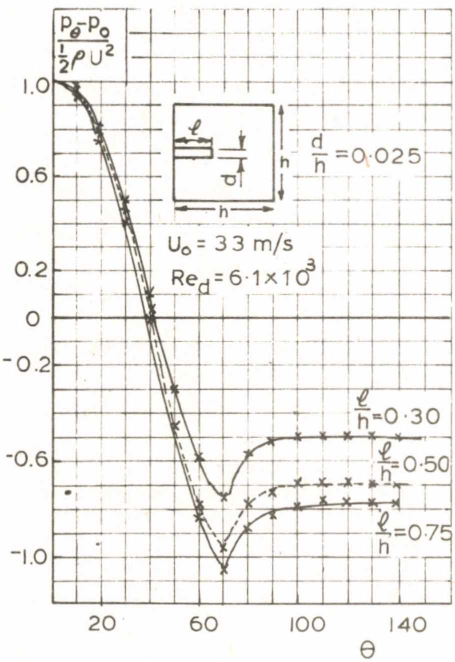

FIG.2a. Pressure Distributions for Cantilever Probe at Different Traverse Positions.

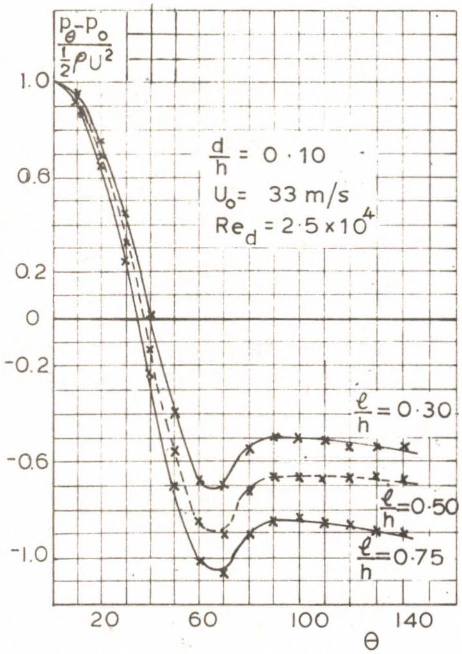

FIG.2b. Pressure Distributions for Cantilever Probe at Different Traverse Positions.

For most of the tests the pressure coefficient was reduced and hence the blockage effect increased at a given insertion depth as the probe diameter was increased.

The comparison between wedge probes and cylinders was of a preliminary nature but to date no clear difference between the two has been found.

CONCLUSION

1) The investigation showed that the pressure distribution characteristics with yaw of constant blockage cylindrical probes are dependent on the probe size and that considerable errors may be obtained if this effect is not allowed for.

2) For cantilevered probes there is an effect due to the three dimensional flow over the end of the probe as well as the wake blockage effect of the constant blockage probes.

3) The tests to date indicate no significant change in blockage between cylindrical and wedge probes.

REFERENCES

1. B.S.1042: Part 2A: 1973 "Methods for the Measurement of Fluid Flow in Pipes" Part 2 Pitot tubes 2A Class A accuracy.

2. ISO 3966 - 1977(E) "Measurement of Fluid Flow in Closed Conduits - Velocity Area Method Using Pitot-Static Tubes".

3. Bryer, D. W. and Pankhurst, R. C., "Pressure-Probe Methods for Determining Wind Speed and Flow Direction", HMSO London 1971.

4. Horsley, D. M., "An Investigation Into the Blockage and Total Head Characteristics of a Wedge Type Probe", B.Eng. Thesis, Univ. of Sheffield, 1969.

5. Jolleys, M., "A Preliminary Investigation Into the Performance of Multi-Venturi Meters", B.Eng. Thesis, Univ. of Sheffield, 1974.

6. Ng, Chee Kong, "An Investigation Into the Blockage Effects of Transverse Cylinder Probes", B.Eng. Thesis, Univ. of Sheffield, 1979.

7. Becker, E, "Beitrag zur Berechnung von Sekundärströmungen, Mitt. Max-Planck - Inst. of Strömungsforchung, Göttingen, 1956, No.13.

Ng, Chee Kong,
Formerly,
Dept. of Mechanical Engineering,
University of Sheffield,
Mappin Street,
Sheffield,
U.K.

Ferguson, T. B.
Senior Lecturer,
Dept. of Mechanical Engineering,
University of Sheffield,
Mappin Street,
Sheffield,
U.K.

ENERGY PROPORTIONS IN CAVITATION WEAR OF MATERIAL

J. Noskievič

ABSTRACT

Mathematical model of cavitation wear of material enables to find the energy proportions in material. Intensity of cavitation is consumed for elastic (reversible) effects in material and for deformations and crumbling of material (non-reversible process). Intensity of cavitation wear of material depends on intensity of cavitation and on elastic properties of material. Intensity of cavitation wear of material is consumed for permanent deformations of material and its crumbling and is consumed during the extension of the area of material damaged by cavitation. Cavitation tests obtain both cavitation properties coefficients of material and also the course of the three components of the intensity of cavitation wear.

1. MATHEMATICAL MODEL OF CAVITATION WEAR

Test of cavitation wear of material are usually demostrated in diagrams $m = f(t)$. Figure 1 shows two typical casses of these courses. If the intensity of cavitation wear is lesser, the damage of material grows together with the growing gradient of courses (Fig. 1 a). A higher intensity of cavitation

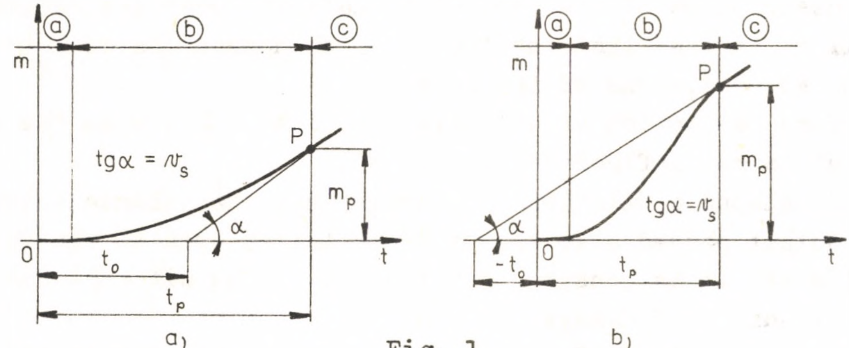

Fig. 1

wear brings a quicker cavitation damage of material. The gradient of the material damage speed grows more quickly, it reaches the peak and falls to the constant value v_s. The inflexional point on the curve $m = f(t)$ corresponds the maximum material damage speed. We may note three stages of development on the course of cavitation wear of material, as it is e.g. in [1] and in the figure 1 :

a/ Incubation period "a" in which the cavitation wear of material is negligibly low. In this stage especially plastic deformations pass through in the material and the material hardens. This area of changes in the material grows in the course of time (sometimes even decreases) according to the qualities of the material and according to the cavitation intensity.

b/ The stage of the developing cavitation wear "b" in which some more plastic deformations connected with the material hardening appear, but material crumbling has already been observable. In the course of time bilateral relation between both the effects on material varies. Crumbling of material appears more often. Material hardening and material cavitation resistance were described in detail in [1].

c/ The stage of the developed cavitation material wear "c" is characterized by a constant gradient of material damage. We reach the balanced condition in the cavitation wear which corresponds to the cavitation intensity and the material properties. A mathematical model with two parameters needed for the description of the cavitation material wear was derived earlier. It describes the transient phenomenon between two balanced conditions of the material:

- before cavitation effect, i.e. in time $t = 0$, when the material is not influenced by cavitation
- a developed cavitation wear stage when the balance between the output passed over from the cavitation area to the material where it is consumed for its destroying with the constant gradient of damage sets in.

Mathematical model of the cavitation material wear is described in detail in [2]. It is obtained by solving a differential equation

$$\frac{d^2 v}{dt} + 2\alpha \frac{dv}{dt} + \beta^2 v = I \,, \tag{1}$$

where v is the instantaneous speed of material damage

$$\left(v = \frac{dm}{dt} \right)$$

α is coefficient indicating material ability of plastic deformation

β is coefficient indirectly proportional to material cavitation strength

I is intensity of material cavitation wear which is the physical meaning the quantity proportional to the energy consumed in material for its crumbling and related to time unit and surface unit.

Solving the equation (1) is used for rating material cavitation tests $m = f(t)$ by means of which parameters α, β of material cavitation properties are determined with intensity of material cavitation damage I [3],[4]. This mathematical model can however be used for studying power relations in material damaged by cavitation.

2. INTENSITY OF MATERIAL CAVITATION WEAR

Physical meaning of the members on the left side of equation (1) is the same as that of the right side, i.e. it represents the intensity of particular components of material cavitation wear. Component $I_\beta = \beta^2 v$ represensts intensity of material cavitation wear caused by own crumbling. It is the energy needed for the overpowering cavitation strength of material which is crumbling; the energy is related to time unit and cavited surface unit. Next component $I_\alpha = 2\alpha \frac{dv}{dt}$ gives intensity of material cavitation hardening. It is again a unit energy (related to surface unit damaged by cavitation) consumed in time unit with plastic deformations of material.

The third component $I_m = \frac{d^2 v}{dt^2}$ represents one part of material cavitation wear intensity needed for the extention of cavited material area. The stage of developing cavitation wear brings the change of thickness of the material layer damaged by cavitation; which is penetrated by the power causing the described changes. The change of the material layer damaged by cavitation evokes the need of power which is given by component I_m. It is in substance the criterion of plastic deformations speed extention in material. So the equation (1) may be transcribed as :

$$I_m + I_\alpha + I_\beta = I \tag{2}$$

In non-dimensional form :

$$\frac{I_m}{I} + \frac{I_\alpha}{I} + \frac{I_\beta}{I} = 1 \quad \text{or} \quad i_m + i_\alpha + i_\beta = 1 , \tag{3}$$

where

$$i_m = \frac{I_m}{I} ; \quad i_\alpha = \frac{I_\alpha}{I} ; \quad i_\beta = \frac{I_\beta}{I}$$

are proportional intensities of cavitation wear. The expressions for proportional intensities of cavitation wear are derived from the mathematical model : $\left(\delta = \frac{\alpha}{\beta} ; \tau = \beta t\right)$

$-1 < \delta < 1 \;; \quad (\delta \neq 0) ; \quad \omega = \sqrt{1-\delta^2}$

$$i_m = e^{-\delta\tau}\left(\cos\omega\tau - \frac{\delta}{\omega}\sin\omega\tau\right) ; \quad i_\alpha = 2\,\frac{\delta}{\omega}\,e^{-\delta\tau}\sin\omega\tau ; \quad i_\beta = 1 - e^{-\delta\tau}\left(\frac{\delta}{\omega}\sin\omega\tau + \cos\omega\tau\right)$$

$\delta > 1 \;; \quad \delta_0 = \delta + \sqrt{\delta^2 - 1}$

$$i_m = \frac{1}{\delta_0^2 - 1}\left(\delta_0^2 e^{-\delta_0\tau} - e^{-\frac{\tau}{\delta_0}}\right) ; \quad i_\alpha = \frac{\delta_0^2 + 1}{\delta_0^2 - 1}\left(e^{-\frac{\tau}{\delta_0}} - e^{-\delta_0\tau}\right) ; \quad i_\beta = 1 - \frac{1}{\delta_0^2 - 1}\left(\delta_0^2 e^{-\frac{\tau}{\delta_0}} - e^{-\delta_0\tau}\right) \tag{4}$$

$\delta = 1$

$$i_m = e^{-\tau}(1-\tau) \qquad i_\alpha = 2\tau e^{-\tau} \qquad i_\beta = 1 - e^{-\tau}(1+\tau)$$

$\delta = 0$

$$i_m = \cos\tau \qquad i_\alpha = 0 \qquad i_\beta = 1 - \cos\tau$$

The rate of single components i_m, i_α, i_β varies in time, as it is shown in fig. 2 ($\delta = 0{,}5$; 1 ; 10). In the beginning the material damage is negligibly low and so in time $t = 0$ is $i_\beta = 0$. In the developed stage (right from point P) the whole power is consumed for material crumbling and so in time $t \geq t_p$ is $i_\beta = 1$. Equation (3) may also be rated from the course of cavitation test $m = f(t)$.

Hardening of material and cavited material area extention prevail in incubation period which is goven by the course of quantities i_α, i_m. Their rate reduces in the course of the second stage to the detriment of crumbling rate growing. Intensity of material cavitation wear varies in the course

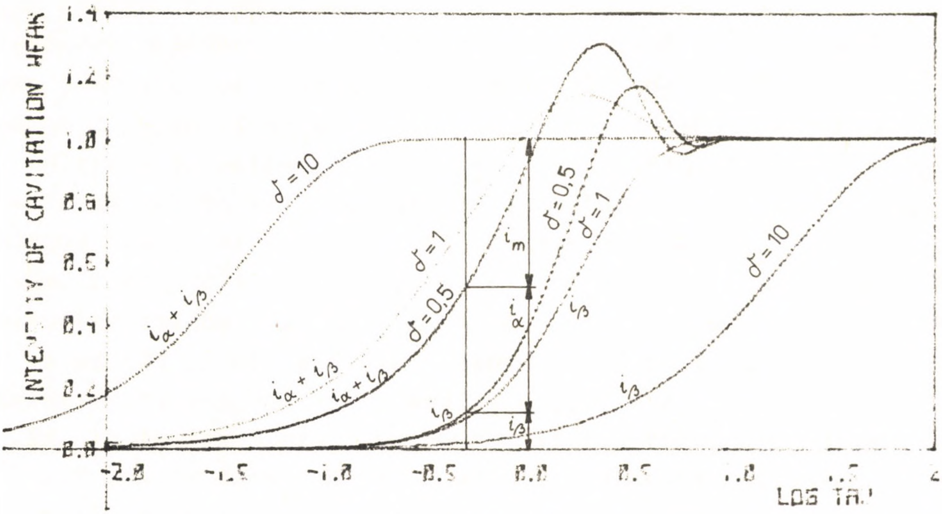

Fig. 2

of cavitation test. It proves the results of material cavitation rated by means of two parameter mathematical model. Time course of cavitation wear intensity may be indicated also by the proportional quantity $i = \frac{I}{I_s}$, where I_s is intensity of material cavitation wear in the developed stage, i. e. in time $t \geqq t_p$. Then $\frac{d\vartheta}{dt} = \frac{d^2\vartheta}{dt^2} = 0$, and from equation (1) $I_s = \beta_s^2 \vartheta_s$.

The course of proportional intensity and material cavitation wear is in figure 3. In incubation period plastic material is given a power multiplexy higher than that in the developed stage of cavitation wear. Material is hardened by cavitation effect, it receives less power and loses ability of plastic deformations.

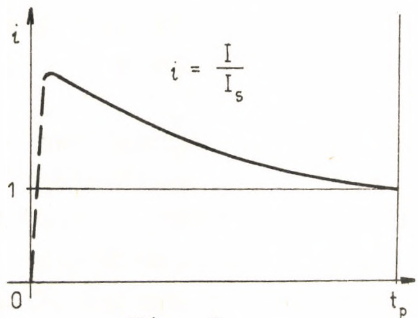

Fig. 3

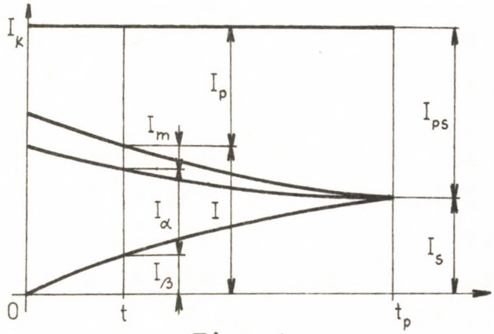

Fig. 4

All the hitherto accounts of power proportions in cavited material were derived with the presumption of constant cavitation intensity. With vibratory facility e.g. the constant cavitation intensity is ensured by constant oscillation frequency, constant amplitude and constant properties of caviting liquid. It must be noted that the third stage of the developed material cavitation wear is typical for its linear course of damage, if the shape of the cavited surface of the model doesn't change essentially, e. g. by making a collar on cavitation specimen in a long-termed test. Diagram in figure 4 gives a survey of power proportions in the course of material cavitation test. Cavitation intensity I_K is constant at the same time. Then one part of I is given to material and is consumed in non-reversible processes, which is the earlier described intensity of material cavitation wear. The second part represents intensity I_p , consumed in elastic deformations of material which are reversible processes. Therefore there is the proportion between cavitation intensity I_K and cavitation wear intensity I : $I_K = I + I_p$ (5)

Analogously there is the proportion for the developed stage of cavitation wear : $I_K = I_s + I_{ps}$ (6)

Cavitation intensity I_K depends e. g. on wave intensity I_v (with vibratory facility), where: [5]

$$I_v = \frac{1}{2} \rho a \omega^2 A^2 = 2\pi^2 \rho a f^2 A^2 , \qquad (7)$$

where

ρ is density of liquid, a is sound speed in liquid,

$\omega = 2\pi f$ is circular frequency, f is oscillation frequency,

A is oscillation amplitude of specimen.

Number of results of the rated cavitation tests brought the proportion for intensity of material cavitation wear I

$$I_s = a \beta_s^m$$

Various materials with various cavitation intensities had their exponent in the scale from $m = 2{,}38$ to $4{,}35$, coefficient from $a = 0{,}00324$ to $1{,}837$. Intensity for elastic material deformations I_p may be expressed e. g. by static tensile strength limit σ_p, e. g. $I_p \sim \sigma_p^2$. With regard to dynamic character of cavitation effect and material fatigue the power dependence is given: $I_p = b\,\sigma_p^n$

There was done the proportion for steel-cast iron, cast-iron and bronze (cavitation test introduced in the report D8 at the conference in Bangalore, India, in 1967, whose author is prof. Varga): $I_K = a\,\beta_s^{2,6285} + b\,\sigma_p^{2,7692}$ (8)

Usage of the described method for the study of power proportions during cavitation test of aluminium is given in diagrams in figure 5. Indication of quantities used in equations corresponds to the indication of quantities in diagrams according to the following table.

quantity indication in diagram	IM	IA	IB	I	A	B	M/MP	T/TP	NI	V/VS
quantity indication in equations	$\dot{i}_m$	$\dot{i}_\alpha$	$\dot{i}_\beta$	i	$\frac{\alpha}{\alpha_\beta}$	$\frac{\beta}{\beta_\beta}$	$\frac{m}{m_p}$	$\frac{t}{t_p}$	$\nu = \frac{m}{v_s t}$	$\frac{v}{v_s}$

Cavitation test was made with vibratory facility with oscillating specimen. At the same time a still (non-oscillating specimen), also aluminium, whose diagram is in figure 6, was subjected to cavitation effects. If we compare the diagrams the influence of the additional tension in specimen, which is caused by its oscillating, is apparent. Cavitation strenght considerably lowers.

3. CONCLUSION

Analysis of power proportions in material cavitation wear enables to evaluate cavitation properties of materials as for their cavitation resistance. A higher part of power for hardening and extention of the area of uspetting prolongs the first stage, i. e. incubation period, and retards development of wear. Application of mathematical model of cavitation wear enables to determine cavitation properties of material and find power proportions in material damaged by cavitation in usually performed cavitation tests.

4. REFERENCES

[1] Noskievič J. : Cavitation strain hardening and cavitation strenght of material
Proc. of the sixth conf. on fluid machinery, Budapest 1979, Vol.2, pp. 751-759

[2] Noskievič J. : Dynamik der Kavitationszerstörung des Werkstoffs
Pumpentagung Karlsruhe´78, Section K 11, Sept. 1978, German Federal Republic

[3] Noskievič J. : Evaluation of cavitation tests (czech)
Conference Hydro-Turbo 1976, Brno, Oct. 1976, Pap. C7.

[4] Noskievič J. : Mathematical model for cavitation damage dynamics of material (in german)
Zeszyty naukowe Politechniki Slaskiej, Gliwice, Poland; Energetyka Z. 66, 1978

[5] Brdička, Samek, Taraba :
Cavitation (in czech), SNTL 1981, Praha

NOSKIEVIČ Jaromír, Prof. Ing. DrSc
Head of the Department of Mechanics
and Fluid Mechanics
Technical University Ostrava
Tř.Vít.Února
CS-708 33 Ostrava-Poruba
Czechoslovakia

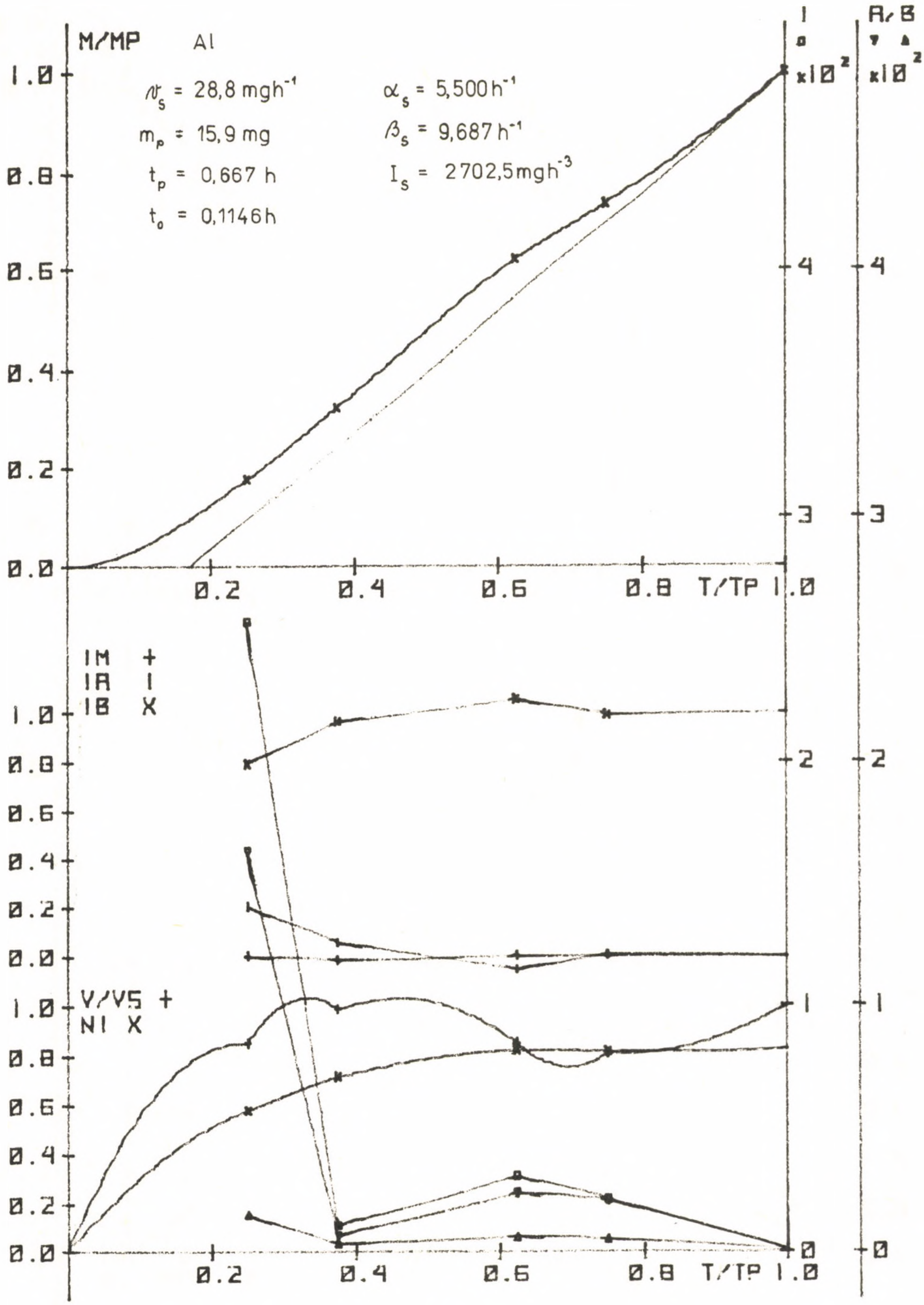
M/MP
Al
ϑ_s = 28,8 mgh^{-1}
m_p = 15,9 mg
t_p = 0,667 h
t_o = 0,1146 h
α_s = 5,500 h^{-1}
β_s = 9,687 h^{-1}
I_s = 2702,5 mgh^{-3}
I
x10^2
A/B
x10^2
T/TP
IM +
IA I
IB X
V/VS +
NI X

Fig. 5

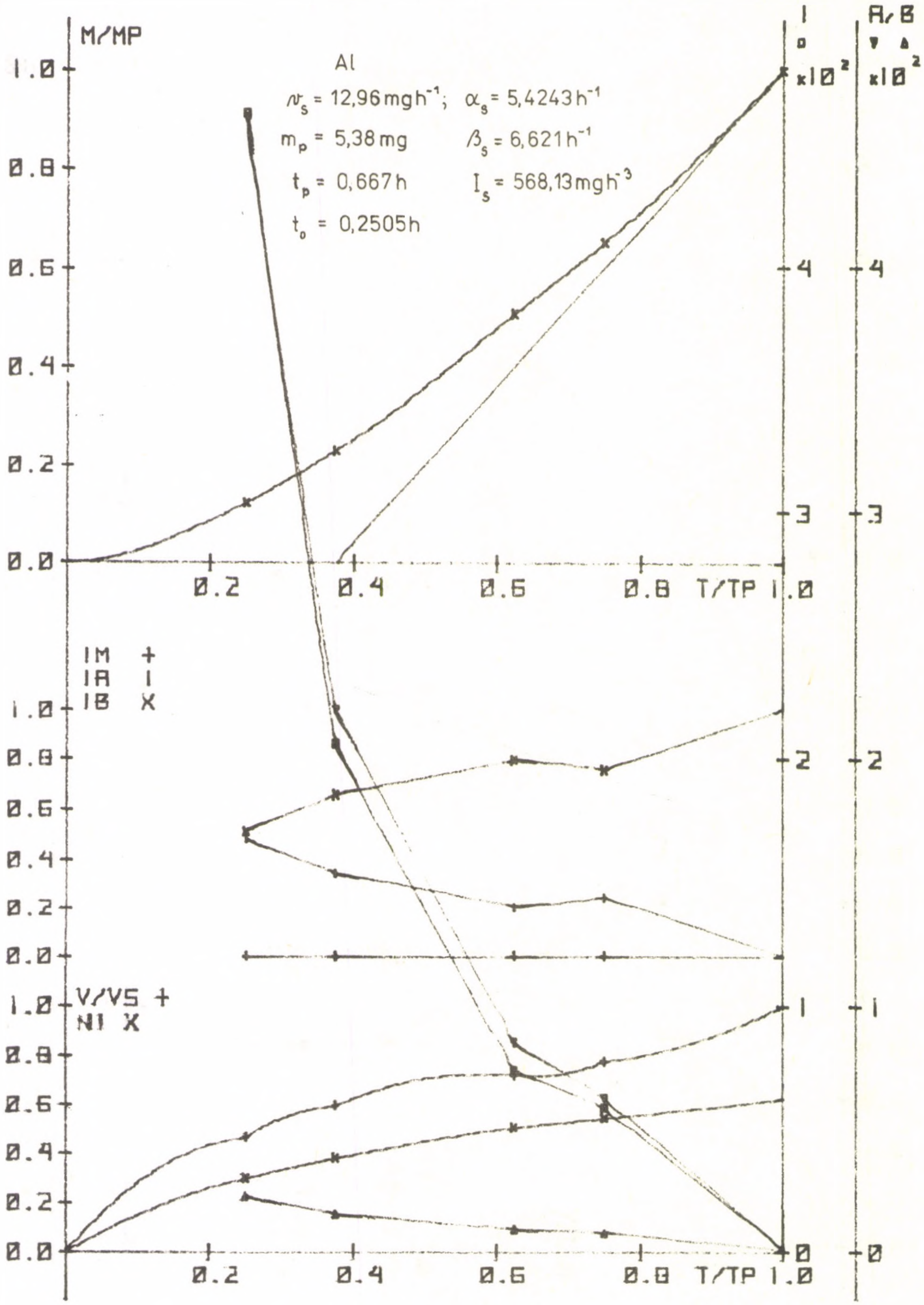
M/MP
Al
v_s = 12,96 mgh^{-1}; α_s = 5,4243 h^{-1}
m_p = 5,38 mg
β_s = 6,621 h^{-1}
t_p = 0,667 h
I_s = 568,13 mgh^{-3}
t_o = 0,2505 h
T/TP
IM +
IA I
IB X
V/VS +
NI X
A/B
x10^2
x10^2

Fig. 6

DETERMINATION OF THE THEORETICAL CHARACTERISTICS OF MIXED-FLOW PUMPS

A. Nyíri and L. Baranyi

SUMMARY

A procedure is presented to determine the theoretical characteristics of a cascade of blades on arbitrary surface of revolution with variable channel width in a pump impeller by tracing back the solution to a circular cascade.

The theoretical characteristics of a pump handling incompressible inviscid fluid can be generally determined through solving the direct problem of a cascade [1]. For the case of a radial trough-flow pump with thin blades having a certain course of channel width the task has been solved by Murata and his co-authors [2]. The results of the latter are plotted on diagrams which can be applied if the inaccuracy intrinsic to the way the data are given is admissible.

A procedure will be shown in order to extend the scope of the method worked out for radial impeller to the general case of a cascade of blades in a pump on arbitrary surface of revolution having the same width distribution as that of the radial one.

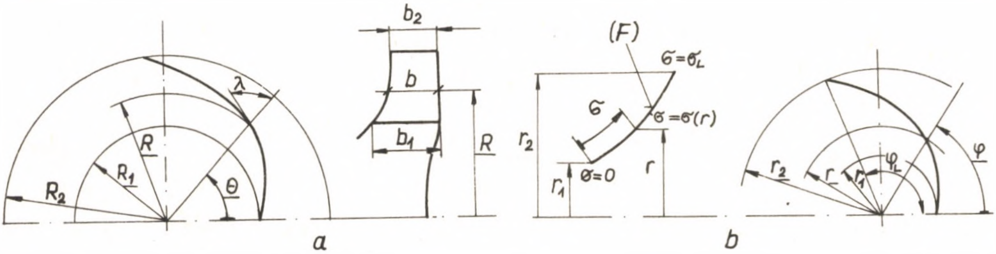

Fig.1

The logarithmic spiral shaped thin blade closing the angle λ with the radial direction is shown on Fig.1a. Generally the cascade of blades are on a surface of revolution (F) the meridional curve of which is given by the function $\sigma = \sigma(r)$ /see Fig.1b/. The channel width varies from b_1 to b_2 in both cases. The task is to find the angle and proportion preserving transformation between the two surfaces securing the same velocity potential in the same way as the conformal mapping between two complex planes.

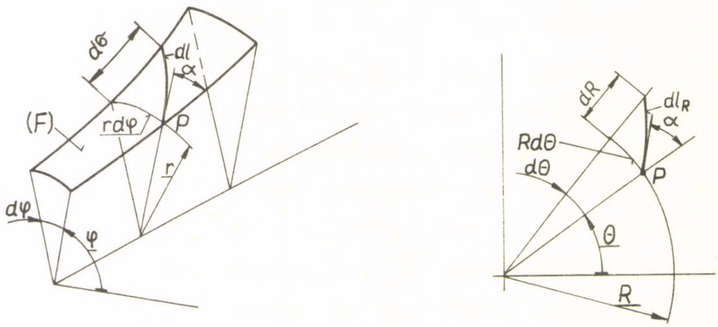

Fig.2

The above conditions are described by the following equations using the notations drawn on Fig.2

$$\tan\alpha = \frac{r\,d\varphi}{d\sigma} = \frac{R\,d\theta}{dR} \quad , \qquad dl = \mu(P)\,dl_R \qquad (1)$$

where the function $\mu(P)$ is to depend solely on point P. It is easy to verify that the mapping function can be chosen as follows:

$$R = R_1 \exp\left(\int_0^\sigma \frac{d\sigma}{r}\right) \quad ; \qquad \theta = \varphi \quad ; \qquad \mu(P) = \frac{r}{R} \qquad (2)$$

and on this basis the connection between the velocity c on the surface (F) and the velocity c_R on the radial plane is obtained as below

$$cr = c_R R \qquad (3)$$

The infinitely thin logarithmic shaped blades of angle λ and number N will correspond to the curve closing the constant angle λ with the meridional direction on the surface of revolution (F) with the same number of blades N. In order to define on both surfaces dimensionless quantities with the same values we can choose without losing the generality that the outer diameters are equal i.e. $r_2 = R_2$.

The theoretical characteristics of a circular cascade when no prewhirl exists can be determined by Murata's diagrams /to be found here also/. The equation of the theoretical characteristics is

$$\Psi_{th}(\Phi) = \Psi_o \left(1 - \frac{\tan\lambda}{k_m}\Phi\right) \qquad (4)$$

where Ψ is the pressure number expressed by the specific energy Y and the peripheral velocity u_2 belonging to the radius R_2

$$\Psi = \frac{2Y}{u_2^2} \qquad (5)$$

and Φ is the flow number defined by the volume rate of flow Q as follows

$$\Phi = \frac{Q}{2\pi R_2 b_2 u_2} \qquad (6)$$

The values for Ψ_o and k_m in Equ. (4) are to be interpolated from the diagrams. The pressure number Ψ_s belonging to the shockless entry is to be taken from there too; with that Ψ_s the corresponding flow number Φ_s can be determined

$$\Phi_s = k_m \cot\lambda \left(1 - \frac{\Psi_s}{\Psi_o}\right) \qquad (7)$$

These quantities can be calculated in the same way for the cascade on the surface (F) if we compute the value of R_1/R_2 upon Equ. (2) like

$$\frac{R_1}{R_2} = e^{-a_L} \qquad \text{where} \qquad a_L = \int_0^{\sigma_L} \frac{d\sigma}{r} \qquad (8)$$

In the classical stream filament theory the relative streamlines in the impeller are considered to be congruent with the blade shape. In this case when there is no prewhirl the relationship between the pressure and flow numbers is well known:

$$\Psi_\infty(\Phi) = 2(1 - \Phi\tan\lambda) \qquad (9)$$

The values belonging to the shockless entry are

$$\Phi_{s\infty}=\left(\frac{R_1}{R_2}\right)^2\frac{b_1}{b_2}\,\mathrm{cotan}\,\lambda \qquad ; \qquad \Psi_{s\infty}=2-2\left(\frac{R_1}{R_2}\right)^2\frac{b_1}{b_2}\,. \tag{10}$$

Now the value of the slope factor can be calculated

$$\lambda_{p\infty}=\frac{\Psi_{th}(\Phi_{s\infty})}{\Psi_{\infty}(\Phi_{s\infty})}=\frac{\Psi_o\left[k_m-\left(\frac{R_1}{R_2}\right)^2\frac{b_1}{b_2}\right]}{2k_m\left[1-\left(\frac{R_1}{R_2}\right)^2\frac{b_1}{b_2}\right]}\,. \tag{11}$$

The slope factor can be defined with the values belonging to the shockless entry of the theoretical characteristics by

$$\lambda_p=\frac{\Psi_{th}(\Phi_s)}{\Psi_{\infty}(\Phi_s)}=\frac{\Psi_s\,\Psi_o}{2\left[\Psi_o-k_m(\Psi_o-\Psi_s)\right]}\,. \tag{12}$$

These last two values are close when the cascade is dense.

The previous expressions may be sufficient approximations if the blade angle is not constant on the surface (F). We can take the angle of the logarithmic spiral fitted on the leading and trailing edges of the blade by

$$\tan\lambda=\frac{\varphi_L}{a_L} \tag{13}$$

where φ_L is the span angle of a blade on its axial view /Fig.1 /.

The determination of the theoretical characteristics outlined above may be a good assistance in designing impeller blading in the simple classical way.

REFERENCES

[1] NYIRI,A.: Determination of the Theoretical Characteristics of Hydraulic Machines, based on Potential Theory. Acta Techn. Acad. Sci. Hung. 69 /197o/ 243-273.

[2] MURATA,S.-OGAWA,T.-GOTOH,M.: On the Flow in a Centrifugal Impeller /2nd Report, Effects of change in Impeller Width/. Bulletin of the JSME, Vol.21, No.151. /1978/ 9o-97.

[3] HOFFMEISTER,M.: ZAMM, Band 4o, Heft 6 /196o-4/ T-135

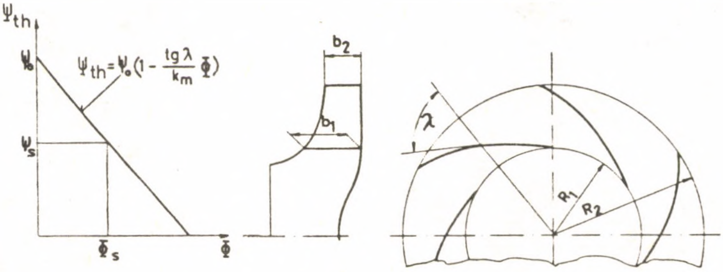

Ψ_{th}
Ψ_0
$\Psi_{th} = \Psi_0 (1 - \frac{tg\lambda}{k_m} \Phi)$
Ψ_s
Φ_s
Φ
b_2
b_1
λ
R_1
R_2

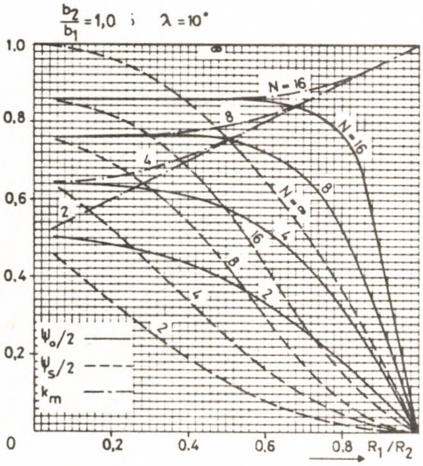

$\frac{b_2}{b_1} = 1{,}0$; $\lambda = 10°$
$\psi_o/2$
$\psi_s/2$
k_m
R_1/R_2

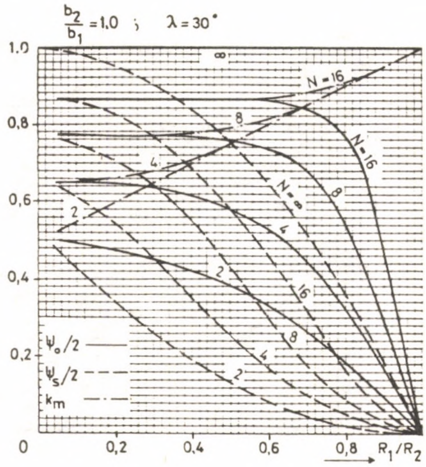

$\frac{b_2}{b_1} = 1{,}0$; $\lambda = 30°$
$\psi_o/2$
$\psi_s/2$
k_m
R_1/R_2

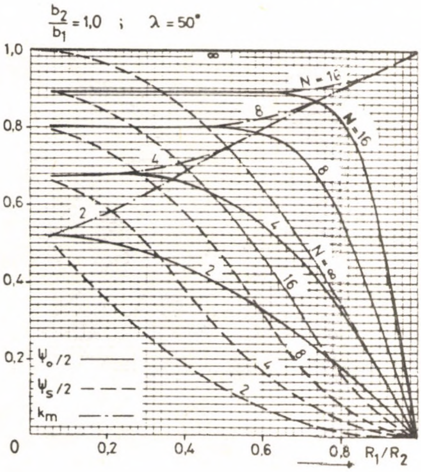

$\frac{b_2}{b_1} = 1{,}0$; $\lambda = 50°$
$\psi_o/2$
$\psi_s/2$
k_m
R_1/R_2

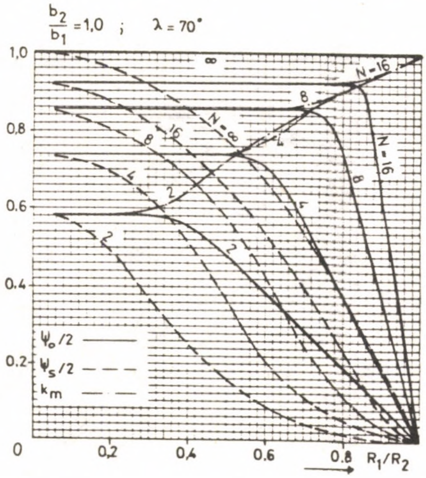

$\frac{b_2}{b_1} = 1{,}0$; $\lambda = 70°$
$\psi_o/2$
$\psi_s/2$
k_m
R_1/R_2

$\frac{b_2}{b_1} = 0{,}8$; $\lambda = 10°$

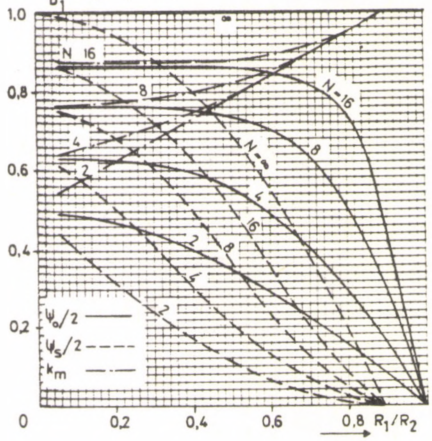

$\frac{b_2}{b_1} = 0{,}8$; $\lambda = 30°$

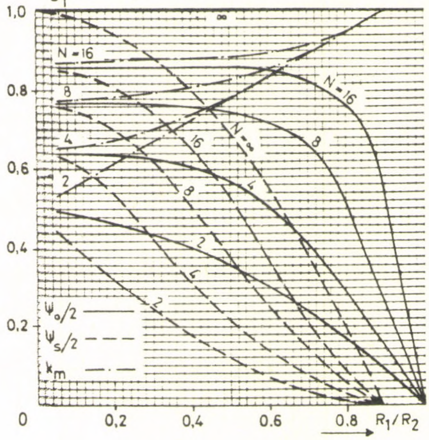

$\frac{b_2}{b_1} = 0{,}8$; $\lambda = 50°$

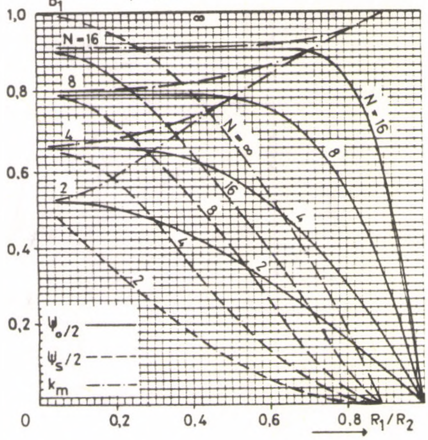

$\frac{b_2}{b_1} = 0{,}8$; $\lambda = 70°$

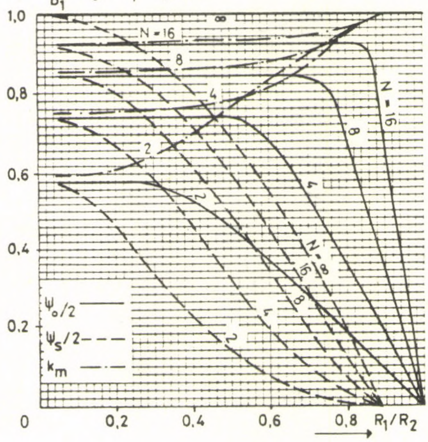

$\frac{b_2}{b_1} = 0{,}6$; $\lambda = 10°$

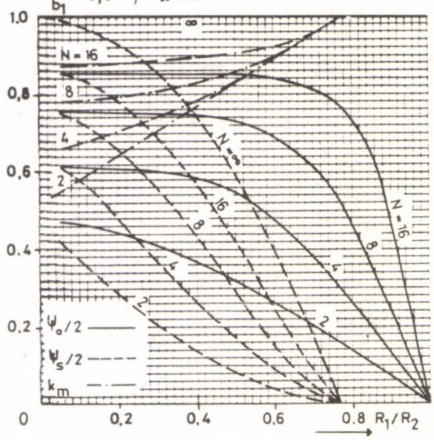

$\frac{b_2}{b_1} = 0{,}6$; $\lambda = 30°$

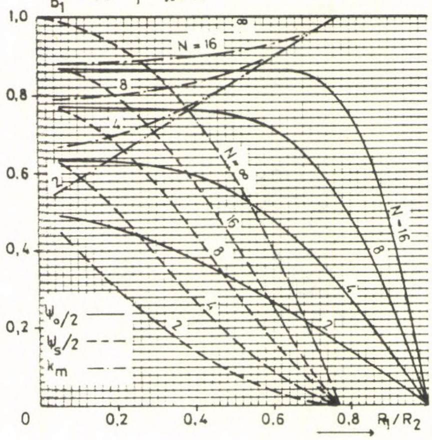

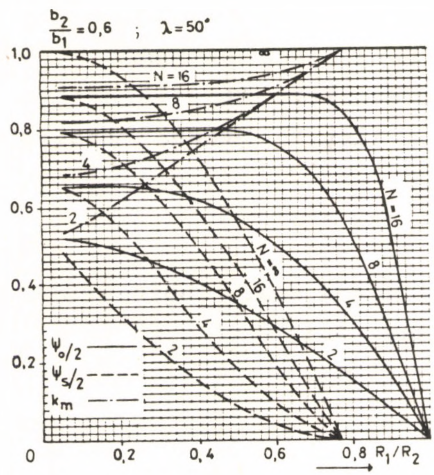

$\frac{b_2}{b_1} = 0,6$; $\lambda = 50°$
N = 16
$\psi_o/2$
$\psi_s/2$
k_m
R_1/R_2

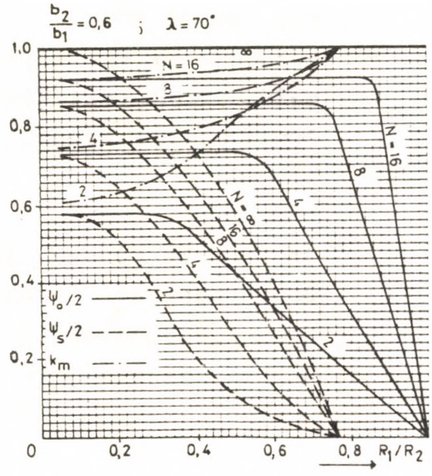

$\frac{b_2}{b_1} = 0,6$; $\lambda = 70°$
N = 16
$\psi_o/2$
$\psi_s/2$
k_m
R_1/R_2

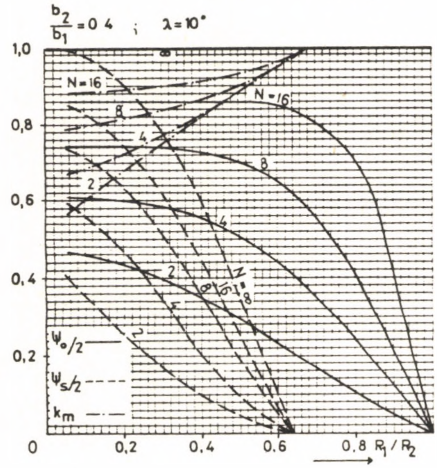

$\frac{b_2}{b_1} = 0,4$; $\lambda = 10°$
N = 16
$\psi_o/2$
$\psi_s/2$
k_m
R_1/R_2

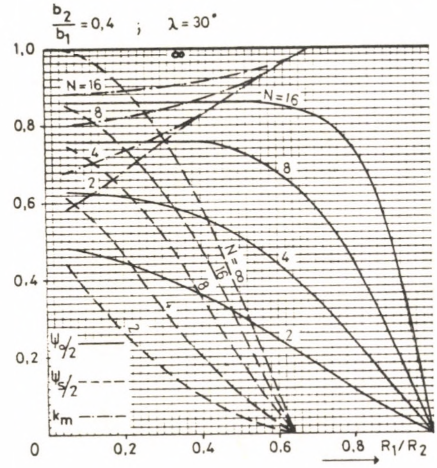

$\frac{b_2}{b_1} = 0,4$; $\lambda = 30°$
N = 16
$\psi_o/2$
$\psi_s/2$
k_m
R_1/R_2

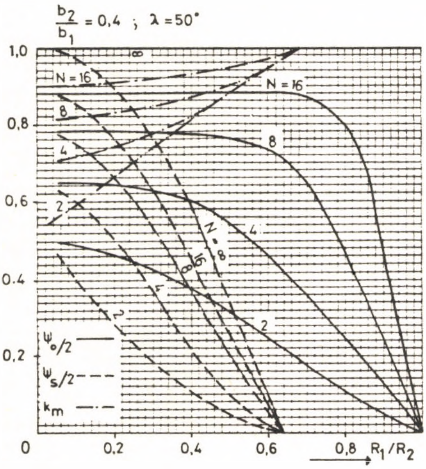

$\frac{b_2}{b_1} = 0,4$; $\lambda = 50°$
N = 16
$\psi_o/2$
$\psi_s/2$
k_m
R_1/R_2

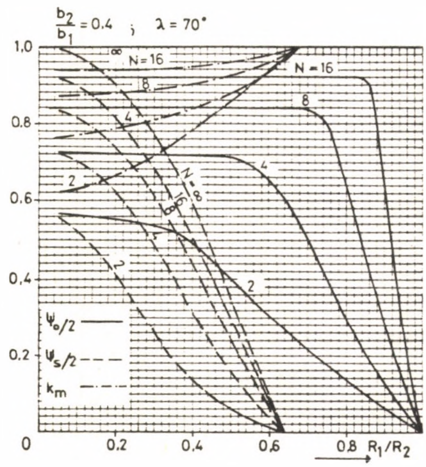

$\frac{b_2}{b_1} = 0,4$; $\lambda = 70°$
N = 16
$\psi_o/2$
$\psi_s/2$
k_m
R_1/R_2

Dr. András NYIRI
Head of the Hydraulic Dep. Ganz-Mávag Budapest
H-1967 Budapest, Könyves Kálmán krt. 76.
Prof. at the Technical University for Heavy Industry, Miskolc

Dr. László BARANYI lecturer
Department of Fluid Mechanics and Heat Engineering
Technical University for Heavy Industry
H-3515 Miskolc-Egyetemváros, Hungary

NUMERICAL METHOD FOR CALCULATING THE FLOW AROUND A CASCADE OF AEROFOILS

A. Nyíri and L. Baranyi

SUMMARY

A FORTRAN 19oo computer program has been written that gives the solution of the 2-D incompressible, inviscid flow problem for a rotating cascade of blades on the mean surface of a stream channel with constant width. The program is based on a known solution of the task. The paper includes the equations to be solved, the applied numerical methods, the flow chart of the computer program and sample calculations in comparison with experimental test and classical solutions.

1. DESCRIPTION OF METHOD AND BASIC EQUATIONS

There are a few solutions to determine the stream pattern around a cascade of foils on a surface of revolution assuming frictionless fluid [1],[4],[7],[1o] . More known papers are for straight cascades to be studied when preparing a computer program for the more general case [5],[6],[9].

A full development of the basic theory is described in [7]. For the time being we take the special case when the channel width is constant. In the paper mentioned the arc length coordinate is used, which is to be transformed to a polar coordinate system by

$$\frac{w(s)}{w_{1x}}ds = w(\varphi)/d\varphi \tag{1}$$

/see Fig.1/. With this the integral equation concerning the relative velocity $w(\varphi)$ to be solved is as follows:

$$w(\varphi)+\frac{1}{\pi}\int_0^{2\pi}\mathcal{K}(\varphi,\varphi')w(\varphi')d\varphi' = F(\varphi) \tag{2}$$

where the kernel function is

$$\mathcal{K}(\varphi,\varphi')=\frac{\dot{y}(\varphi)\sinh\frac{2\pi}{t}\left[x(\varphi)-x(\varphi')\right]-\dot{x}(\varphi)\sin\frac{2\pi}{t}\left[y(\varphi)-y(\varphi')\right]}{\cosh\frac{2\pi}{t}\left[x(\varphi)-x(\varphi')\right]-\cos\frac{2\pi}{t}\left[y(\varphi)-y(\varphi')\right]}\frac{\pi}{t}+\frac{\pi}{t}\dot{y}(\varphi) \; . \tag{3}$$

The limit value of this function when $\varphi' \longrightarrow \varphi$ is

$$\mathcal{K}(\varphi,\varphi)=\lim_{\varphi'\to\varphi}\mathcal{K}(\varphi,\varphi')=\frac{1}{2}\,\frac{\ddot{y}(\varphi)\dot{x}(\varphi)-\ddot{x}(\varphi)\dot{y}(\varphi)}{\dot{x}^2(\varphi)+\dot{y}^2(\varphi)}+\frac{\pi}{t}\dot{y}(\varphi) \; . \tag{4}$$

The right-hand side of Equ. (2) can be composed of three parts

$$F(\varphi)=F_1(\varphi)\ \tan\chi_1+F_2(\varphi)+\omega\left[F_{30}(\varphi)+F_{31}(\varphi)\right] \qquad (5)$$

where

$$F_1(\varphi)=2\dot{y}(\varphi)\quad ; \qquad\qquad F_2(\varphi)=2\,\dot{x}(\varphi)\quad ;$$

$$F_{30}(\varphi)=\frac{2\pi}{Nt}\left[\frac{2r_1^2-r^2(\varphi)}{w_{1x}}+\frac{N\,A_{pax}}{\pi\ w_{1x}}\right]\dot{y}(\varphi)\ ; \qquad F_{31}(\varphi)=\frac{2\pi}{Nt^2}\int_0^{2\pi}\frac{r^2(\varphi')}{w_{1x}}G(\varphi,\varphi')d\varphi'\ ; \qquad (6)$$

$$G(\varphi,\varphi')=-G(\varphi',\varphi)=\frac{\left[\dot{x}(\varphi')\dot{x}(\varphi)-\dot{y}(\varphi')\dot{y}(\varphi)\right]\sinh\frac{2\pi}{t}\left[x(\varphi)-x(\varphi')\right]+\left[\dot{y}(\varphi')\dot{x}(\varphi)+\dot{x}(\varphi')\dot{y}(\varphi)\right]\sin\frac{2\pi}{t}\left[y(\varphi)-y(\varphi')\right]}{\cosh\frac{2\pi}{t}\left[x(\varphi)-x(\varphi')\right]-\cos\frac{2\pi}{t}\left[y(\varphi)-y(\varphi')\right]}$$

Since $G(\varphi,\varphi')$ has a first order singularity at $\varphi'=\varphi$, the Cauchy's principal value of the integral in $F_{31}(\varphi)$ must be taken. Note that if the cascade is either stationary or axial the last term in Equ. (5) vanishes. In the first case $\omega = 0$ and in the second one the sum in brackets becomes zero. In both cases the computational work is being reduced to that of a straight cascade.

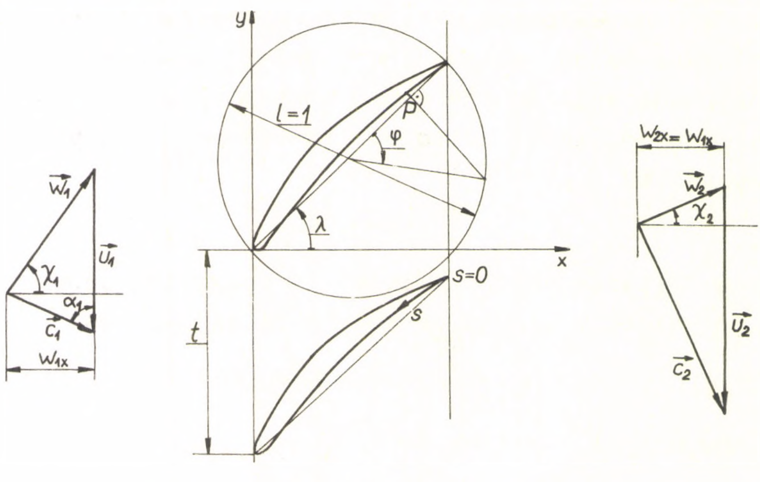

Fig.1

Introducing the trapezoidal integration with N1 pivotal points /even number/ Equ. (2) becomes

$$\sum_{j=1}^{N1}K_{ij}\,w_j=F_{1i}\ \tan\chi_1+F_{2i}+\omega\left(F_{30i}+F_{31i}\right) \qquad (i=1,2,\dots,N1) \qquad (7)$$

where

$$K_{ij}=\frac{1}{\pi}\int\limits_{(\Delta\varphi_j)}\mathcal{K}(\varphi_i,\varphi')d\varphi'+\delta_{ij} \qquad (i,j=1,2,\cdots,N1) \;; \tag{8}$$

$$w_j=w(\varphi_j)\;; \qquad F_i=F(\varphi_i)\;; \qquad \varphi_j=(j-0{,}5)\frac{2\pi}{N1}\;; \tag{9}$$

$\Delta\varphi_j = 2\pi/N1$ and $w(\varphi)$ is considered to be constant over a $(\Delta\varphi_j)$ interval. The choice of such a distribution of the pivotal points results in a proper density in the vicinity of the edges /Fig.2/. The kernel function (3) is very steep when the sum of i and j is near to N1 i.e. the points are on the opposite side of the profile. The problem arising due to the steepness of $\mathcal{K}(\varphi,\varphi')$ is overcome by applying Equ. (8) otherwise

$$K_{ij}=\frac{2}{N1}\mathcal{K}(\varphi_i,\varphi_j)+\delta_{ij} \tag{10}$$

by which sufficient accuracy is attained. Using Equ. (lo) only would lead to a poor solution particularly in the case of thin foils.

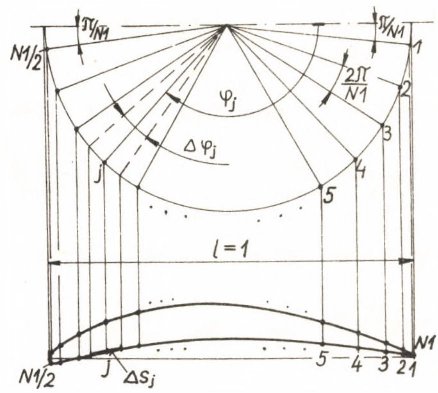

Fig.2

Taking into consideration the results in paper [6] the sum of each column of matrix K_{ij} is zero. Thus the system of linear algebraic equations (7) is indeterminate. Applying the Kutta-Joukowski condition in the form below

$$w_{N1}=-\alpha\, w_1 \tag{11}$$

- where $\alpha \cong 1$ - the system (7) becomes determinate:

$$\sum_{j=1}^{N1-1} K'_{ij} w_j = F_i \qquad (i=1,2,\cdots,N1-1) \qquad (12)$$

where

$$K'_{ij} = K_{ij} - K_{iN1}\,\delta_{j1} \qquad (i,j=1,2,\cdots,N1-1) \qquad (13)$$

The meaning of condition (11) is that the stagnation point is near to the trailing edge. We note that the matrix K'_{ij} is a well conditioned one.

The system of equations (12) is to be solved with three different RHS /see Equ. (7) /. The transformed velocity can be written at the incidence χ_1 and angular velocity ω as follows:

$$w_i = w_{1i} \tan\chi_1 + w_{2i} + \omega w_{3i} \qquad (14)$$

where w_{1i}, w_{2i}, w_{3i} are the three different solutions of Equ. (12). Using transformation (1) the contour velocity as a function of arc length is

$$\frac{w(s_i)}{w_{1x}} = \frac{w_i}{\sqrt{\dot{x}_i^2 + \dot{y}_i^2}} \qquad (i=1,2,\cdots,N1) \qquad (15)$$

and on the surface of revolution is:

$$\frac{w_R(\sigma_i)}{w_{R1\sigma}} = \frac{r_1}{r_i}\,\frac{w(s_i)}{w_{1x}} \qquad (16)$$

furthermore the pressure coefficient on the same surface is:

$$C_p = \frac{p - p_1}{\frac{\varrho}{2} w_{R1}^2} = 1 - \left(\frac{w_R}{w_{R1}}\right)^2 + \left[\left(\frac{r}{r_1}\right)^2 - 1\right]\left(\frac{u_{R1}}{w_{R1}}\right)^2 . \qquad (17)$$

The dimensionless circulation of the absolute velocity is

$$\frac{\Gamma_c}{t w_{1x}} = K_1 \tan\chi_1 + K_2 + \left(K_3 - \varkappa_2^2\right)\frac{u_{2y}}{w_{1x}} \qquad (18)$$

where

$$K_{1,2} = \frac{2\pi}{tN1}\sum_{i=1}^{N1} w_{1,2i} \quad \text{and} \quad K_3 = \frac{N w_{1x}}{r_2^2 N1}\sum_{i=1}^{N1} w_{3i} . \qquad (19)$$

In case of an axial cascade

$$K_3 = 0 \quad \text{and} \quad \varkappa_2^2 = \frac{A_{pax} N}{r_2^2 \pi} = 0 \qquad (20)$$

while $u_{2y} = 0$ stands for a stationary cascade.
By using the well known relationship between the circulation and the pressure number Ψ and flow number Φ the theoretical

characteristics of a pump is:

$$\Psi_P=2(K_2-K_1 \cot an\alpha_1)\phi_P + 2\left[K_1\left(\frac{r_1}{r_2}\right)^2 + \varkappa_2^2 - K_3\right] \qquad (21)$$

and those of a turbine

$$\Psi_T=2(K_2+K_1 \cot an\alpha_1)\phi_T + 2\left[-K_1 + (K_3-\varkappa_2^2)\left(\frac{r_2}{r_1}\right)^2\right] \cdot \qquad (22)$$

The outlet angle χ_2 /Fig.1/ for a pump is given by the relation

$$\tan\chi_2=\left[1-K_1\left(\frac{r_1}{r_2}\right)^2+K_3-\varkappa_2^2\right]\frac{1}{\phi_P}+(K_1-1)\cot an\alpha_1-K_2 \qquad (23)$$

and for a turbine

$$\tan\chi_2=\left[K_1-(1+K_3-\varkappa_2^2)\left(\frac{r_2}{r_1}\right)^2\right]\frac{1}{\phi_T}+(1-K_1)\cot an\alpha_1-K_2 \ . \qquad (24)$$

This method of solution and the computer program can also be used to determine the flow around a single foil if we put $t/l \longrightarrow \infty$ /in practice $t/l \geq 10^4$/.

Further development of this method is in progress for the cascade flow with variable stream sheet thickness.

2. NUMERICAL ANALYSIS

Six areas of numerical analysis are required in the solution of this problem.

a/ Data smoothing

As shown by previous workers any small perturbations in the profile data due to inaccuracy must be removed before entering the differentiating procedure because differentiation amplifies errors, leading to poor solution. The powerful method in [8] is used in which method the graduated values obtained minimize both their r-th differences and their deviations from the values to be smoothed simultaneously. In the program r = 3.

b/ Numerical differentiation

To obtain derivatives for values given at equidistant points the five point formula is used:

$$60hf_k' = f_{k+3} - f_{k-3} - 9(f_{k+2} - f_{k-2}) + 45(f_{k+1} - f_{k-1}) \quad .$$

c/ Evaluating the Cauchy's principal value for the integral

$$I = \int_{x-\frac{\Delta x}{2}}^{x+\frac{\Delta x}{2}} \frac{f(x')}{x-x'} dx' = I_0 + I_1 \tag{25}$$

where

$$I_0 = \int_{x-\frac{\Delta x}{2}}^{x-\varepsilon} \frac{f(x')}{x-x'} dx' + \int_{x+\varepsilon}^{x+\frac{\Delta x}{2}} \frac{f(x')}{x-x'} dx' \quad ,$$

$$I_1 = -2 \sum_{n=0}^{\infty} f^{(2n+1)}(x) \frac{\varepsilon^{2n+1}}{(2n+1)(2n+1)!}$$

The latter expression is obtained by expanding f(x') into Taylor series around x and performing the integral in (25) over the interval $[x-\varepsilon, x+\varepsilon]$ ($\varepsilon < \Delta x/2$; small positive number). The integration sets up from the endpoints of interval $[x-\Delta x/2, x+\Delta x/2]$ and tends towards the pole until the condition

$$|2\varepsilon f'(x)| < E$$

is satisfied, where E is the error bound. As a result we have

$$I \cong I_0 - 2\varepsilon f'(x) \quad .$$

d/ Interpolation

- Newton's general interpolation formula /divided differences/
- Hermite interpolation

e/ Numerical integration

- The rectangle rule
- Simpson's rule
- Romberg's method

f/ Solving the set of linear equations

A subroutine which provides iterative improvement of solution is used available at the Dep. of Computing Techniques at the Technical University in Miskolc.

3. FLOW CHART OF COMPUTER PROGRAM

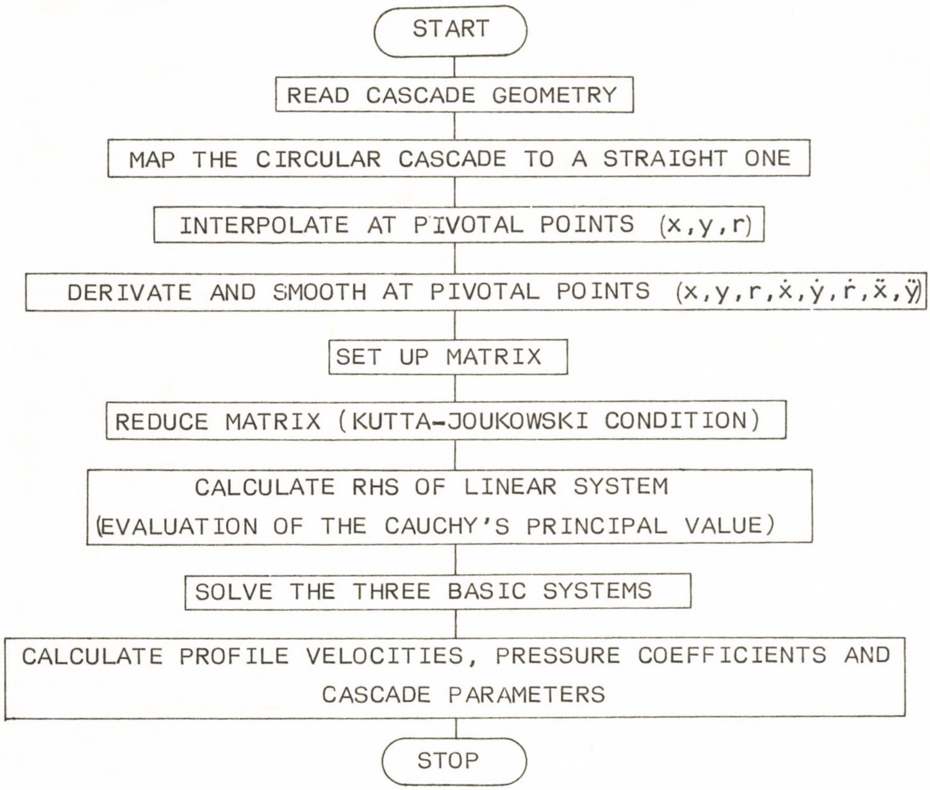

4. SAMPLE CALCULATIONS

The computer program has been tested against a series of axial turbine cascades where test results are available [3], and a number of analytic solutions relating to single foils. The agreement between the theoretical and experimental /or analytic/ distributions is quite satisfactory. Due to lack of space only two examples are shown /see Fig.3, Fig.4/.

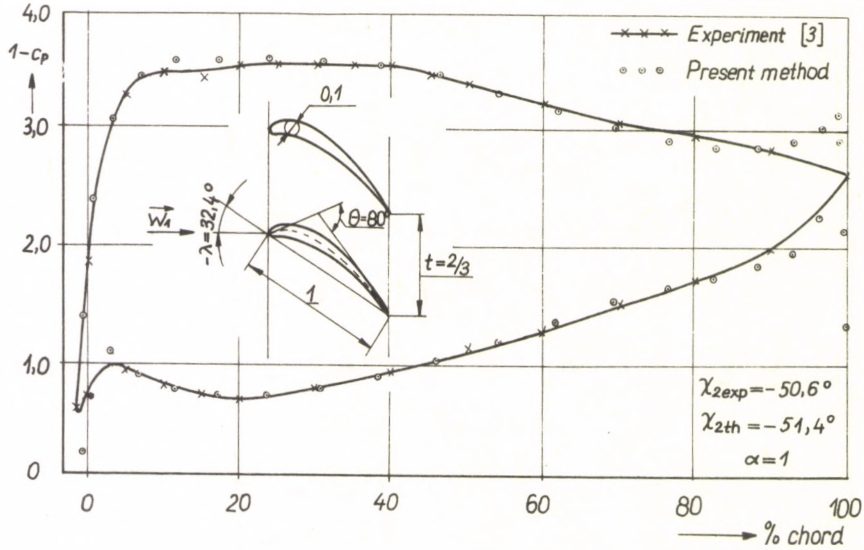

4,0
$1-c_p$
3,0
2,0
1,0
0
0
20
40
60
80
100
% chord
Experiment [3]
Present method
0,1
$\vec{W_1}$
$-\lambda=32,4°$
$\theta=80°$
$t=2/3$
1
$\chi_{2exp}=-50,6°$
$\chi_{2th}=-51,4°$
$\alpha=1$

Fig. 3

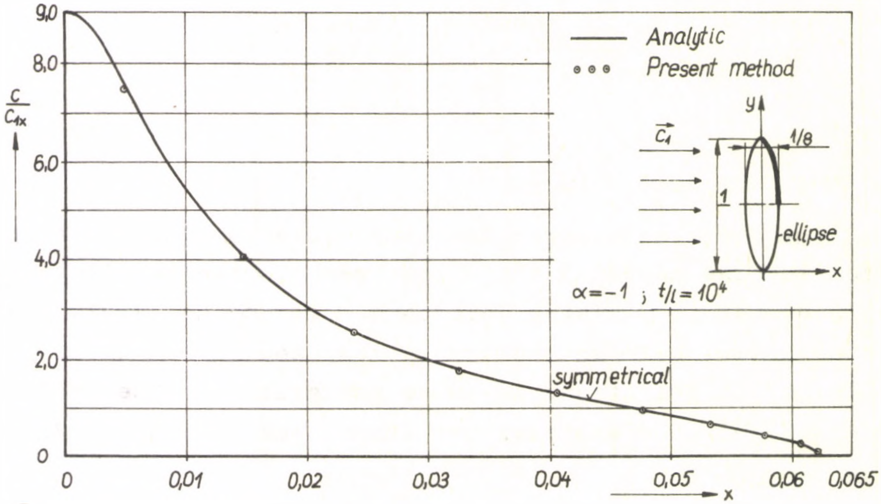

9,0
8,0
$\frac{c}{c_{1x}}$
6,0
4,0
2,0
0
0
0,01
0,02
0,03
0,04
0,05
0,06
0,065
x
Analytic
Present method
y
$\vec{c_1}$
1/8
1
ellipse
x
$\alpha=-1$; $t/l=10^4$
symmetrical

Fig. 4

NOTATION

A_{pax}	Area of a foil's axial projection
c_p	Pressure coefficient
c	Absolute velocity
$\mathcal{K}(\varphi,\varphi')$	Kernel function
K_1, K_2, K_3	Dimensionless constants /cascade parameters/
l	Chord length
N	Number of blades
Nl	Number of pivotal points
p	Pressure
r	Radius
s	Arc length
t	Cascade blade pitch in the mapped plane
x,y	Dimensionless co-ordinates in the mapped plane
$\dot{x},\dot{y},..$	Derivatives with respect to φ
u	Peripheral velocity
w	Relative velocity
α	Trailing edge loading coefficient
α_1	Upstream angle of the absolute velocity
δ_{ij}	Kronecker delta
λ	Stagger angle
ϱ	Fluid density
σ	Arc length co-ordinate on the surface of revolution
φ	Polar angle
Φ	Flow number
χ	Angle included by a direction with the x-axis
Ψ	Pressure number
ω	Angular velocity

Subscripts

i,j	Locations in a profile contour
P	Pump
R	On the surface of revolution
T	Turbine
x,y	Components in the corresponding co-ordinate directions
∞	Infinity
1,2	Upstream and downstream, respectively

REFERENCES

[1] CZIBERE,T.: Solution of the two main problems of the hydrodynamic cascade theory by theory of potentials. /in Hungarian/ Thesis for D.Sc. Miskolc, 1965.

[2] DAHLQUIST,G.-BJÖRCK,Å.: Numerical methods. Prentice-Hall, New Jersey, 1974.

[3] DUNAVANT,J.-ERWIN,J.R.: Investigation of a related series of turbine blade profiles in cascade. NACA TN 38o2, 1956.

[4] KATSANIS,T.: Computer program for calculating velocities and streamlines on a blade-to-blade stream surface of a turbomachine. NASA TN E-4o97, 1968.

[5] LEWIS,R.I.-RYAN,P.G.: Surface vorticity theory for axi-symmetric potential flow past annular aerofoils and bodies of revolution with application to ducted propellers and cowls. J. Mech. Engg. Sci. 14 /1972/ 28o-291.

[6] MARTENSEN,E.: Berechnung der Druckverteilung an Gitterprofilen in ebener Potentialströmung mit einer Fredholmschen Integralgleichung. Arch. Ration. Mech. Analysis 3 /1959/, 235-27o.

[7] NYIRI,A.: Determination of the theoretical characteristics of hydraulic machines, based on potential theory. Acta Techn. Acad. Sci. Hung. 69. /197o/, 243-273.

[8] NYIRI,A.: A method for smoothing empirical function. /in Hungarian/ Alkalmazott Matematikai Lapok 6 /198o/

[9] SMITH,A.M.O.-HESS,J.L.: Calculation of potential flow about arbitrary bodies. Progress in Aeronautical Sciences 1966 8 /Pergamon Press, Oxford/

[1o] WU,C.H.: A general theory of three-dimensional flow in subsonic and supersonic turbomachines of axial-, radial-, and mixed flow type. NACA TN 26o4, 1952.

Dr. András NYIRI

Head of the Hydraulic Dep. Ganz-Mávag Budapest

H-1967 Budapest, Könyves Kálmán krt. 76.

Prof. at the Technical University for Heavy Industry, Miskolc

Dr. László BARANYI lecturer

Department of Fluid Mechanics and Heat Engineering

Technical University for Heavy Industry

H-3515 Miskolc-Egyetemváros, Hungary

EXPERIMENTAL STUDY OF SOME DYNAMIC CHARACTERISTICS OF A LOW-SPEED FRANCIS TURBINE

V.S.Obretenov and V.M.Kichev

I. INTRODUCTION

The operation of water turbines can be considered a steady process in a sense that it is cyclically repeated at least at every second revolution of the impeller. This basic cycle, however, is accompanied by a number of non-stationary phenomena occurring at the hydrodynamic grates as well as in the turbine as a whole. With the non-steady operating conditions of the turbine, some quantitative and qualitative changes in the stream parameters take place; the hydrodynamic forces that appear give rise to some dynamic stresses. Since these phenomena depend on the geometry of the stream part, they can be controlled to a certain extent. This makes it necessary to carry out complex investigations of the non-steady and quasi-steady processes of water turbines.

This paper presents the results of the experimental investigations made on a Francis turbine model with a very low speed: $n_s = 73\ min^{-1}$.

II. EXPERIMENTAL SET AND GENERAL DISCUSSION OF TESTS

Tests have been carried out on an universal turbine stand at the Hydraulic Turbo-machines Laboratory, at the Higher Institute of Mechanical and Electrical Engineering, Sofia, under a head H = 6,5 - 16 mH_2O. Fig.1 shows the model block diagram of the stand. The model turbine has a vertical shaft, the volute chamber has an angle of range $\varphi = 345^0$, the guide vanes are asymmetrical with a positive curvature, the diffuser is crank-like with a hight of $h = 2{,}33\ D_1$. Two impellers have been tested /P073-0 and P073-A1/ with a diameter $D_1 = 0{,}4$ m.

The guide vanes position is controlled by a transducer for linear displacement 1, of the type 7DCPT-1000 Hewlett Packard, mounted to the lever of the controlling mechanism. The different time of closing /opening/ of the guide vanes is achieved by changing the supply voltage of the controlling mechanism.

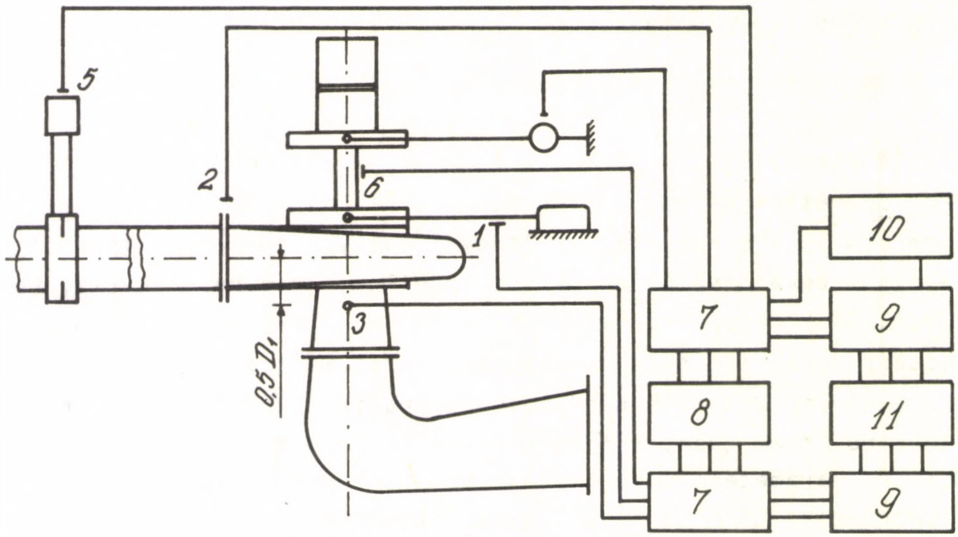

Fig. 1.

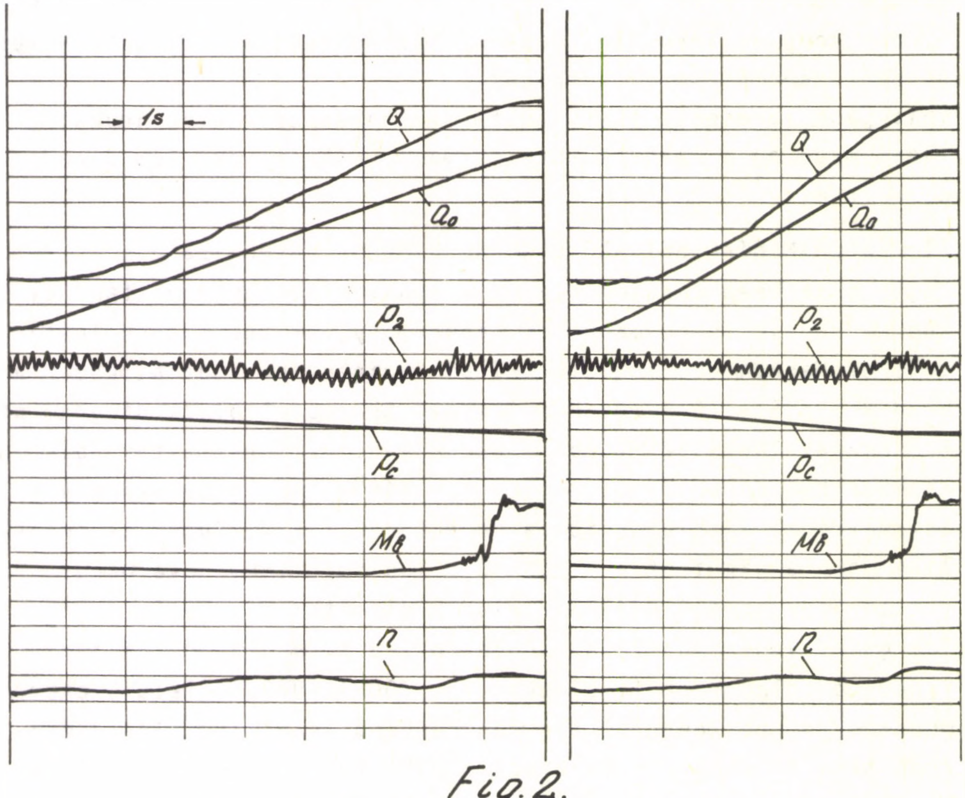

Fig. 2.

The pressure at the case inlet, and after the impeller, is measured respectively by the membrane 2 and the bellows 3 pressure transducers which are of the induction type. The turbine shaft torque is measured by means of a force transducer 4 attached to the hydraulic brake stator. Discharge is measured by an original discharge-meter 5 which is with an elastically supported lokal resistance [1]. The frequency of the turbine rotation is measured by an induction transducer 6.
The signals of the primary transducers are supplied to two measuring amplifiers 7 of the type UM 131, and after passing through auxilliary adjusting stages 9 and 10 of the type 8MW-1 and AS 101/102, they show on the screen of an oscilloscope 8 of the type USG-101 and can be simultaneously recorded on a loop oscil lograph 11 of the type 8LS-1.

III. RESULTS OF THE INVESTIGATIONS

1. Investigating the measured values at various closing times of guide vanes.

Tests have been performed by a P073-A1 impeller. The latter has been worked out after a numerical experiment done by a digital computer [2] and it represents an improved version of the basic P073-D impeller, by means of which similar tests had been carried out.
Fig.2 shows records of the measured values at a linear closing /T_s= 8 s and T_s = 5,5 s/. From the oscillogram given it can be seen that there is a certain delay in discharge variation with respect to guide vanes closing. Along with it, a pressure increase at the volute chamber inlet is observed which is accounted for by the closed circuit operation of the stand. Due to this, the shaft moment also keeps relatively constant for the great part of the closing time and it decreases fast to 0 only at the end of the run. The frequency of rotating decreases to 0 simultaneuosly with the guide vanes closing, due to the considerable resisting moment of the hydraulic brake.
The pressure variation after the impeller has a clearly expressed minimum in the region of the rated opening $a_o = a_o/a_{on} = 1$.

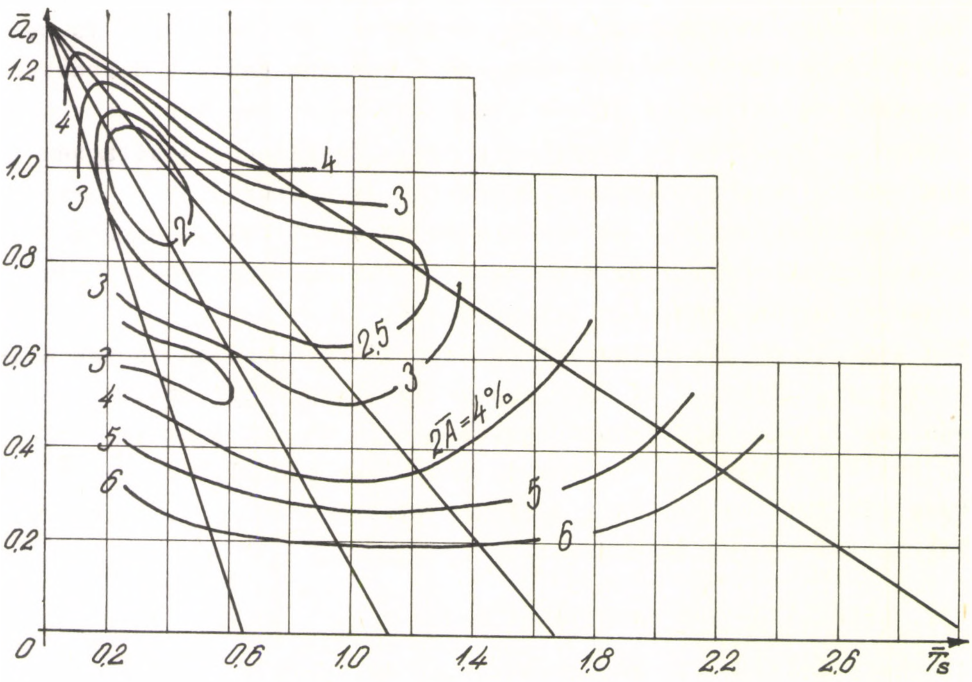
$\bar{a}_0$
1,2
1,0
0,8
0,6
0,4
0,2
0
0,2
0,6
1,0
1,4
1,8
2,2
2,6
$\bar{T}_s$
$2\bar{A}=4\%$
2,5

Fig. 3.

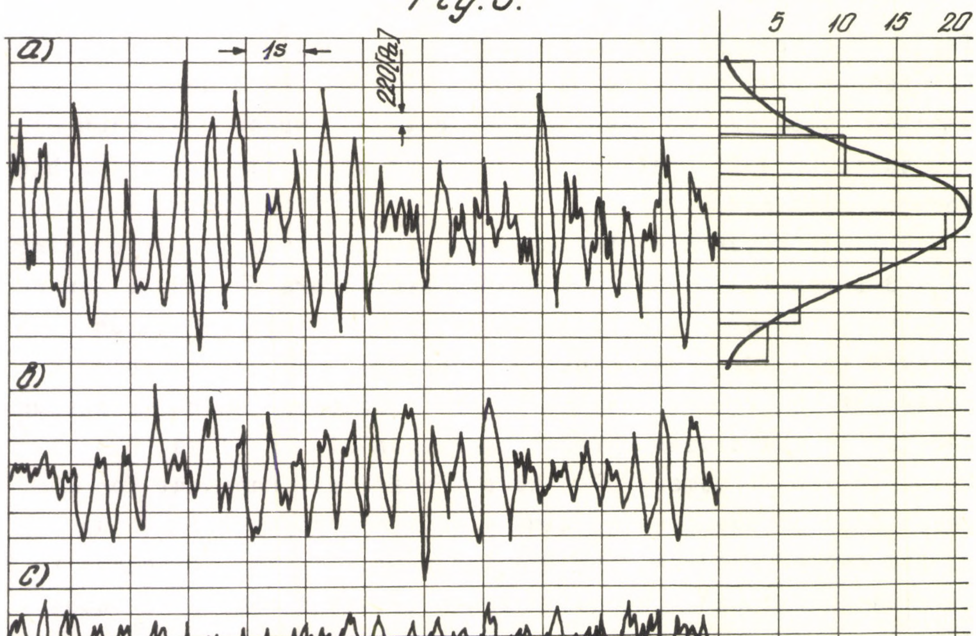
a)
1s
220[Hz]
b)
c)
5
10
15
20

Fig. 4.

This can be also seen from the plotted generalized graphic relation Fig. 3 which represents the change of the double amplitude $2\bar{A} = 2A_{\Delta p}/H$ in a function of the closing time $\bar{T}_s = T_s/T_{sn}$ and the relative opening of guide vanes $\bar{a}_0$. By this relation, the closing time of guide vanes can be determined when the pressure variation after the impeller is at its minimum. The conclusions made can be referred to the original machine supposing the similarity criteria are observed.

2. Investigating the Pressure Variation after the Impeller under Steady Operating Conditions.

Investigations have been carried out at various openings of guide vanes /a_0 = var./ and shaft loads /n_1' = var, a_0= const/ for the two impellers. Figs.4a - 4c present oscillograms referring to three types of operating conditions of the P073-0 impeller (a total of 84 operating conditions have been tesred). The oscillogram processing shows that they are characterized by a normal /Gauss/ distribution of the double amplitude 2A. This is illustrated on Fig.4a by the plotted histogram of the empirical distribution of A and the theoretical curve of the normal distribution describing them.
The obtained-data processing enabled the plotting of the characteristics shown on Figs.5 and 6, which express the relation

$$2\bar{A} = f(\varphi, \psi, a_0) \qquad /1/$$

for the two impellers. The comparative analysis of the two characteristics is good reason to come to the following conclu - sions:
- the pressure variation in the investigated section is of a relatively small amplitude; with the P073-A1 impeller, they are lower for the whole range of tested operating conditions.
- with the P073-A1 impeller the minimum value of 2A coinsides exactly with the maximum value of efficiency /φ_n = 0,275; ψ_n = 4,8/, while with the P073-0 impeller a considerable displacement is observed with respect to the pressure coefficient ψ. Besides, the gradient of $2\bar{A}$ noticeably increases with openings $a_0 < a_{on}$. This is characteristic feature of medium and high-

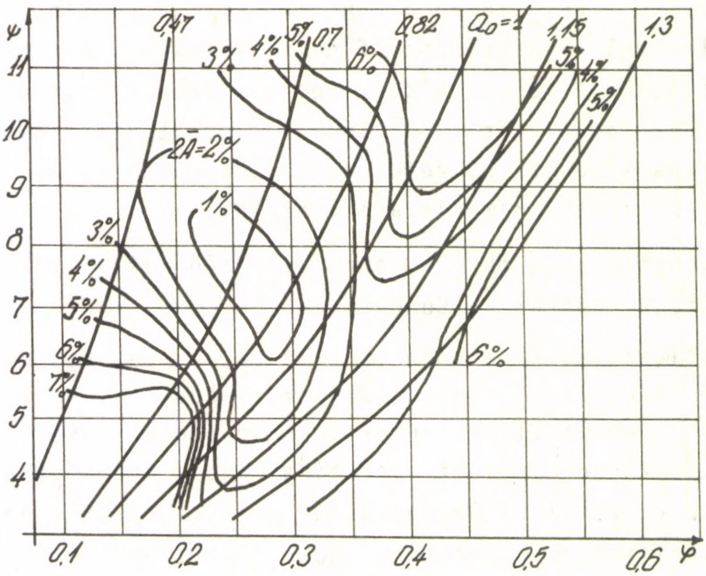

ψ
φ
0,1
0,2
0,3
0,4
0,5
0,6
4
5
6
7
8
9
10
11
0,47
0,7
0,82
1,15
1,3
2Ā=2%
1%
3%
4%
5%
6%
7%

Fig. 5.

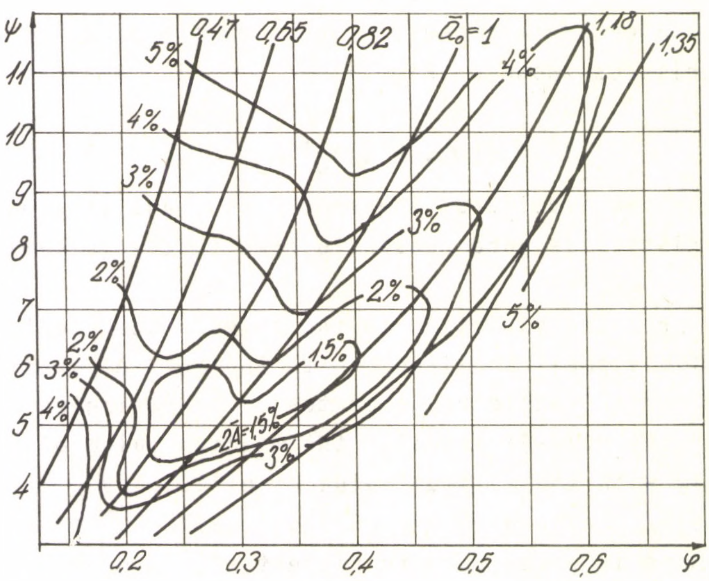

ψ
φ
0,2
0,3
0,4
0,5
0,6
4
5
6
7
8
9
10
11
0,47
0,65
0,82
Ā₀=1
1,18
1,35
5%
4%
3%
2%
1,5%
2Ā=1,5%

Fig. 6

speed Francis turbines, as well [3,4,5]. Apart from the amplitude, a point of interest is the determination of the variation frequency after the impeller and in the diffuser. In these cases, the well-known Rheingans formula /6/ is most frequently applied, and it is:

$$f = n/60k \qquad /2/$$

having in mind that for Francis turbines k = 3,6.
Pazi's investigations /6/ enabled him to recommend some expressions for determinating the frequency and amplitude of pressure variation in the diffuser, and they also account for the turbine operating conditions:

$$f = (0,56 \div 0,60)\left(1 - \frac{n'_{1m}\, Q'_1}{n'_1\, Q'_{1m}}\right)\frac{n}{60} \qquad /3/$$

$$\bar{A} = (0,65 \div 0,85)\left(1 - \frac{n'_{1m}\, Q'_1}{n'_1\, Q'_{1m}}\right)^2 \frac{(n'_1)^2}{g} \qquad /4/$$

In his study, Y.Hosoi [4] pays attention to the influence of the Cu_2 circumference component distribution on the frequency of pressure variation at the diffuser wall. As a result of this study, he offers the following equation for determining f:

$$f = k_1 \left(\frac{D_a}{D_2}\right)^2 \frac{n}{60} - \frac{D_a}{\pi D_2^2} \operatorname{ctg}\beta_2\, C_{m2a} \qquad /5/$$

where the k_1 correction coefficient accounts for the meridian stream deviation at the impeller output from the conditions of a purely axial discharge /Cu_2 = 0/.
One of the tasks of the investigations carried out by us was to determine the applicability of the relations given above /2/-/5/ to low-speed Francis turbines. For this purpose, the values of non-dimensional frequency criterion Φ [4] have been determined:

$$\Phi = f.D_2/\sqrt{gH} \qquad /6/$$

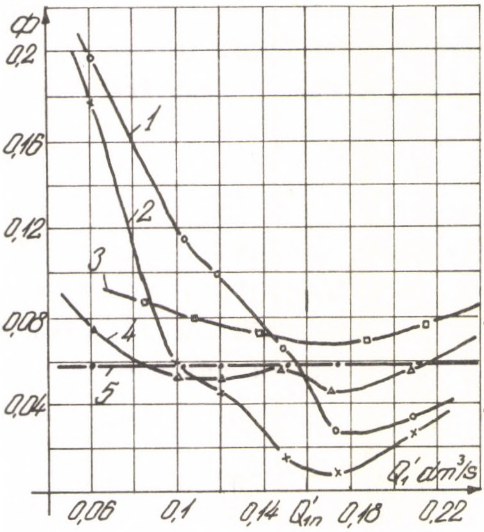

Fig. 7.

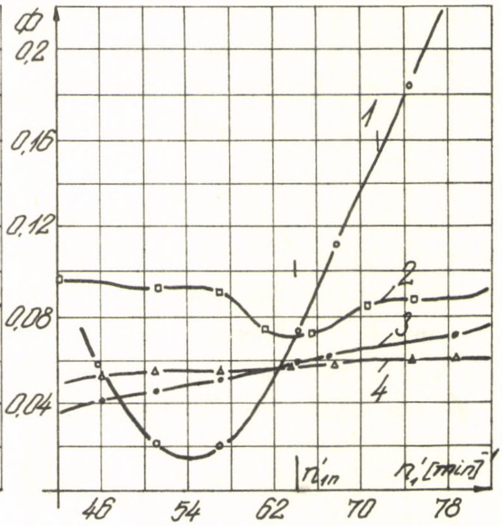

Fig. 8.

1. Hosoi ; 2. Pazi ; 3. PO73-A1- experim.;
4. PO-73-O-experim.; 5. Rheingans.

by the values of f obtained from Eqs. /2/,/4/ and /5/ or experimentally measured. The results of the experimental tests on the speed field in the model turbine stream part were used to obtain the values of f by Eq./5/ [2] . The results obtained have been systematized and are given in a graph on Fig.7 $\Phi = f(Q'_1)$; $n'_1 = n'_{1n}$ and on Fig.8 $\Phi = f(n'_1)$; $a_0 = a_{0n}$. The analysis of these results shows that there is a satisfactory coincidence between the theoretically and experimentally determined values of Φ only in the region of the rated operating conditions, while with $Q'_1 < 0{,}6\, Q'_{1n}$ the values of f /respectively Φ / obtainned from /3/ and /5/ considerably differ from those measured. These differences are still greater with $n'_1 \neq n'_{1n}$ but it should be born in mind that with the normal operation of the turbines, the deviations of n'_1 with respect to their rated values are not so great. Comparatively speaking, the best coincidence in almost the whole range of tested operating conditions has been found when formula /2/ is used. Equation /3/ leads to a very good coincidence, especially with the rated operating conditions. The analysis of the amplitude characteristics $2\bar{A} = f(\varphi, \psi)$ and the values obtained by Eq./4/ shows a lack of convergence even with the rated operating conditions, due to which its application to low-speed Francis turbines cannot be recommended.

IV. CONCLUSIONS

Some more important results obtained by the present investigation are the following:

Astudy was made of the influence of the guide vanes closing time /linear closing/ on the variation of discharge, the pressure at the turbine inlet and after the impeller, the shaft moment and frequency of rotation concerning low-speed Francis turbines. A study was made of the amplitude and frequency of pressure variation after the impeller under various operating conditions of the turbine. The results of these investigations are good reason to recommend the Rheingans and Hosoi's formulas for the frequency of pressure variarion in low-speed Francis turbines. The results of the investigations confirm the predicted better characteristics of the P073-A1 impeller, estimated after an extensive numerical experiment performed by means of a digital computer.

SYMBOLS

$n_s = n.P^{1/2}.H^{-5/4}$ - specific frequency of rotation

H = head mH_2O

P = power kW

n = frequency of rotation min^{-1}

A = amplitude of pressure variation

T_s = closing time of guide vanes

a_0 = opening of guide vanes

$\varphi_2 = Cm_2/U_2 = 8Q/\pi\omega D_2^3$ discharge coefficient

$\psi_2 = 2gH/U_2 = 8gH/\omega^2 D_2^2$ pressure coefficient

Q - discharge m^3/s

D_2 - diameter of the impeller output

D_1 - diameter of the impeller inlet

Cm_2, Cu_2 - meridian and periphery component of the speed of the impeller output

g - accelleration due to gravity

β - angle of vane output

$n_1' = nD_1/\sqrt{H}$

$Q_1' = Q/D_1^2\sqrt{H}$

SUBSCRIPTS

m - optimum value when a_o = const

n - value at rated operating conditions

a - value of the mean point of the impeller output edge

REFERENCE

1. Kichev V.M. Device for Measuring Discharge of Fluid in Time Function. Certificate Bulg. No. 19727 G 01 f 1/00
2. Obretenov V. Investigation and Development of the Francis Water Turbines with Low Specific Speed.Ph.D. thesis, VMEI, Sofia, /Bulgarian/
3. Klein J. Untersuchung der Saugrohrschwingungen einer Francisturbine miltels Modellversuche. VDI - Berichte, 1973, N193
4. Hosoi Y. Characteristics of Pressure Surge Due to Whirling Water from Exit of Water Turbine Runner. Bulletin JSME,1973,v.16,N99
5. Gerich R.,J. Raabe. Measurement of the Unsteady and Cavitating Flow in a Model Francis Turbine of high Specific Speed. Journal of Fluids Engineering, Transactions ASME,XII,1975
6. Паэи Л. Исследование периодических пульсаций давления в отсасывающих трубах гидротурбин. Труды ВНИИГидромаша, 1968, вып.37. /Russian/.

LAWS OF MOVEMENT OF MAGNETIC PROPELLED FEEDING PUMPS

by

ANDRÁS ODROBINA

In chemistry, pharmaceutical-, paint-, and food industry have been increasing number of feeding pumps significantly. At a part of machnines same type, piston or membran are propelled by electromagnet. Our work an attempt to write laws of movement of moving elements of these machnines.

Operating principle of machine

On Figure 1 is shown the scheme of magnetic propelled pump.

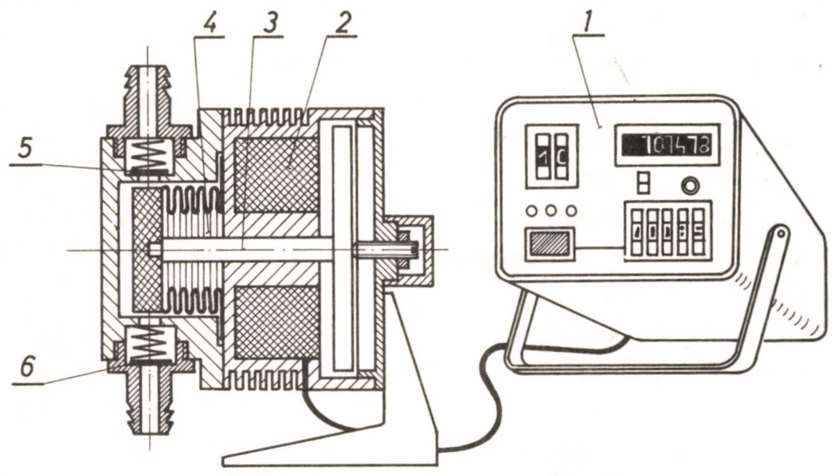

Fig. 1.

At centrollable time intervals given stated time strain by electronic governor unit (1) to the magnet coil (2). As a result, the moving part of the machine (3) moves from the start point to the end point and after strains stopping come back to the start point, as a result of the membran (4) wich is functioning as a spring. The pressure valve (5) and the suction valve (6) are opening and closing as a result of colume's change caused by membran.

SYMBOLS

Sign	Denomination	Unit of measurement
A_d	Surface of membran	m^2
A_s	Surface of valve sitting	m^2
K	Outline of valve	m
M_d	Moving part's volume	kg
M_s	Valve volume	kg
C_d	Spring constant of membran	N/m
C_s	Spring constant of valve	N/m
C_g	Elasticity of cylinder	Pa/m^3
C_m	Constant of magnet	N/m
F_s	Prestretch of valve spring	N
F_d	Prestretch of membran	N
F_m	Starting power of magnet	N
P_n	Pressure of pressure line	Pa
P_h	Pressure in cylinder	P
S_d	Length of stroke	m
V_d	Velocity of membran	m/s
A_d	Acceleration of membran	m/s^2
h	Rise of valve	m
V_s	Velocity of valve	m/s
d_s	Acceleration of valve	m/s^2
ϱ	Density of liquid	kg/m^3
ν	Viscosity of liquid	m^2/s
μ	Throwflowing factor	-
T_B	Time of strain	s
F	Power of magnet	N
V	Volume of cylinder space	m^3

Equations of the laws of movement

These equations are concerning for one pressure stroke. Under the switching-time pulling-pressure is the function of the stroke written by the following equation:

$$F = Fm + Cm . Sd \qquad N \qquad (1)$$

Equilibrium of the powers affecting to moving part, divided by the moving part's mass:

$$\frac{d^2Sd}{dt^2} = \frac{F}{md} - \frac{Cd.Sd}{md} - \frac{Fd}{md} - \frac{Ph.Ad}{md} \qquad \left(\frac{m}{s^2}\right) \qquad 2$$

Volume changing velocity of elastic fluid, closed in the elastic cylinder-space:

$$\frac{dV}{dt} = Ad \cdot \frac{ds_d}{dt} - As \cdot \frac{dh}{dt} - \mu_{(Re)} K.h \sqrt{\frac{2}{\varrho}(Pn-Ph)} \qquad \left(\frac{m^3}{s}\right) \qquad 3$$

μ as a thow flowing factor is the function of Reynolds number. Reynolds number concerned to valve-gap may be written:

$$Re = \frac{\mu \sqrt{\frac{2}{\varrho}(Pn-Ph)} \cdot h}{\nu} \qquad 4$$

μ-Re function concerned to small valves commended by different articles and based on our measuring is shown on Figure 2.

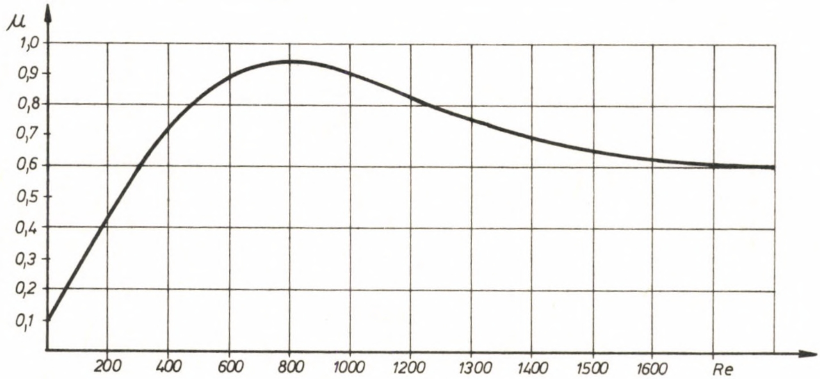

Fig. 2.

Following equation expresses equilibrium of powers affecting to the valve-body, divided by valve mass.

$$\frac{d^2h}{dt^2} = \frac{(Pn-Ph)As}{ms} - \frac{Cs.h}{ms} - \frac{Fs}{ms} \qquad \left(\frac{m}{s^2}\right) \qquad 5$$

Finally can be written equation between the pressure of cylinder space and its elastic volume changing:

$$\frac{dp_n}{dt} = Cg \frac{dV}{dt} \quad . \qquad 6$$

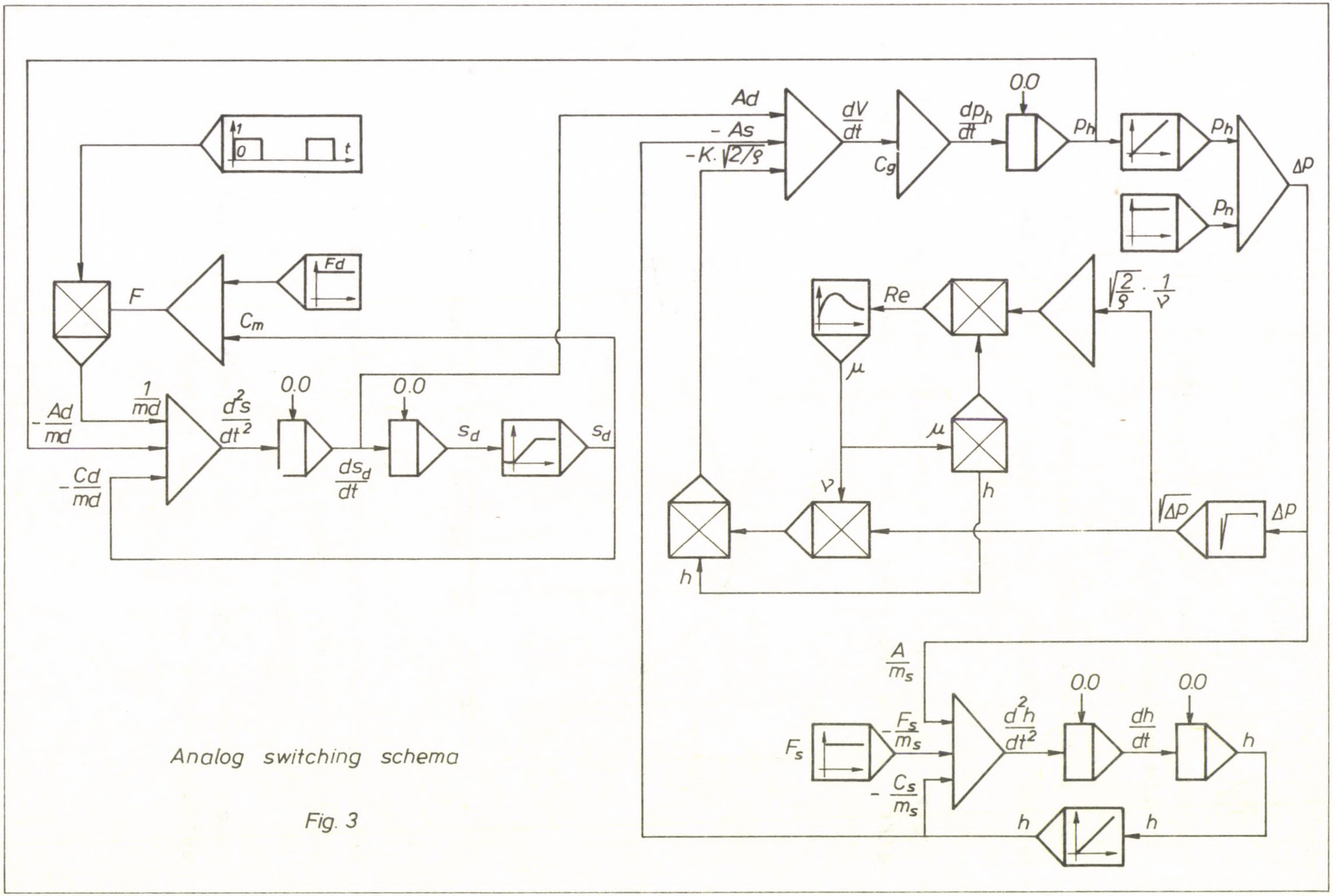

Analog switching schema

Fig. 3

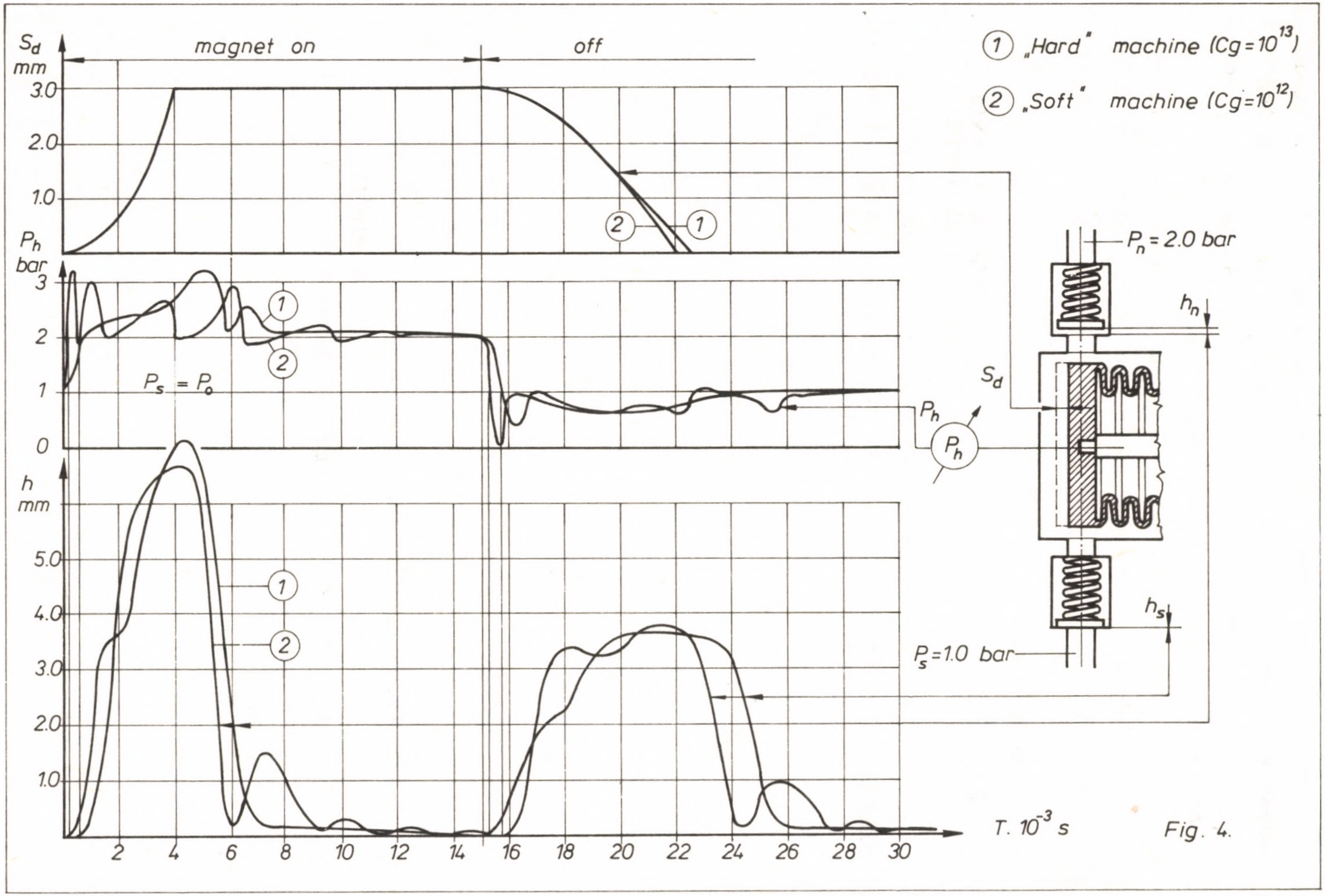

Sd mm
magnet on
off
3.0
2.0
1.0
Ph bar
3
2
1
0
Ps = Po
h mm
5.0
4.0
3.0
2.0
1.0
2 4 6 8 10 12 14 16 18 20 22 24 26 28 30
T. 10^-3 s
① „Hard" machine (Cg = 10^13)
② „Soft" machine (Cg = 10^12)
Pn = 2.0 bar
hn
Sd
Ph
hs
Ps = 1.0 bar

Fig. 4.

Analog seitching schema of the solution of 1-6 equations is shown on Figure 3. Laws of moving identified by analog schema was determined by help of a FORTRAN program functioning in the same way that the scheme.

On Figure 4 are shown laws of moving of machine working with a membran of 40 mm distance and with valves of 12 mm, the valves are spring-loaded.

REFERENCES

HENRYK CHROSTOWSKI: PODSTAWOWE ZAGADNIENIA OBLICZANIA SAMOCZYNNYCH ZAWOROW WZNIOSOWYCH W POMPACH TLOKOWYCH (Rozprawa doktorska) 1979.

ADOLPH V.: BERECHNUNG DER ARBEITSVENTILLE VON KOLBENPUMPEN. (Pumpen und Verdichter 1967).

DR. TECHN. ANDRÁS ODROBINA
TECHNOLOGICAL HIGHSCHOOL POLLACK MIHÁLY
INSTITUT OF SILICATE AND CHEMISTRY
ENGINEERING
PÉCS RÓKUS U. 2.
HUNGARY

FUNCTION OF THE AERODYNAMIC BLADE LOADING AS THE CRITERION TO THE DESIGN OF THE CENTRIFUGAL IMPELLER

Joachim J. Otte

SUMMARY

The general outline of function of the aerodynamic blade cascade loading of centrifugal impeller was considered as a criterion of its rational designing. It was proved that the distribution of function of aerodynamic load along the radius has significant influence on the efficiency and performance characteristics of impellers.

INTRODUCTION

The classical methods of designing centrifugal impellers of fans, pumps and compressors are fundamentally based on the accumulated empirical material and principally resolve themselves into calculating geometry in inlet and outlet section of a row of blades. The very blade on the other hand, is formed after circular arc. This form, however, has no rational justification as far as aerodynamics of flow is concerned. Also in a number of cases the divergence from circular form does not even influence the valuation of the producibility of impellers.

At that very moment the problem of defining criteria arises which would in a synthetic way characterize the flow and which could, in a suitable form for the constructors, be applied to evaluate the geometry of blade cascade. The presented general outline of function of the aerodynamic blade loading of centrifugal impeller according to the definition

$$\Delta\pi = \frac{\Delta p}{\frac{1}{2}\varrho w^2} \tag{1}$$

serves as a suggestion of such a criterion.

The dimensionless function $\Delta\pi = f(r)$ is defined as a ratio of the static pressure difference Δp on both sides of a blade to the dynamic pressure of stream filament in a section with the radius r (fig. 1). The values expresed in $\Delta\pi$ function, i.e. the mean relative velocity

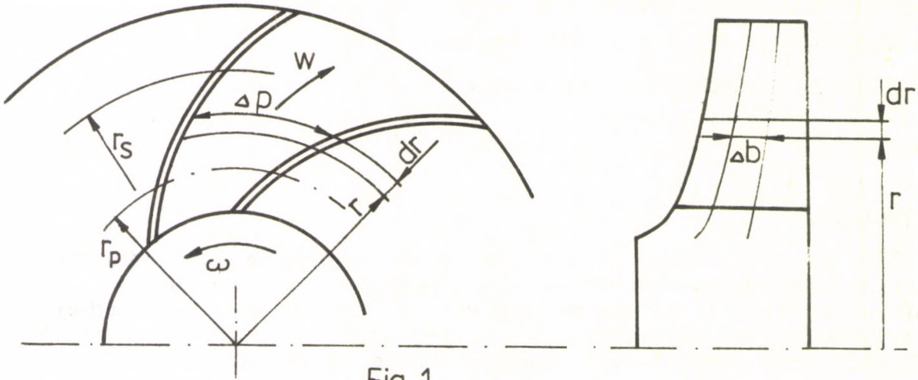

Fig. 1

"w" and the static pressure difference "Δp", are the most important parameters characterizing the flow in the rotating vane passage. The values "w" and " p", i.e. also the function $\Delta\pi$, can be calculated by means of various methods. Below a relatively simple algorithm of the calculations of $\Delta\pi$ function, is presented.

THE ALGORITHM OF THE CALCULATIONS OF AERODYNAMIC LOAD FUNCTIONS

The initial equation is Euler's equation of motion

$$\frac{d\bar{c}}{dt} = - \frac{1}{\varrho} \operatorname{grad} p, \tag{2}$$

which for peripheral direction can be written in the form

$$c_r \frac{d(rc_u)}{dr} = - \frac{1}{\varrho} \frac{\partial p}{\partial \varphi} \tag{3}$$

Passing on to difference approximation of the above differential equation, one obtains

$$- \frac{1}{\varrho} \frac{\partial p}{\partial \varphi} \approx \frac{1}{\varrho} \frac{\Delta p}{\Delta \varphi} = c_r \left. \frac{d(rc_u)}{dr} \right|_m \tag{4}$$

The "m" index denotes that a given value is calculated in the middle of the vane passage.

Taking into consideration that the finite result of the angular pitch comprises the vane passage i.e. that

$$\Delta\varphi = \frac{2\pi\tau}{z} \tag{5}$$

and taking no account of the "m" index, one finally obtains

$$\Delta p = \frac{2\pi\tau}{z} c_r \frac{d(rc_u)}{dr} \tag{6}$$

In the above formula the following values appear:

ϱ - mass density

z - number of blades

τ - tangential blockage factor, defined as

$$\tau = 1 - \frac{zg}{2\pi} \tag{7}$$

where g is angular blade thickness on the radius "r",

c_u - tangential celocity which is calculated from the formula

$$c_u = u - c_r \mathrm{ctg}\beta, \tag{8}$$

c_r - radial velocity which is calculated from the equation of stream continuity.

The introduced notion of function of the aerodynamic blade loading refers fundamentally to stream filament the width of which $\Delta b = \Delta b(r)$ and then the equation of continuity has the form:

$$m = 2\pi r\tau\varrho c_r \Delta b \tag{9}$$

For single curvature blades the calculations can be carried out for the stream comprising the whole width of the impeller. Then the equation of continuity is applied in the following form:

$$\dot{m} = 2\pi r\tau\varrho b c_r \tag{9a}$$

The mean relative velocity "w" which is indispensable to calculate $\Delta\pi$ function according to the formula (1), is calculated from the self--ewident dependence

$$w = c_r/\sin\beta \tag{10}$$

The assignment of the distribution of the mean flow angle $\beta = \beta(r)$ requires certain assumptions. Thus it is suggested here to distinguish three zones (fig. 1) in which the angle of the stream β will be described by the dependencies resulting from various premises. In the middle zone the angle of the stream can be assumed as equal to the vane angle, where-as in the inlet and outlet zones, the angle of the stream will be the resultant of the reaction of the blades and of the flow conditions at the rotor inlet and outlet. The particular zones are separated by r_p radius from which it is assumed that the influence of the conditions in the entry to the row decays. The zones are also separated by r_S radius which is the so-called STANITZ-radius [1]. The r_p radius can be approximately defined by means of the following dependence

$$r_p = r_1\left(1 + \frac{\pi}{z}\sin 2\beta_1^*\right) \tag{11}$$

where β_1^* is the vane angle in the inlet.
Finally in the specified three zones as far as the distribution of mean flow angle $\beta = \beta(r)$ is concerned, one can assume the following assumptions:

$$\begin{aligned} &- \text{for} \quad r < r_p; && \beta = a_1 + b_1 r + c_1 r^2 \\ &- \text{for} \quad r_p < r < r_S; && \beta = \beta^* \\ &- \text{for} \quad r > r_S; && \beta = a_2 + b_2 r + c_2 r^2 \end{aligned} \tag{12}$$

The coefficients a_1, b_1, c_1, a_2, b_2, c_2 are calculated correspondingly in virtue of the following conditions: the angle of the stream in the inlet or outlet, the vane angles in the section with r_p or r_S radius, as well as the derivative values of the vane angle in the same sections.

If in the case of the inlet angle of the stream β_1, its imposed value is the kinematics of flow, then in the case of the outlet angle of the stream β_2, its value must result from satisfying Kutta-Joukowski condition. The value of β_2 angle is thus defined here by means of iteration so as to satisfy the condition $\Delta p = 0$ in the outlet section.

The presented algorithm of calculations enables one to ascertain that the distribution of the function of the aerodynamic blade loading of the centrifugal impeller is dependent on:

- the form of the blade
- the geometry of the impeller in the meridional section
- the number of the blades of the impeller
- the thickness of the blades
- the working point of the impeller.

EXAMPLES OF THE APPLICATION OF THE FUNCTION OF THE AERODYNAMIC LOADING

In order to illustrate the influence of the form of the blade on the distribution of the aerodynamic loading function, the impeller with the blades of the same inlet and outlet angles (β^*_1 and β^*_2), was considered. The first time the blades were formed by the circular arc, the second time, however, according to the dependence $tg\ \beta^* = a + b\nu^2$ (where $\nu = r/r_2$). The distribution of the vane angles was shown in fig. 2 whereas the distribution of the function of the aerodynamic blade loading was presented in fig. 3. As far as the same impellers are concerned, additionally fig. 4 and 5 show the formation of $\Delta\pi$ function in the case of three values of volumetric flow coefficient.

The data named in the paper [2] are another example pointing to the advisability of the application of the aerodynamic loading function in the process of designing. Experimental investigations of impellers were carried out in the above mentioned paper. These impellers had the same inlet vane angle $\beta^*_1 = 30^\circ$ and outlet angle

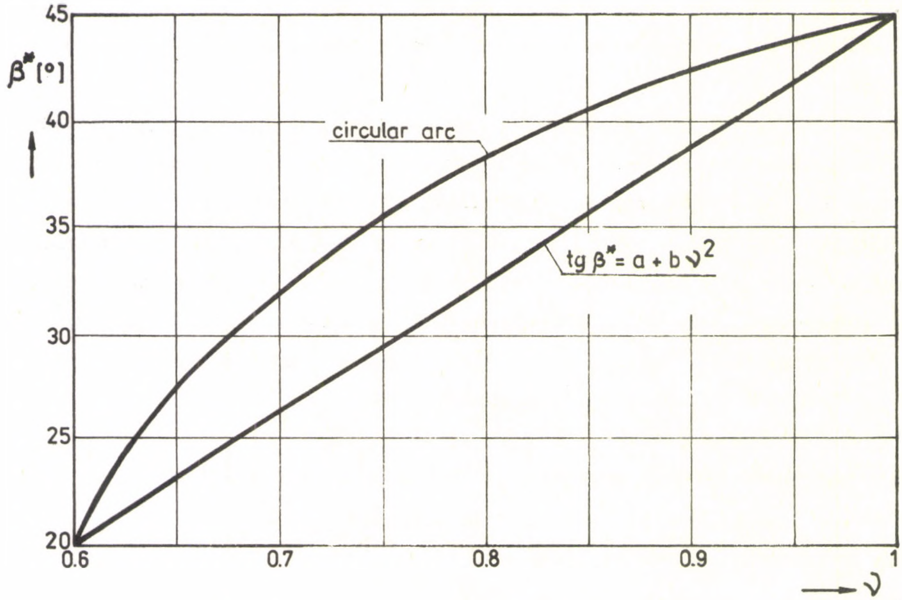
45
β* [°]
40
35
30
25
20
0.6
0.7
0.8
0.9
1
circular arc
tg β* = a + b ν²
ν

Fig. 2

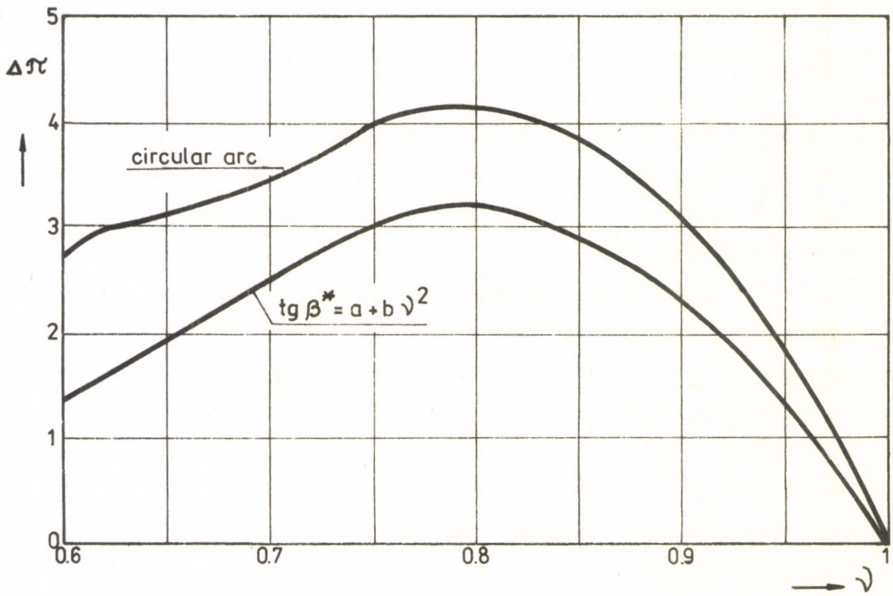
5
Δπ
4
3
2
1
0
0.6
0.7
0.8
0.9
1
circular arc
tg β* = a + b ν²
ν

Fig. 3

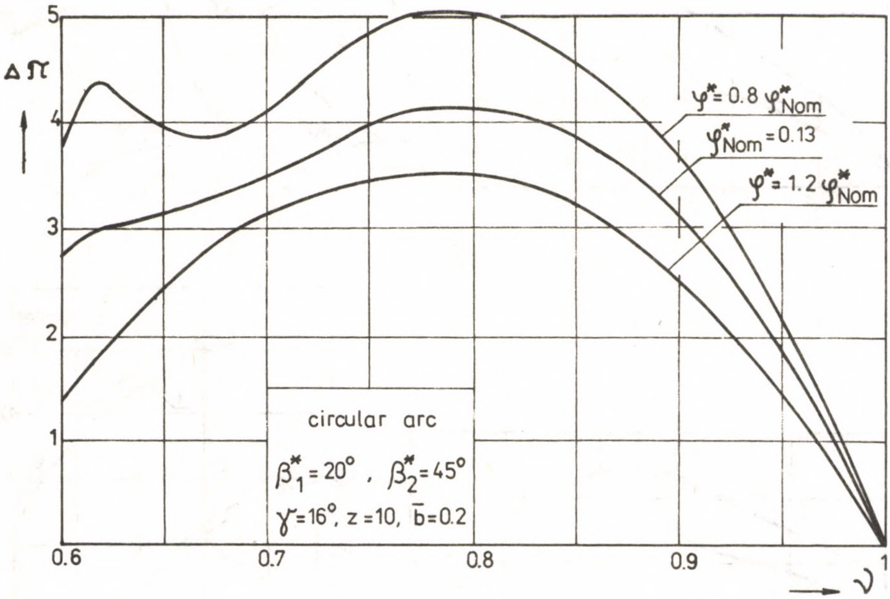

5
4
3
2
1
Δπ
0.6
0.7
0.8
0.9
1
ν
φ* = 0.8 φ*Nom
φ*Nom = 0.13
φ* = 1.2 φ*Nom
circular arc
β*1 = 20° , β*2 = 45°
γ = 16°, z = 10, b̄ = 0.2

Fig. 4

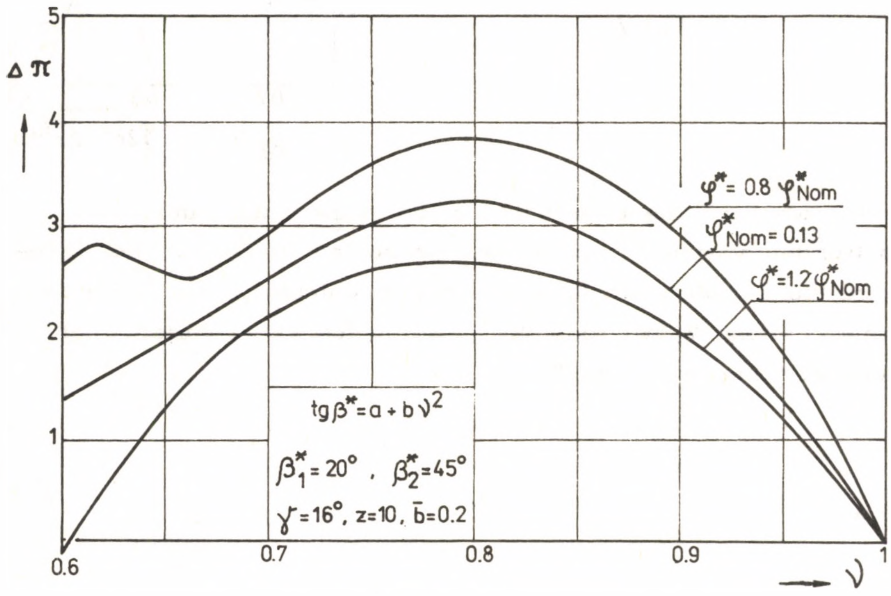

5
4
3
2
1
Δπ
0.6
0.7
0.8
0.9
1
ν
φ* = 0.8 φ*Nom
φ*Nom = 0.13
φ* = 1.2 φ*Nom
tg β* = a + b ν²
β*1 = 20° , β*2 = 45°
γ = 16°, z = 10, b̄ = 0.2

Fig. 5

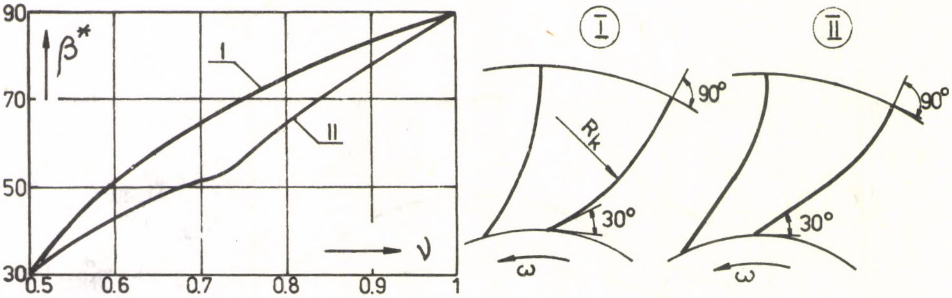

Fig. 6

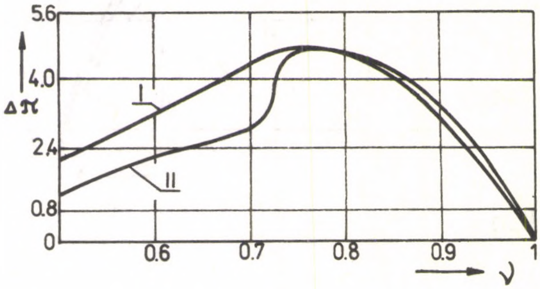

Fig. 7

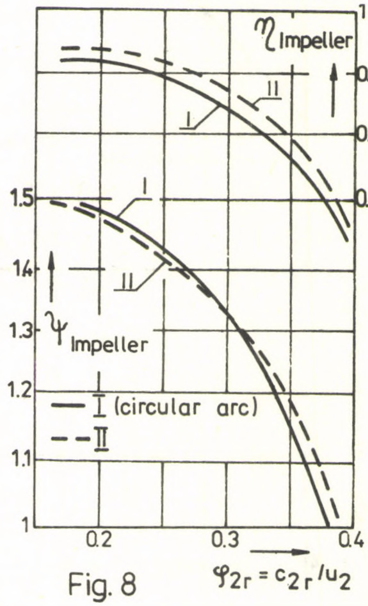

Fig. 8

$\beta_2^* = 90^{\circ}$, whereas the distribution of the vane angle along the radius trended variously, which was presented in fig. 6. The distribution of the aerodynamic loading function calculated for this case, was shown in fig. 7, whereas the performance characteristic of impellers was named in fig. 8.

CONCLUSIONS

The estimation of the function of aerodynamic loading requires the accumulation of the suitable evidence, which is already possible to do making use of the results of measurements concerning the performance characteristics of various impellers.
The investigations which have been carried out hitherto, have made it possible to formulate the following hypotheses:

- there is a boundary, maximum value of $\Delta\pi$ function of loading, the overstepping of which causes a considerable reduction of the impeller efficiency: According to preliminary valuations this maximum (permissible) value $\Delta\pi$ trends on the level about 3.
- out of two impellers of a similar, maximum aerodynamic loading exceeding the boundary value $\Delta\pi = 3$, the impeller giving evidence of a lower value of the function of loading in the inlet section will be characterized by higher efficiency (see fig. 7 and 8).

REFERENCES

[1] TRAUPEL W.: Thermische Turbomaschinen. Springer Verlag, III Auflage.

[2] STOLIARSKIJ M.T.: Sposob powyschenija effektiwnosti wysokonapornych kolies centrobieznych nagnietatielej. Energomaszinostrojenije 1971/7.

OTTE, Joachim Józef, Dr techn.
Silesian Technical University
44-100 Gliwice, ul. Konarskiego 18
POLAND

CAVITATION TESTS ON COPPER BERYLLIUM ALLOYS

U. PIGHINI, G. DI FRANCESCO

SUMMARY

Comparative cavitation tests were performed on Beryllium Copper and Aluminum bronze.

Of Cu-Be alloys, Alloy 25 was chosen since it is the most erosion-resistant of this class.

Among the Aluminum bronzes, ASTM 148-9D alloy was chosen, it being one of the strongest and most utilized Copper-base materials for turbine and pump impellers. Cavitation and cavitation-corrosion tests were performed by using a vibratory device. Rates of mass loss versus time were obtained under various conditions. After a first series of tests, a second one on a special Cu-Be alloy was performed, in order to investigate the influence of Nickel in Beryllium Coppers.

The characteristics of the eroded surfaces of test pieces were compared.

Finally some possible uses of the Cu-Be alloys are listed.

1. INTRODUCTION

On the basis of the study of experimental results [1], it is possible to classify the metals, which show the best cavitation resistance, in three classes, as it is shown in Table 1.

Class	Materials
excellent resistance	Stellites
very good resistance	Nickel Alloys Titanium Alloys
good resistance	Stainless steels Copper alloys

Table 1

According to this Table, one can observe that Copper alloys have a good resistance to cavitation erosion, owning moreover a high strength and corrosion resistance and excellent manufacturing characteristics.

For these features the Copper alloys have several applications in the manufacturing of turbine and pump impellers and of ship propellers.

The alloys, which are more used for the above mentioned applications, are the Copper Alluminum alloys with a percentage of Alluminum between 7% and 12%.

These alloys may contain also Nickel (1% ÷ 7%), Manganese (1% - 14%) and Iron (0,5% ÷ 6%), as it is shown in Table 2.

The mechanical strength of these alloys is very high and allow to reach very good cavitation erosion resistance, as it is also to be expected from the comparatively high values of the CER parameter (i.e.: Cavitation Erosion Resistance) introduced in [1,2] and briefly exposed again in the Appendix.

Alloy no		1	2	3	4	5	6	7	8
Type		Cu 9 Al 1 Fe	Cu 9 Al 2 Mn	Cu 9 Al 2 Mn 1 Fe 1 Ni	Cu 8 Al 6 Mn 1 Ni	Cu 9 Al 3 Fe	Cu 10 Al 5 Ni 5 Fe	Cu 12 Mn 8 Al 3 Fe 3 Ni	Cu 11 Al 4 Ni 4 Fe
ASTM Standard		B148-9B	—	--	-	B148-9A	—	B148-9F	B148-9D
Chemical composition (%)	Cu	88-92	86-89	84-87	82-85	86-89	77-81	70-77	78-82
	Al	8-10.5	8.5-10	8.5-10	7-9	8.5-9.5	8.5-10.5	8-9	10-12
	Ni	—	—	1-2	1-2	—	4-6.5	5-4.5	3-5.5
	Mn	—	1.5-3	1-3	5-6.5	—	—	11-14	—
	Fe	0.5-1.5	—	1-2	-	2-4	4-6	2-4	3-6
Mechanical properties (as cast)	Tensile Strength (daN/mm^2)	50	50	55	52	60	65	70	75
	Endurance Strength 10^8 (daN/mm^2) cycles	15	15	16	16	18	19	20	22
	Vickers Hardness	150	120	130	120	120	200	190	200
CER $(daN/mm^2)^2$	CAVITATION EROSION RESISTANCE	12	10	11	11	15	24	28	33
Applications		Marine Propellers	Marine propellers Pump impellers	Marine propellers Pump impellers	Marine propellers Pump impellers	Marine propellers Pump impellers	Turbine impellers Pump impellers	Marine propellers	Turbine impellers Pump impellers

Table 2

Nevertheless in the field of Copper alloys there are other alloys i.e. the Copper Beryllium alloys which have an higher mechanical strength. Among several alloys, the Alloy 25 is the most important for mechanical uses, as it attains the highest strength and hardness of any Copper base alloy. In the full age hardened condition, tensile strength can exceed 140 daN/mm^2 and hardness can go up to VHN 400.

The chemical composition and mechanical features of this alloy are shown in Table 3, respectively in half age hardened condition ($^1/_2$ HT) and in full age hardened condition (HT). Cavitation tests on Cu-Be alloys are just scarce. Some tests are exposed in [3,4,5,6,7], but their results are deemed not complete and exhaustive.

For this reason the authors decided to examine again the problem, going deeper into the study of these materials, also in the consideration of the encouraging results already attained in previous tests [8].

Alloy type		alloy 25 Half Hard ($^1/_2$ H)	alloy 25 Full Hard (H)
ASTM Standard		B194 B196	B197
Chemical composition (%)	Cu	97.8	
	Be	1.8	
	Co	0.34	
	Si	0.05	
	Zn	0.01	
Mechanical Properties	Tensile Strength (daN/mm^2)	125	130
	Endurance Strength 10^8 (daN/mm^2) cycles	26	28
	Vickers Hardness	342	368
CER $(daN/mm^2)^2$	Cavitation Erosion Resistance	35	45

Table 3

2. EXPERIMENTAL TESTS (1. SERIES)

A first series of cavitation tests was performed on the Alloy 25, with test pieces in the two metallurgical conditions i.e. ½ HT and HT.

Comparative tests were performed on one of the strongest Cu-Al alloys, i.e. ASTM B148-9D, whose features are shown in Table 2 (alloy no. 8).

The erosion tests were performed in a vibratory device, described in a previous paper [9], it having the features shown in Table 4.

Output power supply	500 W
Frequency	20 kHz
Double amplitude	127 µm (p.to p.)
Transducer type	piezoelectric
Test liquids	distilled water salted water
Testpiece immersion depth	6 mm
Erosion time	up to 5 hours
Testpiece diameter	13 mm
Temperature of test liquids	20°C ± 0,5°C

Table 4

The test were performed at first in distilled water and afterwards in salted water, obtained by adding NaCl in H_2O up to saturation. This expedient allowed the authors to realize cavitation corrosion tests with the same duration of the previous normal cavitation tests.

The cavitation tests with testpieces in Cu-Al alloy were very difficult, since the specimens broke very frequently.

On the contrary with Beryllium Copper, tests were much easier and faster.

3. RESULTS OF THE FIRST SERIES OF TESTS

The results of the first series of tests, performed according to what said previously, are shown in Fig. 1 and Fig. 2 and in Table 5.

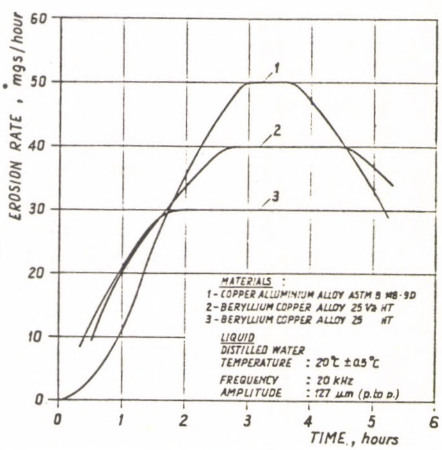

Fig. 1

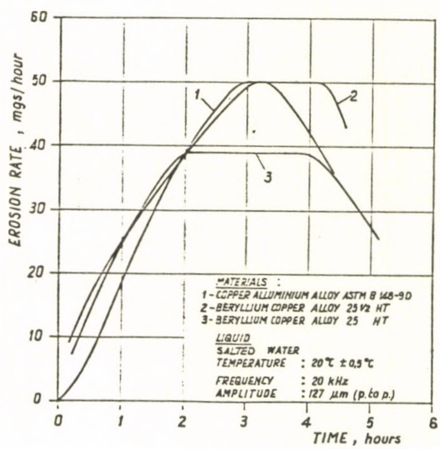

Fig. 2

Material	Distilled water		Salted water	
	Maximum erosion rate (mgs/h)	Erosion resistance (h/mgs) x 10^{-3}	Maximum erosion rate (mgs/h)	Erosion resistance (h/mgs) x 10^{-3}
Alloy 25 HT	30	33,3	39	25,6
Alloy 25 ½ HT	40	25	50	20
ASTM B148-9D	50	20	50	20

Table 5

Fig. 1 shows the erosion rates of the three alloys in distilled water.

On considering the inversed of the peak erosion rate as an index of the erosion resistance [9], one may see how the Alloy 25 in full age hardered state is more resistant than the Cu-Al alloy. The behaviour of the Alloy 25 in half age hardered state is on the contrary less good and intermediate between the former two alloys.

Fig. 2 shows the erosion rates of the three alloys in salted water.

Also in this case the Alloy 25 HT is more resistant than the Copper Aluminium alloy, but the difference of behaviour is lower than that shows in distilled water.

The alloy 25 ½ HT has a behaviour very simular to that of Cu-Al alloy.

4. NOTES ON THE EXPERIMENTAL RESULTS

From the comparative tests performed in distilled water and in salted water it is possible to deduce, clearly, the better behaviour of Beryllium Copper HT to cavitation erosion as compared to the Copper Aluminium alloy.

Fig. 3

The improvement obtained results of 66% in distilled water and of 28% in salted water, as it is shown in Table 5.

Fig. 3, Fig. 4, Fig. 5 and Fig. 6, show respectively the cross section of the test pieces of the Cu-Al alloy and of the Alloy 25 HT after erosion in distilled water and in salted water.

It is possible to observe the different configurations.

While the Copper Aluminium testpiece shows few deep and wide pits, Beryllium Copper shows several small and shallow pits, with a more uniform erosion.

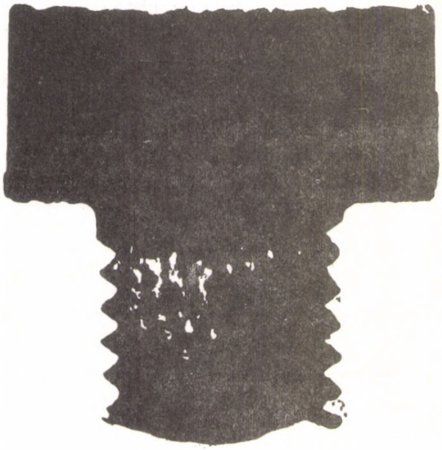

Fig. 4

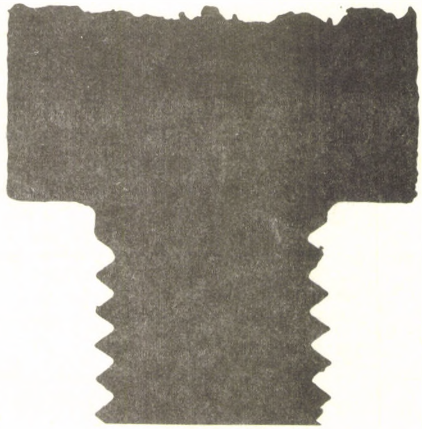

Fig. 5

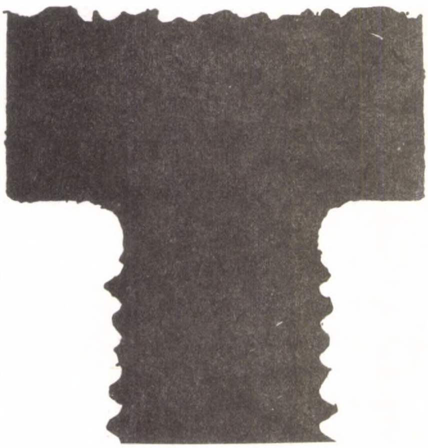

Fig. 6

5. EXPERIMENTAL TESTS (2. SERIES)

On the basis of the results deducted from the 1. series of tests, the authors decided to go on with a further investigation on the Cu-Be alloys.

Alloy 25 was modified increasing its percentage of Beryllium and adding some Nickel with the purpose of increasing the hardness, the strength and the tenacity of the alloy.

This material was prepared on purpose for the present study; its chemical composition and mechanical features are shown in Table 6.

The experimental tests were performed as previously explained for the other alloys.

The test results are shown in Fig. 7 for the tests in distilled water, in Fig. 8 for the tests in salted water and in Table 7.

The results of the former tests are indicated in the same figures with short dashes lines in order to have a direct comparison.

From these figures one can observe that the new alloy has a behaviour similar to that of the normal Alloy 25 HT.

In distilled water there is a little increase in erosion rate of about 3%, while in salted water there is on the contrary a decrease of about 7%.

The configurations of the surfaces of the testpieces, made with Alloy 25 Ni HT are shown in Fig. 9 for the tests in distilled water and in Fig. 10 for

Alloy type		Alloy 25 Ni HT
Chemical Composition (%)	Cu	97.43
	Be	1.90
	Ni	0.25
	Co	0.22
	Zn	0.05
	Fe	0.05
	Al	0.05
	Si	0.05
Mechanical properties	Tensile Strength (daN/mm^2)	130
	Endurance Strength (daN/mm^2)	28 (10^8 cycles)
	Vickers Hardness	391
CER (daN/mm^2)	Cavitation Erosion Resistance	48

Table 6

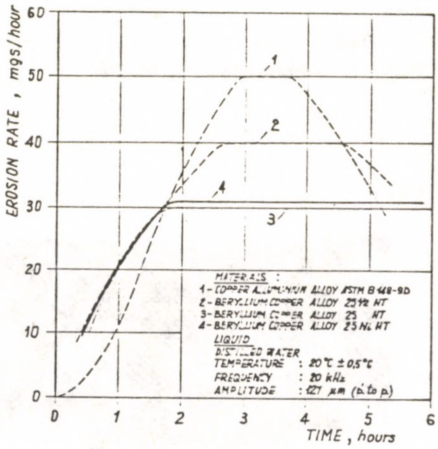

Fig. 7

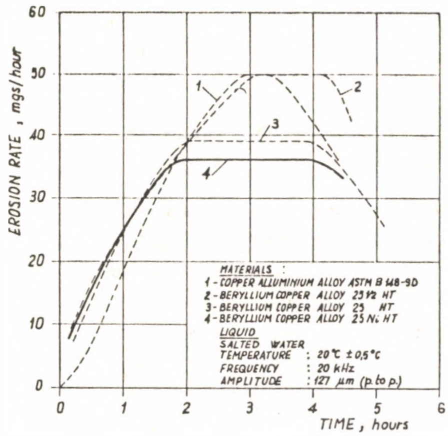

Fig. 8

Material	Distilled water		Salted water	
	Maximum erosion rate (mgs/h)	Erosion resistance (h/mgs) x 10^{-3}	Maximum erosion rate (mgs/h)	Erosion resistance (h/mgs) x 10^{-3}
Alloy 25 Ni HT	31	32.2	36	27.7

Table 7

the tests in salted water.

The aspect of the erosion profiles is similar to that shown in Fig. 4 and Fig. 6 respectively, relative to Alloy 25 HT.

Fig. 9

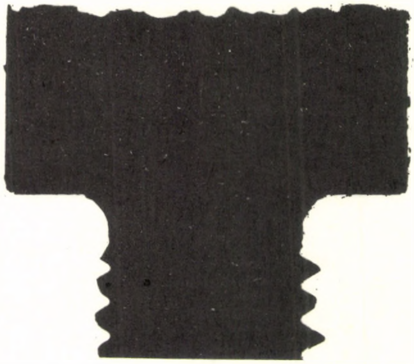

Fig. 10

6. DISCUSSION OF RESULTS

From the comparative tests performed in distilled water and in salted water, it is possible to deduce the better behaviour of the Cu-Be alloy to cavitation erosion as compared to Cu-Al alloy, taken as the reference alloy.

The improvement is more evident in distilled water than in salted water.

Moreover one can pointed out that the erosion surface of the testpieces in Alloy 25 HT is more favourable than that of testpieces in Aluminium Copper, either in distilled water or in salted water. In fact the Cu-Be alloy shows a surface with more numerous and smaller holes as compared to Cu-Al alloy. The authors deem that the Cu-Be alloys could sometimes advantageously replace the Cu-Al alloys, because with them one could have longer working duration for the elements manufactured with these materials, such as pump and turbine impellers, ship propellers, hydrofoils for speed boats.

Moreover the better surface allows an higher efficiency of the impellers and propellers and a higher lift of the hydrofoils.

From the resistance point of view the patter of pits that appear in Beryllium Copper is less dangerous. In fact in case of little thicknesses, this patter allows to lower the piercing effect of erosion and limits the initiation of fatigue cracks.

Beryllium Copper has a tensile strength nearly double in comparison to Copper Aluminium alloys. Consequently it is possible to use machine elements with smaller thickness and therefore with less weight, even with the higher specific gravity of Beryllium Copper.

The only difficulty that exists in the use of these alloys is the higher cost of the materials as compared to Cu-Al alloys, the ratio having a value of about 3:1.

On considering the higher resistance of the Cu-Be alloys, which would allow a lower weight of the machine elements, such ratio might fall to 2:1.

The longer duration and the better surface finish of the elements in Copper Beryllium can shift the cost problems to the second place.

Moreover the use of the Cu-Be alloys could be also important for the replacement of more expensive alloys such as Titanium alloys and Nickel alloys, at least in some applications.

The modification of the Alloy 25 with an higher content of Beryllium and the addition of Nickel did not cause a clear improvement in the behaviour of the alloy. The authors deem that the percentage of Nickel would be higher in order to confer to the alloy a better tenacity, this features being considered very useful for the resistance to cavitation erosion.

7. CONCLUSIONS

The following conclusions have been drawn at the end of the present research:

a. Beryllium Copper, in the full heat treated condition, proves to be more resistant to cavitation erosion than Copper Aluminium alloys.

b. The superiority is inquestionable in distilled water, but less clear in corrosion environment. This behaviour shows that the Cu-Be alloys seem to resist to corrosion less than the Cu-Al alloys.

c. The pits that derive from erosion are smaller and shallower in Cu-Be alloys than in Cu-Al alloys. This is undoubtedly a remarkable advantage, since, mass loss being equal, the solid-liquid contact is better for Cu-Be alloys.

d. The Cu-Be alloys are twice as resistant as Cu-Al alloys. This characteristic enable us to foresee that the machine elements in Cu-Be alloys may have a reduced weight and therefore a limited cost increase as compared to Cu-Al alloys.

e. The good behaviour of the Cu-Be alloys may allow the replacement with these alloys of some more expensive alloys such as Titanium base and Nickel base alloys.

f. It seems advisable to go on with the tests on Cu-Be alloys with an higher percentage of Nickel in order to increase the tenacity and the corrosion resistance of the alloys.

APPENDIX

In reference [2] the CER parameter was defined in the following form:

$$CER = \frac{1}{2} \frac{(k_1 \cdot k_2 \cdot ES)^2}{E} \times (k_3 \cdot VHN)$$

where: k_1, k_3 = oversize coefficients of ES and of VHN, respectively, which take account of the work-hardening effect of material

$k_2 = \frac{ES^*}{ES}$, which takes account of the effect of environment on the endurance strength

ES^* = endurance strength of materials in a given environment (e.g. = = sea water)

ES = endurance strength of materials, in air

E = modulus of elasticity

VHN = vickers hardness.

The value of CER is proportional to the cavitation erosion resistance of metals as it is shown in Table 8.

CAVITATION EROSION RESISTANCE	examples	CER Values $(kg/mm^2)^2$
Very high	Stellites Tantalum Alloys Titanium Alloys Nickel Alloys	> 100
high	Stainless Steels Copper Alloys*	10 - 100
good	Steels Copper Alloys**	1 ÷ 10
fair	Copper, Copper Alloys*** Aluminium Alloys	0.1 ÷ 1
scarce	Aluminium	0,01 ÷ 0.1
no resistance	lead, tin	< 0.01

Table 8

* high resistance
** medium resistance
*** low resistance

ACKNOWLEDGEMENTS

The authors wish to express their thanks to the Metallindustria of Cormano (Milano, Italy) for the partial financial support of the work.

Thanks are also due particularly to Mr. Tirelli for the technical informations given on the Cu-Be alloys.

REFERENCES

[1] Pighini, U.: "Contribution to the study of metal resistance to cavitation erosion", Proc. of the 5th conference on Fluid Machinery, 2, Akademiai Kiado', Budapest, pp. 821-832, 1975.

[2] Pighini, U. et al.: "A new parameter for a rapid evaluation of metal resistance to cavitation attack", Proc. of the 6th conference on Fluid Machinery, 2, Akademiai Kiado', Budapest, pp. 846-856, 1979.

[3] Stewart, W.C. and Williams, W.L.: "Investigation of materials for marine propellers", Proc. Amer. Soc. Test. Mat., 46, pp. 836-845, 1946.

[4] Richards, J.T. Proc. of the 9th Annual Conference, National Association of Corrosion Engineers, Chicago, 1953.

[5] Hohman, A.E. and Kennedy W.L. Materials Protection, 2, pp. 398-402, 1963.

[6] Warkentin, H.S. and Hohman, A.E.: "Which materials for Hydrofoils?" Materials in Design Engineering, 4, pp. 88-90, 1963.

[7] Lichtman, J.Z. and Weingram, E.R. Proc. of the A.S.M.E. Symposium on Cavitation Research Facilities and Techniques A.S.M.E., New York, pp. 185-196, 1964.

[8] Pighini, U. et al.: "Resistance to cavitation erosion of Berillium Copper", Proc. of the Can Cam 79: 7th Canadian Congress of Applied Mechanics, Sherbrooke, Quebec, Canada, 20th May - 1st June, 1979.

[9] Pighini, U. et al.: "Cavitation test with the vibratory method", Proc. of the A.TE.NA. Seminar on Ship Propulsion, Rome, pp. 157-189, 1971 (in italian).

Prof. Ing. Umberto Pighini
Prof. Ing. Giulio Di Francesco

Department of Mechanical and aeronautical
Engineering - Section of Machine Design -
University of Rome
Via Eudossiana, 18 - 00184 Rome (ITALY)

THE SIMULATION OF THE INFLUENCE OF PUMP ROTATION CONTROL ON THE TRANSIENT PHENOMENA IN LARGE-AREA IRRIGATION SYSTEMS.

Karol Prikkel

Summary

The prevailing trend in the present is to irrigate the largest possible areas using a single pumping station. The extension of irrigated surface (20 km^2 and more) entails an increase in power consumption used in order to secure the required pressure and flow rate. With respect to the possibilities of electric motor control, the control of the hydrodynamic pump rotations seems to provide a progressive and technologically feasible answer.

The present paper deals with the possibility of digital simulation of unsteady flow of fluids in large-area irrigation systems using a pump with regulator. The simulation described below enables also to assess the influence of the regulator type and to determine the time constants.

1. Introduction

The unsteady unidimensional, continuous, isothermal flow of a Newtonian fluid can be described by means of Euler movement equation [1]:

$$\frac{\partial c}{\partial t} + c \cdot \frac{\partial c}{\partial x} + \frac{1}{\rho} \cdot \frac{\partial p}{\partial x} + \frac{dh}{dx} \cdot g + \frac{\lambda}{2 \cdot d} \cdot c \cdot |c| = 0 \tag{1}$$

and continuity equation (in an adjusted form) [1]:

$$\frac{\partial p}{\partial t} + c \cdot \frac{\partial p}{\partial x} + \rho \cdot a^2 \frac{\partial c}{\partial x} = 0 \tag{2}$$

The canonical form of partial differential equations (1,2) will be:

$$\frac{dx}{dt} = c \pm a$$

$$\pm \frac{dp}{dt} + \rho \cdot a \frac{dc}{dt} + \rho \cdot a \cdot g \frac{dh}{dx} + \rho \cdot a \frac{\lambda}{2d} \cdot c \cdot |c| = 0 \tag{3}$$

The solution of (3) using the method of characteristics [2] and under the assumption that $a \gg c$; Δx = const. and that the flow takes place in the automodelling area $[\lambda \neq f\,(Re)]$ for K_+, or K_- characteristics gives (Fig.1).

$$\Delta x = \Delta t \cdot a$$

$$\rho \cdot a \cdot c_{i+1,j} \pm p_{i+1,j} = \pm p_{i,j\mp1} + \rho \cdot c_{i,j\mp1} \cdot \left(a - \frac{\lambda}{2 \cdot d} \left| c_{i,j\mp1} \right| \cdot \Delta x\right) - \rho \cdot g \cdot \Delta h \tag{4}$$

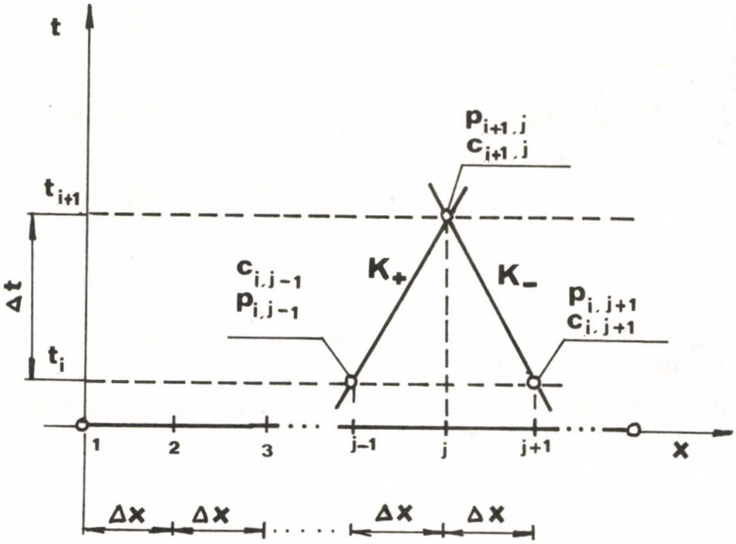

Fig. 1

The solution according to (4) can be applied to the entire pipeline network [3]. The solution yields the time dependency between pressures and flow rates (or velocities) in any given calculation point of pipeline network [3], [4].

2. Description of the Control Process

The high-pressure irrigation system can include - in addition to the pipeline network - also a hydrodynamic pump with regulator. The specific feature of irrigation system control consists in the fact that in view of large irrigated areas, the feedback can include only the electric motor + pump and a relatively short section of the pipeline (Fig.2).

The control process is as follows: The required pressure is preset on the regulator. This pressure is identical with that at the point of reading when the system of irrigation works under a steady mode. Due to the influence of a disturbance variable, the irrigation system should pass from such steady state into another steady state, characterized by a different flow rate, but the pressure corresponding to the desired value.

The disturbance variable can be represented by the parameter of irrigation detail, changed number of intakes, etc.

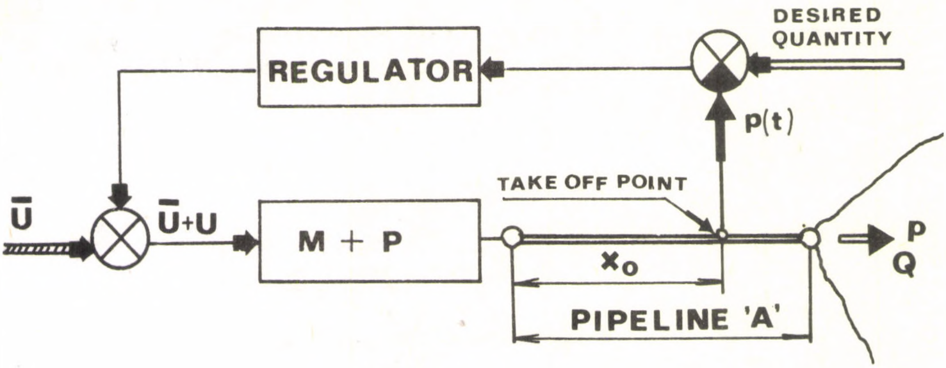

Fig. 2

The digital simulation can be also used to test the properties of theoretically composed regulator.

Let us consider the connection of the regulator according to Fig.3:

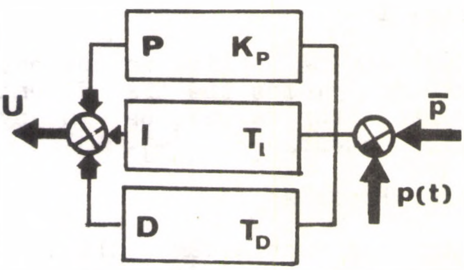

Fig. 3

Let the input variable for the regulator be X = X(t) and output variable U = U(t).

When considering the regulator with the delay of the first order of magnitude and time constant T_1, then the differential equation of such regulator will be:

$$T_1 \cdot \frac{dU}{dt} + U = T_D \cdot \frac{dX}{dt} + K_P \cdot X + \frac{1}{T_I} \int_0^t X \cdot dt \tag{5}$$

When $p(t)$ is the actual pressure read off at the intake point (Fig.2), then in view of the linear approximation when using the method of characteristics [2] the pressure $p(t)$ can be approximated over the examined time interval $\Delta t = t_{i+1} - t_i$ in a linear mode:

$$p(t) = a.t + b \qquad a,b = \text{const.} \tag{6}$$

Input variable for the regulator will be:

$$X(t) = \bar{p} - p(t) = \bar{p} - a.t - b \tag{7}$$

Substituting (7) into (5) we obtain:

$$T_1 \cdot \frac{dU}{dt} + U = - \frac{a}{T_I \cdot 2} t^2 + t\left(\frac{\bar{p}}{T_I} - \frac{b}{T_I} - K_p.a\right) + K_p.\bar{p} - T_D.a - K_p.b \tag{8}$$

The solution of equation (8) is:

$$U = c \cdot e^{-\frac{1}{T_1} \cdot t} - \frac{a.t^2}{2.T_I} + t\left(\frac{\bar{p}}{T_I} - \frac{b}{T_I} - K_p.a + \frac{T_1}{T_I}.a\right) + K_p \cdot \bar{p} - T_D \cdot a - K_p \cdot b - \frac{T_1 \cdot \bar{p}}{T_I} + T_1 \cdot K_p \cdot a - \frac{T_1^2}{T_I} \cdot a \tag{9}$$

where:

$$c = -\left(K_p \cdot \bar{p} - T_D \cdot a - K_p \cdot b - \frac{T_1}{T_I} \cdot \bar{p} + T_1 \cdot K_p \cdot a - \frac{T_1^2}{T_I} \cdot a\right)$$

The equation (9) can be used to read the deviation of voltage which brings about the change in the rotations of electric motor.

3. The Dynamic Behaviour of the Aggregate Motor + Pump

The moment of the electric motor is assumed to be

$$M_m = M_{\check{c}} + J \cdot \frac{d\omega}{dt} \tag{10}$$

where: $M_m = \dfrac{U.I}{\eta_m \cdot \omega}$; $M_{\check{c}} = \dfrac{P}{\eta_{\check{c}} \cdot \omega}$

After the adjustment of (10) and differentiation:

$$\Delta n = \frac{U.I \cdot \Delta t}{4.\pi^2.n.J.\eta_m} - \frac{P.\Delta t}{4.\pi^2.n.J.\eta_{\check{c}}} \tag{11}$$

Rotations in the time t_{i+1} will be

$$n_{i+1} = n_i + \Delta n \tag{12}$$

For the output according to the affinity:

$$P_{i+1} = P_i \cdot \left(\frac{n_{i+1}}{n_i} \right)^3 \tag{13}$$

Pressure of the pump from p-Q characteristics:

$$p_{i+1,\check{c}} = A . n_{i+1}^2 + B . n_{i+1} \cdot Q_{i+1} + C . Q_{i+1}^2 \tag{14}$$

A,B,C are constants which characterize the type of the pump. Equations (11), (12), (13) and (14) describe the dynamic behaviour of the pump following the controlling intervention.

4. The Solution of the Pipeline Section "A"

The pipeline section "A" is connecting the pump with the pipeline network (Fig.2). In the junction "$1_{\check{c}}$", the pipeline is connected with the pump which constitutes a marginal condition. At this point, only the K_- characteristics are known (Fig.4).

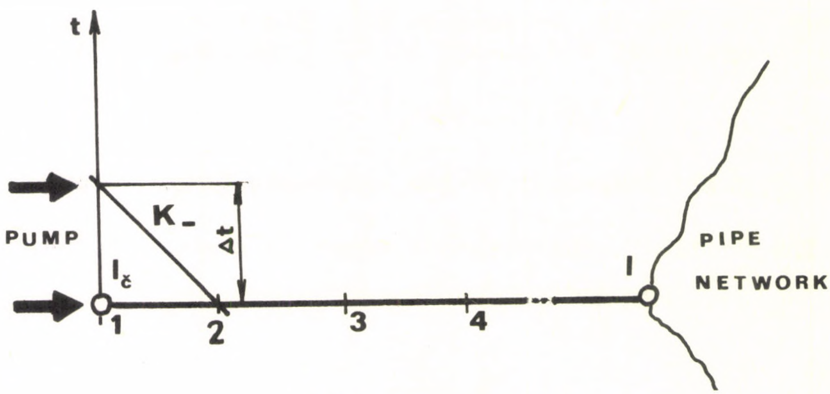

Fig. 4

The simultaneous solution of the equation of characteristics of K_- (4) with characteristics of the pump (14) yields the flow rate in the junction "$1_{\check{c}}$":

$$Q_{i+1,l\check{c}} = \frac{-K_2 - \sqrt{K_2^2 - 4 . K_1}}{2} \tag{15}$$

where:

$$K_1 = \frac{1}{C}\left[A.n_{i+1}^2 - p_{i,2} + \frac{a}{S}\cdot Q_{i,2}\cdot\left(1 - \frac{\lambda.\Delta t}{2.d.\rho.S}\cdot|Q_{i,2}|\right)\right]$$

$$K_2 = -\frac{1}{C}\left(\frac{a}{S} - B.n_{i+1}\right) \tag{16}$$

The density considered in the equations (14), (15) and (16) was $Q = \varrho .S.c$
The pressure in the junction "$1_{\check{c}}$" and time i+1 will be then determined from (14).

Under an unsteady flow of the fluid, oscillation of pressures occurs at the intake point of pipeline section "A" (Fig.2). The principle of the regulator operation is such that the regulator reacts even to small changes in pressure. In view of the fact that the time constant of the motor+pump aggregate is substantially higher than the period of pressure pulsations, it is not desirable for the regulator to respond also to relatively small amplitudes of pressure oscillations. We can assume the insensitivity of the regulator to have the form:

$$|p_{i+1} - \bar{p}| < p_H \qquad \text{than} \quad p_{i+1} = p_i = \bar{p} \tag{17}$$

where p_N is the smallest change in pressure to which the regulator should react.

5. The Adjustment of the Regulator Constants

The digital simulation of the process of control serves also as a kind of prediction as to what constants should be preset on the regulator so as to achieve an optimum control. For an approximative solution of regulator constants, guidelines for experimental regulator setting, formulated by Ziegler and Michols [5] , can be used:
When K_{PK} is the critical intensification of P member, then

$K_p = 0.5\ K_{PK}$ in the case of P regulator

$K_p = 0.45\ K_{PK}$; $T_I = 0.8\ T_K$ for PI regulator.

$K_p = 0.6\ K_{PK}$; $T_I = 0.5\ T_K$; $T_D = 0.12\ T_K$ in the case of PID regulator. T_K is the period of vibration under a critical intensification.

6. Possibilities of Alternative Regulator Connections

The mathematical model of the process of control was derived for the structure of regulator described in Fig.3.

The programme for a digital simulation of the process of control is suitable also for different regulator structures. Individual members, however, must be autonomous, i.e. the change in the intensification of P-member does not entail any change in the time constants T_I, T_D.

Such structures can be found in regulators according to Fig.5.

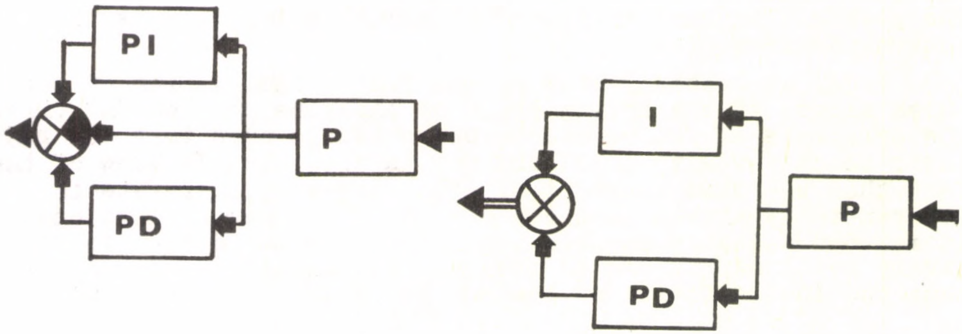

Fig. 5

7. Some Results of the Simulation

7.1 Simple Pipeline Section

The irrigation system consists of one pipeline, one pump with regulator (Fig.6).

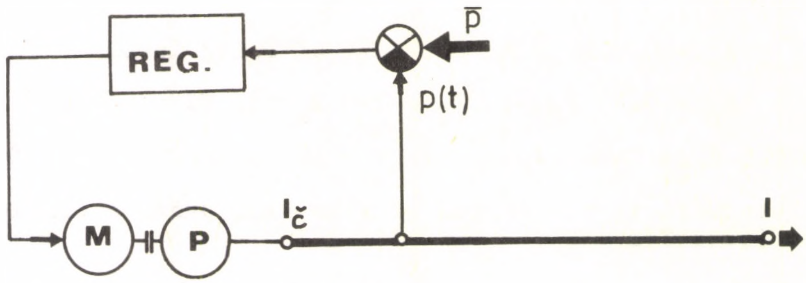

Fig.6

If Q_0 is the steady-state flow rate and after resetting the irrigation detail to a lower intake $Q_{01} < Q_0$, the pressure after the stabilization will have a higher value (Fig.7). If the P regulator is used, after the period of controlling operation, the pressure will settle down to its original value, naturally, with a permanent control deviation (Fig.7).

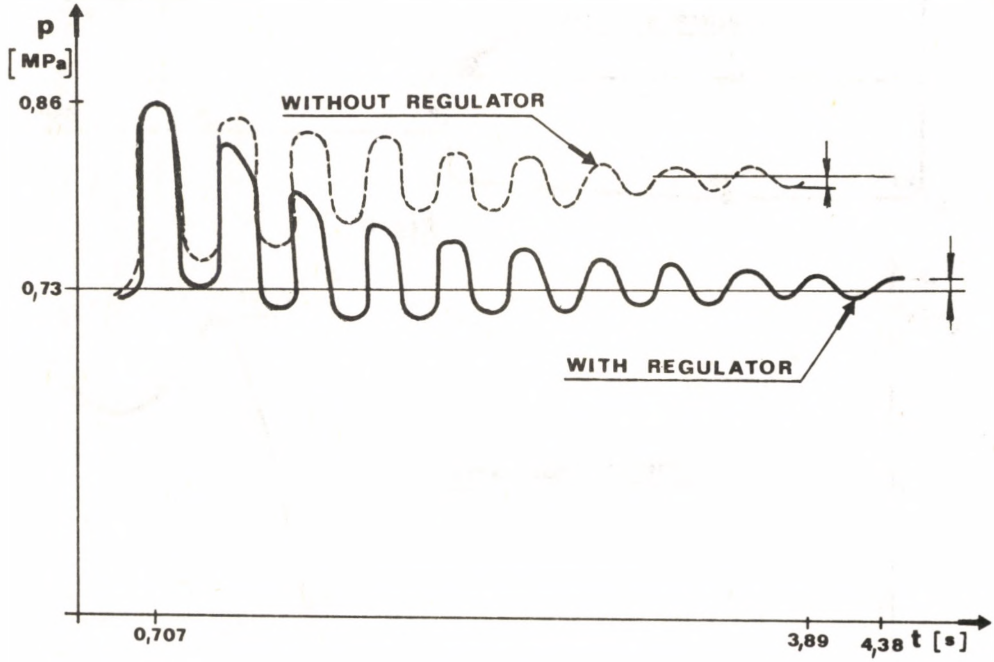

Fig. 7

7.2 Irrigation System with a Complex Pipeline Network

In the case of a large-area irrigation system (Fig.8), when the seal is closed at the predetermined point, the regulator will change pump rotations so as to attain the required pressure level after a temporary pressure increase (Fig.9).

8. Conclusion

Results reached during the solution of specific tasks have indicated that the digital simulation of unsteady fluid flow in a complex large-surface pipeline network of the irrigation system constitutes a rapid and economical method for the "prediction" of the properties of an irrigation system. Complemen-

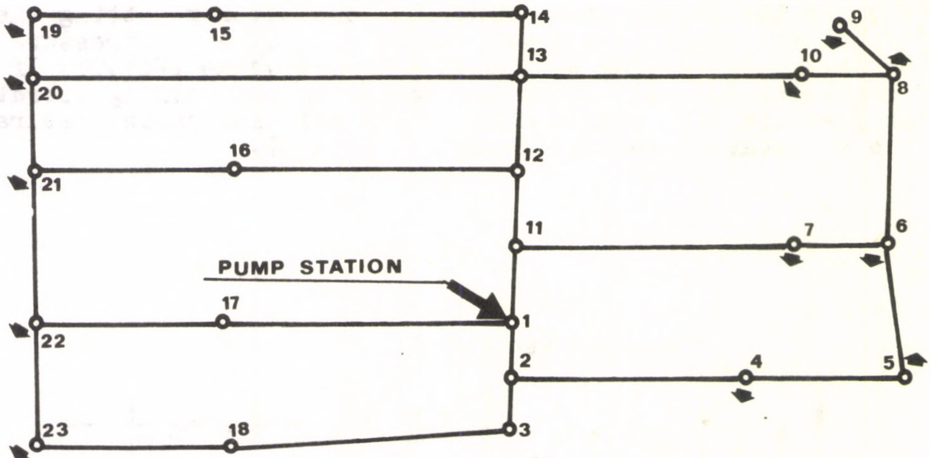

19
15
14
9
13
10
20
8
16
12
21
11
7
6
PUMP STATION
17
1
22
2
4
5
23
18
3

Fig. 8

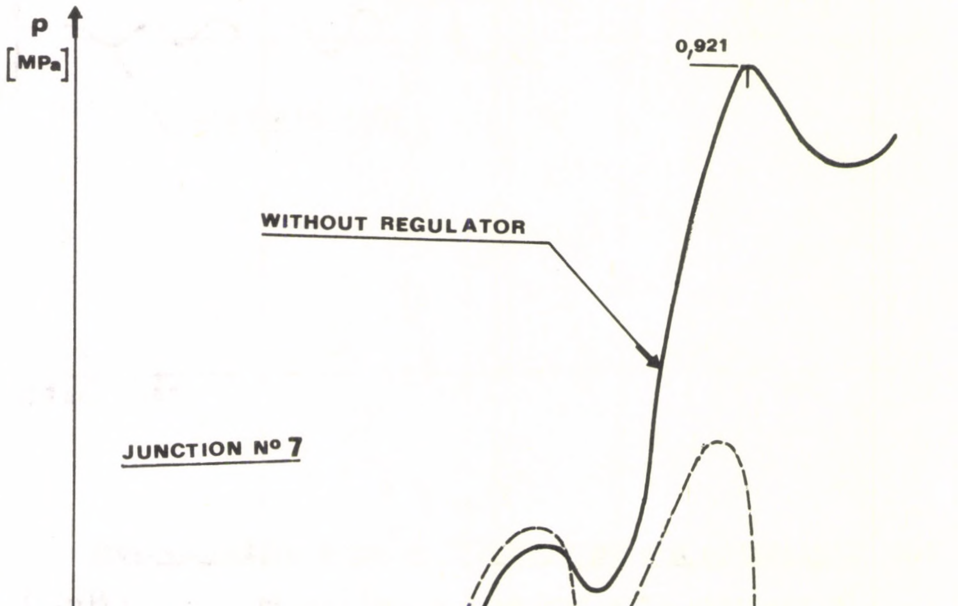

p
[MPa]
0,921
WITHOUT REGULATOR
JUNCTION Nº 7
0,793
WITH REGULATOR
19,29
t [s]

Fig. 9

ted with a simulation of the process of control, it enables to calculate several alternatives in a relatively short time for use in the designing activities.

Some symbols:

a - speed of pressure wave propagation
c - fluid flow speed
d - pipeline diameter
h - geodetic elevation
g - gravitational acceleration
$\underline{p}$ - pressure
p - required value of pressure
t - time

λ - friction factor
ρ - density
T_1, T_D, T_I - time constants
K_P - intensification
Q - mass flow rate
P - power demand
J - moment of inertia
U - voltage

References

[1] TCHARNYI, I.A.: Neustanovivsheiesia dvizhenie realnoi zhidkosti v trubach. Moscow, Nedra 1975.

[2] LISTER, M.: The numerical solution of hyperbolic partial differential equations by the method of characteristics. Ed. WILF, A. and RALSTON, H.S. Wiley, New York 1960.

[3] PACIGA, A.; PRIKKEL, K., KRCHNÁR, J.: Matematický model nestacionárneho hydraulického systému vysokotlakých závlah. (A mathematical model of unsteady hydraulic system of high-pressure irrigations.) Research Project. 1979.

[4] FUZY, O., THUMA, A.: Pressure oscillations in hydraulic systems. Proceedings of the Fifth Conference of Fluid Machinery. Akadémia Kiadó, Budapest 1975.

[5] KUBÍK, S., KOTEK, Z., ŠALAMON, M.: Teorie regulace I. (Regulation theory I.). SNTL, ALFA 1974.

Ing. Karol Prikkel, CSc.
Slovak Technical University
Faculty of Mechanical Engineering
Department of Hydraulic Machines and Mechanisms
Gottwaldovo nám. 17
812 31 Bratislava
Czechoslovakia

A THEORETICAL PROCESS TO DRAW AXIAL FLOW PUMPS CHARACTERISTICS, IN ORDER TO ESTIMATE PREVENTIVELY THEIR "OFF-DESIGN" PERFORMANCE.

Vittorio QUAGGIOTTI
Jacopo MAZZORIN

Machine Institute
University of PADUA

ABSTRACT

A theoretical process to draw axial flow pumps characteristics, in order to estimate preventively their "off-design" performance, has been devised by means of two particular congruency conditions.

The first one singles out the velocity vector triangles in each cylindrical section, where the axial velocity component obviously changes as capacity changes and otherwise the tangential one wouldn't be determinable: it comes out by equalizing two different forms of the airfoil lift coefficient, as function of the attack angle or as function of the flow relative velocity.

The second one leads to connect the tangential velocity component distribution, on the radial direction, with the same distribution of axial velocity component, which has quite to be expected not constant even if design has been referred to the "free-vortex" criterion and then itself, as well as head, has to be regarded as constant in that nominal state.

To this end, a particular preliminary assumption is suggested, which leads, with good approximation, to a simplified arrangement of flow and lets to write a differential equation, then solved by numerical methods.

SYMBOLS

- c absolute velocity
- w relative velocity
- u peripherical velocity
- ω angular velocity
- p pressure
- ρ density
- C_p lift coefficient
- t/l vane solidity that is ratio of the vane spacing to the vane chord length, or, more simply, the "spacing-chord" ratio.

CONNECTIONS

- subscript a - axial
- subscript r - radial
- subscript u - peripherical
- subscript 1 - runner inlet
- subscript 2 - runner outlet
- subscript n - nominal state
- subscript i - internal, that is hub, cylindrical section
- subscript e - esternal, that is tip, cylindrical section.

INTRODUCTION

A hydraulic machine is often requested to satisfy particular requirements also off-design.

It means that design, which first object is just the nominal state, must be secondly revised in order to get precise peculiarities for the whole performances curve.

In such cases a method to estimate and draw it in advance can be a very suitable way to orientate properly any subsequent perfecting.

This problem, referring to the axial flow pumps, is the subject of the present memory, which precisely suggests a theoretical method for the prevision of their characteristics.

When completed the design of the pump, one knows the nominal velocity vectors triangles on each cylindrical section and the various parameters characterizing the correspondent airfoils. As capacity changes, of course the whole fluid-dynamical distribution of stream changes. In particular, besides the obvious variation of the deviations Δc_u produced by the vane system, and just cause of them, it will presumably take place also a variation of the axial velocity component distribution on the radial direction, which has quite to be expected not constant even if design has been referred to the "free-vortex" criterion.

The close and mutual interconnection between the radial distributions of Δc_u and c_a induces, not to introduce rough approximations (like to admit c_a always uniform and then immediately evaluable), to single out two independent congruency conditions between those quantities. One must be stated in order to estimate the local action of each airfoil, which geometrical configuration is known, is invariable and then will produce a well definite peripherical deviation for each possible valve of c_a; the other to take into account, as much as possible, also the dynamical equilibrium described by the equations of motion.

Leaving the last one completely out of consideration, by assuming $\partial c_a/\partial r=0$ in all work condition, seems to be, as above said, too simplicistic.

On the other hand, the only strict application of the laws of motion requires particular boundary conditions, in order to make determinate the problem, anyway leads to numerical complications as to preclude any pratical utilization. This survey will necessarily involve a certain approximation, but will lead to a mathematical model close to the actual flow.

EQUATIONS OF MOTION - PRELIMINARY ASSUMPTIONS

For simplicity we'll consider only the most common case where the predistributing blades are strictly axial and symmetric.

In consequence the whole deviation Δc_u produced by the runner will be, in the following pages, the only tangential component c_{u2} downstream the runner itself. If the viscous effect are neglected and if one assume the flow, as is usual, to be axialsymmetric and stationary (this is certainly valid with good approximation outside the rotating vane system), the equations of motion for an incompressible fluid, in cylindrical coordinates, can be written as follows

$$\frac{\partial p}{\partial r} = \rho \left[\frac{c_u^2}{r} - c_a \frac{\partial c_r}{\partial a} - c_r \frac{\partial c_r}{\partial r} \right] \qquad (1.1)$$

$$c_r \frac{\partial (rc_u)}{\partial r} + c_a \frac{\partial (rc_u)}{\partial a} = 0 \qquad (1.2)$$

$$\frac{\partial p}{\partial a} = \rho \left[- c_r \frac{\partial c_a}{\partial r} - c_a \frac{\partial c_a}{\partial a} \right] \qquad (1.3)$$

In a cross-section 0-0 (see fig.1) far upstream the runner, where flow is undisturbed, the radial gradient of pressure will evidently be zero.

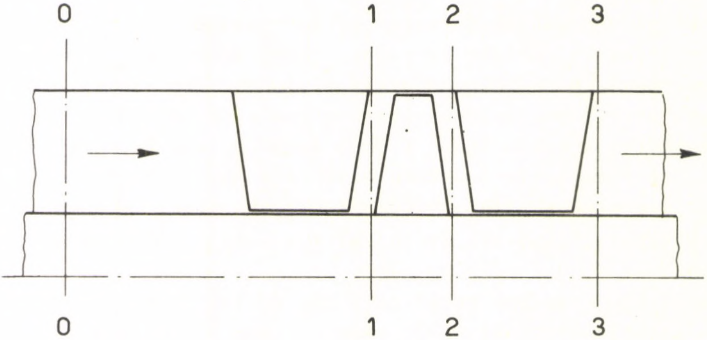

fig. 1

Hence, by referring the eq. (1.1) to the cross-sections 2-2 and 0-0, one easily obtain

$$\frac{\partial p_2}{\partial r} - \frac{\partial p_0}{\partial r} = \frac{\partial p_2}{\partial r} = \rho \left[\frac{c_{u2}^2}{r} - c_{a2} \frac{\partial c_{r2}}{\partial a} - c_{r2} \frac{\partial c_{r2}}{\partial r} \right] \qquad (1.4)$$

Now, if we refer the motion to a rotating system of coordinates, we can state that the energy along a relative stream-line is constant and write the equation of Bernulli, between the same sections 2-2 and 0-0 , as follows

$$p_2 - p_0 = \rho \left[\frac{w_0^2 - w_2^2}{2} + \frac{u_2^2 - u_0^2}{2} \right] \tag{1.5}$$

namely

$$p_2 - p_0 = \rho \left[\frac{c_{a0}^2}{2} - \frac{c_{a2}^2}{2} - \frac{c_{r2}^2}{2} - \frac{c_{u2}^2}{2} + u_2\, c_{u2} \right] \tag{1.6}$$

and then, considering that $\partial c_{ao}/\partial r=0$

$$\frac{\partial p_2}{\partial r} - \frac{\partial p_0}{\partial r} = \frac{\partial p_2}{\partial r} = \rho \left[- c_{a2} \frac{\partial c_{a2}}{\partial r} - c_{r2} \frac{\partial c_{r2}}{\partial r} - c_{u2} \frac{\partial c_{u2}}{\partial r} + \omega \frac{\partial (r c_{u2})}{\partial r} \right] \tag{1.7}$$

By comparing this equation with the eq. (1.4), one obtains

$$c_{a2} \left(\frac{\partial c_{r2}}{\partial a} - \frac{\partial c_{a2}}{\partial r} \right) = \frac{c_{u2}^2}{r} + c_{u2} \frac{\partial c_{u2}}{\partial r} - \omega \frac{\partial (r c_{u_2})}{\partial r} \tag{1.8}$$

Now one can regard as negligible the term $c_{a2}(\partial c_{r2}/\partial a)$, within a sufficiently good approximation. In fact we must think that the radial component c_r of the velocity can reach, in any case, but very small values, together, evidently, with its own change along the axial direction.

That's why the contribution of the aforesaid term to the radial gradient of pressure is certainly very small, at least if compared with the other terms of the eq. (1.4) (in particular with the first one).

The eq. (1.8), with $\partial c_r/\partial a=0$, then becomes

$$c_{a2} \frac{\partial c_{a2}}{\partial r} = - \frac{c_{u2}^2}{r} - c_{u2} \frac{\partial c_{u2}}{\partial r} + \omega \frac{\partial (r c_{u2})}{\partial r} \tag{1.9}$$

which is a fairly credible description of the connection between the radial distribution of c_a and that of c_u in the cross-section 2-2 downstream the runner. It's a relation which keeps valid also with changing of capacity and which must be consequently respected in all the work conditions.

No similar indication is given by the equation of motion with regard to the section 1-1. However some axiomatical considerations lead to think that the adjustment of thestream-lines, from the undisturbed situation of the section 0-0 to that imposed by the runner in the section 2-2, must take place in a gradual way, affecting a portion of the inlet pipe before the runner considerably longer than that occupied by the runner itself.

Hence, also considering the small axial extent of the runner, it seems reasonable to think, as most probable, that the radial differentiation of c_a takes place almost completely upstream the section 1-1 (as shown by the stream surface "a" in fig.2) rather than downstream the same (stream-surface "b" in fig.2) and c_{a1} is consequently little different from c_{a2}.

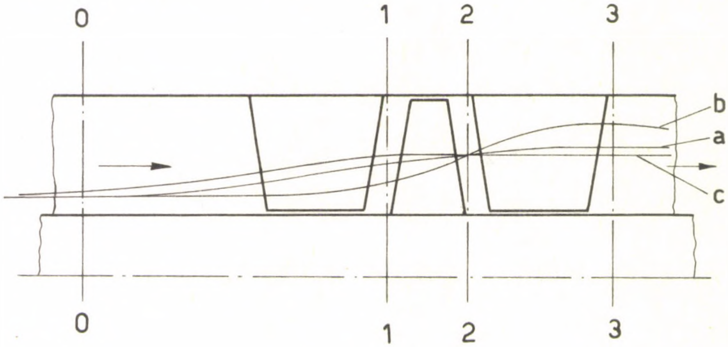

fig. 2

These considerations may find a theoretical explanation in the eq. (1.2) which, at least from a qualitative point of view, allows to state that the flow downstream the runner is nearly cylindrical, by showing that the ratio c_{r2}/c_{a2} is in any case very small.

In fact, the function of the rotating vane system is to produce a deviation c_{u2} inside the stream, whereas that of the stationary one is to annul it again in order to turn its kinetic energy into pressure energy.

Hence, the curve representing the axial distribution of the c_u component, in a generic cylindrical section, must have a point of maximum within the space between the runner and the diffuser. And all these points, for each radius, occur surely very close to cross section 2-2, so we can think that in the whole same section the gradient $\partial c_{u2}/\partial a$ is very little then negligible.

So the eq. (1.2), written as follows for such section,

$$\frac{c_{r2}}{c_{a2}} = - \frac{r \dfrac{\partial c_{u2}}{\partial a}}{\dfrac{\partial (r c_{u2})}{\partial r}}$$

shows that, when $\partial(rc_{u2})/\partial r$ is not also very little and comparable with numerator $r(\partial c_{u2}/\partial a)$, the ratio at the left-hand is always very small.

Otherwise very low values of $\partial(rc_{u2})/\partial r$ can exist only in nominal conditions when design has been referred to the "free-vortex" criterion.

Hence, if we consider that such conditions are in any case characterized by very small radial differentiation of c_a and consequently of c_{r2}/c_{a2}, we can maintain that in any work condition c_{a1} keeps close to c_{a2}.

Then our proposal, as a simplifying hypothesis providing for the problem a positive solution, is to approximate the actual flow with a flow distributed on stream-surfaces like that indicated with "c" in fig.2 for which it's really $c_{r1}=c_{r2}=0$ and $c_{a1}=c_{a2}$.

Such assumption make the problem susceptible of a "nearly two-dimensional" outlet which brings the model much nearer the actual flow than any other simplified hypothesis and which allows to use, for the following investigation about the local action of the various airfoils, all the theoretical and experimental informations given by the technical specialistic literature which, as is known, presuppose that the axial component of velocity is the same at the inlet and outlet of cascade.

LOCAL ACTION OF AIRFOIL

In the following fig. 3 the generic velocity vectors triangles concerning the nominal state (in a generic cylindrical section) are drown with "continuous line". The zero-lift direction (which is a peculiar characteristic of the airfoil in cascade and then invariable as capacity changes, also if the vanes overlap) is drawn with "point and line".

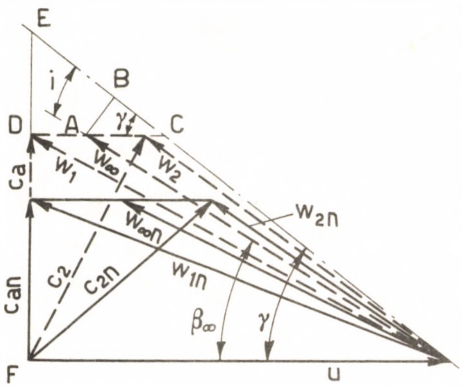

fig. 3

For another generic value of c_a (triangles drawn with "dashed-line") one can always write for the lift coefficient, according with Kutta-Joukowski theory,

$$C_p = \zeta\ 2\pi\ \kappa\ \text{sen}\ i \qquad (2.1)$$

where ζ is a reducing coefficient which values the boundary layer effects.

Experimental data show that ζ is generally included within the range $0.85 \div 0.9$. So it will be

$$Cp = (5.35 \div 5.65)\ \kappa\ \text{sen}\ i \qquad (2.2)$$

where, according to Weinig's diagram extended to cambered airfoils (by considering them as flat plates with the inclination of the zero-lift direction), the cascade coefficient K is a function only of the spacing-chord ratio t/l and of the angle $\gamma=\beta_\infty+i$ and, consequently, is constant as c_a changes.

But, notoriously, it is also

$$C_p = 2 \frac{c_{u2}}{w_\infty} t/1 \qquad (2.3)$$

Then, by comparing with eq. (2.2), one obtains

$$w_\infty \text{sen } i = \mu \, c_{u2} \qquad (2.4)$$

where

$$\mu = (0,35 \div 0,37)\ 1/k\ t/1 = \text{constant.}$$

But fig.3 itself shows that

$$w_\infty \text{sen } i = \overline{AB} = \left(\overline{CD} - \frac{c_{u2}}{2}\right) \text{sen } \gamma \qquad (2.5)$$

where

$$\overline{CD} = u\left(1 - \frac{c_a}{EF}\right) = u\left(1 - \frac{c_a}{u \, tg\gamma}\right) \qquad (2.6)$$

Hence

$$\mu c_{u2} = \left(u - \frac{c_a}{tg\gamma}\right) \text{sen } \gamma - c_{u2} \frac{\text{sen}\gamma}{2} \qquad (2.7)$$

The foregoing eq.(2.7) has to be valid also in the nominal state.
So

$$\mu = \frac{1}{c_{u2n}} \left(u - \frac{c_{an}}{tg\gamma}\right) \text{sen } \gamma - \frac{\text{sen}\gamma}{2} \qquad (2.8)$$

By substituting this equation in the eq. (2.7), one finds

$$\frac{c_{u2}}{c_{u2n}} \left(u - \frac{c_{an}}{tg\gamma}\right) \text{sen } \gamma - c_{u2} \frac{\text{sen}\gamma}{2} = \left(u - \frac{c_a}{tg\gamma}\right) \text{sen } \gamma - c_{u2} \frac{\text{sen}\gamma}{2}, \qquad (2.9)$$

namely

$$c_{u2} = c_{u2n} \left(\frac{u tg\gamma - c_a}{u tg\gamma - c_{an}}\right) \qquad (2.10)$$

or finally

$$c_{u2} = c_{u2n} \left(\frac{c_{an} - c_a}{u tg\gamma - c_{an}} + 1\right) \qquad (2.11)$$

which is a simple linear relation, describing the second congruency condition between c_{u2} and c_a, and gives, together with eq. (1.9), a univocal solution to the problem.

METHODS OF SOLUTION

By considering a discrete number of cylindrical sections, the eq. (2.11) can be represented in a graph c_{u2} against c_a by a sheaf of straight lines, with "r" as a parameter, as shown, for instance, in fig.4.

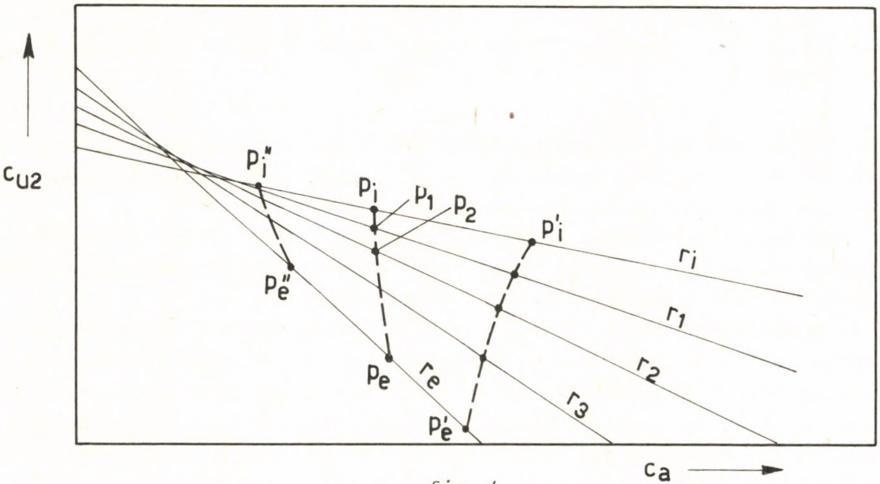

fig. 4

The discrete statement of eq. (1.9) is

$$c_a \cdot \Delta c_a = \omega r \Delta c_{u2} + \omega c_{u2} \Delta r - c_{u2} \Delta c_{u2} - c_{u2}^2 \frac{\Delta r}{r} \qquad (3.1)$$

If a starting value is assumed for $|c_a|^i$ at the hub radius r_i, one can obtain, by using the eq. (2.11) written for r_i, also the corresponding value of $|c_{u2}|^i$, namely the point P_i (see fig.4).

By starting from P_i and solving simultaneously the two equations

$$|c_a|^i \left[|c_a|^1 - |c_a|^i \right] = \left[|c_{u2}|^1 - |c_{u2}|^i \right] \cdot \left[\omega r_i - |c_{u2}|^i \right] + \omega |c_{u2}|^i (r_1 - r_i) - |c_{u2}|^{i^2} \frac{r_1 - r_i}{r_i}$$

$$(3.2)$$

$$|c_{u2}|^1 = |c_{u2n}|^1 \left[\frac{|c_{an}|^1 - |c_a|^1}{\omega r_1 \, \mathrm{tg}\, \gamma_1 - |c_{an}|^1} + 1 \right]$$

it's possible to find $|c_{u2}|^1$ and $|c_a|^1$, namely the point P_1. Then, if P_1 is assumed as the new starting point and the eqs. (3.2) are written again for the radii r_1 and r_2, one can locate the point P_2.

By continuing in succession with this procedure till the tip radius r_e, one draws point by point the curve $P_i - P_e$ and obtain the radial distributions of c_{u2} and of c_a taking place when $|c_a|^i$ has the assumed starting value.

Once these distributions are known, it's possible to execute numerically the following integrations

$$Q = \int_{r_i}^{r_e} c_a \, 2\pi \, r \, dr \simeq 2\pi \, \Delta r \sum_{J=1}^{e} \frac{|c_a|^J + |c_a|^{J-1}}{2} \cdot \frac{r_J + r_{J-1}}{2} \qquad (3.3)$$

$$\frac{gh}{\eta} \simeq \frac{1}{r_e - r_i} \int_{r_i}^{r_e} \omega r\, c_{u2}\, dr \simeq \frac{\omega}{r_e - r_i} \cdot \Delta r \sum_{J=1}^{e} \frac{|c_{u2}|^J + |c_{u2}|^{J-1}}{2} \cdot \frac{r_J + r_{J-1}}{2} \qquad (3.4)$$

where "J" stands for the radius index and η for the hydraulic efficiency, which may be expressed, as a function of capacity, by means of a suitable parabolic relation outcoming from experience.

Such capacity and head concerne, of course, that stream arrangement which is connected with a definite value $|c_a|^i$ of velocity at the hub and then singles out just a point of machine characteristic.

To a different value of $|c_a|^i$ it will correspond a different stream arrangement which is described by another curve ($P_i' - P_e'$, for istance, in fig.4, referring to a high capacity, or $P_i'' - P_e''$, referring to a low capacity).

This curve, by means of eqs. (3.3) and (3.4), will provide another couple of values for capacity and head, that is to say just another point of characteristic. If one follows again and again the foregoing procedure, by changing everytime $|c_a|^i$ with values initially close to the nominal one and then more and more distant, he can get the whole performances curve of machine.

Of course the above procedure has not to be regarded quite as a graphic one, necessarily involving the manual drawing of curves $P_i - P_e$ (which are here acting merely as descriptive examples): indeed, by means of appropriate numerical methods, one can get the characteristic itself directly plotted by a computer, simply referring to the following data

Q_n, h_n, r_i, r_e, ω, z, γ_i, γ_1, γ_2,........γ_e,

where z means the number of cylindrical section taken into account.

Such numerical methods as well as their experimental application and checking will be the object of further research work.

REFERENCES

J.H.HORLOCK - Axial flow compressors - Butterworths 1958.

A.J.STEPANOFF - Centrifugal and axial flow pumps - John Wiley - 1964.

S.LAZARKIEWICZ, A.T.TROSKOLANSKI - Impeller pumps - Pergamon press 1965.

J.H.HORLOCK - Axial flow turbines - Butterworths 1966.

M.MEDICI - Le pompe - Hoepli 1967.

G.VENTRONE - Le turbomacchine - Libreria Cortina 1975.

THEORETICAL APPROACH TO THE RELATION BETWEEN CAVITY LENGTH AND NPSH IN AN IMPELLER PUMP OF GIVEN HEAD-NPSH GRAPH UNDER PULSATILE CAVITATION

by

Raabe, J.

Introduction into the Problem.- An impeller pump of given rotor design is considered, whose head versus NPSH characteristic (see graph in fig. 1) is known from measurements.

Industrial pumps are used to work along the descending branch of this characteristic, so as to have a certain head drop ΔH (about 1 % to 3 % in proposition to the head H).

In the present case a working regime is considered about a point P on the H(NPSH) curve with a certain slope $\tan\gamma = dH/dNPSH$ and a certain radius of curvature R (see graph in fig. 1).

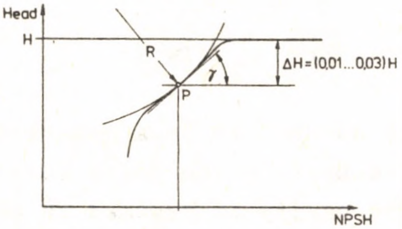

Fig. 1: Head versus NPSH

During stroboscobic observation of the impeller eye through an observation window in the draft, a certain maximum length l_m of cavity is observed on the suction face of the rotor vane, on the zone most susceptible to cavitation, situated close to the shroud, as shown in fig. 2.

In the majority of cases, which is also assumed here, the preliminarily quasi-steady appearing cavity is in reality a pulsatile cavity.

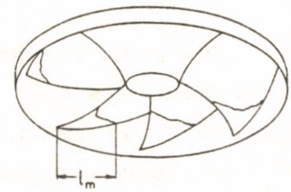

Fig. 2: Impeller eye

As shown in fig. 3, such a cavity consists of a quick sequence of wall attached cavities with the time period T. They originate at the time t = 0 on the critical station A close to the leading edge of the rotor vane, then grow streamwisely with its rear, whilst a re-entrant jet from there between cavity and wall of vane face cuts the wall-attached head of cavity from the wall.

This occurs after a time elapsed t = T. Then the cavity is washed away and collapses finally. Simultanously, at the instant the first cavity separates from wall, a new cavity origi-

nates on the critical point A of that profile contour (in the case considered that at the suction face of impeller vane).
In the following it is assumed that the period T of this pulsating cavity is known from model tests (perhaps through observation by means of a rotoscope). Hence the Strouhal number due to the observed maximum cavity length l_m and the known relative velocity w_1 at the rotor inlet,

$$Sr = l_m/(Tw_1), \tag{1}$$

is assumed to be a constant parameter due to the performance point considered.

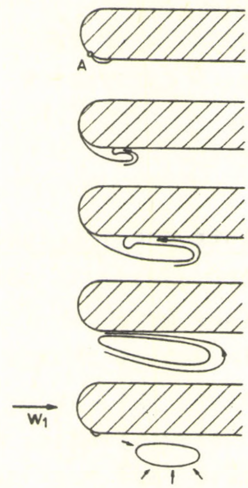

Fig. 3: Pulsatile Cavity

The cavity is assumed to be filled essentially with saturated steam of the working liquid. In agreement with recently made tests on wall-attached cavities by Lush and Peters [2] it is assumed, that the growth of the length l of cavity obeys the corresponding law of a vapourous bubble versus time. Thus

$$l = k\cdot\sqrt{at}, \tag{2}$$

in which a is the known thermal diffusivity of the liquid and k a certain figure.
Finally it is assumed, that the time averaged pressure distribution along the profil of the vane considered is known for the neighbourhood of the critical working point considered. This distribution may be determined by the pressure number due to the critical point defined by

$$\lambda = 2(p_1 - p_{cr})/(\rho w_1^2), \tag{3}$$

in which p_1 and w_1 respectively are the pressure and relative velocity at the outermost station 1 before the impeller inlet, p_{cr} the critical pressure, ρ the liquid density.
The problem arising from these facts and important for the

operation of the pumps is characterized by the following question:

"What maximum of time averaged cavity length l_m (this is the value the unarmed eye can observe stroboscobically) can be assigned to a certain NPSH value?"

And hence:

"What change of head drop ΔH has to be assigned (coordinated) to a certain observed change of maximum time averaged cavity length Δl_m?"

Additional Assumptions.- The head of the re-entrant jet has at an instant of time t elapsed since the origin of the cavity a distance l_S from the rear of the cavity (see fig. 4) given by

$$l_S = vt, \tag{4}$$

in which v is the mean velocity of the jet relative to the rear of the cavity. This velocity v is assumed to originate from the pressure difference between the pressure p_H on the liquid slightly downstream of the rear of cavity and the constant critical pressure p_{cr} in the interior of the cavity, which is close to the pressure of the saturated vapour due to the liquid. Hence

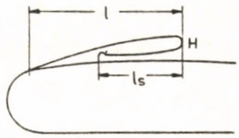

Fig. 4: Cavity

$$v = \sqrt{2(p_H - p_{cr})/\rho}. \tag{5}$$

Imagine the distribution of the time averaged pressure on the cavitation vane face to follow the line "a" (see fig. 5) in the case of non-cavitating flow.

In case of cavitation the branch of the graph "a" is converted into "b", namely a $p = p_{cr}$ = constant line, see fig. 5. The pressure on the station H_m due to the maximum cavity length may be αp_1, in which α is a known figure due to the pressure distribution. Hence from 5) the maximum velocity of

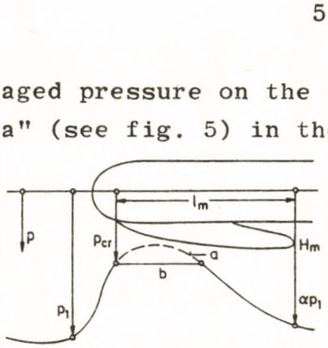

Fig. 5: Pressure Distribution

the re-entrant jet

$$v_m = \sqrt{2[p_1 - p_{cr} - p_1(1 - \alpha)]/\rho}. \tag{6)}$$

A comparison with 3) shows immediately

$$v_m = \sqrt{\lambda w_1^2 - 2(1 - \alpha)p_1/\rho}. \tag{7)}$$

As well known [3] for the here considered whirl-free admission ($c_{u1} = 0$) of an impeller, the NPSH value of a pump can be split into a first term due to the rotor and a second term due to the suction pipe according to

$$NPSH = \lambda w_1^2/(2g) + (1 + \zeta)c_{m1}^2/(2g), \tag{8)}$$

where ζ is the loss coefficient due to the suction pipe, c_{m1} the meridional velocity at station 1, w_1 the relative velocity at station 1, which follows from the given flow Q and the vane angle β_1 and the blade tip speed u_1 at station 1. Substituting λw_1^2 in 7) by 8) yields

$$v_m = \sqrt{2gNPSH - (1 + \zeta)c_{m1}^2 - 2(1 - \alpha)p_1/\rho}. \tag{9)}$$

Finally after the time $t = T$ elapsed the re-entrant jet reaches its maximum length l_m.

Solutin of the Problem.- From 2), 4), 9) results

$$T = ak^2/[2gNPSH - (1 + \zeta)c_{m1}^2 - 2p_1(1 - \alpha)/\rho], \tag{10)}$$

and

$$l_m = k\cdot\sqrt{aT}. \tag{11)}$$

11) gives $k^2 = l_m^2/(aT)$. Putting this into 10) results in

$$T = l_m/\sqrt{2gNPSH - (1 + \zeta)c_{m1}^2 - 2p_1(1 - \alpha)/\rho}. \tag{12)}$$

With T from 12) in 11) yields

$$l_m = ak^2/\sqrt{2gNPSH - (1 + \zeta)c_{m1}^2 - 2p_1(1 - \alpha)/\rho}, \qquad 13)$$

at which the coefficient k follows from certain observed values l_m, a, t assigned to eych other by 11). 13) hints on the fact that the cavity length increases with decreasing NPSH. Differentiation of 13) gives

$$\Delta l_m = - gak^2\Delta NPSH/[2gNPSH - (1 + \zeta)c_{m1}^2 - 2p_1(1 - \alpha)/\rho]^{3/2}, \qquad 14)$$

which reflects that $\Delta l_m > 0$ corresponds to $\Delta NPSH < 0$ in agreement with experience [1].

In general the problem is of interest, how much may l_m increase if only a certain corresponding head drop ΔH is admitted. For this purpose the given H(NPSH) graph of the pump in the neighbourhood of the operating point P is considered in fig. 6.

In a first order approximation $\Delta NPSH$ depends on the head drop by means of the local slope by

$$\Delta NPSH_{1.approx.} = \Delta H\cot\gamma. \qquad 15)$$

In a second order approximation the change $\Delta NPSH$ depends also on the local radius of curvature R of the graph by

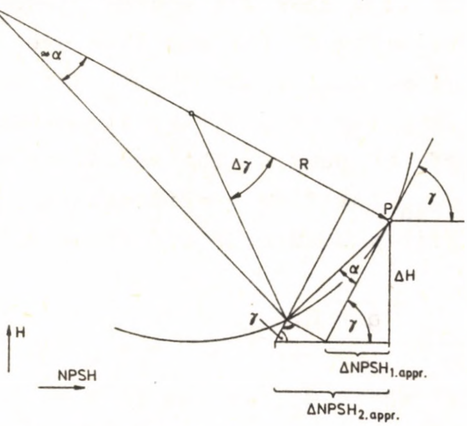

$$\Delta NPSH_{2.approx.} = \Delta H\cot\gamma + \Delta H^2/(\sin^3\gamma\cdot 2R). \qquad 16)$$

Fig. 6: H(NPSH) graph in the neighbourhood of P

Obviously

$$R = \Delta H/(\Delta\gamma\sin\gamma). \qquad 17)$$

Hence

$$\Delta NPSH_{2.approx.} = \Delta H\cot\gamma(1 + \Delta\gamma/\sin 2\gamma). \qquad 18)$$

Introducing this in 14) yields

$$\Delta l_m/\Delta H = - gak^2 \cot\gamma(1 + \Delta\gamma/\sin 2\gamma)/[2gNPSH - (1 + \zeta)c_{m1}^2 - - 2p_1(1 - \alpha)/\rho]^{3/2} = C. \tag{19}$$

In the following the dependance of C on design parameters such as type number (specific speed) n_q', suction head h_S, head H is considered. For this purpose in the appendix it is shown that C results from

$$C = - gak^2 \cot\gamma(1 + \Delta\gamma/\sin 2\gamma)\pi\varphi_{1a}(1 - N_1^2)\xi/\{(gH)^{3/2} n_q'^2 \cdot \cdot [2(\pi\varphi_{1a}(1 - N_1^2)\xi)^{2/3}/S^{4/3} - \alpha(1 + \zeta)(\xi\varphi_{1a})^2 - - 2(1 - \alpha)(\pi\varphi_{1a}(1 - N_1^2)\xi)^{2/3}/n_q'^{4/3}(p_A/(\rho gH) - h_S/H)]^{3/2}\}, \tag{20}$$

at which $n_q' = \omega\cdot\sqrt{Q}/(gH)^{3/4}$ is the dimensionless specific speed (type number), ω the angular velocity, $S = \omega\cdot\sqrt{Q}/(gNPSH)^{3/4}$ the suction specific speed, $\xi = c_{m1}/c_{m1a}$, c_{m1} the mean meridional velocity at the impeller eye, c_{m1a} the meridional velocity close to the shroud, N_1 the hub to tip diameter ratio at the impeller eye, p_A the atmospheric pressure, h_S the suction head of the pump, ζ the suction pipe loss coefficient, $\varphi_{1a} = c_{m1a}/u_{1a}$ the flow coefficient at impeller eye close to the shroud. With a load degree defined by

$$q = Q/Q_{op}, \tag{21}$$

at which Q_{op} is the flow at bep, the flow coefficient for an arbitrary point can be defined by

$$\varphi_{1a} = \varphi_{1aop} q, \tag{22}$$

at which φ_{1aop} is nearly constant. Inserting 22) in 20), the relation 20) reads

$$\Delta l_m/\Delta H = - gak^2 \cot\gamma(1 + \Delta\gamma/\sin 2\gamma)A_0/\{(gH)^{3/2} n_q'^2 [A_1 - - \alpha A_2 q^{4/3} - (1 - \alpha)A_3/n_q'^{4/3}(p_A/(\rho gH) - h_S/H)]^{3/2}\}, \tag{23}$$

at which

$$A_0 = \pi\varphi_{1aop}(1 - N_1^2)\xi, \qquad 24)$$

$$A_1 = 2(\pi\varphi_{1aop}(1 - N_1^2)\xi)^{2/3}/S^{4/3}, \qquad 25)$$

$$A_2 = \xi^2\varphi_{1aop}^2(1 + \zeta), \qquad 26)$$

$$A_3 = 2(\pi\varphi_{1aop}(1 - N_1^2)\xi)^{2/3}. \qquad 27)$$

Since S, φ_{1aop}, ξ , N_1 may be assumed to change very little in an impeller pump, the following conclusions can be drawn from 23):

For a certain H(NPSH) characteristic with known values γ and $\Delta\gamma$ in the critical zone and an experimentally known parameter k (obviously due to a certain Strouhal number, see 1) and according to 11)) the increase of maximum cavity length Δl_m stroboscobically observed due to a certain head drop ΔH is the larger

1) the flatter the H(NPSH) curve is,
2) the smaller the type number n_q' is,
3) the larger the pressure p_A on the level of the suction vessel is in proportion to the head,
4) the smaller the suction head is in relation to the head,
5) the smaller the head is,
6) the larger the thermal diffusivity a of the liquid is,
7) the larger the change of the slope $\Delta\gamma$ in the critical regime is,
8) the larger in relation to p_1 the time averaged pressure αp_1 at the rear of the cavity is,
9) the larger the load degree q is,
10) the larger the suction specific speed is.

APPENDIX

Proof for the conversion of the parameter C (see 19) and 20):
Introducing the ratio of mean meridional velocity in the impeller eye (1) to the value at the shroud (1a) $\xi = c_{m1}/c_{m1a}$ and the flow coefficient $\varphi_{1a} = c_{m1a}/u_{1a}$, the denominator D of C can be transformed into

$$D = u_{1a}^3 [2gNPSH/u_{1a}^2 - (1+\zeta)\xi^2\varphi_{1a}^2 - 2p_1(1-\alpha)/(\rho u_{1a}^2)]^{3/2}. \quad a)$$

u_{1a} can be expressed by the known blade tip speed coefficient ku_{1a} at the impeller eye by means of

$$u_{1a} = ku_{1a} \cdot \sqrt{2gH}. \quad b)$$

The type number n_q' depends on unit speed n_{11} and unit flow Q_{11} by

$$n_q' = n_{11} \cdot \sqrt{Q_{11}}. \quad c)$$

Moreover

$$n_{11} = ku_{1a} \cdot 2 \cdot \sqrt{2} \cdot D/D_{1a}, \quad d)$$

and

$$Q_{11} = \pi/4 \cdot \xi (D_{1a}/D)^2 (1 - N_1^2) \cdot \sqrt{2} \cdot kc_{m1a}, \quad e)$$

at which kc_{m1a} is the coefficient of the meridional velocity $kc_{m1a} = c_{m1a}/\sqrt{2gH}$, N_1 the hub to tip ratio of impeller eye. Inserting e) and d) in c) yields

$$ku_{1a} = n_q'^{2/3} \varphi_{1a}^{-1/3} \xi^{-1/3} 2^{-1/2} \pi^{-1/3} (1 - N_1^2)^{-1/3}. \quad f)$$

Inserting f) in b) gives

$$u_{1a}^3 = \pi^{-1} \varphi_{1a}^{-1} \xi^{-1} (1 - N_1^2)^{-1} (gH)^{3/2} n_q'^2. \quad g)$$

Definition of the suction specific speed $S = \omega \cdot \sqrt{Q}/(gNPSH)^{3/4}$ and $u_{1a} = D_{1a}/2$ results in

$$2gNPSH/u_{1a}^2 = 8\omega^{4/3} Q^{2/3}/(S^{4/3} D_{1a}^2 \omega^2). \quad h)$$

With $Q = \pi/4 \cdot \xi c_{m1a} D_{1a}^2 (1 - N_1^2)$ and $\varphi_{1a} = c_{m1a}/u_{1a}$

$$2gNPSH/u_{1a}^2 = 2\pi^{2/3}\varphi_{1a}^{2/3}(1 - N_1^2)^{2/3}\xi^{2/3}/S^{4/3}. \qquad \text{i)}$$

Assuming (see fig. 5) the pressure p_{1a} close to that at station 1 (p_1) the energy theorem yields

$$p_1 = p_{1a} = p_A - \rho g h_S - \rho c_{m1}^2(1 + \zeta)/2, \qquad \text{j)}$$

at which p_A is the pressure on the level of suction vessel, ζ the suction pipe loss number, h_S the suction head. Hence D in a) with g), i), j) reads

$$D = \pi^{-1}\varphi_{1a}^{-1}\xi^{-1}(1 - N_1^2)^{-1}(gH)^{3/2}n_q'^{2}[2\pi^{2/3}\varphi_{1a}^{2/3}(1 - N_1^2)^{2/3}\cdot$$
$$\cdot\,\xi^{2/3}/S^{4/3} - \alpha(1 + \zeta)\xi^2\varphi_{1a}^2 - 2(1 - \alpha)\pi^{2/3}\varphi_{1a}^{2/3}\xi^{2/3}\cdot$$
$$\cdot\,(1 - N_1^2)^{2/3}n_q'^{-4/3}(p_A/(\rho gH) - h_S/H)]^{3/2}. \qquad \text{k)}$$

REFERENCES

1. Knapp, R./Daily, J./Hammitt, F.: Cavitation. McGraw-Hill, 1970.
2. Lush, P./Peters, P.: Visualisation of the Cavitating Flow in a Venturi-Type Duct Using High Speed Cine Photography. Proceedings of the 11th IAHR Symposium, Amsterdam, 1982.
3. Raabe, J.: Hydraulische Maschinen und Anlagen. Teil 2: Wasserturbinen. VDI, 1970.

LONG-TERM PREDICTIVE CAPABILITY OF EROSION MODELS

P. Veerabhadra Rao and Donald H. Buckley

ABSTRACT

This paper reports a brief overview of long-term cavitation and liquid impingement erosion and modeling methods proposed by different investigators, including the curve-fit approach recently suggested from this laboratory. A table is prepared to highlight the number of variables necessary for each model in order to compute the erosion-versus-time curves. A power law relation based on the average erosion rate is suggested which may solve several modeling problems.

INTRODUCTION

Long-term prediction of erosion due to cavitation and liquid impingement has become very important in view of severe erosion problems associated with hydraulic turbines and pumps due to cavitation, with aircraft surfaces due to rain drops, and with steam turbine blades due to impingement of condensed droplets. Extended periods of reliable operation in all situations reemphasized the necessity for erosion-free performance or the alleviation of erosion. In most cases complete elimination of erosion is not possible. Hence, it is necessary to establish the total erosion of a material for prolonged operation so that the particular component may be changed, or so that highly resistant materials may be used to increase component life.

Although Honegger [1] was the first investigator to notice the effect of exposure time on erosion rate, Fyall et al [2] in 1957, Hobbs [3] in 1962, and Thiruvengadam [4] in the early 1960's clearly observed the influence of time on instantaneous erosion rate. Investigations by Thiruvengadam and Preiser [5], Plesset and Devine [6], Heymann [7], and Tichler and de Gee [8] have become classic studies. There have been, however, several discrepancies in the agreement of the type of erosion-rate-versus-time curves.[1] Using shapes of curves obtained earlier, many models and formulations have been presented by different investigators for the long-term prediction of cavitation and liquid impingement erosion [7 to 13]. The details of the models are reviewed and presented in [14]. Table 1 presents models proposed and the number of variables necessary to predict erosion using these models [13, 14].

---

[1]Curves reported in [5] contain incubation, acceleration, deceleration, and steady-state zones; in [6] incubation, acceleration, steady-state, and deceleration zones; in [7] peak erosion and deceleration zones or acceleration zone and several cycles of peaks of erosion rate; and in [8] incubation, acceleration, first steady-state, deceleration and second steady-state periods.

Table 1. - Predictive models, formulations, and parameters for computation of cavitation and liquid-impingement erosion vs. time curves [13]

Investigator	Type of erosion[a]	Parameters needed for computation
Thiruvengadam [18]	CAV (nomogram)	(1) erosion intensity (2) strain energy
Heymann [7]	CAV and LI (elementary model)	(1) Nominal mean lifetime for original surface (2) Standard deviation for original surface (3) Nominal mean lifetime for substructure (4) Standard deviation for substructure
	LI (elaborated model)	(1) Delay time during which no failure occurs (2) Mean of log-normal distribution on logarithmic time scale (3) Standard deviation of log-normal distribution on logarithmic time scale
Thiruvengadam [9]	LI and CAV	(1) Magnitude of instantaneous erosion rate at first peak, I_{max} (2) Time to attain first peak instantaneous erosion rate, t_m (3) Attenuation exponent, n (4) Weibull shape parameter, α
Hoff and Langbein [10]	LI (rain erosion)	(1) Maximum rate of erosion, e_{max} (2) Incubation period (intercept on time axis from straight line portion of erosion vs. time curve), t
Heymann [11]	CAV and LI	(1) Mean depth of erosion at tangent point, y_T (2) Average erosion rate at tangent point, R_T (3) Exponential constant, B
	LI	(1) Cumulative mean depth of erosion or material loss at tangent point, y_T (2) Normal component of impact velocity, V_o (3) Volume of liquid impinging per unit area per unit time, U_a (4) Generalized nondimensional erosion resistance parameter. N_e
Tichler and de Gee [8]	CAV	(1) Incubation time, t_o (2) Resistance against cavitation erosion under hydrodynamic conditions, as occur in magnetostrictive oscillator R_c (3) Mean depth of erosion at which effect of crater formation becomes manifest, r_b (4) Proportionality constant, symbolizing increase in mean depth of erosion that would be necessary to form number of craters per unit area in final steady-state period, κ (5) Ratio of rate of erosion in the final steady-state period to rate of erosion in first steady-state period, ϕ_∞
Perelman and Denisov [16]	LI	(1) work done on microplastic deformations per cycle of load, due to the energy capacity of microvolumes of the material (2) energy expended on fatigue fracture (3) influence of the surface form (4) kinetic energy of a stream of droplets (5) energy in a stream of droplets absorbed during the incubation period (6) specific energy of fracture determined from macroscopic fracture tests (7) energy absorbed by the material during initial deformation
Thiruvengadam [20]	CAV and LI (nomogram)	(1) erosion intensity (2) erosion strength
Lichtarowicz [19]	LI (graph)	(1) cumulative peak erosion rate (2) time to reach cumulative peak erosion rate
Noskievic [12]	CAV	(1) Cavitation property of material, β (2) Cavitation strength of material or inner friction of material during plastic deformation, α (3) Cavitation damage rate in developed period of cavitation attack, v_s
Rao and Young [13]	CAV and LI	(1) Peak cumulative average erosion rate (2) Time to attain peak cumulative average erosion rate (3) Incubation period (4) Erosion resistance

[a]CAV: cavitation erosion.
LI: liquid impingement erosion-- cylindrical/spherical drop or jet impact including jet with cavitation inducer.

LONG-TERM PREDICTION MODELS

Equations or models for the prediction of erosion rate with respect to time have been proposed by Heymann [7, 11], Tichler and de Gee [8], Thiruvendagam [9], Hoff and Langbein [10], Noskievic [12], Engel [15], Perelman and Denisov [16], and McGuiness and Thiruvengadam [17]. Others [18, 19] have presented nomograms and graphs. A brief description of the important contributions of these models is outlined below in order to explain the current status of erosion-rate-versus-time predictions for long-term exposures.

Heymann's models

Elementary model. Heymann [7] developed an elementary statistical erosion-rate-versus-time model for liquid impingement and cavitation erosion conditions of different materials wherein fatigue is the predominant failure mechanism. The model requires four parameters to obtain instantaneous erosion-rate-versus-time curves (Table 1). The fit of experimental data in certain real situations is very convincing with the use of normal distributions truncated and normalized over a finite time span.

Elaborate model. Heymann's elaborated model [7] permits the specification of a different distribution function for each level below the original surface and of two different functions for the original surface. In this model the log-normal distribution is adopted. The inclusion of the median lifetime for the unaffected surface has significantly improved the predictions.

Curve fit approach. Heymann [11] suggested a simple and straightforward curve-fit approach using tangent (cumulative average) rate of erosion and tangent mean cumulative depth of erosion (volume loss) to predict the erosion rate which follows the peak erosion rate (Fig. 1). Equations suggested for the calculation of normalized average erosion rate (R/R_T) and for time (t_y) to reach a mean erosion rate require three and four parameters, respectively, to compute the erosion-versus-time history (Table 1). For particular liquid impingement and cavitation erosion data sets, this approach appeared promising [11].

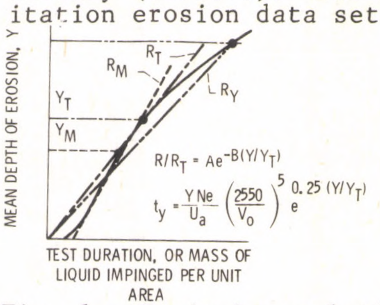

Fig. 1.- Typical cumulative erosion vs. time curve, defining terms used and equations suggested [11].

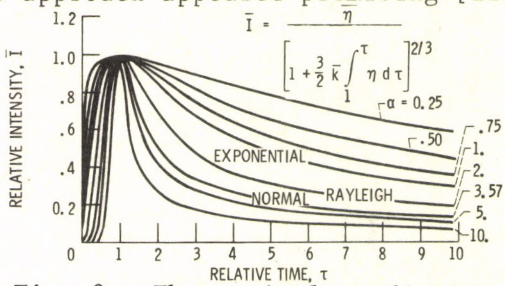

Fig. 2.- Theoretical prediction of the effect of time on intensity of erosion when n = 2 [9]

Thiruvengadam's nomogram and theory of erosion

Strain energy. Using a strain energy (the area of a stress-strain curve is a measure of this energy per unit volume) concept, a nomogram was developed based on cavitation erosion data [20]. This nomogram has been used by design engineers to predict life of materials with a knowledge of erosion intensity and strain energy. Unfortunately, strain energy is a good predictor only for highly ductile materials.

Concept of erosion strength and theory of erosion. In view of the limitations of strain energy, Thiruvengadam later developed the concept of erosion strength (the energy-absorbing capacity of the material per unit volume under the action of erosive forces or the ratio of energy absorbed by the material eroded to the volume of material eroded). Using this concept a theory of erosion [9] was developed to predict nonlinear effects of time on erosion rate, to quantitatively arrive at meaningful correlations in the laboratory, and to extrapolate to field prototypes. Figure 2 presents theoretical prediction curves of relative intensity (or relative erosion rate) versus relative time for an attenuation exponent $n = 2$. The final equation used is also presented in Fig. 2. This theory needs four parameters to compute the erosion-rate-versus-time curve (Table 1). Thiruvengadam also modified his nomogram using the concept of erosion strength instead of strain energy. For design engineers, this nomogram may possibly be useful for the rough estimation of erosion rate under cavitation and liquid impingement erosion conditions.

Hoff and Langbein equation

A simple exponential equation was proposed by Hoff and Langbein [10] incorporating the heterogeneous characteristics of impingement drops based on impact statistics. The proposed equation (Fig. 3) requires only two parameters in order to compute the erosion rate as a function of time (Table 1). It should be noted, however, that by introducing a Poisson distribution into the method proposed by Heymann [7] or by introducing a distribution function into the original method proposed by Hoff and Langbein [10], the two methods are quite similar.

Tichler and de Gee model

Tichler and de Gee [8], on the basis of the observation of two steady-state periods, have formulated an equation to predict the mean depth of erosion as a function of time. It was assumed that the erosion rate is relatively high and the surface is attacked uniformly during the first steady-state period. The surface is saturated with deep isolated craters and the erosion rate is relatively low during the second steady-state period. The final equation suggested for attenuation and second steady-state period and definition of terms used are presented in Fig. 4. The equation needs five parameters to define the mean depth of erosion-rate-versus-time curve (Table 1). A graphical method to determine these parameters was presented by the investigators.

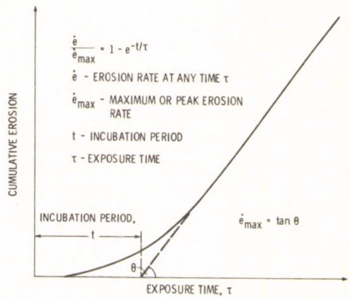

Fig. 3. - Schematic of erosion vs. time curve depicting incubation period according to Hoff and Langbein [10].

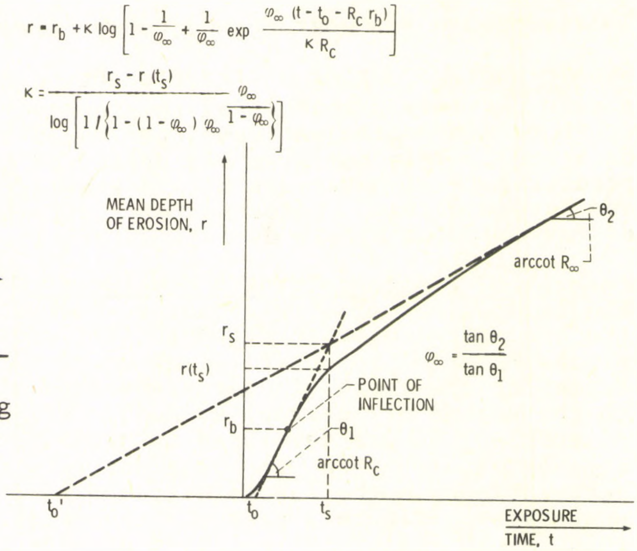

Fig. 4. - Equation and definition of parameters used by Tichler and de Gee [8].

Noskievic Formulation

Noskievic [12] formulated a mathematical relaxation model for the dynamics of cavitation damage of materials using a differential equation applied to forced oscillations with damping. This cavitation erosion model requires three parameters for the prediction of an erosion-versus-time-curve (Table 1). Charts are presented for the use of this method (Fig. 5), which simplifies the hurdle of going through lengthy equations and calculations. The experimental curve of relative cavitation damage (ν) versus log cavitation exposure time log t has to be compared with curves in Fig. 5 by shifting in the direction of the log t axis until a curve of approximate match is found. This enables one to read out δ and τ, which results in a β value.

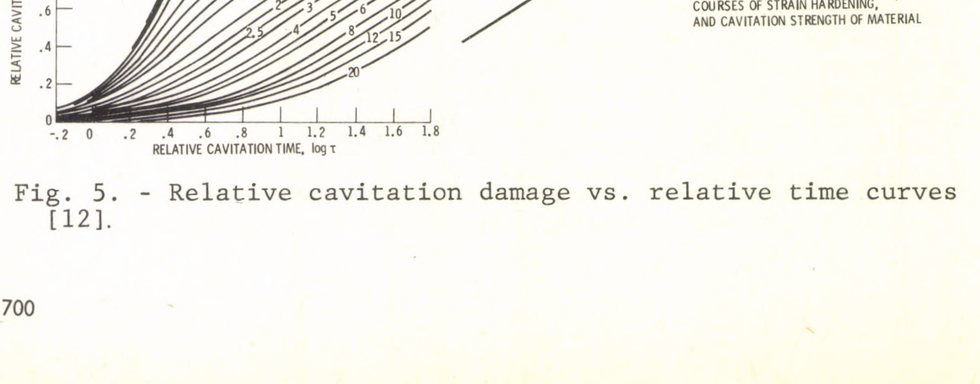

Fig. 5. - Relative cavitation damage vs. relative time curves [12].

Curve-Fit Approach

Data for a large number of materials tested in both a rotating disk device and a magnetostriction oscillator have been analyzed in a new manner that presents normalized cumulative average erosion rate versus normalized time which brings the results to a universal curve fit [13]. With a knowledge of four parameters (Table 1), it may be possible to correlate erosion data between the laboratory model and field device. The agreement of the data analyzed from two previous investigations with entirely different experimental conditions not only showed similarities between cavitation and liquid-impingement erosion, but also reinforced the possibility of the unified nature of erosion. Correction factors for the incubation period and intensity of erosion are suggested.

DISCUSSION

Figure 6 presents normalized-average-erosion-rate-versus-normalized-time curves for stainless steel tested in a rotating disk device [13]. The data are normalized with respect to peak erosion rate and the time corresponding to this peak. Various models proposed by Thiruvengadam [9], and Heymann [11], Rao and Young [13], have also been presented on the curve. The methods proposed in [9] and [11] fit the data following the peak erosion rate. It is noted, however, that normalized time from 0 to 1 cannot be represented by any of the equations presented earlier except the curve-fit approach developed at this laboratory [13]. The methods proposed by Tichler and de Gee [8] and Noskievic [12] have not been used, as the data considered for the analysis were not exposed too long and their plots represent a different dependent parameter. For individual materials, good results can be obtained at a single experimental condition with these two methods. It must be indicated, however, that many calculations are needed with these two methods.

To check the general validity of the models and graphical approaches presented earlier, data reported for cavitation erosion [21, 22] and liquid impingement [23, 24] were analyzed. A typical set of plots are presented in Figs. 7 to 9 as normalized average erosion rate versus normalized time. It is evident that a material tested at a variety of conditions cannot be represented by a single method proposed earlier for

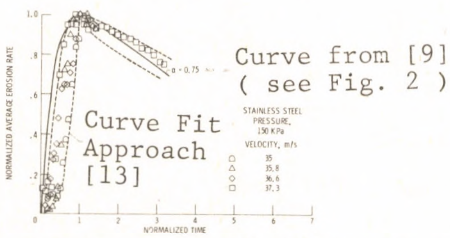

Fig. 6. - Normalized average erosion rate vs. normalized time of stainless steel.

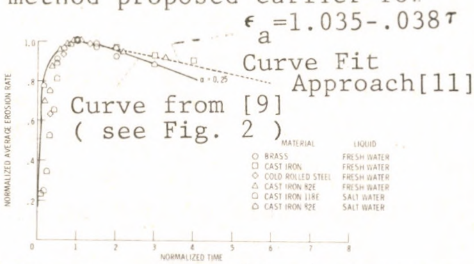

Fig. 7. - Normalized average erosion rate vs. normalized time of different materials - vibratory cavitation.

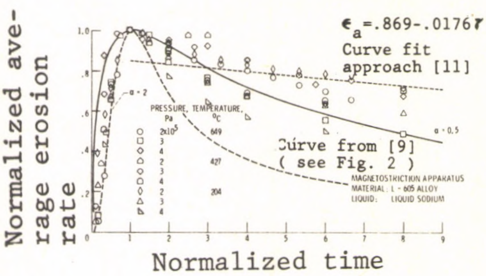

Fig. 8.- Normalized average erosion rate vs. normalized time of L-605 alloy tested in liquid sodium (data source: [22]).

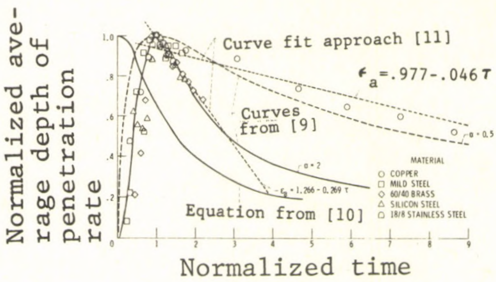

Fig. 9.- Normalized mean depth of penetration rate vs. normalized time for different materials - drop impingement (data source: [23]).

long-term predictions. When individual groups of materials are considered as in Fig. 9, the methods proposed by Thiruvengadam [9] and Heymann [11] are good. To show the involvement of calculations with equations proposed in [8], Table 2 presents parameters necessary to calculate the mean-depth-of-erosion-versus-time curve for stainless steel, mild steel, and brass [23]. In order to use this method, one must know the two steady-state periods. These may, however, not be available for most of the materials tested. The curve-fit approach suggested by this laboratory [13] produces a large scatter band to cover a wide variety of experimental conditions. This method, however, not only calculates erosion rates and times, but also the cumulative erosion.

To solve some of the disadvantages of each of the modeling methods proposed earlier with long-term predictions, a new characteristic law of average erosion rate versus cumulative erosion is presented.

Table 2. - Parameters necessary for Tichler and de Gee formulation [8] (data source: [23])

Parameter	Stainless steel	Mild steel	60/40 brass
t_0 impacts	252×10^3	85×10^3	189×10^3
R_c	2.32×10^{-3}	2.73×10^{-3}	4.20×10^{-3}
r_b, μm	328	360	620
R_∞	5.19×10^{-4}	1.46×10^{-3}	3.44×10^{-4}
$\phi = R_\infty/R_c$	0.244	0.536	0.082
α	1.422	-----	0.763
β	1.813	-----	3.395
$r(t_s)$	369	401	722
r_s	392	453	849
κ	75.62	-----	-----

Characteristic of Erosion-Rate-Versus-Cumulative-Erosion Curve

Figure 10 presents a typical plot of cumulative average volume loss rate versus volume loss of mild steel tested in a rotating disk device. The experimental conditions are: pressure, 0.15 MPa (abs); velocity, 37.3 m/s; diameter of the cav-

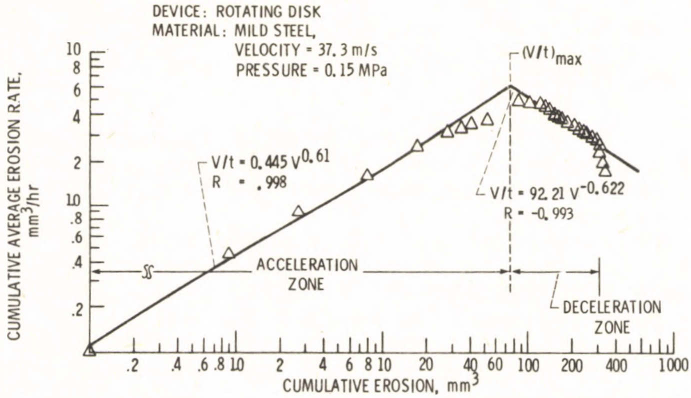

Fig. 10. -Average erosion rate as function of cumulative erosion.

itation inducer, 25.4 mm; and diameter of the test specimen, 63.5 mm. It appears that this curve has acceleration, peak rate and deceleration zones. The acceleration and deceleration zones may be represented by separate power-law relations. The equation for the acceleration zone is written as

$$\mathbf{V}/t = A\mathbf{V}^n \tag{1}$$

or $$\mathbf{V} = (At)^{1/(1-n)} \tag{2}$$

where $\mathbf{V}$ = cumulative volume loss, mm^3; t = exposure time corresponding to $\mathbf{V}$, min; A = coefficient; and n = exponent. Differentiation of Eq. (2) with respect to t results in

$$d\mathbf{V}/dt = A\mathbf{V}^n/(1-n) = \mathbf{V}/(1-n)t \tag{3}$$

Similarly, the deceleration zone after the peak is represented as

$$\mathbf{V}/t = B\mathbf{V}^{-m} \tag{4}$$

or $$\mathbf{V} = (Bt)^{1/(1+m)} \tag{5}$$

where B = coefficient; and m = exponent. Differentiation of Eq. (5) with respect to t results in

$$d\mathbf{V}/dt = B\mathbf{V}/(1+m)t \tag{6}$$

$$= B^{1/(1+m)}\ t^{-m(1+m)}/(1+m) \tag{7}$$

The coefficients, exponents (slopes), and correlation coefficients obtained by least-square fit are marked on Fig. 10. Eqs. (3) and (6) indicate that instantaneous erosion rate $d\mathbf{V}/dt$ for these two zones is a function of cumulative average erosion rate $\mathbf{V}/t$. Further the ratios of these two rates are always constant. The intersection point for these two curves may be obtained by equating Eqs. (1) and (4), i.e.,

$$AV^n = BV^{-m} \tag{8}$$

or $$V = (B/A)^{1/(n+m)} \tag{9}$$

The value of V in Eq. (9) corresponds to maxima on average-erosion-rate-versus-erosion curve, and values of $(V/t)_{max}$ and time corresponding to this peak may be obtained by using either Eq. (1) or (4).

This study establishes that exponents n and m are almost equal, and that a power-law relation also exists between instantaneous erosion rate and exposure time. The advantage of this characteristic relation is that the values of $(dV/dt)_{max}$ and time corresponding to this peak may be calculated with a few number of experimental points. It is generally observed that Eq. (1) terminates at $(dV/dt)_{max}$ and deviates from the experimental points. To the knowledge of the present authors, this type of power-law relationship has not been reported earlier. This relation opens new avenues in erosion scaling and modeling efforts.

CONCLUSIONS

A brief overview of long-term cavitation erosion prediction equations and their capabilities is presented. Data analysis using cavitation and liquid impingement erosion data indicates that the normalized curve-fit approach suggested from this laboratory affords a better prediction for certain sets of data. For individual materials at one experimental condition, however, the methods proposed by Thiruvengadam and Heymann are good immediately following the peak erosion rate.

A unique power law relationship between average erosion rate and cumulative erosion is presented. It is believed that this relationship can solve some long-term modeling problems.

REFERENCES

1. Honegger, E.: Tests on Erosion Caused by Jets. Brown Boveri Review. Vol. 14, No. 4, April 1927, pp. 96-104.
2. Fyall, A. A., King, R. B., and Strain, R. N. C.: Rain Erosion - Part II and Part III, Reports 510 and 513, Royal Aircraft Establishment, Farnborough, 1957.
3. Hobbs, J. M.: Cavitation Erosion Testing Techniques. NEL Rept. 69, East Kilbride, Glasgow, 1962.
4. Thiruvengadam, A.: Cavitation and Cavitation Damage. M. Sc. Thesis, 1959; Prediction of Cavitation Damage. Ph. D. Thesis, 1961.
5. Thiruvengadam, A., and Preiser, H. S.: On Testing Materials for Cavitation Damage Resistance. J. Ship Res., Vol. 8, 1964, pp. 39-56.
6. Plesset, M. S., and Devine, R. E.: Effect of Exposure Time on Cavitation Damage. J. Basic Eng., Vol. 68, 1966, pp. 691-705.
7. Heymann, F. J.: On the Time Dependence of the Rate of Erosion due to Impingement or Cavitation. ASTM STP 408, 1967, pp. 70-110.

8. Tichler, J. W., and de Gee, A. W. J.: Time Dependence of Cavitation Erosion and the Effect of Some Material Properties. Proc. 3rd Int. Conf. Rain Erosion and Associated Phenomena, RAE, 1970, pp. 847-79.
9. Thiruvengadam, A.: Theory of Erosion. Proc. 2nd Meersburg Conf. on Rain Erosion, RAE, 1967, pp. 605-53.
10. Hoff, G., and Langbein, G.: Resistance of Materials Towards Various Types of Mechanical Stress. ibid, 1967, pp. 655-81.
11. Heymann, F. J.: Toward Quantitative Prediction of Liquid Impact Erosion. ASTM STP 474, 1970, pp. 212-48.
12. Noskievic, J.: Dynamics of the Cavitation Damage. Proc. Jt. Symp. on Design and Operation of Fluid Machinery, ASCE-ASME-IAHR, 1978, pp. 453-62.
13. Rao, P. V., and Young, S. G.: Universal Approach to Analysis of Cavitation and Liquid-Impingement Erosion Data. NASA TP-2061, 1982.
14. Rao, P. V., and Buckley, D. H.: Long-Term Predictive Capability of Cavitation and Liquid Impingement Erosion Models - a Comparative Study.
15. Engel, O. G.: A First Approach to a Microscopic Model of Erosion Rate in Drop impact and Cavitation. Proc. 3rd Int. Conf. on Rain Erosion and Associated Phenomena, RAE, 1970, pp. 447-518.
16. Perelman, R. G., and Denisov, Y. D.: The Strength of Materials Under the Action of Droplet Impacts. RAE Lib. Transl. No. 1654, 1971.
17. McGuiness, T., and Thiruvengadam, A.: Cavitation Erosion - Corrosion Modeling. ASTM STP 567, 1974, pp. 30-55.
18. Handbook of Cavitation Damage. Hydronautics, Inc. Rept. 233-8, 1965.
19. Lichtarowicz, A.: Cavitating Jet Apparatus for Cavitation Erosion Testing. ASTM STP 664, 1979, pp. 530-49.
20. Thiruvengadam, A.: Handbook of Cavitation Erosion. Hydronautics, Inc., Tech. Rept. TR 7301-1, June 1974.
21. Kerr, S. L.: Determination of the Relative Resistance to Cavitation Erosion by the Vibratory Method. Trans. ASME, Vol. 59, July 1937, pp. 373-97.
22. Young, S. G., and Johnston, J. R.: Effect of Temperature and Pressure on Cavitation Damage in Sodium. ASTM STP 474, 1970, pp. 67-108.
23. Thomas, G. P., and Brunton, J. H.: Drop Impingement Erosion of Metals. Proc. Roy. Soc. London, Vol. 314A, Jan. 1970, pp. 549-65.
24. Elliot, D. E., Marriott, J. B., and Smith, A.: Comparison of Erosion Resistance of Standard Steam Turbine Blade and Shield Materials on Four Test Rigs. ASTM STP 474, 1970, pp. 127-61.

Dr. P. Veerabhadra Rao
NRC-NASA Research Associate
NASA Lewis Research Center
Cleveland, Ohio 44135

Dr. Donald H. Buckley
Tribology Branch Chief
NASA Lewis Research Center
Cleveland, Ohio 44135.

OPTIMISATION OF THE AXIAL FLOW PUMPS

R. REY and R. NOGUERA

I - INTRODUCTION :

In construction of the axial flow pumps, the designer is required to make, somehow, arbitrary selection among different geometric and hydraulic parameters ; namely, impeller hub to tip diameter ratio, degree of reaction, type of vortex flow, diffusion factor,...

The work presented here is based on the functional relations between specific speed, specific diameter, impeller hub to tip diameter ratio, and two coefficients depending of the degree of reaction. A general method of resolution of the above relations according to each of the following criteria :

a) maximum hydraulic efficiency
b) minimum noise level
c) maximum suction capacity (minimum NPSH)

has been established.

From the basic design data of a machine, i.e head, flow rate, running speed, having adopted the type of vortex flow, the diffusion factor being imposed, and the condition of radial equilibrium respected, this method gives directly :

- rotor outside diameter
- hub diameter
- profile solidity

Furthermore, by employing the NACA 65 airfoil a certain number of relations, concerning the blade deflection and profile losses, have permitted to define at each radius, blade surface curvature and stagger angle of the profile.

Four axial machines (2 fans and 2 pumps) have been designed and constructed, according to the aforementionned method. The experiments carried out over these machines have satisfactorily confirmed the reliability of the method, also four French companies have manifested their interest for this method.

II - GENERALITY CONCERNING PERFECT FLUID FLOW :

The establishment of this part is based on the following assumptions :

- the inlet stage velocities are axial and uniform (Fig.1)
- the flow section between hub and periphery is constant and have a cylindrical configuration
- consistant with a perfect fluid flow, the boundry layer effect is neglected.

Under these conditions, the Euler equation gives the head expression at each radius :

$$H(r) = \frac{U_2 C_{u2}}{g} \qquad (1)$$

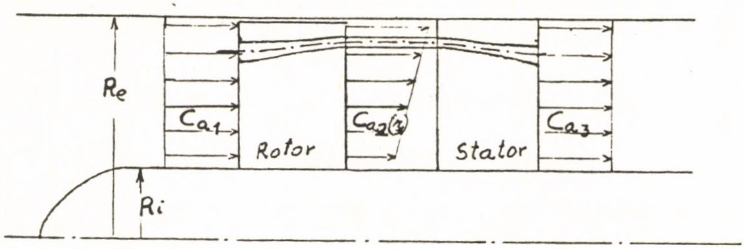

Figure 1 : Axial velocity distribution and stream tube presentation.

Generally, Cu_2 can take the following form : $$C_{u_2}(r) = k_1 r + k_2 + \frac{k_3}{r} \quad (2)$$

Remembering that in construction of axial flow pumps, the most common type of vortex which correspond to a well known hydraulic and geometric properties are :

free vortex flow $k_1 = k_2 = 0$
forced vortex flow $k_2 = k_3 = 0$
constant vortex $k_1 = k_3 = 0$

The first type of generating law is the most widely used one.

1 - Radial Equilibrium

For the general case of a vortex, defined in (2), the respect of the radial equilibrium criteria (1) in the outlet station of the rotor imposes a distribution of axial outlet velocity Ca_2 (r) given by the relation :

$$Ca_2(r) = \sqrt{f(r) + A} \quad (3)$$

f(r) is a function dependant upon the type of the vortex, i.e. k_1, k_2, k_3.

$$f(r) = 2k_1(\omega - k_1)r^2 - 2(k_2^2 + 2k_1k_3)\,Ln\,r + 2k_2(\omega - 3k_1)r + 2\frac{k_2k_3}{r}$$

A is the integration constant which can be calculated from continuity equation.

$$q_v = \int_{Ri}^{Re} 2\pi r\, Ca_2(r)\,.\,dr \quad (4)$$

One can see that in the case of free vortex, the function f(r) cancels and the condition of radial equilibrium is satisfied by a uniform axial flow.

2 - Definition of the Average Radius

The value of the average head, designated by $\overline{H}$, is defined from average power i.e :

$$\overline{H} = \frac{1}{q_v}\int_{Ri}^{Re} H(r)\,.\,dq_v \quad (5)$$

where,

$$dq_v = 2\pi r\, Ca(r)\, dr$$

or,

$$q_v = \pi\,(Re^2 - Ri^2)\,\overline{Ca} \quad (6)$$

where $\overline{Ca}$ is the average velocity (perpendicular to the flow area). Also we define the average radius to be the radius at which the head, H(r) takes its average value i.e $\overline{H}$:

$$H(\overline{R}) = \overline{H} \tag{7}$$

The equation 1 and 2 permit to calculate the local head value :

$$H(r) = \frac{\omega}{g}\left(k_1 r^2 + k_2 r + k_3\right) \tag{8}$$

and the average height is calculated by equation:

$$\overline{H} = \frac{1}{q_v}\int_{Ri}^{Re} H(r)\ 2\pi r\sqrt{f(r)+A}\ dr \tag{9}$$

Except the case of free vortex, the equation cannot be integrated, we have therefore approximated this equation by the following relation :

$$\overline{H} = \frac{1}{Re - Ri}\int_{Ri}^{Re} H(r)\,.dr \tag{10}$$

after simplification, the following expression is obtained :

$$\overline{H} = \frac{\omega}{g}\left[\frac{k_1}{3}\left(Re^2 + RiRe + Ri^2\right) + k_2\,\frac{Re+Ri}{2} + k_3\right] \tag{11}$$

by considering equations 7 and 8 one can write :

$$\overline{H} = \frac{\omega}{g}\left[k_1\overline{R}^2 + k_2\overline{R} + k_3\right] \tag{12}$$

generally, by equating the relations 11 and 12 , two distinct values for the average radius will be resulted :

$$\overline{R} = \frac{Ri + Re}{2} \tag{13}$$

$$\overline{R} = \sqrt{\frac{1}{3}\left(Re^2 + Ri\,Re + Ri^2\right)} \tag{14}$$

where, the first equation corresponds to free and constant vortex ($k_1 = 0$ in the two cases) and the second equation to the vortex for which $k_2 = 0$ (for example, the case of forced vortex).

In spite of this difference it has been shown that in the great majority of cases (i.e hub/tip ratio of $Ri/Re > 0.4$) the values of $\overline{R}$ evaluated by 13 and 14 are nearly equal (a difference of less than 1%). Therefore, the relation 13 is chosen for the definition of average radius for all the types of vortices.

III - REAL FLUID FLOW

For real fluid the same hypothesis are made as that of perfect one, in this case only the rotor and stator profile losses have been taken into consideration.

Taking into account the radial equilibrium criteria, and as indicated in figure 1, the stream tube of constant flow rate, do not have a cylindrical but a conical behavior.

Under these conditions, by applying the momentum theory to the stream tube of the rotor and stator blades respectively, the local head for a horizontal stage of constant flow area, will be expressed as the following :

$$H(r) = \frac{p_3 - p_1}{\rho g} + \frac{C_3^2 - C_1^2}{2g} \qquad (15)$$

which also can be written as :

$$H(r) = \frac{Ca_1 Ca_2}{g} tg\alpha_2 \left[tg(\beta_m - \varepsilon_1) + tg(\alpha_m - \varepsilon_2)\right] - \frac{Ca_1^2}{g} tg\alpha_3 \, tg(\alpha_m - \varepsilon_2) \qquad (16)$$

where, Ca_2, α_2, β_m, ε_1, α_m, ε_2 are the parameters corresponding to the radius defined in Figure 2.

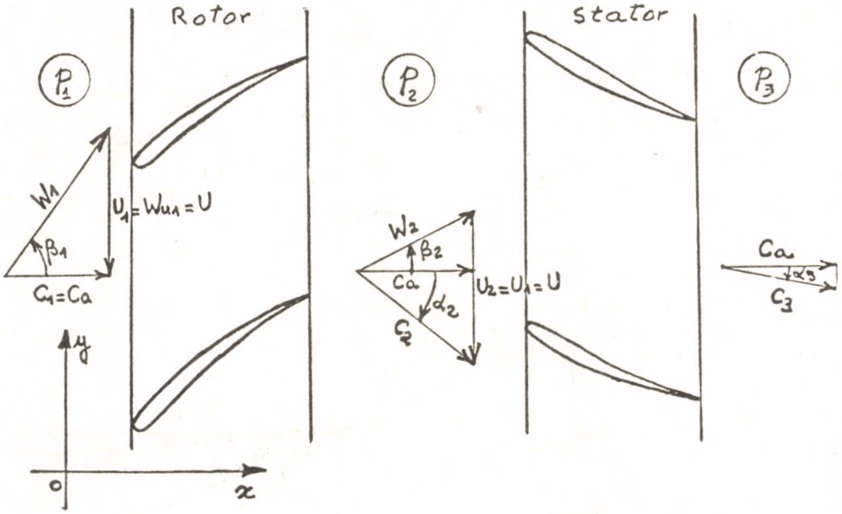

Figure 2 : velocity diagram of a compression stage.

In the foregoing analysis the following conditions and notations have been observed for the above parameters :

$\alpha_3 = 0$, which corresponds, in the preliminary design stage, to the design point operation.

ε_1 et ε_2 are considered to be constant (in the order of 1 to 2 degree, ref (6))

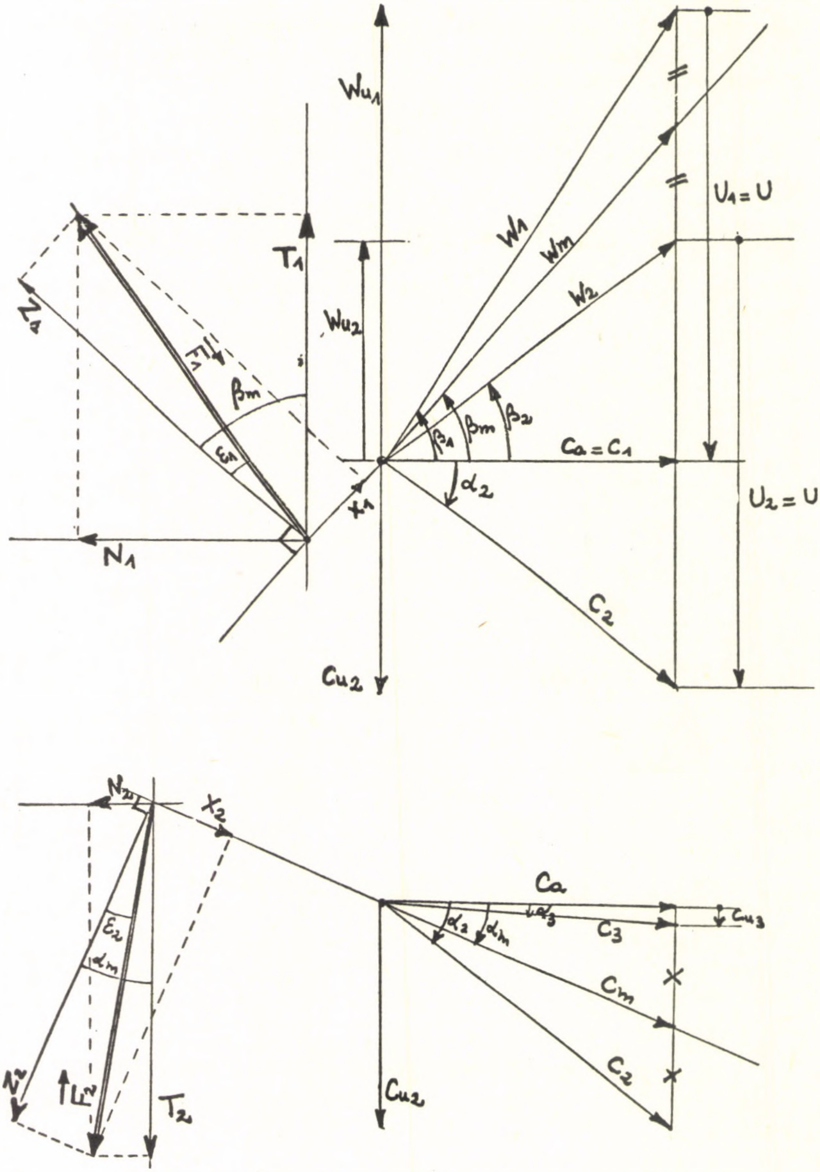

Figure 2A : Details of the aerodynamic parameters and the forces exerted on the rotating and stationary blades (refering to Fig.2)

At the mean radius, other parameters will take particular values :

$$\alpha_2(\bar{R}) = \overline{\overline{\alpha_2}} \quad , \beta_m(\bar{R}) = \overline{\overline{\beta_m}} \quad , \alpha_m(\bar{R}) = \overline{\overline{\alpha_m}}$$

$$\alpha_3(\bar{R}) = \overline{\overline{\alpha_3}} \quad , Ca_2(\bar{R}) = \overline{\overline{Ca_2}}$$

Under these conditions, the average head can be expressed by combining the equations 7 and 16 :

$$\bar{H} = H(\bar{R}) = \frac{Ca_1 \overline{\overline{Ca_2}}}{g} \, tg\overline{\overline{\alpha_2}} \left[tg\left(\overline{\overline{\beta_m}} - \varepsilon_1\right) + tg\left(\overline{\overline{\alpha_m}} - \varepsilon_2\right) \right] \qquad (17)$$

or,

$$\bar{H} = \frac{Ca_1 \overline{\overline{Ca_2}}}{g} K \qquad (18)$$

with K desfined as :

$$K = tg\overline{\overline{\alpha_2}} \left[tg\left(\overline{\overline{\beta_m}} - \varepsilon_1\right) + tg\left(\overline{\overline{\alpha_m}} - \varepsilon_2\right) \right] \qquad (19)$$

By considering equation 17 , the hydraulic efficiency $\overline{\overline{\eta_H}}$, which takes account of profile losses only, will be given by (Ref(2)) :

$$\overline{\overline{\eta_H}} = \frac{tg\left(\overline{\overline{\beta_m}} - \varepsilon_1\right) + tg\left(\overline{\overline{\alpha_m}} - \varepsilon_2\right)}{tg\,\overline{\overline{\alpha_m}} + tg\,\overline{\overline{\beta_m}}} \qquad (20)$$

IV - FONCTIONAL RELATIONSHIP BETWEEN THE NON DIMENSIONAL PARAMETERS OF THE MACHINE

As it will be shown later, two basic equations which relate hub-tip ratio and specific diameter with the specific speed, can be established.

hub-tip ratio
$$T = \frac{Ri}{Re} \qquad (21)$$

specific diameter
$$\Lambda = \frac{Re\,(g\bar{H})^{1/4}}{\sqrt{q_v}} \qquad (22)$$

specific speed
$$\Omega = \frac{\omega \sqrt{q_v}}{(g\bar{H})^{3/4}} \qquad (23)$$

By inserting the value of $\bar{H}$ determined from the equation 18 and by making the following hypothesis :

$$Ca_2(\bar{R}) = \overline{\overline{Ca_2}} = \overline{Ca_2} = Ca_1 \qquad (24)$$

(this hypothesis will be verified later), one can show that :

$$\Omega^2 = \frac{4\pi\left(Re^2 - Ri^2\right)}{K^{3/2}} \; \frac{tg^2\,\overline{\overline{\beta_1}}}{\bar{R}^2}$$

by taking the value of R as given by equation 13 and by introducing T, one obtains (3) :

$$\Omega^2 = \frac{4\pi(1-T)}{K^{3/2}(1+T)}\, tg^2\overline{\overline{\beta_1}}$$

where, the value of hub-tip ratio as a function of specific speed is given by :

$$T = \frac{c - \Omega^2}{c + \Omega^2} \qquad (25)$$

where c is a constant depending only upon the angles at the mean radius $\overline{\overline{\alpha_m}}$ and $\overline{\overline{\beta_m}}$ (*)

$$c = \frac{4\pi\left(tg\overline{\overline{\alpha_m}} + tg\,\overline{\overline{\beta_m}}\right)^2}{K^{3/2}}$$

with simiilar reasoning, and by employing the same hypothesis, the following relation is derived :

$$\Lambda = \frac{d}{2\Omega}\left(c + \Omega^2\right) \qquad (26)$$

with $$d = \frac{K^{1/4}}{\sqrt{\pi c}}$$

In reality, the equation 26 is the parametric form of the famous statistical expression of CORDIER diagram (4), presented in Figure 4.

<u>The Remarks Concerning the Hypothesis</u> :

a) The first approximation has permitted to obtain a simplified expression for the average head. This simplification has only been used for the establishment of the formulas 25 and 26 . These formulas, while being sufficiently simple, reveal the overall behavior of the following phenomena :

The hub-tip ratio and specific diameter decrease when the specific speed increases, this has also been noticed by numerous authors (5) and used by the constructors.

When it is desired to use the correct definition of the mean radius established in 5 , it is then necessary to employ a numerical technique for the establishment of the desired equations relating T and Λ to Ω .

b) For the most commonly used vortices, the numerical integration of the equation 3 shows that the radial distribution of $Ca_2(r)$ is nearly linear, (Figure 3).
Therefore, it is concluded that :

$$Ca_2(\overline{R}) = \overline{\overline{Ca_2}} = \overline{Ca_2} = Ca_1$$

(*) from figure 2 it can be seen that :

$$tg\,\overline{\overline{\beta_1}} = tg\overline{\overline{\alpha_m}} + tg\overline{\overline{\beta_m}} \quad ; \quad tg\overline{\overline{\alpha_2}} = 2 \,.\, tg\overline{\overline{\alpha_m}}$$

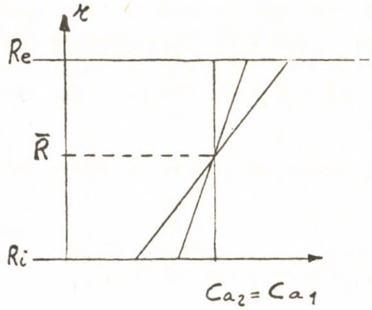

Figure 3 : axial velocity variation at the rotor outlet, for different types of vortex flow.

V - DIMENSIONING OF A COMPRESSION STAGE

Generally, the construction of the machines is based on the expected values of the parameters- :head, flow rate, rotational speed (nearly the same as the synchronous speed) at the design point.

The principal dimensions of the machine, namely, Ri and Re are computed from 25 and 26 , these values will be used for the continuation of the analysis when the values of $(\bar{\alpha}_m, \bar{\beta}_m)$ are chosen.

Now, we are going to see that a particular choice of the above angles, will essentially confer to the machine specific properties, and this depending on our desire to have the mahine possessed, each of the following characteristics :

- maximum hydraulic efficiency,
- minimum size,
- minimum amount of pressure fluctuation (low noise level, in the case the fans),
- maximum suction capacity (minimum NPSH).

As it will be shown later, certain of the above favourable conditions cannot be simultaneously satisfied, and sometimes they are even incompatible.

Also, it is worth noting that the choice of $(\bar{\bar{\alpha}}_m, \bar{\bar{\beta}}_m)$ leads to a definition for the degree of reaction at the mean radius :

$$\bar{\bar{\sigma}} = \frac{tg\,\bar{\bar{\beta}}_m}{tg\,\bar{\bar{\alpha}}_m + tg\,\bar{\bar{\beta}}_m}$$

We are going to study each of the favourable cases in the following :

a) Maximum Hydraulic Efficieny

The definition of hydraulic efficiency is given by the equation 20 . By taking the derivitive of this equation, the optimal values of $(\bar{\bar{\alpha}}_m, \bar{\bar{\beta}}_m)$ can be determined.

By assuming that ε_1 and ε_2 are small with respect to $\bar{\bar{\alpha}}_m$ and $\bar{\bar{\beta}}_m$, and knowing that they are approximately equal, then the optimisation relation is obtained as follows : $\partial \bar{\bar{\eta}}_H / \partial \bar{\bar{\beta}}_m = 0$ after simplification and rearragement one obtains 27 :

$$tg\,\bar{\bar{\beta}}_m = -\,tg\,\bar{\bar{\alpha}}_m + \sqrt{2\left(1 + tg^2\,\bar{\bar{\alpha}}_m\right)} \qquad (27)$$

Also, from figure 4, it is seen that the equation 27 results in a pompe which is evidently smaller than those designed according to the statistical diagram of CORDIER. This is in agreement with the general tendency of the axial flow pumps' constructors, namely, the NPSH being the fundamental parameter, for a given $\overline{\overline{\alpha_m}}$, the $\overline{\overline{\beta_m}}$ is usually chosen greater than that furnished by 27

Inversely, one can still decrease the size by decreasing the value of $\overline{\overline{\beta_m}}$ with respect to the value obtained from 27 .

The limits indicated of figure 4, concerning the values of $\overline{\overline{\alpha_m}}$ (from 14¤ to 22)) corresponds to the utilisation of the NACA 65 airfoil series (7).

c - Low Level of Pressure Fluctuation

This study is based on the Lowson method (8) which lead to a formula for acoustic energy of the pressure fluctuations. This energy is also related to the frequency of the rotor blades passing.

$$W_m = \frac{m^2 Z^4}{2\pi \rho C_0^3} \omega^2 \left(T_1^2 + N_1^2\right) (m Z)^{-2h} \qquad (28)$$

Co : the velocity of sound in the fluid.
m : harmonic number
h : a constant (h ≈ 2 for m = 1)
T_1, N_1 : components of the resultant aerodynamic forces over the rotor bladings (figure 2A)

If one is interested in the particular case, where m = 1, by expressing T_1 and N_1 as a function of H, qv; assigning the angles at the mean radius, after a relatively long development procedure one obtain : $W_1 = \frac{\rho \Omega^2}{\pi C_0^3 Z^2} q_v (g\overline{H})^{5/2} \; tg\,\overline{\overline{\alpha_m}} \left(1 + tg^2 \overline{\overline{\beta_m}}\right)$ (29)

Therefore, the noise level will be as much lower as :

- Ω will be decreased, large Z,
- $\overline{\overline{\alpha_m}}$ will be small,
- for a given $\overline{\overline{\alpha_m}}$ the best value of $\overline{\overline{\beta_m}}$ will be determined by $\frac{\partial W_m}{\partial \overline{\overline{\beta_m}}} = 0$, which results in :

$$tg\,\overline{\overline{\beta_m}} = -\,tg\,\overline{\overline{\alpha_m}} + \sqrt{1 + tg^2 \overline{\overline{\alpha_m}}} \qquad (30)$$

As one can see, the optimum conditions concerning a low noise level is in contradiction with the conditions for optimum efficiency and small size (9).

d - Low Value of NPSH

The optimisation of the required NPSH is based on the classical formulation, i.e. by introducing local dynamic pressure reduction coefficient.

$$NPSH = \frac{C_1^2}{2g} + \lambda \frac{W_{1e}^2}{2g} \qquad (31)$$

Where, W_{1e} is the rotor inlet relative velocity at the Re radius.

When C_1 and W_{1e} are replaced by their respective values, and by introducing the Thoma parameter : $\sigma^* = \frac{NPSH}{H}$, one obtain the general relation :

$$\sigma^* = \frac{1+\lambda}{2K} + \frac{\lambda}{8} d^2 \left(c + \Omega^2\right)^2 \qquad (32)$$

Also, the equation 20 shows that the efficiency will be higher as $\bar{\bar{\alpha}}_m$ is increased (within the limitation imposed by the camber of the available profiles, one can take, for example, in the case of the NACA 65 airfoil series, a maximum value of 22¤ - 24¤ for $\bar{\bar{\alpha}}_m$). The relation 27 is used for the optimal choice of $\bar{\bar{\alpha}}_m$ and β_m

b) Minimum Size

For a given head and flow rate, in order to design the machine according to minimum size criteria, it is sufficient to have Λ minimized (relation 22). As it is shown in figure 4 (after the relations 25 and 26 also, by using the optimization equation 27) the size of the machine decreases when :

- Ω is large, which is evidently consistent with the actual rules of art.
- $\bar{\bar{\alpha}}_m$ is large for a given fixed value of Ω .

As one can see, the last condition is in agreement with the conditions of having a high efficiency.

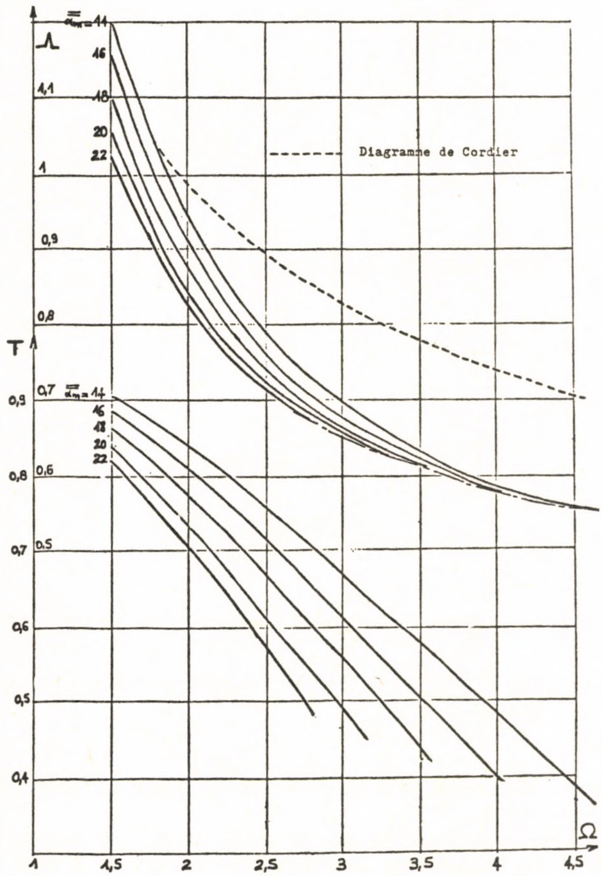

Figure 4 : The variation of specific diameter and hub/tip ratio with the specific speed. (Réf. equation 27)

Where c, d and K are functions of $\overline{\overline{\alpha_m}}$ and $\overline{\overline{\beta_m}}$ (as defined previously).
Then, to have the NPSH minimised is equivalent to :
- using a small value for Ω,
- a large value for $\overline{\overline{\alpha_m}}$,
- a value for $\overline{\overline{\beta_m}}$ which satisfies the equation : $\dfrac{\partial \sigma^*}{\partial \overline{\overline{\beta_m}}} = 0$ (33)

This last equality leads to an equation of fourth degree which should be resolved, numerically or graphically.

The solutions are presented in figure 5, where, the optimal values of $\overline{\overline{\beta_m}}$ corresponding to the equations 27 and 30 are figured.

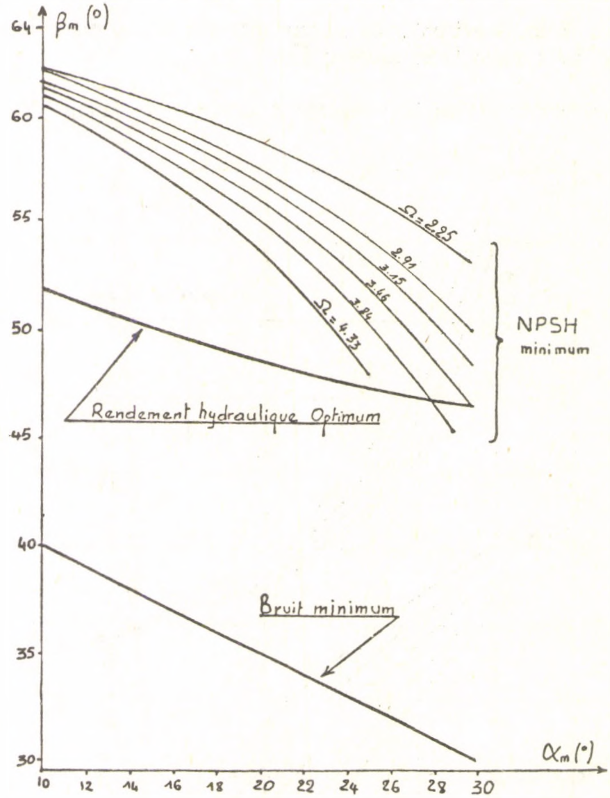

Figure 5 : Optimum choice of the couple $(\overline{\overline{\alpha_m}}, \overline{\overline{\beta_m}})$, according to the adopted design criteria.

VI - Generalisation

The formulas presented throughout this paper permit to completely dimension the stage of an axial flow compression machine.
For a given basic design data (H,qv) the type of optimisation (hydraulic efficiency, size, noise level, NPSH) being imposed, the considerations of section V lead to a choice of : specific velocity (therefore, rotational speed) large or small, also the most adapted (or else, compatible with the employed profile) values of $\overline{\overline{\alpha_m}}$ and $\overline{\overline{\beta_m}}$.

The relations 25 and 26 permit to compute hub/tip ratio and specific diameter, then from 21 and 22 the hub and tip radius (Ri, Re) can be determined.

Now, depending on the type of selected vortex, the relation 5 permit to calculate the corresponding values of k_1, k_2 and k_3.

Thus, one can determine the velocity triangles at each radius. Then, by imposing an acceptable value of local diffusion coefficient (10), in the order of 0,4 to 0,5, the cascade solidity (l/t) can be found by the following relations :

rotor : $$D = 1 - \frac{\cos\beta_1}{\cos\beta_2} + \frac{\cos\beta_1}{2\,l/t}\left|tg\beta_1 - tg\beta_2\right|$$

stator : $$D = 1 - \cos\alpha_2 + \frac{\cos\alpha_2}{2\,l/t}\left|tg\alpha_2\right|$$

On the other hand, in order to assure the desired fluid deflection at different radius, the general method appeared in (11), (12) and (13) can be readily employed.

Notations

C : absolute velocity,
Ca : axial velocity,
Cu : tangential component of C,
W : relative velocity,
U : tangential velocity,
N : rotational speed,
H : stage head,
qv : flow rate,
Re : blade tip radius,
Ri : hub radius,
Z : rotating blade number,
g : gravitational acceleration,
p : static pressure,
T : hub/tip ratio,
r : radius,
D : coefficient of diffusion.
w : angular velocity
α : absolute flow angle
β : relative flow angle
ε : drag angle
α_m : mean angle defined as : $tg\,\alpha_m = \frac{tg\alpha_2 + tg\alpha_3}{2}$
β_m : mean angle defined as : $tg\,\beta_m = \frac{tg\beta_1 + tg\beta_2}{2}$
Λ : specific diameter
Ω : specific speed
ρ : fluid density
σ : degree of reaction

REFERENCES

(1) : A. HOUBERECHTS
"Les Turbines" - Ed. Vander - 1972

(2) : R. COMOLET
"Etude analytique du rendement manométrique local d'un étage de turbomachine axiale".
Thermique et aéraulique - Tome 2 - n°1 - 1972

(3) : R. REY
"Méthode générale de détermination d'un étage de turbomachine axiale de compression".
Thèse de Docteur Etat Es-Sciences - Université PARIS VI - 1981.

(4) : R. OUZIAUX.
"Contributions diverses à l'étude des machines volumétriques et des turbomachines".
Thèse de Docteur Etat Es-Sciences - Université de LILLE - 1969.

(5) : BALJE
"Axial cascade technology and application to flow path design".
Journal of Engineering for power - 1968.

(6) : HERRIG, EMERY, ERWIN.
"Systematic two-dimensional cascade tests of NACA 65 - Series compressor blades at low speeds".
NACA TN 3916 - 1957.

(7) : R. REY.
"Représentation fonctionnelle des propriétés cinématiques des grilles d'aubes planes".
Entropie - 1976.

(8) : LOWSON
"The sound field for singularities in motion".
Proc. Roy. Soc. - A 286 - 1965.

(9) : SUNYACH, ARBEY, COMTE-BELLOT, PAPAILLIOU, BARIO, OYFFERS, BRIDELANCE.
"Bruit des ventilateurs axiaux équipés de profils très porteurs".
Rapport DGRST - 76 - 7 - 1018 et 1019 - 1979.

(10) : LIEBLEIN
"Incidence and deviation - angle correlations for compressor cascades".
Journal of basic Eng. - 1960.

(11) : NASA SP 36 - 1965.
"Aerodynamic design on axial flow compressors".

(12) : BALJE.
"A study on design criteria and matching of turbomachinery".
Journal of Eng. for power - 1962.

(13) : R. COMOLET
"Mécanique des grilles d'aubes planes".
Bulletin des Etudes et Recherches EDF - n°2 - 1974.

AUTHORS :

Robert REY,
Ingénieur ENSAM,*
Docteur Es-Sciences,
Maître-Assistant à l'ENSAM.

Ricardo NOGUERA,
Ingénieur (CARABOBO University)**
Docteur-Ingénieur,
Maître-Assistant à l'ENSAM.

* Ecole Nationale Supérieure d'Arts et Métiers.
** Venezuela.

STATISTICAL EVALUATION OF THE INFLUENCE OF THE CHIEF DIMENSIONS OF CENTRIFUGAL PUMPS WITH DOUBLE-VANE IMPELLERS ON THEIR WORK PARAMETERS

Jerzy ROKITA

SUMMARY

It has been assumed that between the chief dimensions of double-vane impeller pumps and their work parameters there are some determinable interdependences. The existing correlations have been determined and aveluated. It has been found that only some chief dimensions of the pump affect distinctly its work parameters. The possibility has been pointed out of determining the chief parameters of pumps for preset work parameters.

1. INTRODUCTION

Centrifugal pumps with double-vane impellers are used for pumping liquids containing solid-body grains. Pfleiderer's method of calculating the chief dimensions of the impellers of centrifugal pumps cannot be applied in the case of double-vane impellers, as the distribution of relative velocities along the perimeter of the outside diameter of the impeller is not known and theoretically not determinable. The existence of vortices and dead spaces in the inter-vane ducts makes it impossible also to determine the distribution of the meridional components of absolute velocity in the discharge section of the impeller.

In such a situation the chief dimensions of double-vane impellers may be selected basing on empirical relations between the chief dimensions of double-vane impellers and the work parameters of the pumps. It is on such a conception that Stepanoff's [1] proposition of selecting the chief dimensions of centrifugal pumps with multi-vane impellers is based.

It has been assumed that between the chief dimensions and the work parameters of centrifugal pumps with double-vane impellers there are relations which can be determined.

Therefore, a large collection of data was gathered concerning Polish-made pumps [2, 3] as well as pumps producted in other countries.

2. CHIEF DIMENSIONS OF DOUBLE-VANE IMPELLERS AND DIMENSIONLESS DISCRIMINANTS

The geometrical dimensions of impellers considered in the performed analysis are:

- diameters d_0, d_1, d_2,
- widths b_1, b_2,
- vane angles β_1, β_2.

These dimensions have been presented directly in Fig.1. The following dimensionless discriminants were introduced:

- peripheral velocity constant u_2

$$K_{u2} = \frac{u_2}{\sqrt{2\,g\,H}} \qquad /1/$$

- meridional velocity constant at the impeller outlet c_{2m}

$$K_{c\,2m} = \frac{c_{2m}}{\sqrt{2\,g\,H}} \qquad /2/$$

- velocity constant in the impeller neck c_0

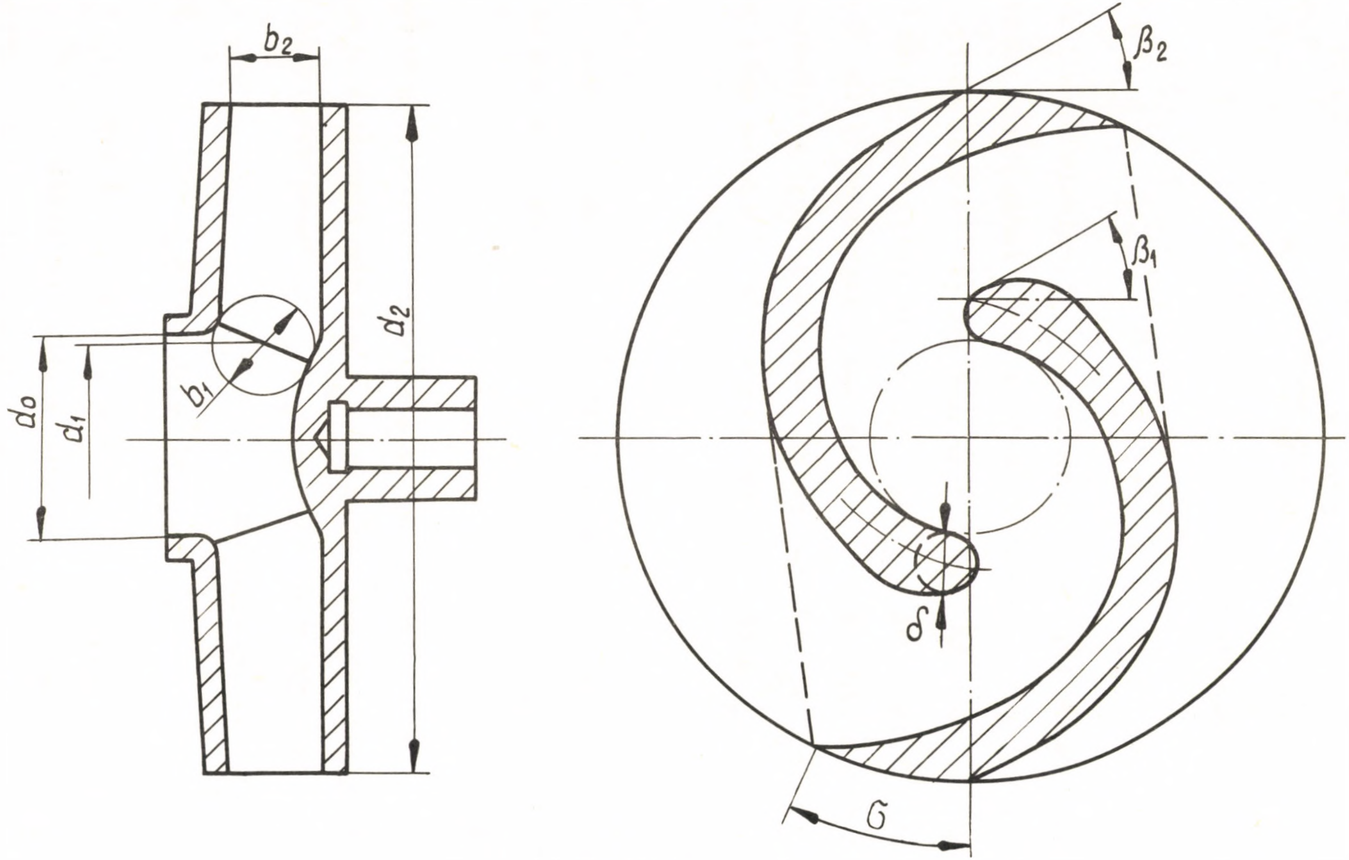

Fig. 1

$$K_{co} = \frac{c_o}{\sqrt{2gH}} \qquad /3/$$

- kinematic specific speed

$$n_{sq} = n\, Q^{1/2}\, H^{-3/4} \qquad /4/$$

The values of the discriminants were calculated for all the considered pumps /30 in all/ and analysed. Independent of the fact whether the impeller had or had not got lateral rotor-disks, the velocities c_{2m} were determined while taking into account the discharge area of the pump, expressed by the formula $(\pi d_2 - 2\,\sigma_2)\,b_2$. If the impeller had no lateral rotor-disks, the velocity c_{2m} determined in this way is of course only conventional.

3. CORRELATIONS BETWEEN THE DIMENSIONLESS /NON-DIMENSIONAL/ DISCRIMINANTS OF THE IMPELLER AND THE KINEMATIC SPECIFIC SPEED

It has been found that there is a distinct correlation between the peripheral velocity constant K_{u2} and the kinematic specific speed n_{sq} /Fig.2/. The relation K_{u2}-n_{sq} has been described by means of the linear equation

$$K_{u2} = 0{,}871 + 0{,}0063\, n_{sq} \qquad /5/$$

The maximum deviation does not exceed 4,9 %, and two thirds of all the deviations are contained within the limit of 2,5 %. In Fig.2 the black dots concern pumps with volutes with increasing cross-sections, whereas the white dots concern pumps with volutes whose cross-sections are constant. We see that the

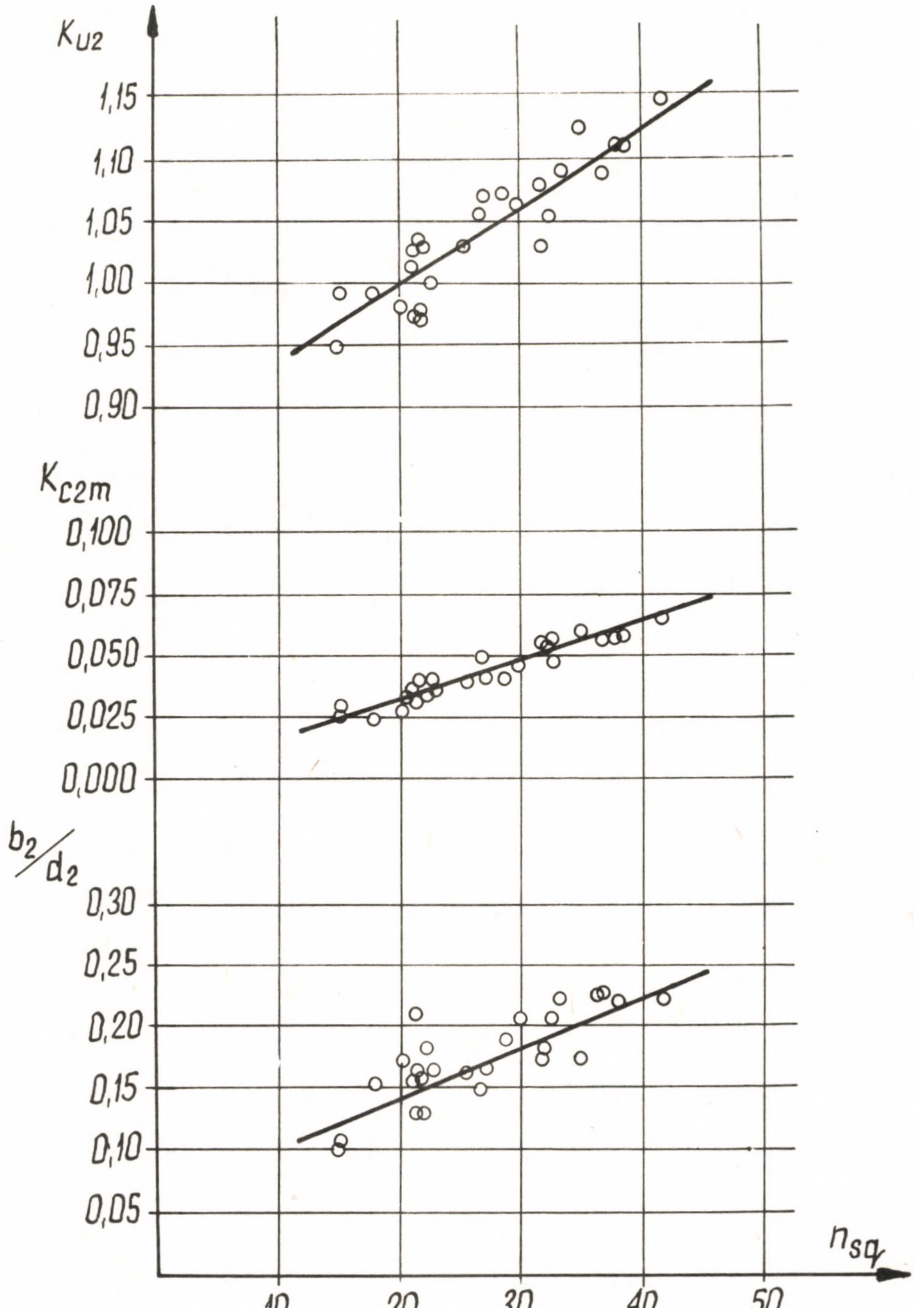
K_{U2}
1,15
1,10
1,05
1,00
0,95
0,90
K_{c2m}
0,100
0,075
0,050
0,025
0,000
b_2/d_2
0,30
0,25
0,20
0,15
0,10
0,05
n_{sq}
10
20
30
40
50

Fig. 2

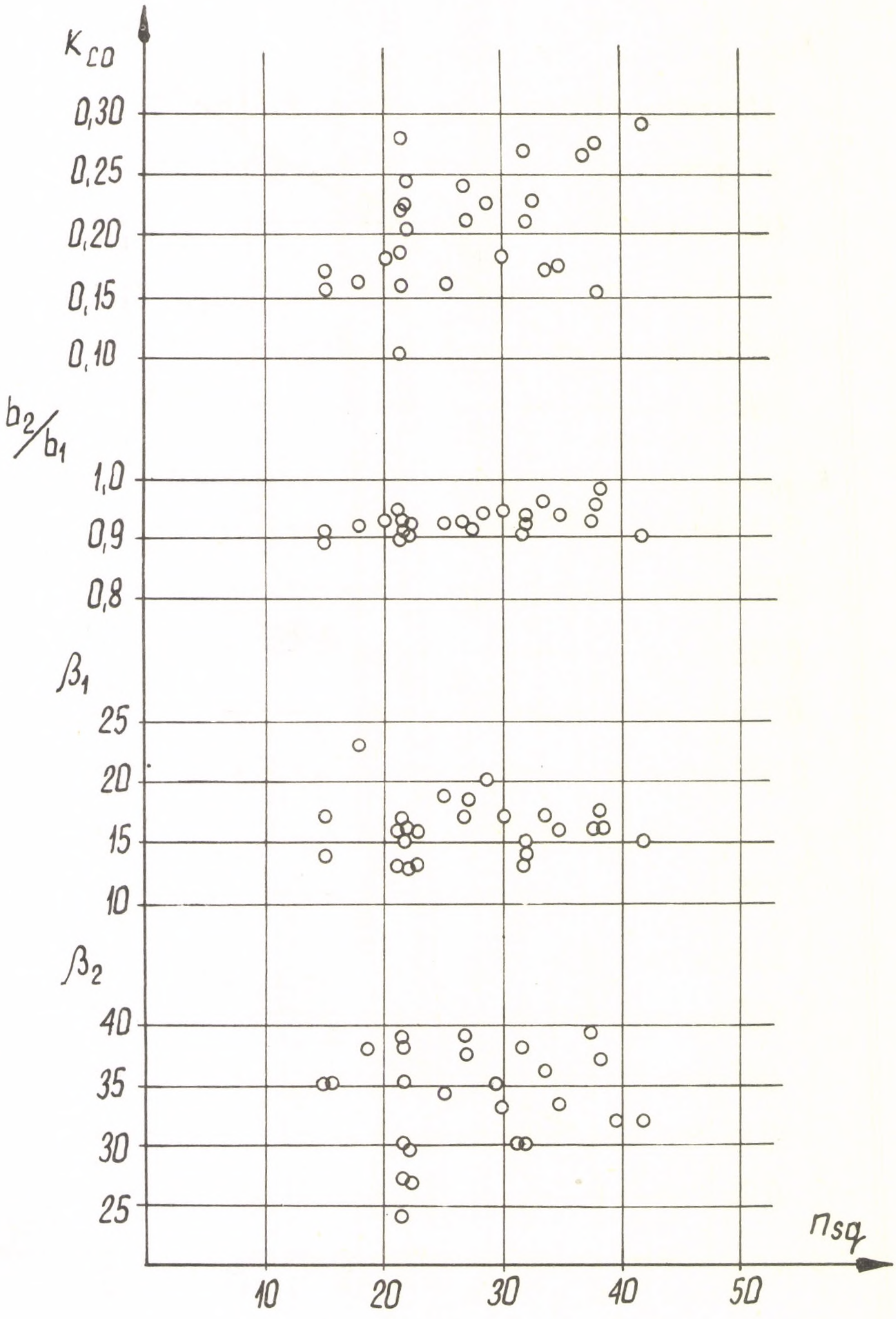
K_{CO}
0,30
0,25
0,20
0,15
0,10
b_2/b_1
1,0
0,9
0,8
β_1
25
20
15
10
β_2
40
35
30
25
n_{sq}
10
20
30
40
50

Fig. 3

shape of the volute does not affect much the value of the peripheral velocity constant K_{u2}.

A conspicuous correlation exists also between K_{c2m} and n_{sq} /Fig.2/. The relation $K_{c2m}-n_{sq}$ is described by the linear dependence

$$K_{c2m} = 0,002 + 0,0016\ n_{sq} \qquad /6/$$

The maximum relative deviation amounts to 24 %, but two thirds of all the deviations do not exceed 10 %.

Threre is also a correlation /Fig.2/ between the relation b_2/d_2 and n_{sf}, which is expressed by the following equation:

$$b_2/d_2 = 0,061 + 0,004\ n_{sq} \qquad /7/$$

In this case, however, larger deviations occur.

Fig.3 presents the values of K_{co}, b_2/b_1, β_1 and β_2 in comparison with the value of the kinematic specific speed n_{sq}. A considerable scatter of results is to be observed particularly in the case of the values of K_{co}, though this does not affect much the work parameters of the pump. The remaining values are contained within the ranges: $b_2 = (0,90 \div 0,95)\ b_1$; $\beta_1 = 13 - 18^o$, $\beta_2 = 28 - 40^o$. The diameter d_1 is contained in the range $d_1 = (0,75 \div 1)\ d_2$.

4. CONFIGURATION OF THE PUMP VOLUTE

The volutes of pumps with double-vane impellers have either constant or increasing flow sections. The shape of the volute does not exert, however, any visible effect on the value of the peripheral velocity constant K_{u2}, because even when the volute is spiral-shaped, the volute tongue deviates considerably from the outer diameter of the impeller. In this way the favourable offects of flow section changes are neutralized.

The efficiency of a pump is determined in a large degree by the flow capacity of the liquid-discharge system, which again is influenced by the cross-section of the diffuser inlet. In the case of the analysed pumps the inlet velocity constant of the diffuser c_{diff}, expressed by the formula

$$K_{c\ diff} = \frac{c_{diff}}{\sqrt{2\ g\ H}} \qquad /8/$$

reaches values in the range $K_{c\ diff} = 0,15 \div 0,25$.

5. THE EFFICIENCY OF PUMPS

The efficiency of pumps increases both with the growth of the capacity of the pump and with the growth of the kinematic specific speed. The deduced dependence formulates both these effects:

$$\eta = 0,545\ n_{sq}^{0,12}\ Q^{0,07} \qquad /9/$$

(where Q is expressed in m^3/s).

The efficiency of pumps with double-vane impellers reaches, particularly at high capacities, considerable values.

6. RECAPITULATION

The chief dimensions of centrifugal pumps with double-vane impellers doubtlessly exert a distinct effect on their work parameters, though not all the dimensions influence them in an equally conspicuous degree.

The lifting height of a pump depends mainly on the outer diameter of the impeller and on the kinematic specific speed. Even considerable variations of the other dimensions /d_0, d_1, β_1, β_2/ do not affect visibly the lifting height, because correlation /5/ is intrinsic in its character.

The capacity of a pump, on the other hand, is determined by the impeller widths b_1 and b_2. The correlations /6/ and /7/ are quite evident, relation /6/ being more essential, as it takes into account more effects /blanking off (screening) of the outlet section of the impeller, volumetric efficiency of the pump/.

The determined relations make it possible to select sensibly the dimensions of pumps with double-vane impellers. It is to be expected with good probability that the assumed work parameters of the pump will be achieved. These relations hold true in a rather large range of n_{sq} values.

REFERENCES

1. STEPANOFF A.J.: Centrifugal and axial flow pumps, J.Wiley Inc., New York 1957.
2. ROKITA J.: Analiza doboru geometrycznych cech konstrukcyjnych wirników dwułopatkowych pomp odśrodkowych, Zeszyty Naukowe Politechniki Śląskiej, Seria: Energetyka, zeszyt 54, Gliwice 1976 /in Polish/.
3. ROKITA J., BAUM B.: Analiza doboru geometrycznych cech konstrukcyjnych kadłubów pomp odśrodkowych do hydraulicznego transportu ciał stałych, Zeszyty Naukowe Politechniki Śląs-

kiej, Seria: Energetyka, zeszyt 56, Gliwice 1976 /in Polish/.

NOMENCLATURE

H - lifting height of the pump

Q - capacity of the pump

n - rotational speed of the pump

g - acceleration of gravity

u_2 - peripheral speed at the diameter d_2

c_{2m} - meridional component of absolute velocity at the impeller outlet

c_o - velocity in the neck of the impeller

c_{diff} - velocity at the diffuser inlet

η - efficiency of the pump

ROKITA Jerzy, Dr techn.
Silesian Technical University
44-100 Gliwice, ul. Konarskiego 18
POLAND

PUMPING STATIONS OPERATED BY DROWNED PUMPS WITH SLANTING AXES

by

O. RÖSER

Institute for Hydraulic Planning

Budapest, HUNGARY

SUMMARY

A prime objective of the technical development of flow-technical machines is the reduction of investment costs. This was our goal too in trying to design pumping stations supplied by drowned pumps and slanting axes, an arrangement which has been developed recently by a number of pump-factories. By investigating possible solutions we arrived to a conclusion that investment costs are very favourable if drowned pumps are used and submerged to their site of operation via a rail deployed onto the slope of the channel. Based on this arrangement a set of experiments has been pursued in Hungary around the beginning of the 80's. Also some permanent pumping stations were constructed in this way. For some elements of this design also notices of patent have been forwarded. In this lecture, our experiences in planning, construction and operation are presented and discussed.

INTRODUCTION

Planning of pumping stations along river sections or beside reservoirs with heavily fluctuating water levels was always one of the most difficult problems. If the pump was below minimum, the power-house above maximum (flood) water level the driving axes are very long. To eliminate large dimensions and to reduce costs several approaches were recently proposed; one fairly often applied method is the use of floating pumping stations. Even today, a number of such stations are operated in Hungary.

Some are several decades old. Investment costs of such plants were significantly lower than those of the stable stations but their operation was not without trouble. Sometimes navigation was disturbed, then the drifting of ice was hindered and also winter harbours were needed. The advent of drowned pumps with slanting exes revolutionized the construction of pumping stations operated under heavily fluctuating water levels. This, however, called for a drastic change in the basic concepts of construction. No economic advantage would have risen from a particular solution where this new type of machine and a traditional type of arrangement of the project would have been combined.

If small pumps are needed often they are directly drowned in the river. If the size of a pump is large, different complications may arise, especially if the river bank is only moderately sloping. To let a pump be drowned in this situation, large cranes, or costly bridge-structures are needed. To overcome such difficulties several types of the drowned pump with slanting axis were developed. In this arrangement the pump is on wheels, and is let down on a slanting rail to its site of operation below the water level. Local transportation is made possible on their own wheels, on rails, or on other appropriately constructed trail.

T A B L E

About Submersible Motor Propeller Pumps
placed in oblique position

Number	Plant name	Realisation		Pump					Pipe diameter (mm)	
		Degree	Year	Producer	Type	Piece	H (m)	Q/p. (l/s)	pressure	protecting
1.	Tolnai Holtàg	in work	1982	EMU	KP 334-2	2	13	470	400	1 000
2.	Vargahossza	experiment	1981	Flygt	PL 7080	1	6	1 000	-	1 000
3.	Biharugra	in work	1983	EMU	KP 602	2	4	1 400	800	-
4.	Körösladány	preliminary plan	1981	Flygt	PL 7080	3	4	1 700	-	1 000
5.	Bp.Mozaik u.	experiment	1982	Flygt	PL 7060	1	4	900	-	800
6.	Kanda fok	execution plan	1982	EMU	KP 334-2	2	13	470	400	1 000

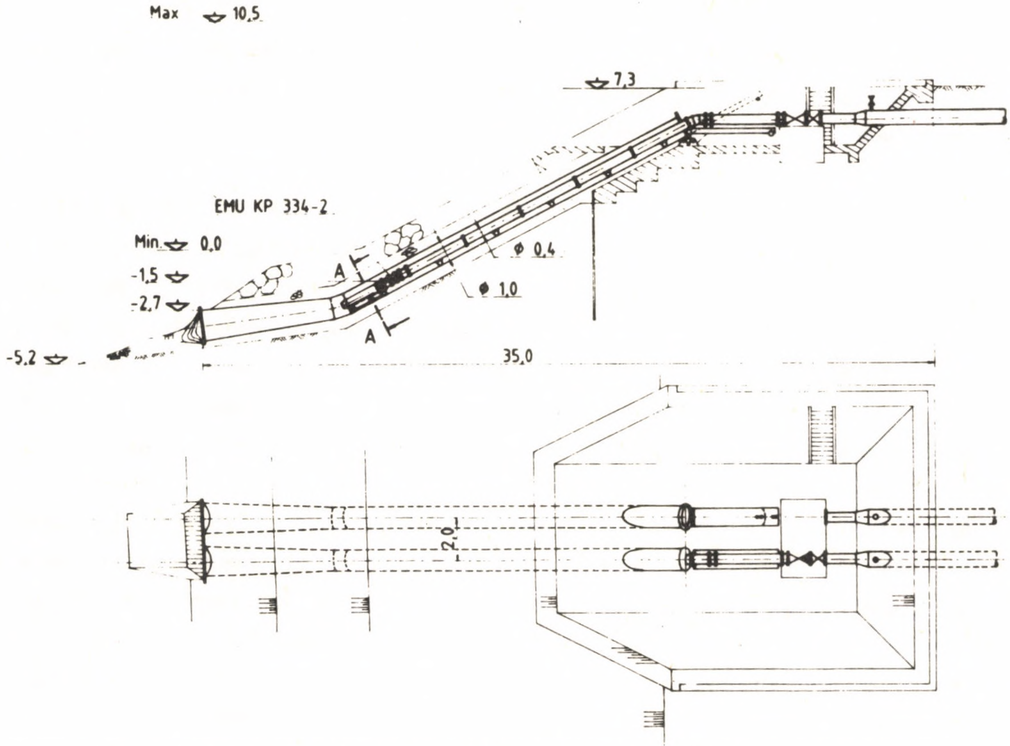

Fig. 1. Pumping Plant " Tolnai Holtág " with EMU two Stage Submersible Motor Propeller Pump placed into a protecting Pipe in oblique position.

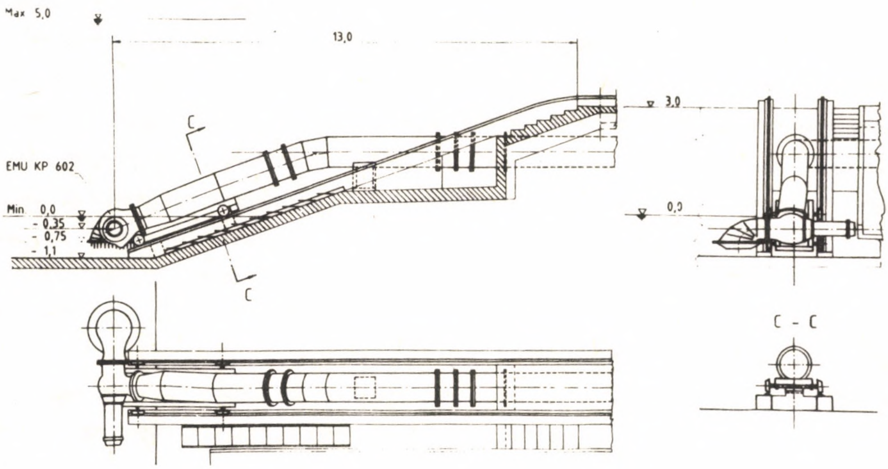

Fig. 2. Pumping Plant " Biharugra " with EMU Submersible Motor Volute Casing Propeller Pump placed in oblique track.

EXISTING VANE-TYPE DROWNED PUMPS WITH SLANTING AXES

Around the beginning of the 80's some pumping stations had been brought into existance in Hungary supplied by vane-type drowned pumps with slanting axes. The most important data about these stations has been listed in one of the enclosed tables. Some characteristic solutions are presented also in figures and by additional short information.

In Fig.1. a sketch of a **pumping station located on the dead Danube branch of Tolna** is presented /1/. At this site, a 28° steep rail has been made of steel pipes and was submerged in to the slope of the embankment. This solution has meant protection, at the same time, against larger floating solids and drifting ice. The pumps are moved inside the pipes on wheels. These wheels are made of Danamid plastics and are mounted radially in 90° to each other on the pump-body and pressure pipe. In this case, KP 334–2 type drowned, two-phase vane-pumps have been installed made by EMU. On this type, similarly to other submerged pumps for water supply, the engine is located underneath the pump itself. Pressure pipe can be joint to a pressure stud looking upward. By this stud the pump can be let down, is lifted, or held in position during operation. Operational water levels were determined on the basis of minimum water stage during upfill of the dead branch. This has made possible a bended formation of the lower part of the protective pipe, and a placement of it in the river bed without special modification of the embankment. On the conic end of the protective pipe a rough grating has been applied. Pumps were placed into the protective pipe during fall, 1981. They survived the hard winter period without failure. The pumping station was in full operation since spring, 1982. It is operated since without any problem.

In Fig.2. the development of the **pumping station of Biharugra** is presented /2/. Here the newly installed drowned pumps are mounted on carts and are moved and operated on a slanting rail deployed onto the slope of the suction-canal of the existing pumping station. Selection and design of these pumps has been influenced significantly by the suction-canal of the existing pumping station and by its appr. 1.1 m deep water. Available conditions and limitations were tried to be overbridged by the use of a KP 602, EMU made vane-type, scroll-cased, drowned pump. The pump-units were deployed according to Fig.2. with horizontal axes, and downward turned cranked suction-connes mounted on a cart that was moved on a slanting rail parallel to the pressure pipe. Due to the fact that the pumps were not placed into the streaming river but in a protected, calm bay, there was no need for special protection, e.g. for a protecting pipe mentioned earlier in this lecture.

Operational testing of this novel and revolutionary pumping station was in spring, 1983. Its most important results will be presented during the discussions of this Conference.

In Fig.3., one of the construction alternatives of a Flygt made vane-type drowned pump, called PL-pump is presented. Such arrangement was recommended by us for the reconstruction of the pumping station of Körösladány and also for other plants. A specific characteristic

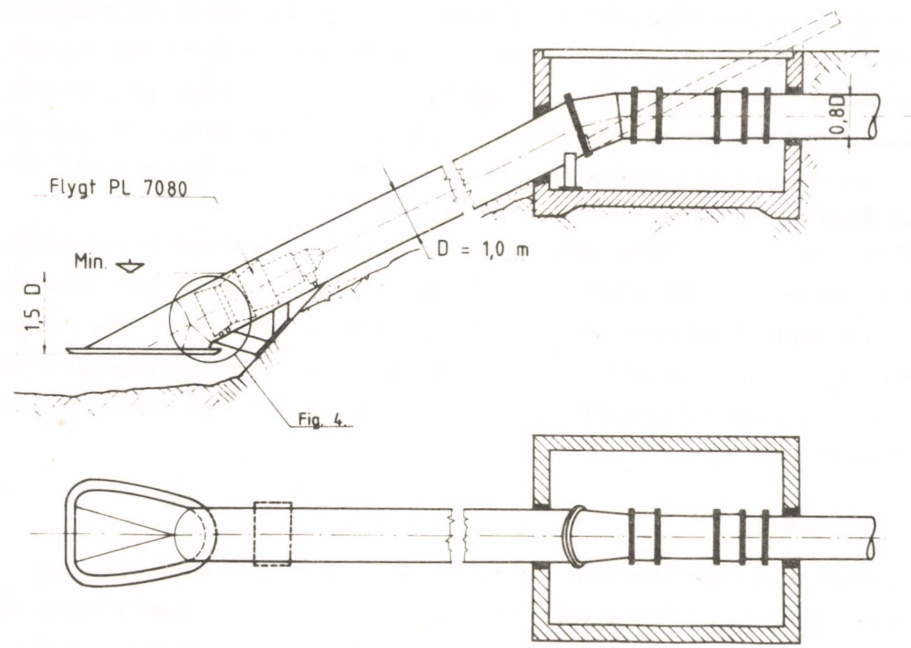

Fig. 3. Plant installation with Flygt Submersible Motor Propeller Pump typ "PL" in oblique position.

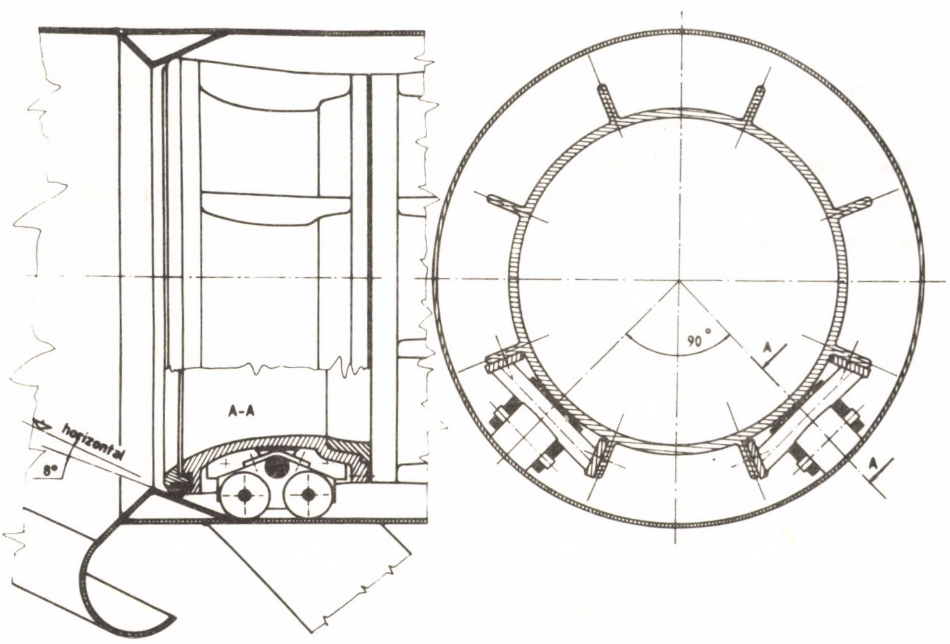

Fig. 4. Detail from former Figure.

of the PL-type pumps is the location of engines just above the runner. By this arrangement the depth of construction could be decreased. The machine itself has been placed originally in a protective pipe playing the role of a pressure pipe as well. For the solution of the problems arising from this slanting arrangement, exchanging the original vertical axis, a number of experiments have been executed recently at **Vargahussz** and on the Danube shore just beside **str. Mozaik in Budapest** in cooperation with Co. Flygt /4/.

These experiments reaffirmed the usability of our mechanical-structural design worked out to make possible this slanting construction. The statment is especially valid as far as the location of the heavily loaded wheel (with a very limited space requirement), the design of a suction opening without the possibility for the air to enter it, and the conic closing surface for the elimination of the damaging effect of the floating load, are concerned. Detailed solutions are visible in Fig.4.

CONCLUSIONS

Experiments and operation confirmed that the use of pumps drowned in a river or lake, and moved on slanting rails is a viable solution for a technically well-based pumping station. Economic evaluation – basically the initial question in this topic – was favourable at our existing plants. A decrease in civil engineering work has shown up 30 to 50 per cent saving of the construction costs compared to those of the vertical arrangement. Time of construction has been shortened too.

Summation: a reduction in cost and time of construction has led to a cheaper realization of pumping stations supplied by the relatively more expensive drowned engines compared to the traditional plants. According to our experiments and experiences, the technical solutions of the slanting arrangement – discussed in this lecture – can be well used and applied in everyday engineering practice.

LITERATURE

1. ADUVIZIG–MTO: Construction plan of water supply for the dead Danube branch at Tolna.
Planners: K. Prekop – O. Röser, Baja, Hungary, 1981.
Design no: 380–019.

2. VIZITERV: Reconstruction of the pumping station of Biharugra.
Planner: O. Röser, Budapest, Hungary, 1981.
Design no: 22 816.

3. RÖSER, O.: The use of drowned pumps with slanting axes in irrigation and land-drainage systems.
VIZITERV-INFORMATION, Budapest, 1982–3.

4. VIZITERV: Comprehensive evaluation of tests performed in Budapest on the slopes of the Danube embankment with an experimental deployment of a Flygt PL 7060-type drowned pump with slanting axial arrangement.
Planner: O. Röser, Budapest, 1982.
Design no: 23 453.

Dr. Röser Ottó
Institute for Hydraulic Planning
VIZITERV
Budapest, Münnich Ferenc u. 36.
H – 1051

FLOW THROUGH OPENINGS IN ROTATING DISCS

J. Rydlewicz

Some centrifugal pumps (Fig. 1) require axial thrust reduction devices consisting of sealing rings BS and balancing holes BH in the impeller shroud. This produces the desired reduction in the pressure difference and the axial thrust. However there is also another effect, due to induced secondary flow $\dot{V}_{BS} = \dot{V}_{BH}$ through the balancing holes resulting in reduced pump flowrate.

In designing an impeller, it is essential to match both the number and bore of the balancing holes to reduce of the recirculating flowrate.

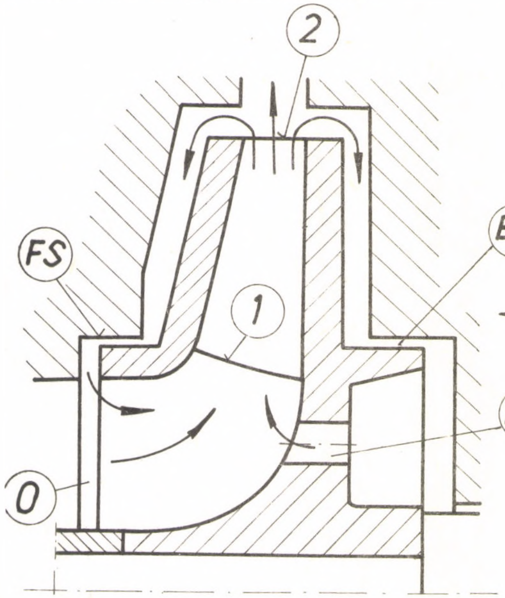

Fig. 1

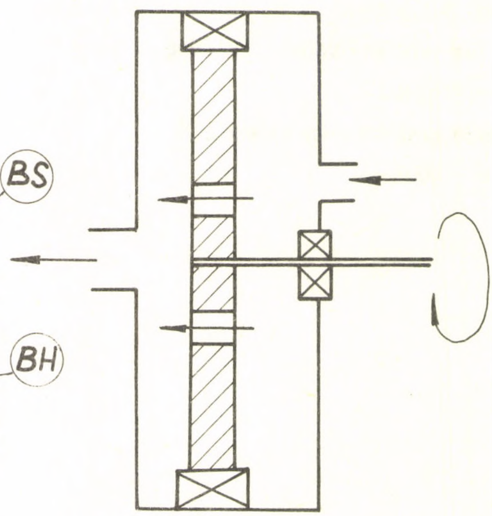

Fig. 2

The phenomena taking place in a pump can be simulated by using a flow model consisting of a spinning disc with holes parallel to the axis of rotation (Fig. 2).

The flow through holes can be given by the expression

$$\dot{V} = A \mu v = A \mu \sqrt{2 \frac{\Delta p}{\varrho}}$$

where A - holes area

μ - coefficient of discharge

For flow through static holes the value of coefficient μ is assumed to be constant over a large range of flows. For flow through openings (balancing holes) in rotating disc the value of μ_{BH} is not constant and should be fixed by various conditions of flow.

The laboratory tests are performed by using the model impeller with balancing holes (Fig. 3a) and without holes (Fig. 3b)

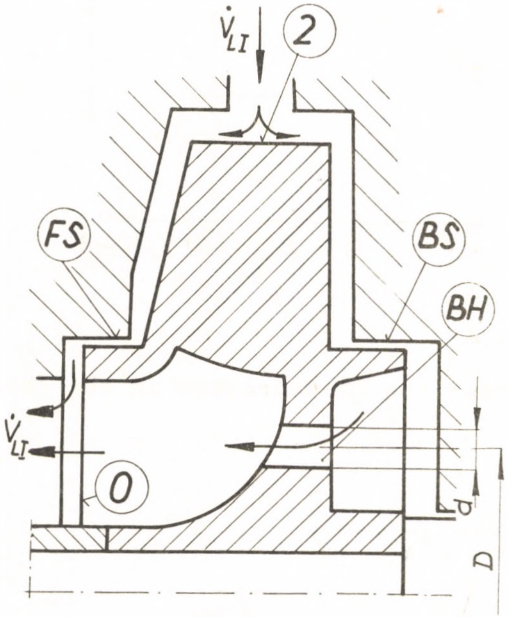

Fig. 3a

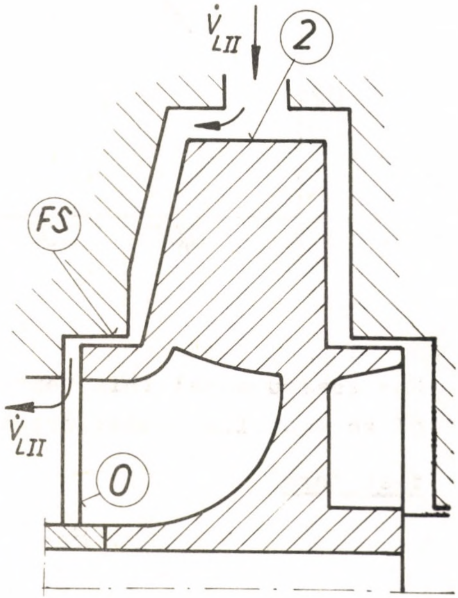

Fig. 3b

For the same conditions the rate of flow through balancing holes is given by the expression

$$\dot{V}_{BH} = \dot{V}_{LI} - \dot{V}_{LII} \quad \text{by} \quad (\Delta p_{02})_I = (\Delta p_{02})_{II}$$

The experimental data collected for such configuration show, that coefficient μ_{BH} is not constant and depends amongst other factors on rotational speed n (Fig. 4).

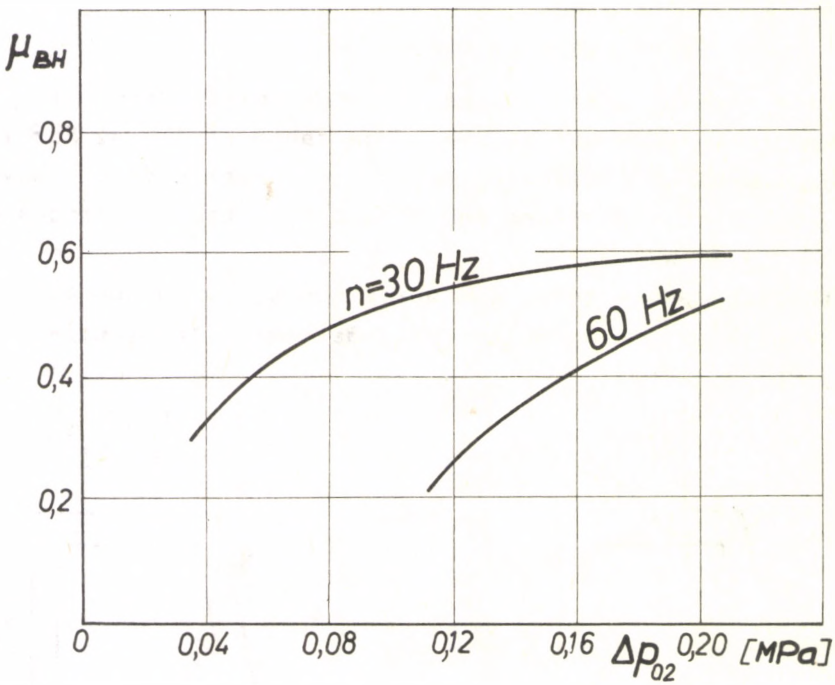

Fig. 4

For tested model this dependence can be expressed in the form of an empirical relationship.

<u>1-st form</u>

$$\mu_{BH} = \frac{1}{1{,}5 \cdot 10^{16} X^5 + 1{,}7}$$

$$X = \frac{n\,D\,d}{\nu\, Re^{3/2}} \qquad Re = \frac{v\,d}{\nu} \qquad v = \sqrt{2\,\frac{\Delta p_{BH}}{\varrho}}$$

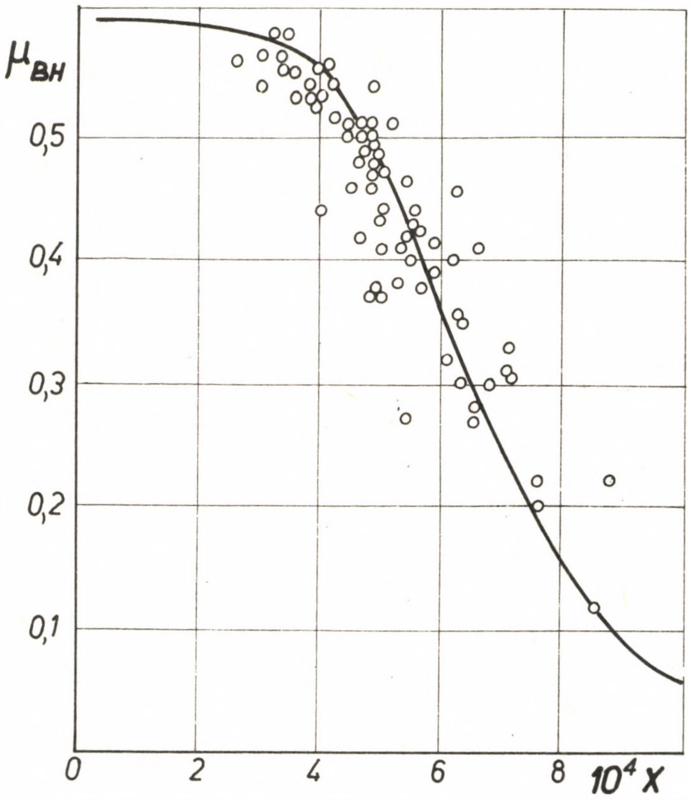

Fig. 5

<u>2-nd form</u>

The coefficient μ_{BH} is a algebraic sum of a coefficient $(\mu_{BH})_{n=0}$ of static holes and addend dependent on theoretical speed of flow v and peripheral speed of holes u .

$$\mu_{BH} = (\mu_{BH})_{n=0} - \frac{1}{0{,}23\left(\frac{v}{u}\right)^5 + 1{,}7}$$

$$(\mu_{BH})_{n=0} = 0{,}59 \qquad v = \sqrt{2\,\frac{\Delta p_{BH}}{\rho}} \qquad u = \pi D n$$

The expressions are exact for the tested model.
More universal relationship can be reach as a result of a successive research.

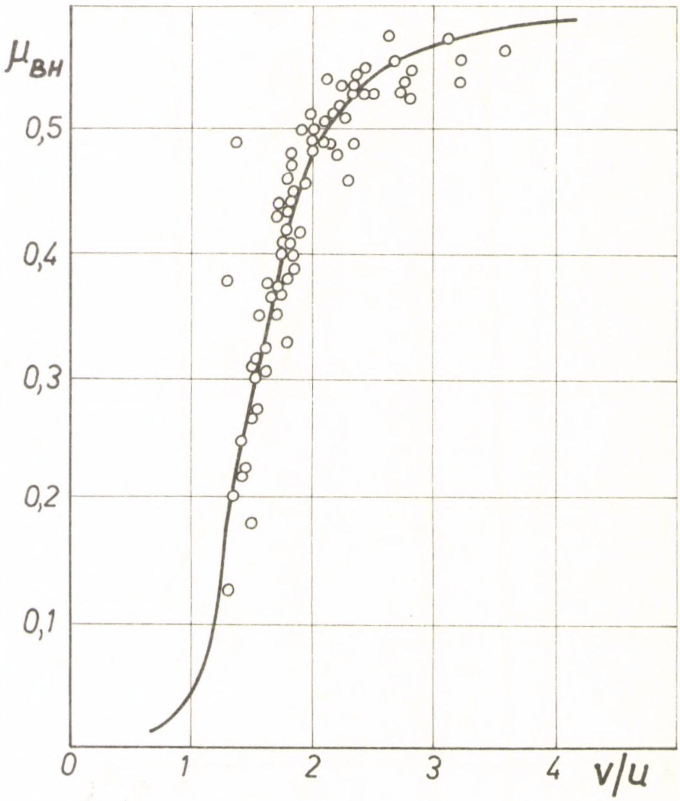

Fig. 6

List of symbols

A - area

d, D - diameter

n - rotating speed

Δp - pressure difference

Re - Reynolds number

u - peripheral speed

v - theorelical speed

$\dot{V}$ - rate of flow

μ - coefficient of charge

ρ - liquid density

Index

O, 1, 2 - control point

I, II - 1-st, 2-nd form of model

BH - balancing hole

BS - back sealing

FS - front sealing

L - leakage

RYDLEWICZ Janusz, Doc. Dr Inż.
Instytut Maszyn Przepływowych
Politechnika Łódzka
(Institute of Fluid - Flow Machinery
Lodz Technical University)
ul. Gdańska 155
Pl - 90 - 924 Łódź - Poland

ANALYSIS OF THE BOUNDARY LAYER DEVELOPMENT IN A CENTRIFUGAL PUMP IMPELLER

Antonio Satta, Marina Ubaldi, Pietro Zunino
Istituto di Macchine, Università di Genova

Abstract

The results of a boundary layer calculation on the internal surfaces of a centrifugal pump impeller are presented.
The analysis is based on an integral three dimensional boundary layer model which incorporates all the effects of the centrifugal forces, due to the curvatures of the coordinate lines, and of the Coriolis forces.
The boundary layer integral parameters are then used to calculate the flow losses on the blades and on the end wall surfaces of the impeller.

1. Introduction

The evaluation of the losses in the flow elements of the turbomachines is often obtained with the aid of empirical correlations. They can offer reliable predictions only for machines similar to those which have been utilized to calibrate the experimental coefficients and give few informations to improve the performances of the analyzed flow element.
Only a physical model able to interpret the complex development of the viscous flow allows to know the distribution of the flow losses in the elements of a turbomachine and to optimize the aerodinamic profiles.
This paper proposes a method for the calculation of the flow losses in centrifugal pump impellers, based on an integral boundary layer model which is simple enough for industrial applications.

2. Basic equations

The incompressible three dimensional boundary layer on curved and rotating surfaces can be analyzed by means of the integral momentum equations, the entrainment equation or the kinetic energy equation for three dimensional flows, written in an orthogonal curvilinear coordinate system, constituted by the external streamline, the normal and the straight line perpendicular to the surface.

Hub and shroud boundary layer. - The three dimensional behaviour of the end wall boundary layer on a shrouded pump impeller is caused by the deficit of the components tangent to the surface of the centrifugal and Coriolis forces.
For the case of the wall boundary layer of a low specific speed impeller the effects of the forces normal to the wall on the turbulence production and on the momentum balance can be neglected. Then the following system formed by the two integral momentum equations and by the entrainment equation is adopted:

$$\frac{1}{U_e^2}\frac{\partial}{\partial s}(U_e^2\,\Theta_{ss}) + \frac{1}{U_e}\frac{\partial U_e}{\partial s}\,\delta_s^* + \frac{1}{U_e^2}\frac{\partial}{\partial n}(U_e^2\,\Theta_{sn}) + \frac{1}{U_e}\frac{\partial U_e}{\partial n}\,\delta_n^* +$$

$$- K_{12}(\Theta_{sn} + \Theta_{ns}) - K_{21}(\Theta_{ss} - \Theta_{nn}) - 2\frac{\omega_3}{U_e}\,\delta_n^* - \frac{C_{fs}}{2} = 0 \qquad (1)$$

$$\frac{1}{U_e^2}\frac{\partial}{\partial s}(U_e^2\,\Theta_{ns}) + \frac{1}{U_e^2}\frac{\partial}{\partial n}(U_e^2\,\Theta_{nn}) + K_{12}(\Theta_{ss} - \Theta_{nn}) - 2K_{21}\,\Theta_{ns} +$$

$$+ (K_{12} + 2\frac{\omega_3}{U_e})\,\delta_s^* - \frac{C_{fs}}{2}\,m = 0 \qquad (2)$$

$$\frac{\partial(\delta-\delta_s^*)}{\partial s} + (\delta - \delta_s^*)\left(\frac{1}{U_e}\frac{\partial U_e}{\partial s} - K_{21}\right) - \frac{\partial\delta_n^*}{\partial n} - C_E = 0 \qquad (3)$$

If the streamwise flow and the cross flow are described by the power law and the Mager profile, the system of the partial differential equations (1),(2),(3) is hyperbolic [1] with two real characteristics which in each point are close to the external and the wall streamlines, in agreement with the physical problem [2]. The system is integrated with a finite difference explicit procedure, verifying the Courant-Friedrichs-Lewy stability condition in each point.
The domain of integration on the surface of the hub or of the shroud is limited sidewise by two contiguous blades and by the stagnation streamlines. Upstream it is closed by a circumference arc with known turbulent axisymmetrical boundary layer and downstream by the normal to the streamlines which passes through the point on the pressure side at the trailing edge.
Boundary conditions along the boundary crossed by the flow entering the integration region are supplied for the three principal unknowns Θ_{ss}, H_{12}, m. In agreement with the hypotesis of Moore [3], zero cross flow is supposed on the pressure side wall and along the upstream boundary.
Once the values of Θ_{ss}, H_{12} and m are known, all the parameters of the three dimensional boundary layer can be evaluated together with the mass flow rate, the streamwise momentum and kinetic energy carried by the cross flow out of the pressure side corners and into the suction side corners.

Blade boundary layer. - In the case of low specific speed impellers, the blade boundary layer can be considered two dimensional. It can be calculated by means of the following momentum and kinetic energy equations:

$$\frac{1}{U_e^2}\frac{\partial}{\partial s}(U_e^2\,\Theta_{ss}) + \frac{1}{U_e}\frac{\partial U_e}{\partial s}\,\delta_s^* + \frac{1}{U_e^2}\frac{\partial}{\partial n}(U_e^2\,\Theta_{sn}) - K_{21}\,\Theta_{ss} = \frac{C_{fs}}{2} \qquad (4)$$

$$\frac{1}{U_e^3}\frac{\partial}{\partial s}(U_e^3\,\delta_{ss}^{**}) + \frac{1}{U_e^3}\frac{\partial}{\partial n}(U_e^3\,\delta_{sn}^{**}) - K_{21}\,\delta_{ss}^{**} = C_{Ds} \qquad (5)$$

The three dimensional effects of the tangential components of the centrifugal forces due to the K_{12} curvature and of the Coriolis forces due to the ω_3 component on the initial part of the blade are neglected. On the contrary, the influence of the secondary flows out of the pressure side and into the suction side is taken into account by means of the terms $\partial(U_e^2\,\Theta_{sn})/\partial n$ and $\partial(U_e^3\,\delta_{sn}^{**})/\partial n$. The influence of the normal components of centrifugal and Coriolis forces on the turbulence production has been introduced in the integral model by adding a correction term to the dissipation coefficient C_{Ds} in the kinetic energy integral equation. This term is a function of H_{12} and of the mean Richardson numbers of curvature Ri_C and rotation Ri_R [4].

3. Results of the boundary layer calculation

The above model has been applied to a low specific speed impeller, which is an experimental and theoretical test case of a work group of the "Société Hydrotéchnique de France". The geometrical data are quoted in [5]: from this reference the meridional section and the design operating point data of this pump, shown in fig. 1, have been derived. The inviscid velocity distributions have been obtained by a quasi-three dimensional calculation [6].

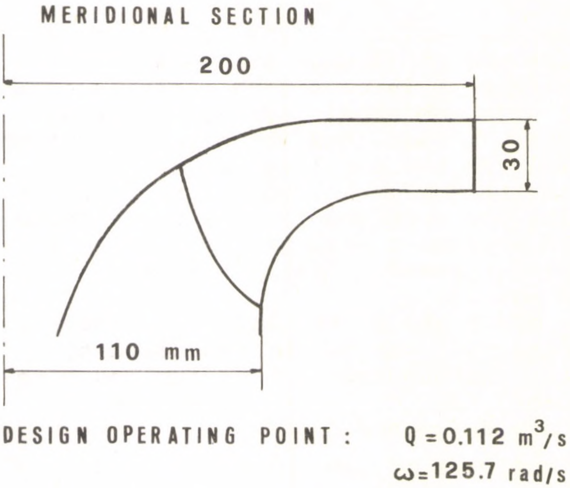

fig. 1

The external and wall streamlines are shown in fig. 2 and 3 on the frontal views of the blade channels at the hub and at the shroud. The three dimensional boundary layer development is described in fig. 4 and 5 by means of the distributions of the integral parameters H_{12}, Θ_{ss} and of the angle of the wall streamline ε_o for the external streamline a, c, e on hub and shroud. On the hub the cross flow, caused by the ω_3 component, is limitated by the adverse effect of the curvature K_{12} and by the low thickness integral parameters of the boundary layer. The positive velocity gradients on a large part of the channel lower the shape factor H_{12} to values near to relaminarization.

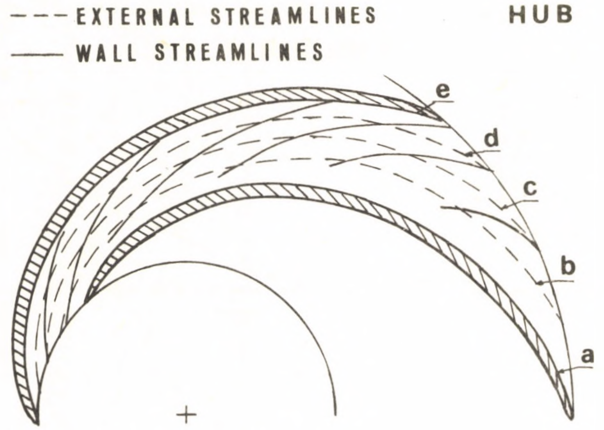

fig. 2

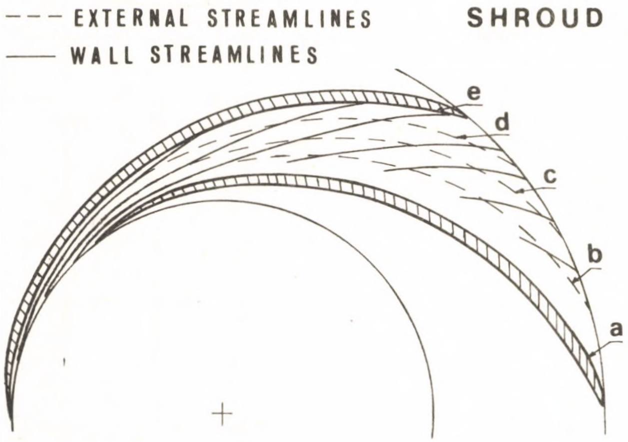

fig. 3

On the shroud the streamline divergence and the presence of the cross flow limitate the growth of the shroud boundary layer in spite of the strong negative velocity gradients on a large part of the channel.
Because of the positive velocity gradient a completely two dimensional calculation on the blade suction side (fig. 6) predicts a thin boundary layer with low values for the H_{12} shape factor. The stabilizing effect of the Coriolis force, although limitated by the adverse effect of the curvature K_{13}, results in an increased value for H_{12} and a decrease of C_{fs}. The streamline convergence K_{21} and the secondary flows entering the blade region act to thicken the boundary layer. Besides the secondary flows cause a further decrease of C_{fs} and a small decrease of H_{12}.

Because of negative velocity gradients a completely two dimensional calculation on the blade pressure side (fig. 7) predicts boundary layer separation. The secondary flow out of the pressure side and expecially the destabilizing effect of the Coriolis force act to decrease the boundary layer thickness integral parameters and bring the boundary layer far from separation.

4. Flow losses evaluation

The losses on the end wall and blade surfaces of the impeller can be evaluated as a drop of the relative total pressure of the combined inviscid-boundary layer flow as regards the inviscid flow.
In each meridional station the power losses $\Delta\dot{E}$, due to the three dimensional boundary layer development on the axisimme-

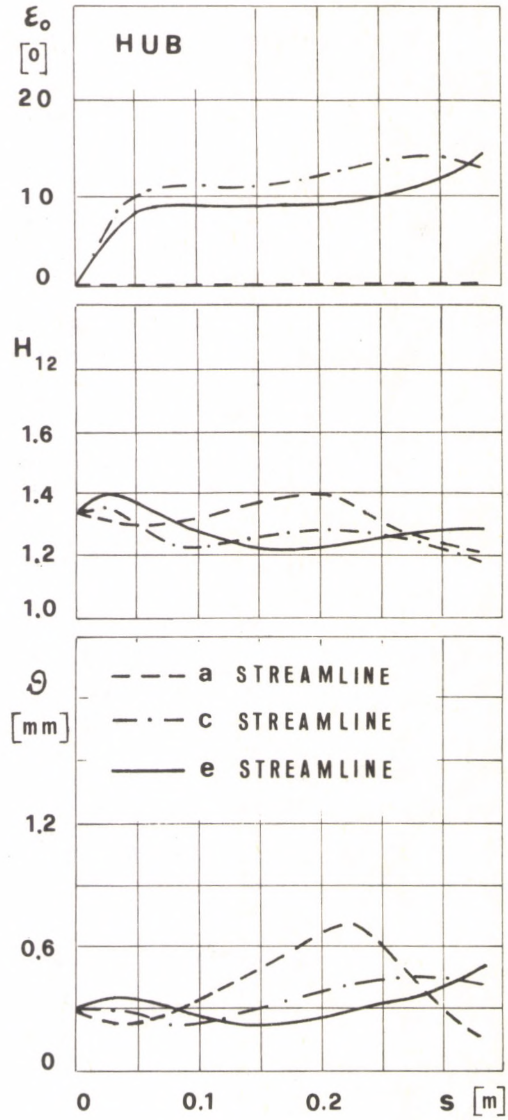

fig. 4

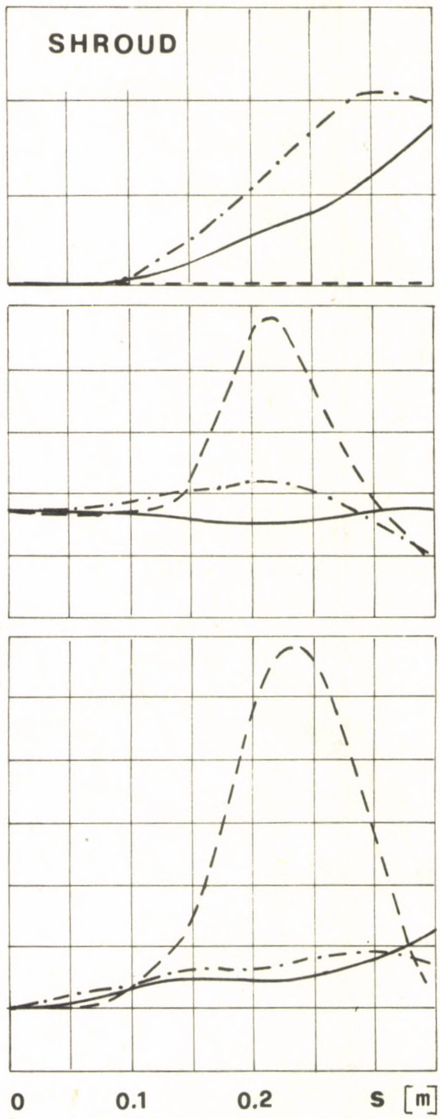

fig. 5

tric rotating surfaces of hub and shroud, can be expressed in function of the integral parameters:

$$\Delta\dot{E} = N\ \rho/2 \int_{\bar{\phi}}^{\bar{\phi}+2\pi/N} U_e^3\ [(\delta_{ss}^{**}+\delta_{ns}^{**})\ \cos\beta + (\delta_{sn}^{**}+\delta_{nn}^{**})\sin\beta]\, R d\phi \qquad (6)$$

In the same way the power losses on the suction and pressure sides of the blades can be obtained by the expression:

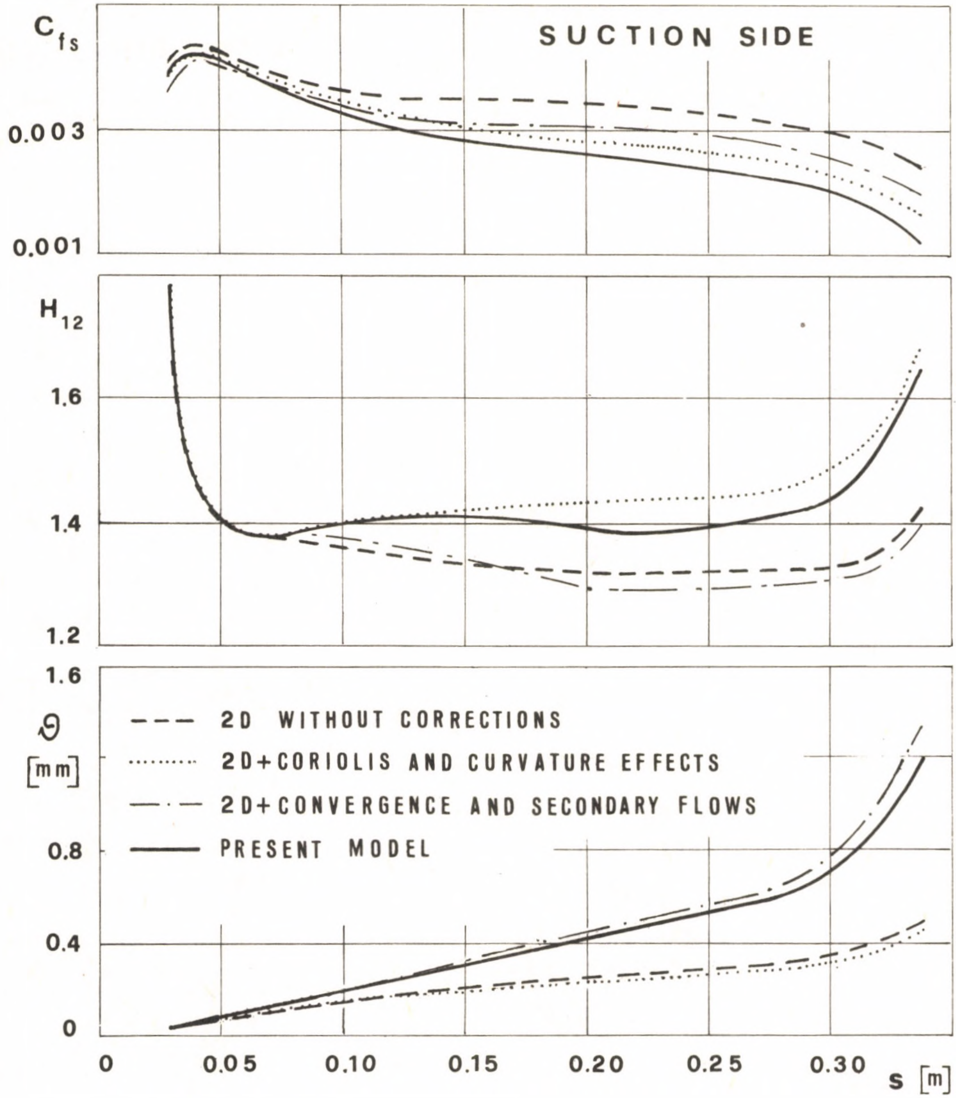

fig. 6

$$\Delta\dot{E} = (\rho/2)\ N\ h\ U_e^3\ \delta_{ss}^{**} \tag{7}$$

The distribution of the boundary layer losses on the hub, shroud, suction and pressure side surfaces are shown in fig. 8 in function of the mean meridional coordinate. The power losses have been divided by the theoretical power $\dot{E}_t$ calculated by the chan-

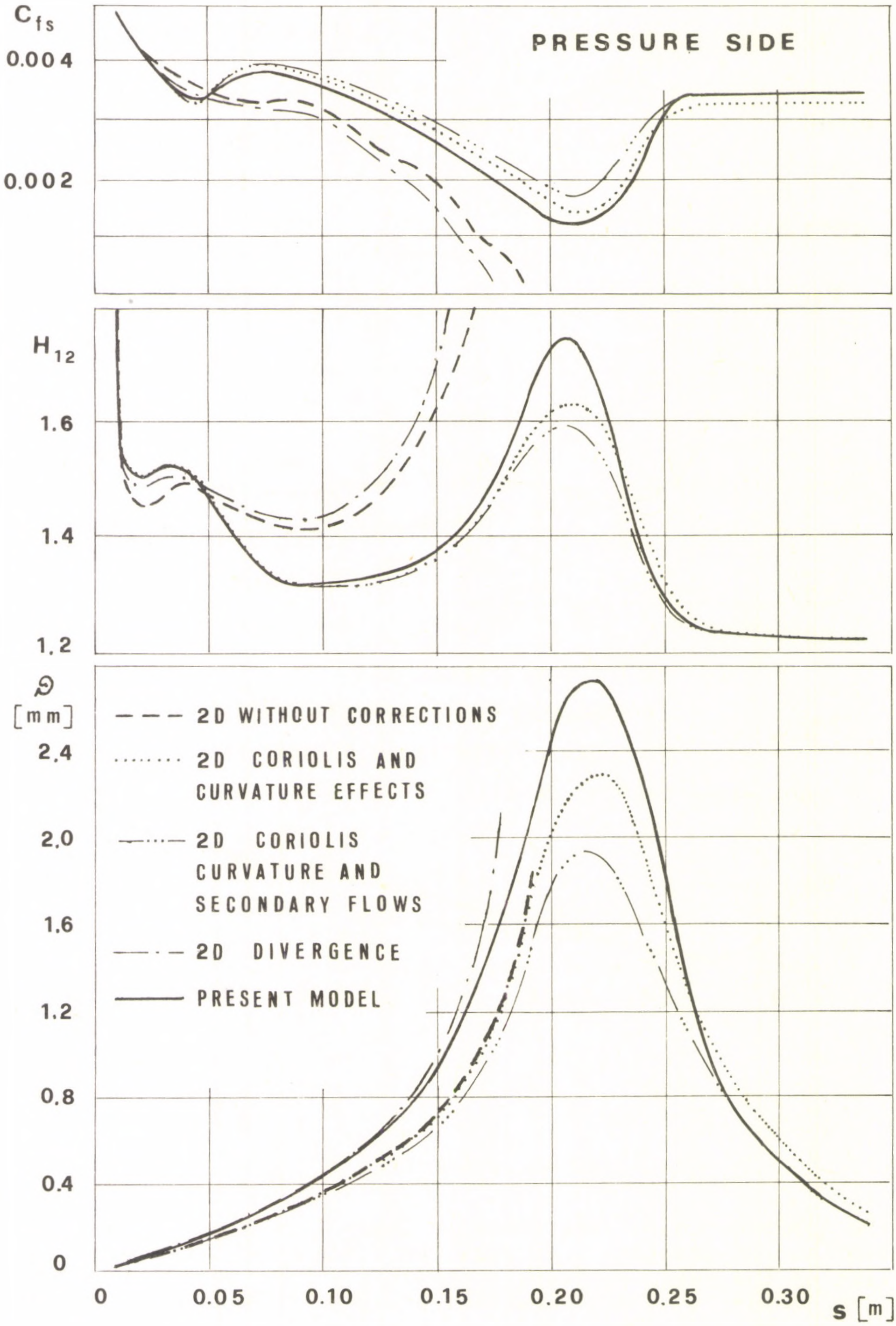
C_{fs}
0.004
0.002
PRESSURE SIDE
H_{12}
1.6
1.4
1,2
δ
[mm]
2,4
2,0
1,6
1,2
0,8
0,4
0
2D WITHOUT CORRECTIONS
2D CORIOLIS AND CURVATURE EFFECTS
2D CORIOLIS CURVATURE AND SECONDARY FLOWS
2D DIVERGENCE
PRESENT MODEL
0
0.05
0.10
0.15
0.20
0.25
0.30
s [m]

fig. 7

ge of the moment of momentum of the inviscid flow from the inlet to the impeller outlet. The mixing losses in the wakes behind the blades are calculated by means of the expression proposed by Scholz [7] for axial cascades: under the hypotesis of instantaneous mixing at the impeller exit, it is valid also for rotating radial cascades. The value obtained is

$$\Delta\dot{E}_{mix} / \dot{E}_t = 0,3\%.$$

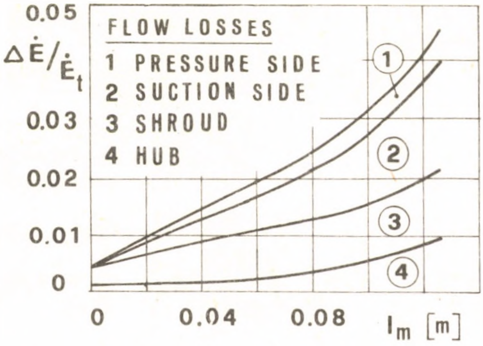

fig. 8

5. Conclusions

A method for the calculation of unseparated boundary layer and flow losses in centrifugal impellers has been presented. The results of its application to a shrouded pump impeller with backswept blades evidence the importance of all the effects introduced in the integral model.
Improvements to the procedure could be obtained by evaluating the influence of the boundary layer blockage on the inviscid calculation. The boundary conditions imposed for the hub and shroud boundary layer calculation and the validity of the velocity profiles for the analysed flows should be experimentally verified.

Nomenclature

C_{Ds}, C_E, C_{fs}	Streamwise dissipation coefficient, entrainment coefficient and skin friction coefficient
$\dot{E}$	Power
h	Blade height
$H_{12} = \delta^*_s/\theta_{ss}$	Shape factor
K_{ij}	Curvatures of the coordinate lines
l_m	Meridional coordinate
$m = \tan \varepsilon_o$	Cross flow parameter
N	Blade number
Q	Volumetric flow rate
R, z, ϕ	Cylindrical coordinates
s, n, y	Orthogonal curvilinear coordinates

U_e Free stream velocity

u, v, w Local velocity components in s, n, y directions

β Angle between the streamwise velocity and the meridional direction

δ Boundary layer thickness

$\delta_n^* = -1/U_e \int_o^\delta v\, dy;\ \delta_s^* = 1/U_e \int_o^\delta (U_e - u) dy$ Displacement thicknesses

$\delta_{nn}^{**} = -1/U_e^3 \int_o^\delta v^3\, dy;\ \delta_{ns}^{**} = -1/U_e^3 \int_o^\delta uv^2\, dy;$ Kinetic energy thicknesses

$\delta_{sn}^{**} = 1/U_e^3 \int_o^\delta v(U_e^2 - u^2) dy;\ \delta_{ss}^{**} = 1/U_e^3 \int_o^\delta u(U_e^2 - u^2)\, dy$

ε_o Angle of the limiting wall streamline with respect to the free stream velocity

$\Theta_{nn} = -1/U_e^2 \int_o^\delta v^2 dy;\ \Theta_{ns} = -1/U_e^2 \int_o^\delta u\, v\, dy;$ Momentum thicknesses

$\Theta_{sn} = 1/U_e^2 \int_o^\delta v(U_e - u) dy;\ \Theta_{ss} = 1/U_e^2 \int_o^\delta u(U_e - u) dy$

ρ Density

ω Angular velocity

$\omega_1, \omega_2, \omega_3$ Angular velocity components in s, n, y directions

References

[1] Satta A., Ubaldi M., Zunino P.: Proc. XXXVII ATI Congress, Padua, 1982, (In Italian).

[2] Wang K.C: J.Fluid Mech., vol.48, part 2, pp.397-404, 1971.

[3] Moore J.: ASME paper 73-GT-58, 1973.

[4] Van den Braembussche R.A., Zunino P.: ASME paper 81-GT-97, 1981.

[5] Borciani G.: XXXVII ATI Congress, Padua,1982 (In Italian).

[6] Satta A., Ubaldi M., Bologna P.: XXXVII ATI Congress, Padua, 1982 (In Italian).

[7] Scholz N.: "Aerodynamics of Cascades", AGARDograph N.220, 1977.

A DIFFUSION FACTOR CORRELATION FOR THE PREDICTION OF THE REVERSE FLOW ONSET AT THE CENTRIFUGAL PUMP INLET

B. Schiavello

SUMMARY

This paper deals with the reverse flow onset phenomenon at the centrifugal pump inlet. The triggering mechanism is produced mainly by the relative flow in the impeller. The inlet reverse flow onset capacity can be detected by means of both "direct methods", which use flow traverses or wall pressure measurements, and "not-direct methods", which are based on the incipient cavitation detection. Also, the problem of predicting the inlet reverse flow onset is discussed. It is shown that on the basis of a systematic experimental data set a correlation derived from the Diffusion Factor in the impeller relative flow appears to be the most effective.

1. INTRODUCTION

When centrifugal pumps operate at part flows, a highly unsteady flow suddendly appears, at a certain capacity, in the suction pipe. As soon as capacity is slightly decreased, a steady annular swirling reverse flow arises at the pipe wall. The velocity pattern shows near the wall a reversed axial component, which is named "reverse flow", and a tangential component, which is named "prerotation". The capacity at which the reverse flow appears at the leading edge of the impeller blade tip section is defined as "critical capacity", Q_{cr}/Q_N. At smaller capacities, the swirling reverse flow pattern develops more and more and changes the level of noise and vibrations, as well as pressure, torque and thrusts' pulsations.
An extensive literature review on the reverse flow and prerotation phenomena is presented in [1] and [2].
The influence of the impeller and volute geometry, inlet guide vanes and suction throttling devices has already been partially investigated. However, such investigations were not systematic. Often more than one influencing parameter was modified thus introducing compensating effects. Although no theory has been formulated which adequately relates the reverse flow onset to the pump design parameters, the impeller design appears to be very crucial.

2. TRIGGER MECHANISM OF THE INLET REVERSE FLOW

When the pump capacity is decreased, the incidence of the flow at the impeller inlet, especially at the tip blade section, increases. A high relative velocity and a subsequent rapid pressure recovery is generated on the blade suction side. This was clearly detected in centrifugal pumps by [3] through visualizations under stroboscopic light of the impeller flow at the condition of cavitation inception. Fig. 1 shows the curve of NPSHi (Net Positive Suction Head at incipient cavitation) against the pump capacity. At NPSHi-peak capacity a developing cavitation was

localized at the impeller tip blade leading edge, on the suction side, denoting high local relative velocity. The NPSHi-peak capacity was just before the reverse flow onset critical capacity.
As it is well documented in literature the curve in Fig. 1 is also typical of mixed- and axial-flow impellers and inducers. Furthermore some flow visualizations display a separation at or near the impeller blade leading edge. Therefore a general common mechanism can be supposed. When capacity is decreased, the incoming flow reaches a high positive incidence, which causes a high blade loading on the suction side of the tip blade at or near the leading edge. At a certain capacity the limiting stalling incidence is reached and local separation starts. As the flow rate is furtherly reduced and the back pressure increased, a reverse flow arises immediately for centrifugal impellers, with a delay for mixed- and axial-flow rotors. The prerotation arising immediately after is forced by the reverse flow through shear stresses.

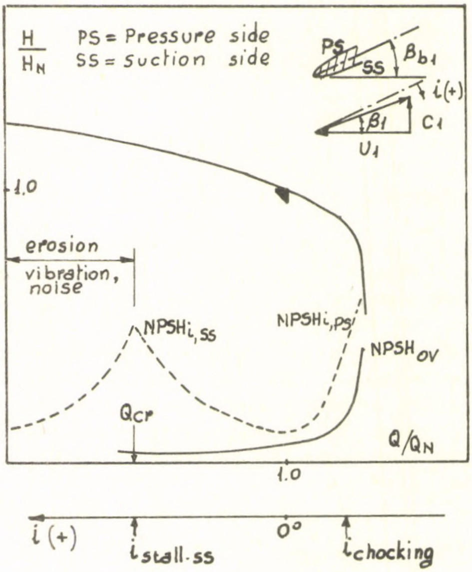

Fig. 1

According to the experiments [4] the reverse flow is practically eliminated by throttling the impeller eye in such a way to maintain shockless flow conditions at any capacity. Then, clear emphasis is given to the crucial role of the inlet relative flow incidence angle i.

3. TEST MODELS

A research program on the reverse flow was started in order to obtain quantitative information. As a first step four impellers of same specific speed Nq = 37.2 have been investigated: a reference one (A) and three variants (A1, A2, A3). The basic approach in designing the impeller variants followed two main assumptions:

1. Constant matching capacity between impeller and volute in order to exclude the volute influence.
2. Impeller design which greatly differs from one to the other for one parameter or design criterium at time.

The impeller B (Nq = 32) was tested in the same volute.
A second series of configurations (C,C1,B1) were also tested in order to extend the investigation to higher Nq: 43.6 (B1) and 48.2 (C,C1).
The leading criteria in selecting and designing the impeller variants are described in [1] , [5] . It was assumed that the reverse flow is

strictly related to the boundary layer separation on the blade suction side at tip near the leading edge. A qualitative analysis of the physics of the tip streamtube (Fig. 2) suggested[1] that:

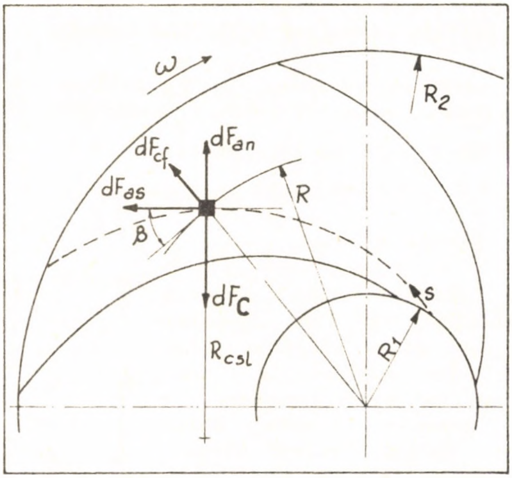

Fig. 2

a) The centrifugal force field, dF_{cf} (Eqn A1), has no influence on the boundary layer separation. Infact, the adverse pressure gradient, which is generated by the centrifugal forces, is the same, at a given radius, in the boundary layer region and in the main stream.
b) The influence of the Coriolis force, dF_C (Eqn A2), on the separation of the boundary layer on the blade suction side is secondary. Such influence is partially compensated by the streamlines curvature effect in the relative flow for highly backward curved vanes, since they are typical of the centrifugal pump impellers. Moreover, the Reynolds effect (inertia force effect) is prevailing on the Coriolis force influence (rotation effect), when the kinematic viscosity of the fluid, f.i. water, and the rotation speed are low, as typically for the pumps.
c) The aerodynamic forces field, dF_{an} and dF_{as} (Eqn A3), arising from the diffusion and streamline curvature effects in the relative flow, influence very critically the boundary layer separation. Infact, it is clearly shown in all the types of impellers, i.e. centrifugal-, mixed- and axial-flow, by the link between the NPSHi,ss peak and Q_{cr}/Q_N (Fig. 1)
d) The three-dimensional flow effects on the boundary layer behaviour, as either the main stream diffusion ratio of the secondary flows, arising from the removal of end wall boundary layer and from the aerodynamic blade loading distribution along the blade span, appear to be crucial on the reverse flow critical capacity.

Special attention was given to the effects of 1) the mainstream diffusion ratio (variant A1) in the relative flow and 2) the aerodynamic blade loading level and spanwise distribution from hub to tip. Since such phenomena control both the secondary flows' level and the migration of boundary layer (low energy fluid) from hub to tip, they strongly affect the susceptibility to separation of the impeller shroud-blade suction side corner boundary layer. The variant A2 was designed with reduced and equalized aerodynamic lift coefficient. This design concept was furtherly and drastically forced in the variant A3 and, especially, C1.

Detailed information on the test models geometry are given in [1], [5].

4. CRITICAL CAPACITY DETECTION METHODS

The critical capacity Q_{cr}/Q_N follows the affinity laws. This can be measured by means of several techniques [6] on:

a) Model tests in laboratory.

b) Full scale machines in situ.

4.1 Direct Methods

The reverse flow appears suddenly in the impeller suction pipe at the outer wall. It generates a sudden change of both the velocity and pressure fields, which have become fully three-dimensional, when they were one-dimensional for $Q > Q_{cr}$. The "direct-methods" consist of detecting such sudden change of the flow parameters.

A. Flow visualizations [3]

B. Flow traverses. The test facility and experimental procedures for traversing with 5-hole probes the flow field in the pump suction pipe both at nominal and part flow rates are described in detail in [1], [2]. At a certain capacity, lower than the nominal one, it can be seen that $C_x = 0$ at the outer wall in the test section (Fig. 3a). This capacity is function of the axial distance x/D_{hyd} (hyd: hydraulic) between the test section and the impeller tip blade leading edge. According to [1] the critical capacity, Q_{cr}/Q_N, is obtained by extrapolating the experimental plot $Q_{cr,x}/Q_N = f(x/D_{hyd})$ for $x/D_{hyd} = 0$ (Fig. 3b).
The same criterium can be applied to the velocity swirling component ($C_u > 0$) as well as to the total pressure ($P > P_{suction}$).

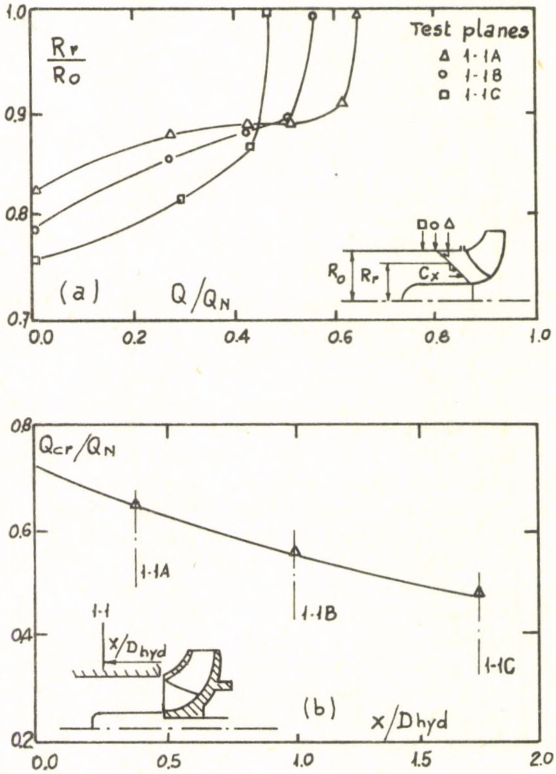

Fig. 3 a) b)

C. Oscillating vanes [7]

D. Wall static pressure. When the reverse swirling flow reaches a test section, the pipe outer wall static pressure suddenly increases. The critical capacity is obtained by applying the extrapolation criterium described in 4.1.B.

5.2 Not-Directs Methods

The not-direct methods are based on the liaison between the reverse flow onset and the peak of the incipient cavitation curve. The development and collapse of the cavitation bubbles cause, at given capacity, the variation of:

A) Energy (Head) Level (Fig. 4-A)
B) Sound Pressure Level (SPL) or
   Noise Level (Δ SPL = SPL-SPL$_{REF}$; REF = no cavitation) (Fig. 4-B)
C) Suction Pressure Fluctuations (Fig.4-C)
D) Volute Pressure Fluctuations (Fig.4-D)
E) Pump Casing Axial Vibrations (Fig.4-E)
F) Shaft Torque Fluctuations (Fig.4-F)

All these methods, which have been applied to a mixed-flow pump model (Nq = 92.5), are described in [8]. Fig. 4 gives an example (Q/Q_N =0.79). It should be pointed out that some scattering was caused by a flow recirculation at impeller discharge present at Q_N as well. For the noise curve no evident discontinuity was observed. A conventional value SPL = 5dB (Eqn A4) was chosen for comparison of noise level against the capacity. The detailed flow surveys, such as wall pressure measurements and flow traverses according 4.1.B and 4.1.D were also performed. All methods show a peak of τ_i in the range Q/Q_N = 0.67÷0.79 and a large increase of τ_i towards shut off. The different values of the critical capacity are collected in Table 1. It is clear that the not-direct methods A, C, D, E are in good agreement (with τ_i/τ_N - Q/Q_N curves having very similar shape) also compared with direct methods B and C.

Table 1

Method	$\tau_{i,cr}/\tau_{iN}$	Q_{cr}/Q_N
Flow traverse (4.1.B)	-	0.71
Wall pressure (4.1.D)	-	0.71
Energy Level (5.1.A)	-	0.70
Noise (5.1.B)	1.5 (1.4)	0.79(0.67)
Suction Pressure Fluct. (5.1.C)	1.3 (1.2)	0.70(0.79)
Volute Pressure Fluct. (5.1.D)	1.2 (1.1)	0.70(0.79)
Axial Vibrations (5.1.E)	1.8	0.70
Torque Fluct. (5.1.F)	1.1 (1.0)	0.79 (1.0)

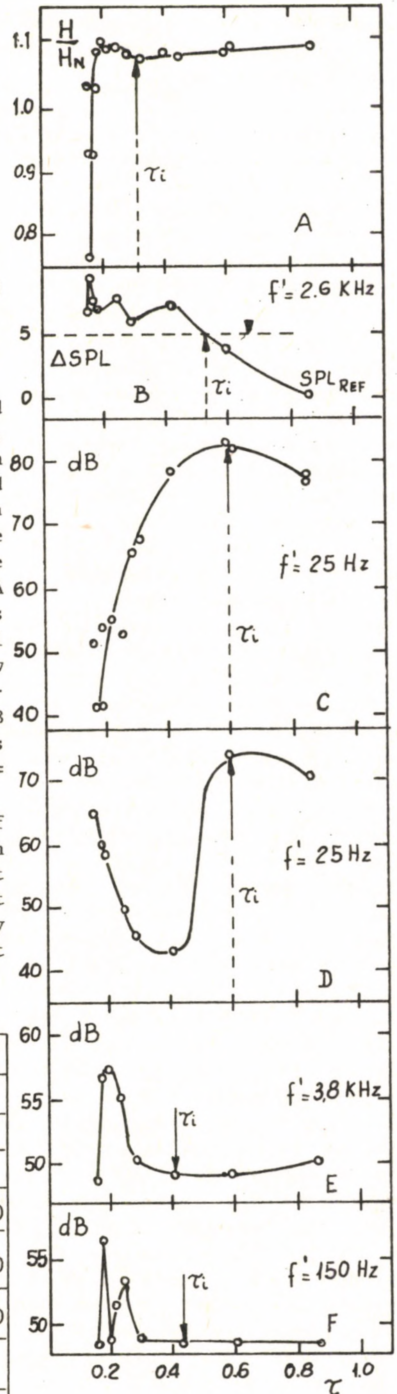

Fig. 4

5. CRITICAL CAPACITY PREDICTION CORRELATION

The elaborated set of experimental data concerns velocity traverses and wall pressure measurements at the impeller inlet and exit sections for several capacities [1], [2], [5].
The critical capacity Q_{cr}/Q_N reached considerably different values for the tested configurations: 0.45÷0.95.
The tests clearly pointed out [6], [9] that there is no univocal link $Q_{cr}/Q_N = f(N_q)$.
According to [9], the onset of the reverse flow cannot be related either to the pressure peak forced by the volute at the impeller exit or to the overall (centrifugal and aerodynamic) pressure average increase through the impeller. But, when the centrifugal forces pressure gradient is excluded by considering exclusively the "reduced static pressure", $h^{(r)}$ (Eqn A5), a relationship between the aerodynamic pressure increase and the reverse flow onset is evident and self-consistent i.e. the impellers with higher aerodynamic pressure increase show higher Q_{cr}/Q_N. An aerodynamic pressure coefficient at the impeller tip, $Cp_{a,T}$, is defined as in cascade flow (Eqn A6). From Fig. 5 it can be deduced that, at the critical capacity, there is a well defined liaison between the critical aerodynamic pressure coefficient, $Cp_{a,T,cr}$, the design aerodynamic loading, $(C_{LA}\sigma)_{T,des}$, and the secondary flow losses, $\omega_{SF,T,cr}$ (Eqns A7,A8), for the impeller tip blades cascade. A basic conclusion is that the aerodynamic pressure field, generated by the relative flow, is crucially affecting the impeller tip blade boundary layer separation and then the onset of reverse flow in centrifugal pumps.

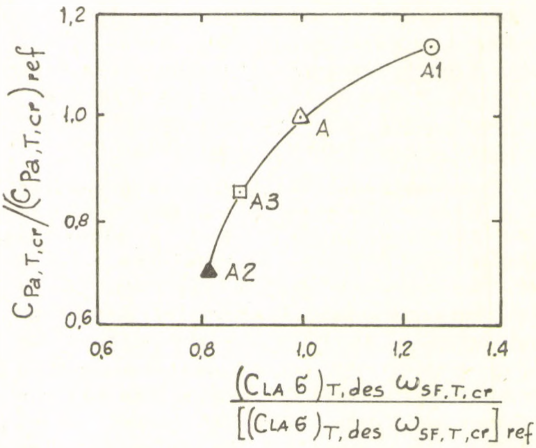

Fig. 5

The accurate prediction of the impeller exit relative flow (velocity W_2 and angle β_2) at design and off-design conditions is a very delicate step for whichever approach to the critical capacity prediction problem. The relative flow in centrifugal impellers is obtained by superimposing the: 1) "displacement flow" (vortex flow with Q = 0), 2) "relative through flow" (channel flow with Q > 0). The ideal slip factor due to the "displacement flow" was determined with the Busemann's theory, which applies to thin, uncambered blades radial-flow cascades. A relative flow angle at impeller exit, β_2', was computed. An additional deviation, $\delta = \beta_2' - \beta_2$ (β_2: relative flow angle), is introduced by the "relative through flow" because of the blade camber, if present, and both three-dimensional and viscous flow effects. The deviation δ was estimated (Eqn A9) on the basis of the classical deviation angle correlations for axial cascades (Carter, NACA). These correlations were properly transformed for radial-flow cascades by establishing a physical relation between the phenomena responsible for the deviation angle in both axial and radial flow fields. The global slip factor, K_{th} (Eqn A10), was calculated and compared to the experimental slip factor, derived from the velocity traverses at the impeller exit. The comparison results quite acceptable ($\simeq$ 5%), exception made for variants C and C1, requiring further refinements in the Busemann's theory application (effect of the impeller inlet-to-outlet diameter ratio).

As far as the off-design prediction of the impeller exit relative flow is concerned the "displacement flow" was assumed as invariable in relation with capacity i.e. the Busemann's zero flow head coefficient h_o is invariant against Q. Fig. 5 displays that Q_{cr}/Q_N is determined primarily by the relative velocity diffusion and the aerodynamic circulation, secondarily by three-dimensional and viscosity effects. The blade suction side boundary layer separation in straight stationary cascades is commonly predicted with the Diffusion Factor correlation (Eqn A11). The statistical critical value is DF = 0.6. The diffusion factor basic concepts were adopted and revised for centrifugal rotors by considering only the relative flow field and excluding any influence of the centrifugal flow field. The critical diffusion factor (at Q_{cr}/Q_N) for the blade tip section was ranging from 0.47 (impeller C) to 0.63 (impeller A2). The impeller A2, designed for uniform aerodynamic load distribution from hub to tip with low twisted blades, appears very similar to a rotating radial-flow cascade. All the other impellers are characterized by more or less pronounced three-dimensional effects. They are generated by:

a) A non uniform hub-to-tip distribution of the aerodynamic blade loading. This diminishes the maximum diffusion through a factor f_{3D} (Eqn A12).
b) The meridional curvature of the impeller tip shroud. This increases the separation susceptibility of the blade suction side boundary layer according to a factor f_{TC} (Eqn A13).

Moreover, the friction and secondary flow losses deteriorate the relative velocity diffusion process by increasing the boundary layer thickness . This loss influence is expressed through the factor f_{SF} (Eqn A14). In Fig. 6 the limit value $DF_{T,cr}$ is plotted against the correlating parameter $(K_{3D,SF,TC})_{cr}$ (Eqn A15), which includes the three-dimensional flow and viscosity and tip shroud curvature effects. According to Fig. 6 the prediction of the critical

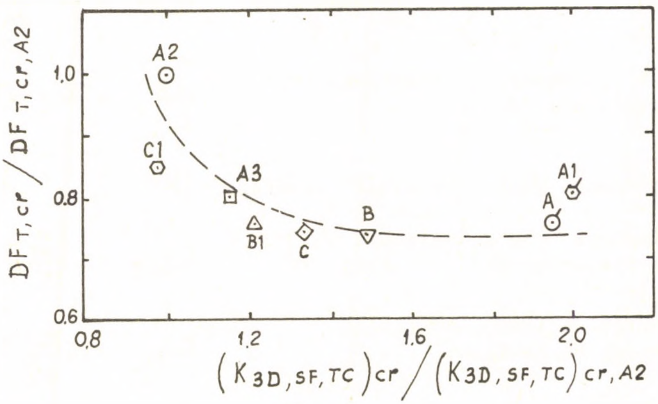

Fig 6

capacity can be formulated as follows:

$$Q_{cr}/Q_N = F\,(DF_{T,cr})$$

$$DF_{T,cr} = DF_{cr,2D} \cdot (K_{3D,SF,TC})_{cr}$$

$$DF_{cr,2D} = 0.6$$

with an accuracy of 5% on Q_{cr}/Q_N.

Various other theoretical approaches [6] as:

a) Diffusion Ratio (De Haller)
b) Lift coefficient (Carter)
c) Stalling incidence angle
d) Diffusion factor with absolute flow circulation (Rodgers) [10]
e) "Pump Diffusion Factor" (Sen) [11]

or empirical correlations [12] have been applied to the tested configurations. Such analysis, described in detail in [5], shows that the criteria elaborated on the basis of the Diffusion Factor concepts are the most effective and complete from the phenomenon physical description point of view, although certain formulations and applications [10], [11] are not entirely correct, either theoretically or experimentally.

APPENDIX A . DEFINITIONS AND FORMULAS

- Centrifugal force (Fig. 2) $$dF_{cf} = R\,\omega^2\,dm \quad \text{(A1)}$$

- Coriolis force (Fig. 2) $$dF_c = 2\,\omega\,W\,dm \quad \text{(A2)}$$

- Aerodynamic (blade) forces (Fig. 2)
  - normal (n) $$dF_{an} = \frac{W^2}{R_{csl}}\,dm$$
  - streamwise (s) $$dF_{as} = \frac{d(W^2/2)}{ds} \quad \text{(A3)}$$

- 'Y' parameter fluctuations amplitude (Fig. 4) $$dB = 20\,\log\,(Y/Y_{REF})_{f=f'} \quad \text{(A4)}$$

- "Reduced static pressure" (average) $$\bar{h}^{(r)} = \bar{h} - U^2/2g \quad \text{(A5)}$$

- Impeller tip aerodynamic pressure coefficient (Fig. 5) $$Cp_{a,T} = \frac{\bar{h}^{(r)}_{2T} - \bar{h}^{(r)}_{1T}}{W^2_{1T}/2g} \quad \text{(A6)}$$

- Friction loss coefficient (mean streamline) $$\omega_M = \frac{\Delta H_{12,f}}{W^2_{1M}/2g} \quad \text{(A7)}$$

- Secondary flow losses (Stewart's correlation 13) $$\omega_{SF} = \omega_M\,\frac{\sin\beta_{ch}}{AR \cdot \sigma} \quad \text{(A8)}$$

- Additional angle deviation $\delta = \beta_2' - \beta_2 = \delta_{2D}^* + \Delta\delta_{2D}^* + \delta_{3D,\omega}$ (A9)

  δ_{2D}^* = two-dimensional deviation angle at optimal incidence, $i=i^*$ (Carter's correlation)

  $\Delta\delta_{2D}^*$ = Variation of δ_{2D}^* at off-design incidence, $i \neq i^*$ (NACA correlation)

  $\delta_{3D,\omega}$ = deviation angle due to three-dimensional (3D) and viscous (ω) effects (Author'a correction)

- Overall theoretical (th) slip factor $K_{th} = C_{u2,th} / C_{u2,th,\infty}$ (A10)

- Diffusion Factor (axial flow cascade) $DF = 1 - \frac{W_2}{W_1} + \frac{|W_{u1} - W_{u2}|}{2\,\sigma\,W_1}$ (A11)

- Correction factors (Fig. 6)
  - 3D-flow $f_{3D} = [(C_{LA}\sigma)_T/(C_{LA}\sigma)_H]_{cr}$ (A12)
  - Tip shroud curvature $f_{TC} = b_1 / R_{TC,1}$ (A13)
  - Viscosity $f_{SF} = \omega_{SF,cr}$ (A14)

- Overall correction factor on $DF_{T,cr}$ (Fig. 6) $K_{3D,SF,TC} = f_{3D} \cdot f_{SF} \cdot f_{TC}$ (A15)

NOMENCLATURE

AR - blade aspect ratio (height/chord)
b - blade height
C - absolute velocity
C_{LA} - aerodynamic lift coefficient
C_{Pa} - aerodynamic pressure coeff.
D - diameter
DF - diffusion factor
f - frequency or correction factor
$\overline{h}$ - average static pressure
$\overline{h}^{(r)}$ - average "reduced static pressure"
H - total head
ΔH - head losses
i - relative incidence angle
K - slip factor
Nq - specific speed (rpm, m /s,m)
NPSH - Net Positive Suction Head
Q - capacity
R - radius
SPL - sound pressure level
U - peripheral velocity
W - relative velocity
x - axial distance (Fig. 3)
β_b - blade angle
β' - relative flow angle (Busemann)
β - overall relative flow angle
β_{ch} - blade chord angle
δ - relative flow deviation angle
σ - solidity (chord/pitch)
τ - cavitation coefficient ($NPSH/(U_{1T}^2/2g)$)
ω - angular velocity or loss coeff.

Subscripts

1(2) - impeller blade leading (trailing) edge
12 - impeller inlet to outlet
2D - twodimensional
3D - threedimensional
∞ - infinite blade number
a - aerodynamic
A2 - test configuration A2
C - Coriolis
cf - centrifugal
cr - critical
csl - streamline curvature
des - design point
f - friction
H - impeller hub section
i - incipient cavitation
M - blade mean section
N - nominal
o - suction pipe outer wall
ov - overall (Fig. 1)
r - reverse flow (Fig. 3)
ref - configuration A (Fig. 5)
SF - secondary flow
T - impeller tip section
TC - tip shroud curvature
x - velocity axial component
u - velocity tangential component
ω - viscous

REFERENCES

[1] JANIGRO, A. and SCHIAVELLO, B.: "Prerotation in Centrifugal Pumps. Design Criteria", Off Design Performance of Pumps, Von Karman Institute, LS 1978-3, March 1978.

[2] SEN, M.: "Prerotation in Centrifugal Pumps", Off-Design Performance of Pumps, Von Karman Institute, LS 1978-3, March 1978.

[3] MINAMI, S., KAWAGUCHI, K., and HOMMA T.: "Experimental Study on Cavitation in Centrifugal Pump Impellers", Bull. JSME, Vol 3, N. 9, Sep. 1960, pp. 9-19.

[4] MURAKAMI, M. and HEYA, N.: "Improvement of Pump Performance by Impeller Eye Throttling", ASME 69-FE-26, 1969.

[5] SCHIAVELLO, B. and SEN, M.: "Experimental Investigation on Centrifugal Pump Design Criteria for Minimum Reverse-Flow Delivery", Improveement in Turbomachines and Related Techniques, Worthington European Technical Award, Vol. V, HOEPLI, Milan 1981 pp. 191-239.

[6] SCHIAVELLO, B.: "Débit Critique d'Apparition de la Récirculation à l'Entrée des Roues de Pompes Centrifuges: Phénomène Determinants, Méthodes de Détection, Critéres de Prévision", Fonctionnement des Turbomachines a Débit Partiel, SHF - Session n. 119, La Houille Blanche N. 2/3 - 1982 (In French).

[7] SEN, M., BREUGELMANS, F. and SCHIAVELLO, B.: "Reverse Flow, Prerotation and Unsteady Flow in Centrifugal Pumps", Fluid Mechanics Jubilee Conf., Paper N. 3-1, NEL East Kilbride, Glasgow, Nov. 1979.

[8] BOCCAZZI, A. and GIULIANI, P.: "Analysis of NPSH-Q Curve by means of Several Detection Methods for a Mixed Flow Pump", Proceedings National Conf. ATI-Saint Vincent, Sept. 1980 (In Italian).

[9] SCHIAVELLO, B. and SEN, M.: "On the Prediction of the Reverse Flow Onset at the Centrifugal Pump Inlet", Performance Prediction of Centrifugal Pumps and Compressors, ASME, 22nd Annual Fluids Engineering Conf., New Orleans, Luoisiana, March 9-13, 1980.

[10] RODGERS, C.: "A Diffusion Factor Correlation for Centrifugal Impeller Stalling", ASME Paper 78-GT-61, 1978.

[11] SEN, M.: "Study of Inlet Flow of Centrifugal Pumps at Partial Flow Rates", Thèse de Doctorat, Universitè Libre de Bruxelles et Institut Von Karman, Juin 1980.

[12] GRIANKO, L.P. and PAPIRA A.N.: "Determining Flow Parameters at the Impeller Inlet of a Multistage Centrifugal Pump during Hydraulic Stagnation", Lopastnie Nasosi (Bladed Pumps), Mashinostroenie Leningrad Dept. 1975, pp. 50-66 (In Russian).

[13] STEWART, W.L., WHITNEY, W.J. and WONG, R.J.: "A Study of Boundary Layer Characteristics of Turbomachine Blade Rows and their Relation to Overall Blade Loss", Trans. ASME, Series D, Journal Basic Engng., Vol. 82, 1960, pp. 588-592.

Aknoledgements The author would like to thank Dr. M. Sen for supervision of the experiments at Von Karman Institute for Fluid Dynamics (Rhode St Génese, Belgium). Also the author is indebted to Mr. A. Boccazzi of Centro Nazionale Propulsione e Materiali (Peschiera Borromeo, Italy) for the collaboration in the incipient cavitation investigation area.

SCHIAVELLO BRUNO - Associate Director Hydrodynamics
Worthington Group
270 Sheffield Street
Mountainside 07041, N.J., U.S.A.

INVESTIGATION OF THE FLUID FLOW WITHIN THE RETURN PASSAGES OF MULTI-STAGE CENTRIFUGAL PUMPS

R.Schilling, O.Eichler, D.Klemm and H.Offenhäuser

SUMMARY

The paper deals with the numerical and experimental investigation of the inviscid but rotational meridional flow of an incompressible fluid within a return passage of a multi-stage centrifugal pump. A second-order finite difference solution procedure has been developed using boundary-fitted coordinates. The first numerical results are shown and compared with measured data.

1. INTRODUCTION

Designing multi-stage centrifugal pumps it is very important to know the flow field within the return passage and the inlet flow conditions of the second stage and of the following ones.

The fluid flow in turbomachinery is unsteady, three-dimensional and turbulent. In spite of large computers available, a full numerical solution of this difficult flow problem cannot be obtained. Therefore, the simplified flow model of WU [1] is used in order to predict the steady inviscid fluid flow within turbomachineries. Following this theory, the real three-dimensional flow can be described as a superposition of two two-dimensional flows in the hub to shroud plane (H-S) and in the blade to blade plane (B-B), see Fig.1.

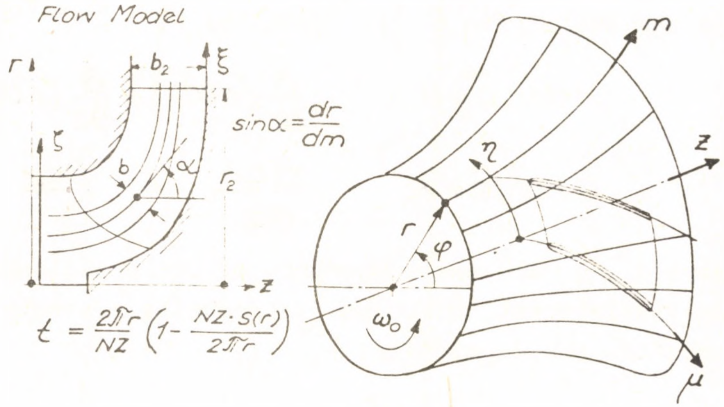

Fig.1 Mathematical Model of the Quasi 3D Flow Through an Impeller.

The present paper deals with the H-S flow within return passages of multi-stage centrifugal pumps supposing a known B-B flow within the stay vanes and the return vanes, see Fig.2.

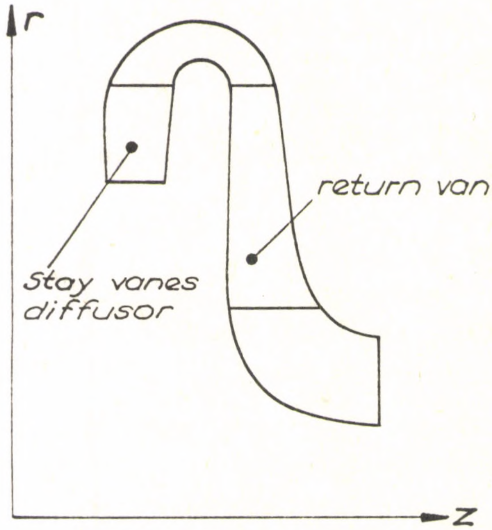

Fig.2 Meridional Contour of a Return Passage of a Multi-Stage Centrifugal Pump.

2. MATHEMATICAL FORMULATION OF THE PROBLEM,BASIC EQUATIONS

The flow is considered to be steady, inviscid but rotational and axisymmetric. The governing equations are the continuity and the definition of the vorticity .

$$div\ \vec{c} \equiv 0 \qquad \frac{\partial}{\partial r}(rtc_r) + \frac{\partial}{\partial z}(rtc_z) = 0 \qquad (1)$$

$$rot\ \vec{c} = \lambda \qquad \frac{\partial c_r}{\partial z} - \frac{\partial c_z}{\partial r} = \lambda \qquad (2)$$

where c_r, c_z are the components of the meridional flow and t is the displacement thickness. Introducing a stream function which satisfies the continuity

$$c_r = -\frac{1}{rt} \cdot \frac{\partial \Psi}{\partial z} \quad (3a) \qquad\qquad c_z = +\frac{1}{rt} \cdot \frac{\partial \Psi}{\partial r} \quad (3b)$$

we obtain the Poisson equation for the stream function

$$\underset{rz}{\Delta}\Psi - \left(2+\frac{r}{t}\frac{\partial t}{\partial r}\right)\frac{1}{r}\frac{\partial \Psi}{\partial r} - \frac{1}{t}\frac{\partial t}{\partial z}\frac{\partial \Psi}{\partial z} = -\lambda r t \tag{4}$$

Using the definitions for the swirl ϑ and the total pressure of the flow p_t

$$\vartheta = r \cdot c_\varphi \tag{5}$$

$$p_t = p + \frac{\varrho}{2}\left(c_r^2 + c_\varphi^2 + c_z^2\right) \tag{6}$$

the EULER equation for the r- and z-direction may be rearranged as follow, see [2]:

$$\lambda = \frac{1}{c_z}\left\{\frac{1}{2}\,\frac{1}{r^2}\frac{\partial}{\partial r}\left(\vartheta^2\right) - \frac{1}{\varrho}\,\frac{\partial p_t}{\partial r}\right\} \tag{7}$$

$$\lambda = -\frac{1}{c_r}\left\{\frac{1}{2}\,\frac{1}{r^2}\frac{\partial}{\partial z}\left(\vartheta^2\right) - \frac{1}{\varrho}\,\frac{\partial p_t}{\partial z}\right\} \tag{8}$$

The EULER equation in φ -direction yields an equation for the calculation of the swirl ϑ as a function of c_r and c_z

$$\frac{\partial}{\partial r}\left(r c_r \vartheta\right) + \frac{\partial}{\partial z}\left(r c_z \vartheta\right) = 0 \tag{9}$$

which may be applied in the vaneless spaces of the pump. Within the stay and return vanes the swirl ϑ can be estimated supposing an infinitely high number of vanes.

Coordinate Transformation

The partial differential equations (4) and (9) are to be solved numerically taking into account the appropriate boundary conditions. Because of the complexity of this boundary value problem it is convenient to introduce a boundary-oriented coordinate system (ξ,η). The advantage of this method is that the flow calculations using a finite difference method can be carried out in a fixed rectangular domain with an uniform grid. The boundary-fitted coordinates have to be generated numerically solving the following Poisson equations

$$\Delta_{rz} \xi = f \qquad (10a) \qquad\qquad \Delta_{rz} \zeta = h \qquad (10b)$$

where f, h are the so called "forcing functions" depending on (r, z) or (ξ, ζ), which provide a control over the spacing of the coordinate lines in the physical domain. An arbitrary point in the transformed plane P (ξ, ζ) can be mapped into the physical plane P (r, z) by solving the following Poisson equations

$$c_1 r_{\xi\xi} + c_2 r_{\zeta\zeta} + c_3 r_{\xi\zeta} + d^2 (f r_\xi + h r_\zeta) = \frac{1}{r} d^2 \qquad (11a)$$

$$c_1 z_{\xi\xi} + c_2 z_{\zeta\zeta} + c_3 z_{\xi\zeta} + d^2 (f z_\xi + h z_\zeta) = 0 \qquad (11b)$$

Similarly the Poisson equation for the stream function (4) and the swirl transport equation (9) has to be transformed

$$c_1 \Psi_{\xi\xi} + c_2 \Psi_{\zeta\zeta} + c_3 \Psi_{\xi\zeta} + c_4 \Psi_\xi + c_5 \Psi_\zeta = -\lambda r t \cdot d^2 \qquad (12)$$

$$\frac{\partial}{\partial \xi}\left(\frac{1}{\sqrt{c_2}} r c_\xi \vartheta\right) + \frac{\partial}{\partial \zeta}\left(\frac{1}{\sqrt{c_1}} r c_\zeta \vartheta\right) = 0 \qquad (13)$$

In the equations (11) and (12) c_1 to c_5 are the transformation coefficients and d is the Jacobian determinant.

The velocities of the transformed domain may be evaluated from the corresponding derivations of the stream function .

$$c_\xi = -\frac{1}{r} \frac{\sqrt{c_2}}{d} \cdot \frac{\partial \Psi}{\partial \zeta} \qquad (14a)$$

$$c_\zeta = \frac{1}{r} \frac{\sqrt{c_1}}{d} \cdot \frac{\partial \Psi}{\partial \xi} \qquad (14b)$$

The relations between the velocities of the physical and the transformed domain are as follows:

$$c_r = \frac{r_\xi}{\sqrt{c_2}} c_\xi + \frac{r_\zeta}{\sqrt{c_1}} c_\zeta \tag{15a}$$

$$c_z = \frac{z_\xi}{\sqrt{c_2}} c_\xi + \frac{z_\zeta}{\sqrt{c_1}} c_\zeta \tag{15b}$$

$$c_\xi = \frac{\sqrt{c_2}}{d} (z_\zeta c_r - r_\zeta c_z) \tag{16a}$$

$$c_\zeta = -\frac{\sqrt{c_1}}{d} (z_\xi c_r - r_\xi c_z) \tag{16b}$$

Boundary Conditions

At the inlet of the domain c_r is supposed to be uniform while at the outlet c_r is assumed to be zero. The solid boundaries are stream-lines Ψ = const, where the difference of the values of the stream function is given by the volume flow rate.

3. NUMERICAL SOLUTION

The coordinate transformation was performed at the Institut für Strömungslehre und Strömungsmaschinen, Fachgebiet Strömungsmaschinen der Universität Karlsruhe. On this basis there was developed a second-order finite difference procedure for the calculation of the potential flow within simple geometries using Gaussian line elimination [3]. This basic program was extended at VOITH GmbH to the real case of rotational flow within complex geometries using the field method of STONES [4], which is about 10-times faster than the line-elimination.

4. TEST RIG FOR TESTS IN AIR

In order to prove the mathematical model air tests were performed. For this purpose a special test rig was built up.

On the test rig (fig.3) the original pump impeller of the 1st stage, which is also used for tests in water, is driven by a 3-phase a.c.motor. By frequency control, the pump impeller speed can be adjusted within a wide range up to the maximum speed of

2940 min^{-1}. The speed is measured by means of an induction meter. The tests were conducted at a speed of 2500 min^{-1}.

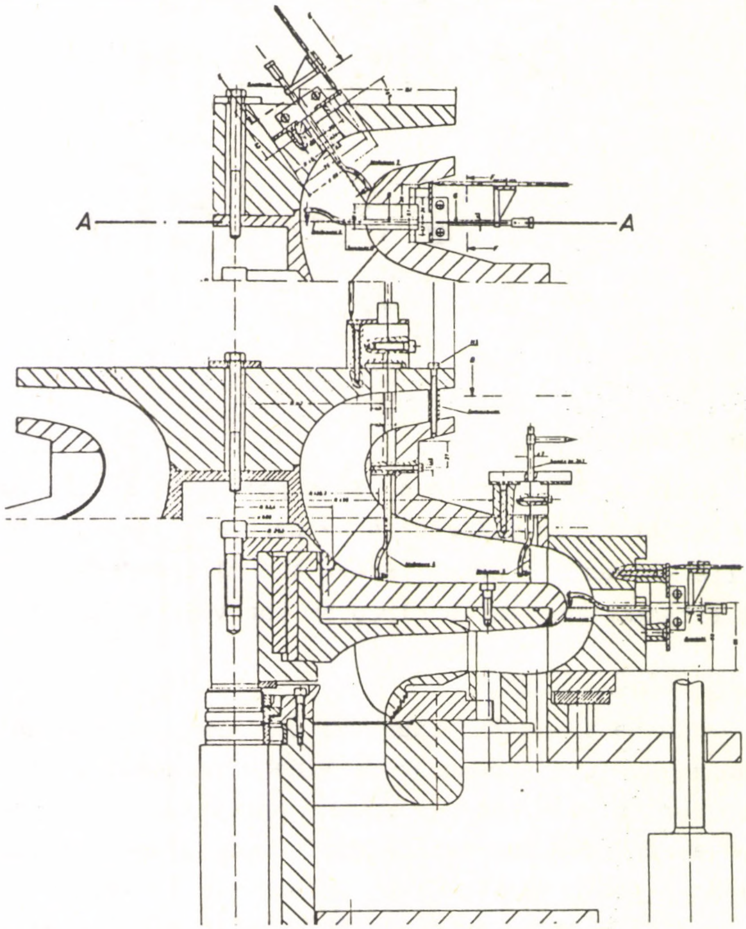

Fig.3 Test Assembly

The impeller sucks in air directly through an inlet nozzle, which simultaneously serves for discharge measurement, as it was calibrated at this point with the help of a calibration nozzle. The impeller blows into the downstream diffuser; from there, the air flows through the return chamber and the return vanes into the next stage. The 2nd-stage impeller is not installed; only the vaneless airstream passage of this impeller is modeled. With the help of flow restrictor rings provided at the outlet, the desired flowrate is adjusted.

The entire airstream passage from the entrance into the diffuser of the 1st stage to the entrance into the impeller of the second stage can be equipped with a number of flow measuring probes for the measurement of flow fields. The cover walls, in which the probes are fastened, can be turned towards the vanes.

5. MEASUREMENT TECHNIQUE

For measuring the velocities with respect to magnitude and direction, calibrated flow measuring probes in the form of cranked quadruple tubes were used. By simple turning of the probe, the direction in the flow plane is read off on the basis of zero balancing, by means of an angle scale dial pointer attached to the shaft.

All other values (total pressure, static pressure, component of the flow direction in the plane of the probe shaft and, thus, the velocity) must be determined with the help of calibration curves via suitably measured pressures.

The hook-shaped probes have the drawback that, for measurements conducted near the wall, through which the shaft is passed, either a large opening or a ring-shaped slot is required for turning the probe, which falsifies the test results. In order to minimize this disturbing influence, the direction is roughly determined in a preliminary test. For the main test, the probe is adjusted in this direction, and the wall opening is closed to such an extent that, during the test, only the fine adjustment of the probe is possible.

For indication of the total pressure, the static pressure and, thus, the dyn. pressure, as well as for indication of the differential pressure for determining the direction in the shaft plane (meridian plane), projected-scale pressure gauges according to Betz were used.

The differential pressure for determining the direction vertical to the probe shaft was ascertained by means of an inductive diferential pressure cell with digitizer on the load side.

6. RESULTS

The numerical analysis was carried out for a centrifugal pump of low specific speed. The measurements were performed considering several operation points.

However, the comparison between numerical and measured results is restricted to the best point, where only small separation zones occur in the stay vanes (diffuser) and in the return vanes. The numerical theory and the experiments show a good agreement concerning the circumferential velocity c_u at lower radii, see Fig.4.

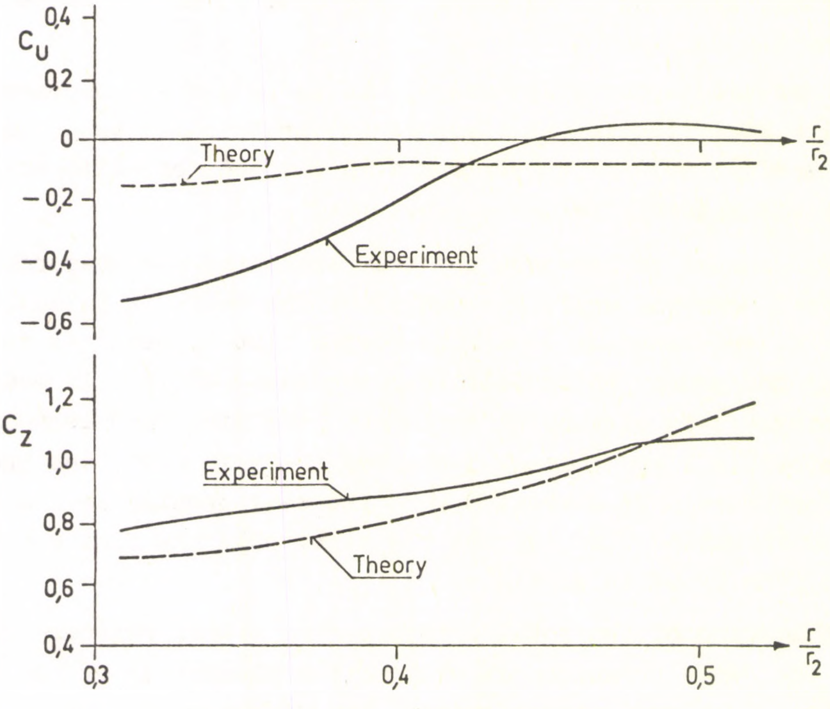

Fig.4 Theoretical velocities in circumferential (c_u) and axial (c_z) direction in section A-A compared with experimental results.

This behaviour may be understood because the flow angle at the stay vane and return vane outlet clearly differs from the blade angle, which was supposed to be equal to the flow angle in this step of our investigations.

The next step will also include a B-B analysis, see [5], in order to get a better agreement.

7. NOMENCLATURE

$c_1 - c_5$	transformation coefficients
c_r, c_z	meridional velocity components
c_ξ, c_ζ	transformed velocities
c_φ, c_u	circumferential velocities
d	Jacobian determinant
f, h	forcing functions
p, p_t	static, total pressure respectively
r, z	meridional coordinates
t	displacement thickness
ξ, ζ	transformed coordinates
ϱ	density
ϑ	swirl
λ, Ψ	vorticity, stream function respectively
$\underset{rz}{\Delta} = \frac{1}{r}\frac{\partial}{\partial r}\left(r\frac{\partial}{\partial r}\right) + \frac{\partial^2}{\partial z^2}$	delta operator

8. LITERATURE

[1] Wu, C.H.: A general theory of the 3D flow in subsonic and supersonic turbomachines of axial, radial and mixed flow type. NACA, TN 2604, 1952.

[2] Schilling,R., Liess,Ch., Weidtmann,J.: Überlegung zur Berechnung der reibungsfreien Strömung im schaufellosen Raum von Kaplan-Turbinen. Interner VOITH-Bericht Nr.1305, 1981.

[3] Felsch,K.O., Steck,E.: Berechnung der 2D Potentialströmung im schaufellosen rotationssymmetrischen Raum. Forschungsbericht im Auftrag der Firma J.M.VOITH GmbH, 1982.

[4] Stones,H.L.: Iterative solution of implicit approximations of multidimensional partial differential equation. NAG FORTRAN Library Manual.

[5] Schilling,R.: Numerical analysis of the quasi-3D incompressible inviscid flow in turbomachines. Proc.of 11th IAHR Symposium, Amsterdam, 1982.

ADDRESS OF THE AUTHORS

Dr.-Ing.habil. R. Schilling,
Dipl.-Ing. O. Eichler,
Dipl.-Ing. D. Klemm,
Dipl.-Ing. H. Offenhäuser,

J.M. VOITH GMBH
St.Pöltener Str. 43
D-7920 Heidenheim

DETECTION OF THE SERVICE LIFE OF TURBINE COMPONENTS

G. Schramm, G. Schilg, W. Hahn

Formula symbols and indices

A	area	r	radius
a	temperature conductivity	s	wall strength
Bi	Biot number	T	temperature
b	lever arm	$\dot{T}$	temperature transient
E	modulus of elasticity	α	heat transfer coefficient
E	fatigue degree	α_T	linear heat expansion coefficient
F	force		
Fo	Fourier number	$2\varepsilon_a$	amplitude of dilatation
M	moment	τ	time
N	number of load reversals	ϑ	Poisson's ratio
P	pressure	λ	heat conductivity
p	unit pressure	$\sigma_{B/\tau/T}$	creep-rupture stability

A	surface crack	kr	critical	U	turning
B	rupture	lin	linear	W	wall
E	inlet	m	medium	W	material
F	fluid	R	wheel chamber		
Fl	flange	S	screw		
		spr	jump		

1. Introduction and aim

The limits of the service life of a component are reached when the functionality isn't guaranteed any more because of abrasion or when undue extensions or cracks occur caused by material fatigue. This paper will deal with the service life effected by material fatigue, as components of steam or gas turbines are often applied at temperatures of more than 350 °C so that material fatigue is decisive for component failures.

For the engineer the question arises: How strong is the consumption of service life of the component under the service conditions at a given material quality? For answering this question the effects on service life must be known. They can be divided into two groups:

1. Stress resulting from service conditions
2. Material parameters typical for fatigue.

There is a complex dependence of service life on service stress, material properties and constructive solutions, thus a technical processing is impossible without simplification. The following processing stages can be stated:

(1) Analysis of the operating condition and detection of the load collektiv.

(2) Calculation or measurement of time-dependent temperature fields and thermal stresses.

(3) Detection of the total load of the component.

(4) Estimation of component stress by comparison with material parameters and detection of the component damage and service life consumption, resp.

The problems arising are, on the one hand, the exact calculation of unsteady thermal stresses for components of an intricate shape, in grooves and at cross-sectional variations, and on the other hand, the summation of creep-rupture stress and dilatation-rupture stress. In the first case, remarkable advance was achieved by developing finite-element procedures, which are, however, associated with high expenditures. In the second case, the methods of damage accumulation don't offer sufficient security so that experimental investigations on original components are required.

2. Detection of component stress

The total stress is composed of mechanical and thermal steady and unsteady stresses.

At thermally stressed components the unsteady thermal stresses play a dominant role, in many cases. Therefore it is often decisive to know them.

2.1. Detection of temperature fields

Apart from experimental methods, the temperature profile on a component wall can be computed by solving the Fourier differential equation. A confined solution of this equation is not possible. By means of EDP-programmes based on finite elements good approximation can be achieved, depending to the processing efforts.

Using simplified assumptions for the boundary conditions and component geometry approximation equations can be set up, which can be applied for the estimated detection of the temperature profile. Typial parameters for heat transfer and heat conduction are the Biot-number and the Fourier-number.

2.2. Determination of thermal stresses using simplified assumptions

If the temperature profile of the component wall is known, the thermal stress can be computed according to the relation

$$\sigma_{(x)} = \frac{E\alpha_T}{1-\nu}\left(T_m - T_{(x)}\right). \tag{1}$$

Summarizing the material parameters in a material factor $\Phi_W = E\,\alpha_T/1-\nu)$ and expressing the wall temperature as a function of the fluid temperature variation equation (1) can be written in the following way:

For a temperature variation of the fluid with a constanct transient $\dot{T}_F = dT_F/d\tau$ it holds

$$\sigma_{lin} = \frac{\Phi_W}{a}\,\Phi_{lin}\,s^2\,\dot{T}_F. \tag{2}$$

For an erratic temperature variation of the fluid at ΔT_F = const. it holds

$$\sigma_{Spr} = \Phi_W\,\Phi_{Spr}\,\Delta T_F. \tag{3}$$

Thereby the tension factors Φ_{lin} and Φ_{spr} are functions of the Biot-number, the Fourier-number and the component shape. Their dependence on these parameters on principle is shown in figure 1 for linear temperature alteration and in figure 2 for erratic temperature alteration. At the Dresden

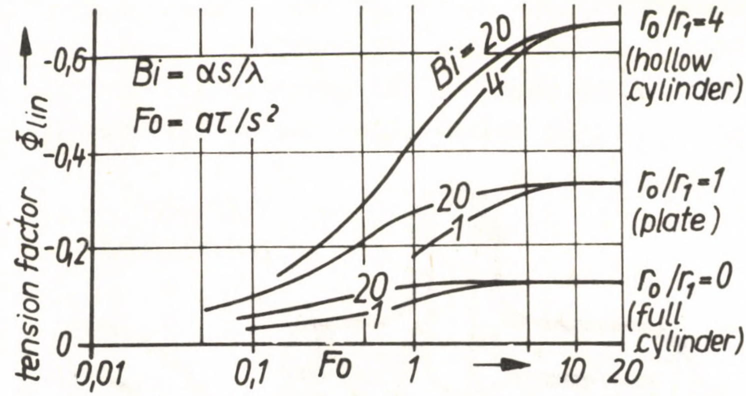

Fig. 1 Tension factors Φ_{lin} for lineare changes of temperature

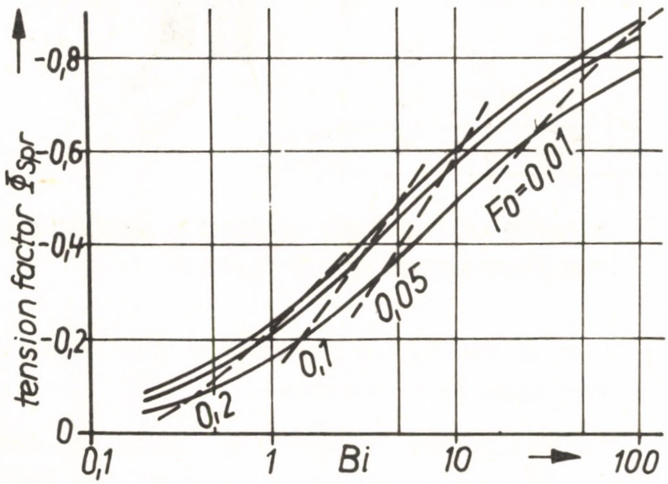

Fig. 2 Tension factors Φ_{spr} for jump-like changes of temperature

University of Technology a working documentation for the approximate calculation of tensions was developed and used in practice by this method.

2.3. Limits of simplifying assumptions

The tension factors can be applied for simple geometrical forms like plate, cylinder and sphere, successfully. These are e.g.at the high-pressure unit of a superheated steam turbine shown in figure 3

- the cylindrecal zone of the external casing (internally heated thin-walled hollow cylinder)
- the shaft in the range of the intermediate stuffing box (externally heated thick-walled hollow cylinder).

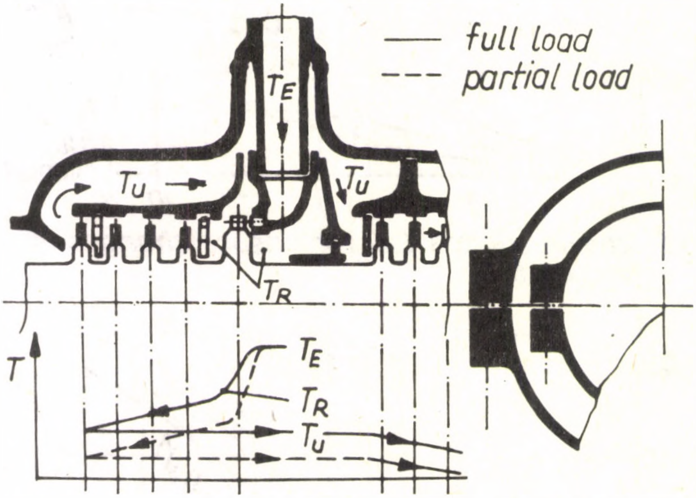

Fig.3 Scheme of the high-pressure section of a superheated steam turbine

From the behaviour of the fluid parameters the required Biot- and Fo-numbers can also be determined.

This method can't be applied if there are great deviations from the simple shapes, e.g. at the flange of the divided casing or the range of big flanged sockets.

It has already been stated in /1/ and /2/ that additional stresses occur at components according to figure 4 through the different temperature developments and the restricted dilatations caused by them, in the casing wall and joint flange. After determining the boundary coditions

- the flange remains even on the level of the joint flange and can shift into x-direction
- the inclination of the casing wall in the vertex remains

constant and the wall can shift into y-direction
- flange and casing wall have equal inclinations in section A

the thermal stresses in the wall and the flange can be computed on the basis of a finite-element programme. By a comparison to the approximation computation for the cylindrical wall it is possible to determine the additional stresses acting as a consequence of moment ΔM. Moment ΔM can also be determined approximately according to /2/. Knowing ΔM the flange can be computed with regard to the moments $b \cdot F_p$, M_{Fl}, M_W and the forces F_S and F_P as a deformeble plate separated from the cylindrical wall in section A. Results of this computation method are shown in figure 4. For

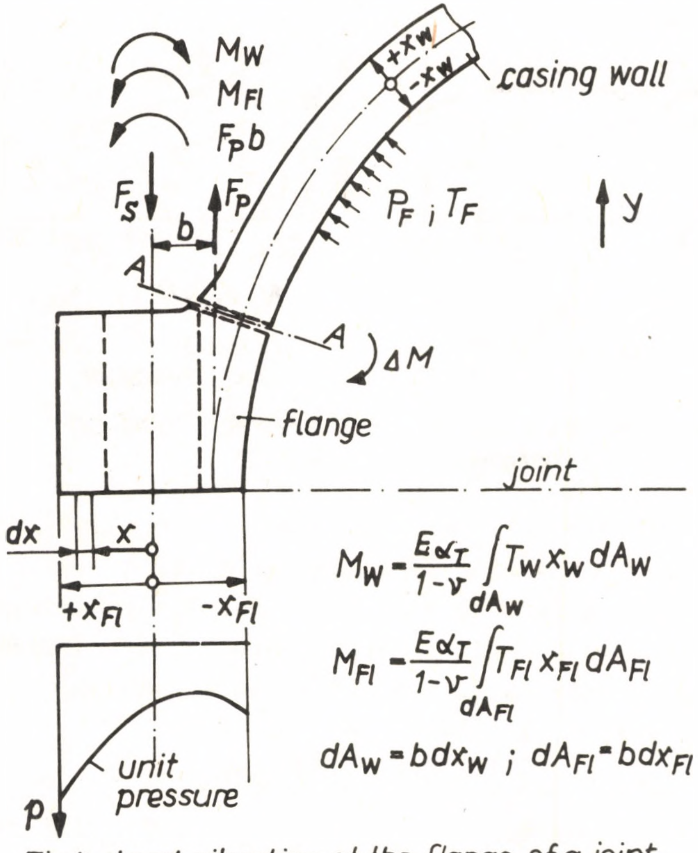

Fig.4 Load situation at the flange of a joint

typical temperature developments in casing wall and flange regarding the moment $F_p \cdot b$ the represented behaviour of the unit pressure $p = f(x)$ is resulting.

3. Evoluation of the component stress by comparison to material parameters

The service life consumption of a component thermally stressed occurs due to superposition of creep-rupture fatigue because of the steady and of dilatation-rupture fatigue because of the unsteady stress (figure 5).

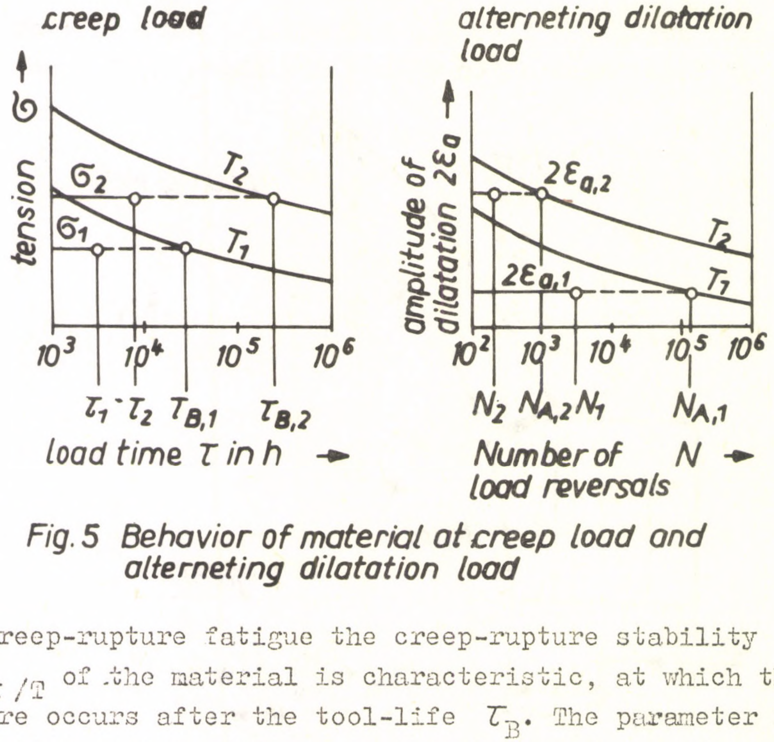

Fig. 5 Behavior of material at creep load and alterneting dilatation load

For creep-rupture fatigue the creep-rupture stability $\sigma_{B/\tau/T}$ of the material is characteristic, at which the rupture occurs after the tool-life τ_B. The parameter for dilatation-rupture fatigue is the alternating surface crack number N_A, at which a surface crack is to be expected for a certain amplitude of dilatation $2\,\varepsilon_a$.

4. Statements on service life consumption

The fatigue degree of the material is decisive for service life consumption. The simplest method for summarizing the fatigue shares from creep-rupture fatigue and dilatation-rupture fatigue is the linear damage accumulation

$$E = \sum_{i=0}^{i} \frac{\tau_i}{\tau_{B,i}} + \sum_{j=0}^{j} \frac{N_j}{N_{A,j}} \quad . \tag{4}$$

Theoretically, the service life is exhausted when the fatigue value is E = 1. Practically, however, a broad range of results can't be excluded due to uncertainties at

the detection of the load collectiv

the determination of material parameters as well as

the method of linear damage accumulation itself.

Thus, it is impossible to compute the precise failure criterion in the component, but a warning time can be determined, according to which repairings, inspection cycles and reconstructions can be planned more easily. Due to the uncertainties mentioned above at steam turbines E_{kr} = 0,6...0,25 and at gas turbines $E_{kr} \approx 0,1$ is proposed for the critical fatigue degree.

5. Research work required for increasing security of service life determination

From the description of the basic method of service life determination the problems still to be solved for incrasing the security of the statements become obvious.

The following complexes can be listed:

(1) Detection of the state of tensions within the component

The computation of tensions in components of intricate shapes is possible by means of complicated finite element programmes. The results of computation are to be checked by measurements on original components. At the Dresden University of Technology, a model casing test stand is being prepared for measuring thermal stresses and deformations. As a model the simplified external casing of the high-pressure unit of a superheated steam turbine in the scale of about 1:5 was used.

(2) Providing material parameters

Various influences like

- frequency time and hold-up time of the load cycles

- component shape
- temperature level
- surface condition
- corrosion

make the provision of reproducible expressive values for dilatation-rupture stability more difficult. The numerous measured values available for different steels must be systemized.

(3) Validity of damage accumulation

In order to determine the complex effect of the individual influences as well as the behaviour of the components at different degrees of damage experimental investigations on models and original components are required.

(4) Acquisition and processing of operating characteristics

A complete knowledge of the stresses occuring during the total operating time is the supposition for service life investigations. This is only feasible by means of automated measuring and data processing facilities. Currently, the producers of turbines, also in the GDR, are doing comprehensive research work in this field.

References

/1/ Buchmann, K.; Hahn, W.; Schilg, G.: On the evaluation of thermal stresses in simple components. (Zur Beurteilung der Wärmespannungen in einfachen Bauteilen thermischer Turbomaschinen). Wiss. Z. Techn. Univers. Dresden 28 (1979) 3, pp. 647 - 654.

/2/ Plotkin, E.P.; Berljand, V.J.; Svarc, A.V.: The influence of the flange at the joint on thermal stresses within the casing wall of a steam turbine. (Vlijanie flancev goricontalnogo razema na tempez raturnye naprjazenija v stenke korpusa parovoi turbiny). Energomachinostroenie, Leningrad 17 (1971) 10, pp. 9 - 11.

COMPARISON OF TWO METHODS FOR CALCULATING THE VELOCITY DISTRIBUTION IN ROTATING CASCADES

A. Sebestyén - E. Steck - K.O. Felsch

CASCADE MODELS AND ASSUMPTIONS

To compute the velocity distribution along the pressure and suction sides of radial grids, a purely radial impeller of constant width b and backwards curved blades is considered, see Fig.1. For the simple description of the blade profiles according to the finite difference method, a finite blade thickness is produced by turning the skeleton line round the rotation axis. In the following let the skeleton line be a logarithmic spiral with a helical angle $\beta_S = 42^{\circ}$. Forms of leading and rear edges of the blade models are different: the computing method based on the Fredholm integral equation applies rounded blade edges, whereas the difference method sets out from sharp-edged blade corners.

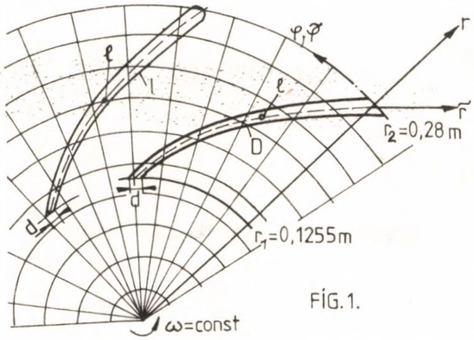

FIG.1.

Let the flow be plaine and steady in the relative system co-rotating at ω = const. Let the density ρ be constant and the dynamic viscosity μ disappear.

CALCULATIONS BY MEANS OF A FINITE DIFFERENCE METHOD

The steady-state frictionless relative flow is described by the two Euler equations and the continuity equation. They can be transformed with the help of the vorticity function

$$\zeta = \frac{1}{r} \cdot \left[\frac{\partial}{\partial r} \left(r\, w_{\varphi} \right) - \frac{\partial w_r}{\partial \varphi} \right]$$

and of the reduced static pressure

$$p^* = p - \frac{\rho}{2}(r\omega)^2$$

according to [1] into an equivalent substitute system for the scalar energy magnitude of the reduced total pressure

$$p_t^* = p + \frac{\rho}{2}\left(w_r^2 + w_\varphi^2\right)$$

such as:

$$\operatorname{div} \vec{w} = 0 \qquad \frac{\partial}{\partial r}\frac{p_t^*}{\rho} = (\zeta + 2\omega)\, w_\varphi ,$$

$$\frac{1}{r}\frac{\partial}{\partial\varphi}\frac{p_t^*}{\rho} = -(\zeta + 2\omega)\, w_r$$

As in the absolute system the flow would be a potential flow $\zeta = -2\omega$ leads to the direct conclusion that the reduced total pressure p_t^* is constant.

Introducing a stream function Ψ , meeting the continuity identically with

$$w_r = \frac{1}{r}\frac{\partial\Psi}{\partial\varphi} , \qquad w_\varphi = -\frac{\partial\Psi}{\partial r}$$

the Poisson equation suitable for numerical handling

$$\Delta\Psi = 2\omega$$

is obtained.

For description of the flow through curved blades a co-ordinate transformation into profile oriented non-orthogonal co-ordinates $\tilde{r},\tilde{\varphi}$

$$\tilde{r}(r,\varphi) = r , \qquad \tilde{\varphi}(r,\varphi) = \mp\left(\frac{r}{r_2}\right) + \varphi$$

is carried out.

Thereby the concentric circles r = const are sustained as co-ordinate lines, whereas the initial straights φ = const become general spirals. Furthermore, to increase the numerical accuracy an implicit co-ordinate distorsion $\hat{r}(\tilde{r}), \hat{\varphi}(\tilde{\varphi})$ is applied.

It is expedient to develop the following dimensionless magnitudes:

$$\tilde{R} = \frac{\tilde{r}}{r_2} , \quad \tilde{\Phi} = \frac{\tilde{\varphi}}{\gamma} , \quad \gamma = \frac{2\pi}{z} , \quad W_{\tilde{R}} = \frac{w_{\tilde{r}}}{r_2\omega} , \quad W_{\tilde{\Phi}} = \frac{w_{\tilde{\varphi}}}{r_2\omega} , \quad P^* = \frac{p^*}{\rho(r_2\omega)^2} ,$$

$$\Psi = \frac{\Psi}{r_2^2\omega\gamma} , \quad \Omega = \frac{\zeta}{\omega} , \quad \varphi_r = \frac{w_{r2}\cdot m}{r_2\,\omega} , \quad \Psi_t = \frac{\Delta p_t}{\rho/2\,(r_2\omega)^2}$$

where z is the blade number, $W_{r2.m}$ the radial component of the relative velocity averaged by volume, φ_r the volume coefficient and Ψ_t the total pressure coefficient.

Written in dimensionless form, with velocity components to be calculated from the stream function Ψ , the Poisson equation becomes:

$$\gamma \underset{\hat{R}\hat{\phi}}{\Delta} \Psi = 2,$$

$$W_{\tilde{R}} = \frac{\sqrt{1+\cot^2\beta_s}}{\tilde{R}} \frac{d\hat{\phi}}{d\tilde{\phi}} \frac{\partial\Psi}{\partial\hat{\phi}}, \qquad W_{\tilde{\phi}} = -\gamma \frac{d\hat{R}}{d\tilde{R}} \frac{\partial\Psi}{\partial\hat{R}}$$

The dimensionless Laplace operator $\underset{\hat{R}\hat{\phi}}{\Delta}$ refers to co-ordinates $\hat{R}$ and $\hat{\phi}$.

For the calculation of the cascade flow the Poisson equation has to be solved numerically, taking the relevant boundary conditions into consideration. Because of periodicity it is enough to seek the solution within the integration range between two blades.

At the control volume inlet - far enough from the cascade were the non-orthogonal co-ordinate system develops into a polar one by a twice continuously differentiable manner, the velocity components are fixed by the given velocity field.

$$W_{\tilde{R}} = \frac{\varphi_r}{\tilde{R}}, \quad W_{\tilde{\phi}} = W_{\tilde{R}} \cot\alpha - \tilde{R},$$

The stream function is linear

$$\Psi = \varphi_r \tilde{\phi} + \text{const},$$

the unknown integration constant has to be computed from the azimuthal component $W_{\tilde{\phi}}$. Analogue requirements have to be made at the control volume outlet in a sufficient distance behind the cascade, where the co-ordinate system becomes again orthogonal. However there the circumferential component $W_{\tilde{\phi}}$ is unknown and has to be determined to meet a physically interpretable downwash condition on the rear blade edge. At present problem the sum of the azimuthal components on both blade edges should disappear. In case of infinitely thin blades this downwash condition changes into the Kutta-Joukowsky condition. On the pressure side the value of the stream function is zero, on the suction side its value is equal to the volume coefficient. For both sides of control volume boundaries of the inlet and downwash range, periodical boundary conditions have to be specified.

The elliptic boundary value problem is numerically solved by an implicit difference method of second order of consistence [2]. For this all differentials are approximated by symmetrical difference ratios. The algebraic difference equations are solved row by row by Gaussian elimination [2]. The linear theory permits the superposition of elementary solutions. The coefficients of the linear combination for the stream function Ψ have to be adjusted hereby to the boundary conditions.

CALCULATION BASED UPON THE FREDHOLM INTEGRAL EQUATION

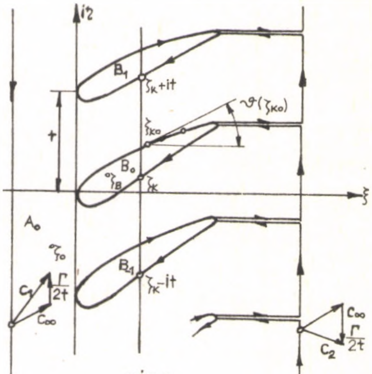

FIG.2

According to the method developed at the Department of Hydraulic Machines of the Technical University Budapest, first the circular blading is transformed into an infinite straight cascade. The transformation relationships are:

$$\zeta = \frac{Nt}{2\pi}\ln\frac{r}{r_1} \qquad \eta = \frac{Nt}{2\pi}\varphi$$

where N is the number of the impeller blades and r_1 the radius of the blade front edge. In the obtained straight cascade [4] - see Fig.2 - for any point ζ_{ko} of the blade contour the complex integral equation

$$-\frac{\gamma(\zeta_{ko})-iq(\zeta_{ko})}{2}+\frac{e(\zeta_{ko})}{2\pi}\oint_k^c\left[q(\zeta_k)+i\gamma(\zeta_k)\right]\sum_{\mu=-\infty}^{+\infty}\frac{1}{\zeta_{ko}-\zeta_k-i\mu t}\,|d\zeta_k|=0$$

may be written, where γ and q are tangential and normal velocity components, resp. on the contour $q=u_\eta\cdot\cos\Theta(\zeta_k)$ and $u_\eta=\frac{2r^2\pi}{Nt}\cdot\omega$. Decomposing the equation into a real and an imaginary part results in

$$\frac{\gamma(\zeta_{ko})}{2}-\frac{1}{t}\oint_k^c\gamma(\zeta_k)K_1\left(\frac{\zeta_{ko}-\zeta_k}{t}\right)|d\zeta_k|=c_{\infty\xi}\cos\vartheta(\zeta_{ko})+$$

$$+c_{\infty\eta}\sin\nu(\zeta_{KO})+\frac{1}{t}\oint_K^C u_\eta(\zeta_K)K_{II}\left(\frac{\zeta_{KO}-\zeta_K}{t}\right)|d\zeta_K|$$

solution of which gives the distribution $\gamma(\zeta_{KO})$ and where the kernel functions of the equation with the known functions of influence [4]:

$$K_I\left(\frac{\zeta_{KO}-\zeta_K}{t}\right)=-\phi\left(\frac{\zeta_{KO}-\zeta_K}{t}\right)\cos\nu(\zeta_{KO})-\Psi\left(\frac{\zeta_{KO}-\zeta_K}{t}\right)\sin\nu(\zeta_{KO})$$

$$K_{II}\left(\frac{\zeta_{KO}-\zeta_K}{t}\right)=\Psi\left(\frac{\zeta_{KO}-\zeta_K}{t}\right)\cos\nu(\zeta_{KO})-\phi\left(\frac{\zeta_{KO}-\zeta_K}{t}\right)\sin\nu(\zeta_{KO})$$

In the knowledge of $\gamma(\zeta_{KO})$ the rotating system velocity on the contour is

$$W(\zeta_K)=\gamma(\zeta_K)-u_\eta(\zeta_K)\cdot\sin\nu(\zeta_K)$$

Kernel function K_I of the integral equation is continuous, but K_{II} has a pole at $\zeta_K=\zeta_{KO}$. Decreasing blade thickness the numerical solution of the integral equation [4] becomes a more difficult and in case of an infinitely thin blade, kernel function K_I degenerates into a singular one.

The integral equation has an infinite number of solutions.The individual solution can be met by specifying a uniqueness condition. It has been defined according to [5].

RESULTS

A cascade with the radius ratio R_1 = 0,448, number of blades z = 9 and blade thicknesses d = 8, 12, 16, 20 mm measured at the inlet, was tested. While the solution of the computation method (I), based on the Fredholm integral equation is valid only for not too thin blades, by the difference method (D) cascades of disappearing blade thickness or a thickness of d = 4 mm could also be computed.

In Fig.3 pressure and suction side wall velocities are plotted for a case of shockless entry as well as the characteristic curve for d = 8 mm. Based on the pressure side velocity distributions a satisfactory accordance is observed. Deviations of the velocity distribution along the suction side are due partly to the difference of the blade edge models and the

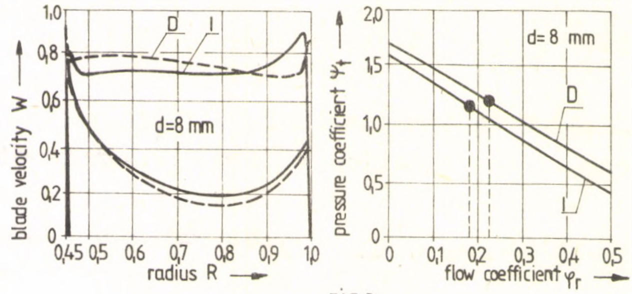

FIG.3

downwash conditions, partly to the different volume number values regarding to the so-called shockfree inlet $\varphi_r = \varphi_{r\,opt}$. Comparison of the theoretical characteristic curves is similarly satisfactory, stressing again the decisive influence of the downwash condition on the rear edge of the blade.

VARYING THE BLADE THICKNESS AND EXTRAPOLATING TO INFINITELY THIN BLADES

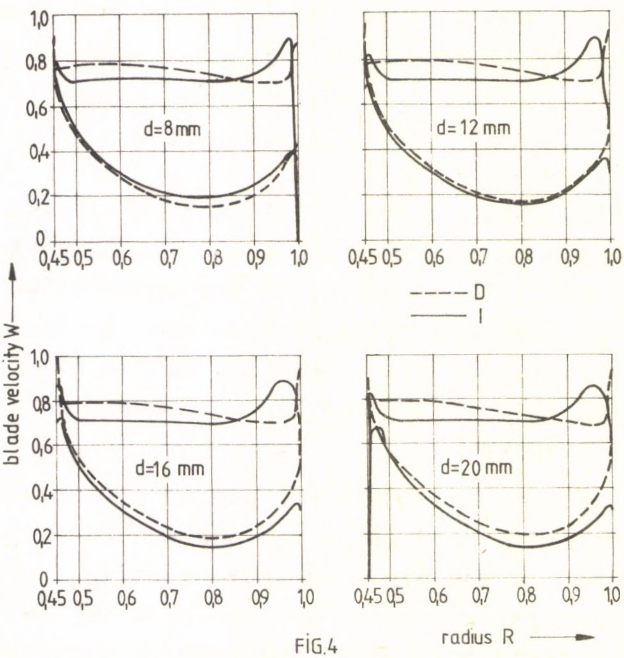

FIG.4

Velocity distributions

Comparing blade thicknesses d=12,16,20 mm to blade thickness d=8, velocity distributions surround the blades are plotted in Fig.4 at working points of shockfree inlet. As to suction side curves, no fundamental change for thickness variations are observed, whereas the pressure side results correspond well especially for thickness d=12 mm.

This property becomes plausible when considering that both downwash conditions for d=12 mm yield the same value for the relative velocity volume component at the intersection of the skeleton line and the blade rear edge.

CHARACTERISTICS AND DISTINCT BLADE VELOCITIES IN COMPARISON WITH THE SOLUTION OF BUSEMANN

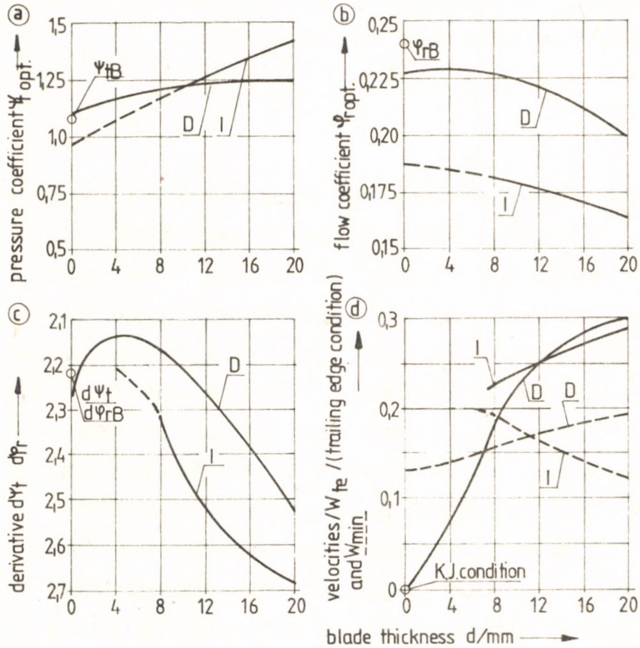

FIG. 5

Fig.5 a,b shows pressure coefficients $\Psi_{t\,opt}$ and volume numbers $\varphi_{r,opt}$ referring to the optimal points in function of blade thickness d. For d=0 the result obtained with the difference method can be compared to the analytical solution of Busemann [3]. Both the pressure coefficient $\varphi_{t,opt}$ and the volume number $\varphi_{r,opt}$ show the same tendencies for both calculating systems. If the curve shapes obtained with the Fredholm integral equation are extrapolated to the blade thickness d=0, the deviation from the Busemann solution can be explained by the reduced numerical accuracy for small blade thicknesses.

Fig.5c shows the slopes of characteristics as function of the blade thickness. In method (I) the rate of changes increases in function of blade thickness monotonically,and that in case of (D) starting from d = 0 is small and gets greater latter. If this effect has a numerical nature or so - it must be cleared up by a discretization analysis.

In Fig.5d the velocities at the intersection of the skeleton line and the rear blade edge are plotted over d (full line). Curve shapes for both computation methods increase monoton - ously, while the difference method result changes consequently into the Kutta-Joukowsky condition at the transition d = 0. In this diagram also the wall velocity minima are recorded on the pressure side of the blade. Reason for contradictory tendencies at indeed relatively satisfactory agreement may be found in the difference of the blade edge conditions.

COMPUTING TIME

Beside accuracy of the results also the running time rate is of great importance in all numerical methods. In Fig.6 the CPU times are plotted for both computation methods in function of the blade thickness. Contrary to method (I) which shows no difference worth mentioning in computing time for different blade thicknesses, the CPU-time increases with greater blade thickness for method (D). This effect occurs not because of worsening of the convergence but because of the increase of the number of net points to be calculated in the inlet and downwash range, whereas the number of net points in the blade domain remain constant.

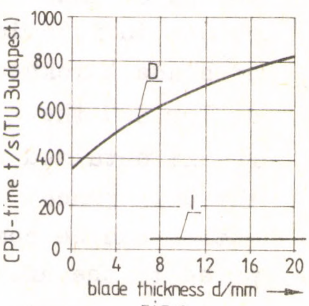

FIG.6

By means of this diagram the advantages of a rapid computing method become evident.

CONCLUDING REMARKS

Comparison of two methods for the computation of an inviscid flow through plane, rotating radial blading yields a satisfactory accordance in all essential tendencies. The fundamental deviations are based on the difference of the applied - in themselves - consequent blade conditions. The method based on solution of the Fredholm integral equation shows an important superiority with regard to the computing rapidity, whereas the difference method is not impaired by the blade thickness.

REFERENCE

1 Steck,E.; Schilling,R.: Berechnung des Betriebsverhaltens von Radialgittern am Beispiel der reibungsfreien Strömung. Strömungsmechanik und Strömungsmaschinen 26, (1976)

2 Steck,E.: Berechnung des Betriebsverhaltens rotierender Radialgitter, Karlsruhe, Universitat /TH/, Dr.Ing.Diss. 1981.

3 Busemann,A.: Das Förderhöhenverhaltnis radialer Kreiselpumpen mit logarithmisch spiraligen Schaufeln. Z.f.angew. Math.Mech. 8,5 (1928)

4 Fűzy O. - Thuma A.: Calculating the velocity distribution of a blade airfoil cascade given by its geometry. Proc. of the 3rd Conference on Fluid Mechanics and Fluid Machinery, Budapest, 1969.

5 Fűzy O. - Sebestyén A.: Generalization of the downwash condition for a dynamic case. Proc. of the 7th Conference on Fluid Machinery.

Dr.-Ing. STECK,E. - Prof. Dr.-Ing. FELSCH,K.O.
Inst. für Strömungslehre und Strömungsmaschinen,Univ.Karlsruhe
D-7500 KARLSRUHE, Kaiserstrasse 12

Dr.-Ing. SEBESTYÉN,A. Dept. of Hydraulic Mach. T.U. Budapest,
H-1521. BUDAPEST, Stoczek-u. 2/D.

THE INFLUENCE OF THE PHYSICAL PARAMETERS OF FILLING LIQUIDS ON THE CONSTRUCTION AND TORQUE TRANSFER OF HYDRODYNAMIC COUPLINGS

Sebestyén,Gy. - Katona, L. - Demény, J.

The paper deals with the problems of using water and waterbased inflammable liquids as working liquids for hydrodynamic power transfer in couplings; discusses construction problems arising from the obligation of taking the physical parameters of water into consideration.

A./ INTRODUCTION

The application of water in hydrodynamic power transfer is not unknown. It has been used mainly in high duty couplings connected to cooling systems (scoop tubes) with good results. There is a more limited application also for constant-filled couplings where again it is the basic medium of the emulsion working liquid.

It is a well known fact that in hydrodynamic power transfer mechanisms - and to narrow down the circle, in hydrodynamic couplings - the manufacturers suggest, or prescribe, certain kinds of filling liquids. Up till now these included chiefly oils of hydrocarbon base, whose non-desirable operational properties were restricted with the addition of certain additives. However, serious accidents at workplaces exposed to the danger of fire soon brought up the necessity of using high-flash liquids which do not promote burning, are either inflammable or only so to a low degree. At the same time the extremely fast rising of oil prices made it necessary to fully exclude oil as a potential working liquid, if possible, from power transfer.

The use of oils of hydrocarbon base though not an absolute necessity, gave also a convenient and simple solution for the problem a greasing those parts of hydrodynamic structures as needed greasing.

In the past 10, or rather 5 years, several attempts and results were attained for a wide-range application of water as the most natural and cheapest filling - with all the consequences included.

B./ THE PRESENT SITUATION

The hydrodynamic power transfer structures working with at present known non-inflammable working liquids - meaning hydrodynamic couplings and their construction - have been applied to the physical parameters of the new filling liquid.The changes which were necessary for the inside construction as well as the change of density and viscosity as compared to that of hydrocarbons have exerted favourable influence of the geometrical measures of the couplings.

B.1./ The influence of physical parameters of the filling liquid on the torque transfer

The determination of the torque transfer of the hydrodynamic coupling can be made from the following correlation:

$$M = \rho\, K_M\, n_1^2 . D^5$$

where K_M is the torque factor, and

$$K_M = A\, q\, \Delta\vartheta \qquad q = q(c_r)$$

and

$$c_r = c_r(\nu)$$

where

- ρ is the density of the medium
- n_1 is the primary speed
- D is the characteristic diameter
- A is the constant containing geometrical data, too
- q is the specific volume flow
- $\Delta\vartheta$ is the specific spin change
- c_r is the friction factor
- ν is the kinematic viscosity.

In case of the same hydrodynamic coupling (n_1 = const), the influence of working liquid can be taken into consideration (in comparison with the earlier correlations):

$$\frac{M}{M^*} = \frac{\rho}{\rho^*}\left(\frac{\nu^*}{\nu}\right)^m$$

where $*$ marks the reference liquid.

It can be stated from the correlation that density is directly proportional to torque transfer. The judgement about viscosity is less certain [1]. Our earlier investigations [2] have shown that "m" changes 1/10-1/25 depending on the modification, in other words, the influence of the change in viscosity can be, under certain circumstances, neglected.

Nowadays in order to eliminate the use of oils of hydrocarbon base synthetic liquids are being searched and used over a wide range of composition and their application has brought favourable changes in density (e.g. $\rho = 1200 \sim 1300$ kg/m^3), yet the viscosity properties have reduced the advantages brought about by the change in density.

Fig.1. shows the changes of viscosity in synthetic liquid (a) silicon oil, hydrocarbon oil (b) and water (c) as functions of temperature, with density changes also presented.

Besides Fig.1. shows the outstanding properties of water in power transfer.

The temperature operation range of the couplings had been earlier determined partly by the comperatively low flash point of the filling liquid; partly by the strength tolerance of the

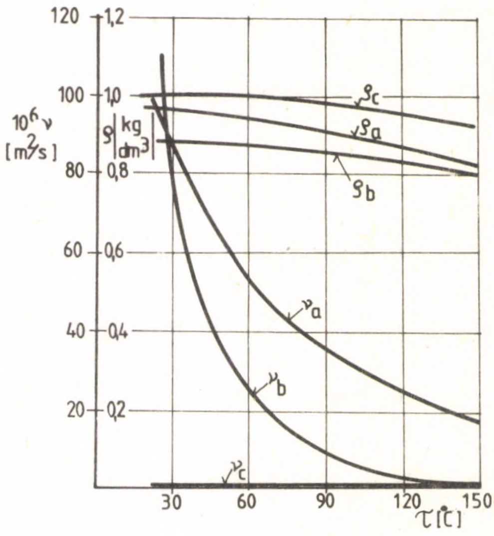

Fig.1

housing and structural elements made usually of aluminium moulding. In this respect, today the Ist de - gree of safety operation is in the range t=130-150°C. In the case of hydrodynamic couplings working with non-hydrocarbon filling liquids (primarily water and water-base working liquids),which begin to operate at higher temperatures, the safety installations have a temperature range of 150-210°C, representing the IInd degree.

These values are in close contact with the physical parameters of the filling liquid. Fig.2. presents the changes of the saturation pressure as function of temperature.

B.2./ Consideration of other influences of the filling liquid

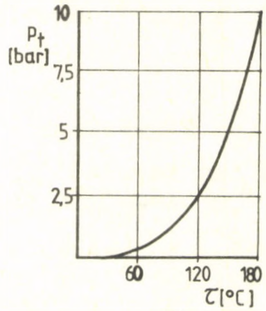

Fig.2

The most important damage caused by water and water-base filling liquids is corrosion, in structures where the material is prone to corrosion. In this respect the employment of emulsion has given no solution either because of the wide temperature range and the unwanted changes appearing in the constitution of the emulsion.

If in regard of construction the hydrodynamic couplings working with hydrocarbon liquids are considered - where the gearing and working space are common - the corrosion can cause full breakdown.

It is quite obvious that with the exception of special corrosion free and water-greased gearings, the protection of the gearing from the working medium is an essential task for the construction.

In the case of non-water base, non-inflammable synthetic liquids the keeping up of the greasing quality is, together with the anti-corrosion properties, essential just as well as the sealing of the spaces, which often demand special materials. Several synthetic filling liquids are suitable for press transfer, but do not come up to the requirements of health and environment defence in view of the wide temperature range (irritating vapours, poisonous liquids, etc.) [3].

Our own researches [4] have shown that silicon oil derivates as synthetic liquids, have met the requirements for filling liquids in all respects; however, high prices make their application practically impossible for workshop operation.

The working liquids of hydraulic systems form a separate category. In the mines these liquids can be advantageously stored and therefore their application as liquids in hydrodynamic couplings is being considered. The marks and characters of such working liquids are:

HFA (water-oil emulsion)
HFB (oil-water emulsion)
HFC (water glycol mixture)
HFD (water-free liquid)

The prescribed temperature limits as well as the expenses from meeting environment defence prescriptions for synthetic liquids rarely support the application of these liquids. [5], [6], [7].

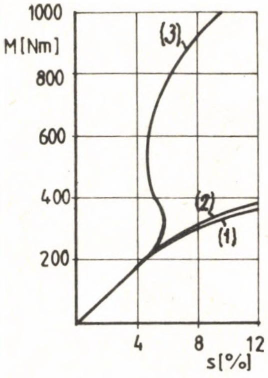

Fig.3

Fig.3. gives characteristics of a hydrodynamic coupling for water (1), for emulsion oil (2) and oil-water emulsion of 5% (3) at a some partly degree of filling liquid. According to the curve (3) at slip s = 4-6% the "deformation" of filling liquid caused vibration in the hydrodynamic coupling.

The cheap and in vast quantities disposable filling liquid for couplings is water, if the requirements rendering it wellapplicable can be satisfied.

B.3./ The construction of hydrodynamic coupling in case of water and water-base filling liquid

If water and water-base, non-inflammable filling liquid is applied, the influence of the physical parameters of the filling liquid must be taken into consideration in the construction of the coupling to ensure safe operation.

In the present consideration no attention is paid to the elements of the structure in contact with the filling liquid, with the exception of the gearing. The protection of the former parts is chiefly a matter of choosing the proper material. Here the problems and solutions of gearing as well as the safety methods and processes are discussed.

As for gearing protection there are two solutions known so far in the present constructions. The first - more widely used - method is, starting from the earlier construction of hydrocarbon-filled couplings, that a sealing element is placed between the working space and the gearing with the purpose of keeping liquid out of the gearing space. This sealing ring seals - especially in the temperature range of the safety devices - the space under pressure. The pressure decreasing way leads

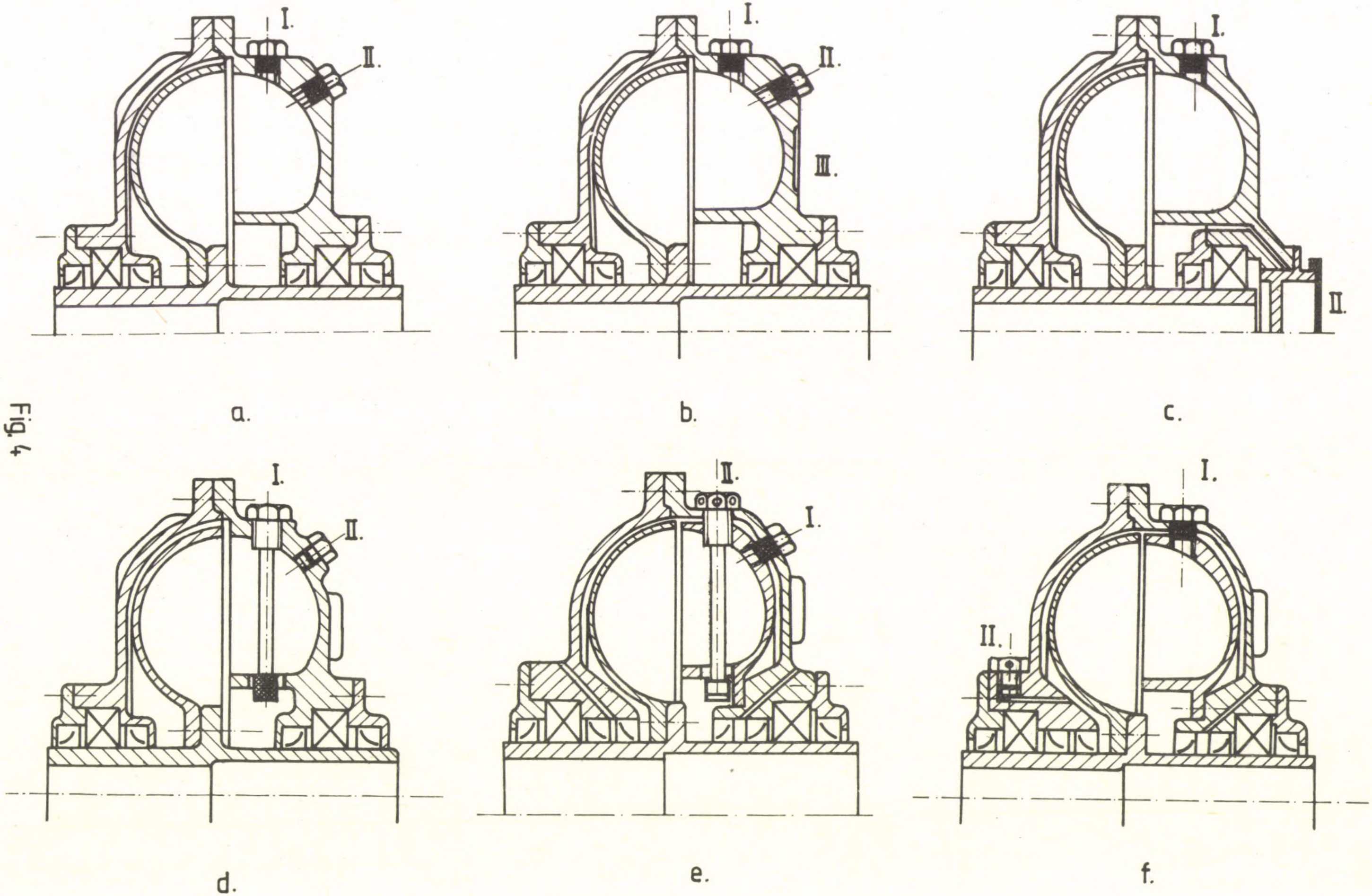

Fig. 4

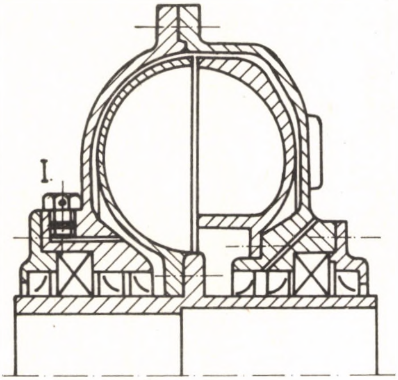

Fig. 4/9

through the gearings (Fig.4.) [8],[9]. The second method is making a double seal between the working space and the gearing for the protection of the latter. The space between the seal-rings can lead into a puffer-space, or into the atmosphere. Corrosion damage to the gearing can thus be greatly diminished, practically eliminated.

Another important field is the creation of safe operation; there have been several variations so far. The hydrodynamic coupling shown in section presented in Fig.4. aims at perfection only from the point of view of working space, sealings and safety measures; the connection on the engine side and the conditions on the driven side are not shown in detail.

As regards the safety elements of the coupling almost every variation kept the plug fuse element of hydrodynamic couplings operating with hydrocarbon filling liquid; though there are constructions based on a single cleavage disc working in the temperature range $t = 130\text{-}150^{o}C$.

The cleavage disc safety device - actually a device of the IInd safety degree - is placed basically on the principle of being independent of the additional pressures and yet sense the saturation pressure and work accordingly.

The main kinds of safety elements and their locations are shown in Table I.

The construction and operation characteristics of the safety devices can be followed from the illustration.

The safety measures taken at the mounting of the whole coupling serves also for the safety of the operation.

Finally it can be mentioned that where the conditions are specially exposed to the danger of fire outbreak and aluminium may be the source of danger when employed, couplings with steel plated casing may be recommended.

CONCLUSIONS

1. When reviewing the reference and development work it can be stated that in the field of hydrodynamic power transmission the conditions for using water-filled hydrodynamic couplings are good enough for replacing couplings with hydrocarbon filling liquids.
2. If water filling is used, the hydrodynamic couplings have

I. Table

Mark*	Ist safety degree $t_{oper.}$ °C	way	location	IInd safety degree $t_{oper.}$ °C	means	location	IIId degree	gearing protection	
a	140	OBCS	on outer casing	170	OBCS	on outer casing		one sealing ring	
b	120	OBCS	on outer casing	150	OBCS	on outer casing	casing cracks	one sealing ring	[9]
c	130	OBCS	on outer casing	>170	HT	tied to theoretical center of axis		one sealing ring	[10]
d	150	OBCS	reaches into coupling inside	150	HT	on outer casing + OB combined		one sealing ring	[8]
e	140	OBCS	on outer casing	150	HT	deeply reaching into coupling inside		double sealing ring with leading out	OBV BME
f	140	OBCS	on outer casing	150	HT	on casing near the axis		double sealing ring with leading out	OBV BME
g	140	HT	on casing near the axis of rotation	-	-	-		double sealing ring with leading out	OBV BME

OBCS = plug fuse, HT = cleavage disc,
OBV = State Enterprise for Mining Machinery,
BME = Technical University, Budapest

* Variation corresponding to marks see in Fig.4.

better specific performance parameters than those using oil filling, which leads to smaller sizes.

3. The application of emulsions, with due regard to the relatively high safety temperature and the prescriptions for the use of emulsions, must be preceded by very serious considerations.

   Though silicon oils can be used in traditional oil-type couplings in principle without limitation, when the safety devices start working, very high values get lost.

4. Careful consideration must be given in forming the sealing systems to high operation performance; to up-to-date and safe operation in selecting the safety elements, and to quick servicing conditions.

REFERENCES

[1] ROZWADOWSKI,E.: Analiza wplywu parametrow fizycznych cieczy roboclej oraz niektorych parametrow geometrychny elementow przeplywowych na parametry energetyczne sprzegla hydrodinetycznego. Hydroforum-80. Porabka Kozubnik 1980.2. 362-378.

[2] SEBESTYÉN,GY., DEMÉNY,J., KATONA,L. and BALÁZS,K.: The influence of filling liquid's characteristics on the torque transmission of hydrodynamic couplings. Proc.of the sixth Conf.on Fluid Machinery, Budapest, 1979. 1025-1032.

[3] MOLNÁR,J., LEHOTZKY,K., M.SZEBERÉNYI,S., A.PAKSY,K. és MOLNÁR,A.: Tíz hidraulikus munkafolyadék akut toxikológiai vizsgálata. Munkavédelem. 1977.XXIII. 1-3. 19-24.

[4] SEBESTYÉN,GY., VARGHA,L., STVRTECZKY,F. and KATONA,L.: Working fluid of high flash-point in fluid couplings. Proc.5.Conf.on Fluid Machinery,Budapest,1975. 979-985.

[5] BLANPAIN,G.: Étude des propriétés des fluides difficilement inflammables liees a l'elimination des huiles de transmissions hydrauliques. Industrie minerale-mine. 1974. V-VIII-IX. 1-14, 103-120.

[6] GUSE,W.: Schwerentflammbare Druckflüssigkeiten-Eigenschaften und Verwendung. Ölhydraulik und Pneumatik. 24 (1980) Nr.6. 449-454.

[7] Arbeiten mit Druckflüssigkeiten; Auswahl-Betriebsprobleme-Instandhaltung. = Ölhydraulik und Pneumatik. 25 (1981) 12. 889-896.

[8] FLUIDRIVE Performance and life tests on fluidrive 390 and 475 akwafil fluid couplings. Test report No (75) 10.

[9] Predohranitel'naja gidromufta GPV 400. IGD Moszkva 1977.

[10] BEKLENKO,V.P. LEUSTENKO,A.V.: O szrizsenii pozsaro-opasznoszti gidromuft. Ugol 1978. 12. 45-47 p.

[11] Beschreibung und technische Daten von Wassergefülltes hydrodinamischen Kupplungen Typ HDK-V-XXX-1. Budapest, 1982. OBV.

SEBESTYÉN, Gyula
Dr.Eng.Cand. of T.Sc.
Associate professor
Techn.Univ.Budapest

KATONA, Lajos
Head of Dept.
OBV. Budapest,X.
Fertő u.8.

DEMÉNY, Judit
Dr. Eng.
First assist.

INVESTIGATION OF PUMP NOISE SCALE EFFECT

Sebestyén,Gy., Rizk,M., Szabó,Á.

In the paper the authors present results of investigations made with experimental pump. In the investigation the effect of changes in speed on the flow noise level was searched. It has been shown that the value of noise level in the range significant for the investigation of cavitation changes by the ~4th exponent of the increase in the speed, while in the range of mechanical noises the characteristic frequencies show changes according to diverse exponents of pheripheral velocity depending on cavitation whether it occurs.

A./ INTRODUCTION

The extent and intensity of cavitation appearing in hydraulic machines and other places obstructed to visual observation are increasingly determined by detecting methods which include the measuring of characteristic pressure, the determination of sound pressure level, the registration of machine vibrations, and other methods of examinations [1], [2], [3], [4].

The reason for the increase in noise level when cavitation begins in steady flows with constant velocity was determined to be the appearance of noise generators, which had been identified as the vibrations of bubbles at resonance frequency, or the pressure thrust from bubble collapse, and/or the jet impacts appearing at the collapse of the configuration of cavitation flow.

In the case of hydraulic machines the possibility of investigating constant flow velocity is restricted to a very narrow section of all research. That is why a wider investigation of the noise effect caused by changes in speed has become justified.

B./ DESCRIPTION OF THE EXPERIMENTAL EQUIPMENT

The investigations were made at the pump test rig of the Department of Hydraulic Machines of the Technical University of Budapest (Fig.1.: 1.pump with balance-motor, 2.imp.reg. and marker, 3. orifice, 4. booster pump, 5. tank, 6. noise meas. devices, 7. photo and observation). The semi-open impeller placed in pump had 4 blades, whose sketchline is $\beta = 15^{\circ}$ logarithmic spiral, outer diameter D_2=155mm, blade thickness s=6 mm. Noise examination was made by a Brüel and Kjaer acceleration sensor and narrow-band frequency-analyser mounted on the scroll.

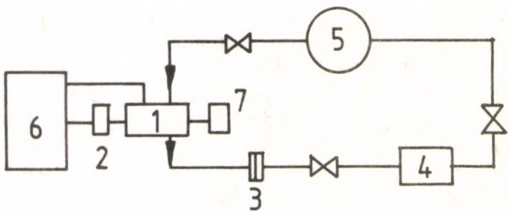

Fig.1

Frequency range for measurement was 20 kHz. In the investigation use was made of earlier investigation results which yielded the possibility of determining the intensity of cavitation flow (and in this connection the extent and measure of proceeding of the cavitation) by noise level measurement at any discrete frequency at least in the f > 5 kHz range.

C./ INVESTIGATION RESULTS

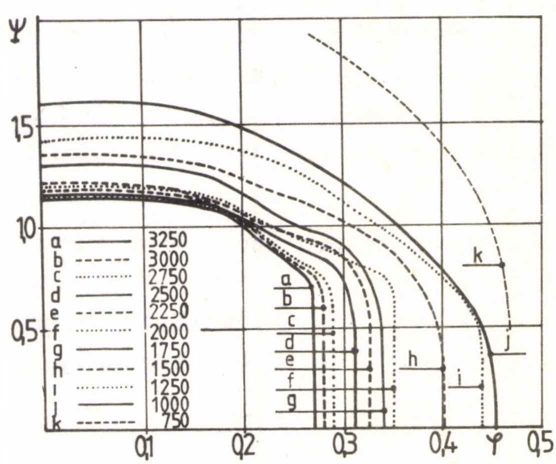

Fig.2

The examinations were made in the n=800 - 3250 r.p.m. speed range. The $\varphi - \psi$ dimensionless character curves are shown in Fig.2. Here

$\varphi = \frac{Q}{A_2 u_2}$ is the flow rate coefficient

Q rate of flow

$A_2 = D_2^2 \pi / 4$, where D_2 is the outer diameter of the impeller,

u_2 peripheral velocity

$$\psi = \frac{2gH}{u_2^2}$$ head coefficient, and H head.

As seen in Fig. it can be stated that the law of affinity can be used only to a limited degree in the n = 3200-2000 r.p.m. speed range; under that value the conversion correlations are not valid even to a limited degree.

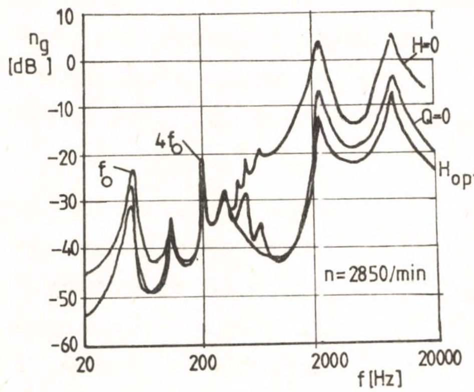

Fig.3

For an overall view of the noise investigation results Fig.3. shows noise level pictures of some well defined points on the curve of the pump.

The acceleration level is defined with the correlation $n_g = 10 \lg (g/g_0)^2$ where

g is the concrete acceleration measured at the given frequency,

g_0 is the relative acceleration (=gravitation acceleration).

In the investigations the data given for the acceleration are the ones made in only one direction. Earlier investigations have shown [5] that the acceleration vector in its direction is dependant of the flow conditions. Its position in space and its absolute value is changing with the changes in the flow conditions, expecially when cavitation appears and develops. Therefore the measurement of the projection component in any direction of the acceleration vector gives qualitatively correct result.

In Fig.3. the characteristic points and ranges of the spectrum are the following:

f_0 is the frequency corresponding to the speed

$4f_0$ is the blade frequency

20-1000 Hz is the basic range of mechanical noises

1000-2000 Hz is the transient range

2000-20000 Hz is basically the range characteristic of cavitation noises.

Here the near-parallel shape of the curves show that measurements at any frequency are suitable for investigating noises characteristic of the flow structure.

The given spectrum also refers to the fact that in the frequency range the results obtained by measuring unscreened noises - in unison with the measurement results at discrete frequencies - reflect primarily the characteristic features of noises connected with flow conditions. These statements are in good accordance with the results of cavitation noise investigations made earlier.

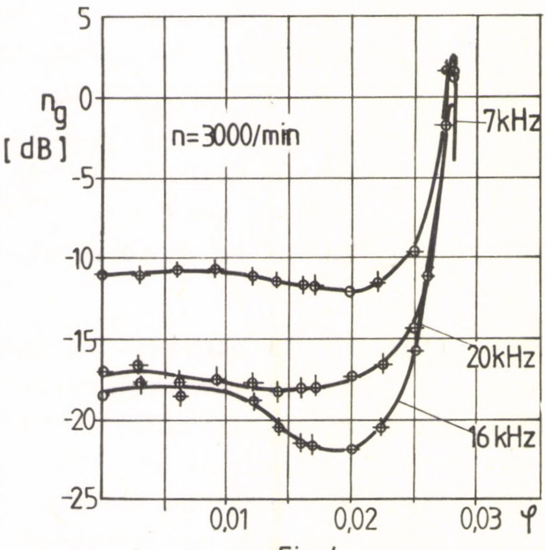

Fig. 4

From the results of investigations made at discrete frequency Fig. 4. shows the so-called noise level curve. It must be mentioned that the minimum of the noise level curve belongs to the optimum efficiency operation range (impact-free entry into the rotating cascade), the noise level peak appearing with greater φ indicates the development of cavitation on the pressure side of the blade - surpassing the maximum intensity range to the blocking state - (which is the recurving part of the noise level curve).

The diagram of Mc.Nulty and Pearsall [6] containing the characteristic of flow-acoustic cavitation number is shown in Fig.5. The correspondence between the two diagrams is, qualitatively, adequate.

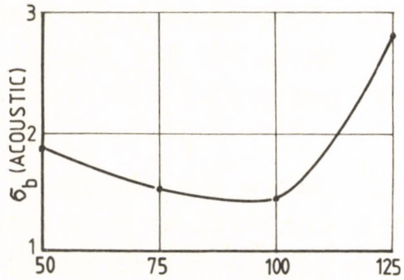

Fig.5

Though in the given arrangement the basically mechanical noises are at relatively low levels, they (f_o,$4f_o$) give direct information of the extent of noise level changes with the changing of the speed.

In Fig.6. the changes in the noise level of the basic generating frequency, or the blade frequency, resp., are shown as functions of the speed. By force of the correlation between intensity and velocity

$$I \sim v^m$$

authors could state the following relations: the value of m

for $n < 2000$

$m_{f_o} = 3,6$ and

$m_{4f_o} = 3,3$

for

$n > 2000$

$m_{f_o} = m_{4f_o} = 11$

are essentially the same.

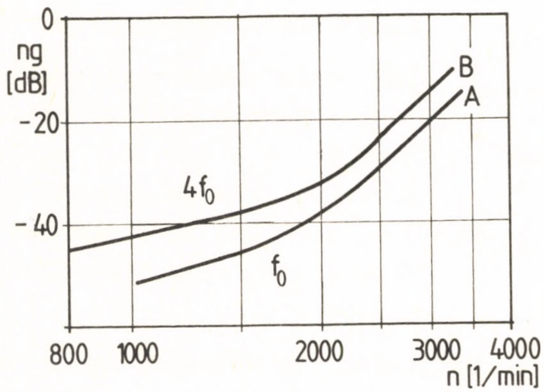

Fig.6

It must be noted that f_o values were examined for Q=0 and H=0 resp., while $4f_o$ values were examined in a speed-range above n= 1500 ~ 2000/rpm. for Q=0 and H=0, resp., where intensive cavitation developed on the impeller blades. According to this there was superimposed to the mechanical noise a connected cavitation noise becoming more intensive with increasing speed. Here the separation of the cavities act as first rate noise radiators, the bubbles as monopols. The radiated performance is of 0 order for noise radiator $P \sim v^5$ and in case of a dipole $P_d \sim v^6$ and $P_d \sim v^7$, resp. [7], [8], [9], [10], [11].

Depicting the noise level curves as functions of φ (Fig.7.)

- in the range $\varphi = 0$ and the best efficiency point - the levels are different because of different speeds, owing to the limited applicability of the law of affinity for the present case; after the best efficiency point they are diverse because of their characters.

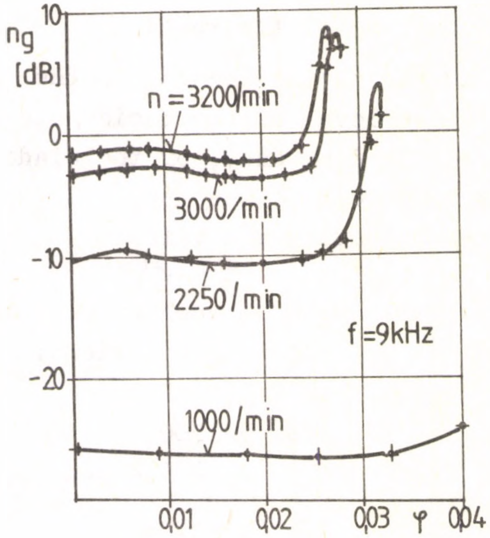

Fig.7

Fig.8. shows the changes of the noise level as functions of the speed. The curves are divided to two characteristic sections: partly showing the range where the law of affinity is valid; partly the range where this law is excluded ($n < 2000$/min).

The scale numbers referring to the change of the speed, here are $m_A = 4-8$, and $m_B=4-6$, where we ordered the state: H=0, to A and to B the Q=0 flow state, resp. ($n > 2000$, $m_A=m_B= 4$).

In an earlier work we had investigated the velocity scale number of cavitation flow. Fig.9. gives the investigation results.

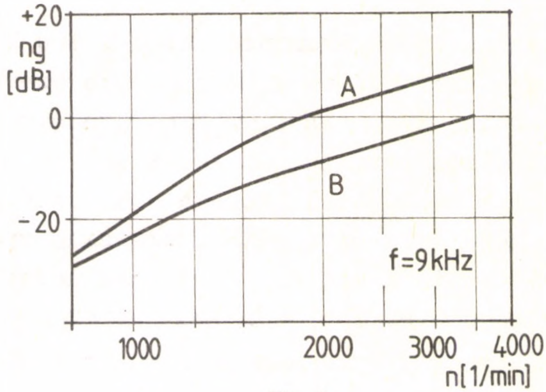

Fig.8

The influence of flow velocity and vibration intensity is proportional to $m \cong 5$ exponent of the velocity. These results are corroborated by the research results of other authors, too [12].

CONCLUSIONS

The investigation results of cavitation and vibration in pumps can be summed up as follows:

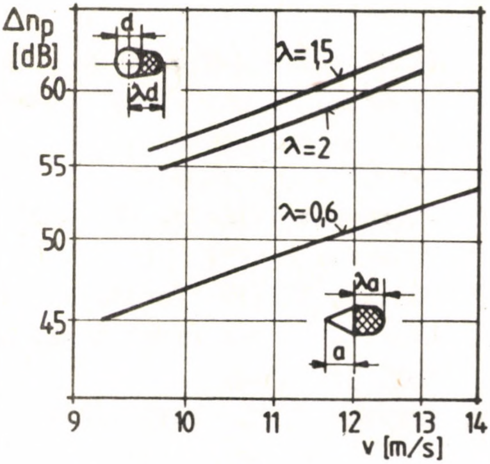

Fig.9

a./ In case of changes of the impeller speed at generating frequencies (f_o is the frequency corresponding to the speed, and, as in the present case, $4f_o$ is the blade frequency), the noise level changes according to the m= 3,5 and 11, resp. exponent of the frequency quotients.The latter result is the function of the effect of noise generators changing with the development of cavitation.

b./ In the range where the law of affinity is valid - with noise investigation at discrete frequency - the noise level changes according to m_n = 6 exponent of the revolution number quotients. Beyond the validity of the affinity law the value of the exponent m $\geqq$ 6.

c./ Since results obtained from noise investigations made with different velocities but identical cavitation show that the noise level changes according to the $\sim$ 5th exponent of the velocity quotients. In view of a. and b. in the range of the law of affinity, the noise intensity can be converted over a wide range of the speed, whereas in the operation ranges outside the power of that law the intensity can be converted for the operation in question only with a narrow case of velocity change.

REFERENCES

1 VARGA,J.J., SEBESTYEN,G., FAY,A.: Detection of cavitation by acoustic and vibration-measurement methods. La Houille Blanche Nr.2/1969.

2 KERCAN,V., SCHWEIGER,F.: Cavitation phenomena detection by different methods. Proc. of the sixth Conf. on Fluid Mach. Budapest, 1979.

3 OBA,R., ITO,Y.: Cavitation Shock Pressures in a Venturi. Reports of the first High. Speed Mech. Tohoku Univ.1975. Vol. 32 33-49.

4 SEBESTYÉN,GY., STVRTECZKY,F., SZABÓ,Á. and VERBA,A.: Investigation of cavitation in pumps by direct and indirect methods. Acta Technica Tom. 71(3-4), pp.431-474 (1971)

5 SEBESTYÉN,GY., RIZK,M., SZABÓ,Á.: Some properties from cavitation-vibration tests on centrifugal pumps. (Proc.Joint Symp. on Design and Operation on Fluid Mach. COLORADO STATE UNIV. - Fort Collins. 1978)

6 McNULTY,P.J., PEARSALL,I.S.: Cavitation Inception in Pumps. Journal of Fluids Engineering, March 1982, Vol. 104/99.

7 SHALNEV,K.K., VARGA,J. and SEBESTYÉN,GY.: Accurate Determination of the Scale Effect Formula for Cavitation Erosion. Acta Technica 66/4.

8 BLOHINCEV,A.I.: Akustika neodnorodnoy dvishustsheysya sredu Gostehisdat, Moskva - Leningrad 1946.

9 CURLE,N.: The Influence of Solid Boundaries upon Aerodynamic Sound. Proc. Royal Society of London 231 (1955),Ser.A.

10 GERARD,J.H.: Measurements of the Sound From Circular in an Air Stream. Proc.Phys.Society 68 (1955).

11 STOWELL,E.Z., DEMING,A.F.: Noise from two-blade propellers NACA (1935). TN 526.

12 RAMAMURTHY,A.A., BHASKARAN,P.: Velocity Exponent for Erosion and Noise Due to Cavitation.J.of Fl.Eng.1979/3.

SEBESTYÉN,Gyula Dr.Eng.
Cand.of T.Sc.Ass.Prof.
Techn.Univ. Budapest

RIZK,Mohamed Dr.Eng.
T.U.Cairo
EGYPT.

SZABÓ,Ákos
sen.res.eng.
T.U.Budapest

PREDICTION OF THE REVERSE FLOW AND PREROTATION IN CENTRIFUGAL PUMPS

H.Mete Şen

SUMMARY

This paper is based on the impeller inlet flow and related phenomena in centrifugal pumps at partial capacities. The impeller design parameters which might affect the onset of the reverse flow and prerotation were investigated experimentally. It was found that the aerodynamic blade loading and its spanwise gradient are the dominant design parameters for the control of the reverse flow and prerotation in suction pipe. A correlation factor was presented to predict the starting of the reverse flow at the impeller inlet.

1.INTRODUCTION

When centrifugal pumps operate at the best efficiency point and high capacities, the flow in the suction pipe is one-dimensionel,i.e. axial. If the capacity is reduced by throttling to a certain value, a three-dimensionel swirling flow starts at the impeller inlet. The flow at the outer periphery of the impeller eye is reversed. This flow phenomena is called "Reverse Flow and Prerotation". Reverse flow and prerotation propagates upstream in the suction pipe if the capacity is further reduced. The capacity which reverse flow and prerotation starts at the tip of the blade leading edge(section 0 in Fig.1) is named "Pump Critical Capacity". This is the main parameter to be identified in this paper.

Reverse flow causes abnormal suction pipe wall static pressure rise, noise, vibration, erosion on the blades and rarely surge. These undesirable phenomenon limit the centrifugal pump reliable operating range at partial capacities. Due to the nature of the problem, theoretical approach to the problem is very limited. Therefore, this study is based on experimental investigation in order to find out the governing parameters which influence the onset of the reverse flow and prerotation.

An extensive literature review on the subject is given in (1).

8 full size centrifugal pump models were tested. Overall and detailed flow surveys at the impeller inlet and exit were carried out. The impeller design parameters which have effect on the reverse flow onset and intensity, were clarified. Effect of the reverse flow on the pump overall performance is shown. A correlation factor based upon the impeller tip section diffusion ratio is proposed to predict the pump critical capacity.

2. TEST MODELS DESİGN CRITERIA

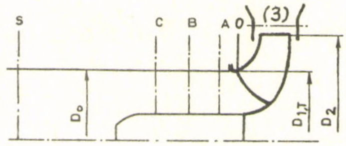

Fig. 1

The studies on the présent subject show that the reverse flow and prerotation in the suction pipe is directly related to the three-dimensional flow separation on the suction side of the impeller blade near the shroud (1)(2)(3)(4)(5)(6). Diffuser and volute do not directly affect the starting mechanizm of the reverse flow (1). Therefore, the impeller itself was taken as a basic element regarding the onset and intensity of the reverse flow. Three major impeller design parameters which are the most important and dominant parameters, were studied.

- Impeller inlet to outlet area ratio (meridional velocity ratio): A_0/A_2
- Value of the impeller tip section aerodynamic blade loading: $(C_{LA}\cdot\sigma)_T$
- Aerodynamic blade loading spanwise gradient: $(C_{LA}\cdot\sigma)_T/(C_{LA}\cdot\sigma)_H$

8 models in two series were designed. The following limitations were taken into account on the design of the test models, for both series.

- Pump design nominal point characteristics; Q_N, $(H_m)_N$ were kept the same
- The impeller-volute matching point was kept the same

3. TEST MODELS

The non-dimensional impeller design parameters are given in Table 1. Radial and meridional views of the test impellers are shown in Fig. 2.

I-A : It is the reference configuration of the I series. It has conventional-industrial design.

I-A1 : The main design criterium is the inlet to outlet area ratio which was increased 28% referred to the reference impeller A.

I-A2 : The main design criterium is the aerodynamic blade loading. It has almost uniform aerodynamic blade loading spanwise distribution. Aerodynamic blade loading at the tip section is reduced by reducing the aerodynamic lift coefficient; $\left[(C_{LA})_T\right]_{I-A2} = 0.7\left[(C_{LA})_T\right]_{I-A}$

I-A3 : The aerodynamic blade loading at the tip section is further reduced; $\left[(C_{LA})_T\right]_{I-A3} = 0.6\left[(C_{LA})_T\right]_{I-A}$

II-A : It is the reference configuration of the II series which has a conventional design. II series has higher specific speed than I series.

II-A1 : It has a particular design which aerodynamic blade loading decreases from tip to hub. Its blade exit angle increases from tip to hub where all the other configurations have uniform blade exit angle.

I-B, II-B : These configurations are out of the parametric study. They have lower specific speeds than the their series.

Model / Parameter	I - SERIES					II - SERIES		
	A(ref)	A1	A2	A3	B	A	A1	B
N_S	37.2	37.2	37.1	37.1	32.	46.	46.	43.6
Φ	0.120	0.120	0.128	0.136	0.098	0.130	0.118	0.146
ψ	0.865	0.865	0.833	0.834	0.940	0.903	0.859	0.805
z	5	5	6	7	5	6	5	6
AR	0.162	0.154	0.156	0.145	0.137	0.266	0.271	0.191
A_2/A_0	1.311	0.976	1.183	1.088	1.266	1.285	1.280	1.057
$(\beta_{2,T}-\beta_{1,T})_b$	5.	9.7	3.6	3.9	6.	6.	4.4	6.7
$\frac{(C_{LA}\cdot\sigma)_T}{(C_{LA}\cdot\sigma)_H}$	2.25	2.37	1.19	1.79	1.32	1.74	0.69	1.59
$\frac{(C_{LA}\cdot\sigma)_M}{(C_{LA}\cdot\sigma)_{M\,ref}}$	1.	1.12	1.01	0.81	1.42	1.38	1.45	1.05

Table 1

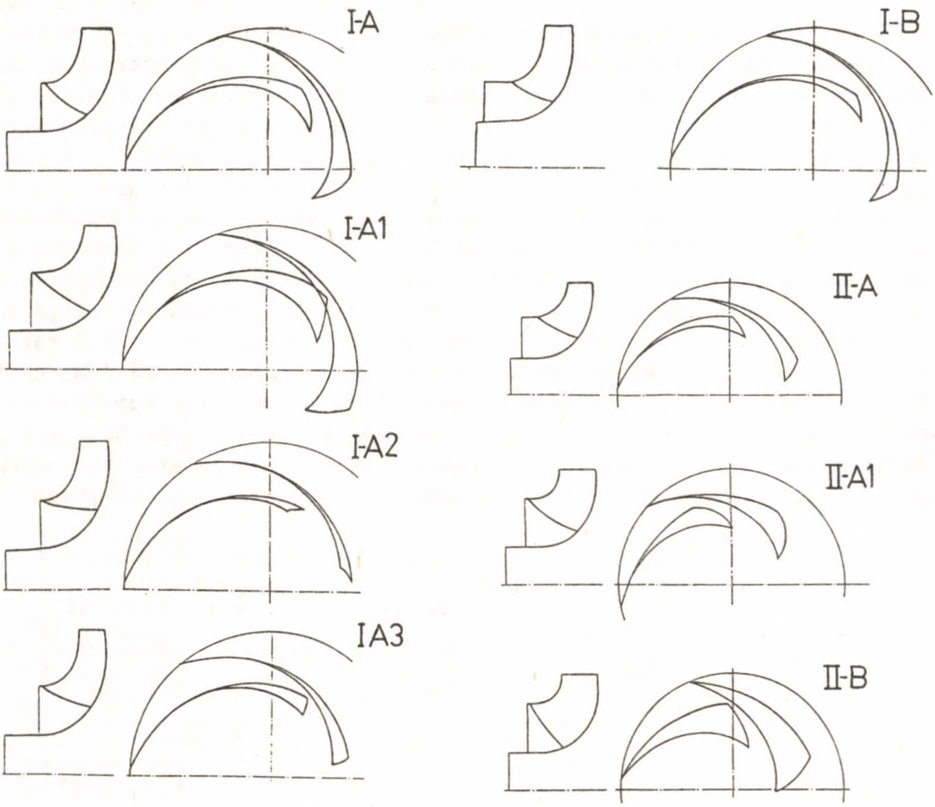

Fig. 2

4. EXPERIMENTAL ARRANGEMENT

The experiments were carried out in the pump facility of the von Karman Institute which operates as a close loop. The locations of the pump test sections are shown in Fig.1. A series of wall tappings are drilled around the circumference of the inlet test sections A,B,C and exit test section 3. Three-dimensional flow traverses were done at the inlet test planes, at different angular positions with properly designed five-holes probes. Two-dimensional impeller exit flow traverses were done at the test section 3, with wedge probes.

5. TEST RESULTS

This paper presents the main results of the study. The detailed results of the experiments are published in (1)(7). The major test results concerning the reverse flow, are summarized in Table 2.

Fig.3 shows the overall performances of the I series. Pump I-A1 has the most stable and highest head performance. I-A2 has the most unstable and lowest head performance of I series. Pump II-A has higher head curve than the pump II-A1, at partial capacities. The increasing order of the shaft power at partial capacities is the same as that of the head curve. Pump II-A has the highest pump critical capacity ($Q_{cr}=0.88Q_N$) and pump I-A2 has the lowest pump critical capacity ($Q_{cr}=0.53Q_N$) as given in Table 2. In the reverse flow region of the impeller inlet, the streamlines have high amount of total energy which is up to 55% of the pump manometric head. This energy is carried back by the reverse flow and dissipates in the suction pipe. Fig.4 shows the circumferentially averaged energy losses caused by the reverse flow, at the inlet test section A for I series. All the test results showed that the increasing order of the pump critical capacity, reverse flow losses, pump shaft power, head performance and head stability at partial capacities is the same. Pumps having high critical critical capacity, give higher reverse flow losses, higher shaft power, higher head and more stable head performance, than the pumps

Test Model	II-A (ref.)	II-B	I-A1	II-A1	I-B'	I-A	I-A3	I-A2
$Q_{cr}/Q_{N,des}$	0.97	0.79	0.77	0.77	0.70	0.63	0.59	0.46
$Q_N/Q_{N,des}$	1.10	0.97	0.89	1.05	1.03	0.91	0.87	0.86
$Q_{N,des}/(Q_{N,des})_{ref}$	1.	0.76	1.33	0.95	1.01	1.33	1.33	1.33
$Q_m/Q_{N,des}$	1.15	1.18	1.	1.17	1.18	1.04	1.	1.
$[(W_{1,T}/W_2)_{N,des}]/[(W_{1,T}/W_2)_{N,des}]_{ref}$	1.	0.85	0.85	0.81	0.85	0.81	0.77	0.77
$[(W_{1,T}/W_2)_{cr}]/[(W_{1,T}/W_2)_{N,des}]_{ref}$	1.01	0.94	0.94	0.87	0.94	0.92	0.95	0.98

Table 2

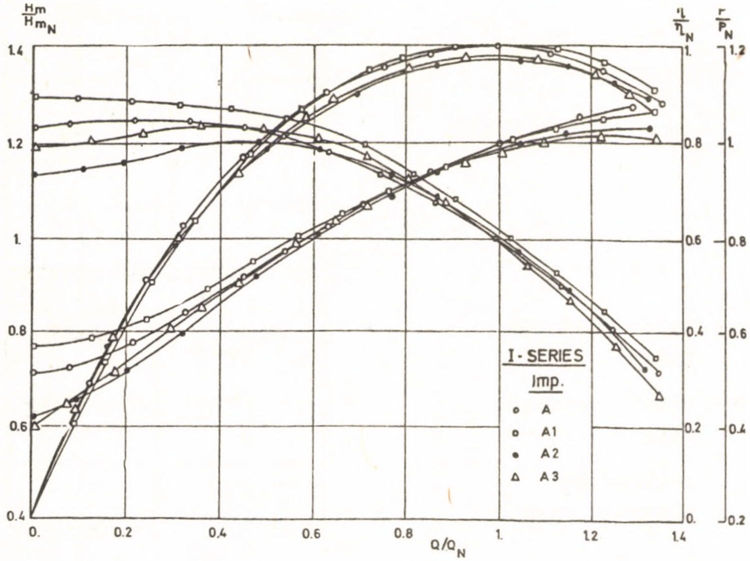

Fig. 3

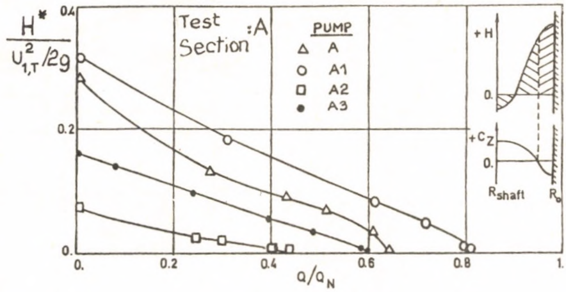

Fig. 4

having low critical capacity.

Fig.5 shows the total, static and centrifugal pressure rise through the impeller, at the blade tip, mean and hub streamlines for the pumps I-A, I-A1, I-A2. The aerodynamic pressure rise: $(W_1^2-W_2^2)/2g$ = Overall static pressure rise - Centrifugal pressure rise; gives a clear interpretation of the studied impeller design parameters, concerning the onset of the reverse flow. Pump I-A2 which has the lowest critical capacity, gives almost zero aerodynamic pressure rise and uniform spanwise aerodynamic pressure distribution at the nominal capacity. Pumps having high critical capacity such as I-A1, have higher aerodynamic pressure rise and larger aerodynamic pressure spanwise gradient than those having lower critical capacity. The trend of the aerodynamic pressure rise for all impellers is correlated to the trend of the pump critical capacity.

The above results state that the onset of the reverse flow and prerotation is related exclusively to the aerodynamic flow field phenomena.

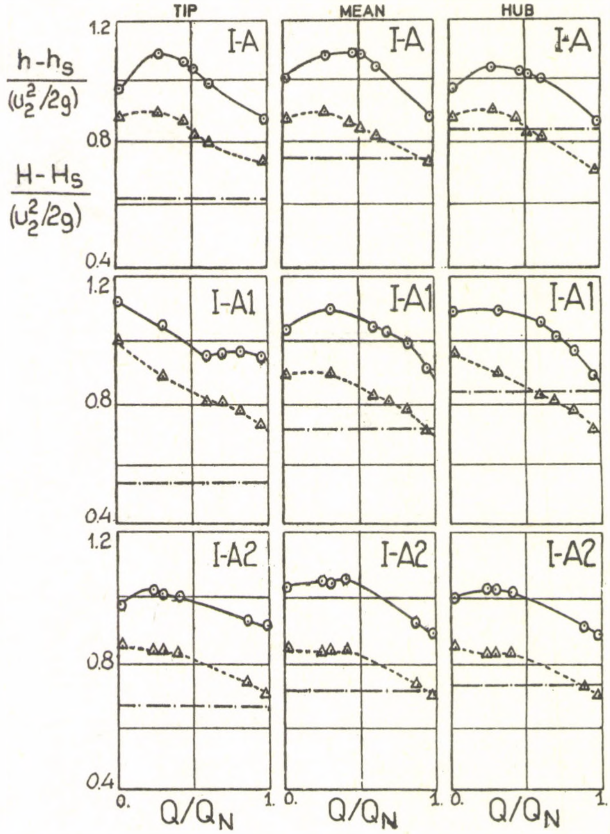

Fig. 5

—○— total pressure rise

—△— static pressure rise

—·—· centrifugal pressure rise

6. PARAMETERS AFFECTING PUMP CRITICAL CAPACITY

On the base of the test results, all the impeller design parameters were examined in order to find out the governing parameter or parameters, regarding the starting of the reverse flow and prerotation. It was clarified that none of the parameters, considered individually, controls the pump critical capacity. The following parameters have the strongest effect:

- Aerodynamic blade loading ($C_{LA}\cdot\sigma$) and its spanwise gradient $(C_{LA}\cdot\sigma)_T/(C_{LA}\cdot\sigma)_H$
- Impeller inlet to outlet area ratio (A_o/A_2)
- Aspect ratio (AR)

If the impeller-volute matching point differs too much from the nominal point, this peculiarity has to be taken into account. This is the case for the II series pumps.

After examining all possible combined effects, the following empiric relationship was found as a direct measure of the pump critical capacity magnitude. It is the " Pump Parameter " - PP :

$$PP = \left[(C_{LA} \cdot \sigma)_M + \frac{(C_{LA} \cdot \sigma)_T}{(C_{LA} \cdot \sigma)_H} \right] \cdot AR \cdot \frac{A_o}{A_2} \cdot \frac{Q_m}{Q_{N,des}}$$

It is a design point parameter and is directly calculated from the chosen design parameters. The value of the Pump Parameter increases with increasing critical capacity, as shown in Fig.6. If low critical capacity is required, pump parameter has to be kept in small value.

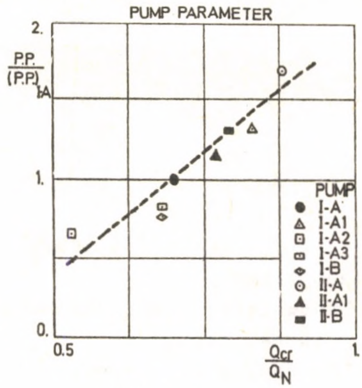

Fig. 6

From the design point of view, aerodynamic blade loading and its spanwise gradient are the most effective controls on the reverse flow and prerotation. Small values of these two design parameters give small pump critical capacity.

7. PREDICTION OF CRITICAL CAPACITY

In general, there is a certain limit of the relative velocity diffusion to predict the stall, in turbomachines. Rodgers (8) shows that the diffusion ratio $(W_{1,RMS}/W_2)$ is a correlating parameter to predict the impeller stalling for centrifugal compressors. In pump case, this correlation indicates the general tendency, but is not enough accurate to predict the pump critical capacity. It is evidenced from the experimental results (Table 2) that diffusion ratio at the impeller tip streamline $(W_1/W_2)_T$, is the dominating flow criterion for the stalling limit. If the impeller has high diffusion ratio at the tip section, for nominal capacity, it will have relatively small margin till stall. Therefore, high value of impeller tip diffusio ratio at the nominal capacity, causes early stalling of the flow,hence high pump critical capacity.

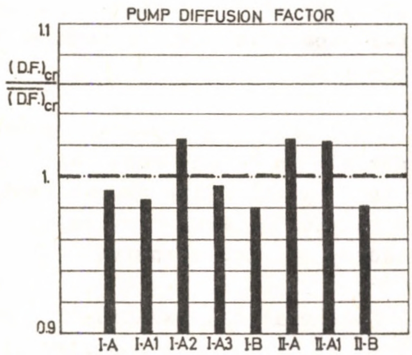

Fig. 7

Based upon the above considerations and Rodgers' study, a " Diffusion Factor " is presented to predict the pump critical capacity. It consists of impeller tip diffusion ratio, blade-to-blade loading, meridional shroud curvature and meridional velocity ratio. Diffusion Factor (DF) is:

$$DF = f_1 \cdot \left(\frac{W_1}{W_2}\right)_T + f_2 \cdot \left[\frac{\left(\frac{Cu_2}{2\sigma W_1}\right)_H}{\left(\frac{Cu_2}{2\sigma W_1}\right)_T} - 1\right] + f_3 \cdot \frac{\bar{b}}{\bar{R}_s}\left[1+\left(\frac{W_2}{W_1}\right)_T\right] + f_4 \cdot \left[\frac{(Cm_2)_M}{Cm_o}\right]$$

f_1, f_2, f_3, f_4 : constant coefficients

W_1, W_2, Cu_2 are calculated from the design values, under the following assumptions:

- There is no prerotation($Cu_1=0$), for the capacities higher than pump critical capacity
- The design slip factor is constant, between nominal and critical capacities.

The average limit value of the diffusion factor at the pump critical capacity, is 1.7 . Fig.7 shows the diffusion factor of the tested pumps, for critical capacity. By using this correlation, pump critical capacity is predicted with an average error of 4%.

8. CONCLUSIONS

Pump head instability at partial capacities is not attributed to the intensity of the reverse flow and prerotation. Pump shaft power at partial capacities,can be reduced significantly by reducing pump critical capacity.

Pump critical capacity strongly depends on the impeller design. It is possible to change critical capacity in a wide range for the same nominal point, by selecting proper design criterion. Pump critical capacity can be reduced by selecting relatively small values of aerodynamic blade loading and its spanwise (from tip to hub) gradient.

Pump critical capacity is predicted by a modified diffusion factor, which is based upon impeller tip streamline diffusion ratio.

ACKNOWLEDGEMENT

This study was carried out at the von Karman Institute (Belgium) in collaboration with Worthington Nord S.P.A.(Italy). The author wishes to thank Research Engineer B. Schiavello, formerly from Worthington Nord, for his contribution on this research.

REFERENCES

1. Şen, M., "Study of inlet flow of centrifugal pumps at partial flow rates", Ph.D. thesis, Université Libre de Bruxelles, June 1980
2. Fischer, K., Thoma, D., "Investigation of the flow conditions in a centrifugal pump", Trans. of the ASME, Vol.54, pp.141, 1932
3. Minami, S., Kawaguchi, K., Homma, T., "Experimental study on cavitation in centrifugal pump impeller", Bull. of JSME, Vol. 3, no:9, 1960
4. Toyokura, T., Kubota, N., Akaike, S., "Studies on back-flow mechanizm of turbomachines", Bull. of JSME, Vol.12, no:50, 1969
5. Lenneman, E., Howard, J.H.G., "Unsteady flow phenomena in rotating centrifugal impeller passages", Trans. of the ASME, J. of Eng. for Power, January 1970
6. Young, G.A.J., "The flow in the rotating passages of a centrifugal pump impeller", BHRA, SP 530, 1956
7. Schiavello, B., Sen, M., "On the prediction of the reverse flow onset at the centrifugal pump inlet", ASME 25. Annual International Gas Turbine Conference, March 1980
8. Rodgers, C., "A diffusion factor correlation for centrifugal impeller stalling", ASME,Paper 78-GT-61, 1978

NOMENCLATURE

A	area
AR	blade aspect ratio ($\bar{b}/c_M$)
b	blade height
c	chord
C	absolute velocity
C_{LA}	aerodynamic lift coefficient
DF	diffusion factor (section 7)
g	gravitatidnol constant
h	static pressure height
H	total pressure height
H_m	pump manometric head
H	head loss due to reverse flow
N	rotational speed
N_S	specific speed ($N_S = N.Q^{0.5}/H_m^{0.75}$; m^3/s, m)
P	pump shaft power
PP	pump parameter (section 6)
Q	volume flow - capacity
R_s	shroud curvature redius in meridional plane
U	peripherical velocity
W	relative velocity
Z	blade number
β_b	blade angle (measured from tangential direction)
η	pump efficiency
σ	solidity (chord/pitch)
ϕ	flow coefficient (C_{m2}/U_2)
ψ	head coefficient ($H_m/(U_2^2/2g)$)

SUBSCRIPTS

o	impeller eye
1	blade leading edge
2	blade trailing edge
cr	critical (starting of reverse flow

des	pump design point	ref	reference pump
H	blade hub section	S	suction head measurement section
m	meridional component or impeller-volute matching point	T	blade tip (shroud) section
M	blade mean section	u	tangential component
N	pump nominal (best efficiency) point - experimental	z	axial component

SUPERSCRIPT

-	average

Dr. H. METE ŞEN
Assistant Professor

Hydraulic Machinery Department
Mechanical Engineering Faculty
Technical University of İstanbul
Gümüşsuyu, İstanbul
Turkey

NON-ROTARY PISTON PUMPS WITH DISCHARGE ADJUSTABLE BY MEANS OF POWER STROKE

S. Simov, D. Vulkov, N. Kotzev

I. NOTATION

Q_n - rated pump discharge
Q_R - adjusted pump discharge
D - piston diameter
S_n - rated stroke of the piston
S_e - power stroke
n - rotation frequency of the pump cam shaft
ω - angle speed of the cam shaft
r - radius of the cam shaft
η - total pump efficiency
η_m - mechanical pump efficiency
m_p - mass of the pump
P - power of the pump shaft
x_R - ram displacement
μ - discharge coefficient
ρ - power liquid density
P_v - pressure at the pump discharge valve opening
P_1 - pressure at the pump suction side
a - width of the channel connecting the power cylinder with the hole of the ram adjusting the pump discharge
S - area of the piston

II. INTRODUCTION

Contemporary production in the chemical, oil-refining, pharmaceutical and food industries, as well as in water purifying stations and in a number of other productions, where liquids need to be mixed in a certain proportion, requires the application of non-rotary pumps adjustable in discharge /dosing pumps/.

A characteristic feature of this type of pumps is their low efficiency, from 25 to 60%, and their considerable mass, over 130 kg per 1 kW effective power.

The well-known methods and design solutions for adjusting the discharge in non-rotary piston pumps are unsatisfactory as regards the simplicity of construction and technology of production, we well as with respect to the possibility of increasing the frequency of rotation.

III. ANALYSIS OF THE BASIC METHODS OF DISCHARGE ADJUSTING

From the basic equation of piston pumps actual discharge

$$Q = \frac{\pi D^2}{4} s n \eta_Q$$

it follows that the discharge can be varied in:

a/ varying the frequency of rotation;

b/ varying the piston stroke.

One of the most expedient methods of discharge adjusting with this type of pumps, is by varying the frequency of the cam shaft rotation. Since this method does not lead to constructive changes and complication in the piston pump, it proves to be most adequate from hydraulic point of view. The chief disadvantage of the method is the use of a costly electrical engine with an alternating frequency of rotation, its relatively low total efficiency compared to engines with a constant frequency of rotation , as well as the expensive additional electrical equipment installed to the machine. This is the reason why, in spite of the possibilitiy for technical implementation of this method of discharge adjusting, it proves to be economically unprofitable, and has not been widely applied in industrial production, although it has considerable advantages.

With contemporary dosing pumps, the most widely applied is the method of varying the piston stroke by means of a gear additionally built into the pump, the driving electrical engine having a constant frequency of rotation.

The built-in additional gear considerably increases the mass of the pump and decreases its total efficiency, which makes its design and technologocal implementation more complicated,

and its manufacture becomes more expensive.
There exist a number of design solutions for varying the piston stroke which can be classified in the following way:

a/ Piston pumps with discharge adjustable by a link gear;

b/ Piston pumps with discharge adjustable by a crank-like suspended worm gear;

c/ Piston pump with discharge adjustable by a worm gear and a device for changing eccentricity.

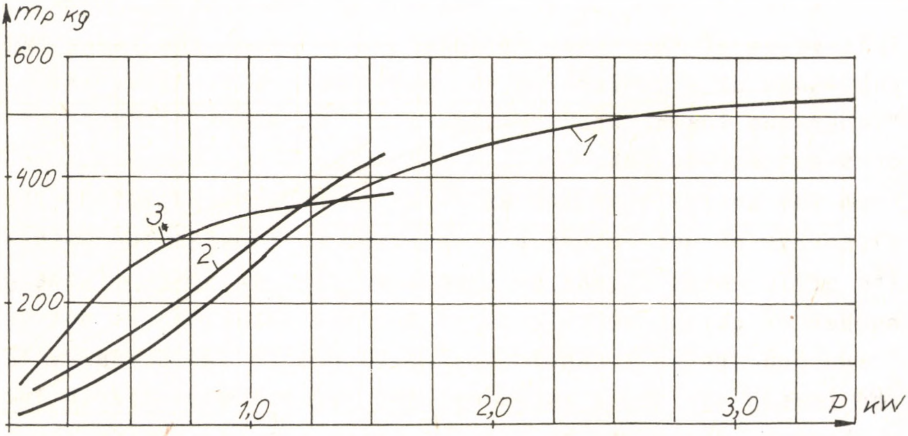

fig.1

Fig. 1. shows the relation between the pump mass and the shaft power P, obtained on the basis of data published by various companies producing dosing pumps [2,3,4,5,6,7,8]. Curve 1 refers to dosing pumps with link gears; curve 2 - to pumps with a crank-like suspended worm gear; curve 3 - to pumps with a worm gear and a device for changing eccentricity. Graphs 1,2 and 3 in Fig.1 show the considerable mass per 1 kW power of the pump shaft.
The mechanical efficiency η_m is also considerably decreased in dosing pumps with worm gears: for one-pitch worm gears η_m = 0,51 + 0,70; for two-pitch worm gears η_m = 0,55 + 0,79 [1]. It can be seen that a considerable part of the

input energy /49 to 21%/ is lost by turning into heat. The considerable decrease of the mechanical efficiency leads to a considerable decrease of the total efficiency, as well. Companies, manufacturing pumps of that type do not usually publish any data on efficiency.

The following case should be taken as an example to illustrate the low efficiency: an estimation of the total efficiency η = 24,19% has been done concerning a pump, manufactured by the Milroyal Company /France/ which secures a maximum discharge Q = 14,23 ℓ/min , at a maximum pressure of 0,7 MPa .

This value of the total efficiency is within the range of the published data concerning the pumps manufactured by the "Tcherveno Zname" Works /Bulgaria/ [8], the efficiency of which does not exceed 30%.

From the analysis of the existing methods of adjusting the discharge of non-rotary piston pumps as regards the mass and the efficiency, it may be concluded that in spite of the great number of design solutions, an optimum solution has not yet been found concerning technological performance and economy. This is the reason why it is expedient and necessary to search for new methods of discharge adjusting which should combine the advantages of the existing methods and avoid their disadvantages.

IV. NON-ROTARY PISTON PUMPS WITH DISCHARGE ADJUSTABLE BY MEANS OF VARYING THE POWER STROKE

The methods of discharge adjusting in non-rotary piston pumps well-known for the present are based on effecting some changes on their mobile elements. In order to simplify the construction and to reduce the mass of that type of pumps, as well as to increase, to a certain extent, their efficiency,use is made of the principle of affecting the stationary actuating cylinder by varying the operating process hydrailically. Thus, at a constant frequency of rotation of the engine actuating the pump, it becomes possible to avoid the gears for varying the stroke for this type of pumps.

A schematic diagram for constructing a non-rotary piston pump with discharge adjustable by the power stroke, is shown in Fig. 2. This method of discharge adjusting has been defended by two Author's Certificates [9, 10]. The design and the principle of operating are the following: a side hole is made in the cylinder block with an axis parallel to the axis of the actuating cylinder. The ram that is situated in the hole has such a form

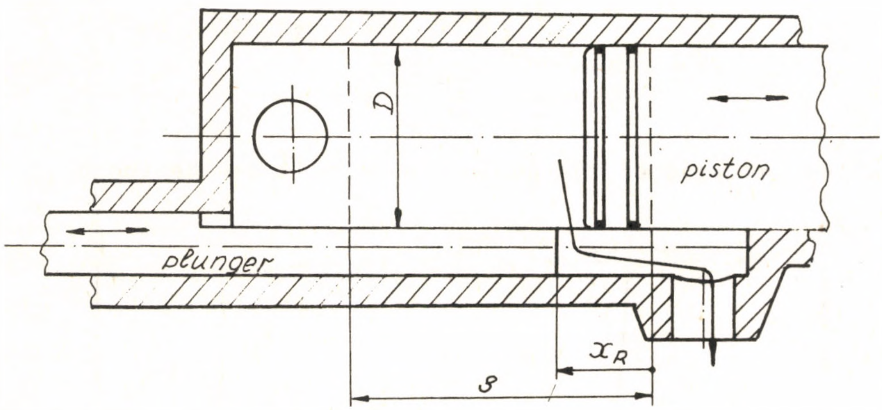

Fig. 2.

that a part of its surface participates in the cylinder surface of the actuating cylinder.

Of the ram is in its extreme right position, the pump will deliver the rated discharge. When the ram moves to the left at a distance of x_R , then, during the delivery stroke, a part of the working area fluid will be discharged through the space left free by the ram towards the pump suction side. Discharging continues till the piston front surface is on the same level with the right front surface of the ram. In this case, the discharge delivered by the pump will be less than the rated discharge.

If the ram is in its extreme left position, then the pump discharge will be zero, since the working area fluid will be entirely drawn back into the suction space. Thus, it becomes possible to vary the discharge gradually from its rated value to zero; in this case, avoiding the complex gears for varying the piston stroke, its power stroke is varied instead:

$$s_e = s_n - x_R$$

After carrying out the theoretical investigations, an equation has been obtained concerning the adjusted discharge Q_R in relation to the displacement x_R of the ram:

$$Q_R = Q_n \left\{ \frac{s - x_R}{2r} + \frac{x_R - r\left[1 - \cos 2\,\mathrm{arctg}\, \dfrac{\dfrac{-S\omega}{\mu a\sqrt{\frac{2}{\rho}(P_v - P_1)}} + \sqrt{4\left(\dfrac{S\omega}{\mu a\sqrt{\frac{2}{\rho}(P_v - P_1)}}\right)^2 + 4\left(2 - \dfrac{x_R}{r}\right)\dfrac{x_R}{r}}}{2(2 - x_R/r)}\right]}{2r} \right\}$$

From the analysis of the above equation it can be found

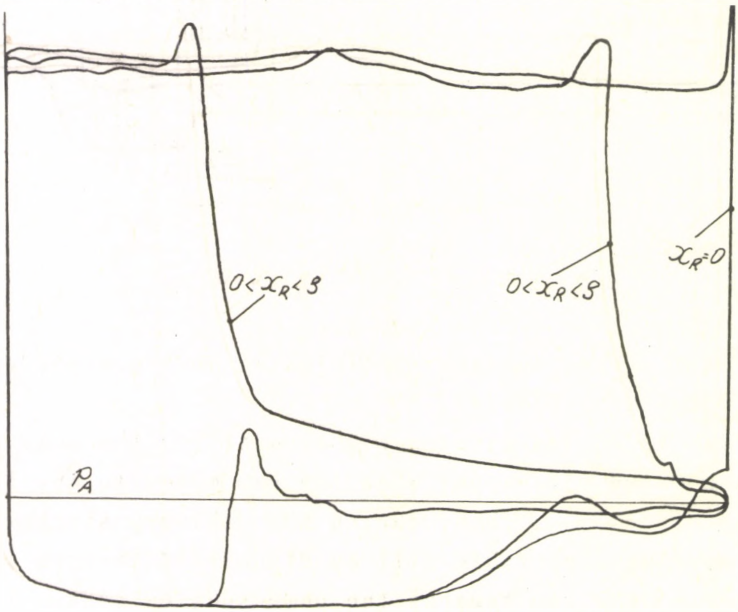

fig. 3

that the term

$$A = \frac{x_R - r\left[1 - \cos 2\,\mathrm{arctg}\dfrac{\dfrac{-S\omega}{\mu a\sqrt{\frac{2}{\rho}(P_v - P_1)}} + \sqrt{4\left(\dfrac{S\omega}{\mu a\sqrt{\frac{2}{\rho}(P_v - P_1)}}\right.+4\left(2 - \dfrac{x_R}{r}\right)\dfrac{x_R}{r}}}{2(2 - x_R/r)}\right]}{2r}$$

has relatively small values. As a matter of fact, it displaces the adjusted pump characteristics to the right, and it has zero values for x_R = 0, and $x_R = 2r$

Fig. 3. show experimental indicators diagrams of non-rotary piston pumps with discharge adjustable by varying the power stroke from x_R = 0 and $0 < x_R < s_n$, respectively. The pump experimental characteristic is shown in Fig. 4. It can be seen that the effect of the term A is really negligible and it only displaces it to the right.

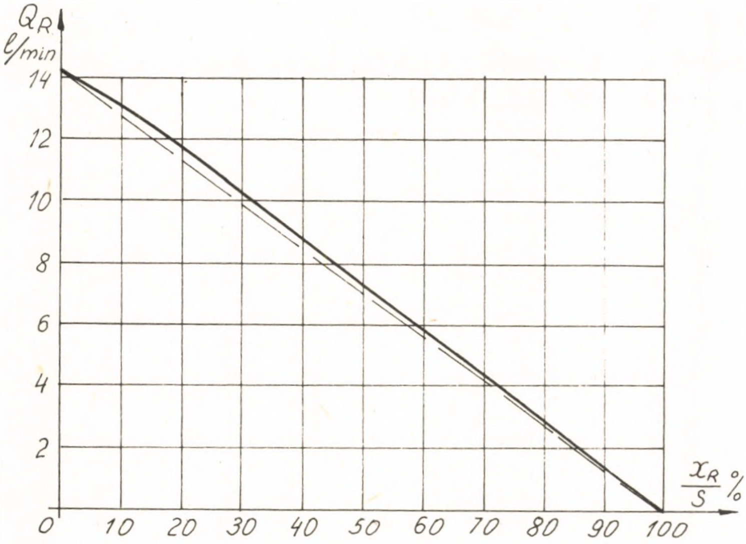

fig. 4

V. CONCLUSIONS

On the basis of the experimental investigations it has been found that non-rotary piston pumps with discharge adjustable by varying the power stroke have a certain significance; since they are simple in construction and technology, it is possible to reduce their mass and, to a certain extent, to increase their total efficiency. It can be assumed that they will find their proper practical application.

REFERENCE

1. Dloukhiy V., Machine Drives, L., Machine-building, 1982
2. Catalogues of the Company Lewas /Austria/
3. Catalogues of the company Milroyal /France/
4. Catalogues of the Company Milton Roy /France/
5. Catalogues of the Company AKA /Sweden/
6. Catalogues of the company Hauke /Austria/
7. Catalogues of the Company Fujitsu Fanuc Ltd. /Japan/
8. Catalogues of the "Tcherveno Zname" Works /Bulgaria/
9. Simov S. et al. Adjustable Displacement Machine, Author's Certificate No. 29809, 1981.
10. Simov S., Adjustable Displacement Machine, Author's Certificate No. 32062, 1982.

A UNIVERSAL AERODYNAMIC DIAGRAM OF THE FAMILY OF SINGLE AIRFOILS

Ernest Sisak

Abstract

The universal diagram of a family of single airfoils is the plotting in one graph of both the geometric parameters and the aerodynamic characteristics of the airfoils of that family. The coordinate system of this diagram is given by the geometric parameters,-maximum thickness ratio d/l, or maximum ordinate ratio of the mean line f/l, and the angle of attack of the flow, α. In this system, the curves of equal value of the aerodynamic characteristics, i.e., lift, drag and lift/drag ratio, are plotted by means of the dimensionless coefficients C_a, C_w and C_a/C_w for the airfoils of the considered family.

The data required for the universal aerodynamic diagram are obtained from the individual characteristics of the respective airfoils, published in the literature.

This paper provides examples of universal diagrams for single airfoil families in the coordinate systems (d/l, α) and (f/l, α), respectively. The method also holds for combinations of single aerodynamic airfoils whose individual characteristics are known.

The universal aerodynamic diagram of the family, or the combination, respectively, of single airfoils can be applied in the practical computations of hydraulic and wind machines and of aircraft. The most important of these are described in the paper.

1. <u>The Universal Aerodynamic Diagram of the Family of Single Airfoils</u> is the general representation, in one graph, of all the geometric and aerodynamic characteristics of the single airfoils of a given family. It is obtained from the coordinate system given by the geometric characteristics of the airfoils, d/l and f/l, with the angle of attack α as an independent variable. In this system the curves of equal coefficients of lift C_a = = const., of drag C_w = const. and lift/drag ratio, C_a/C_w = const are plotted for the airfoils of the family which can be obtained from the catalogues of airfoils providing the individual experimental characteristics measured in the wind tunnel /1, 2, 3/. The universal diagrams given in the literature are systematized in a different manner /4/ or, respectively, refer to airfoil cascades /5, 6/.

As an example, Fig.1 gives the universal aerodynamic diagram in the (d/l, α) system of the NACA 4412, 4415, 4418, and 4424 family of airfoils, in the range of maximum thickness ratio between 12 and 24 %, at $Re = 3.10^6$. Fig.2 provides an example of

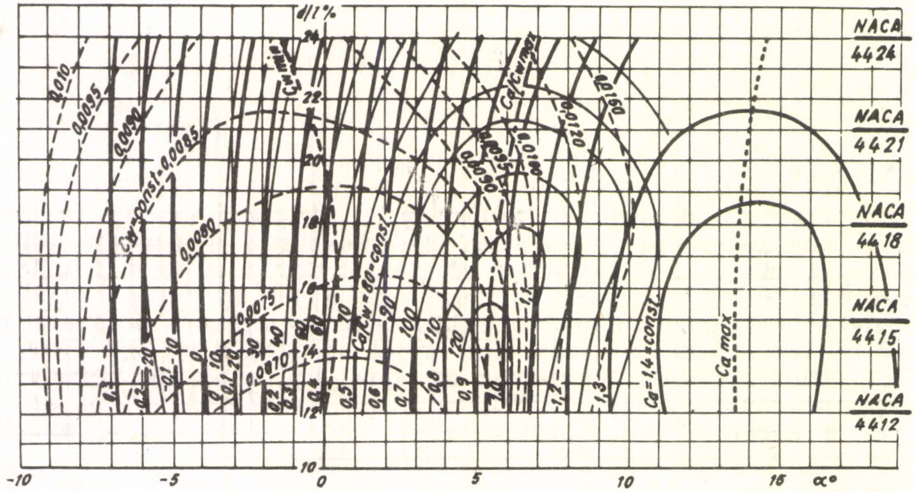

Fig.1 The universal aerodynamic diagram of the NACA 4412, 4415, 4418, 4421 and 4424 family of airfoils in the $(d/l, \alpha)$ system; d/l = 12 to 24 % ; Re = 3.10^6.

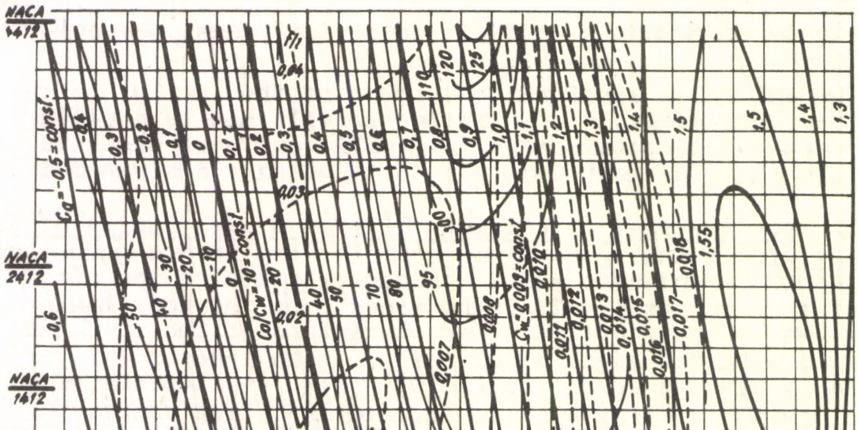

Fig.2 The universal aerodynamic diagram of the NACA 0012, 1412, 2412 and 4412 family of airfoils in the $(f/l, \alpha)$ system ; f/l = 0 to 4,0 % ; Re = 3.10^6.

this characteristic in the (f/l, α) system, for the NACA 0012, 1412, 2412, 4412 family of airfoils, in the 0 to 4 % range of maximum ordinate ratio of the mean line with $R_e = 3.10^6$. The family of airfoils of the first example is characterized by its maximum ordinate ratio of the mean line of 4 % for all airfoils, while in the second example the maximum thickness ratio, of 12 %, is constant.

1.1 The universal aerodynamic diagram of the family of single airfoils has the following advantages :

- it shows in a synoptic form the functional relation between the geometric and aerodynamic characteristics of the family of airfoils ;
- it permits to study the influence of the main geometric parameters on the aerodynamic characteristics of the airfoils ;
- by joining the points of $C_{a\ max}$, $C_a/C_{w\ max}$ and $C_{w\ min}$ of the airfoils in this diagram, the curves of the maximum values of lift and lift/drag ratio, and, respectively, of the minimum values of the coefficient of drag, are obtained for the considered family of airfoils, thus providing real data for an optimized computation.

2. Applications of the Universal Aerodynamic Diagram of the Family of Single Airfoils.

2.1 Determination by means of extra- and intrapolation of the individual characteristics for values of d/l and f/l other than the nominal ones provided by the catalogues.

(a) Intrapolation. For all thicknesses, or respectively, all maximum ordinates of the mean line within the range covered by wind tunnel measurements, the individual aerodynamic characteristic can be plotted for intermediate values of d/l and f/l.

(b) Extrapolation. The lower part of the graph of Fig.3 plotted for the family of airfoils Gö 795, 796, 797, 798 provides the measurements made in the 8 to 20 % range of maximum thickness ratio. The upper part represents the range extended by extrapolation, with the geometric (or analytic) extension of the curves up to a maximum thickness ratio of 30 %. Such high values are required, for example, in the computation of blades in the hub region

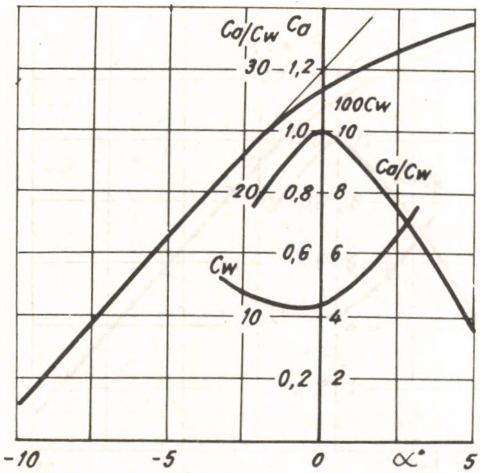

Fig.4 The individual aerodynamic characteristic of an airfoil with a maximum thickness ratio d/l = = 30%, obtained from the extrapolated diagram of Fig. 3.

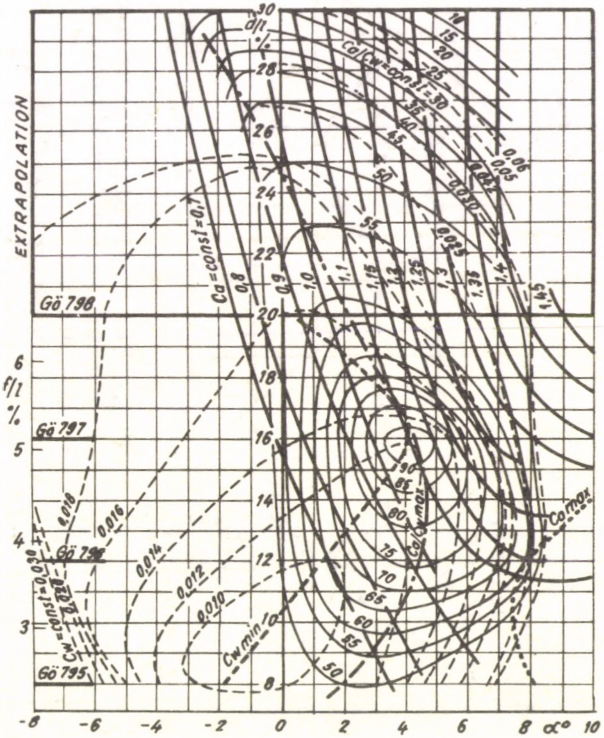

Fig.3 The universal aerodynamic diagram of the Gö 795, 796, 797, 798 family of airfoils in the (d/l, α) system; Re = 3.8.10^5; - at the bottom: in the measured range d/l = 8 to 20 %; - at the top: in the extrapolated range d/l = 20 to 30 %.

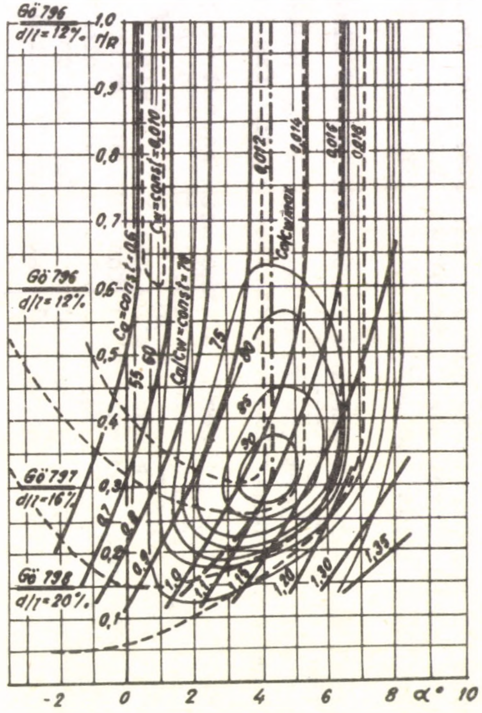

Fig.5 The universal aerodynamic diagram in the (r/R, α) system of a runner blade of a horizontal-axis highspeed wind turbine, consisting of Gö 796, 797, 798 airfoils; Re = 3,8.10^5.

of high-speed horizontal-axis wind turbines. Fig.4 gives the individual aerodynamic characteristic at a thickness ratio of 30 % obtained from the extrapolated diagram of Fig. 3.

2.2 The universal aerodynamic diagram of high-speed, horizontal-axis wind turbine blades. This diagram is the general representation, in one graph, of all geometric and aerodynamic characteristics of the airfoils of the runner blade, in which the influence of the cascade is not felt. It is plotted in the (r/R, α) system, together with the associated values of the maximum thickness ratio of the airfoils, determined in terms of the admitted distribution of d/l along the radius r.

Fig.5 provides an example of the universal aerodynamic diagram of a blade consisting of Gö 796, 797, 798 airfoils ($R_e = 3.8 \times 10^5$). The figure also shows the curves of maximum lift/drag ratio and minimum drag coefficient along the radius, which are of help in the determination of the most favourable values of the angle of attack between hub and periphery. If the values of the angles of attack are close to the curve of maximum lift/drag ratio, the turbine blade works in optimum aerodynamic conditions, with high aerodynamic efficiency. Satisfactory results are obtained from the universal diagram if the values of the angle of attack at nominal operating point, computed or admitted along the radius, are also plotted in it. For comparison, Fig.6 provides the incomplete diagram of a blade in which the airfoil FX 77-W-153 ($R_e = 3.10^6$) would be admitted in the $r/R \in (0{,}5\ ,\ 1)$ range. With the usual angles of attack, blades consisting of Wortmann airfoils are clearly better which is also evident from this comparison based on an incomplete diagram.

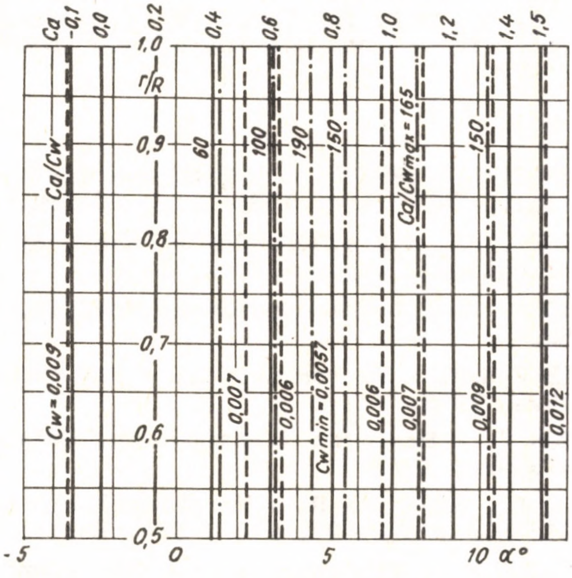

Fig.6 The incomplete universal diagram [$r/R \in (0{,}5\ ,\ 1)$] of a blade with an FX 77-W-153 airfoil ; $Re = 3.10^6$

It should be noted that the aerodynamic conditions are greatly modified at the periphery of the blade; at $r/R = 1$, the lift is zero, hence the shape of the characteristic curves changes correspondingly. The phenomenon occurring at the periphery should therefore be studied as particular case in terms of the conditions existing in this area.

3. Final Remarks.

- The universal diagram of the family of single airfoils, or of the blade, respectively, is obtained from the individual aerodynamic characteristics of the component profiles experimentally measured in the wind tunnel. Thus, the universal diagram is as accurate as the basic diagrams are and an analysis based on it is correspondingly safe.

- The universal aerodynamic diagram of the blade at nominal operating point contains also all the characteristics determining the aerodynamic operation of the blade at values other than the nominal one, when $\alpha \neq \alpha_{nom}$. It provides useful data for computing the strength and for the study of the governing system.

- For large values of the maximum thickness ratio (larger than the greatest measured values), the literature does not provide any experimental data or relations permitting an approximation of the aerodynamic characteristics of the component airfoils. Extrapolation based on the universal diagram gives fairly accurate results.

- The universal diagram can be obtained for any combination of airfoils, not only for families in an aerodynamic sense. It can be applied in the computation of highspeed wind turbine blades and of aircraft wings.

References

1. PRANDTL L., BETZ A. : Ergebnisse der Aerodynamischen Versuchsanstalt, I-IV, Lfg, 1921-1932, Göttingen.
2. ABBOT J.H., A.E.v.DOENHOFF : Theory of Wing Sections, Dover Publications, Inc.New York, 1958
3. RIEGELS F.W. : Aerodynamische Profile, R.Oldenbourg, München, 1958.
4. FATEEV E.M. : Vetrodvigateli i vetroustanovki, Selhozgiz, Moskva, 1948.
5. ANTON V. : Doctoral dissertation, Polytechnical Institute of Timişoara, 1972
6. DOGE R., HERRMANN R. : Maschinenbautechnik 8(1959), Heft 12, S.655-660 ; 9(1960), S.571-574, Berlin.
7. MOLLY J.P. : Windenergie in Theorie und Praxis. C.F.Müller, Karlsruhe, 1978.

SISAK ERNEST
Dr.eng., Res.Eng.
Polytechnical Institute
1900 Timişoara
Romania

STATIONARY COLLECTOR SYSTEM FOR WIND-ENERGY CONVERSION

Ernest Sisak

Abstract

Based on a new aerodynamic scheme, the relation of the power coefficient C_p is established. Unlike other methods (A.Betz), in which an intermediate level is taken into account, in the proposed procedure the working power is directly compared to the total power of the flow. In this system, which was patented in Romania, a specially constructed stationary collector generating a secondary flow is used for the conversion of wind energy. The air turbine required for the conversion is placed into this secondary flow. The use of a stationary collector without any revolving parts in the wind distinguishes this installation from the Andreau-Enfield system, in which a hollow-vane runner is used for generating the secondary flow. The measurements provided in the paper were carried out in natural conditions on the first machine constructed according to the new procedure.

1. The Power Coefficient.- The ratio between the working power obtained through conversion and the total power of the wind taking part in the conversion is defined as power coefficient C_p. This coefficient determines the degree of utilization of the energy of the moving fluid. Assuming a flow with uniform velocity before the system and with a mass of air flowing through an area S of an obstacle, A.Betz /1, 2/ determined the maximum theoretical power coefficient, $C_{p\ id} = 0.593$. The present paper determines a new relation for this power coefficient, defining conversion in terms of the total mass of the flow contributing to the conversion. This new relation contains in an explicit form all the parameters characterizing the obstacle from an aerodynamic point of view, in variable flow conditions. The maximum theoretical power coefficient resulting in this hypothesis approaches 1.0 ; from a practical point of view, the areas close to the extreme values, 0 and 1, are of no concern.

1.1 Aerodynamic Body of Arbitrary Outline.- Consider an aerodynamic body of infinite span and of arbitrary outline placed in the uniform infinite flow of velocity V (Fig.1).

The total kinetic power of the flow undisturbed by the obstacle is

$$P_b = 1/2\rho\ Q V^2 = 1/2\rho\ S V^3 \qquad (1)$$

where Q is the total mass discharge and S is the area through which this mass flows.

The force F resulting from the action of the wind upon the obstacle may be decomposed into two components : lift A and drag W. The drag force W is determined by means of Newton's drag relation, (2) :

$$W = 1/2\rho\ C_w\ S_c\ V^2, \tag{2}$$

where S_c designated the characteristic aera of the obstacle.

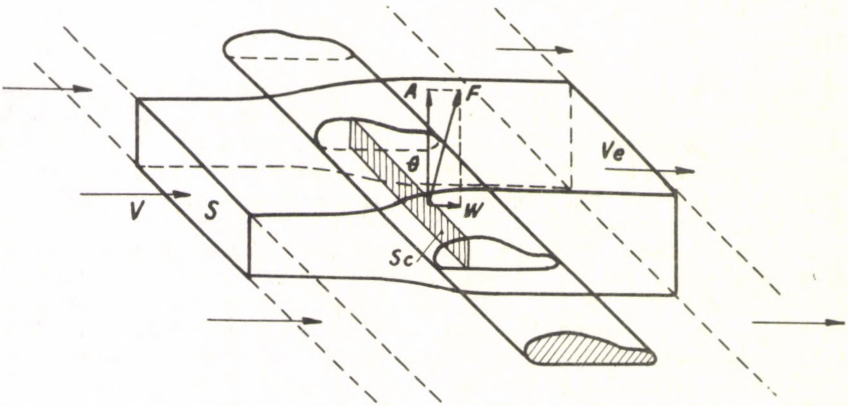

Fig.1 Aerodynamic scheme of a body of arbitrary outline.

The power dissipated by the obstacle in the flow of uniform velocity V is :

$$P_d = W.V = 1/2\rho\ C_w\ S_c\ V^3 \tag{3}$$

The actual output is given by the difference betwee Eqs.(1) and (3) :

$$P_u = P_b - P_d = 1/2\rho\ S\ V^3 - 1/2\rho\ C_w\ S_c\ V^3 = 1/2\rho\ V^3(S - C_w S_c) \tag{4}$$

The same output can be written as the difference between the power before and behind the obstacle :

$$P_u = 1/2\rho\ Q\ V^2 - 1/2\rho\ Q\ V_e^2 = 1/2\rho\ S\ V^3(1 - V_e^2/V^2) \tag{5}$$

Denoting by K the ratio of velocities V_e/V we obtain :

$$P_u = 1/2\rho\ S\ V^3\ (1 - K^2) \tag{6}$$

The two outputs in Eqs.(4) and (6) being equal, we obtain :

$$S - S_c\ C_w = S(1 - K^2),$$

from which we get the area S :

$$S = S_c\ \frac{C_w}{K^2} \tag{7}$$

From Eq.(7) it can be seen that the area S differs from the exposed area S_c of the obstacle by the factor C_w/K^2, which is of variable magnitude, influenced by the aerodynamic characteristics of the body by means of C_w, and by the flow conditions by means of $K = V_e/V$.

The power coefficient characterizing the energy conversion is given by P_u/P_b :

$$C_p = 1 - C_w \frac{S_c}{S} = 1 - K^2 \qquad (8)$$

which is obtained directly from Eqs.(6) and (1), or Eqs.(4) and (1), respectively

$$C_p = 1 - K^2$$

Table 1 lists the values of the power coefficient C_p at various values of the velocity ratio K before and behind the obstacle : $C_p = 1 - K^2$.

Table 1.

$K = V_e/V$	0	1/4	1/3	1/2	2/3	3/4	1
$C_p = 1 - K^2$	1	15/16	8/9	3/4	5/9	7/16	0

Conversion takes place in the desired direction if the mass of fluid determined by area S of the undisturbed flow of velocity V is greater than the mass flowing through area S_c with the same velocity, hence $S > S_c$; this condition is fulfilled in accordance with Eq.(7) when $C_w > K^2$ or, it is at its limit if $C_w = K^2$. From here we obtain the smallest theoretical value of the velocity ratio at which conversion becomes feasible :

$$K = \sqrt{C_w} \qquad (9)$$

The maximum theoretical coefficient is

$$C_{p\ id} = 1 - C_w \qquad (8')$$

Curve 1 of Fig.2 represents the variation of the power coefficient $C_p = f(K)$ resulting from Eq.(8) (in a continuous line); separately, the magnified portion approaching $C_p = 1$, indicates the limit at which conversion becomes possible (in accordance with Eqs. (9) and (8')). Fig.2 also contains Curve 2, determined by A.Betz :

$$C_p = 1/2\ (1 + K)\ (1 - K^2) \qquad (10)$$

A.Betz's method differs from the one presented in this paper in that it operated with the term 1/2(1 + K), which at K = 1/3 yields $C_{pB} = 2/3\ C_p = 2/3 \cdot 8/9 = 16/27 = 0.593$.

Observations regarding the power coefficient :

- Assuming that there exists an obstacle of infinite span in the unlimited flow of uniform velocity, the power coefficient C_p varies with the velocity ratio V_e/V between zero and a value that in ideal conditions approaches 1.

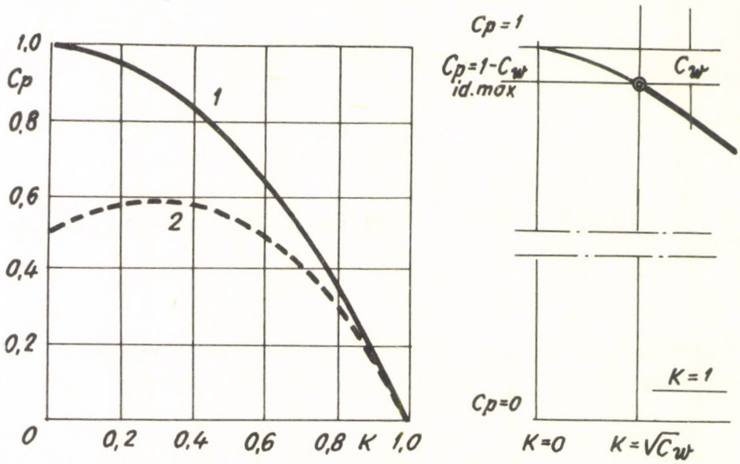

Fig.2 Variation of the power coefficient C_p as a function of the velocity ratio $K = V_e/V$: Curve 1 (Eq. (8) ; Curve 2 (Eq. (10) A.Betz.

- Under the above assumptions, area S contains the entire mass of fluid which takes part in the energy conversion with the given obstacle.

- Considering C_w to be an equivalent global drag coefficient of the obstacle, the method can be generalized and holds for any obstacle.

1.2 Aerodynamic Body with Minimum Drag.-Fig.3 represents a wing-shaped body of infinite span in an infinite flow of uniform velocity V. The pressure acting at any point of the outline is determined by means of the dimensionless pressure coefficient k_p using Eq.(11) :

$$k_p = 1 - (V_m/V)^2 = \Delta p/(1/2\rho\ V^2) \qquad (11)$$

The total force acting on the wing can be expressed with the mean pressure Δp_m :

$$F_t = \Delta p_m\ L.1 = 1/2\rho V^2\ k_{pm}\ L.1 = 1/2\rho V^2\ L(k_{pm}.1) \qquad (12)$$

in which $(k_{pm}.1)$ is the area between the pressure distribution curve and the chord of the airfoil, Fig.4. Force F_t is proportional to area $(k_{pm}.1)$, in which k_{pm}, the height of the rectangle whose base is given by chord 1 of the airfoil, is a mean global value obtained through the measurement of the above-mentioned area.

The output can be expressed using Eq.(12) :

$$P_{ul} = F_t.V = 1/2\rho L\ V^3(k_{pm}.1) = 1/2\rho\ V^3\ S_c\ k_{pm} \qquad (13)$$

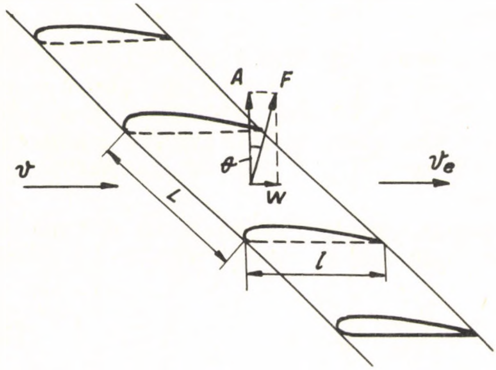

Fig.3 Aerodynamic scheme of a body of minimum drag.

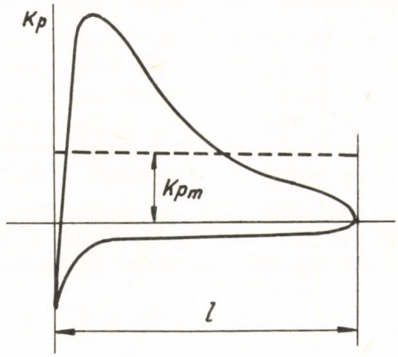

Fig.4 Pressure distribution and equivalent area.

The power coefficient P_{lu}/P_b from Eqs.(13) and (1) becomes, after a number of simplifications :

$$C_{pl} = \frac{S_c}{S} k_{pm} = \frac{K_l^2}{C_w} k_{pm} , \tag{14}$$

where Eq.(7) was used.

From the limiting condition $C_{pl} = 1$ we have :

$$K_l = \sqrt{C_w/k_{pm}} , \tag{15}$$

therefore the maximum theoretical power coefficient for wings is :

$$C_{pl\ id} = 1 - C_w/k_{pm} \tag{16}$$

1.3 Aerodynamic Body of Open Outline.-Consider the hollow aerodynamic body with an open outline represented in Figs.5 and 6.

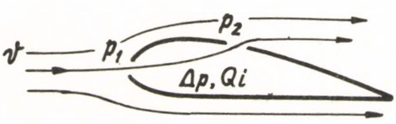

Fig.5 Aerodynamic body with an open outline at points 1 and 2.

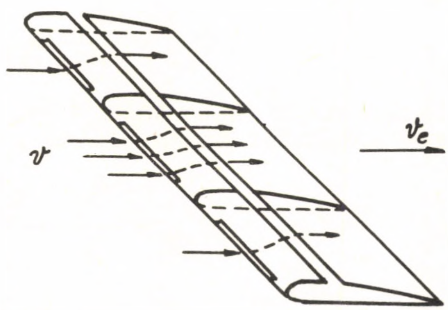

Fig.6 Aerodynamic scheme of a body with open outline.

In a body with a discontinuous contour, the pressure distribution is different from the pressure distribution in a body wit continuous outline; the modification consists in the reduction of the area determined by the pressure distribution curve, the extent of this reduction expressing the occurring losses.

In numerous wind tunnel experiments on the symmetrical slotted single airfoil Gö 460 (Re = 4.60×10^5), in which slots are provided at distances $\bar{x}$ = 0.05 ; 0.30 and 0.55 from the leading edge, the values obtained for the area ratio in the open-contour body ranged between 0.905 and 0.950 /3/ as compared to the body with continuous outline.

Relation (13) of the total force can be written in a similar form for the body with discontinuous contour, while the other conditions do not change :

$$F'_t = 1/2\,\rho\, V^2\, L(k'_{pm} \cdot 1) \tag{12'}$$

in which F'_t denotes the total force, and k'_{pm} denotes the mean pressure coefficient, of the body with open outline.

The F'_t/F_t ratio is considered to be a mean pressure factor of the open-outline body, expressing the modified height of the rectangle $(k_{pm} \cdot 1)$; introducing the notation for this ratio η_p, we obtain :

$$\eta_p = F'_t/F_t = k'_{pm}/k_{pm} \tag{17}$$

in which Eqs.(12) and (12') were used.

Under the action of the pressure difference due to the external flow, $\Delta_p = p_1 - p_2$ between points 1 and 2 (Fig.5), a secondary flow is generated in the hollow body, having a discharge Q_i. The power of this secondary flow is

$$P_i = Q_i\, \Delta' p \tag{18}$$

which in accordance with Eqs.(11) and (15) becomes :

$$P_i = Q_i\, 1/2\rho\, V^2\, k_{pm}\, \eta_p. \tag{19}$$

The power coefficient relating P_i (Eq.(19)) to the total power (1) will then be :

$$C_{p2} = \frac{Q_i}{Q}\, k_{pm}\, \eta_p. \tag{20}$$

Eq.(7) is used in this case, too. Writing $Q_i/Q_c = V_T S_T / V S_c = \eta_v$ and substituting in Eq.(18), we have :

$$C_{p2} = \frac{Q_i}{Q}\,\frac{K_2^2}{C_w}\, k_{pm}\, \eta_p = \eta_v\, \eta_p\, \frac{K_2^2}{C_w}\, k_{pm} \tag{21}$$

For wings with open outline the limiting condition $C_{p2} = 1$ is obtained when

$$K_2 = \sqrt{\frac{C_w}{k_{pm}} \frac{1}{\eta_v \eta_p}} \quad (22)$$

Substituting in Eq.(8) finally yields

$$C_{p2\ id} = 1 - \frac{C_w}{k_{pm}} \frac{1}{\eta_v \eta_p} . \quad (23)$$

The ratio Q_i/Q_c, designated with η_v, is a flow discharge factor determined by the flow discharge of the internal circuit in which the turbine stands, and by the discharge given by the flow velocity V passing through the area of the obstacle.

Eq.(23) is the power coefficient of the body with open outline in which, unlike Eq.(14) for C_p of the body with continuous outline a global factor appears :

$$\eta_p \eta_v = (k'_{pm}/k_{pm})(Q_i/Q_c) \quad (24)$$

affecting the energy exchange by this new procedure.

In these equations, the velocity ratio $K = V_e/V$ is characteristic of the external flow, while C_w, k_p and η characterize the collector itself, as internal elements.

1.4 A Special Case of Bodies with Symmetric Outlines.- In bodies with symmetric outline such as cylinders with circular cross-section, wings with symmetrical outline etc., the resultant lift forces acting on the two halves are equal and in opposite direction, the total lift equalling zero. The problem of creating a secondary flow and of utilizing the latter in the conversion of wind energy reduces to the preceding case if the outline is opened at points that are symmetrical to an axis placed in the direction of flow (Fig.7). In this case the internal flow is defined by the pressure difference p, which is the same on both faces, and by the discharge Q_i, which equals the sum of the discharge through the two symmetrical channels : $\frac{1}{2} Q_i$.

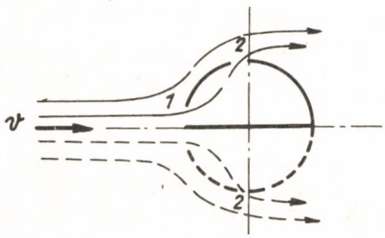

Fig.7 Symmetrical body with open outline.

2. Energy Conversion Procedure with Stationary Collector.- Eq.(21) defines the conditions under which a hollow aerodynamic body with open outline (i.e., an outline that is interrupted at points of different pressure) creates an internal flow in which energy is converted by a conversion machine with the power coefficient C_p of the shape described in this paper. A body of this special construction thus achieves the function of collecting the energy of the unlimited flow in which it is placed, unlike the up-

lift of aircraft or the torque of revolving machines. The proposed patented procedure thus determines a new function of stationary bodies with an outline of minimum drag, i.e. the utilization of pressure distribution in creating a secondary flow for energy conversion /4/. This aerodynamic body, named "collector", is stationary in relation to the flow in which it is placed; no rotation is required except perhaps for the adjustment of the body in the direction of the flow.

2.1 <u>Installation for Wind Energy Conversion Using a Stationary Collector</u>.- The wind energy conversion machine developed at the Timişoara Polytechnic Institute is based on the aforementioned procedure and has the following characteristics :

Collector :

Geometric shape	circular cylinder
cylinder diameter	$D = 0.8$ m
cylinder height	$H = 1.4$ m
area of wind exposure	$S_c = 1.12$ m^2
adjustment device	directional vane

Aero-electric power unit :

- Air turbine :

turbine type	axial,with an upstream vane
nominal output	$P = 110$ W
nominal wind velocity	$V = 11$ m/s
rpm	$n = 950$ rev/min.

- Generator :

type	alternating EP 1110
current	dc (rectified)
voltage	$U = 6$ V
kind of excitation	autoexcitation
rpm	$n = 950$ rev/min.

Fig.8 shows the sketch of this installation, consisting of three parts :

- a central part containing the turbine-generator power unit
- two parts which are symmetrical to the central one and which serve for collecting the energy, being provided with outlets.

The parts are separated by span disks.

The secondary circuit consists of the admission tube of the central part, the guide vane, the impeller and the internal connecting channels with outlets, which are symmetrical in the two parts.

Fig.9 indicates the first results that have been obtained with this system in natural conditions, for the power measured at the generator outlet. Losses in the measured range were about 90 W. The power at the turbine shaft at a wind velocity of 16 m/s is 110 W, which is below the theoretical output.

The present results confirm the conversion procedure using a

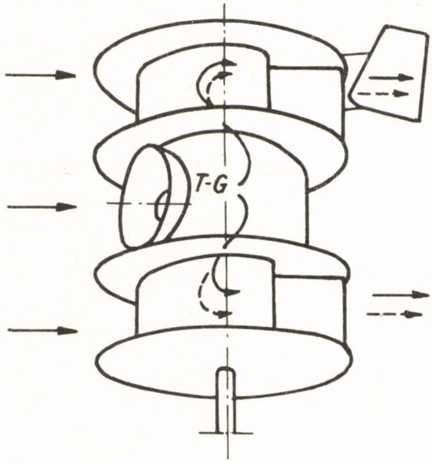

Fig.8 Experimental device of windenergy conversion with stationary collector.

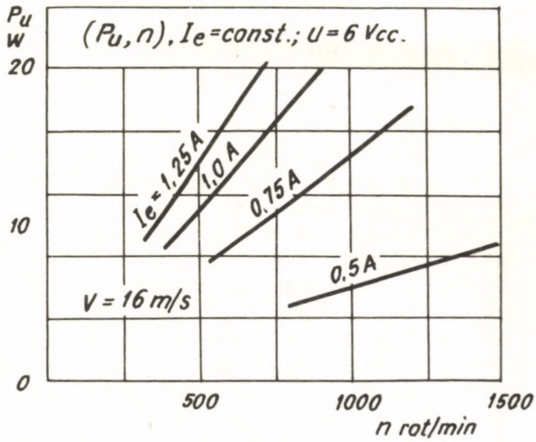

Fig.9 Output (measured in natural conditions) versus speed of rotations.

stationary collector and provide the first data measured with the described installation. Further research and development is being carried out at the Polytechnic Institute Timişoara.

References

1. A.BETZ, Die Windmühlen im Lichte neuerer Forschung. Die Naturwissenschaften, Vol.XV. No.46, Nov.18, pp.905-914
2. E.M.FATEEV, Vetrodvigateli i vetroustanovki. Ed.OGIZ Moskva, 1948
3. I.SISAK, Experimental investigation on airfoils with slots. Communication, Inst.Polit.Timişoara, 1978
4. E.SISAK, Patent RSR Nr.70225 (1979)

SISAK ERNEST
Dr.Eng., Res.Eng.
Polytechnical Institute
1900 Timişoara
Romania

HYDRAULIC DESIGN OF PUMP-TURBINE GUIDE VANES

J. Špidla and B. Seďa

Summary

The paper deals with the hydraulic design of guide vanes for reversible pump-turbines and its verification on a scale model. The presented design procedure is based on a simplified solution of the flow through a fixed double cascade and on the boundary layer estimation. The guide vane design is carried out for the optimum efficiency point of the runner characteristics for pump mode operation. This point determines the value of the angle of attack of the flow on the guide vanes. This angle may be obtained from the theoretical performance characteristics. A linearly decreasing flow velocity along both the suction and pressure sides of the guide vane and no boundary layer separation are assumed in the calculation.

The proposed design procedure was verified experimentally. For this purpose, comparative tests of a model pump-turbine were carried out, by testing successively the guide vanes previously designed and the guide vanes designed in accordance with the proposed procedure. The model allowed the observation of the visualized flow around the guide vanes. The obtained results are presented and discussed.

1. Introduction

The distributor, designed as a system of fixed stay vanes and adjustable guide vanes represents a significant part of the reversible pump-turbine. The guide vanes allow the turbine output to be controlled and further, they serve as a closing device. The stay vanes are important in stiffening the spiral case and head cover structures heavily stressed through water pressure and other external loads. The fundamental tasks of the distributor as a whole are to convert a portion of the potential energy of the fluid into the kinetic energy in the turbine mode operation of the machine and to convert a portion of the kinetic energy of the fluid into the potential energy in the pump mode operation. These conversions involve inevitable some energy losses. Since the flow in a diffuser is generally accompanied with higher losses than the flow through a confuser, the distributors of pump-turbines are designed primarily with respect to the pumping mode conditions. In order to minimize the energy losses, thorough calculations have to be performed using a reliable computational model of the flow with all main sources of losses included. The numerical analysis allows the theoretical optimization of the hydraulic design of the distributor and the experiments are performed in order to verify physically the obtained results.

2. Computational model of the flow

The real three-dimensional flow through the distributor is modelled assuming a two-dimensional potential flow of an incompressible and inviscid fluid through a fixed double cascade of vanes with finite thickness. An axisymmetric flow surface is assumed. The viscosity of the fluid is considered to be significant only in the boundary layer. In the case of an unseparated flow the interactions between the viscid and potential flow layers are insignificant and thus are neglected. The interactions between the distributor and the runner and between the distributor and the spiral case are not considered. The boundary conditions of the flow are satisfied in their mean integral values. The above mentioned potential flow is described by Fredholm integral equation of the second kind with a supplementary condition /1/. The numerical solution of this equation is performed on the computer using a program coded in FORTRAN IV. This computer program allows the analysis of both single and double cascades, thus respecting the interaction between the stay and guide vanes. However, the double cascade analysis is limited to cases with blade number ratios 1:1 or 1:2 only. The computational procedure gives the values of the flow velocities at any point of the blade profile, i. e. at the leading edge too, what allows the investigation of the flow loss characteristics of the cascade.

Based on the knowledge of the velocity distribution along the blade profile, the behaviour of the boundary layer is estimated. The boundary layer momentum thicknesses are calculated and the possibility of flow separation, leading to higher energy losses, is evaluated. For this purpose the method proposed by E. Truckenbrodt /2/ is applied. Such a procedure satisfies well the needs of a comparative analysis, even when some other refined computational models of the boundary layer may be used.

3. Hydraulic design of the guide vane profile

The design of guide vanes represents a very difficult procedure and it results actually as a compromise on various, frequently contradictory requirements in hydraulics, strength, etc. In this section, only the procedure in designing a guide vane profile with low losses at specified hydrodynamic parameters will be described.

Using computational model of the flow described above series of cascades were analysed. Taking into account the obtained results, a linear variation of the flow velocity along the blade profile surface can be assumed. This holds for both the suction and pressure sides. All calculations are performed for the mean cross-section of the distributor. The final shape of the blade profile is obtained in course of a step by step shape modification and calculation, untill the required velocity distribution is reached.

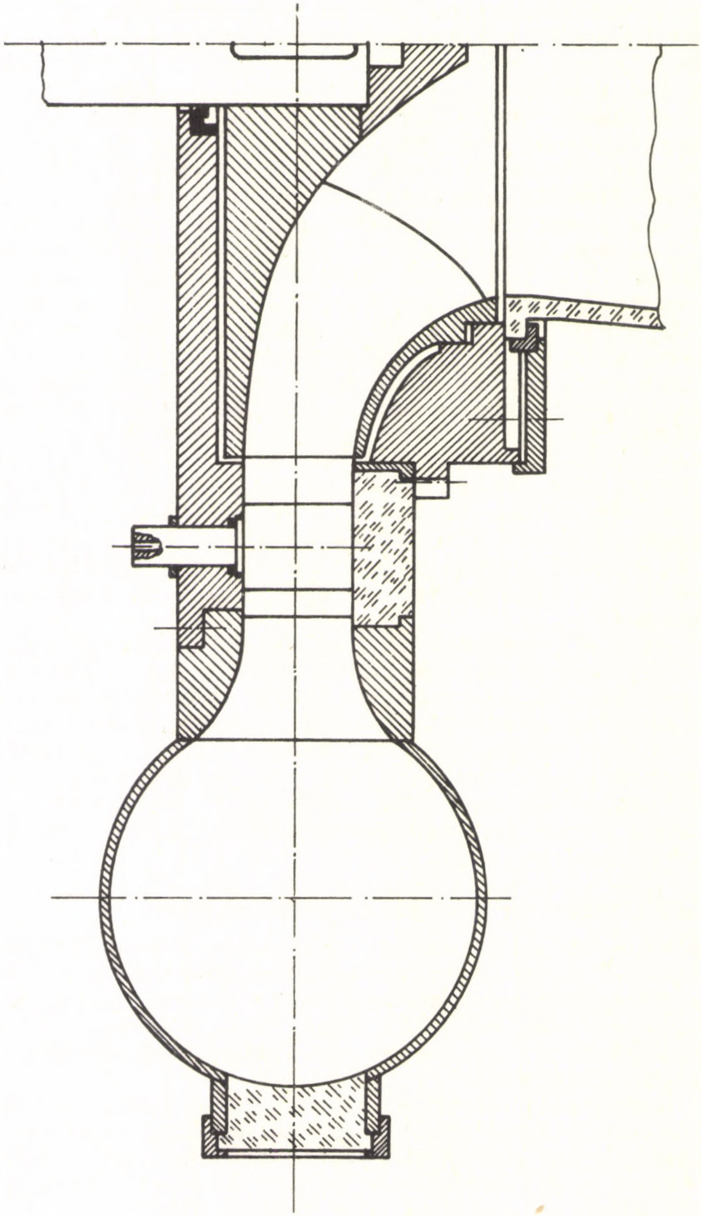

Fig. 1 Sectional view of the model pump-turbine

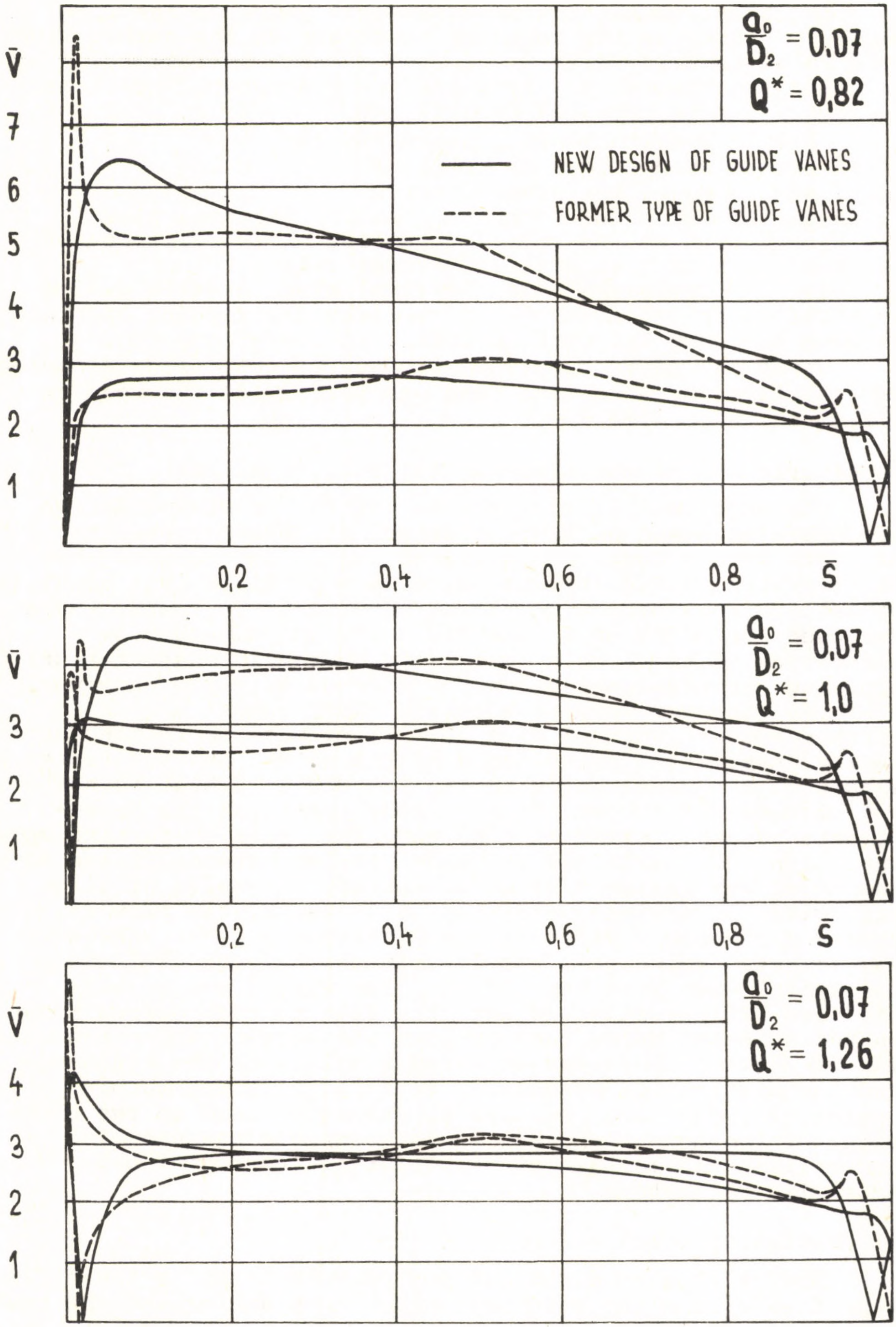

Fig. 2 Calculated velocity distribution around the guide vanes

In calculations, the mean integral value of the flow angle is chosen as the boundary condition at the runner side. This value is derived from the runner characteristics, relating the theoretical head and the discharge. The characteristics can be obtained by applying:

/i/ proper computational procedures, or
/ii/ accumulated empirical data, or
/iii/ scaled model performance tests.

It should be taken into account, that in the real flow the circulation at the spiral case side of the distributor is lower than that determined theoretically.

The appropriateness of the final blade profile design is verified by calculations for various distributor openings in both the pump and turbine modes of operation, too.

Using the above described procedure, the design of guide vane profile for an actual case was performed. The results are given in section 5.

4. Description of the experimental investigations

The experimental verification of the presented design procedure is based on the comparison of relevant results of tests with a model pump-turbine, using successively two distributors with different guide vane profiles. The conditions of testing were otherwise almost identical. In tests, there was used the model of a recently designed pump-turbine possessing at $n_q=41$ relatively good hydraulic characteristics. Applying the presented procedure only guide vanes were newly designed, however without altering their number and stem pitch diameter. The use of a NC milling machine in manufacturing ensured the coincidence of the actual and the designed shapes of the model guide vanes. The model turbine runner has a diameter of 400 mm. In pump mode operation the measurements were performed at 1500 rpm. The tests in turbine mode operation were performed at heads varying between 35 and 40 m. The model was designed so as to satisfy the needs of flow visualization around one of the guide vanes. The flow was observed through a visor in the distributor cover whereas the selected guide vane was illuminated through a visor in the spiral case /see Fig. 1/. In flow visualization milk was used. It was injected into the flow through narrow holes in the selected guide vane on both its suction and pressure sides. The flow was observed at various values of the discharge and the distributor opening in both the pump and turbine operating modes, with particular attention paid to the behaviour of the boundary layer. A lab-computer was used in controlling the measurements and for evaluation of the hydraulic parameters.

5. Results and conclusions

The calculated distributions of velocities in the diffuser-type flow around the original guide vanes and around the newly

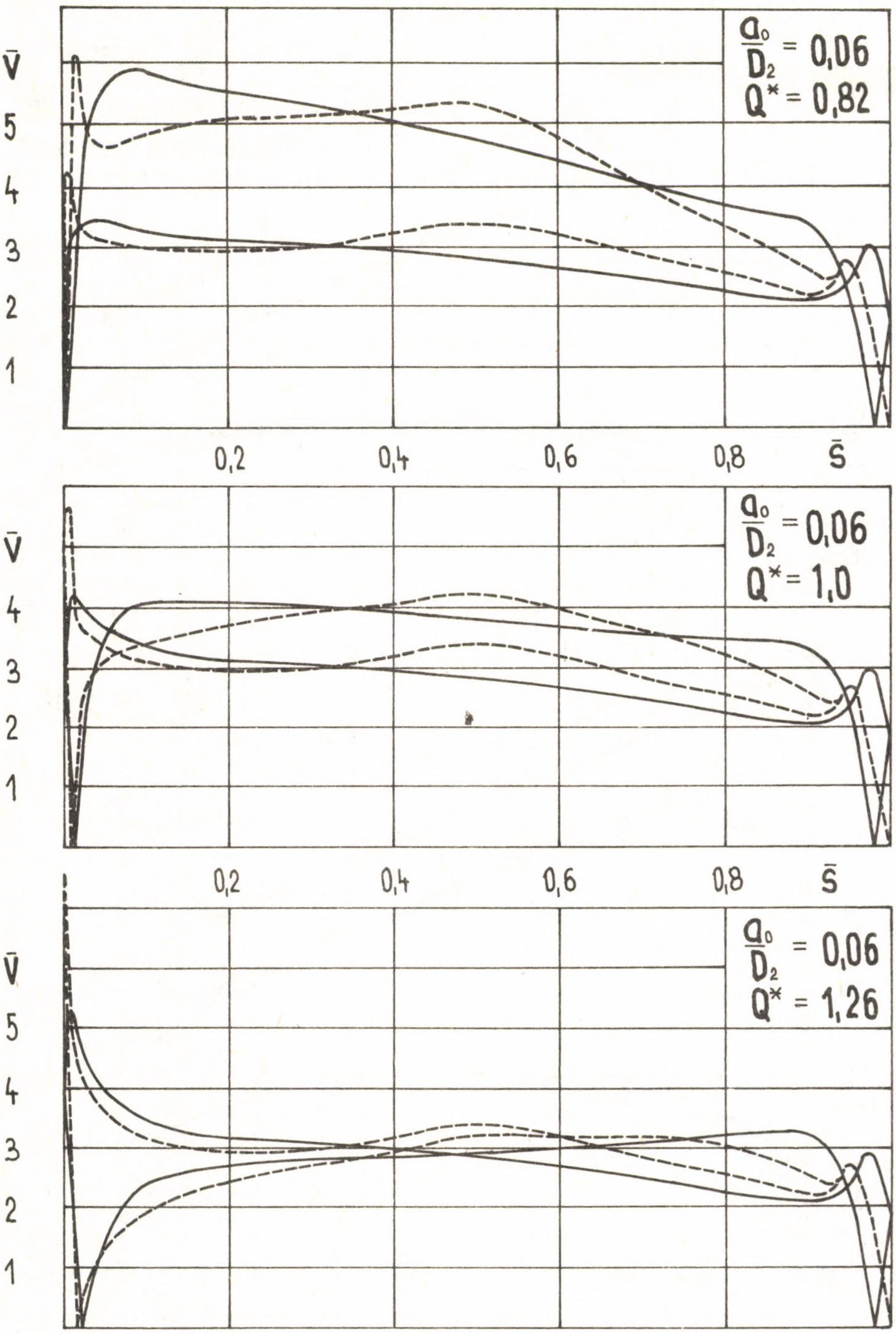

Fig. 3 Calculated velocity distribution around the guide vanes

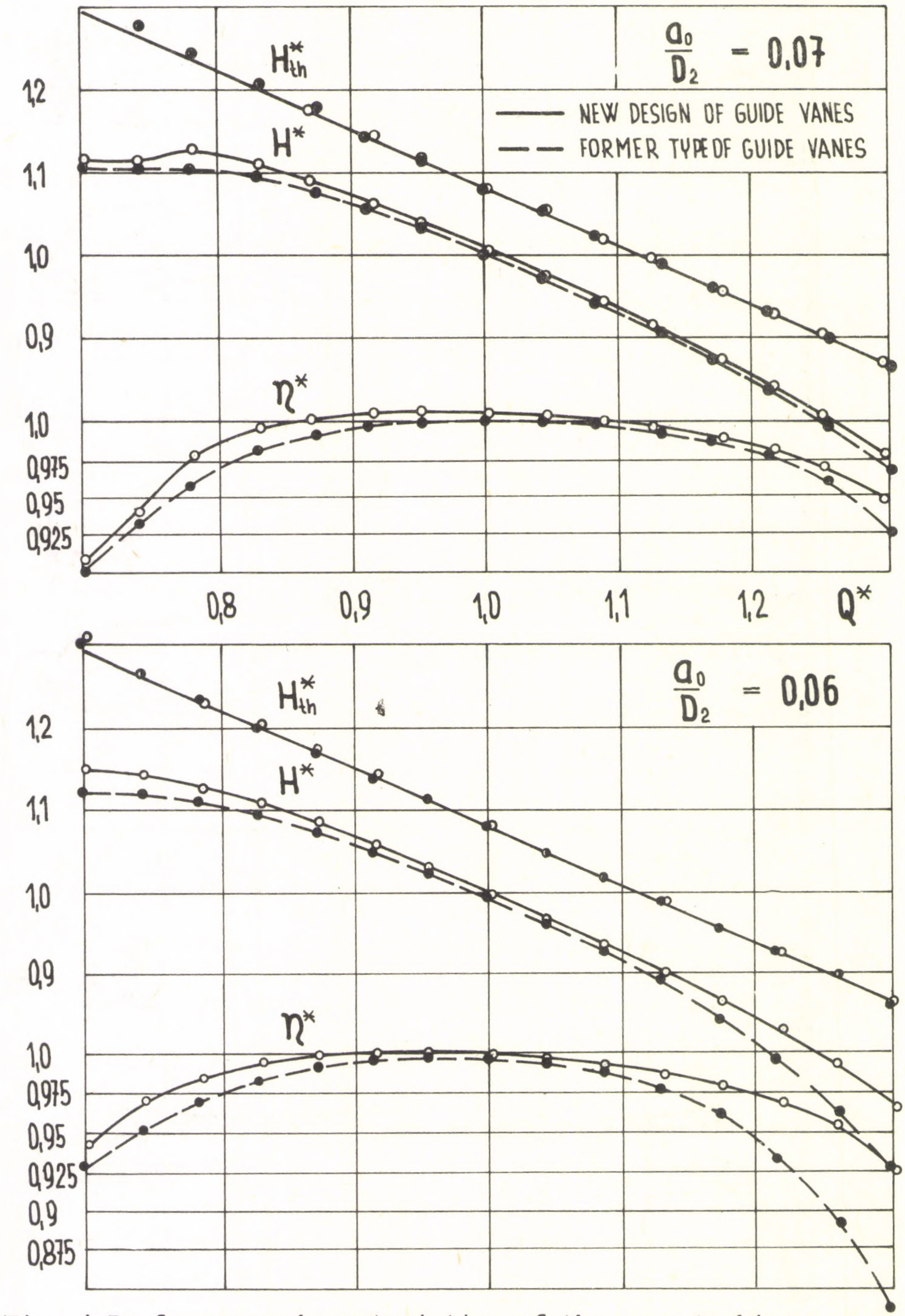

Fig. 4 Performance characteristics of the pump-turbine in the pumping mode operation

designed guide vanes are plotted in Fig. 2. and Fig. 3. The calculations were performed for two distributor openings and three values of the angle of attack. The performance characteristics of the model in the pump mode operation obtained experimentally with both types of guide vanes are shown in Fig. 4. By comparison of all plotted curves the influence of the velocity distribution on the energy losses in the distributor may be estimated. The sensitivity of the leading edge shape with respect to the angle of attack may be easily deduced from Fig. 2 and Fig. 3. The velocity peaks appear either on the suction side /$Q^* = 0.82$/ or on the pressure side /$Q^* = 1.26$/ causing boundary layer separation just behind the leading edge of the blade. This defficiency does not appear at the newly designed guide vane profile. Also the velocity distribution along the middle part of the profile is at the new design more favourable and the boundary layer separation point is always shifted more towards the trailing edge. Herefrom follows the lowering of the losses. This may be seen in Fig. 4, where the characteristics corresponding to the new guide vane design show an increase in both efficiency η^* and head H^*. In order to verify indirectly the correctness of the measured quantities, theoretical characteristics of both alternatives were determined. In Fig. 4 is shown, that for both alternatives the straight line H^*_{th} is identical. In the turbine mode of operation, no changes in performance of practical importance were detected.

The presented results investigations show, that even a relatively simple computational model of the flow applied in the design of the distributor helps substantially in attaining good energy conversion properties. However, it should be noted, that an increase of the overall performance of a reversible pump-turbine can be ensured only when all main functional parts, such as spiral case, distributor, runner and draft tube are mutually well adjusted and the losses are proportionally distributed.

References:

/1/ Waisser Z.: The Solution of Flow through the Stator Blades of Hydraulic Machines /in Czech/ In: Hydro-Turbo, Luhačovice 1974 pp. 58-71.

/2/ Truckenbrodt E.: Ein Quadraturverfahren zur Berechnung der laminar und turbulent Reibungsschicht bei ebener und rotationssymetrischen Strömung. Ing. Arch., XX Bd, 1952, Heft 4, pp. 211-228.

Ing. Jiří ŠPIDLA
Research Institute
ČKD Blansko, k. p.
BLANSKO
Czechoslovakia

Bohuslav SEĎA
Research Institute
ČKD Blansko, k. p.
BLANSKO
Czechoslovakia

PREDICTION OF CAVITATION DAMAGE IN HYDRAULIC TURBOMACHINERY

K. Steller

1. Prediction of cavitation and erosion zones

Cavitation in a hydraulic machine can be distinguished by various stages of its development and sites of occurence, various influence upon the functional properties of the machine, increasing or decreasing dynamic impingement, and vibroacoustic and erosion effects. The change of some cavitation signs in an impeller pump can be illustrated by the curves in fig.1 while fig.2 shows such change in a Francis turbine.

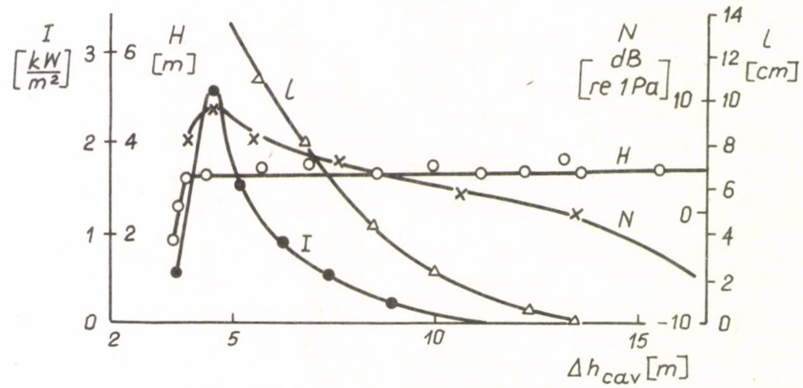

Fig.1. Diagnostic characteristics of a diagonal pump (H - head, l - length of the cavitation cloud, I - intensity of cavitation pulses, N - level of the hydroacoustic noise of 120 kHz frequency, Δh_{cav}=NPSH-Net Positive Suction Head)

In the sequence of many years certain general relationships between cavitation and operational properties of the machines were established. The relationship

$$\sigma = \text{const} \cdot n_{SQ}^{4/3} \tag{1}$$

between the cavitation number σ and the specific speed n_{SQ} is an obvious example. Also methods of determining the cavitation sensitivity of machine components of known geometry have been developed. These enable both predicting cavitation in definite machines and indicating places subject to the most intensive cavitation erosion. An example of such evaluation concerning the stationary circular cascade (guide wheel) in a reversible hydraulic machine [2] will be discussed in the following.

Assuming the two-dimensional model of flow through a circular cascade characterized by a given circulation[1)] and the source (sink) of intensity Q/b situated in the centre (Q -

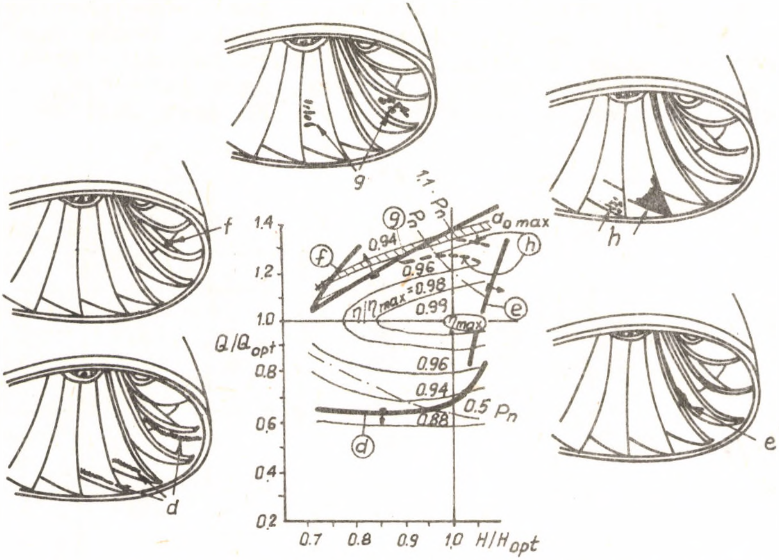

Fig.2. Cavitation course in the runner of a Francis turbine with specific speed $n_{sQ} = 70$ (d,e,f,g,h lines denote the boundaries of cavitation) [1]

flow rate, b - guide blade span) we can evaluate cavitation sensitivity of the guide wheel and indicate the places most susceptible to cavitation damages.

While in the turbining regime the cavitation sensitivity is a univocal function of the position of guide blades it depends in the pumping regime also on the similarity number

$$q = Q/\Gamma_0 b \tag{2}$$

where $\Gamma_0 = (\pi D^2)n/60$ is the circulation at the outlet of the impeller with diameter D and rotation speed n . The cur-

---

1) Circulation is equal $\Gamma_\infty = 0.25Q(R_1+R_2)/(R_2-R_1)^2$ where Q is the flow rate while R_1 and R_2 denote the minimum and maximum radii of the spiral casing, respectively.

2) The quantities σ_∞ and σ_{cr} are cavitation numbers defined by the following formulae:

$$\sigma_\infty = 2(p_\infty - p_v)/\varrho v^2_\infty \quad \text{and} \quad \sigma_{cr} = 2(p_\infty p_{min})/\varrho v^2_\infty$$

where p, p_v, ϱ and v denote pressure, saturated vapour pressure, liquid density and velocity while subscripts ∞ and min refer to the quantities in an undisturbed flow and to their minimum values as measured at the blade surface. By the critical cavitation number σ_{cr} we mean the value of σ that corresponds to cavitation incipience or desinence (which is usually assumed to occur when the local pressure value is equal p_v).

ves showing cavitation sensitivity of the guide wheel of a reversible hydraulic machine mounted at Żydowo Power Station h^ve been presented in fig.3. The curves indicate that one should expect no cavitation in turbining regime ($\sigma_\infty > \sigma_{cr}$)[2] while the blade edges are subject to the most intense erosion

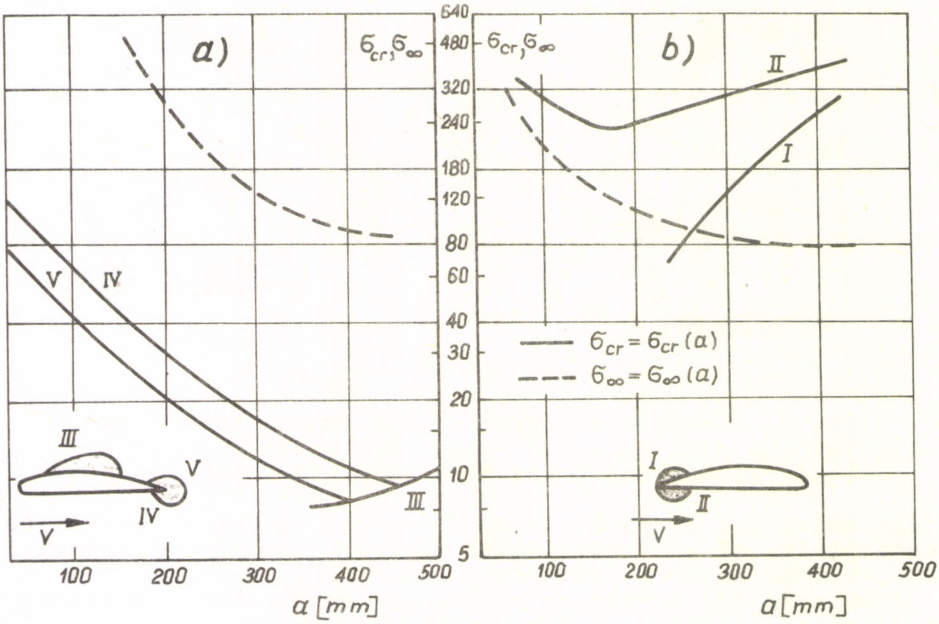

Fig.3. Cavitation sensitivity of the guide wheel of the reversible machine mounted at Żydowo Pump Storage Power Station in turbining (a) and pumping regime (b); acc. [2]

in pumping regime. It follows from $\sigma = \sigma(a_0)$ curves that the cavitation damage hazard occurs first of all on the suction side of the blades (zone II) and gets more and more increased as the guide wheel is being opened. At the openings $a_0 > 275$ mm cavitation cloud develops also at the pressure side. High value of $\Delta\sigma = \sigma_{cr} - \sigma_\infty$ difference allows to expect extremely strong liquid microjet impacts and cavitation cloud pulsations leading to both surface erosion and fatigue failure of the blades.

Results of field inspection confirmed this prediction (fig.4); evident effects of cavitation erosion may be seen near blade edges. One should notice that the pressure side erosion covers only the lower parts of the blades, which is due to the streamline curvature in the meridional plane. Despite of neglecting this phenomenon the numerical computations allowed for fairly reliable prediction of cavitation erosion zones. One should suppose that further development of the numerical methods of cavitation prediction will enable even better determination of the places subject to the most intense cavitation erosion. Certainly, the course of cavitation erosion is determined not only by the cavitation sensitivity of a particular flow system and the stage of cavitation development. Erosion rate is

Fig.4. Cavitation pits at the guide blade of a reversible machine

seriously affected by the cavitation intensity, the physico-chemical properties of the working liquid, the resistance of the structural material to cavitation impingement and corrosion processes that usually accompany cavitation.

2. Cavitation intensity as related to cavitation erosion

Cavitation intensity is usually meant as the quantitative characteristics of the phenomenon. However, the notion has not been defined precisely. Cavitation intensity can be measured, for instance, by the averaged density of the energy flux coming out from the collapsing cavities, that is the quantity determined by duration of this pulse process, acoustic impedance of the medium as well as the number, amplitude and frequency of pressure pulses acting at the definite area of the flow-limiting surface. Assuming that the acoustic impedance of the medium is constant we can evaluate cavitation intensity using an indicator formed from averaged statistical characteristics of a definite pulse process. We can use, for instance, the estimator of the spectral power density

$$\hat{G}_x(f) = \frac{1}{B_e T} \int_0^T x^2(t,f,B_e)dt \tag{3}$$

or the indicator of the energy flux

$$ME = \frac{1}{T} \sum_{i=1}^{N} n_i p_i^2 \tag{4}$$

where T denotes the time of averaging (pulse counting), $x(t,f,B_e)$ - the component of the input signal $x(t)$ at the outlet of a narrow-band filter with the band width equal B_e and mean frequency equal f, n_i - the number of pressure pulses with the amplitude p_i . The estimator $\hat{G}_x$ informs about the frequency structure of a cavitation process while the indicator ME carries information about its amplitude composition.

The results shown in fig.5 indicate that material damage is closely related to the value of the ME indicator. Fig.5a shows the photograph of an eroded specimen with marked places showing positions of a pressure transducer[3] installed to receive pressure pulses from collapsing cavities interchangeably with the specimen. Fig.5b presents circular diagram illustrating

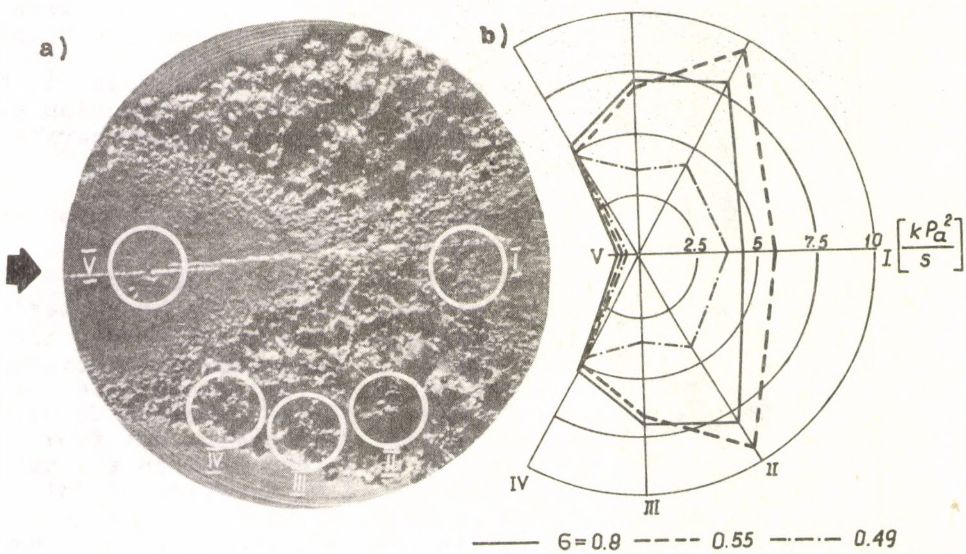

Fig.5. The relationship between the material damage and the values of the ME indicators; a) the area of an eroded specimen at $\sigma = 0.8$ with marked positions of the pressure transducer (I ... V), b) cavitation intensity distribution at various cavitation conditions

the spatial distribution of the ME indicator for σ = const.

Amplitude distributions of pressure pulses (fig.6) show a wide spectrum and very high ratio of "non-damaging" to "damaging" collapses. For the material under consideration the evaluated resistance threshold was about 600 mV.

Cavitation intensity can be measured using also some vibroacoustic quantities like the level of acoustic radiation or the level of vibrations of the flow-limiting walls. A common indicator is the acoustic power as defined by the following formula:

$$W(R) = \int_{(A)} I_a dA \tag{5}$$

where $I_a = p_a^2/\rho c$ denotes the unit flux of acoustic energy emitted by the source at the distance R, p_a - acoustic pressure, c - sound velocity in the medium with density ρ while A is the area of the surface crossed by the flux.

The applicability of acoustic pressure (emitted by the collapsing cavitation bubbles) for evaluation of the flow state and the erosion hazard has been indicated among others by

---

3) Piezoelectric transducer PCB with the membrane of 5.5 mm diameter, 0.145 mV/kPa fidelity and 500 kHz resonance frequency.

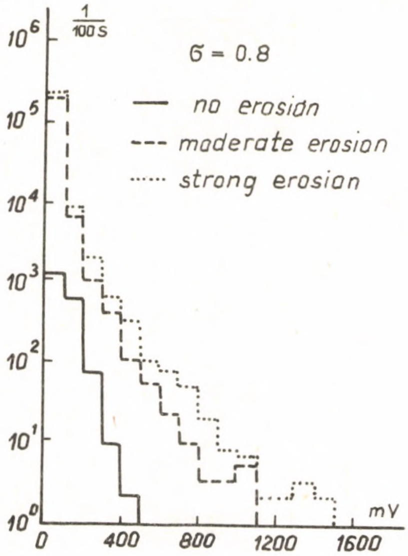

Fig.6. Histograms of pressure pulses and respective effects of cavitation action

F.G.Hammitt [3] and A.S.Ramamurty and P.Bhaskaran [4]. From this point of view it is worthwhile to mention the results obtained in the cavitation tunnel with a cylindrical cavitator at the laboratory of the IF-FM, Pol.Ac.Sci. in Gdańsk. The acoustic pressure (amplitudes, frequencies and effective values) was measured using hydrophones situated at various places of the flow. The effective value of the acoustic pressure appeared extremely useful for describing the state of flow and indicating the cavitation intensity most dangerous from the erosion point of view. The influence of the cavitation development stage (σ) upon the effective value of the acoustic pressure (U_{ef}) for 4 different situations of the hydrophone has been shown in fig.7 while the amplitude distribution of the pressure pulses for a particular situation may be seen in fig.8.

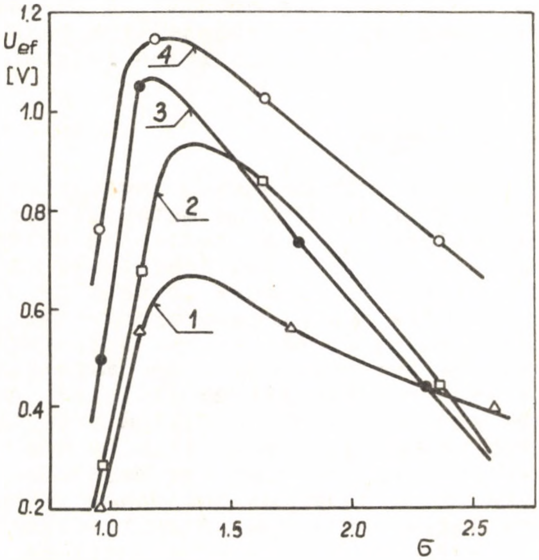

Fig.7. Degree of cavitation influence upon the acoustic pressure value for 4 different hydrophone positions

It follows from the above that there exists a good correlation between the results of the amplitude analysis and the effective values of the acoustic pressure, and that the location of the hydrophone affects only the pressure value (the level of cavitation intensity) and not the shape of the $U_{ef}(\sigma)$ curve. It could be inferred from the maximum of the acoustic pressure

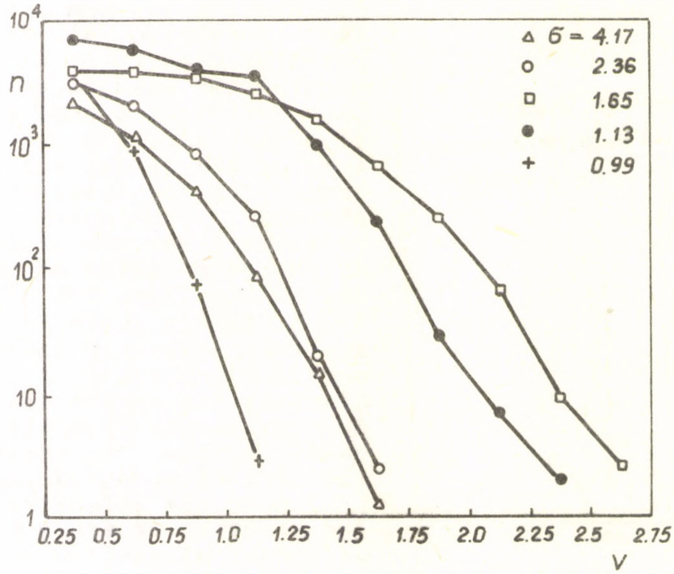

Fig.8. Amplitude distribution of acoustic pressure pulses at various degrees of cavitation

occurring at $\sigma \approx 1.2$ that these were the conditions corresponding to the maximum erosion hazard. This supposition has been confirmed by the results obtained for specimens inlaid into the tunnel wall.

3. On prediction of cavitation damages

The knowledge of hydrodynamic or vibroacoustic cavitation signs is still not sufficient for prediction of material performance in definite flow conditions. Such a prediction requires first of all the knowledge of the material resistance to the action of cavitation. Cavitation resistance is usually evaluated from the test results obtained at laboratory test facilities. This is certainly a relative evaluation allowing for no direct inferring about the performance of the material in conditions different from the test conditions. This is due to the different level, shape and number of so called effective pressure pulses and various response of materials to the change of cavitation impingement. This problem has been discussed in 5 . It has been indicated there at the non-univocal classification or non-uniform differentiation of evaluations of materials tested both in laboratory and field conditions.

<u>3.1. The proposal of predicting material performance in the initial period of damage.</u> Results of testing an aluminium alloy (PA) and zinc (Zn) at various cavitation intensities have been shown in fig.9. The specimens were subjected to cavitation tunnel of our Institute during the period of so called initial damage (fig.9). The choice of such an exposition period

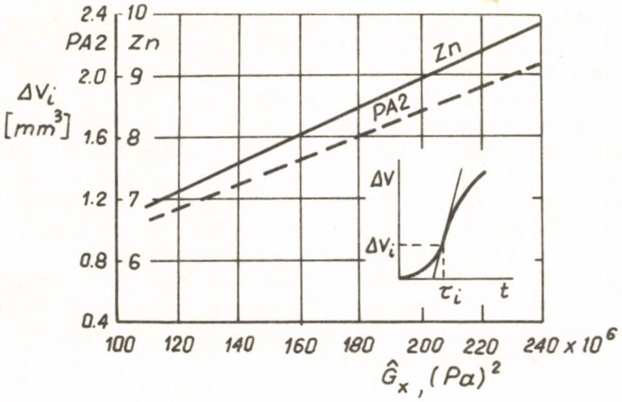

Fig.9. The relationship between the loss of zinc (Zn) and aluminium alloy (PA2) in the initiation period and the spectral power density $\hat{G}_x$

followed from the aiming to keep almost constant impingement conditions, so that the energy taken off by the specimens could be assumed constant and proportional to the energy delivered.

Relations $\Delta V = f(\hat{G}_x)$ following from the above proved to be linear. The results obtained allow to expect the similar relationship for other materials. The confirmation of this supposition will form the basis to conclude about the performance of definite materials in various (especially field) conditions of cavitation. This means that knowing the results of testing the respective specimens in laboratory conditions (with well-determined cavitation intensity) and the cavitation intensity in field we will be able to predict the field performance of the same material. The average rate of damage initiation can be determined from the following relationship

$$\left(\frac{\Delta V}{t}\right)_n = \left(\frac{\Delta V}{t}\right)_m \frac{R_{cav,m}}{R_{cav,n}} \frac{(\eta\, ME)_n}{(\eta\, ME)_m} \tag{6}$$

where ΔV is the volume loss of the material in the period t , R_{cav} is the instantaneous material resistance [6], $\eta < 1$ - the efficiency of energy absorption by the material [4)], ME - the indicator of energy flux, the quantities with subscript n refer to field conditions while those with subscript m to the model tests. Using the simplified assumption of $\eta_n = \eta_m$ and $R_{cav,n} = R_{cav,m}$ we can estimate approximately the erosion rate in field conditions from the formula

$$\left(\frac{\Delta V}{t}\right)_n = \left(\frac{\Delta V}{t}\right)_m \frac{ME_n}{ME_m} \tag{7}$$

---

4) According to [7] the efficiency of energy absorption η can be described by the Weibull distribution, that is

$\eta = 1 - \exp(-\tau\alpha)$ where $\tau = t/t_{r\ max}$

is the relative time of cavitation action and α - the coefficient of the statistical function.

3.2. The methods of predicting cavitation erosion in a prototype. One of the methods consists in estimating the erosion in a prototype by comparing test results with results obtained in field conditions. In both cases the tests are conducted using the same reference material characterized by weak cavitation resistance and the main material - subject of evaluation. The latter one is tested only at the laboratory. The field performance of the essential material is deduced from the results of these three tests. The procedure described above is rather troublesome and leads to highly uncertain predictions.

Basing upon the equality of Strouhal numbers and the kinematic similarity of a model (m) and a prototype (n), N.I.Pylaev and Y.U.Zdel' [8] propose to estimate the erosion extent in water turbines from the following formula

$$\left(\frac{\Delta V}{t}\right)_n = \left(\frac{\Delta V}{t}\right)_m \left(\frac{H_n}{H_m}\right)^{3.5} \left(\frac{D_{1n}}{D_{1m}}\right)^3 \tag{8}$$

where H is the head and D_1 - the characteristic diameter of the runner.

A.S.Lashkov [9] proposed a relationship which is very much alike to (8), except of exponent values.

Both methods of predicting as mentioned above, require determining the volume loss rate $(\Delta V/t)_m$ from model investigations. This requirement is very difficult and frequently even impossible to meet. That is why it is expedient to search for other methods of erosion prediction in hydraulic machinery. One of possible solutions is to relate the mean depth of penetration rate MDPR with the cavitation intensity $I \propto \eta ME$. For the needs of approximate evaluations we can assume the constant resistance of a material ($\bar{R}_{cav}$) and the efficiency η of energy absorption. Basing upon the relationship

$$I = \bar{R}_{cav}\ MDPR \tag{9}$$

and the knowledge of the cavitation intensity indicator ME in field and during laboratory tests (ME_m) as well as the $MDPR_m$ value we can estimate the $MDPR_n$ value from the formula

$$MDPR_n = MDPR_m \frac{ME_n}{ME_m}\ . \tag{10}$$

The preliminary verification of this dependence using aluminium specimens proved the validity of the assumptions made. However, further verifying investigations are expedient.

All the presented erosion prediction concepts are based on less or more justified assumptions. At this stage of our knowledge it seems necessary due to the lack of more precise erosion predicting methods [10] to consider the simplified solutions as allowable.

References

[1] ULITH P.: Kavitationsgrenzen bei Francisturbinen, Voith Information, 3, 1981.

[2] STELLER J.: Profile Sensitivity to Cavitation and Prediction of this Phenomenon for Guide Wheels of Reversible Machines (in Polish), Proc.of the HYDROFORUM'80 Conf., Porąbka-Kozubnik, 1980.

[3] HAMMITT F.G., M.K.DE: Instrument System for Monitoring Cavitation Noise, Report UMICH 014456-80-I, Univ.of Michigan, 1981.

[4] RAMAMURTY A.S., P.BHASKARAN: Velocity Exponent for Erosion and Noise Due to Cavitation, Proc.ASME/CSME Appl. Mech., Fluids Eng.and Bioeng.Conf., Niagara Falls, N.Y. 1979.

[5] STELLER K.: Change of the Relative Material Resistance Due to the Change of Cavitation Conditions, Proc.of the Sixth Conf.on Fluid Machinery, vol.2, Akademiai Kiado, Budapest, 1979.

[6] STELLER K.: New Concept of Evaluation of the Resistance of Materials to the Cavitation Erosion (in Polish),Trans. of the Inst.of Fluid-Flow Machinery, no.80, 1981.

[7] THIRUVENGADAM A.P.: Further Studies of Scaling Laws Governing Cavitation Erosion, I.Mech.Eng., Paper no. C 188/77, 1977.

[8] PYLAEV N.I., Y.U.ZDEL': Kavitatsiya v gidroturbinakh, Mashinostroenie, Leningrad, 1974.

[9] LASHKOV A.S.: Metod prognozirovaniya kavitatsionnogo iznosa gidroturbin, Energomashinostroenie, no.1, 1974.

[10] HAMMITT F.G.: Cavitation Erosion; The State of the Art and Predicting Capability, Appl.Mech.Rev., vol.32, no.6, 1979.

STELLER Kazimierz, Ass.Professor
Institute of Fluid-Flow Machinery
Polish Academy of Sciences,
80-952 Gdańsk, ul.Fiszera 14
Poland

MODEL TESTS ON A SEMI-AXIAL PUMP TURBINE

F. Strohmer, G. Horacek

ABSTRACT

Due to their good hydraulic characteristics semi-axial pump turbines are used in the medium range of pumped storage plants. This paper describes model tests performed with a semi-axial pump turbine model and shows the results of these tests.

The aim of the model tests was the optimization of the hydraulic water passage, the measurement of the hydraulic characteristics over the whole operating range, the investigation of the cavitation behaviour, the investigation of the hydraulic forces and torques as well as the proof of the guaranteed values for the customer.

INTRODUCTION

The growing demand of electric energy entailed also an increase in the construction of pumped storage plants for generation of the necessary peak energy. The use of reversible pump turbines reduces both investment cost of the hydraulic machinery and civil engineering cost.

At present pumped storage plants with reversible pump turbines operate - considering also tidal power plants - at heads rangeing from 2 m to 1300 m. Fig. 1 shows the application range of reversible pump turbines carried out at present.

In the low head and medium head range pumped storage plants are constructed increasingly in a more economical way due to the continuing development of the hydraulic machines. In high head plants their economy was increased by the tendency towards high heads and large unit output.

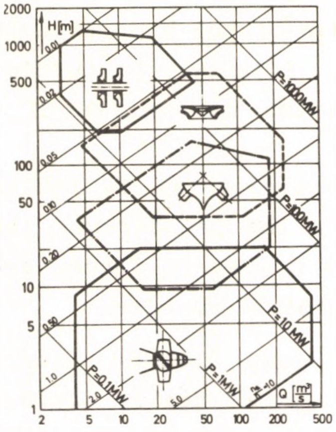

Fig. 1 Application range of reversible pump turbines

In the following model tests with a semi-axial pumped turbine model are described and the results of these tests are shown.

SEMI-AXIAL PUMP TURBINES

Hydraulic Features

Due to their good hydraulic characteristics both in turbining and pumping, semi-axial pump turbines are used in the medium head range of pumped storage plants. Due to their design with adjustable runner blades and adjustable wicket gates these turbines can be operated with the corresponding optimum efficiency points over a large output range. By the possibility to close the runner blades the required starting torque is greatly reduced thus enabling starting in the water. This results in a shorter transition time to the pumping mode as compared with Francis turbines.

Model Tests

For a pumped storage plant with the characteristic data
- turbining H = 18 to 33 m, P = 42 MW
- pumping H = 19 to 31 m, Q = 160 to 72 m^3/s

a semi-axial pump turbine was optimized in a model test whereby the runner centerline being already fixed by the existing draft

tube and the upstream connection to the penstock.
The requirement of a large regulating range of the discharge in the pumping operation as well as of high efficiency in turbine operation over the full operating range led to the use of a double controlled semi-axial pump turbine.
It was the aim of the model tests to optimize the hydraulic contour, proof of the guarantee values in the presence of the customer as well as determination of the hydraulic forces and torques as basis for dimensioning the prototype machine.

Fig. 2 shows a section of the model pump turbine (scale 1 : 16,47). All water leading parts are geometrically similar to the actual plant (runner diamter 6,18 m). Making the discharge ring of plexiglass enabled good observation of the cavitation behaviour of the runner.

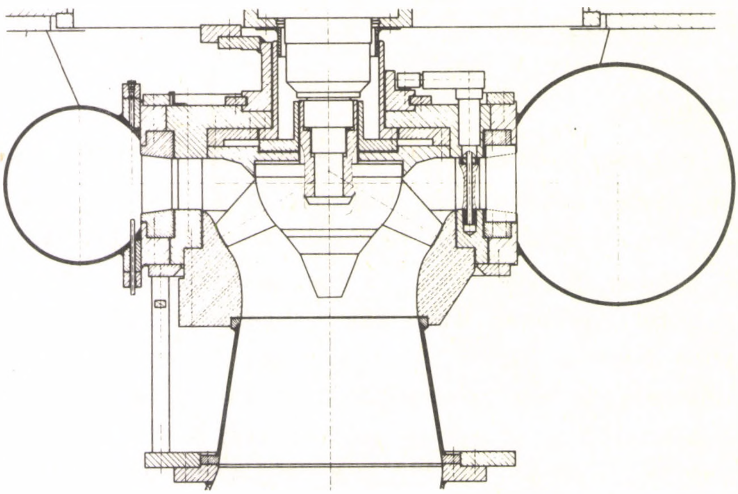

Fig. 2 Section of a semi-axial model pump turbine

The model tests were carried out on one of the vertical pump turbine tests rigs of VOEST-ALPINE AG, Linz.

This test rig shows the following characteristics:

- closed circuit for cavitation tests
  (Q_{max} = 1200 l/sec, H_{max} = 150 m, P_{max} = 330 kW)
- automatic data acquisition and processing
- measuring accuracy of the individual measured quantity ±0,1%
  repeatability better than ± 0,15 %
  total error of efficiency measuring ± 0,3%.

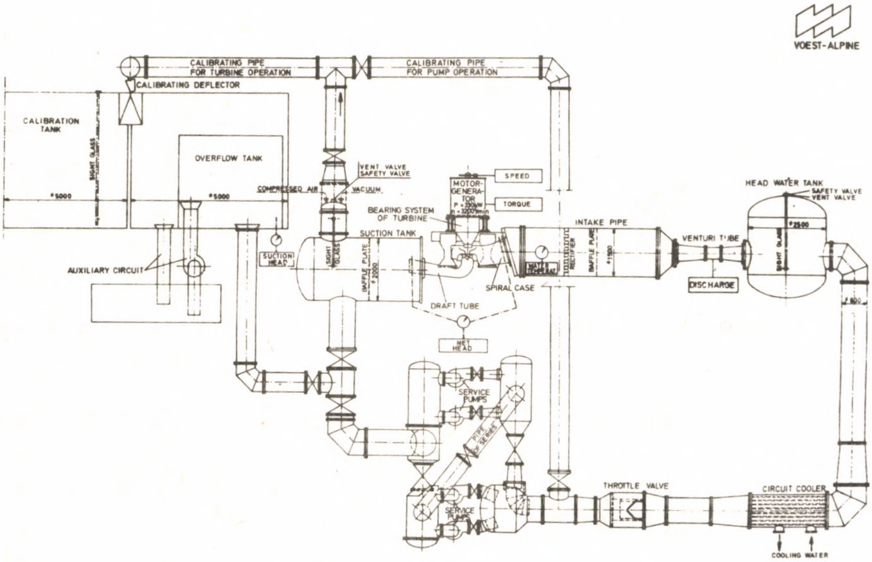

Fig. 3 Scheme of the test stand

Several runners which differed in the number of blades, shape of blades and angle of inclination of the rotating axis were examined in preliminary tests and the influence on efficiency and cavitation behaviour was investigated. By probe measuring analyses of losses were carried out and the relevant modifications were derived.

As example of such measurement, the distribution of the meridional speed Kcm, distribution of angular momentum and the total energy P_{total} at the runner inlet and outlet for the point of optimum turbine efficiency are shown in Fig. 4.

The measurement was made with a semispherical 4-hole probe by which the vector of the speed can be recorded. The calibration curves were numerically represented in order to enable the evaluation by means of an EDP program. It was the purpose of these investigations to determine the individual losses.

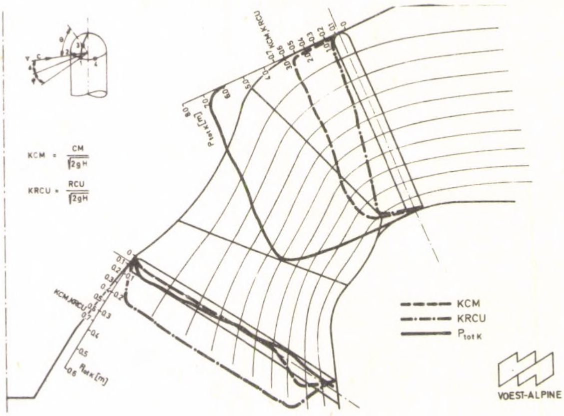

Fig. 4 Velocity-, angular momentum and pressure distribution during turbining

For cavitation reasons finally a runner with eight blades was provided. Due to the low heads and the resulting low cavitation intensity, minor cavitation at the inlet edges both at the suction and pressure side were permitted.

Fig. 5 shows the hill diagram for turbine operation in the unit sizes. The characteristic curves for pump operation are shown in Fig. 6 dimensionless.

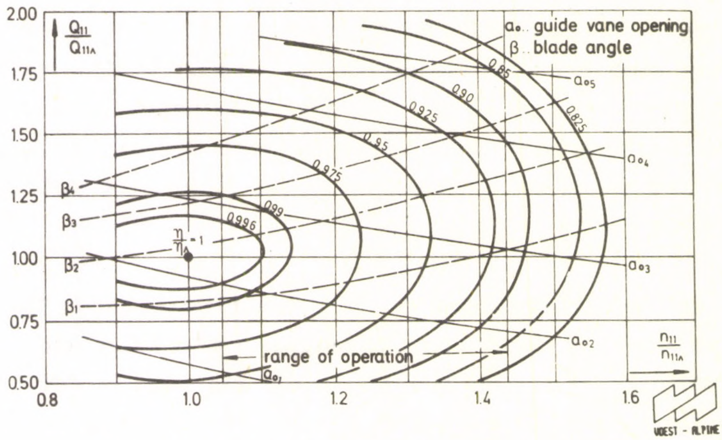

Fig. 5 Hill diagram for turbining

The pump characteristics are the envelope curve of various openings of the wicket gates for one constant runner blade opening and show the dependence of the pressure number or efficiencies and the discharge number.

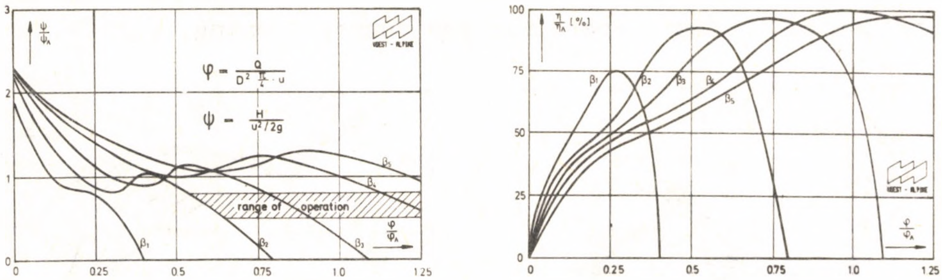

Fig. 6 Dimensionless pump characteristics

After investigation of the model pump turbine during turbine and pump operation the characteristics in the remaining quadrants were measured. This four-quadrant characteristic curve serves to simulate the starting and shut-off procedures as well as the operating transitions by means of EDP programs. Fig. 7 shows a four-quadrant curve for a selected runner position.

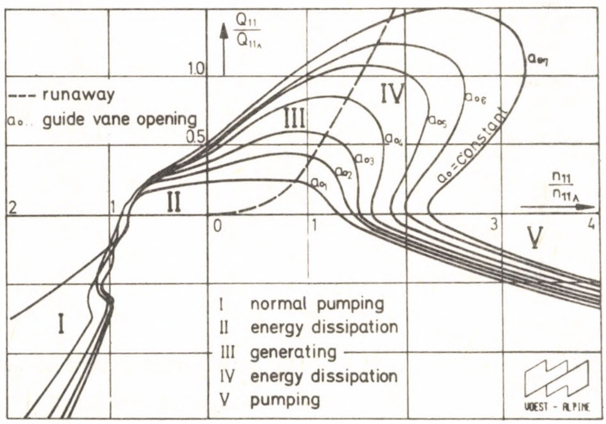

Fig. 7 Four-quadrant diagram for a runner opening

With increasing machine size the knowledge of the strength of individual turbine parts is very important. For safe dimensioning, particularly of the drives the static and dynamic forces and torques of wicket gates and runner were measured over all quadrants. Fig. 8 and Fig. 9 show the course of the wicket gate torque and the axial thrust over all quadrants as function of the unit speed for one runner opening.

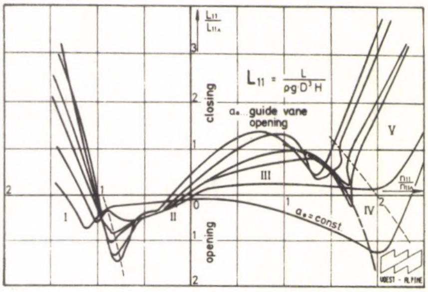

Fig. 8 Hydraulic wicket gate unit torque

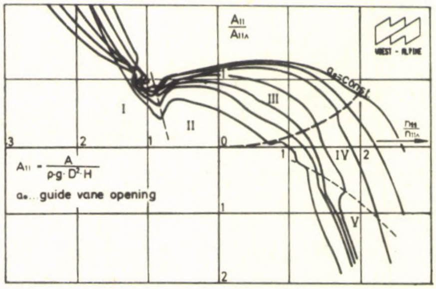

Fig. 9 Hydraulic axial unit thrust

The measuring arrangement for determination of the runner blade torque may be seen from Fig. 10.

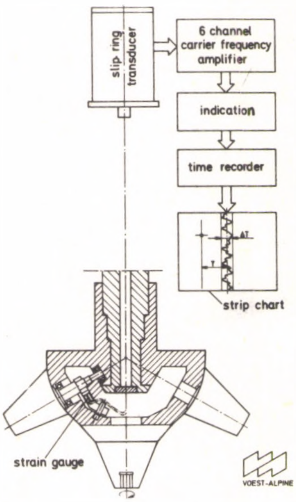

Fig. 10 Measuring arrangement for determination of runner blade torque

The hydraulic torque was measured with the strain gauge fixed on a bending rod and the signal was transmitted via a slip ring transmitter to the carrier frequency amplifier. The amplitude of the torque vibrations was recorded by means of an UV oscillography. The results of these measurements are shown for turbine operation in Fig. 11 and for pump operation in Fig. 12.

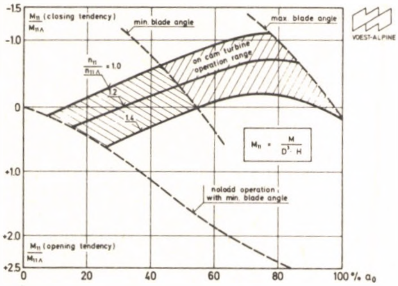

Fig. 11 Runner blade unit torque, turbining

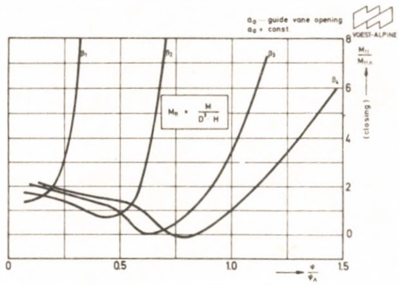

Fig. 12 Runner blade unit torque, pumping at constant wicket gate opening

For judgement of the operational behaviour measurements of pressure fluctuations along the water passage were performed.

Start-up Procedure

The pump characteristics $\psi = f(\varphi)$ are usually determined during tests in a closed test circuit at constant speed, operating points are obtained by the intersections of the dynamic characteristic and the pump characteristic.

However, at the prototype the geodetic head difference between head- and tailwater level is to be overcome - besides the dynamic characteristic which are losses depending on the discharge in the penstock - that cannot be simulated in model tests in a closed circuit.

The tests subsequently described herein aimed at the determination of a proper start-up procedure for the pumping mode by determining the discharge and head characteristics depending on the opening time of the wicket gates.

As may be gathered from the measurements of the static characteristics (Fig. 13), the pump characteristics show instabilities at large runner blade openings which are caused by the rotating stall in the area of the inflow edge.

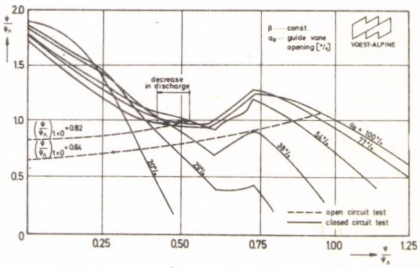

Fig. 13 Dimensionless characteristic for a runner blade opening

Two specific cases were investigated during the tests in an open circuit:

- dynamic and geodetic characteristic is below the minimum ψ - value of instability for a_0 = 100 %
- dynamic and geodetic characteristic is above the minimum ψ - value of instability for a_0 = 100 %

The results for $\left(\frac{\psi}{\psi_\Lambda}\right)_{t=0}$ = 0,82 are presented in Fig. 14 and prove that the discharge φ/φ_Λ is again decreasing as from a_0 = 54 % in accordance with the characteristic determined in the closed test circuit.

During the tests performed at $\left(\frac{\psi}{\psi_\Lambda}\right)_{t=0}$ = 0,64 the stable leg of the characteristic was reached in spite of the instabilities for smaller a_0-values as shown in Fig. 13.

If the minimum ψ - value of the instable pump characteristic coincides with the dynamic and geodetic characteristic, an operating point is given at the stable leg of the pump characteristic. This procedure entails a sudden increase of the discharge and the pressure number as can be seen in Fig. 14 (approx. 50 % a_0).

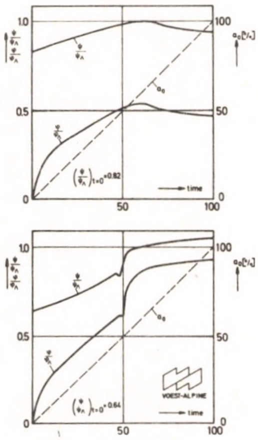

Fig. 14 Simulation of the start-up procedure in the open test circuit

In order to avoid these areas during pump start-up - instabilities in the characteristic are not inevitable at smaller runner blade openings - the following start-up procedure was established:

- start-up to synchronous speed at closed wicket gates and runner blades
- opening of wicket gates to operating position thus ensureing the stable leg of the H-Q-curve to be reached
- opening of runner blades to operating position.

CONCLUSION

Model tests are necessary for the layout of a pump turbine and form the basis for the design of the prototype plant.

The results received from model testing a semi-axial pump turbine give a good survey of the tests to be performed in the course of development.

Besides the tests for a hydraulic optimization for a safe and reliable design of the prototype also measurements of the wicket gate- and runner blade torques as well as start-up investigations are necessary.

Strohmer Franz, Dr. techn. Dipl.-Ing.
Manager of Hydro Power Engineering Department

Horacek Gerhard, Dr. techn. Dipl.-Ing.
Head of Hydraulic Laboratory

VOEST-ALPINE AG / TLM 1
Postfach 2
4010 Linz - Austria

Designations

D (m)	runner diameter	η (%)	efficiency
H (m)	head	β	runner blade opening
n (rpm)	speed	a_0	wicket gate opening
n_q (rpm)	specific speed	ψ	pressure number
u (m/s)	circumferential speed	φ	discharge number
g (m/s^2)	acceleration due to gravity	n_{11}	unit speed
ρ (kg/m^3)	specific density	Q_{11}	unit discharge
P (MW)	output	L_{11}	unit wicket gate torque
		A_{11}	unit axial thrust
		M_{11}	unit runner blade torque
		t	time

Indices

T turbine

P pump

$\wedge$ optimum

FRICTION LOSSES IN ROTATING CURVED PIPES

Mircea A.Tămaş

Summary

Considering the results of previous papers, the present work proposes a general method to obtain the friction factor and the velocity profiles for laminar flow in rotating curved pipes of circular cross section, for any value of rotation or curvature.

1. Introduction.- It is well known the importance of understanding the complex hydrodynamic phenomena in rotating passages of turbomachines and so, the case of the laminar flow in a rotating curved pipe can be considered as a first step in the investigation of flow through the impeller channels.

2. Symbols

ρ = density
ν = kinematic viscosity
p = field of static pressure
$\bar{q}$ = angular velocity
R = radius of circular cross section of pipe
L = pipe length
$\bar{C}_Z$ = position vector
Re = Reynolds number
S = Strouhal number
$\bar{c}$ = position vector of $\bar{O}$ with respect to $\bar{O}'$
V_n, V_t, V_y = components of velocity in orthogonal curvilinear coordinates.
$\bar{V}$ = relative velocity
R_c = radius of curvature
$\bar{f}'$ = field of gravitational acceleration with respect to the inertial system ($\bar{O}'$)
$\bar{Q}^T$ = transpose of the orthogonal tensor
ξ = distance from pipe wall

3. Navier-Stokes Equations, in the Case of Laminar Flow

Let be ($\bar{O}$; x, y, z) a non-inertial frame of reference. The Navier-Stokes equations can be written /4/, in orthogonal curvilinear coordinates (r, Θ, y) (fig.1):

$$\frac{\partial V_n}{\partial \tau} + V_n\frac{\partial V_n}{\partial r} + \frac{V_t}{r}\frac{\partial V_n}{\partial \Theta} + V_y\frac{\partial V_n}{\partial y} - \frac{V_t^2}{r} + \frac{V_y^2\cos\Theta}{R_c} - 2q V_y\cos\Theta =$$
$$= -\frac{1}{\rho}\frac{\partial p_M}{\partial r} + \nu\left[\frac{\partial^2 V_n}{\partial r^2} + \frac{1}{r}\frac{\partial V_n}{\partial r} + \frac{1}{r^2}\frac{\partial^2 V_n}{\partial \Theta^2} + \frac{\partial^2 V_n}{\partial y^2} - \frac{2}{r^2}\frac{\partial V_t}{\partial \Theta} - \frac{V_n}{r^2} - \right.$$
$$\left. - \frac{1}{R_c}\left(\frac{\partial V_n}{\partial r}\cos\Theta - \frac{\partial V_n}{r\partial\Theta}\sin\Theta\right) - \frac{V_n\cos^2\Theta}{R_c^2} + \frac{V_t\sin\Theta\cos\Theta}{R_c^2} + \frac{2\cos\Theta}{R_c}\frac{\partial V_y}{\partial y}\right] \tag{1}$$

$$\frac{\partial V_t}{\partial \tau} + V_n \frac{\partial V_t}{\partial r} + \frac{V_t}{r}\frac{\partial V_t}{\partial \theta} + V_y \frac{\partial V_t}{\partial y} + \frac{V_n V_t}{r} - \frac{V_y^2 \sin\theta}{R_c} + 2q V_y \sin\theta =$$

$$= -\frac{1}{\rho}\frac{\partial p_M}{r\,\partial\theta} + \nu\left[\frac{\partial^2 V_t}{\partial r^2} + \frac{1}{r}\frac{\partial V_t}{\partial r} + \frac{1}{r^2}\frac{\partial^2 V_t}{\partial \theta^2} + \frac{\partial^2 V_t}{\partial y^2} + \frac{2}{r^2}\frac{\partial V_n}{\partial \theta} - \frac{V_t}{r^2} - \right.$$

$$\left. -\frac{1}{R_c}\left(\frac{\partial V_t}{\partial r}\cos\theta - \frac{\partial V_t}{r\,\partial\theta}\sin\theta\right) + \frac{V_n \sin\theta\cos\theta}{R_c^2} - \frac{V_t \sin^2\theta}{R_c^2} - \frac{2}{R_c}\sin\theta\frac{\partial V_y}{\partial y}\right] \tag{2}$$

$$\frac{\partial V_y}{\partial \tau} + V_n \frac{\partial V_y}{\partial r} + \frac{V_t}{r}\frac{\partial V_y}{\partial \theta} + V_y \frac{\partial V_y}{\partial y} - \frac{V_y}{R_c}\left(V_n\cos\theta - V_t\sin\theta\right) + 2q\left(V_n\cos\theta - V_t\sin\theta\right) =$$

$$= -\frac{1}{\rho}\cdot\frac{\partial p_M}{\partial y} + \nu\left[\frac{\partial^2 V_y}{\partial r^2} + \frac{1}{r}\frac{\partial V_y}{\partial r} + \frac{\partial^2 V_y}{r^2\,\partial\theta^2} + \frac{\partial^2 V_y}{\partial y^2} - \frac{1}{R_c}\left(\frac{\partial V_y}{\partial r}\cos\theta - \frac{\partial V_y}{r\,\partial\theta}\sin\theta\right) - \right.$$

$$\left. - \frac{2\cos\theta}{R_c}\frac{\partial V_n}{\partial y} + \frac{2\sin\theta}{R_c}\frac{\partial V_t}{\partial y} - \frac{V_y}{R_c^2}\right] \tag{3}$$

and the equation of continuity is:

$$\frac{\partial V_n}{\partial r} + \frac{V_n}{r} + \frac{\partial V_t}{r\,\partial\theta} + \frac{\partial V_y}{\partial y} - \frac{1}{R_c}\left(V_n\cos\theta - V_t\sin\theta\right) = 0 \tag{4}$$

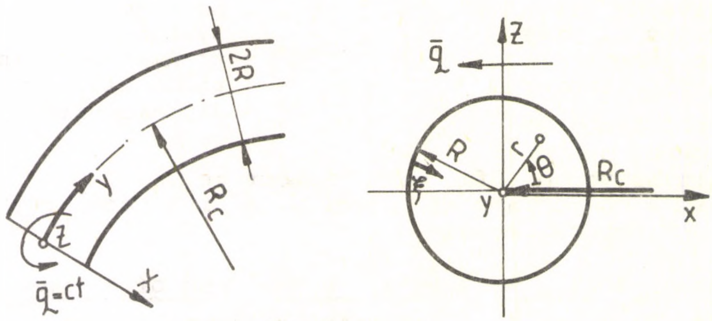

Fig. 1

p_M is the motion pressure obtained in /4/, and has the expression, in this particular case:

$$\frac{1}{\rho}\nabla p_M = \frac{1}{\rho}\nabla p - \bar{Q}^T\cdot\bar{f}' + \left[\bar{q}\cdot\left(\bar{C}_z - \bar{C}\right)\right]\bar{q} - q^2\left(\bar{C}_z - \bar{C}\right) \tag{5}$$

which is similar with Johnston /7/ or Ito /1/ relationship.

4. <u>Boundary Layer Equations</u>.- The following assumtions are made:

a) incompressible fluid; b) fully developed flow; c) steady laminar flow; d) continuity of secondary flow; e) the origin of the non-inertial frame concurs with the origin of the inertial frame; f) the flow in the pipe is formal divided in two regions:

a thin "boundary layer" near the wall, where the secondary flow takes place and the viscous forces are important and a frictionless core (this assumption is justified by the results of the previous paper and of course, by the effects of rotation and curvature upon the laminar flow); g) constant rotation; h) constant curvature.

According to Schlichting classical way and using the above assumptions, the equations of motion in the boundary layer become:

$$\begin{cases} -\dfrac{V_t^2}{R}+\dfrac{V_y^2\cos\theta}{R_c}\left[1-\dfrac{2\Omega R_c}{V_y}\right]=-\dfrac{1}{\rho}\dfrac{\partial p_M}{\partial r} & (6)\\ V_n\dfrac{\partial V_t}{\partial r}+\dfrac{V_t}{R}\dfrac{\partial V_t}{\partial\theta}-\dfrac{V_y^2\sin\theta}{R_c}\left[1-\dfrac{2\Omega R_c}{V_y}\right]=-\dfrac{1}{\rho}\dfrac{\partial p_M}{R\partial\theta}+\nu\dfrac{\partial^2 V_t}{\partial r^2} & (7)\\ V_n\dfrac{\partial V_y}{\partial r}+\dfrac{V_t}{R}\dfrac{\partial V_y}{\partial\theta}+\dfrac{V_yV_t\sin\theta}{R_c}\left[1-\dfrac{2\Omega R_c}{V_y}\right]=\nu\dfrac{\partial^2 V_y}{\partial r^2} & (8)\end{cases}$$

The term $\left[1-\dfrac{2R_c\Omega}{V_y}\right]$ shows the complex influence of rotation and curvature, (it is known that both, the Coriolis forces - effects of rotation - and the centrifugal forces - effect of curvature - set up secondary flows), and confirms the results of Hoffmeister /8/. It is interesting to study the opposite influences of rotation and curvature, in the present case, upon the secondary flow, especially when $2R_c\Omega/V_y \cong 1$ /9/ (that means also $S \cong P_c$, where $S=2R\Omega/\tilde{V}_y$ and $P_c=R/R_c$), but that is not our present purpose. Ito /2/ presents such an example and shows the two opposite secondary flows which neutralize the effects upon the axial velocity profile, and also obtains a theoretical formula for the friction factor, but only in the particular case of small rotation and small curvature. For us, it is important to know the friction factor for significant values of rotation and so $S \gg P_c$, even if the curvature is sensible.

Outside the boundary layer, according to experimental data and like /1/, /5/,/6/, the equations of motion offer the possibility to express the parameters of secondary flow, such as:

$$\left(\frac{\partial p_M}{\partial\theta}\right)_\delta=\frac{\rho R\sin\theta}{R_c}(V_y)_\delta^2-2\Omega\rho(V_y)_\delta R\cdot\sin\theta \tag{9}$$

$$V_x=-\frac{1}{\rho}\frac{\partial p_M}{\partial y}\,\frac{1}{\dfrac{\partial V_y}{\partial x}-\dfrac{V_y}{R_c}+2\Omega} \tag{10}$$

Considering a definite thickness δ and using (9) and the boundary conditions /6/, the equations (6),(7),(8) can be integrated through the boundary layer:

$$-\frac{1}{R}\frac{d}{d\theta}\int_0^\delta V_t^2 d\xi - \frac{\sin\theta}{R_c}\int_0^\delta \left[V_t^2+(V_y)_\delta^2 - V_y^2\right] d\xi +$$

$$+2\Omega\sin\theta\int_0^\delta \left[(V_y)_\delta - V_y\right] d\xi = \nu\left(\frac{\partial V_t}{\partial \xi}\right)_0 \quad (11)$$

$$-\frac{1}{R}\frac{d}{d\theta}\int_0^\delta V_t V_y\, d\xi + (V_y)_\delta \frac{1}{R}\frac{d}{d\theta}\int_0^\delta V_t\, d\xi + (V_y)_\delta \frac{\sin\theta}{R_c}\int_0^\delta V_t\, d\xi -$$

$$-\frac{2\sin\theta}{R_c}\int_0^\delta V_t V_y\, d\xi + 2\Omega\sin\theta\int_0^\delta V_t\, d\xi = \nu\left(\frac{\partial V_y}{\partial \xi}\right)_0 \quad (12)$$

According to (d):

$$\int_1^2 V_x\, dz = \int_0^\delta V_t\, d\xi \quad (13)$$

and from (10), because $\frac{\partial p_M}{\partial y} = ct$ /4/:

$$\frac{d(V_y)_\delta}{d\theta} = -\frac{(V_y)_\delta R\cdot\sin\theta}{R_c}\left[1-\frac{2\Omega R_c}{(V_y)_\delta}\right] + \frac{\frac{\partial p_M}{\partial y} R^2 \sin^2\theta}{\rho\int_0^\delta V_t\, d\xi} \quad (14)$$

5. <u>Solutions of Integral Equations</u>.- The Pohlhausens's approximative method, which has been used with success by Ito /1/ and also /5/,/6/ is considered to obtain the velocity expressions:

$$V_t = \frac{\delta^2 (V_y)_\delta \sin\theta}{\nu}\left[2\Omega - \frac{(V_y)_\delta}{R_c}\right]\cdot G_1(\eta) + \frac{\Lambda}{\nu}\left[2\Omega - \frac{(V_y)_\delta}{R_c}\right]\cdot G_2(\eta) \quad (15)$$

$$V_y = (V_y)_\delta \cdot G_3(\eta) \quad (16)$$

where Λ is the shape factor and $\eta = \xi/\delta$,

$$G_1(\eta) = \frac{1}{3}\eta - \frac{1}{2}\eta^2 + \frac{1}{6}\eta^4 \tag{17}$$

$$G_2(\eta) = \frac{1}{6}\eta - \frac{1}{2}\eta^3 + \frac{1}{3}\eta^4 \tag{18}$$

$$G_3(\eta) = 2\eta - 2\eta^3 + \eta^4 \tag{19}$$

Considering the non-dimensional coefficients:

$$\delta = \bar{\delta}\left(\frac{\nu^2 R}{g(V_y)_{\delta,\theta_0}}\right)^{1/4} \tag{20}$$

$$\Lambda = \bar{\Lambda}\left(\frac{\nu^2 R (V_y)_{\delta,\theta_0}}{g}\right)^{1/2} \tag{21}$$

$$(V_y)_\delta = (\bar{V}_y)_\delta \cdot (V_y)_{\delta,\theta_0} \tag{22}$$

where $\theta_0 = 0$, the integral equations become:

$$\begin{aligned} &-\frac{d}{d\theta}\left\{A\left[\frac{17}{315}\bar{\delta}^5(\bar{V}_y)_\delta^2 \cdot \sin^2\theta + \frac{101}{1260}\bar{\delta}^3(\bar{V}_y)_\delta\bar{\Lambda}\cdot\sin\theta + \frac{19}{630}\bar{\Lambda}^2\bar{\delta}\right]\right\} - \\ &-\sin\theta \cdot P_c \cdot A\left[\frac{17}{315}\bar{\delta}^5(\bar{V}_y)_\delta^2 \cdot \sin^2\theta + \frac{101}{1260}\bar{\delta}^3(\bar{V}_y)_\delta\bar{\Lambda}\cdot\sin\theta + \frac{19}{630}\bar{\Lambda}^2\bar{\delta}\right] = \\ &= \frac{53}{35}\bar{\delta}(\bar{V}_y)_\delta^2 \cdot (R_0)_{\delta,\theta_0}^{-1} \cdot \sin\theta + \frac{3}{5}\bar{\delta}(\bar{V}_y)_\delta \cdot \sin\theta + 3B\frac{\bar{\Lambda}}{\bar{\delta}} \end{aligned} \tag{23}$$

$$\begin{aligned} &-\frac{d}{d\theta}\left\{B\left[\frac{167}{126}\bar{\delta}^3(\bar{V}_y)_\delta^2 \cdot \sin\theta + \frac{263}{252}\bar{\Lambda}\bar{\delta}(\bar{V}_y)_\delta\right]\right\} - \\ &-\sin\theta\left\{P_c \cdot B\left[\frac{41}{63}\bar{\delta}^3(\bar{V}_y)_\delta^2 \cdot \sin\theta + \frac{74}{126}\bar{\Lambda}\bar{\delta}(\bar{V}_y)_\delta\right]\right\} + \\ &+\sin\theta\left\{\left[2\bar{\delta}^3(\bar{V}_y)_\delta \cdot \sin\theta + \frac{3}{2}\bar{\Lambda}\bar{\delta}\right] \cdot P_c\left[(R_0)_{\delta,\theta_0} - (\bar{V}_y)_\delta\right]\right\} + \\ &+(\bar{V}_y)_\delta \frac{d}{d\theta}\left\{B\left[2\bar{\delta}^3(\bar{V}_y)_\delta \cdot \sin\theta + \frac{3}{2}\bar{\Lambda}\bar{\delta}\right]\right\} = 60\frac{(\bar{V}_y)_\delta}{\bar{\delta}} \end{aligned} \tag{24}$$

$$\frac{d(\bar{V}_y)_\delta}{d\theta} = -P_c \cdot \sin\theta\left[(\bar{V}_y)_\delta - (R_o)_{\delta,\theta_o}\right] - \frac{I_1 \cdot \sin^2\theta}{B\left[\frac{1}{15}\bar{\delta}^3(\bar{V}_y)_\delta \cdot \sin\theta + \frac{1}{20}\bar{\Lambda}\bar{\delta}\right]} \tag{25}$$

where:

$$(R_o)_{\delta,\theta_o} = \frac{2q\,R_c}{(V_y)_{\delta,\theta_o}} \quad , \quad A = B^2$$

$$B = 1 - (\bar{V}_y)_\delta \,(R_o)^{-1}_{\delta,\theta_o} \quad , \quad I_1 = \frac{4}{\pi}\int_0^{\pi} \frac{(\bar{V}_y)_\delta}{\bar{\delta}}\, d\theta$$

6. <u>The Friction Factor</u>

According to /1/ the mean axial-velocity is:

$$\tilde{V}_y = \frac{2}{\pi}\int_0^{\pi}(V_y)_\delta \cdot \sin^2\theta\, d\theta - \frac{2}{\pi R}\int_0^{\pi}(V_y)_\delta \int_0^{\delta}\left(1 - \frac{V_y}{(V_y)_\delta}\right) d\xi\, d\theta \tag{26}$$

and so

$$\tilde{V}_{y/o} = I_2 - I_3\, R_e^{-1/2}\, S^{-1/4}\, \tilde{V}_{y/o}^{\;1/4} \tag{27}$$

where:

$$\tilde{V}_{y/o} = \tilde{V}_y \big/ (V_y)_{\delta,\theta_o} \quad , \quad I_2 = \frac{2}{\pi}\int_0^{\pi}(\bar{V}_y)_\delta \sin^2\theta\, d\theta$$

$$I_3 = \frac{3 \cdot 2^{3/4}}{5\pi}\int_0^{\pi}(\bar{V}_y)_\delta\, \bar{\delta}\, d\theta \quad , \quad R_e^{\cdot} = \frac{2R\,\tilde{V}_y}{\nu}$$

According to /4/ the friction factor is:

$$\lambda = -\frac{4R}{\tilde{V}_y^2}\,\frac{1}{\varrho}\left(\frac{\partial p_M}{\partial y}\right) \tag{28}$$

and so

$$\lambda = 2^{9/4}\, I_1\, R_e^{-1/2}\, S^{3/2}\, P_c^{-5/4}\, (R_o)^{-5/4}_{\delta,\theta_o} \tag{29}$$

where

$$(R_o)_{\delta,\theta_o} = I_2 \cdot S \cdot P_c^{-1} - I_3 R_e^{-1/2} S^{1/2} P_c^{-3/4} (R_o)_{\delta,\theta_o}^{1/4} \tag{30}$$

7. Numerical Results.- Using the numerical solutions of the equations (23),(24),(25), obtained on a Felix C 256 electronic computer, the axial velocity profiles can be plotted and also, with (29), the friction factor is calculated.

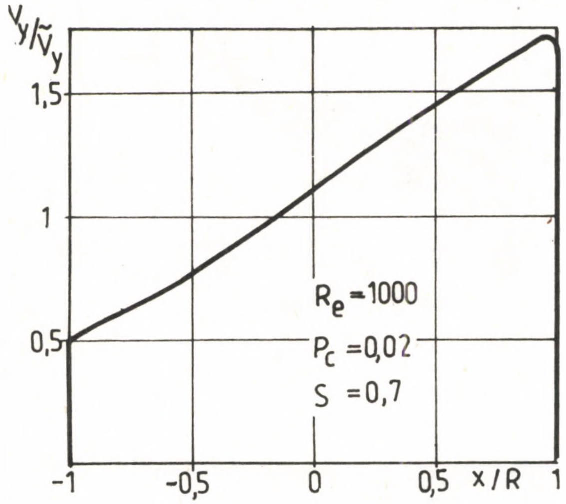

Fig. 2

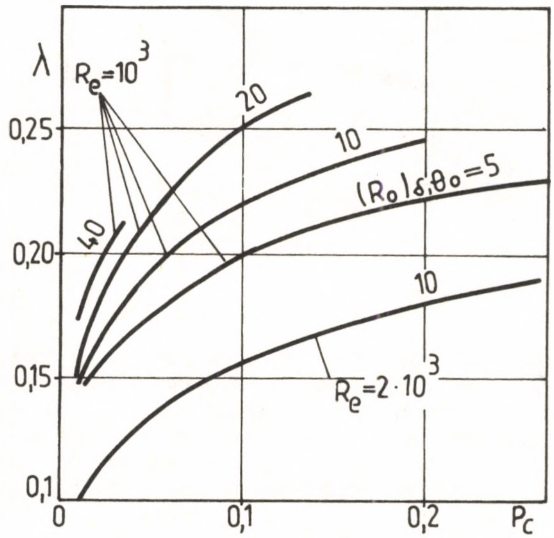

Fig. 3

The general expression (26), fig.2 and fig.3, show that the friction factor λ and the axial velocity are functions of S, Re and P_c; so, the generality of the method is confirmed. The values of λ obtained with the present method are compared with experimental data /3/ (fig.4 and fig.5) and a very good agreement, for the case of laminar flow, is observed.

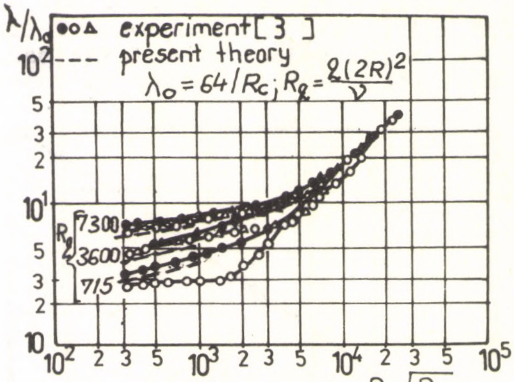

Fig.4(P_c=0,086) $Re\sqrt{P_c}$

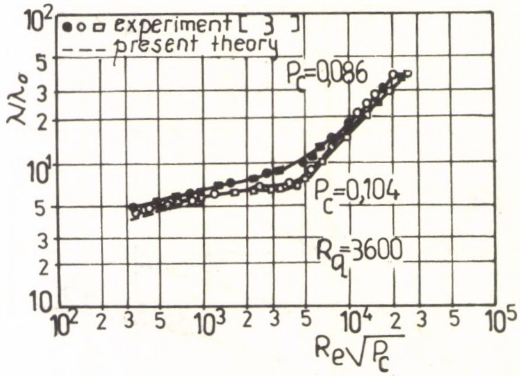

Fig. 5

8. Conclusions.- Considering the previous results obtained in /1/, /4/, /5/, /6/, the paper offers a general method for computation the friction factor in rotating curved pipes, for any value of rotation and curvature and unlike the other models it is showed clearly the influence of rotation, curvature and Reynolds number upon the axial velocity profile and friction factor.

References

1. Ito,H., K.Nanbu, Flow in Rotating Straight Pipes of Circular Cross Sections, Trans.ASME, Sept.1971

2. Ito,H., T.Motai, Secondary Flow in a Rotating Curved Pipe, Rep.Inst.High Speed Mech., Vol.29,1974

3. Euteneuer,G.-A., M.Piesche, Druckabfallmessungen in stationär rotierenden, gekrümmten Koralstrecken mit quadratischem sowie kreisförmigem Durchflussquerschnitt, Forsch.Ing.Wiss. 44,1978

4. Tămaş,M.A., Theoretical Model of Flow in Rotating Straight Pipes, Bul.şt.şi tehn., Timisoara 1982

5. Tămaş,M.A., Friction Losses in Curved Pipes, in the case of Laminar Flow, Bul.şt.şi tehn., Timişoara 1983

6. Tămaş,M.A., Friction Losses in Rotating Straight Pipes, Studii de mec.aplic., Bucureşti,1983

7. Johnston,J.P., R.M.Hallen, D.K.Lezius, Effects of Spanwise Rotation on the Structure of Two-dimensional Fully Developed Turbulent Channel Flow, J.Fl.Mech., vol.56, 3, 1972

8. Elbing,G., Messungen der turbulenten Strömung im rotierenden Radialrad einer Arbeitsmaschine, Berlin,1975

9. Johnson, M.W., Secondary Flow in Rotating Bends, Trans. ASME, oct.1978.

Mircea A. Tămaş

Assoc. Prof.

Institutul Politehnic "Traian Vuia" Timişoara
Facultatea de mecanică
Catedra de maşini hidraulice
1900 TIMISOARA
Bd.Mihai Viteazul nr.1
ROMANIA

FLUID FLOW BEHAVIOUR AT OFF DESIGN CONDITION OF TURBOMACHINERY

Tanaka, T.

Summary

The turbomachinery tested had a good efficiency characteristics. Its fluid flow behaviour at off design condition was that the position at where the annulus wall pressure head became a maximum in the impelling section moved toward the leading edge with the decrease in flow ratio. The turbomachinery, whose outlet return flow starts at a high flow ratio before the inlet return flow starts, therefore, may form a flat efficiency curev at off design condition.

1. Introduction

In recent years the turbomachinery which has a high efficiency, not only at design condition but also at off design condition, has high potential. To exploit this potential the fluid flow behaviour at off design condition has to be clear. Especially the mechanism of occurrence of return flows at impeller inlet and outlet sections and the effect of those return flows on performance characteristics have to be explained in detail more than ever since they are very much significant for the improvement in efficiency characteristics.

There are several experimental reports regarding the fluid flow behaviour at off design condition of turbomachinery, such as investigations by Toyokura [1], Scheeler [2], Murata [3], Tanaka [4], and so on. They are very helpful for the understanding of the mechanism of occurrence of inlet and outlet return flows. However, some of those explanations and results, especially the fluid flow behaviour in radial direction, are concluded or estimated from the experimental data in two dimensional measurements. Moreover, there are some uncertain and indetailed explanations, not only the fluid flow behaviour but also the effect of those return flows on performance characteristics.

In this point of view the three dimensional velocity measurements are proceeded for a turbomachinery for various flow ratios, and the mechanism of occurrence of inlet and outlet return flows and the interrelations with the efficiency characteristics are investigated.

2. Experimental Setup and Procedure

The turbomachinery, which was used for this investigation is one of the semi-axial flow propeller pumps. Fig. 1 shows its cross section. The shape of the mean line of the blade profile is due to the blade angle distribution (that is due to the camber variation). Fig. 2 shows the blade profile at mean radius of the impeller tested and Fig. 3 its blade angle distribution.

The velocity distributions at impeller inlet and outlet sections were measured by using a five hloe spherical pitot tube. The diameter of the spherical head is 6 mm. The holes on the spherical head are 0.6 mm diameter. The spherical head is joined with a mechanical part which allows its vertical movement as well as the horizontal and radial movements.

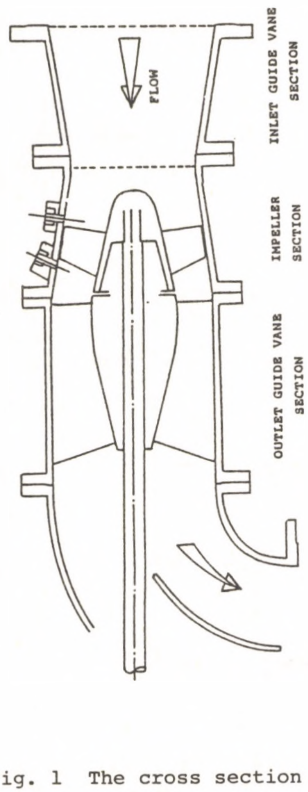

Fig. 1 The cross section of the turbomachinery tested.

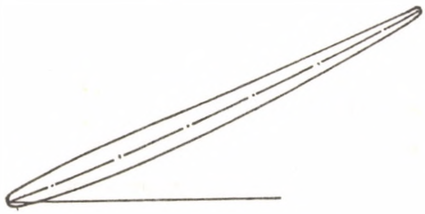

Fig. 2 The blade profile at mean radius.

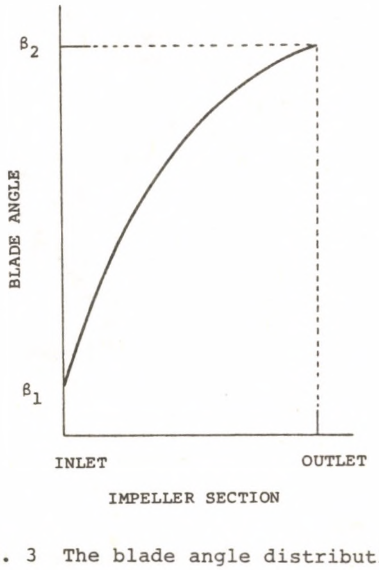

Fig. 3 The blade angle distribution at mean radius.

Some of the important characteristics of the experimental impeller used in this program are listed in Table 1. Other detailed performance measurements are reported in references [4] and [5].

Table 1. Blade characteristics of the impeller tested, and the flow coefficient at the optimum efficiency point.

	At tip	At mean radius	At hub
Vane angles at inlet	17°33'	22°33'	38°20'
Vane angles at outlet	24°36'	30°00'	42°05'
Vane angles at mid chord axis	24°44'	30°40'	44°20'
Length of vane	150	137	111
Number of blades		8	
Optimum flow coefficient		0.368	

3. Test Results

3.1 Efficiency Characteristics

Fig. 4 shows the performance characteristics of the turbomachinery tested. The rotational speeds examined are 940, 850, 750, 650, and 550 rpm.

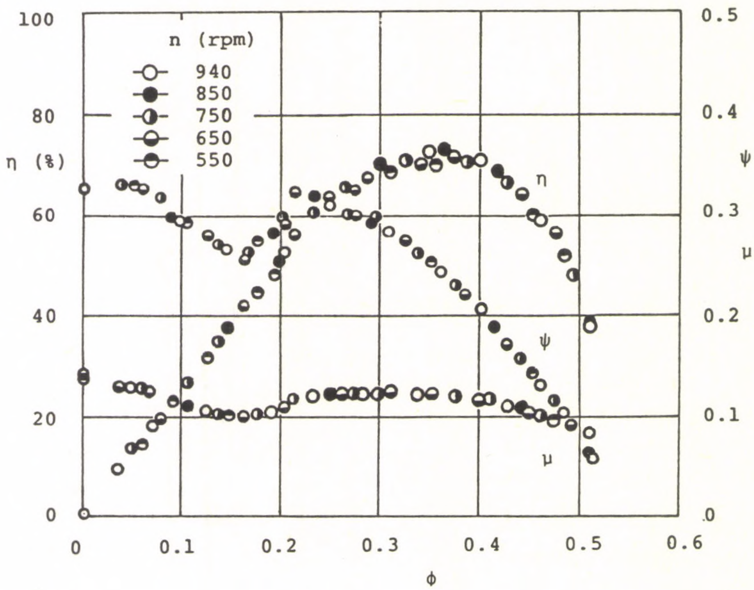

Fig. 4 The performance characteristics of the turbomachinery tested.

The power coefficient is constant for the wide range of flow ratio and the head coefficient keeps its value growth for the decrease in flow ratio, even at a small flow coefficient. The efficiency, therefore, forms a flat curve. The efficiency at the optimum condition is, however, effected slightly by the change in rotational speeds.

3.2 Observation of Inlet Return Flow

Figs 5 (a), (b), and (c) show the velocity distribution at impeller inlet of axial, tangential, and radial components, respectively.

Fig. 5(a) shows that for the same decrease in flow ratio, the magnitude of axial component of the velocity becomes much smaller at the outer radius than that at the inner radius. The occurrence of inlet return flow may be, therefore, due to the separation of fluids from the blade surfaces at the casing wall. The inlet return flow started at the flow ratio 0.573. The velocity distribution, whose flow ratio is smaller than 0.484, therefore, differs entirely from those whose flow ratios is larger than 0.623. The negative value of axial component of the velocity at the casing wall becomes large with the decrease in flow ratio. However, its expanding rate at the outer radius is fairly smaller than those at the inner radius. This indicates that the center of the inlet return flow moves gradually toward the inner radius (hub side) with the decrease in flow ratio.

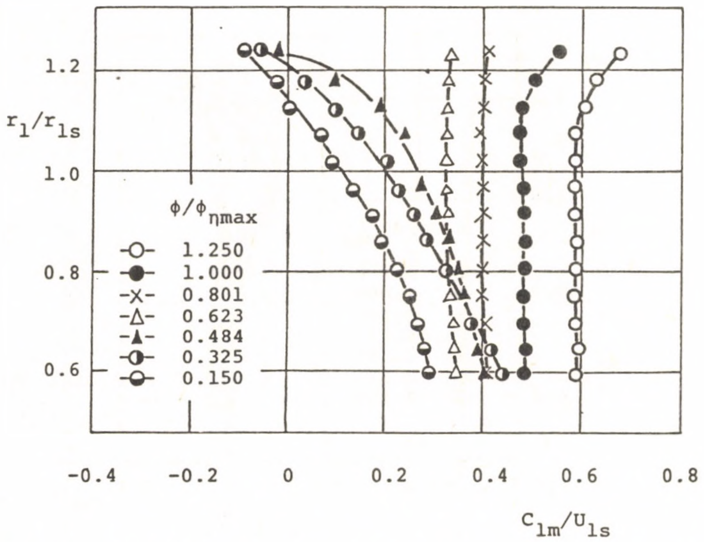

Fig. 5(a) The axial velocity distribution at impeller inlet.

This could be also understood from Fig. 5(c). The fluid flow at those flow ratios have the radial component of the velocity, which is directed inward radius. The position at where the radial component of the velocity becomes the maximum moves gradually toward the inner radius as the decrease in flow ratio. Its maximum value, however, decreased with the decrease in

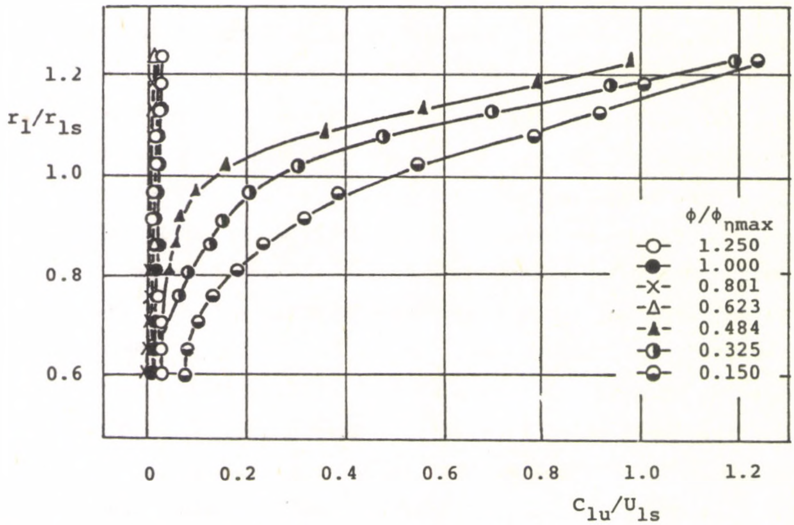

Fig. 5(b) The tangential velocity distribution at impeller inlet

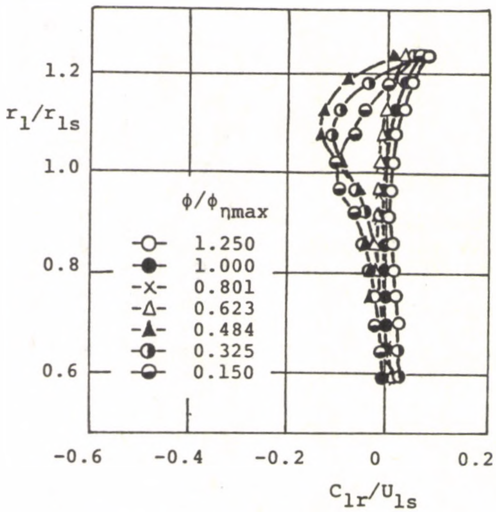

Fig. 5(c) The radial velocity distribution at impeller inlet.

flow ratio. The reason for this is that for the decrease in flow ratio the inlet return flow region may expand more axially at the inner radius as the center of the inlet return flow moves radially inward.

The latter could be also understood from Fig. 5(b). The fluid flow at those flow ratio have the tangential component of the velocity whose magnitude becomes large with the decrease in flow ratio. Its expanding ratio is, however, much larger at the inner radius. This tendency becomes much clear when the flow ratio becomes much smaller.

Fig. 6 shows an illustration of the inlet return flow. The tangential component of the velocity may appear near the outer radius as soon as the inlet return flow starts and the return flow region at the periphery may start its rotation around the axis. The flow condition at a flow ratio with an inlet return flow is shown by the line. Then, the flow condition with a much smaller flow ratio may be shown by the dotted line since the inlet return flow may expand much to axial and radial directions. The position at where the velocity distribution was measured is shown by a double dotted line.

It may be understood from the illustration that the radial component of the velocity of the main flow which directed inward radius may decrease its magnitude with the decrease in flow ratio as the inlet return flow expands its rotational flow region axially upstream when the flow ratio becomes much smaller.

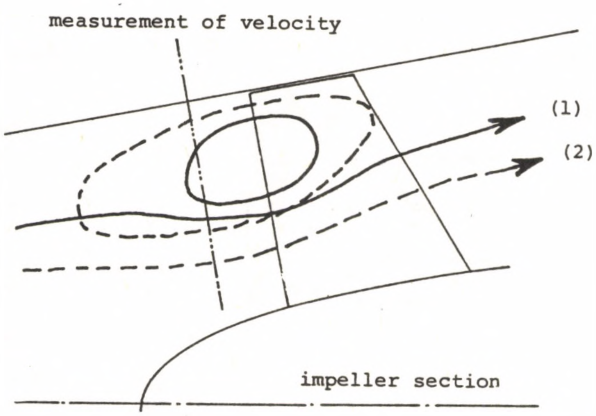

Fig. 6 The illustration of the inlet return flow.

3.3 Observation of Outlet Return Flow

Fig. 7(d),(e), and (f) show the velocity distribution at impeller outlet of axial, tangential, and radial components, respectively.

The outlet return flow started near the hub at the flow ratio 0.653. The outlet return flow region expands rapidly outward from the hub side toward the outer radius with the decrease in flow ratio, whereas the decreasing rate of axial component of the velocity becomes gentle at the inner radius. It could be, therefore, understood that the center of the outlet return flow moves rapidly toward the outer radius whereas the magnitude of axial component of the velocity does not expand that much at the inner radius.

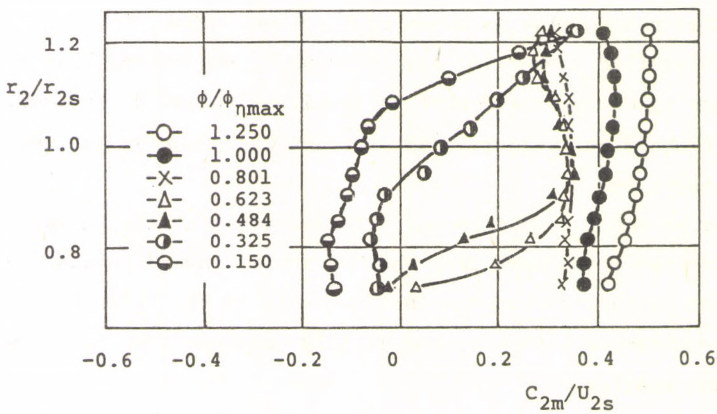

Fig. 7(d) The acial velocity distribution at impeller outlet.

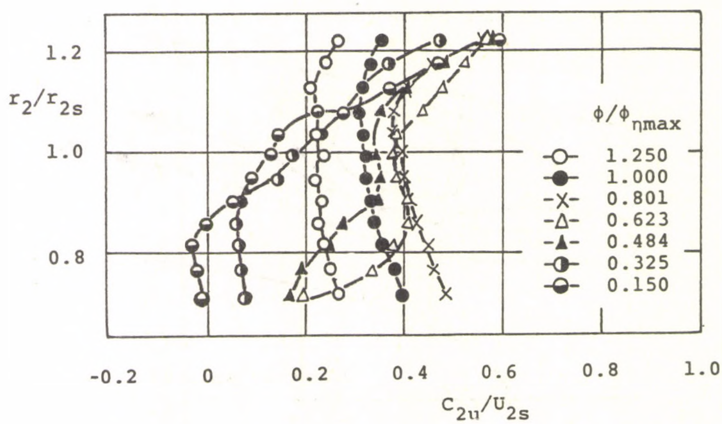

Fig. 7(e) The tangential velocity distribution at impeller outlet.

Fig. 7(e) shows the velocity distribution of the tangential component. At the flow ratio larger than 0.801, the tangential component of the velocity distributed uniformly throughout the radius, except at the casing wall and the hub, each becomes a maximum value. At the flow ratios 0.623 and 0.484, it became large gradually at the outer radius, especially at the casing wall (The base of discussion is on the mean radius.), whereas it became small rapidly at the inner radius, especially at the hub.

This decreasing tendency at the inner radius becomes more obvious with the decrease in flow ratio and its region expands more toward the outer radius (see 0.325). Finally, the tangential compoent of the velocity may distribute throughout the radius with a contimuously decreased gradient (slope) from the casing wall toward the hub (0.150).

From the above observation it could be considered that the fluid flow at impeller outlet shifts rapidly toward the outer radius with the decrease in flow ratio, resulting to large differences between the casing wall and the hub in axial and tangential velocity heads.

Fig. 7(f) shows that the radial component of the velocity, which is directed outward radius appears slightly near the hub even at the high flow ratio 1.250 and it becomes large gradually with the decrease in flow ratio. At the flow ratio 0.801 it developed at the hub with a maximum value toward the mean radius. Its magnitude, however, becomes zero at the hub after the outlet return flow starts. For the further decrease in flow ratio, the position at where the radial component of the velocity becomes a maximum moves radially toward the outer radius. For example, it was maximum at the

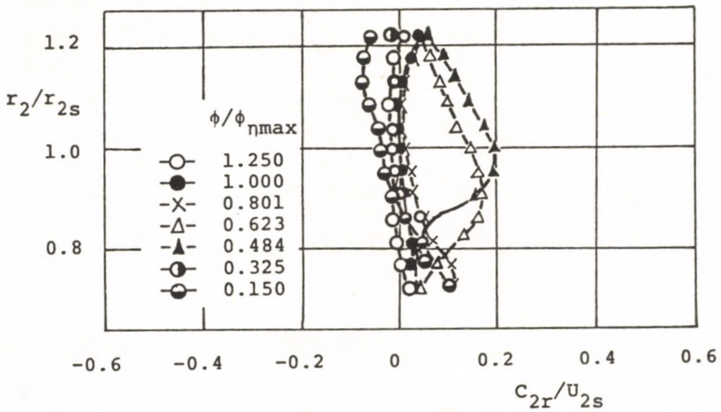

Fig. 7(f) The radial velocity distribution at impeller outlet.

radius r_2/r_{2s}=0.900 for the flow ratio 0.623 and its position moved to the mean radius for the flow ratio 0.484. Its maximum value became large with the decrease in flow ratio. Such radial component of the velocity may be caused at the impelling section by the centrifugal forces whose effect may become large with the decrease in flow ratio.

From the above observation it is clear that the radial component of the velocity, which is directed outward radius has a strong relation with the occurrence of the outlet return flow. The outlet return flow, therefore, may be occurred due to the increase in radial component of the velocity near the hub for the decrease in flow ratio.

At the flow ratio 0.325 the radial component of the velocity, which is directed inward radius appeared slightly near the casing wall. It became more clear at the flow ratio 0.150 and distributed between the mean radius and the periphery. The radius at where the radial component of the velocity becomes the maximum moves toward the inner radius with the decrease in flow ratio. The reason for this is that the main flow in the impelling passage, which shifted outer radius might expand again toward the inner radius with the decrease in flow ratio. The reason for this could be seen in Fig. 8.

Fig. 8 shows the annulus wall pressure head distribution along the axis for various flow ratios. There is a position at where the annulus wall

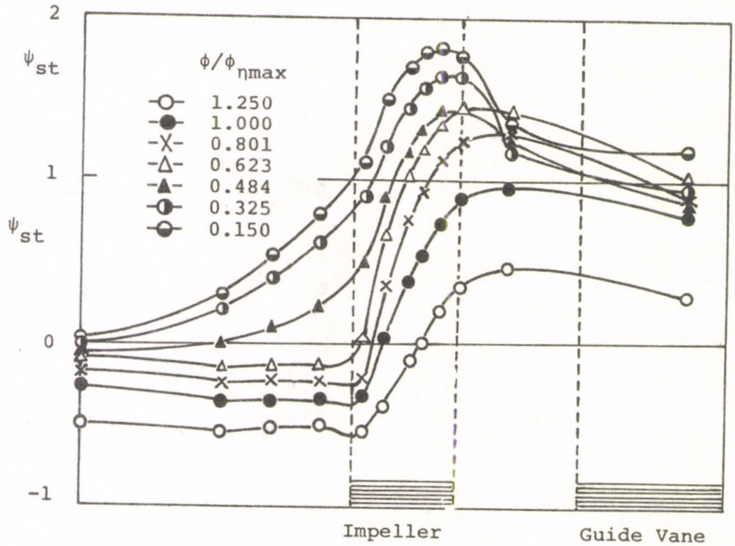

Fig. 8 The annulus wall pressure head distribution.

pressure head becomes a maximum in the impelling section (see 0.484). This is the place at where the main flow, which is effected by the outlet return flow, is hitting the casing wall. It could be also seen that its position moves axially upstream toward the leading edge with the decrease in flow ratio (see 0.325 and 0.150). The reason for this is that for the decrease in flow ratio the outlet return flow expands its flow region radially outward and axially upstream, and the effect on the main flow may becmoes much larger. The position, therefore, moves toward the upstream.

Accordingly the main flow, which hitted the casing wall changes its flow direction radially inward at the impeller outlet. The radial component of the velocity which is directed radially inward, therefore, could be seen near the outlet pheriphery as described before.

4. Conclusion

From the above observation it may be concluded that the turbomachinery tested had a good efficiency characteristics. Its fluid flow behaciour at off design condition was that the position at where the annulus wall pressure head became a maximum in the impelling section moved toward the leading edge with the decrease in flow ratio. The turbomachinery, whose outlet return flow starts at a high flow ratio before the inlet return flow starts, therefore, may form a flat efficiency curve at off design condition.

5. References

1. Toyokura, T.,"Studies on the Characteristics of Axial Flow Pumps, Part 3, Trans of JSME, Vol.26, No.168, August 1960, p.1084.
2. Scheer, W.,"Untersuchungen und Beohachtungen uber die Arbeits weise von Axialpumpen unter besonderer Beruchsichtigung des Teillastbereiches, Pumpen in Kraftwerk", BWK, Nr,11(5), November 1959, p.503.
3. Tanaka, S. and Murata, S.,"On the Partial Flow Rate Characteristics of Axial Flow Compressor and Rotating Stall, 2nd Report", Trans of JSME, Vol.41, No.343, March 1975, p.1948.
4. Tanaka, T.,"An Experimental Study of Backflow Phenomena in a High Specific Speed Propeller Pump", ASME paper No.80-FE-6.
5. Tanaka, T.,"An Experimental Study of Diagonal Flow Propeller Pump: Design Performance with Various Types of Blading", ASME Paper No.77-WA/FE-9.

Takaharu TANAKA
Department of
Mechanical Engineering,
Kobe University,
Kobe, Japan.

CAUCHY KERNEL INTEGRAL EQUATIONS FOR STEADY-STATE BLADE CASCADE FLOW

Dr. Antal Thuma

SUMMARY

In blade cascade flow analysis, the complex conjugate of the absolute velocity can be written by means of Cauchy's integral formula. The determination of the velocities along the profile contour leads to an integral equation of the second-kind with Cauchy type kernel. By convenient transformations we may achieve that this complex-variable integral equation has a continuous kernel. Thereby also the integral equations with real variables formed of the real or imaginary part will have continuous kernels.

1. STATING THE PROBLEM

In the region S^+ of the straight cascade in Fig.1, a steady-state irrotational and solenoidal (no sources) flow is assumed. The complex conjugate $\overline{c}(z)$ of absolute velocity meets the Cauchy-Riemann equations, hence it is regular inside region S^+. Cauchy's integral formula yields

$$\overline{c}(z) = \frac{1}{2\pi i}\oint_K \frac{\overline{c}(z)}{\zeta - z}\, d\zeta \tag{1}$$

where K results from uniting $K' \cup K'' \bigcup_{\mu=-\infty}^{+\infty} K \quad (\mu = 0, \pm 1, \pm 2, \dots)$

and $\zeta \in K$, $z \in S^+$. Integrating along each element of contour K and shifting lines K' and K" to infinity:

$$\overline{c}(z) = \frac{\overline{c}_1 + \overline{c}_2}{2} + \frac{1}{2\pi i}\sum_{\substack{\mu=-\infty \\ \mu \neq 0}}^{+\infty} \oint_{K_\mu} \frac{\overline{c}(\zeta)}{\zeta - z}\, d\zeta + \frac{1}{2\pi i}\oint_{K_0} \frac{\overline{c}(\zeta)}{\zeta - z}\, d\zeta \tag{2}$$

Let us find limit value $\lim\limits_{z \to \zeta_0} \overline{c}(z)$ where $\zeta_0 \in S^+$ and $\zeta_0 \in K_0$.

Since function $\overline{c}(z)$ meets Lipschitz's condition for an exponent ≤ 1, and is continuous along curve K_0:

$$\overline{c}(\zeta_0) = \frac{\overline{c}_1 + \overline{c}_2}{2} + \frac{1}{2\pi i} \sum_{\substack{\mu=-\infty \\ \mu \neq 0}}^{+\infty} \oint_{K_\mu} \frac{\overline{c}(\zeta)}{\zeta - \zeta_0} d\zeta + \frac{1}{2\pi i} \oint_{K_0} \frac{\overline{c}(\zeta) - \overline{c}(\zeta_0)}{\zeta - \zeta_0} d\zeta \tag{3}$$

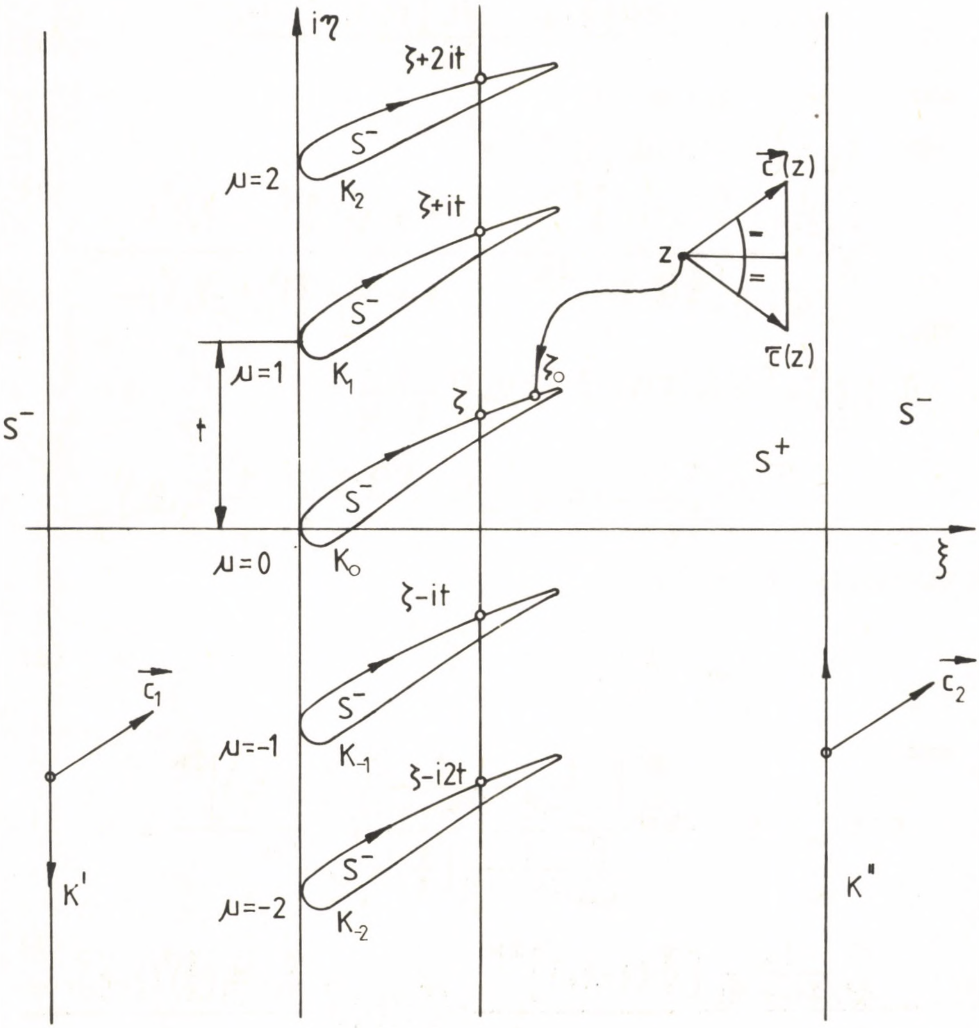

Fig. 1.

Summarizing leads to the form:

$$\tau(\zeta_0) = \frac{\tau_1+\tau_2}{2} + \frac{1}{2\pi i}\oint_{K_0} \frac{\tau(\zeta)\frac{\pi}{t}(\zeta-\zeta_0)\,\mathrm{cth}\,\frac{\pi}{t}(\zeta-\zeta_0)-\tau(\zeta_0)}{\zeta-\zeta_0}\,d\zeta \qquad (4)$$

2. CONTINUITY OF THE KERNEL OF THE INTEGRAL EQUATION

Let $G(\zeta,\zeta_0)$ denote the argument of the integral in (4):

$$G(\zeta,\zeta_0) = \frac{\tau(\zeta)\frac{\pi}{t}(\zeta-\zeta_0)\,\mathrm{cth}\,\frac{\pi}{t}(\zeta-\zeta_0)-\tau(\zeta_0)}{\zeta-\zeta_0} \qquad (5)$$

and $F(\zeta-\zeta_0)$ its part:

$$F(\zeta-\zeta_0) = \frac{\pi}{t}(\zeta-\zeta_0)\,\mathrm{cth}\,\frac{\pi}{t}(\zeta-\zeta_0) = \frac{\sum\limits_{n=0}^{\infty}\frac{1}{(2n)!}\left[\frac{\pi}{t}(\zeta-\zeta_0)\right]^{2n}}{\sum\limits_{n=0}^{\infty}\frac{1}{(2n+1)!}\left[\frac{\pi}{t}(\zeta-\zeta_0)\right]^{2n}} = \frac{1+\frac{1}{2!}\left(\frac{\pi}{t}\right)^2(\zeta-\zeta_0)^2+\dots}{1+\frac{1}{3!}\left(\frac{\pi}{t}\right)^2(\zeta-\zeta_0)^2+\dots} \qquad (6)$$

Thus

$$G(\zeta,\zeta_0) = \left[\tau(\zeta)F(\zeta-\zeta_0)-\tau(\zeta_0)\right]\frac{1}{\zeta-\zeta_0} = \frac{\tau(\zeta)-\tau(\zeta_0)}{\zeta-\zeta_0}F(\zeta-\zeta_0) + \frac{F(\zeta-\zeta_0)-1}{\zeta-\zeta_0}\tau(\zeta_0) \qquad (7)$$

Obviously, from (6):

$$\lim_{\zeta\to\zeta_0} F(\zeta-\zeta_0) = 1 \qquad (8)$$

and

$$F(\zeta-\zeta_0)-1 = \frac{\sum\limits_{n=0}^{\infty}\left[\frac{1}{(2n)!}-\frac{1}{(2n+1)!}\right]\left[\frac{\pi}{t}(\zeta-\zeta_0)\right]^{2n}}{\sum\limits_{n=0}^{\infty}\frac{1}{(2n+1)!}\left[\frac{\pi}{t}(\zeta-\zeta_0)\right]^{2n}} =$$

$$= \frac{\sum\limits_{n=1}^{\infty}\frac{2n}{(2n+1)!}\left[\frac{\pi}{t}(\zeta-\zeta_0)\right]^{2n}}{\sum\limits_{n=0}^{\infty}\frac{1}{(2n+1)!}\left[\frac{\pi}{t}(\zeta-\zeta_0)\right]^{2n}} = \left(\frac{\pi}{t}\right)^2(\zeta-\zeta_0)^2\,\frac{\frac{2}{3!}+\frac{4}{5!}\left(\frac{\pi}{t}\right)^2(\zeta-\zeta_0)^2+\dots}{1+\frac{1}{3!}\left(\frac{\pi}{t}\right)^2(\zeta-\zeta_0)^2+\dots} \qquad (9)$$

hence

$$\lim_{\zeta \to \zeta_0} \frac{F(\zeta-\zeta_0)-1}{\zeta-\zeta_0} \bar{c}(\zeta_0) = 0 \tag{10}$$

On the other hand, as assumed before:

$$|\bar{c}(\zeta)-\bar{c}(\zeta_0)| \leq A|\zeta-\zeta_0|^{\alpha} \tag{11}$$

where $0 < \alpha \leq 1$, $\quad \forall \zeta, \zeta_0 \in K \; \exists A \in R_+$

hence

$$\lim_{\zeta \to \zeta_0} \left| \frac{\bar{c}(\zeta)-\bar{c}(\zeta_0)}{\zeta-\zeta_0} F(\zeta-\zeta_0) \right| = \lim_{\zeta \to \zeta_0} \left| \frac{A}{|\zeta-\zeta_0|^{1-\alpha}} F(\zeta-\zeta_0) \right| \tag{12}$$

$$= \begin{cases} A & \text{if} \quad \alpha = 1 \\ \text{bounded} & \text{if} \quad 0<\alpha<1 \end{cases}$$

The integral of G along line (a,b) containing point ζ_0 exists

$$\int_a^b G(\zeta,\zeta_0)\,d\zeta = \int_a^b \frac{\bar{c}(\zeta)-\bar{c}(\zeta_0)}{\zeta-\zeta_0} F(\zeta-\zeta_0)\,d\zeta + \tag{13}$$

$$+\bar{c}(\zeta_0)\int_a^b \frac{F(\zeta-\zeta_0)-1}{\zeta-\zeta_0}\,d\zeta$$

3. FLOW CONDITION

The transformed vector of absolute flow velocity in the straight cascade is composed of the transformed relative and circumferential velocities

$$\bar{c} = \bar{w} + \bar{u} \tag{14}$$

The flow condition requires the relative velocity vector $\bar{\bar{w}}$ to be tangential to the profile.

According to Fig.2, $i\bar{c}(\zeta)d\zeta = [c_n(\zeta)+ic_t(\zeta)] \cdot |d\zeta|$ and $c_n = u_n$. Thus, the flow condition is:

$$\bar{c}(\zeta) = [\, c_t(\zeta) - i\, u_n(\zeta)]\, e^{-i\vartheta(\zeta)} \tag{15}$$

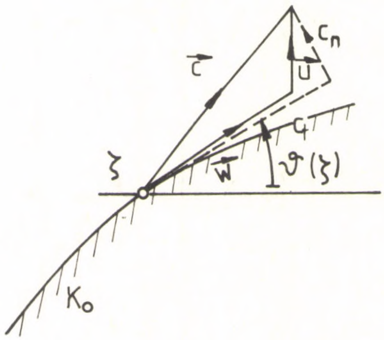

Fig. 2.

Substituting this flow condition into (4) (be $\bar{c}_\infty = (\bar{c}_1 + \bar{c}_2)/2$)

$$[c_t(\zeta_0) - i\, u_n(\zeta_0)]\, e^{-i\vartheta(\zeta_0)} = \bar{c}_\infty - \tag{16}$$

$$- \frac{1}{2\pi} \oint_{K_0} \left([u_n(\zeta) + i\, c_t(\zeta)] \frac{\pi}{t}\, \mathrm{cth}\, \frac{\pi}{t}(\zeta - \zeta_0) - [u_n(\zeta_0) + i\, c_t(\zeta_0)] \frac{1}{\zeta - \zeta_0} \right) |d\zeta|$$

or

$$c_t(\zeta_0)\, e^{-i\vartheta(\zeta_0)} + \frac{1}{2\pi} \oint_{K_0} \left(i\, c_t(\zeta) \frac{\pi}{t}\, \mathrm{cth}\, \frac{\pi}{t}(\zeta - \zeta_0) - i\, \frac{c_t(\zeta_0)}{\zeta - \zeta_0} \right) |d\zeta| =$$

$$= i\, u_n(\zeta_0)\, e^{-i\vartheta(\zeta_0)} - \frac{1}{2\pi} \oint_{K_0} \left(u_n(\zeta) \frac{\pi}{t}\, \mathrm{cth}\, \frac{\pi}{t}(\zeta - \zeta_0) - \frac{u_n(\zeta_0)}{\zeta - \zeta_0} \right) |d\zeta| \tag{17}$$

These equations will be completed by the Kutta-Joukowsky condition, namely $\bar{w} = 0$ at the outlet edge, that is, $\bar{c} = \bar{u}$.

4. DETERMINATION OF VELOCITY DISTRIBUTION ALONG THE PROFILE CONTOUR

Equation (17) of complex variables will be separated into integral equations from the real and the imaginary part,respectively. Both equations are Fredholm type integral equations one of them is of the second-kind, and the other of the first-kind. The equations have continuous kernels. Both equations are suitable for calculation. Concerning numerical solution, let us refer to the literature [2], [3].

REFERENCES

[1] Smirnov, V.: Cours Mathématiques Supérieurs. Tome III. 2éme partie Editions MIR, Moscou 1972.

[2] Fűzy,O. and Thuma,A.: Calculating the Velocity Distribution of a Plane Airfoil Cascade Given by its Geometry Proceedings of the Third Conference on Fluid Mechanics and Fluid Machinery, 1969.

[3] Thuma,A., Wozny,E., Kherraf,M.: Calcul d'un écoulement permanant à travers une grille d'aubes plan à l'aide des intégrales du type Cauchy. Revue Scientifique de l'Université de le Science et de la Technologie d'Oran. 1982. (in press)

Dr.Antal Thuma

Department of Hydraulic Machines,
Technical University,
Budapest, XI. Stoczek u.2. D.
1521

COMPUTATION OF TRANSIENT FLOWS IN WATERPIPELINES

Béla Tolvaj

SUMMARY

Nowadays drinking and industrial water necessary for water supply can be provided in most cases from sources being situated far away from the consumers. The waterpipeline made of concrete can bear an overload much lower than the one made of steel. That's the reason why the waterpipelines must be designed in such a way that the high pressure due to transient flows occuring at start, break down or adjustments do not endanger the pipelines. The computation process presented in this paper enables us to calculate the velocity and pressure values appearing in the flow, and on the basis of this calculation the pipeline can be checked or in case of necessity it can be changed.

1. COMPUTATION OF THE TRANSIENT FLOWS

Before starting the computation the pipeline must be divided into M sections, where inside of it the wave velocity $\underline{a}$, the diameter of the pipe D, the pipe friction coefficient λ, and the angle of declination α are constant. In a section like this the transient flow can be described by a system of differential equations consisting of the equations of motion and continuity [1], [2], [3]:

$$\frac{\partial v}{\partial t} + v\frac{\partial v}{\partial x} + \frac{\partial Y}{\partial x} + \frac{\lambda v|v|}{2D} = 0 \tag{1.1}$$

$$a^2 \frac{\partial v}{\partial x} + \frac{\partial Y}{\partial t} + v\frac{\partial Y}{\partial x} + gv\sin\alpha = 0 \tag{1.2}$$

where $v(x,t)$ is the flow velocity, $Y(x,t) = \frac{p}{\rho} + gh$ is the potential energy, g is the gravitational acceleration, ρ is the liquid density, h is the geodetical height.

Let us introduce for the denomination of the individual sections the index i /i = 1...M/ and let us correspond them the grid boundaries Δx_i, Δt shown in Fig.1. The grid size in t direction has the same value in order to simplify the boundary conditions. For denomination of the grid points let us introduce the j, and for the time k indices [Fig.1].

Solving the system of differential equations consisting of Equs. (1.1) and (1.2) by the method of the characteristics [1], [2], [4] and supposing that in each grid point of the k-th time point $v_{i,j,k}$ and $Y_{i,j,k}$ are known /initial condition/ the values of the velocity and potential energy of the /k+1/th time point can be determined from the equations

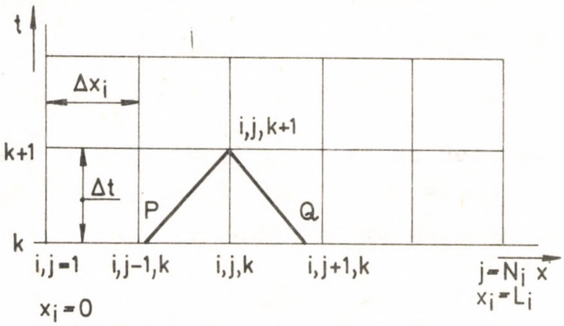

Fig.1.

$$V_P=\frac{V_{i,j,k}-a_iT_i\,(V_{i,j,k}-V_{i,j-1,k})}{1+T_i\,(V_{i,j,k}-V_{i,j-1,k})} \quad (1.3); \qquad V_Q=\frac{V_{i,j,k}-a_iT_i\,(V_{i,j,k}-V_{i,j+1,k})}{1-T_i\,(V_{i,j,k}-V_{i,j+1,k})} \quad (1.4)$$

$$Y_P=Y_{i,j,k}-T_i\,(V_P+a_i)(Y_{i,j,k}-Y_{i,j-1,k}) \quad (1.5)$$

$$Y_Q=Y_{i,j,k}+T_i\,(V_Q-a_i)(Y_{i,j,k}-Y_{i,j+1,k}) \quad (1.6)$$

$$B_{P_i}=V_P+\frac{Y_P}{a_i}-\left[\frac{g}{a_i}\sin\alpha_i+\frac{\lambda_i}{2D_i}|V_P|\right]V_P\Delta t \quad (1.7)$$

$$B_{Q_i}\;V_Q-\frac{Y_Q}{a_i}+\left[\frac{g}{a_i}\sin\alpha_i-\frac{\lambda_i}{2D_i}|V_Q|\right]V_Q\Delta t \quad (1.8)$$

$$V_{i,j,k+1}=\frac{B_{P_i}+B_{Q_i}}{2} \quad (1.9); \qquad Y_{i,j,k+1}=\frac{B_{P_i}-B_{Q_i}}{2}\,a_i \quad (1.1o)$$

where $T_i=\Delta t/\Delta x_i$. The computation is convergent if the following inequality holds true in every section: $T_i \leqq (v_i+a_i)^{-1}$

2. BOUNDARY CONDITION

At the beginning /j=1/ and the end /j=N_i/ of the pipe-sections the Equs. (1.9) and (1.1o) are not valid. The values $Y_{i,1,k+1}$; $v_{i,1,k+1}$ and $Y_{i,N_i,k+1}$; $v_{i,N_i,k+1}$ can be determined on the one hand from so-called equation of characteristics

$$Y_{i,1,k+1}=a_i\,(v_{i,1,k+1}-B_{Q_i}) \quad (2.1); \qquad Y_{i,N_i,k+1}=a_i(B_{P_i}-v_{i,N_i,k+1}) \quad (2.2)$$

and on the other hand from the boundary conditions

$$Y_{i,1,k+1} = f_1(v_{i,1,k+1}) \quad \text{and} \quad Y_{i,N_i,k+1} = f_2(v_{i,N_i,k+1}).$$

The most important boundary conditions occuring at the water-pipelines are as follows:

2.1. Pipe junction

This can be seen on the Fig.2. Rewriting this boundary condition on the basis of [1] according to our denominations the following Equs. can be written:

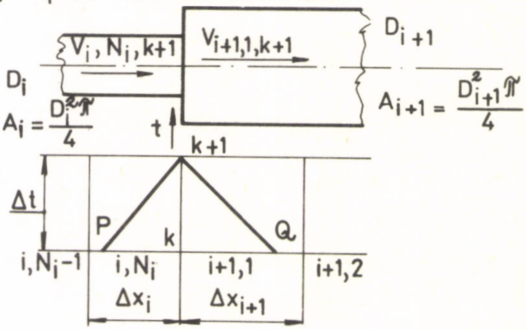

Fig.2.

$$Y_{i,N_i,k+1} = \frac{A_i B_{P_i} - A_{i+1} B_{Q_{i+1}}}{\frac{A_i}{a_i} + \frac{A_{i+1}}{a_{i+1}}} \quad (2.3); \qquad Y_{i+1,1,k+1} = Y_{i,N_i,k+1} \quad (2.4)$$

$$v_{i,N_i,k+1} = B_{P_i} - \frac{Y_{i,N_i,k+1}}{a_i} \quad (2.5); \qquad v_{i+1,1,k+1} = \frac{A_i}{A_{i+1}} v_{i,N_i,k+1} \quad (2.6)$$

2.2. Boundary condition for the flow into open air

This can be seen on the Fig.3. The relationship $Y_{i,N_i,k+1} = f_2(v_{i,N_i,k+1})$ can be determined from the Bernoulli equation between the points i,N_i and A valid for /k+1/th time. The unknowns $Y_{i,N_i,k+1}$ and $v_{i,N_i,k+1}$ can be computed from Equs. (2.7) and (2.2)

$$Y_{i,N_i,k+1} = \frac{p_0}{\varrho} + g h_{i,N_i} + \frac{\xi}{2} v_{i,N_i,k+1}^2 \qquad (2.7)$$

$$v_{i,N_i,k+1} = \xi^{-1}\left[a_i + \sqrt{a_i^2 + 2\xi\left(B_{P_i} a_i - \frac{p_0}{\varrho} + g h_{i,N_i}\right)}\,\right] \qquad (2.8)$$

$$Y_{i,N_i,k+1} = a_i\left(B_{P_i} - v_{i,N_i,k+1}\right) \quad (2.9) \text{ where } \quad C_0 = B_{P_i} a_i - \frac{p_0}{\varrho} + g h_{i,N_i}.$$

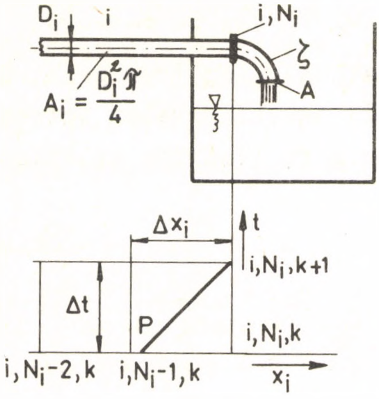

Fig.3

The formula (2.8) is valid only if the inequality $C_o \geq 0$ holds, because otherwise air inflow is started at the pipe end.

2.3. Air in the pipeline

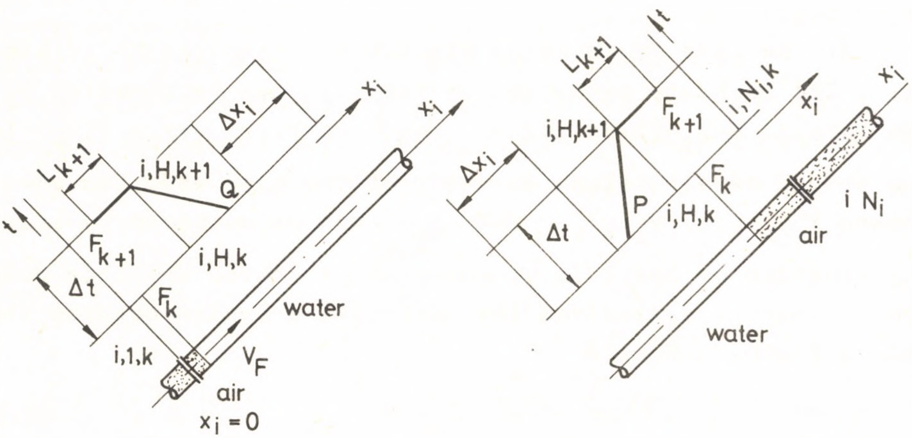

a b

Fig.4.

Air comes from the air pressure tank, from the pipe ends falling into open air and through air ventils and is situated as shown in Fig. 3., 4. At the grid points where air is present Y and v can not be determined from the Equs. (1.3) - (1.lo). In a case according to Fig.4 the boundary condition should not be given at the point j=1, but where water is present /j=H/. This point can be determined from the length of the air column s_{k+1}: $H = 2 + \text{entier}\left[\frac{s_{k+1}}{\Delta x_i}\right]$; $s_{k+1} = s_k + \Delta t\, V_{F_k}$.

The unknowns $Y_{i,H,k+1}$; $v_{F_{k+1}}$; $v_{F_{k+1}}$ can be computed from the equation of the characteristics going from point Q into /i,H,k+1/ and from the Bernoulli equation valid between the points F_{k+1} and /i,H,k+1/ furthermore from the equation of continuity:

$$V_{i,H,k+1} = C_1^{-1}\left(-C_2 + \sqrt{C_2^2 + 2C_1C_3}\right); \qquad (2.10)$$

$$Y_{i,H,k+1} = a_i\left(V_{i,H,k+1} - B_{Q_i}\right) \quad (2.11); \qquad V_{F_{k+1}} = V_{i,H,k+1} \qquad (2.12)$$

where
$$C_1 = \pm \frac{\lambda_i}{D_i} L_{k+1}; \qquad C_2 = a_i + \frac{L_{k+1}}{\Delta t};$$

$$C_3 = \frac{p_{\ell k+1}}{\varrho} + \frac{V_{i,H,k}}{\Delta t} L_{k+1} + g(h_{i,H} - \sin\alpha_i L_{k+1}) + a_i B_{Q_i}.$$

We have to start with the computation of c_3. If $c_3 > 0$, then c_1 must be computed with the upper sign, otherwise with the lower sign.

In the case depicted on Fig.4.b the computation is similar. The boundary condition of the pipe can be computed by the formula $H=N_i-(1+\text{entier}(s_{k+1}/\Delta x_i))$ where $s_{k+1}=s_k+\Delta t v_{F_k}$ is the length of air column situated at the pipe end. The unknowns $Y_{i,H,k+1}$; $v_{i,H,k+1}$ and $v_{F_{k+1}}$ can be computed by using the equation of continuity, equation of characteristics going from P into /i,H,k+1/ and the Bernoulli equation between the points F and /i,H,k+1/

$$V_{i,H,k+1} = C_4^{-1}\left(-C_5 + \sqrt{C_5^2 + 2C_4C_6}\right) \qquad (2.13)$$

$$Y_{i,H,k+1} = a_i\left(B_{P_i} - V_{i,H,k+1}\right) \quad (2.14); \qquad V_{F_{k+1}} = V_{i,H,k+1} \qquad (2.15)$$

where
$$C_4 = \pm L_{k+1}\frac{\lambda_i}{D_i}; \qquad C_5 = a_i + \frac{L_{k+1}}{\Delta t}; \qquad L_{k+1} = s_{k+1} - \Delta x_i(N_i - H - 1)$$

and
$$C_6 = B_{P_i} a_i + \frac{L_{k+1}}{\Delta t} V_{i,H,k} - g(h_{i,H} + \sin\alpha_i L_{k+1}) - \frac{p_{\ell k+1}}{\varrho}.$$

Now we have to start with the computation of c_6. If $c_6 > 0$ c_4 must be computed with the upper sign, otherwise with the lower sign.

2.4. Boundary condition for a pump provided with an air pressure tank

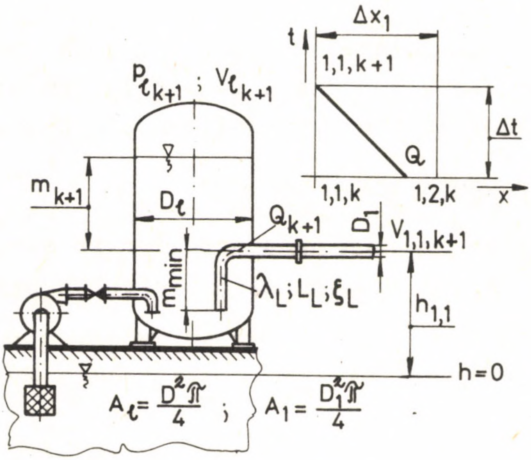

Fig.5

At the pumping station shown in Fig.5 there are three different sections after the break down of the pump:

a/ the air pressure tank and the pump on the way to stop is feeding the pipeline together;

b/ the air pressure tank is feeding the pipeline alone;

c/ the air pressure tank is getting empty and air gets into the pipeline.

The case a/ is disregarded now. This occurs only if the inertia of the rotating masses is very large. In the case b/ - supposing an isotherm equation of state - the value Q_{k+1}; $Y_{1,1,k+1}$; $V_{1,1,k+1}$ can be determined from the characteristics equation (2.1) from the Bernoulli equation between the air pressure tank surface and the beginning of the pipeline /i=1, j=1/, and from the equation of continuity

$$V_{1,1,k+1} = C_7^{-1}\left(-a_1 + \sqrt{a_1^2 + 2C_7C_8}\right) \quad (2.16) \qquad Q_{k+1} = A_1 V_{1,1,k+1} \quad (2.17)$$

$$Y_{1,1,k+1} = a_1\left(V_{1,1,k+1} - B_{Q1}\right) \quad (2.18)$$

where $C_7 = \xi_L + \frac{\lambda_L L_L}{D_L} + 1 - \left(\frac{A_1}{A_\ell}\right)^2$; $\quad m_{k+1} = m_k + \frac{Q_k}{A_\ell}\Delta t$;

$$C_8 = \frac{p_{\ell_{k+1}}}{\varrho} + g\left(m_{k+1} + h_{1,1}\right) - B_{Q1} ; \quad p_{\ell_{k+1}} = \frac{V_k\, p_{\ell_k}}{V_k + Q_k \Delta t} ;$$

and V_k is the volume of the air column. A_ℓ is the cross section of the air pressure tank. Meanings of the other letters can be seen on Fig.5.

If during the computation $m_{k+1} < m_{min}$, then the air pressure tank has got empty and there is air in the pipe. In this case the computation is similar mentioned in chapter 2.3 .

3. APPLYING THE COMPUTATIONAL PROCESS

The computation will be presented for an example shown in Fig.6 when transient flow appears after the break down of the pumping station.

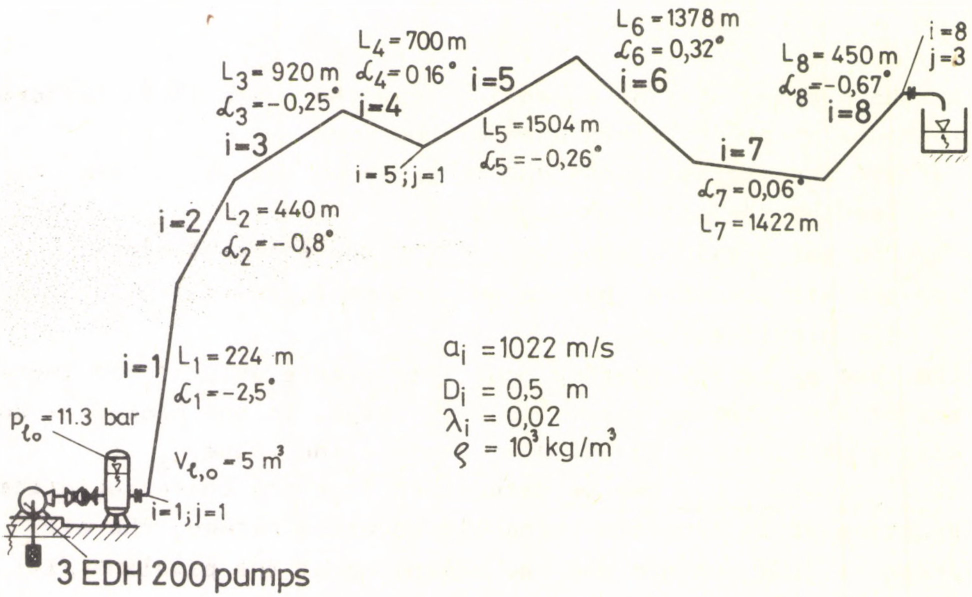

Fig.6

Data of the pipeline and the pumping station are shown in Fig.6. The velocity and potential energy at the beginning /i=1, j=1/ at the middle /i=5, j=1/ and at the end /i=8, j=3/ sections of the pipeline are shown in Fig.7.

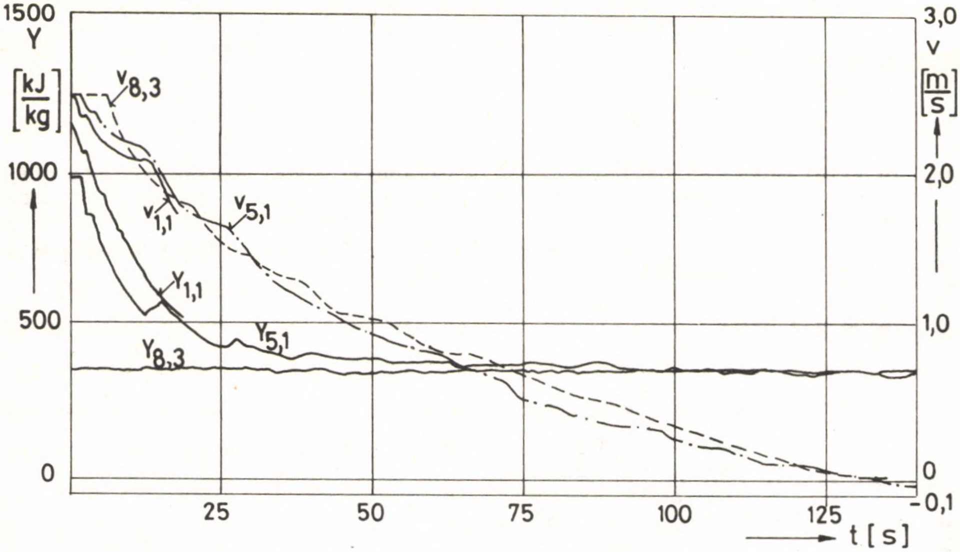

Fig.7

It can be seen that the pressure tank of large size reduces the velocity, furthermore the values of Y do not reach their stationary ones.

REFERENCES

1. Czibere,T.-Kalmár,L.-Tolvaj,B.: Berechnungen der in Rohrleitungen entstehenden instationären Flüssigkeitsströmungen, Publ. Techn. Univ. Heavy Industry, Miskolc, Series C. Machinery,Vol.36. /1981/ pp. 13-58.

2. Streeter,V. and Wylie,B.: Hydraulic transients, McGraw-Hill Book Company, New York /1967/

3. Jaeger,Ch.: Technische Hydraulik, Verlag Birkhauser Basel /1949/ pp. 25o-326.

4. Kozák,M.: A szabadfelszinü nempermanens vizmozgások számitása, Akadémiai Kiadó, Budapest /1977/

Dr. Béla TOLVAJ
Department of Fluid Mechanics and Heat Engineering
Technical University of Heavy Industry, Miskolc-Egyetemváros

VELOCITY AND PRESSURE DISTRIBUTIONS IN THE IMPELLER PASSAGES OF CENTRIFUGAL PUMP.

Michal Varchola

The paper presents some findings from an extensive experimental investigation concerning radial pumps under different modes of operation. Its outcomes include isotachs of veloc.and isobars of pressures, characterizing the structure of flow in the impeller channel.

Symbols:

φ_m	- angle of probe setting
β	- angle of relative velocity
w	- relative velocity
c	- absolute velocity
u	- peripheral velocity
c_u	- peripheral component of absolute velocity
p_1, p_2, p_3	- pressure data of the probe
p_{st}	- static pressure
ϱ	- density
T_1	- time of arc illumination
T_{10}	- time of illumination at $\Delta p = 0$
$T_a = \frac{2\pi}{\omega}$	
T_2	- time of arc obscuration
ω	- angle velocity
K	- constant determined by calibration
$\lambda = \frac{1}{\sin^2 \varphi_p}$	- calibration coefficient of the probe
ξ	- calibration coefficient of the probe
φ_p	- angle at which the intake data of the probe are equal to the static pressure
δ	- angle of velocity gradient from the plane of flow
Q/Q_n	- flow rate coefficient
Q_n	- flow rate at maximum efficiency

INTRODUCTION

The intensification of labour and improvement of the effectiveness of pumping equipment operation are due primarily to improved efficiency and performance parameters and to the attainment of required output and cavitation characteristics.

Knowledge on the mechanism of flow in the hydrodynamic pumps did not as yet reach the level which would prevent further improvements of hydraulic properties of hydrodynamic pumps.

Tasks involving the acquisition of data on the mechanism of the flow, either theoretical or experimental, are therefore highly topical. Several experimental studies are thus far known which deal with the measurement of the speed and pressures in the channel of impeller. It may be said that these experimental studies are characterized by differences in methods used for the velocity or pressure determination and by differences in the shape of blades of the impeller and in the type of diffuser.

Methods used for the determination of velocity include visualization, thermoanemometry, laser anemometry or methods based on the measurement using different probe types, capable of measuring the velocity vector and pressure - both planary and spatial measurements. The complex character of the given measuring apparatus problem (it always involves the transfer of signal from the rotor to the stator), indirect determination of the velocity vector affect the accuracy of such experiments and their completeness.

Flow parameters were always measured within the framework of experiments for testing the theoretical flow solutions in the impeller area. Theoretical solutions aim at the determination of all velocity and pressure components on the surface of the blades and in the channels. Remarkable results were achieved also here, e.g. [10].

The further advance of theoretical solutions, however, requires more detailed and complete experimental data on the mechanism of flow in the impellers of different geometrical configurations, with different number of blades and different input and output elements of the pump (e.g. diffusers).

Experimental Equipment and Measurement Methods

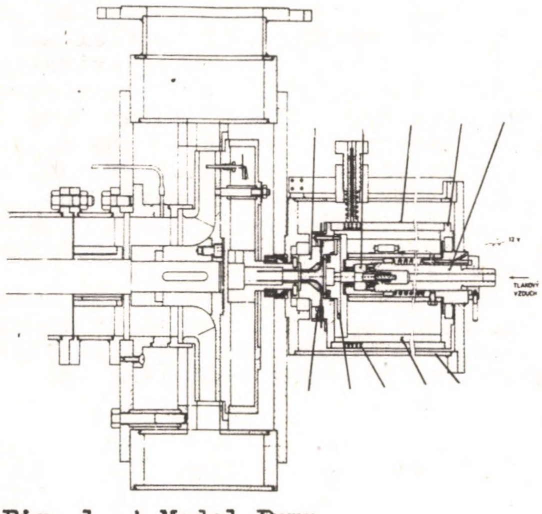

Fig. 1 A Model Pump

The test model pump is shown in Fig.1. For experiment purposes, the hydraulic solution of the impeller was selected according to [2]. Dimensions and designation of measurement points in the channels are given in Fig.2. The measurement of velocity and pressure was carried out on radiuses r/r_2=0.97, 0.83, 0.66, 0.5, the probe being set up in three sections in the meridian plane X, Y, Z - Fig. 2.

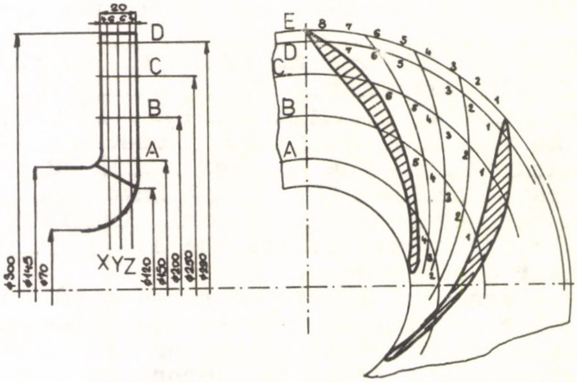

Fig.2 Diagramme of the Impeller and Measurement Points in the Channel

The experiments were conducted at the rotations of n = 750 1/min, fulfilling the conditions as proved by validity measurements at n = 1450 1/min. They were carried out at the values of Q/Q_n = 1.2, 1.0 and 0.5.

The measured signal was transferred from the rotor to the stator by means of a rotating pressure reader, directly connected to the pump, Fig. 1. The rotating pressure reader consists of a set of mercury differential manometers located in the field of centrifugal forces (gravitational forces are relatively small). The equilibrium in the rotating differential manometer having the form of a circular tube in which the rotation axis is shifted with respect to the manometer centre, is reached as a result of the operation of centrifugal forces on the fluid (fluid is relatively steady). The operation principle (Fig. 3) is based on the measurement of the arc length, proportional to the difference between pressures conducted to both ends of the manometer.

A source of light is situated in the inside of the stator and a phototransistor opposite the light source on the outside which, coupled to the equipment, makes it possible to automatically evaluate the measured data (Fig. 3).

It may be proved that :

$$p.T_A^2 = K\left[\cos\left(\frac{2\pi.T_1}{T_A}\right) - \cos\left(\frac{4\pi.T_{10}}{T_A} - \frac{2\pi.T_1}{T_A}\right)\right]$$

where: $T_1 + T_2 = T_a \quad (\ell_1 + \ell_2 = 2\pi . R_a)$

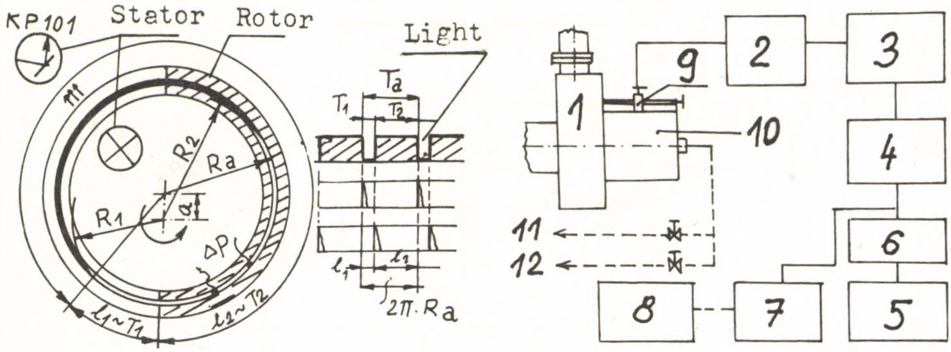

1-Model Pump, 2-Converter, 3-Universal Impulse Counter BM520
4-Adapter for Printing Equip. BP5200, 5-Typewriter CONSUL 257
6-Printing Equipment BP 4450, 7-Teleprinter TESLA, 8-Computer ADT-4316, 9-Holdre with Phototranzistor, 10-Rotating Pressure Reader, 11-Towards the Differential Manometer, 12-Pressure Air from the Compressor

Fig. 3 The Diagramme of the Transfer of Signal from the Rotor to the Stator and Its Evaluation

Cylindrical air-blown probes [3] of Ø 2.8 mm diameter with four holes ø = 0.4 mm, rotated by 45° were used for the measurement - Fig. 4.

Prior to the measurement, the probe was accurately calibrated, the calibration data being shown in Fig. 4. From obtained pressure data, three successive data were chosen, the middle one being the highest (p_3).

Flow parameteres were evaluated according to the following relationships:

$$\mathrm{tg}\,[\,2(\varphi_m - \beta)] = \frac{p_1 - p_2}{p_1 + p_2 - 2p_3} = \frac{p_1 - p_2}{p_A}$$

$$W = \sqrt{\frac{\sqrt{(p_1 - p_2)^2 + p_A^2}}{\rho \cdot \xi \cdot \lambda}}$$

$$p_{st} = p_3 - \frac{p_A}{4} - \frac{2-\lambda}{4} \cdot \sqrt{(p_1 - p_2)^2 + p_A^2}$$

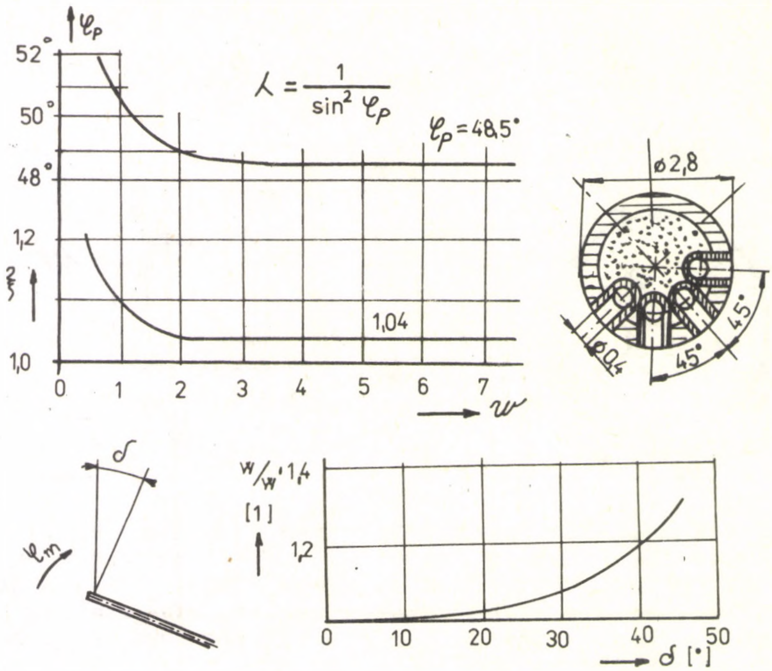

Fig. 4 Calibration Diagrammes of the Cylindrical Probe

where ξ and λ are determined by the calibration, Fig. 4. The calibration determined that the accuracy of measurement is sufficient if the angle β from measured values moves over the range of $\pm 20^{\circ}$ and the speed $w > 1.5$ m/s.

The flow angle, velocity w and static pressure were measured using the calibration diagrammes. The inaccuracy of velocity values moved over the range of $\pm$ 4 %, direction of velocity over the range of $\pm$ 2 %. It needs to be said that in the vicinity of the blades and at the points of tear, the inaccuracies greatly increase. The pump flow rate was measured by means of a calibrated orifice plate from the difference of pressures with the accuracy of $\pm$ 2.5 %.

The accuracy of measurement was also verified by comparing the meridian velocity components in the given section from the flow rate and the mean value of this velocity, obtained by means of graphic integration from measured values.

Differences in the flow rate measured by the orifice plate and from the velocity field of meridian velocity components moved over the range of + 5 - 8 %.

Experimental Results and Their Evaluation

The distribution of relative velocities for the working point of the pump at a maximum efficiency is shown in Fig. 5 which represents the isotachs of relative velocities over the entire channel area in the meridian plane Y (see Fig. 2).

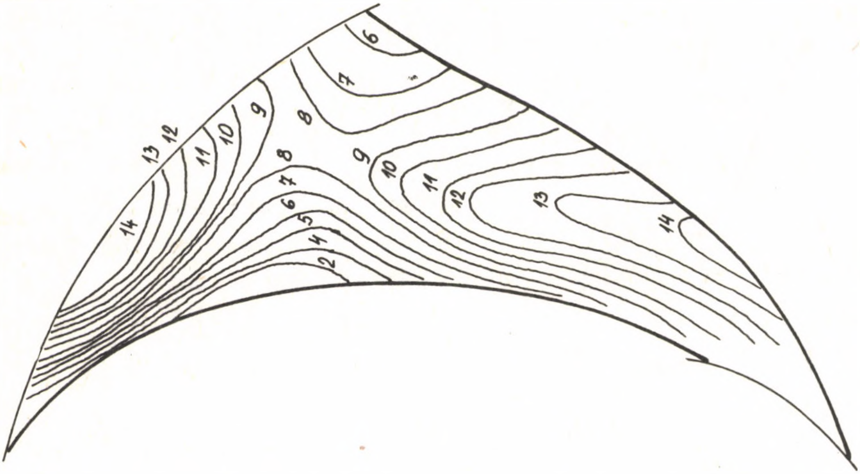

Fig. 5 Isotachs of Relative Velocities at $Q/Q_n = 1$ in the Middle of the Channel (w [m/s] at n = 24.16 [1/s])

The distribution of relative velocities at the same plane, but at ø/Q_m = 0.5 is given in Fig. 6.

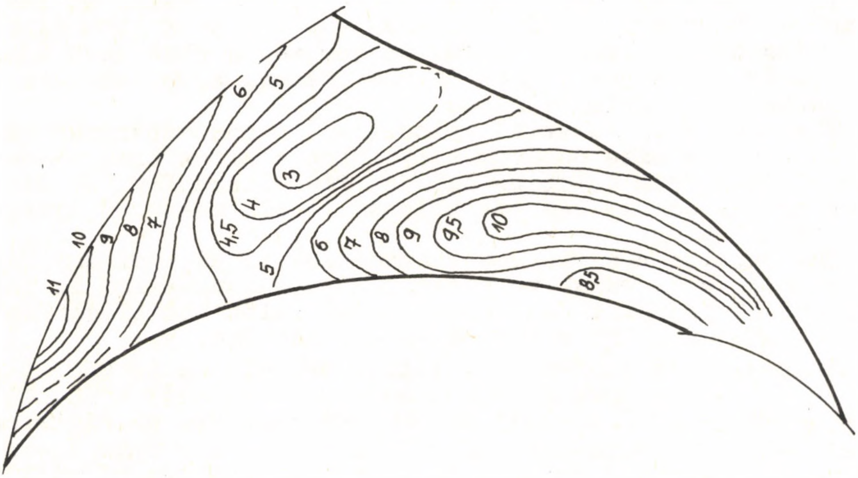

Fig. 6 Isotaches of Relative Velocities at $Q/Q_n = 0.5$ in the Middle of the Channel (w [m/s] at n = 24.16 [1/s])

The complementary courses in Fig. 7 and Fig. 8 indicate that the velocity field has a marked threedimensional character.

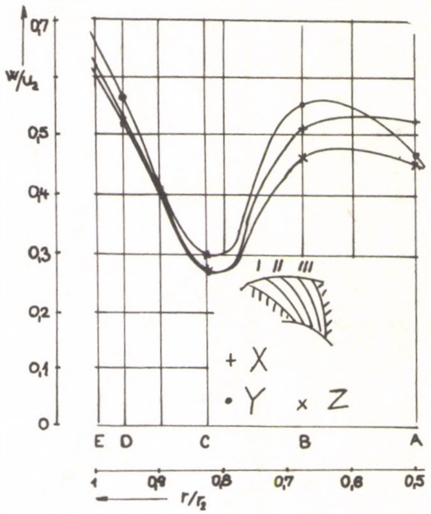

\+ At the Front Disk
• In the Middle of the Channel
× At the Back Disk

Fig. 7 The Course of Relative Velocities Over the Channel Width at $Q/Q_n = 1$ Along the Line of Flow II

The direction and size of relative velocities varies not only along the radius and in the peripheral direction, but also in the plane perpendicular to the plane of anticipated primary flow. This is, apparently, not only the result of the influence of boundary layer formed at the walls of both disks and blades of the impeller. The measurements show that transversal eddy flows are formed in the channel area, changing the character of primary flow.

The course of relative velocities is characterized by the fact that their size periodically changes along the chosen lines of flow from inlet to outlet, Fig. 7 and Fig. 8. The same periodical course was established in all measured operation modes of the pump.

The results are characteristic also in view of the fact that at $\phi/\phi_m = 1$, relative velocities are increasing in the direction of pressure to suction sides, with the exception of the area of output from the impeller, see Fig. 5.

This area of increased relative velocities is characterized by a sudden pressure drop and substantially changing meridian velocities as well as by a decrease of absolute peripheral velocity components, Fig. 9 and Fig. 10. This surprising development may be explained by the presence of eddy currents occurring as a result of force operation of impeller blades, diffuser and fluid at the interface of different qualitative conditions.

With the decreased rate of flow $\phi/\phi_m = 0.5$, the area of increased velocities is moving over to the pressure side, the character of flow, however, remaining the same.

A characteristic picture of flow processes in the channel can be obtained from the course of pressures, Fig. 9 and Fig.10.

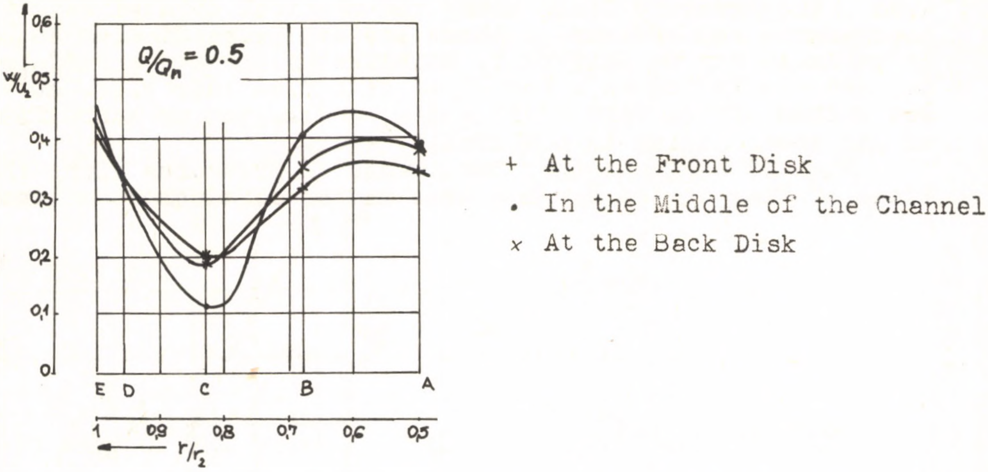

Fig. 8 The Course of Relative Velocities over the Width of the Channel at $Q/Q_n = 0.5$

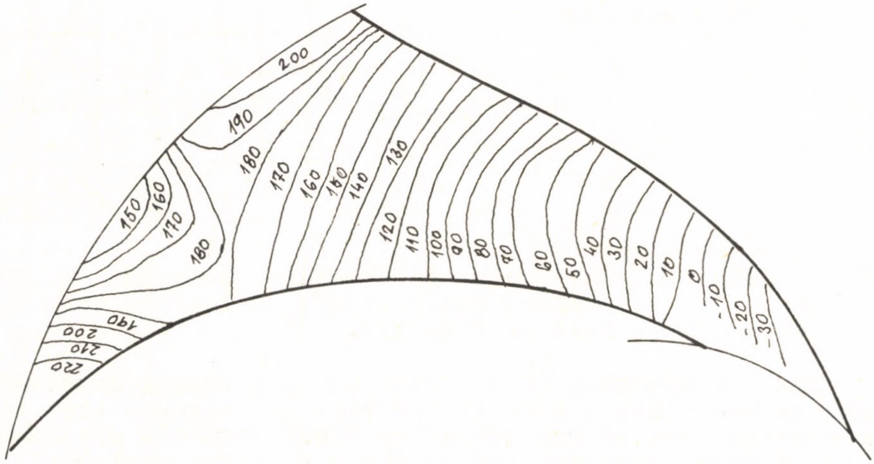

Fig. 9 Isobars of Static Pressures at $Q/Q_n = 1$ in the Middle of the Channel (P/ϱ [J/kg] at n = 24.16 [1/s])

The flow is qualitatively differing in characteristic regions of covered and uncovered channels. We may see that particularly at the output, areas are formed with considerably uneven distribution of pressure, as compared to the areas of covered channel. Accordingly, the structure of flow in the channel may be characterized by three qualitatively differing areas. Area of covered channel, where the pressure field is the most homogeneous and areas at the input and the output, characterized by increased inhomogeneity of all flow parameters (w, P/ϱ). Another important finding indicates that in the covered area , the pressure field along the vertical channel height is homogeneous and pressure isobars are not perpendicular to blade walls. It may be said that, essentially, pressure differences are decreasing as a result of rate flow reduction. At very low values of the rate of flow $\phi/\phi_m = 0.1$, the pressure field at the equal radius is practically even.

Fig. 10 suggests that the course of pressures along the lines of flow in the covered area may be considered as linear.

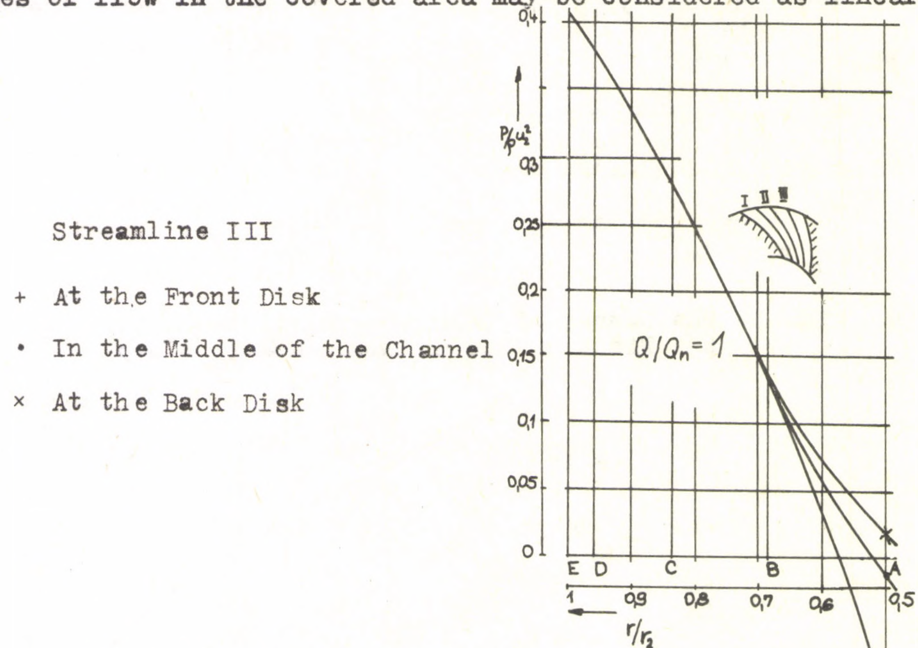

Fig. 10 The Course of Pressure Over the Channel Width at $Q/Q_n = 1$ along the Line of Flow III.

The distribution of pressure and peripheral components of absolute velocities, Fig. 11 and Fig. 12 suggests that the characteristic area at the output is "inefficient", not taking part in the further pressure and absolute velocity peripheral component increases. It is this area which is the subject of strong secondary influences. These influences do not include only real properties of fluids. On the contrary, this area suggests that the influence of real fluid properties is much weaker than the effect of mutual link between the rotor (impeller) and the stator (diffuser, input areas).

During the transition of current from the rotor to the stator, i.e. from impeller into the diffuser under the influence of cyclic changes and as a result of sudden change in external flow conditions, very complex force conditions are created which lead to strongly developed three-dimensional phenomena /secondary flow).

• - In the Middle of the Channel
+ - At the Front Disk
x - At the Back Disk

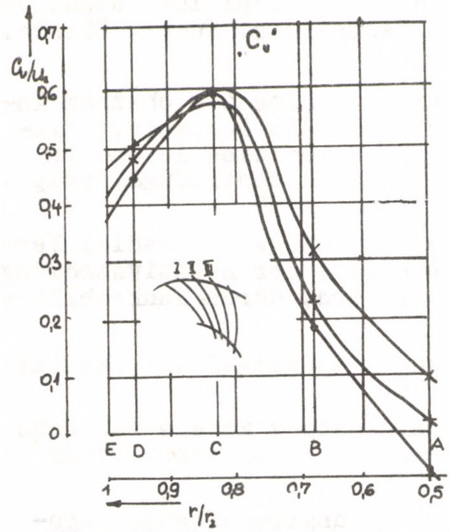

Fig. 11 The Course of c_u Components of Absolute Velocities at $Q/Q_n = 1$ along the Line of Flow II.

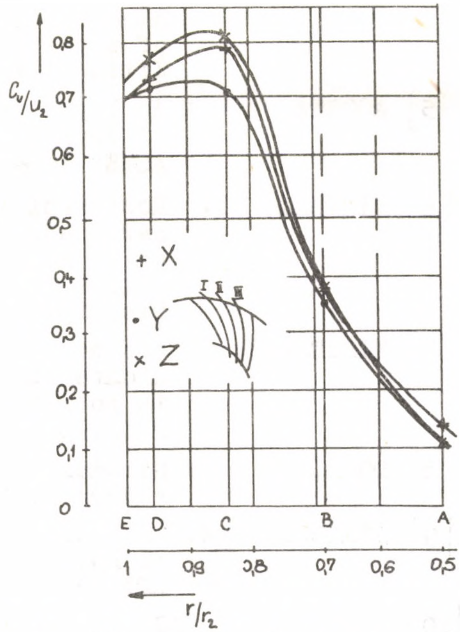

Fig.12 The Course of c_u Components of Absolute Velocities at $Q/Q_n = 0.5$ along the Line of Flow III

CONCLUSION

Obtained data from experimental measurements indicate that the flow in impeller channels is very complicated and does not possess a potencial character.

From the aspect of energy transfer from the shaft to the fluid, the uncovered area at the output does not participate in the increment ot total specific energy of the pump.

References

[1] VARCHOLA, M.: Prúdenie v radiálnom hydrodynamickom čerpadle. (Flow in the radial hydrodynamic pump.) SVŠT Bratislava, 1979. (Dissertation Thesis.)

[2] STRÝČEK, O. : Lopatky obežných kolies, čsl. vynález AO č.162 856. (Impeller blades, Cz. invention AO No.162 856.)

[3] STRÝČEK, O., VARCHOLA, M.: Systém merania rýchlosti a tlakov pevnými štvorotvorcými guľovými sondami. (System of measurement of speeds and pressures by solid four-hole spherical probes.) Collection of SjF SVŠT Papers, Bratislava 1974.

[4] VARCHOLA, M.: Rotačný snímač tlakov. (Rotating Pressure Rea-

der.) Collection of Lectures on Application of Experimental Methods in Fluid Mechanics, Žilina 1981.

[5] ACOSTA : An Experimental and Theoretical Investigation of Two-dimensional Centrifugal Pumps. "Trans. ASME" 1954 No. 7.

[6] MITYSKA, M.: Rozložení relativních rychlostí v oběžném kanálu radiálního odstředivého čerpadla. (Distribution of relative velocities in the impeller channel of a radial centrifugal pump.) Dissertation Thesis Brno 1959.

[7] FISTER, W. : Sichtbarmachung der Stromungen in Radial Verdichter Stufen, besonders der Relativstromung in rotirendedn Laufrädern, durch Funkenblitze. BWK 1966, No. 9.

[8] DOMM, U. : Stromunguntersuchungen an umlaufenden Radialrädern. BWK 1962, No. 9.

[9] ŠKARBUĽ, S.N.: Techenie viazkoi zhidkosti v kanale rabotchego kolesa centrobezhnogo kompresora. Trudy LPI 1962 N3 Leningrad.

[10] BOLTE, W. :Zur Berechnung der Reibungsbehafteten Stromung in den Laufrädern. VDI Zeitschrift 117/1975/No.15/16.

[11] SAKURAI, T.: Study on Flow in Centrifugal Pump Impellers. The Second International JSME Symposium Tokyo 1972.

[12] HOWARD, J.G. - LENNEMAN, E.: Measured and Predicted Secondary Flows in a Centrifugal Impeller. Trans. ASME Series A 1971 No. 1.

[13] MURAKAMI, M. - KIKUYAMA, K. - ASAKURA, E.: Velocity and Pressure Distributions in the Impeller Passages of Centrifugal Pumps. Teoreticheskie osnovy inzhenernych raschetov, 1980. T 102 No.4.

Ing. Michal Varchola, CSc.
Slovak Technical University
Faculty of Mechanical Engineering
Department of Hydraulic Machines
Gottwaldovo nám. 17
812 31 Bratislava
Czechoslovakia

CAVITATION EROSION AND MECHANICAL PROPERTIES OF MATERIALS

J.J.VARGA

ABSTRACT

A good correlation exists between the erosion reistance (ER) and the product of some material properties and the incubation time. The "normalized erosion resistance" (Ne) is a better characteristic than the ER. The erosion resistance of ferrous materials is determined in the first place by the square of hardness, by the ultimate resilience and by the incubation period. In case of non ferrous materials the erosion resis - tance is determined by the hardness (or ba the Ne), by the incubation time and by the compressibility, which is also a very important material property. The merit rating can also offer very valuable information.

1. INTRODUCTION

There have been numerous investigations to determine the relationship between the mechanical properties of materials and the cavitation damage. In spite of all endevour, an objective measurement for the erosion resistance of materials still does not exist. One reason is that there is no material property that could singly characterize the erosion resistance. Further reason can also be that the concept "erosion resistance" has not been clarified unambigously yet. Sometimes the values of erosion rate given in weight or volume or by their reciprocal values are used as erosion resistance. In other cases the "mean depth of penetration rate" (volume loss rate/exposed area) is used.

Heymann [1] proposes that the erosion resistance should be nondimensionalized by referring to the similarly tested resistance of a standard reference material. The "normalized erosion resistance" (Ne) then can be defined as the measured erosion rate of the reference material divided by the measured erosion rate of the material to be evaluated.

From the literature we can learn the investigated material properties comprised almost everything (tensile strength, 0,1% proof stress, Young modulus, hardness, elongation etc), with the exception of the compressibility of materials, that $\beta = 3(1-\nu)/E$ (where ν = Poisson ratio, E = Young modulus). The compressibility is also an important material property. The circumstances described above led to physical hypotheses to understand how material can absorb the energy released by collapsing cavity.

Hobbs [2] e.g. supposed that it can be: 1. by elastic deformation, 2. by plastic deformation, 3. by fracture. By this way of thinking he introduced the concepts of "proof resilience", the "ultimate resilience" (UR = (tensile strength)^2/elastic modulus), and the "work done to cause fracture".

This situation encouraged us to investigate some combinations of material properties in which the compressibility and incubation period were included. The base of the investigation were the NEL495 and 496 reports [3],[4], that had summarized the results of carefully executed and excellently documented vibratory cavitation tests. Some results of the comprehensive research work are summarized as follows:

2. FERROUS MATERIALS

NEL report No 495 summarizes the results of the vibratory cavitation tests of 35 different ferrous alloys. Determining the Ne values and comparing them with the erosion resistance values (ER = min/mm^3) used by Hobbs a good correlation between them has appeared:

Ne - ER R = 0,973 Regression line: y=29,708 + 5,176x

As it was expected there is a good correlation between the ultimate resilience (UR) and the square of hardness (HV^2):

UR - HV^2 R = 0,970 Regression line: y=8,765 + 41,5 x

The importance of the incubation time should be evident from the following:

HV - ER	R = 0,812 while	HVxInc - ER	R = 0,956
UR - ER	R = 0,881	URxInc - ER	R = 0,944

HV^2 - ER	R = 0,870	HV^2xInc - ER	R = 0,965
HV^2/β-ER	R = 0,871	HV^2/βxInc-ER	R = 0,966
UR - HV^2	R = 0,970	URxInc-HV^2xInc	R = 0,994

The correlations connected with Ne are:

HV^2xInc - Ne	R = 0,954
NexInc - ER	R = 0,967

UR - ER R=0,881; UR - Ne R=0,930; UR/β - Ne R=0,9333

and they demonstrate that the Ne better reflects the erosion resistance than ER. It is justified by the tests made on different 22 Cr-Ni and Cr-Ni-Mo alloys published in Hobbs former work [2]. Hobbs got R = 0,65 correlation between UR - ER and R = 0,60 between the proof resilience - ER. Though the R = = 0,9526 correlation between Ne and ER is good nevertheless the different material properties systematically result better correlation with the Ne values than the ER ones. E.g. Ne - UR R = 0,7981; ER - HV R = 0,801; Ne - HV R = 0,8872 etc.

From the data presented it can be ascertained that the erosion resistance of these materials are determined by the square of the hardness, the tensile strength (by means of UR) and the incubation period. The influence of the compressibility is less perceptible because the compressibility of the materials changes only slightly.

3. NON FERROUS MATERIALS

Among the 38 materials examined by Miss Laird and Hobbs there were 8 cast and wrought bronzes, 10 nickel, 7 aluminium and 4 titanum alloys. In the NEL report No 496 the following correlations are published:

HV - ER R=0,751; HV^2-ER R=0,715; Tens.strength-ER R=0,732; (Tensile strength)^2 - ER R=0,742; Proof stress/hardness - ER R=0,898.

From the results of our examination it is to be mentioned that contrary to the ferrous materials the correlation between Ne and ER is poor (R = 0,621). On the other hand the correlation R = 0,8654 between ER - Inc. period is remarkable. Besides incubation time compressibility has importance. E.g. Ne - ER R = 0,621; NexInc - ER R = 0,928; $Ne/\beta x Inc$ - ER R = 0,945.

The moderate correlation between hardness and ER increases taking into consideration the incubation period: HVxInc - ER R = 0,910. In the same way: URxInc - ER R = 0,828.

It is worth mentioning the fact that determining the correlation factors for the different material groups, much better correlations can be obtained. E.G. $Ne/\beta x Inc$ - ER R = 0,958 for the bronzes, R = 0,951 at nickel alloys, R = 0,968 at aluminiums. The same can be learned from the NexInc - ER relation. For bronzes R = 0,976, for nickels R = 0,951, for aluminiums R = 0,968.

The same result can experienced in the $HV^2/\beta x Inc$ - ER and in other relations. This refers to the fact that normally it is not resonable to examine materials which considerably differ from each other. In the merit rating of the separate material groups almost the same sequence has been formed (Table 1.).

At non ferrous materials the hardness and the incubation period better characterize the erosion resistance than the square of the hardness and incubation time: HVxInc - ER R = 0,910; $HV^2 x Inc$ - ER R = 0,0803.

The use of NE offers better correlation. The influence of the compressibility can be well perceived. This refers to the fact that the erosion resistance of the non ferrous materials is determined first of all by the incubation period and the compressibility.

4. SOME REMARKS

The data issued are the results of a more comprehensive investigation that aims - among others - to approach the dimension of the erosion resistance.

TABLE 1

	CAST BRONZES										
	$\frac{Ne}{\beta}$ × Inc	Hv × Inc	Hv^2 × Inc	Ne × Inc	Ne	ER	Inc	Σ Ne Hv Inc	Σ ER Hv^2 Inc	Σ UR Hv^2 Inc β^{-1}	Σ Ne Inc
F1	5	5	5	5	5	5	5	5	5	5	5
F2	6	6	6	6	6	6	6	6	6	6	6
F3	8	8	8	8	8	8	8	8	8	8	8
F4	7	7	7	7	7	7	7	7	7	7	7
F5	2	2	2	2	2	2	2	2	2	2	2
F6	1	1	1	1	1	1	1	1	1	1	1
F7	3	3	3	3	3	3	3	3	3	3	3
F8	4	4	4	4	4	4	4	4	4	4	4
	NICKEL ALLOYS										
H1	9	9	9	9	10	9	9	9	9	9	9
H2	8	8	8	7	8	8	8	8	8	8	8
H3	7	7	7	5	6	7	6	7	7	7	7
H4	3	2	2	3	3	5	2	2	3	3	2
H5	2	6	3	1	1	2	7	4	1	1	6
H6	4	3	4	4	4	3	1	3	4	4	1
H7	6	4	6	8	7	4	3	5	5	5	4
H8	1	1	1	2	2	1	4	1	2	2	3
H9	5	5	5	6	5	6	5	6	6	6	5
H10	10	10	10	10	9	10	10	10	10	10	10

	WROUGHT BRONZES										
	$\frac{Ne}{\beta}$ × Inc	Hv × Inc	Hv^2 × Inc	Ne × Inc	Ne	ER	Inc	Σ Ne Hv Inc	Σ ER Hv^2 Inc	Σ UR Hv^2 Inc β^{-1}	Σ Ne Inc
G1	6	5	6	5	5	6	6	6	6	6	6
G2	8	8	8	8	7	5	8	8	8	8	8
G3	7	6	7	7	6	7	5	5	7	7	5
G4	3	3	3	3	3	3	4	4	3	3	4
G5	5	4	4	6	8	8	3	3	4	4	3
G6	4	7	5	4	4	4	7	7	5	5	7
G7	9	9	9	9	9	9	9	9	9	9	9
G8	2	2	2	2	1	2	2	2	2	2	2
G9	1	1	1	1	2	1	1	1	1	1	1
	ALUMINIUM ALLOYS										
J1	7	7	7	7	7	7	7	7	7	7	7
J2	6	6	6	6	6	6	6	6	6	6	6
J3	3	3	3	2	2	3	2	3	3	3	3
J4	5	5	5	5	5	5	5	5	5	5	5
J5	4	4	4	4	3	2	4	4	4	4	4
J6	1	1	1	1	1	1	3	1	1	1	2
J7	2	2	2	3	4	4	1	2	2	2	1
	TITANIUM ALLOYS										
K1	3	2	3	3	2	2	3	3	3	3	3
K2	4	4	4	4	4	4	2	4	4	4	4
K3	2	3	2	2	3	3	1	1	2	2	1
K4	1	1	1	1	1	1	4	2	1	1	2

MERIT RATING OF NON FERROUS MATERIALS

5. REFERENCES

[1] Heymann,F.I.: Toward Quantitative Prediction of Liquid Impact Erosion. ASTM stp 474,1969.

[2] Hobbs,J.M.: Experience with a 20-Kc Cavitation Erosion Test. ASTM stp 408.1966.

[3] Hobbs,J.M. and Miss Laird,A.: Comparative Erosion Tests on Ferrous Materials. Prt II. Vibratory Cavitation Tests.NEL report No 495.1971.

[4] Miss Laird and Hobbs,J.M.: Comparative Erosion Tests on Non Ferrous Materials,Part II. Vibratory Cavitation Tests. NEL report No 496. 1971.

Prof. Dr.J.J.Varga
Budapest, TU. H1521.

AXISYMMETRIC DIFFUSER FLOWS WITH MASSIVE SEPARATION

K. VARSAMOV , A. KIROV

Summary

This paper describes a theoretical model and numerical results for high Reynolds number flows in axisymmetric diffuser with massive separation. Constant pressure is assumed in the separated flow region, which starts from the line of separation of the turbulent boundarylayer. A boundary value problem of mixed boundary conditions is formulated for the potential incompressible flow consisting of the non-flow condition across the diffuser wall and the free-streamsurface, where also the constant pressure condition is applied. An algorithm for numerical solution of this problem is presented and some results are compared with experimental data .

1. Introduction

The study on flows experiencing massive separation is of considerable importance for different engineering applications , therefore it has been investigated for a long period of time the last decades especially. Large reviews on that problem can be found in the monographs [1] and [2] . Currently there are several successful solutions of the problem concerning separated flows over airfoils, based on potential flow analysis ,

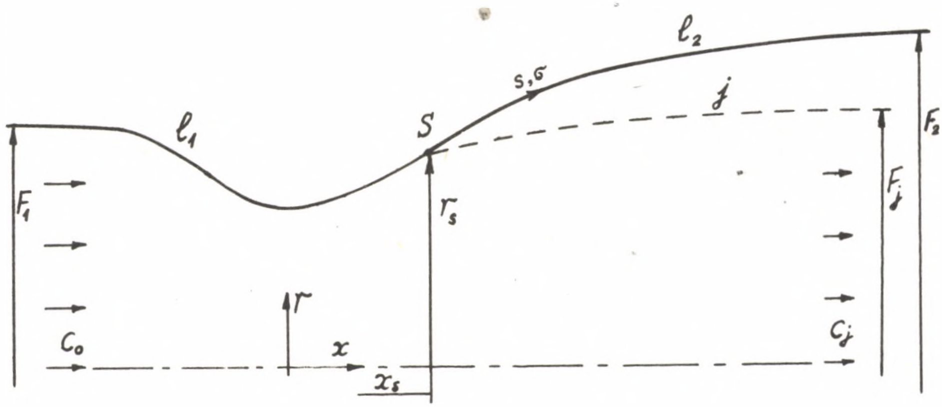

Fig.1.

boundary layer computations and different models for the separated flow region (see[2],[3],[4] etc.) .

In a similar approach to the flow analysis in axisymmetric diffuser the present work is based on the following assumptions :

- the Reynolds number is high enough to apply " potential flow-turbulent boundary layer " model in accord with the conventions arising in the inner problems and discussed in [5] .
- in the separated region between the main flow and the diffuser wall , the fluid is at rest (jet model). The stream surface j (Fig.1) beginning from the separation line of the turbulent boundary layer (point S) is a surface of tangential jump of the velocity of the potential flow, the vortex strength on j has a constant value, equal to Cj.
- the interaction of the boundary layer and the main stream is not accounted for .

2.Definition of the Problem

The analysis of the flow with the above given simplifications is governed by the following system of equations :

$$(1) \qquad C(S) + \int_{\ell_1+j} C(\sigma)\, K(S,\sigma)\, d\sigma = \varphi(S) ,$$

$$(2) \qquad \tau_o \left[S , \ell_j , C(S) \right] = 0 ,$$

$$(3) \qquad r_j(S) = r_s + \int_{x_s}^{x} \frac{V_j}{U_j}\, d\xi ,$$

satisfying also the boundary conditions :

$$(4) \qquad C_n \Big|_{\ell_1+j} = 0 , \qquad C \Big|_j = const = C_j , \qquad C_j = C_o F_1 / F_j ,$$

where C (S) - velocity on boundaries, τ_0 - wall shear stresses, U, V - axial and radial velocity components. The rest of the nomenclature is obvious from Fig. 1.

Equations (1) ÷ (4) define a nonlinear boundary value problem, which even in the case of given position of point S (Equation 2 is not needed) can be solved only by successive approximations (See[7],[8]). To clarify this point assume that surface j is known in a given iteration (this means that Cj is also known). The solution of Eq.1 yields the velocity distribution C (S) on l_1 and j . The right hand side (S) of Eq.1, the kernel K and the technique of its numerical solution are described in [6]. For known velocity C (S) on l_1 in a given iteration, the turbulent boundary layer growth can be calculated in order to find the next iteration for point S from Eq. 2.

Thus, it becomes possible to construct the next approximation for the surface j from Eq. 3 going back to the solution of Eq. 1.

3. Numerical Solution

Based on the previous numerical experience of the authors for the solution of system of equations (1), (3), (4), the following iterative technique is used :

$$C^{(i+1)}(S) + \int_{l_1+j^{(i)}} C^{(i+1)}(S)\, K(S,\sigma)\, d\sigma = \varphi^{(i)}(S, l_1, j^{(i)}) \Rightarrow C^{(i+1)}(S) \tag{5}$$

$$\tau_0\left[S, j^{(i)}, C^{(i+1)}(S) \right] = 0 \Rightarrow S^{(i+1)} \tag{6}$$

$$C_j^{(i+1)} = const = C_s^{(i+1)} \,,\quad F_j^{(i+1)} = C_0 F_1 / C_j^{(i+1)} \tag{7}$$

$$r_j^{(i+1)} = r_s^{(i+1)} + \int_{x_s}^{x} \left(\frac{V_j}{U_j} \right)^{(i+1)} d\xi \Rightarrow j^{(i+1)} \tag{8}$$

where

$$V_j^{(i+1)} = C_j^{(i+1)} . \cos\alpha^{(i)} , \quad U_j^{(i+1)} = C_j^{(i+1)} . \sin\alpha^{(i)} ,$$

$$tg\alpha^{(i)} = \left(\frac{V_j}{U_j}\right)^{(i)} .$$

Some numerical details are skipped and can be partly found in the references [6],[7],[8] . For the numerical solution of Eq.6 the well known method of Truckenbrodt is applied, choosing the initial parameters of the boundary layer upstream - δ_o^*-displacement thickness, δ_o^{**} - momentum thickness, δ_o^{***} - energy loss thickness, Re - Reynolds number . When solving Eq. 8 a smooth detachment condition is observed expressed by a continuous first derivative of the contour j .

A FORTRAN computer program was written which solves the problem by the algorithm , the main steps of which are :

1. Input data - the offsets of the surfaces l_1 and l_2; the initial parameters of the boundary layer δ_o^*, δ_o^{**}, δ_o^{***}, Reynolds number .
2. The potential analysis problem is solved following Eq. 5 yielding the velocity distribution attributed to the next iteration .
3. The parameters of the boundary layer are calculated. If no separation occurs steps 4 and 5 are omitted, otherwise the separation point S is determined. When the separation point does not change in two successive iterations, step 4 and 5 are also omitted .
4. The initial position of the surface j is r_j=const. = r_s and the velocity distribution on it is determined from Eq. 7 .
5. The surface j is determined in next iteration from Eq. 8 . After reaching the required precision ε_r in two neighbouring iterations or the maximum allowed number of iterations the control is passed to step 2. The number of iterations for the determination of j does not exceed the number of outer ite-

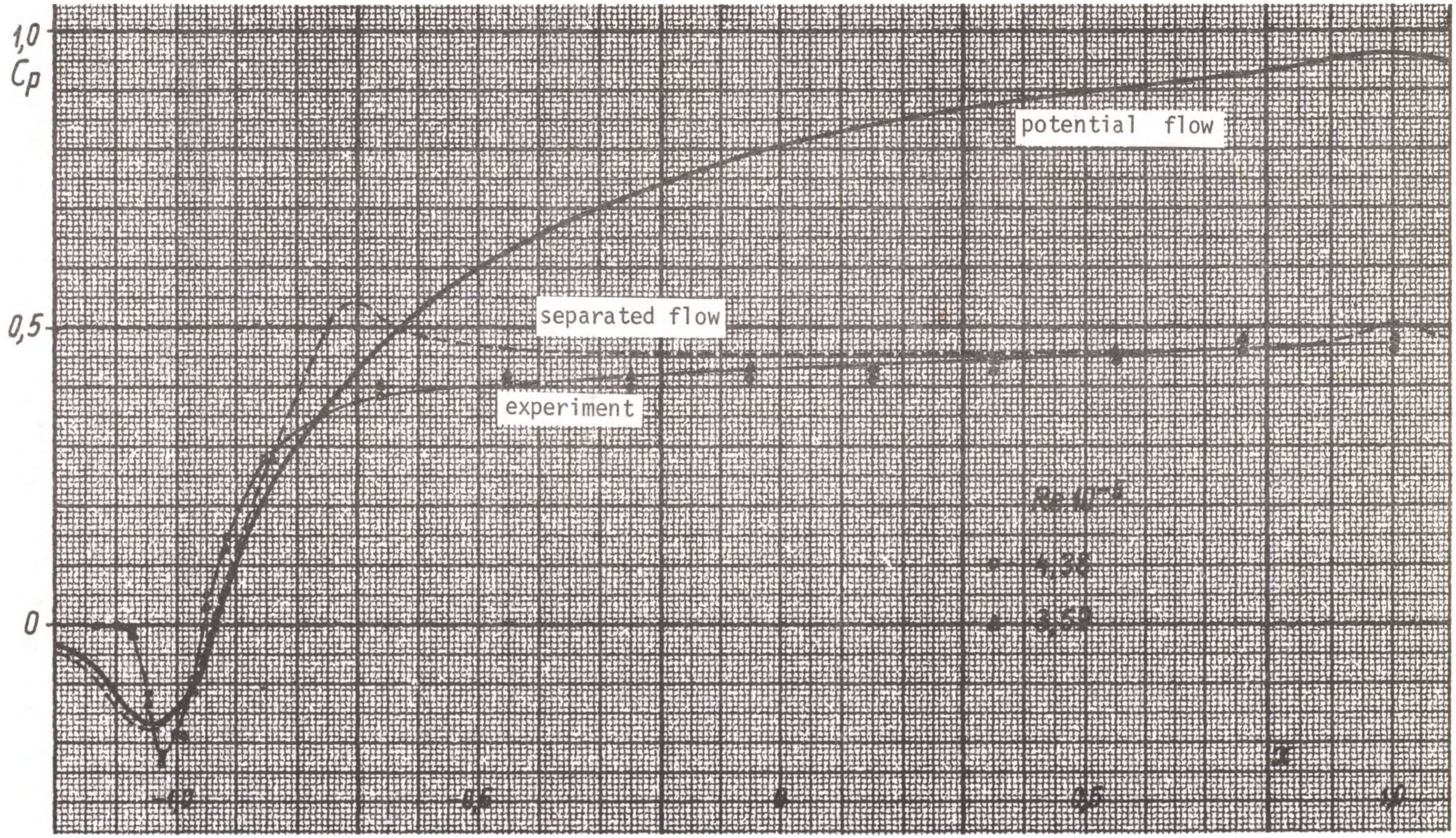

Fig.2.

rations (for the analysis problem) plus two .

6. The pressure coefficient distribution is computed $C_p = 1 - C_j^2$ and if needed the energy loss coefficient , etc.

From the numerical experiments the following conclusions can be drawn :

- the number of inner iterations for the adjusting of surface j is about 3 - 5 for a precision of $\varepsilon_r = 10^{-2}$;
- the number of iterations for determination of point S is about 4 - 5 .

An example of the flow in wide angle (30°) diffuser of F_2/F_1 equals 4 and Re = 10^6 is presented in Fig. 2. The agreement of the computations with experimental results is good for the region far from point S. The considerable difference in the neighbourhood of point S is attributed to the fact that no special care is taken for the contour of surface j to be smoothed properly .

4. Conclusion

The limited experience from the numerical experiments carried out and the comparisons with few experimental results does not give sufficient information about the applicability of the presented method. Further numerical investigations and comparisons with experimental results are needed with the use of other methods for boundary layer computations in order to estimate, if it is necessary to add to the theoretical model the flow in the separation zone and its interaction with the potential flow.

References

1. Chang P." Separation of Flow ", MIR, 1972 (in Russian)
2. Goghish L., Stepanov G. " Separated Turbulent Flows ", NAUKA, Moscow, 1979 (in Russian).
3. Jacob K. " Theoretische Bestimmung der Kennkurven von Tragfluegelprofilen mit Klappen, Stroemungsabloesung und Bodeneinfluss, DGLR-Vortrag Nr. 76-206, 1976 .
4. Butter D.J. " Two-Dimesional Separated Flows " EUROMECH 148, Bohum 1981.
5. Deutsch M.E., Zariankine A.E. " Gazdynamics of Diffusers and Inlet/Outlet Tubing of Turbomachines ", ENERGIA , Moscow, 1970 (in Russian)

6. Varsamov K., Haimov A. " Axisymmetric Potential Flow about a Multiply-Connected Body in Duct ", Proc. VI Conf.Fluid Machinery, vol.2, Academiai Kiado, Budapest , 1979.
7. Varsamov K., Kirov A., Haimov A. " Design of Additional Elements for Multielement Axisymmetric Diffusers ", IV Nat.Congress Theoretical and Applied Mech., Proc., vol.4, Varna , 1981 (in Bulgarian).
8. Varsamov K., Haimov A. " Axisymmetric Jet Flow Past Body of Revolution", Theoretical and Applied Mechanics, 1983 (to be published).

Kiril Varsamov ,
Associate Professor
Institute for Mechanical and Electrotechnical Engineering ,
Sofia 1156, BULGARIA

Alexander Kirov,
Assistant Professor
Institute for Mechanical and Electrotechnical Engineering,
Varna 9010 , BULGARIA

TURBULENT FLOWS OF THE NON-NEWTONIAN AND DRAG REDUCTION FLUIDS IN THE ENTRANCE ZONE OF A PIPE

Verba, A. - Embaby, M.H. - Angyal, I.

SUMMARY

A theoretical analisys is given for the turbulent flows of the non-Newtonian and drag-reduction fluids in the entrance zone of a circular or a square cross section pipe.
The theoretical results were checked by an experimental study using aqueous solutions of carboxymethyl cellulose and polyethyleneoxide in a square cross section pipe. A brief description on the theoretical model is presented. Some theoretical and measured results are shown.

THE THEORETICAL MODEL

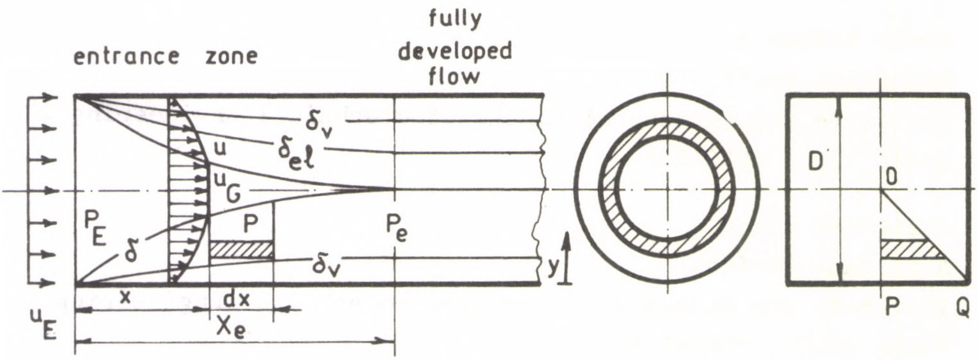

Fig. 1.

The upper part of Fig. 1 regards the flow of a drag-reduction fluid, while the lower one that of a non-Newtonian fluid.
The thickness of the boundary layer inceases downstream from the entrance cross section. The end of the entrance zone is defined by the boundary layer thickness δ = D/2. The flows consist of more layers. The velocity distribution of the laminar sulayer at the wall:

$$u^+ = y^{+\frac{1}{n}}, \qquad 0 \leq y^+ \leq \delta_v^+ \qquad (1)$$

The velocity distribution of a non-Newtonian fluid in the turbulent part of the fully developed flow [1] :

$$u^+ = A \ln y^+ + B \ , \qquad \delta_v^+ \leq y^+ \leq \delta^+ \ , \tag{2}$$

$$A = 2{,}46/n^{0{,}75} \ , \tag{3}$$

$$B = \frac{3{,}475\,[1{,}96+0{,}81n - 0{,}7n \ \ln(3+1/n)]}{n^{0{,}75}} - \frac{0{,}566}{n^{1{,}2}} \ . \tag{4}$$

In the fully developed flow of a drag-reduction fluid according to Virk [2], two turbulent layers, the elastic and the Newtonian ones can be distinguished inwards from laminar sublayer. Their velocity distributions are:

$$u^+ = 11{,}7 \ln y^+ - 17 \ , \qquad \delta_v^+ \leq y^+ \leq \delta_{el}^+ \ , \tag{5}$$

$$u^+ = 2{,}5 \ln y^+ + 5{,}5 + \frac{9{,}2 \ln \delta_{el}^+}{11{,}7} \ , \qquad \delta_{el}^+ \leq y^+ \leq \frac{D^+}{2} \ . \tag{6}$$

The non-Newtonian fluid is supposed to comply with the Power - law:

$$\tau = K\left(\frac{du}{dy}\right)^n \ . \tag{7}$$

For the drag-reduction fluid n=1 and $K=\eta$. The later is the viscosity of the solvent.

Assumptions:

1. The flow is steady and the velocity distribution u_E at the entrance is uniform.
2. The velocity distribution in each layer within the boundary layer is the same as in the corresponding layer of the fully developed flow. In the core the velocity u_G is uniform along the cross section.
3. In the entrance zone the ratio of widths of the single layers compared agrees with those of the corresponding layers in the fully developed flow.
4. The lines of constant velocities in the square cross section are parallel to the wall. So the investigation of the triangle OPQ presented in Fig.1 proves sufficient.

5. The pressure along the cross section is uniform.

6. For drag-reduction flow the onset wall shear stress and the slope increment $\emptyset$ are known. Their definition can be seen in [2], [3].

The model is based upon the momentum balance, the continuity equation and the previously known velocity distributions mentioned above. The momentum balance of the boundary layer:

$$\frac{dx}{D}\frac{\tau_w}{\varrho} = \frac{u_G}{D^2}\delta(D-\delta)\ du_G - \frac{2u_G}{D^2}\ d\left[-\int_0^{\delta} u\left(\frac{D}{2}-y\right)\ dy\right] - $$

$$- \frac{2}{D^2}\ d\left[\int_0^{\delta} u^2\left(\frac{D}{2}-y\right)\ dy\right]. \tag{8}$$

The continuity equation:

$$u_E D^2 = 8\int_0^{\delta} u\left(\frac{D}{2}-y\right) dy + u_G\left(D-2\delta\right)^2 . \tag{9}$$

The Reynolds-number that holds good for both fluids is needed:

$$R_e = \frac{D^n u_E^{2-n}\varrho}{8^{n-1}KC} , \tag{10}$$

$$C = \left(\frac{a}{n} + b\right)^n . \tag{11}$$

For the circular section [4] : a=0,25; b=0,75.

For the square cross section: a=0,2121; b=0,6766.

In the core: $dp = -\varrho u_G du_G$. (12)

After making the lengths and velocities dimensionless, the numerical solution of equations (8)...(11) gives:

1. The change of the pressure drop and the width of the layers along the entrance zone.

The dimensionsless pressure drop:

$$\overline{\Delta p} = \frac{2\left(p_E - p_e\right)}{\varrho u_E^2} . \tag{13}$$

2. The change of the local friction factor:

$$f = \frac{2\,\tau_w}{u_E^2\,.} \quad . \tag{14}$$

3. The velocity distribution in the cross sections.
4. The length of the entrance zone.
5. The incremental entrance pressure drop factor:

$$\bar{K} = \frac{2\,(p_E - p_e)}{\varrho\, u_E^2} - 4\, f_{fd}\, \frac{x}{D} \quad . \tag{15}$$

It can be shown, that the influence of the laminar sublayer is negligible, so it was not taken into account by the numerical solution. The results calculated by the Reynolds-number for the non-Newtonian fluids were given in the function of the power n, while for the drag-reduction fluids in that of the concentration.

THEORETICAL AND MEASURED RESULTS

Measurements were made in a pipe of 24x24 mm square cross section. The details of the measuring devices and methods are presented in [3], [5]. The Δp pressure drop measured and calculated by the non-Newtonian fluid characterized with n=0,771 is shown in Fig. 2. Measurements comprises the range n=0,726...1,0 and the case shown in the figure gave the highest difference between the calculeted and measured values. According to the analysis of non-Newtonian fluids the increase of the Reynolds-number or the decrease of n has a decreasing effect on the friction factor f, the pressure drop $\bar{\Delta}p$ and the incremental entrance pressure drop factor $\bar{K}$ and an increasing effect on the entrance length x_e/D.

According to the analysis on drag-reduction fluids supposing a constant c concentration, the increase of the Reynolds-number has a decreasing effect on the friction factor f, the pressure drop $\bar{\Delta}p$ and the incremental entrance pressure drop factor $\bar{K}$ and an increasing effect on the entrance length x_e/D.

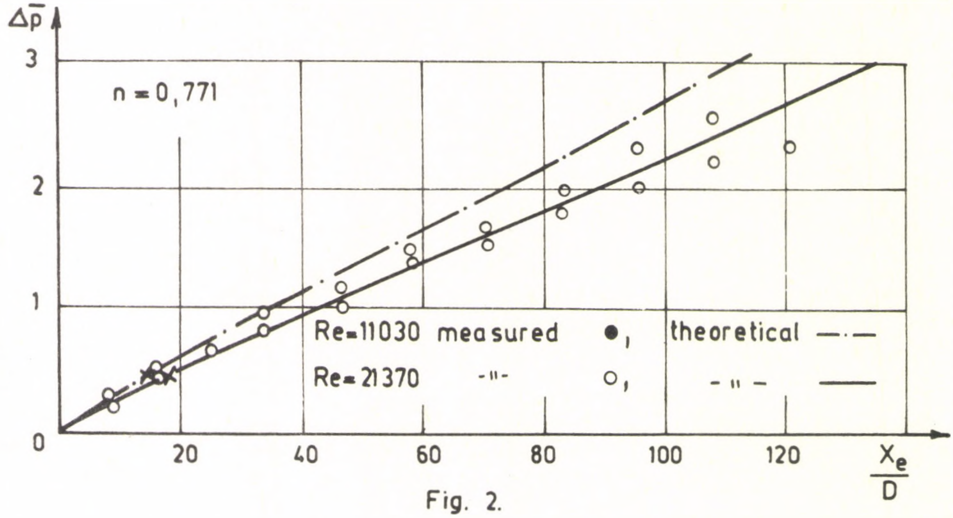

Fig. 2.

In Fig. 3 the change in x_e/D is shown in function of the Reynolds-number at different concentrations. The curve denoted with mdr belongs to the maximum drag-reduction. The change of the pressure drop along the entrance zone is shown in Fig. 4 at different concentrations. Entering, on a relatively short distance the drag-reduction fluid induces a higher pressure drop than the Newtonian one. Moving on along flows the drag-reduction fluid has already a less pressure drop.

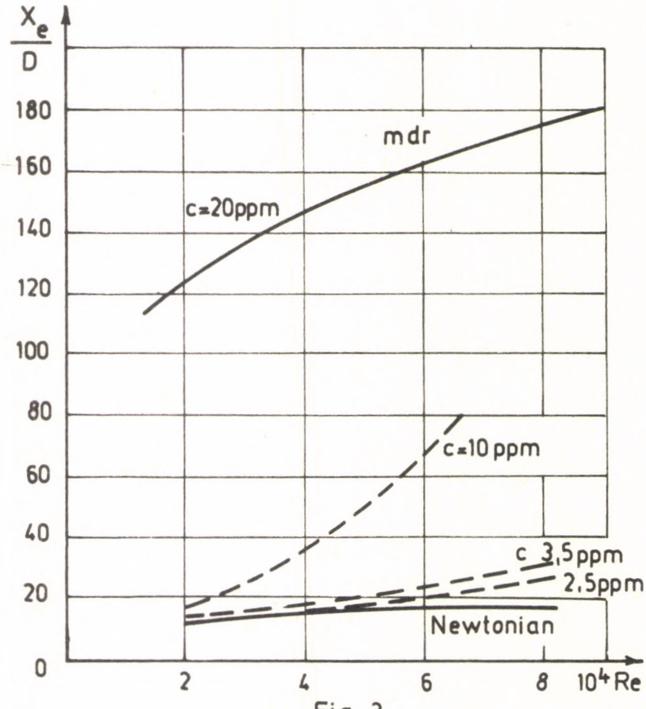

Fig. 3.

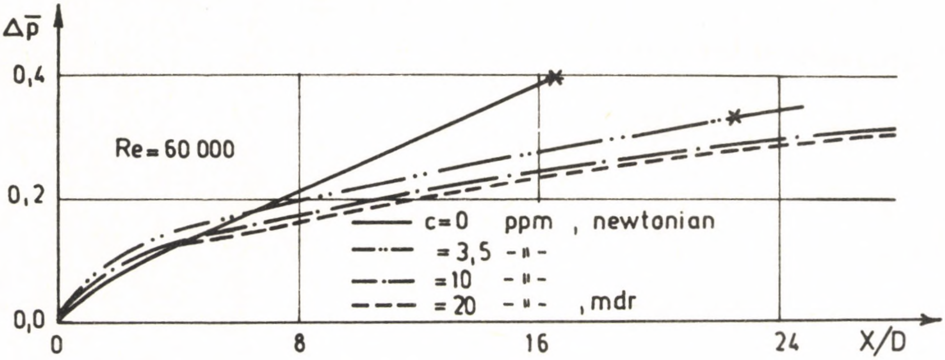

Fig. 4.

In Fig.5 the calculated and measured friction factors are shown in function of the pipe length at maximum drag-reduction which was obtained at c=20 ppm concentration. In the fully developed flow, the friction factor of the water $f=5,8 \cdot 10^3$ without polyethyleneoxide that means about a 70 per cent drag reduction can be arrived by adding 2o ppm polyethyleneoxide to the water.

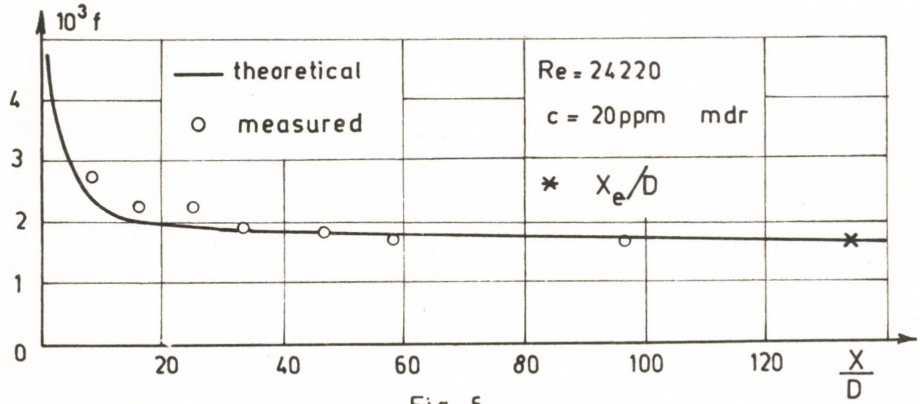

Fig. 5.

NOTATIONS, not defined in the text or in the figures.

dimensionless length=length$^+$=length^n $u^{*(2-n)}/K$	m
dimensionless velocity=velocity$^+$=velocity/u^*	m/s
K: non-Newtonian consistency	kg/ms^{2-n}
p: pressure	kg/ms^2

$u^* = \sqrt{\tau_w/\varrho}$: shear velocity m/s

η : viscosity kg/ms

ϱ : density kg/m^3

τ : shear stress kg/ms^2

τ_w: wall shear stress kg/ms^2

Subscript:

fd: fully developed

REFERENCES

[1] Dodge, D.W., and Metzner, A.B: AICHE J, vol.5,No 2, pp. 189-204

[2] Virk, P.S: AICHE J, vol. 21. No 4, pp.625-656, 1975.

[3] Embaby, M.H.: Candidate Thesis, TU. Budapest, 1981.

[4] Kozicki, H.W., and Chon C.H. and Tiu: Ch. Eng. Sc. Vol 21, Feb.,1966, pp.665.

[5] Verba, A. - Embaby M. - Angyal, I.: Newtoni és nem-newtoni folyadékok áramlásának mérése négyzet-keresztmetszetü csatornában. III. Áramlásmérési Kollokvium, Miskolc, 1980 okt. 16-17.

Dr. Attila VERBA, Head of the Dept.
István Angyal, Assistant
TU, Budapest
Department of Mechanical Engineering
for the Chemical Industry
H-1521 Budapest

Mohamed Hamed Embaby
Faculty of Engineering
Shibin El-Kom,
Egypt, Shibin El-Kom.

RESULTS CONCERNING THE APPLICATION
OF PLANE CASCADE AT THE STUDY OF RADIAL-AXIAL
RUNNERS OF THE HYDRAULIC MACHINES

by

I.Voia

INTRODUCTION

The application of plane cascade to the study of radial-axial runners is based on the following observations:

- on the basis of the laboratory experiment (EL) the universal characteristic is established for a radial-axial runner;
- by applying a conformal transformation (TC) to the runner blade for each flow surface, the correspondence to a plane straight cascade is established.

These correspondences are suggestively presented in fig.1., where the geometrical parameters of the plane cascade are given as well. Thus, it results the possibility that the hydrodynamic parameters of the runner would be studied in correlation with the geometrical parameters of plane cascades.

The extensive use of digital computers favoured the method development by the possibility of the automatic achievement of plane transformation.

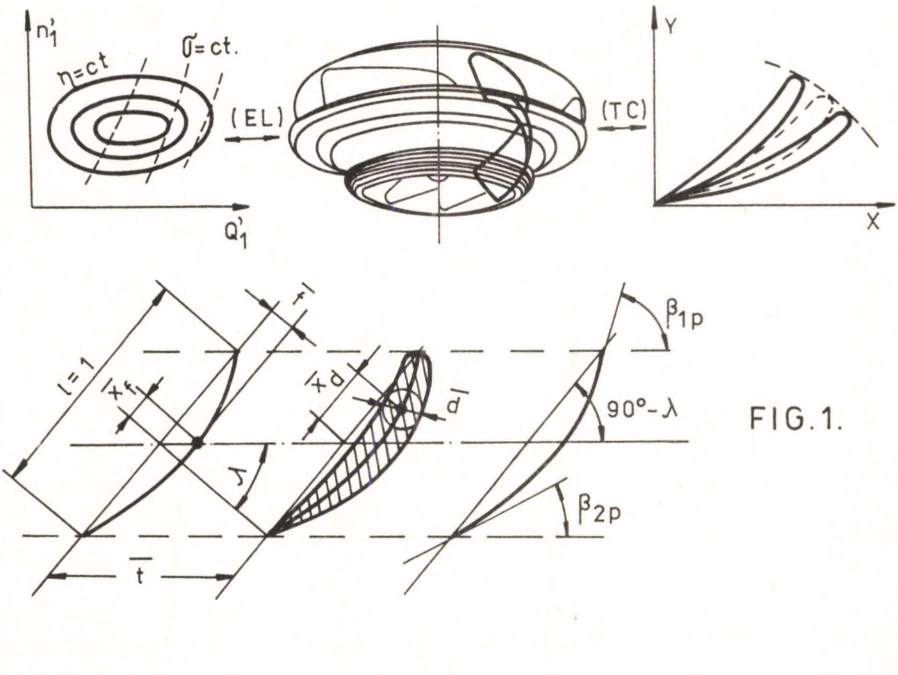

FIG.1.

For the axial-symmetrical surface of isothermal curvilinear coordonates $S(\xi,\eta)$, the conformal transformation in the plane $N(X,Y)$ is done with the relations given by M.Strscheletzki /1/, fig.2, thus:

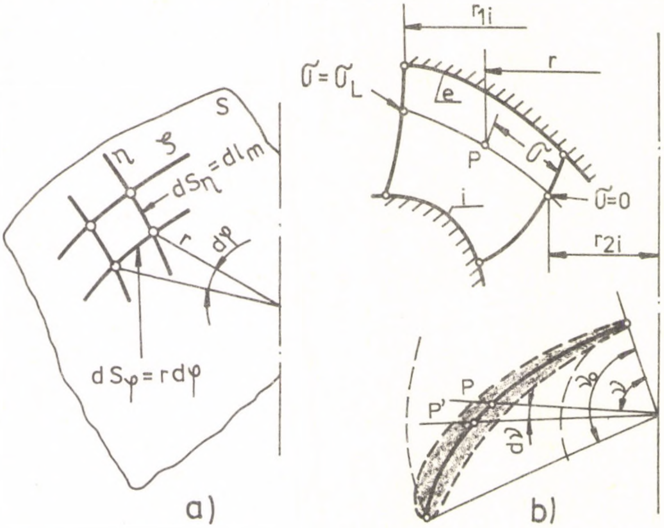

FIG.2.

$$\theta \equiv \begin{cases} X = R\displaystyle\int_{\varphi_1}^{\varphi_2} d\varphi \\ Y = R\displaystyle\int_{r_1}^{r_2} \frac{dl_m}{r} \end{cases} \qquad (1)$$

with R arbitrarily chosen. A more convenient form for engineering calculation is given by the /2/, thus:

$$(TC) \equiv \begin{cases} X = R_o \varphi \\ Y = R_o \displaystyle\int_0^{\sigma} \frac{d\sigma}{r} \end{cases} \qquad (2)$$

$$\text{with} \quad \frac{1}{R_o} = \frac{1}{\sigma_L}\int_0^{\sigma_L} \frac{d\sigma}{r}$$

The transformation can be applied both to the blade camber-line and the blade foil. It is obvious that for particular form of the meridian line (e.g. axial or radial forms) the relations are simplified. The method can be applied both in the analysis of runners tested in the laboratory and for generating new runners. The study is based on the search of some dependences having the form:

$$(n'_1, Q'_1, \eta, \sigma) = f(\lambda, \bar{t}, \beta_{1p}, \beta_{2p}, \bar{f}, \bar{x}_f, \bar{d}, \bar{x}_d) . \qquad (3)$$

As these dependences are quite complicated, the left side values forming an implicit function while the right side variables are theoretically infinite in number, the problem is dealt with in a simplified way by searching the main dependences only.

ANALYSIS OF SOME RUNNERS CHARACTERISTICS

Parameters of the optimum duty for Francis turbines

The experimental results concerning the testing of 9 variants of rotors for Francis turbines, on the same fix line, present the positions of the optimum points as illustrated in fig.3. The rotors were calculated by different methods and different authors, so that the blades geometry differs considerably from one rotor to another.

When analyzing the plane cascades resulted of the conformal transformation (2), some main dependences can be established between the geometrical and hydrodynamical parameters As for each blade there is an infinite number of plane cascades possible, an arithmetic mean value was chosen from the runner crown and the runner ring. The results are grafically illustrated in fig.4-7. In fig.4-5 the dependences are given in the form of $Q'_{1opt}=f(\lambda_m)$ and $f[(\sin\beta_2)_m]$ respectively, and in fig.6-7 the main dependences for the optimum speeds:

$n'_{1opt}=f(\beta^{m}_{1p})$

and $f(\bar{f}_m)$, respectively.

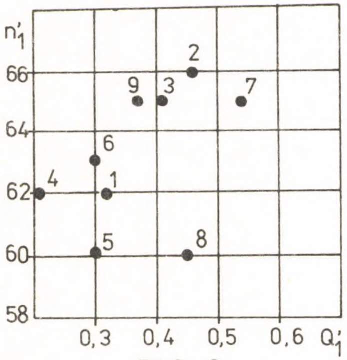

FIG. 3.

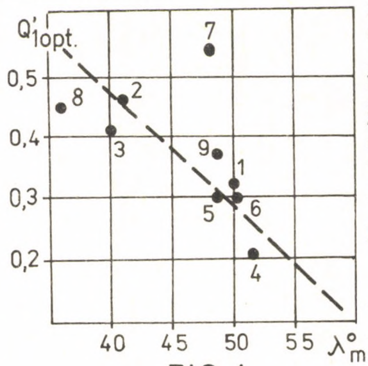

FIG. 4.

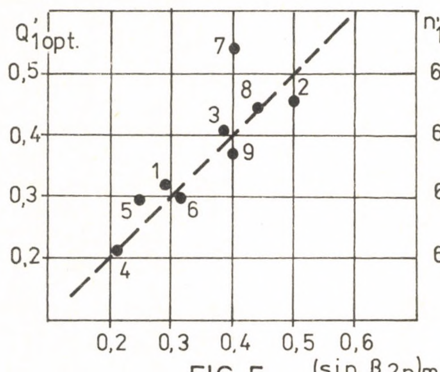

FIG. 5.

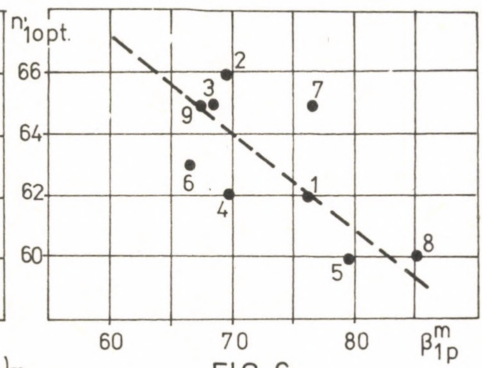

FIG. 6.

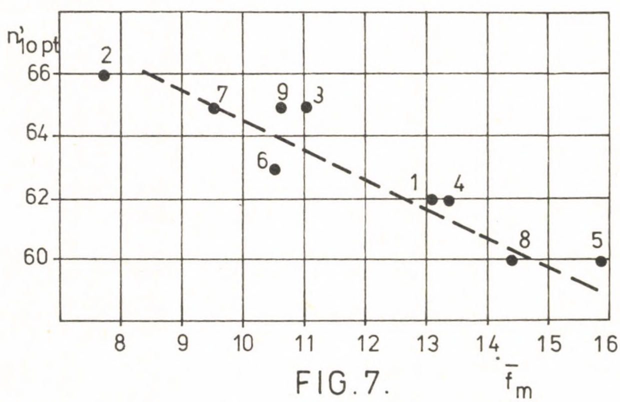

FIG. 7.

For these variants the relative average gap varied within the limits $\bar{t}_m=(0,306\div0,468)$. The dependence $Q'_{1opt}=f(\beta^{m}_{2}, \lambda_m)$ is illustrated in fig.8. as well, for another series of 7 Francis rotors which were tested in an identical fix line.

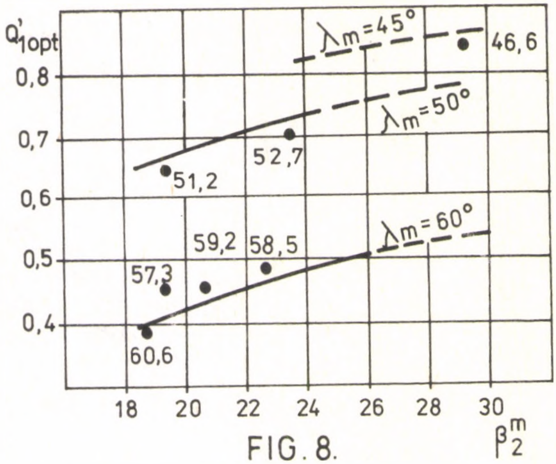

FIG. 8.

Thus, it results that the main dependences are the flow increase with angle and the reduction of inclination of the cascade respectively. For the speed, the latter decreases as the β_{1p} angle and $\bar{f}$ camber increase.

Influence of inlet conditions at rotor

If α_o is the outlet angle of the guide blade as compared to the transport speed u, the dependences $Q'_1 = f(\alpha)$ for four high head Francis rotors, tested on the same fixed line, are illustrated in fig.9. As it results from this figure, the λ_m cascade inclination determins the position of the flow characteristic as compared to the rotor inlet conditions. The rotors III and IV having the λ_m inclination very close, also have close characteristics. In these characteristics the positions of the optimum points are indicated for the values β_{1p}^m and β_{2p}^m. According to fig. no.10. the incidence angles "i" can be calculated the representation of which, depending on α_o, is given in fig.11. From the analysis of this figure it results that:

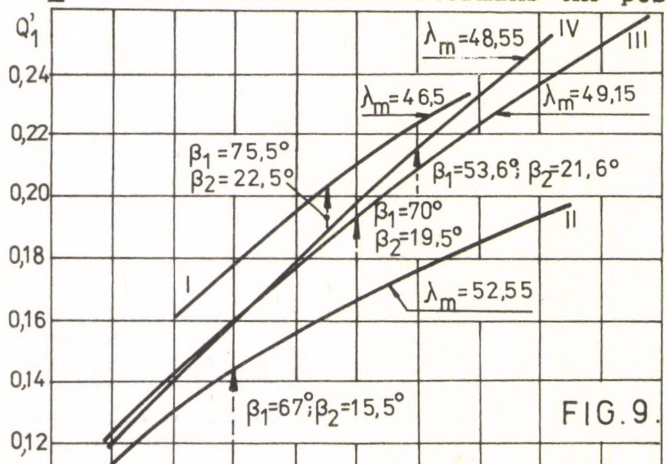

FIG. 9.

- the highest value of efficiency is at the "i_e" positive incidence (variant I);
- the low incidences (variant IV) extend the efficiency curve but the maximum remais reduced;
- the weakest performances are presented by variant II with negative incidences at both runner crown.

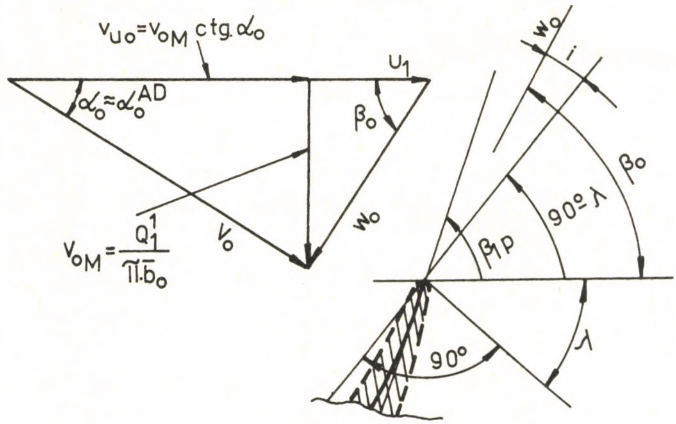

v_uo=v_oM ctg.α_o
U_1
α_o=α_o^AD
β_o
w_o
V_o
v_oM = Q_1^1 / π·b̄_o
β_1p
90°-λ
β_o
i
90°
λ

FIG.10.

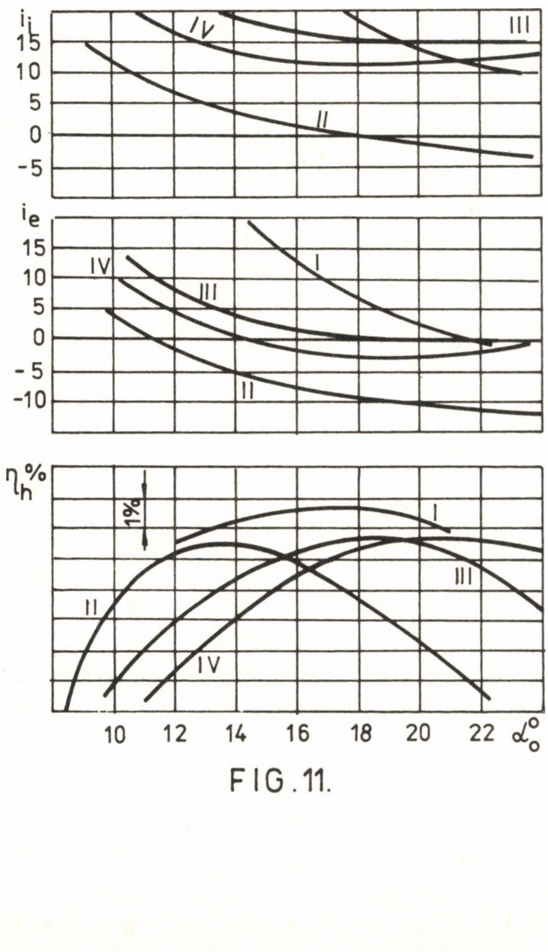

i_i
15
10
5
0
-5
IV
III
II
i_e
15
10
5
0
-5
-10
IV
III
I
II
η_h%
1%
I
II
III
IV
10
12
14
16
18
20
22
α_o°

FIG.11.

ROTOR BLADES GENERATING

For the achievement of some runners variants, the plane cascade is successfully used in generating the blades, thus making possible the systematical modification of the characteristics.

For this purpose the plane cascade is first generated, after which by application of the inverse function to (2) $(TC)^{-1}$, the geometry of the spatial blade /2/ results.

The meridian foil is previously adopted and the edges position in meridian plane, and the hydrodinamic field is traced and the kinematic elements are calculated an the axial-symmetrical surface /4/.

The plane cascade generating is done on the basis of the values(λ, t, β_{1p}, β_{2p}, $\bar{f}$, $\bar{x}_f$: $\bar{d}$, $\bar{x}_d$) or some of them.

In fig.12,13 and 14 ,the elements resulted when generating a runner variant are presented as well as the blade geometry and respectively the universal characteristic of the model runner tested in the energo-cavitational stand Reşiţa.

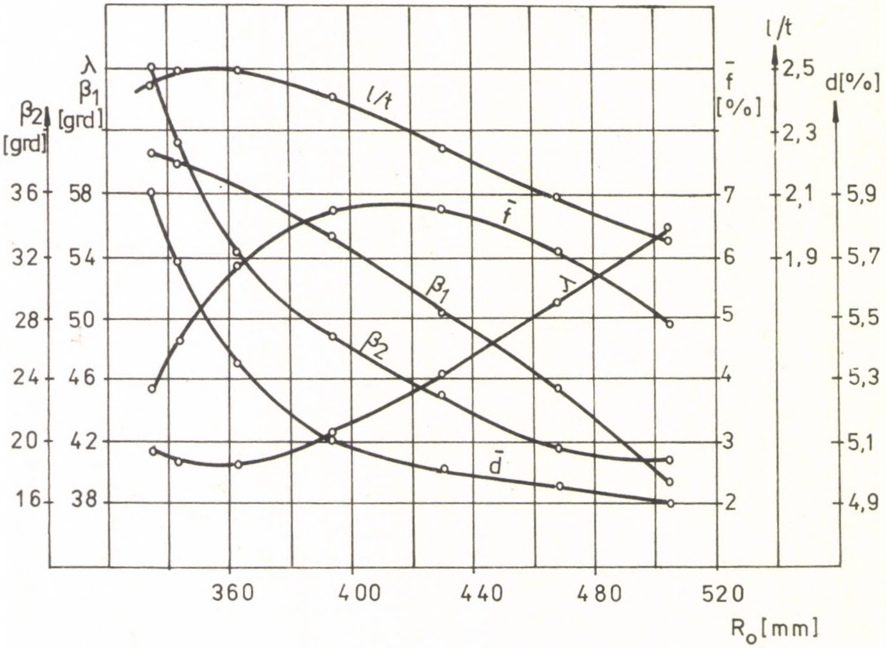

FIG.12.

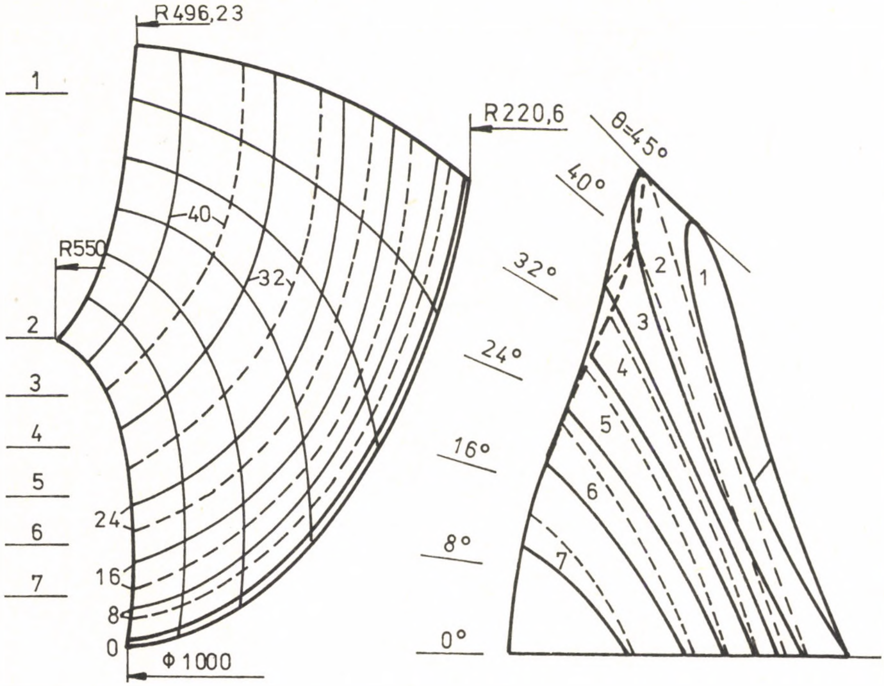

R 496,23
R 220,6
θ=45°
40°
32°
24°
16°
8°
0°
R550
1
2
3
4
5
6
7
40
32
24
16
8
0
Φ 1000

FIG. 13.

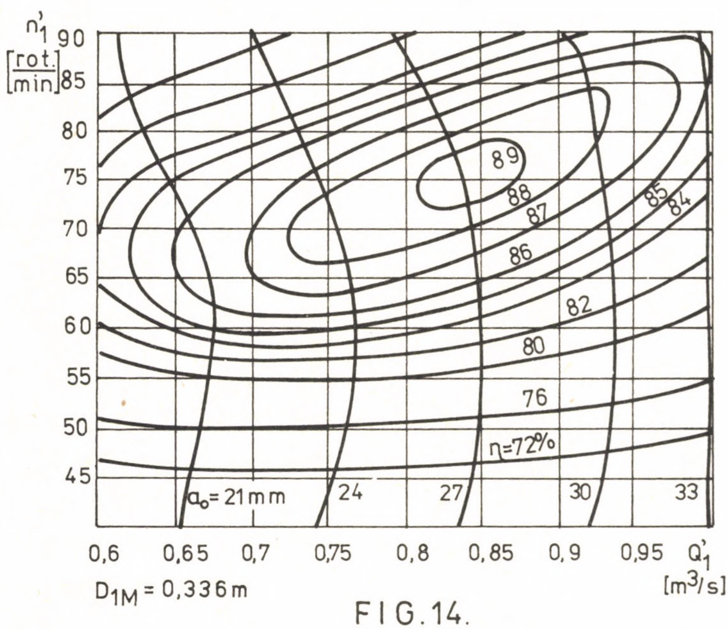

n'1 [rot./min]
90
85
80
75
70
65
60
55
50
45
89
88
87
86
85
84
82
80
76
η=72%
a0= 21mm
24
27
30
33
0,6
0,65
0,7
0,75
0,8
0,85
0,9
0,95
Q'1 [m3/s]
D1M = 0,336 m

FIG. 14.

As a conclusion,the systematic application of the plane cascade to the study of radial-axial rotors represents an efficient method in the development of the models range, permitting the maximum and systematic use of the experimental results obtained an models.A complex programme for exploiting this method is under performing in the Reşiţa laboratory for Francis and pump-turbines.

Bibliography

1.Strscheletzky M.:" Zur konformen Abbildung von Stromflächen in rotationssymmetrischen Hohlräumen" Voith Forschung und Konstruction ,Heft 14,Aufzatz 2.
2.Moulin C.,Wegner M.,Ermeef R.,Vinh-Pong:"Méthodes des tracé des turbomachines hydrauliques"La Hoille Blanche Nr.718-1977
3.Voia I.:"Application of Plane Cascade Profiles to the study of Radial-Axial Runners of Hydraulic Machines"Rev.Constructie de Maşini nr.1-1983.
4.Voia I.:"Paramètres cinématiques,énergétiques et de cavitation des roues Francis"Hydro-turbo '81 ,Brno 1981.

Iacob Voia -Dr.engineer.scientific researcher.

Scientific Research and Technological Engineering Center for Hydroenergetic Equipmement

Address: Calèa Caransebeşului Nr.16.
1700 Reşiţa-România

COMPUTER-AIDED SYNTHESIS OF AN IMPELLER OPTIMUM VERSION IN IMPROVING WATER TURBINES

I.V. Vuchkova, V.S. Obretenov, V.K. Mitsova

I. INTRODUCTION

Improving the power and cavitation characteristics of water turbines is one of the basic problems of hydroturbine building. The solution of this problem requires the application of up-to-date methods of investigating the flow in the turbine stream part when estimating the impeller vane systems. Along with it,still greater importance is attached to the use of mathematical methods in planning and experimental investigations on the basis ofthe profound application of the experimental theory, as well as to the commitment of the solution to the investigation's economic effectivity.

The present paper offers a method of synthesizing an optimum version of a Francis turbine impeller which has been applied in improving the turbines of the "Aleko" Water Power Station in Bulgaria.

II. A SCHEME FOR THE INVESTIGATION

The offered solution of the problem for synthesizing an optimum version of a water turbine impeller comprises the following basic stages:

1. Stand tests of the basic version which is to be improved.
2. Theoretical investigations of the basic impeller operating process by means of a computer-aided mathematical experiment.

For this purpose, use was made of an Applied Programs Package APP/ for computer-aided investigating of vane hydraulic machines, worked out at the Central Institute of Automation, Sofia (1). The APP represents an improved and extended version of the algorithm (2) for solving the direct hydrodynamic problem. With preset operating conditions and geometric parameters of the vane, the APP secures the determination of the distribution of relative speed W and the pressure p along the profile, the peripheral component of the absolute speed at the impeller output C_{u2}, the relative profile losses ζ_1, and the cavitation coefficient σ_k. Thus, the power and cavitation features of the investigated impellers' vane systems can be assessed.

3. Analysis and comparison of the results obtained from stand tests with those of the computer-aided theoretical investigation. Assessment of the possibility for using APP in investigating the same-speed impellers.

4. Planning of theoretical investigations of the various versions of the basic impeller. For this purpose, statistical methods are used, the theory of experimental planning in particular. An appropriate plan is chosen (3).

5. Profiling the required versions of the impeller in the items of the plan.

6. Computer-aided solution of the direct hydrodynamic problem concerning these versions.

7. Processing the results obtained (4). Approximation by the least-squares method is used, as a result of which the regression coefficients of the multifactor relations is found, and the impeller optimum version is determined.

8. Making the impeller /an optimum version/.

9. Stand testing of this impeller.

10. Comparing the results obtained with those of the theoretical investigations /Item 6/. Final conclusions.

III. INVESTIGATION RESULTS

The above scheme has been applied when making a new impeller for the Francis turbines at the "Aleko" Water Power Station, which are of a low specific frequency of rotation: $n_s = 73\ \mathrm{min}^{-1}$. Power testing of the basic P073-0 impeller made at the Hydraulic Machines Department at the Higher Institute of Mechanical and Electrical Engineering, Sofia (5) pointed to a certain discharge displacement Q'_1 of the optimum (n) operating conditions compared to the estimated (o) operating conditions, i.e. $Q'_{1n} > Q'_{1o}$, where $Q'_1 = Q/D_1^2\sqrt{H}$ is the discharge reduced per meter. The power and cavitation features of the basic impeller were investigated by means of the APP (1) on a computer. The practical application of the APP in studying the vane grades of low-speed Francis turbines is given in (6). Comparing the experimental results with the data obtained from the computer-aided investigation showed that the operating process of low-speed Francis turbines can be studied by means of the APP (1). Afterwards, a series of 6 basic impeller versions and 18 modifications was worked out by varying the number of vanes m /Table 1/. Vane profiling in this case has been done by using one-dimension methods. The P073-A1 and P073-A2 impellers are designed with different inlet angles β_1, and the P073-C1 and P073-C2 - with different evolution angle of the vane φ . Profiling of the P073-P impeller vanes has been done under the conditions of equal-speed meridian stream, and as for all remaining types - under the conditions of a potential meridian stream.

Table 1.

No	Impeller	Type of meridian stream	β_1^o	φ^o	m
1-4	P073-0	potential	69,5	57-60	15,11,13,17
5-8	P073-A1	potential	80	57-60	15,11,13,17
9-12	P073-A2	potential	60	57-60	15,11,13,17
13-16	P073-C1	potential	69,5	47-50	17,11,13,15
17-20	P073-C2	potential	69,5	67-70	13,11,15,17
21-24	P073-P	equal-speed	69,5	57-60	15,11,13,17

The study of the impellers characteristics from Table 1 has been done by solving the direct hydrodynamic problem according to Plan No. 14 (3). The number of calculations is considerably reduced in comparison with the one in (7), where the solution concerns all possible combinations of the independent β_1, m, Q and φ parameters. The obtained data processing is done by means of the REGRA program (4), the following relations being obtained:

$$\zeta_1 = f(\beta_1, m, Q_1') \qquad /1/$$

$$\zeta_1 = f(\varphi, m, Q'_1) \qquad /2/$$

$$\sigma_\kappa = f(\beta_1, m, Q'_1) \qquad /3/$$

$$\sigma_\kappa = f(\varphi, m, Q'_1) \qquad /4/$$

The relative profile losses ζ_1 are determined by the well-known method of the "Polzunov" Central Turbine and Boiler Institute (8), and the cavitation coefficient of the impeller σ_κ is:

$$\sigma_\kappa = \frac{W_\kappa^2 - U_\kappa^2}{2gH} + \frac{U_2 C_{u2}}{gH} \qquad /5/$$

where W_κ, U_κ is the relative and peripheral speed at a profile point where the rarefaction is at its maximum;

H is the head;

g is the gravitational acceleration.

Relations /1/ - /5/ have been obtained by approximation after the least-squares method in the following form:

$$y = B(0) + \sum_{I=1}^{3} B(I)\,X(I) + \sum_{I=1}^{2}\sum_{I>J}^{3} B(I,J)\,X(I)X(J) + \sum_{J=1}^{3} B(I,I)\,X^2(I) \qquad /6/$$

where $X(1)$, $X(2)$, $X(3)$ are the independent factors which in this case are β_1 (or φ), m and Q'_1, respectively; y is the function (ζ_1 or σ_κ).

Figs. 1-6 show a part of the results obtained in the computer-aided solution of /6/, namely:

- variation of the cavitation coefficient σ_κ /Figs.1-2/;
- variation of profile relative losses /Figs. 3-4/;
- variation of the relative circulation $\zeta_2 = C_{u2}^2/2gH$ and total $\zeta_3 = \zeta_1 + \zeta_2$ losses for the various types of impellers /figs. 5-6/.

IV. ANALYSIS OF THE RESULTS OBTAINED

The purpose of the analysis of the theoretical data obtained in studying the power and cavitation characteristics of the whole series of impellers is to solve the basic problem, i.e. to choose the optimum version. This analysis is a good reason

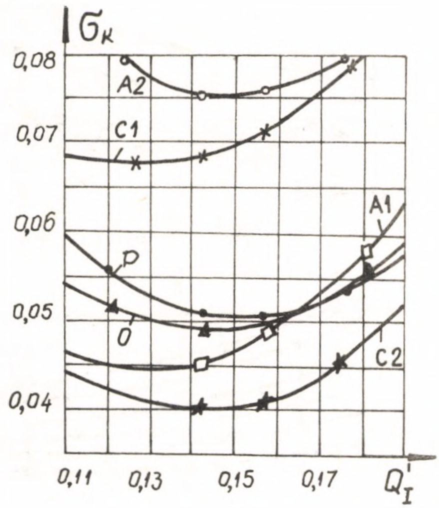

Fig. 1

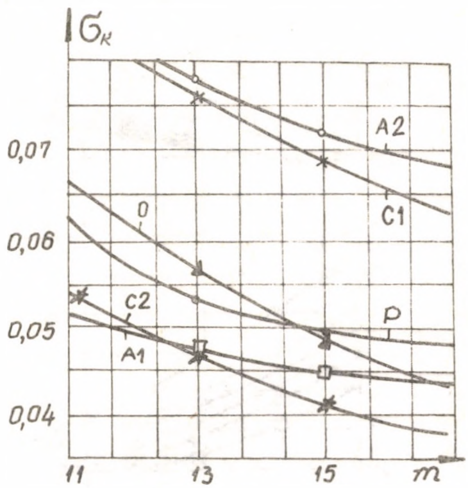

Fig. 2

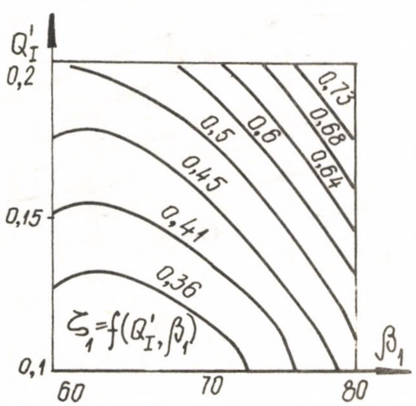

Fig. 3

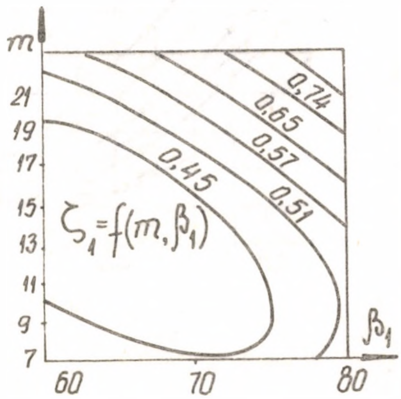

Fig. 4

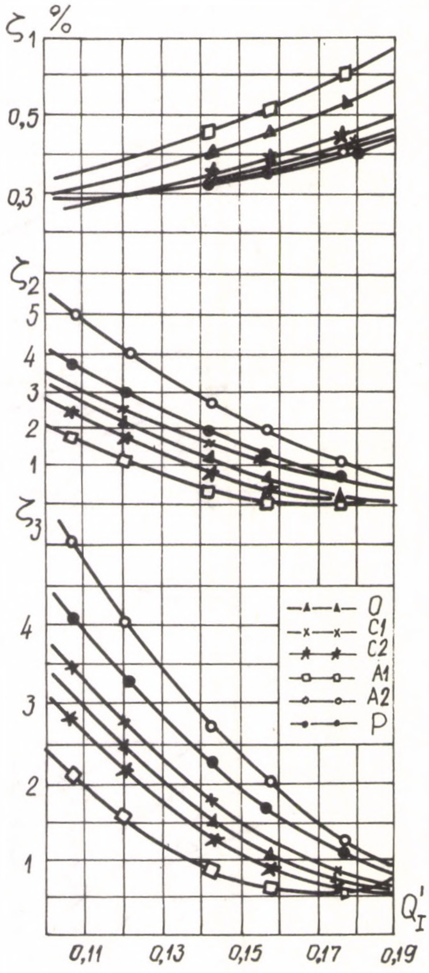

ζ1 %
0,5
0,3
ζ2
5
4
3
2
1
ζ3
4
3
2
1
O
C1
C2
A1
A2
P
Q'I
0,11
0,13
0,15
0,17
0,19

Fig. 5

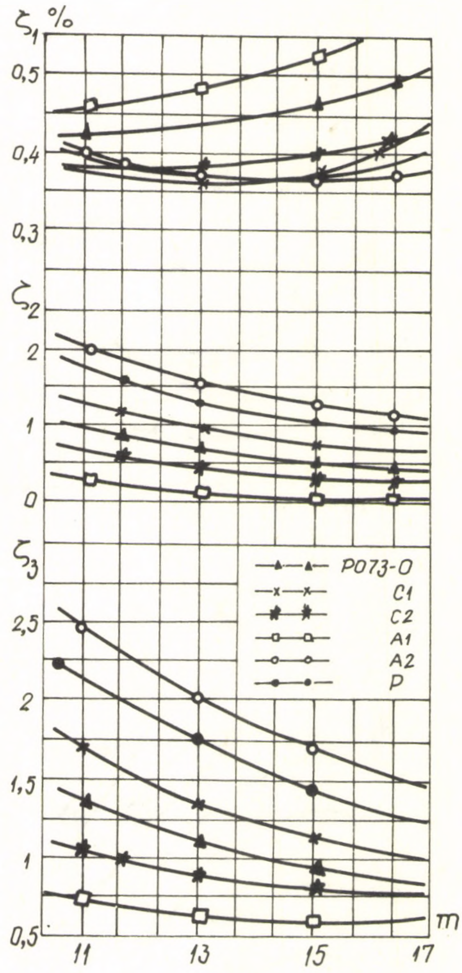

ζ1 %
0,5
0,4
0,3
ζ2
2
1
0
ζ3
2,5
2
1,5
1
0,5
P073-O
C1
C2
A1
A2
P
m
11
13
15
17

Fig. 6

to come to the following conclusions:

- The relative circulation losses increase with the increase of the inlet angle β_1 and the angle of the guide vanes opening, as well as with the decrease of the evolution angle φ .
- The relative circulation losses increase with the decrease of the β_1 angle and the evolution angle φ , having their minimum for a defined value of Q_1' .
- The variation of the total relative losses ζ_3 under various turbines operating conditions corresponds in quality to the variation of ζ_2 due to their greater value. This, to a great extent, determines the optimum turbine operating conditions.
- The number of vanes on some of the tested impellers considerably affects both ζ_1 and ζ_2 . Increasing m leads to improving the impeller cavitation indices.
- The Values of the cavitation coefficient σ_K increase fast together with the increase of $Q_1' > Q_{1n}'$.

The variation of the pressure coefficient $\bar{p} = -\sigma_K$ along the profile (7) has also been analysed, whereby it is shown that the pressure distribution for the mean cross-section of the P073-A1 impeller is the most favourable. With it, the zone of rarefaction is the shortest and it lies most closely to the output edge, the pressure on the sectional are being the highest at the same time.

As a result of the complex assessment of the tested impellers characteristics, we come to the conclusion that the P073-A1 / m = 13/ impeller satisfies to the highest degree the preset requirements. This is also confirmed by the experimental tests carried out afterwards /Table 2/.

Experimental results from Table 2 show that the improved P073-A1 impeller has the lowest cavitation coefficient σ_y /the Thomas coefficient/, while the maximum value of its efficiency is by 5,6% higher than the efficiency of one of the turbines at "Aleko" Water Power Station.

Table 2.

No.	Impeller	D_1	Q'_1	η	σ_y
		m	m^3/s	-	-
1.	"Aleko" W.P.S.	2,0	0,155	0,862	0,033
2.	P073-0	0,4	0,163	0,905	0,033
3.	P073-A1	0,4	0,158	0,918	0,029

V. CONCLUSION

Economic effectivity of the proposed approach in improving turbine impellers is chiefly determined by the following factors:

1. Reducing the volume of experimental tests because of replacing a considerable part of the required physical experiment by a numerical computer-aided experiment.

2. Increasing the turbine efficiency as a result of improving its stream part.

3. Machine-time economizing due to the reduction of the volume of calculations when using mathematical methods of planning the numerical experiment.

In this particular case when improving the Francis turbines at "Aleko" Water Power Station, the economic effectivity of the applied approach is estimated at 450 thousand Leva.

REFERENCE

1. Vuchkova I., V. Mitsova. An Algorithm and a Computer Program for Obtaining the Impeller Theoretical Characteristics When Designing Vane Hydromachines, Proc. Central Institute of Automation, v.XV, S., 1980.

2. Viktorov G., I.Vuchkova. Calculation of the Liquid Flow in an Arbitrary Grid on the Current Axis-symmetrical Surface in the Variable Thickness Layer. Proc. Ac.of Sc.of USSR, Fluid Mechanics, No.5. M. 1969.

3. Vuchkova I., H. Yonchev et at.,A Catalogue of Successively Generated Plans, Technika, S., 1978.

4. Vuchkova I., V. Mitsova. Computer-aided Design of Vane Machines. COMCONTROL, Varna, 1981.
5. Grozev, G., V. Obretenov. A New Model Impeller for the "Aleko" Water Power Station. Scientific Session at the Higher Inst. of Mech. and Electr. Engineering, b.IV, S., 1979.
6. Vuchkova I., V. Obretenov. A Study of the Operating Process of a Radial-axis Impeller for a Low-speed Hydroturbine at the "Aleko" Water Power Station., Scient. Session, Higher Inst. of Mech. & Electr. Engineering, Power Machine Building Section, S., 1981.
7. Obretenov V., I. vuchkova. Computer-aided Design of a Highly Effective Impeller for a Francis Water Turbine, Proc. of the Higher Inst. of Mech. & Electr. Engineering, v. 37, S., 1982.
8. Rauchman B. Grade Profile Losses of a Radial-axis Turbine in a Two-dimensional Non-flat Current. Power Machine Building, No. 12, M., 1963.

INFLUENCE OF AERODYNAMIC LOAD ON THE SHAPE OF VELOCITY PROFILES IN THE AXIAL FLOW COMPRESSOR STAGE

Andrzej Witkowski

SUMMARY

The theoretical and experimental investigations of the flow structure in the axial flow compressor stage at the three operating conditions have been described. In the theoretical part the relationships for simplifying analysis of real flow have been developed. A series of velocity free stream profiles obtained from an axisymmetric flow calculation upstream and downstream of a row campressor impeller blades have been fitted together with diffrend boundary layers model profiles. The results of theoretical prediction are compared with experimental investigation. The analysis of influence of aerodynamic load of axial compressor impeller on the annulus boundary layer parameter has been presented.

INTRODUCTION

The shape and inclination of velocity profiles downstream of axial compressor inpeller have been conditioned by the magnitude flow loss fraction in the stage as well as by operating conditions. To be able to work out effective methods of defining aerodynamic performances of axial flow compressor stage with known geometry it is necessary to know the methods of setting the quasireal velocity profiles. The problem has been solved by fitting main velocity distribution into annular boundary layer velocity profiles where friction forces dominate.

THEORY

Mainstream Flow

The mainstream flow for the compressor stage was calculated by the Streamline Curvature Method program using design flow angles [1]. The general equation of axisymmetric motion for a fluid flowing relative to a turbomachine rotor in cylindrical rotating coordinates, r, ϑ, z is:

$$W \frac{\partial W}{\partial q} + PW^2 + QW + R = 0 \qquad (1)$$

The procedure for utilizing equation (1) to obtain a solution on a prescribed stream surface is to estimate the function P(q), Q(q), R(q) [1] so that equation 1 can be integrated on the condition that the continuity be satisfied.

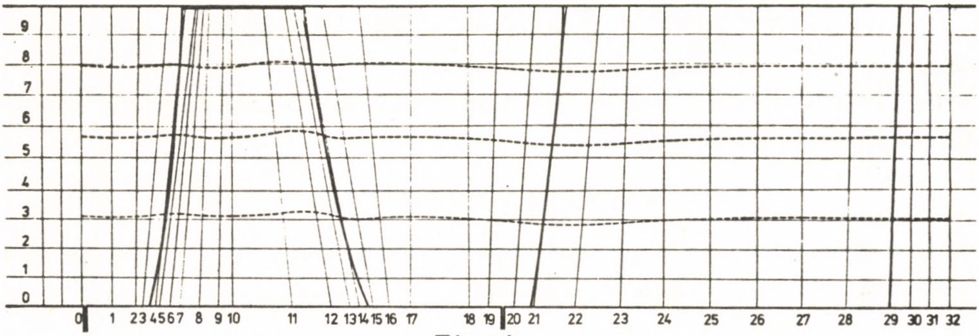

Fig. 1

The flow calculation in model compressor stage OSS 750/06/I [2] has been performed in 33 quasi-orthogonals and 11 streamlines (Fig. 1). The computer program STO-PZDW [3] has been applied.

End Wall Boundary Layer Theory

Velocity distribution obtained from solving axial symmetrical flow model has been used to set boundary layer parameters [4]. These calculations have been performed with the use of momentum integral equation [5]

$$\frac{d}{dz}(W_z^2\Theta_z) + H\,\Theta_z\,\frac{dW_z}{dz} = \frac{d}{dz}(W^2\delta f_z) + \frac{\tau_z}{\varrho} \qquad (2)$$

To define boundary layer parameters $\delta^*, \Theta_z, \delta f_z$ it is necessary to know velocity profiles close to the walls.

The Velocity Distribution in Turbulent Boundary Layers

In turbulent boundary layer the unknown exceed in number the governing equations and some degree empiricism must be introduced. Additional information among others can be obtained in the formulas which make computing velocity distribution in turbulent boundary layers possible. The simplest model of so called power law velocity profile has been used here for introductory definition of boundary layer parameters. Computing formulas introduced by Coles [6] and Kool [7] have been experimentally verified as well.

Coles model. The Coles profile may be written in its velocity defect form to evaluate the boundary layer thicknesses and the form parameter

$$\frac{C_{me} - C_m}{C_m} = \frac{\omega}{k}\left\{\Pi\,[2 - W(Y/\delta)] - \log_e y/\delta\right\} \tag{3}$$

$W(y/\delta)$ is a universal wake function which analytical expression was suggested by Hinze [8]

$$W(y/\delta) = 1 - \cos(\pi y/\delta) \tag{4}$$

The well established empirical expression worked out by Ludwig and Tillmann has been used to calculate wall friction

$$\omega^2 = 0.123 \times 10^{-0,678}(\Theta\ W_m/\nu)^{-0,268} \tag{5}$$

To evaluate the initial values of the Coles wake parameter the equation resulting from equation 6 transformation has been used [8]:

$$1.5\,\Pi^2 + (3.179 - \frac{k}{\omega}\frac{H-1}{H})\Pi + (2 - \frac{k}{\omega}\frac{H-1}{H}) = 0 \tag{6}$$

Local parameter Π distribution along the radius in the real flow have been defined taking into account experimentally set values C_m/C_{me} and ω from equation

$$\Pi_{local} = \frac{[1 - (C_m/C_{me})_{exp}\ ]\frac{k}{\omega\ exp} + \ln y/\delta}{1 + \cos\pi\ (y/\delta)} \tag{7}$$

Other boundary layer parameters have been computed from the dependence:

$$\delta^* = \omega\cdot\delta\ \frac{1}{k}(1 + \Pi) \tag{8}$$

$$\Theta = \omega\cdot\delta\ \frac{1}{k}(1 + \Pi) - \omega^2\cdot\delta\ \frac{1}{k^2}(2 + 3.179\Pi + 1.5\Pi^{-}) \tag{9}$$

<u>Kool's model [7].</u> The hole boundary layer profile is written as

$$\frac{C_m}{C_{me}} = 1 - b(1 - y/\delta)^n(1 - e^{-Ky^+}) \tag{10}$$

where:

$$y^+ = \frac{y.C_\tau}{\nu}$$

and

$$c_{\tau} = c_e \sqrt{\frac{c_f}{2}}$$

Other boundary layer parameters have been computed from the dependence

$$\delta^*_m = \delta \cdot b \cdot \frac{1}{n+1} \tag{12}$$

$$\Theta_m = \delta \ b\left(\frac{1}{n+1} - b\ \frac{1}{2n+1}\right) \tag{13}$$

EXPERIMENTAL INVESTIGATIONS

Test Stand

The results of theoretical predictions are compared with experimental investigation which has been performed on the test stand for determining the flow structure in axial compressor stage (Fig. 2). The flow system of the examined compressor stage consists of an impeller row with eighteenth blades the design beeng free vortex, discharge back stator vane and the outflow curvilinear diffuser. A detaited description of the research stand is in the authors paper [2]. Flow traverses were made before and behind rotor at three flow coefficients C_m/U_T = 0,317, 0,37 and 0,4475. In the main stream of five hole probe was used but for the boundary layer flows a three tube Conrad type probe was needed to make accurate measurements close to the walls.

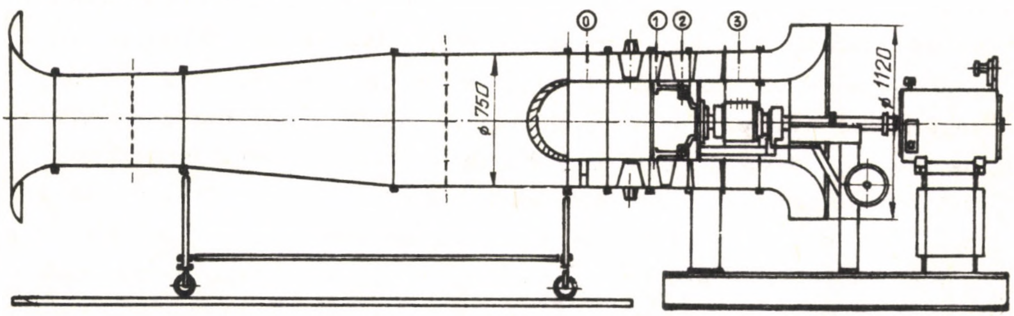

Fig. 2

Results of experiments

Mainstream velocity profiles. Figures 3, 4 and 5 show the theoretical and experimental results for the axial velocity distribution at the upstream and downstream of the rotor. The influence of annulus boundary layer growth on theoretically defined velocity distributions in the main flow has been considered by applying blockage factor. The resulting velocity free stream profiles have been matched with boundary layer velocity profiles. The same tendences in theoretically and experimentally set in meridional velocity profiles in the downstream of the impeller should be stressed. The meridional velocity along the radius may increase, remain constant or decrease depending on the flow ceofficient. These changes in axial velocity are very important when considering the boundary layers.

Boundary Layer Parameters. The influence of the operating conditions and traversing probe position on the velocity profiles shape in the boundary layers and the values of the boundary layers parameters Θ, δ^*, H, ω and Π has been checked. Figures 6, 7, 8, 9, 10, 11 and 12 show the comparison between theoretically and experimentally set boundary layers velocity profiles at the hub in upstream and downstream impellers. These theoretically set have been computed using the power law velocity profiles and Coles and Kools formulas. In every cases measuring velocity profiles are best aproximated by Coles formula specially in the inner region of the boundary layer. From equation 8 the distribution of local values of free parameter across the layer has been set making use of experimentally defined values δ and C_m/C_{me}. Figs. 6, to 12 show that local Π does not remain exactly constant across the layer, taking very large positive and negative values particularly nearerer to the outer edge of the layer. The free parameter Π calculated locally takes the same value as that one determined from (7) only at the point of intersection between experimental and theoretical velocity curves. From equations 6, 7, 9 and 10 the values of annulus wall skin friction coefficient C_f, annulus wall boundary layer shape factor H, free parameter Π and boundary layer thicknesses $\delta^*$and Θ have been set. The boundary layer thickness grows between of the impeller inlet and outlet measuring cross section when C_m/U_T = 0,37 and C_m/U_T = 0,4475

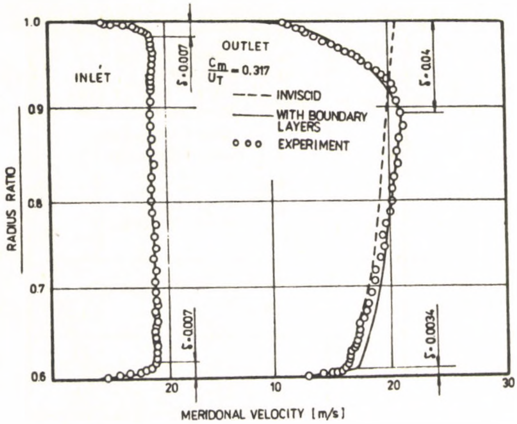

Fig. 3

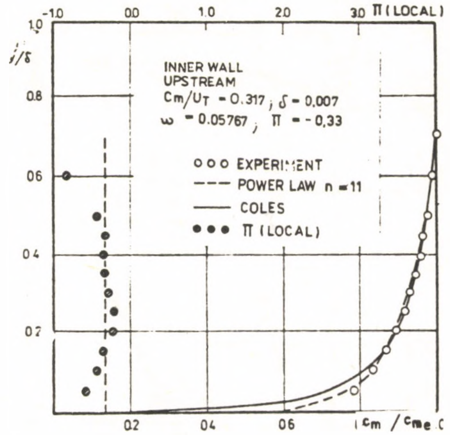

Fig. 6

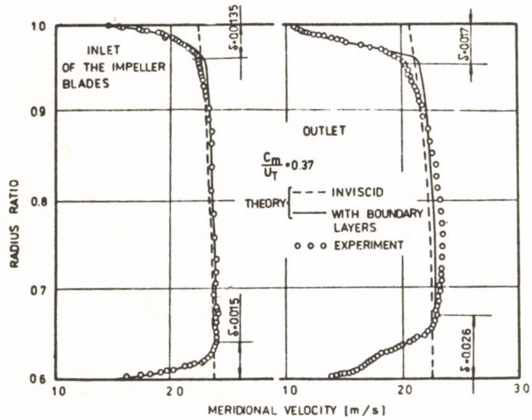

Fig. 4

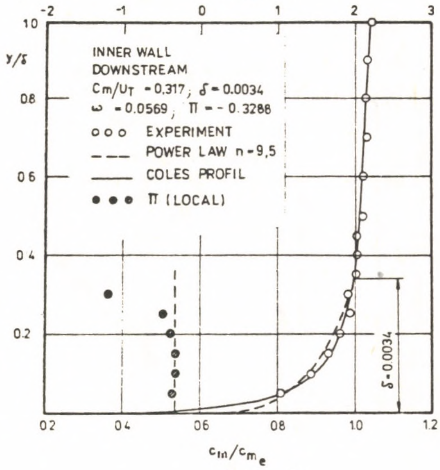

Fig. 7

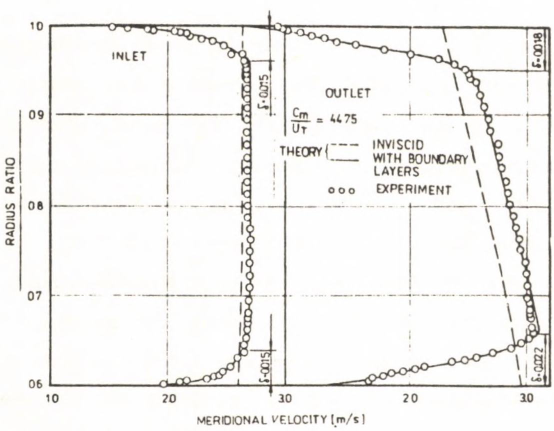

Fig. 5

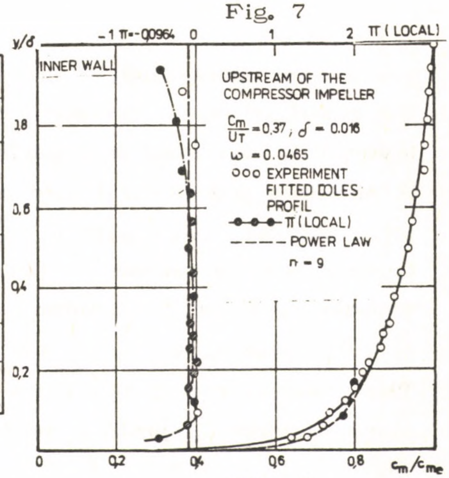

Fig. 8

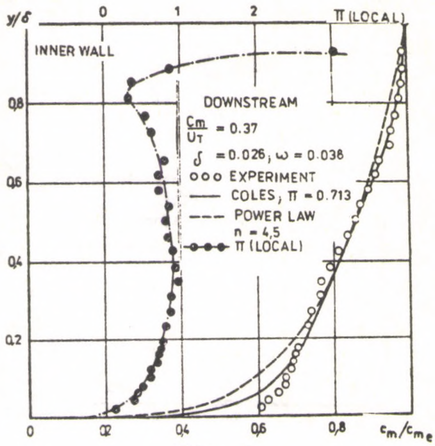

Fig. 9

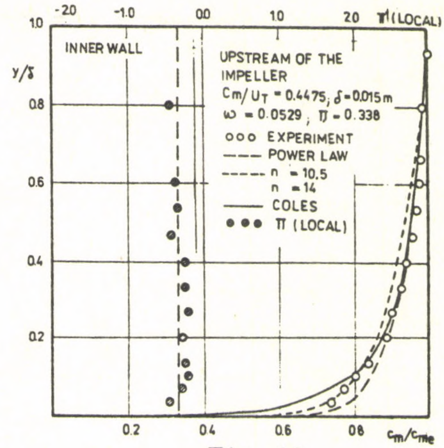

Fig. 10

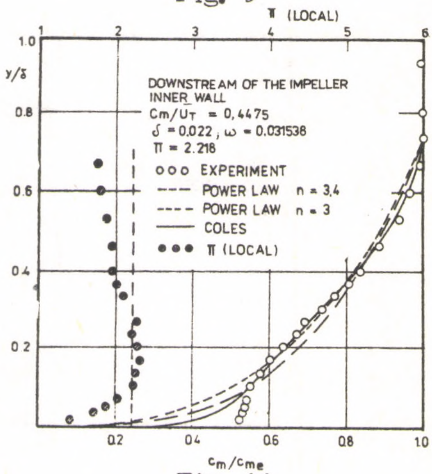

Fig. 11

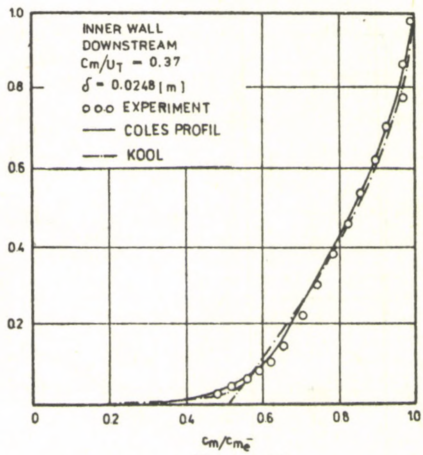

Fig. 12

but it decreases slightly when C_m/U_T = 0,317 what is most probably the result of flow separation at the hub. With the growing boundary layer, the wall friction ceofficient is decreasing and the form parameter H and free parameter Π are increasing. The influence of the position of measuring cross section on the profiles shaping in the boundary layer region is shown on Figures 13 and 14. On Figure 13 the velocity profiles in boundary layer on the inner wall in the distance of 0,015 and 0,025 m behind impeller blades have been compared. The greatest the distance the thicker is the boundary layer and the slope of velocity profile. Similar tendences can be noticed on Figure 14. In both cases the thicker boundary layer is the higher free parameter value and the smaller value of coefficient C_f.

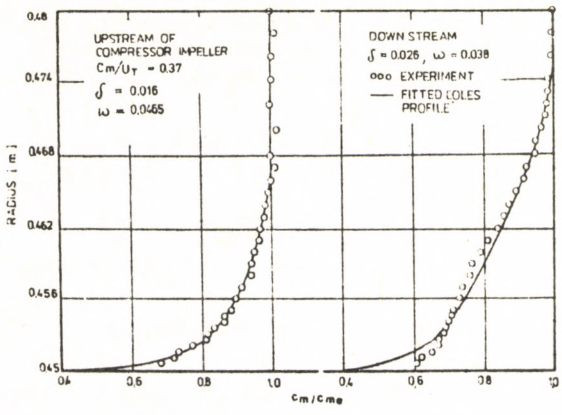

Fig. 13

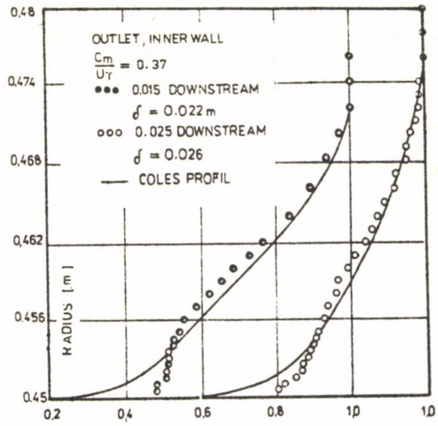

Fig. 14

CONCLUSIONS

A method for calculating the flow in axial compressor stage including the effects of the boundary layers has been developed and experimentally verified. Streamline Curvature Method has been proved satisfactory for the mainstream flow calculation. The mainstream profiles with boundary layer profiles have been matched. If the sublayer is excluded, a turbulent boundary layer velocity profile is best represented by the Coles profile. The shape of velocity profiles between blade rows depends on the choice of working condition and cross section position. With the boundary layer growth the wall friction coefficient decreases but the shape parameter H and free parameter Π increase. The free parameter Π has been computed making use of experimentally set velocity values and boundary layer thicknesses. It has proved not to be constant across boundary layer taking the values which differ considerably from the computed by Coles formula values particularly in the outer region of boundary layer.

REFERENCES

[1] WITKOWSKI A.: Zastosowanie quasiortogonalnych współrzędnych do obliczeń przepływu w wieńcach sprężających o przestrzennie ukształtowanych kanałach międzyłopatkowych. Zeszyty Naukowe Pol. Sl., Energetyka, z. 72, Gliwice 1973 r.

[2] WITKOWSKI A.: Stanowisko do badań struktury przepływu w osiowym stopniu sprężającym. Zeszyty Naukowe Pol.Sl., Energetyka, z. 72, Gliwice 1979 r.

[3] WITKOWSKI A.: Program ALGOL 1900 obliczeń przepływu osio-wo-symetrycznego w stopniu sprężającym o dowolnej geometrii metodą krzywizny linii prądu. Praca wewnętrzna IMiUE. Gliwice, 1981 r.

[4] WITKOWSKI A.: Badania teoretyczne i doświadczalne struktury przepływu w osiowym stopniu sprężającym. Zeszyty Naukowe IMP PAN nr 114/1022/81, Gdańsk 1981 r.

[5] MELLOR G.L., WOOD G.M.: An Axial Compressor End Wall Boundary Layer Theory. Trans ASME, Journal of Basic Engn., June 1971.

[6] COLES D.: The law of the wake in the turbulent boundary layer. J. Fluid Mech., I, 1956 p. 191.

[7] J. DE RUYCK, C. HIRSCH, P. KOOL: An Axial Compressor End Wall Boundary Layer Calculation Method. Trans. ASME J. of Engn. for Power, vol. 191, 1979.

[8] LEWKOWICZ A.: Two and Three Dimensional Incompressible Turbulent Boundary Layers. Ph. D. Thesis. Liverpool, 1965.

NOMENCLATURE

C - absolute fluid velocity

C_f - wall friction coefficient

H - shape factor

k - von Karman constant

n - power

W - relative fluid velocity

y - transverse coordinate (across boundary layer)

z - axial coordinate

δ - absolute thickness of boundary layer

δ^* - displacement thickness

Θ - momentum thickness

Π - Coles parameter

ω - wall friction

Subscripts

m - in meridional coordinale

e - at the edge of the boundary layer

1 - at inlet

2 - at outlet

Witkowski Andrzej, Dr techn.
Silesian Technical University
44-100 Gliwice, ul. Konarskiego 18
POLAND

RESULTS OF THE CALCULATION OF THE AXISYMMETRIC FLOW IN AN AXIAL FLOW COMPRESSOR AND COMPARISON WITH MEASURED DATA

H. Wolf

ABSTRACT

A numerical method for the calculation of the axisymmetric flow is applied to an axial flow compressor stage. The calculated radial distributions of the axial velocity are compared with experimental data in the planes at the entry to and the exit from blade rows. Secondly an approximation method is derived which can be applied to the design of blading as well as the calculation of a given blading. The comparison of the results obtained by this simple approach shows very small differences.

1. INTRODUCTION

At the sixth Conference on Fluid Machinery in BUDAPEST in 1979 we presented a paper on the calculation of the axisymmetric flow in axial flow turbomachines [1]. In the following years we have continued our investigations. We have continously improved both the method and the computer programme and calculated numerous axial flow gas turbine and compressor stages and as far as possible compared the results with experimental data, too. Some results were published in [2].

This paper deals with our investigations on axial flow compressor stages. For the purpose of the comparison the data of the compressor stage from BOOS [3] are available. This compressor stage was designed for high subsonic Mach numbers and the flow measurements were performed from hub to tip upstream and downstream of the rotor and stator blading. These investigations resulted in essential information on the secondary and leakage flows in the rotor and stator blading and on the differences of the losses and the deflection angle compared with the values of straight cascades.

The exact determination of the radial flow distribution in axial flow stages requires the solution of the boundary value problem for the complete meridional plane with consideration of the tangential velocity distribution in this plane. This distribution is given by the cascade geometry or obtained by the law of moment of momentum for the range outside the cascades, respectively. But the detailed blade geometry is only known for the calculation of a given blading (direct problem). The design of blading (indirect problem) requires a more or less iterative procedure. This procedure takes a great deal of time and is expensive, too. The extent of solving the indirect problem can be reduced essentially if the influence of the meridional streamline curvature on radial equilibrium can be evaluated in a simple way. In part 3 an approach for determination of the complete radial equilibrium is suggested. This approximation renders possible the integration of the differential equation of radial equilibrium in the case of the indirect as well as the direct problem.

2. NUMERICAL CALCULATION AND RESULTS

The flow is assumed to be steady and axisymmetric. The losses of mechanical energy caused by friction on the blade surfaces and on the annulus walls and by secondary and leakage flows are taken into consideration by loss coefficients which increase in a determined way within the cascades from section to section. Therefore experience is necessary to evaluate the increase dependent on the x-coordinate. We can obtain some information by boundary layer calculations.

Due to axisymmetric flow the quantities are only dependent on the meridional plane coordinates. A grid in the meridional plane, as shown in Fig.2, is used for the calculation. The grid consists of a number of parallel straight lines x=const. the so-called calculation sections (RS) and the calculation streamlines z=const. The complete numerical calculation is performed in the intersection points (RP) of these two groups of lines. The method for solving the system of nonlinear partial differential equations was described in [2]. The differential equation system involves in addition to the continuity and energy equation the important condition of the radial equilibrium, and furthermore, involves relations on the kinematic conditions within and outside the cascades and function of the thermodynamic quantities. The following function for the static pressure dependent on x and r or x and z, respectively, is assumed in the numerical solution procedure

$$p(x,r) = \sum_{i=0}^{m} b_i(x)\, P_i(2z-1) \tag{1}$$

where P_i are the LEGENDRE polynominals. Because $P_o=1$, the first term in eqn.(1) does not influence the radial pressure gradient, it is used for fulfilling the continuity equation. Due to the iterative solving procedure we also have to assume a first approximation of the stream function $\Psi(x,r)$ and we have to take into consideration that the total quantities of the flow, e.g. the total enthalpy, are carried along the streamlines Ψ=const. The continuity equation is identically fulfilled by the relations

$$c_x = \frac{1}{\rho r k}\frac{\partial \Psi}{\partial r} \qquad c_r = -\frac{1}{\rho r k}\frac{\partial \Psi}{\partial x} \tag{2}$$

A first flow state can be determined by using a first approximation of the distribution p(x,r). This flow fulfills all equations except the radial equilibrium equation. We have to correct the coefficients b_i in eqn.(1) in such a way that the deviation from the radial equilibrium becomes zero. The first approximation of the coefficients b_i can be rough. The start approximation of the stream funktion results from an assumed distribution of a constant flux density and the given mass flow rate in every calculation section RS. So we can calculate the gradient of the streamlines in every RP. The solution of the boundary value problem is given, if that pressure distribution is found out to be the deviation of the radial equilibrium F(x,z) is zero in every RP. But since the number of the streamlines and, consequently, the number of the calculation points in every section RS is generally greater than m (3-5) we define m integrals for every RS

$$G_i(x) = \int_{z=0}^{1} F(x,z) z^{i-1} dz \tag{3}$$

and require the integrals to become zero by the iteration process.

In Fig.1 the calculated radial distributions of the axial and radial velocity components and of the static pressure are shown together with the measured axial velocity. The measured values are a little lower than the calculated ones although the mass flow rate has exactly the equal value. The difference between the theoretically and experimentally obtained density has the opposite tendency. After involving considerations on the accuracy of the experimental investigations we can conclude that the difference is mainly caused by measurement uncertainties.

Some of the calculated meridional streamlines are shown in Fig.2. The curvature of these streamlines is only small. But if we consider the proportion of the terms in the radial equilibrium equation we obtain the values in Table 1 for the mean radius.

Table 1

	rotor row inlet	rotor row outlet	stator row outlet
$\frac{c_x \partial c_r/\partial x + c_r \partial c_r/\partial r}{c_u^2/r}$	0,7653	1,0623	-3,4272

3. AN APPROXIMATION METHOD

The meridional flow in axial flow turbomachines can be rather exactly calculated using numerical methods according to part 2. However we can only apply this method or similar ones for solving the direct problem because the detailed blade geometry must be known. Of course, we can design a blading in an iteration procedure although the expense is enormous and the application of an approximation is mostly more favourable. The deviations caused by the approximations can be easily evaluated by comparison with the results of the more accurate method. In this part we present a simple approach.

If we apply the equation of the radial equilibrium

$$c_x \frac{\partial c_r}{\partial x} + c_r \frac{\partial c_r}{\partial r} - \frac{c_u^2}{r} = -\frac{1}{\rho}\frac{\partial p}{\partial r} + \frac{F_r}{\rho} \tag{4}$$

to the range outside the blade rows the blade force is zero and, furthermore, if we introduce the entropy and the total quantities, we can transform eqn.(4) to

$$\frac{1}{\rho^*}\frac{\partial p^*}{\partial r} = (T - T^*)\frac{\partial s}{\partial r} + \frac{c_u^2}{r} - c_x\frac{\partial c_r}{\partial x} + c_x\frac{\partial c_x}{\partial r} + c_u\frac{\partial c_u}{\partial r} \tag{5}$$

Assuming perfect gas and adiabatic conditions ($\partial T^*/\partial r = 0$) we obtain

$$\frac{\partial s}{\partial r} = -\frac{R}{p^*}\frac{\partial p^*}{\partial r} \tag{6}$$

and eqn.(5) yields

$$RT^*\frac{T}{T^*}\frac{dp^*}{p^*} = \left(\frac{c_u^2}{r} - c_x\frac{\partial c_r}{\partial x} - c_r\frac{\partial c_r}{\partial r}\right)dr + \frac{1}{2}dc^2 \tag{7}$$

The first term in brackets in eqn.(7) can be calculated as follows: Due to design of axial flow blading a distribution of the tangential component of the mean stream velocity

$$\frac{c_{u\infty}}{\hat{c}_{u\infty}} = \left(\frac{r}{\hat{r}}\right)^q \tag{8}$$

is stated and the exponent q is chosen. If, furthermore, the specific blade work shall be constant along the blade length, the relation

$$\frac{\Delta c_u}{\Delta \hat{c}_u} = \left(\frac{r}{\hat{r}}\right)^{-1} \tag{9}$$

is valid. Using eqns.(8) and (9) we can easily calculate the term c_u^2/r in eqn.(7)

$$\frac{c_u^2}{r} = \frac{\hat{c}_{u\infty}^2}{r}\left(\frac{r}{\hat{r}}\right)^{2q} \mp \frac{\hat{c}_{u\infty}\Delta\hat{c}_u}{r}\left(\frac{r}{\hat{r}}\right)^{q-1} + \frac{1}{4}\frac{\Delta\hat{c}_u^2}{r}\left(\frac{r}{\hat{r}}\right)^{-2} \tag{10}$$

Our investigations have shown that the influence of the other two terms in brackets of eqn.(7), especially the curvature term as the more important one, can be taken into consideration, if the following approximation in regard of eqn.(10) is made.

$$\frac{c_u^2}{r} - c_x\frac{\partial c_r}{\partial x} - c_r\frac{\partial c_r}{\partial r} = \alpha^*\frac{\hat{c}_{u\infty}^2}{r}\left(\frac{r}{\hat{r}}\right)^{2q} \mp \beta^*\frac{\hat{c}_{u\infty}\Delta\hat{c}_u}{r}\left(\frac{r}{\hat{r}}\right)^{q-1} + \gamma^*\frac{\Delta\hat{c}_u^2}{4r}\left(\frac{r}{\hat{r}}\right)^{-2} \tag{11}$$

The correction factors $\alpha^*, \beta^*, \gamma^*$ are essentially dependent on the related blade width and on the exponent q. An influence of Mach number is to be expectet, too.

We substitute the expression in brackets of eqn.(7) by eqn.(11) and if we neglect the temperature alteration, the differential equation can be integrated. The error is very small for small integration steps. The integration for $q \neq 1$ yields

$$\frac{\varkappa+1}{2\varkappa}\ln\frac{p_{i+1}^*}{p_i^*} + \frac{1}{2}\frac{\varkappa+1}{\varkappa-1}\ln\frac{1-\frac{\varkappa-1}{\varkappa+1}Ma_{i+1}^{*2}}{1-\frac{\varkappa-1}{\varkappa+1}Ma_i^{*2}} = \frac{1}{1-\frac{\varkappa-1}{\varkappa+1}Ma_i^{*2}}\left\{\alpha^*\frac{\hat{M}a_{u\infty}^{*2}}{2q}\left[\left(\frac{r_{i+1}}{\hat{r}}\right)^{2q} - \left(\frac{r_i}{\hat{r}}\right)^{2q}\right]\right.$$

$$\left.\mp\beta^*\frac{\hat{M}a_{u\infty}^*\Delta\hat{M}a_u^*}{q-1}\left[\left(\frac{r_{i+1}}{\hat{r}}\right)^{q-1} - \left(\frac{r_i}{\hat{r}}\right)^{q-1}\right] - \gamma^*\frac{\Delta\hat{M}a_u^{*2}}{8}\left[\left(\frac{r_{i+1}}{\hat{r}}\right)^{-2} - \left(\frac{r_i}{\hat{r}}\right)^{-2}\right]\right\} \tag{12}$$

For q = 1 the second term has to be replaced by the expression

$$\mp\beta^*\hat{M}a_{u\infty}^*\Delta\hat{M}a_u^*\ln\frac{r_{i+1}/\hat{r}}{r_i/\hat{r}} \tag{13}$$

The Mach numbers nave to be related to the velocity of sound a_1^* or a_2^* , respectively.

The stepwise calculation begins at the mean radius using the known values of the one dimensional calculation. After the first calculation inclusive the comparison of the mass flow rate with the given value the Mach number at the mean radius has to be corrected and the calculation has to be repeated. For determining the total pressure $p^*(r_{i+1})$ by using loss coefficients it is sufficient to use the known velocity $c(r_i)$ or $w(r_i)$, respectively.

In the case of total pressure $p^*(r)$ = const. we can easily integrate eqn.(7). We obtain the radial distribution of the axial velocity component ($q \neq 1$)

$$c_x = \sqrt{\hat{c}_x^2 + \left(1+\frac{\alpha^*}{q}\right)\hat{c}_{u\infty}^2\left[1-\left(\frac{r}{\hat{r}}\right)^{2q}\right] \mp \left(1+\frac{2\beta^*}{q-1}\right)\hat{c}_{u\infty}\Delta\hat{c}_u\left[1-\left(\frac{r}{\hat{r}}\right)^{q-1}\right] + (1-\gamma^*)\frac{\Delta\hat{c}_u^2}{4}\left[1-\left(\frac{r}{\hat{r}}\right)^{-2}\right]} \qquad (14)$$

For $q = 1$ the third term of the root has to be replaced by the expression

$$\mp 2\beta^*\hat{c}_{u\infty}\Delta\hat{c}_u \ln\left(\frac{r}{\hat{r}}\right)^{-1} \qquad (15)$$

In the case of the indirect problem we usually cannot take into consideration the exact distribution of the losses especially in the range of the walls, because the blade twist would be very complicated. The application of eqn.(14) is favourable. Using this equation together with eqns.(8) and (9) and a chosen exponent q we obtain the radial distribution of the angles $\alpha_{1,2}(r)$. The problem consists in the evaluation of the factors α^*, β^*, γ^*. For the investigated axial flow compressor stage (Fig.2) with q = o,6 we obtained $\alpha^* = 0{,}771$ $\beta^* = 0{,}608$ $\gamma^* = 0{,}711$.

If we will take into account the influence of secondary and leakage flow on losses and flow angles especially in the case of a given blading we have to apply eqn.(12) and to calculate step by step. The results of this approach are also shown in Fig.1. The agreement with the results of the numerical method according to part 2 is good. Of course, this good agreement is also caused by the fact that accurate values of the correction factors were known for this example. In our further investigations in this field we will obtain more knowledge on the correction factors α^*, β^*, γ^*.

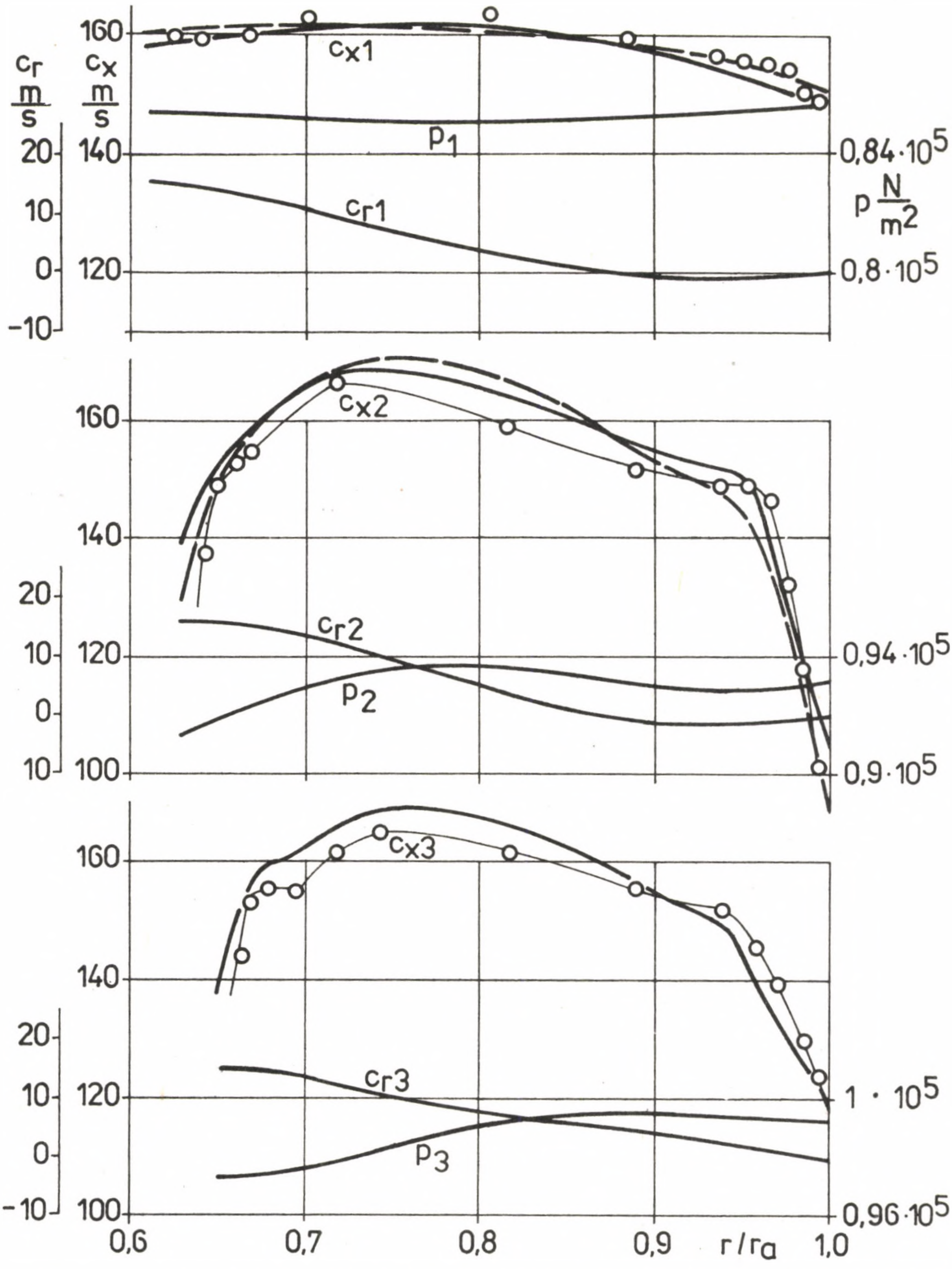

Fig. 1 Radial distributions of velocity components and pressure in the reference planes of the compressor stage r_a = 0,205 m, n = 175 1/s, $\dot{m}$ = 13,89 kg/s
numerical method—— simple approach— — measured O

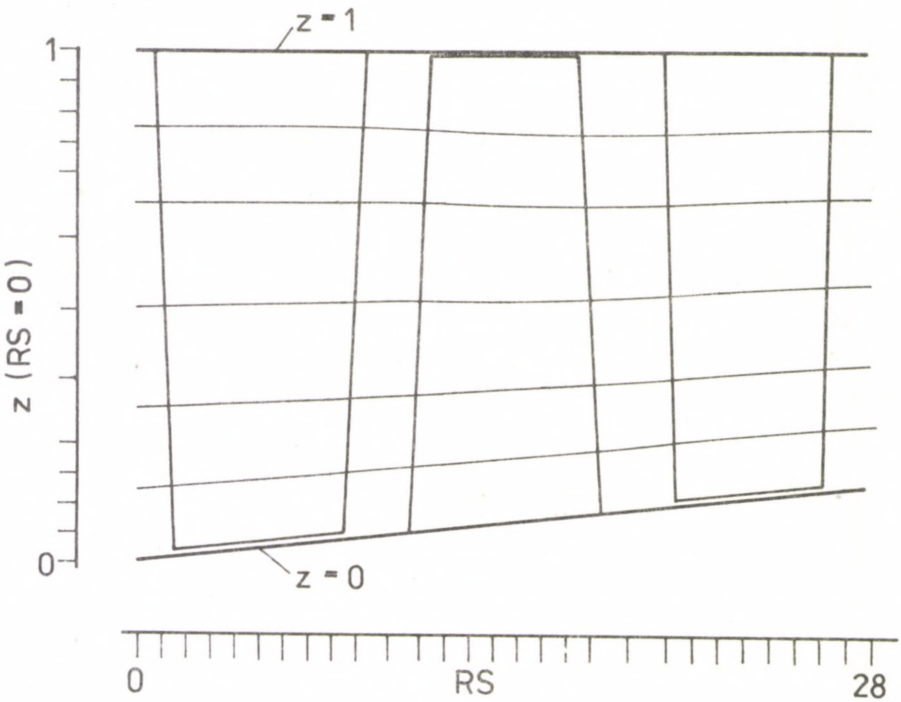

Fig.2 Meridional plane of the axial flow compressor stage and some calculated streamlines

NOTATION

c	absolute velocity
c_x, c_r, c_u	axial, radial and tangential components, respectively, of c
F_r	radial component of blade force
k	blockage factor
Ma^*	Mach number related to critical condition
$\dot{m}$	mass flow rate
n	rotational speed
p, p^*	static pressure, stagnation pressure
r, $\hat{r}$	radial coordinate, reference radius
s	specific entropy
T, T^*	absolute temperature, absolute stagnation temperature

x	axial coordinate
z	dimensionless radial coordinate
α	angle between absolute velocity and peripheral velocity
$\varkappa$	specific heat ratio
ρ, ρ^{*}	density, density of stagnation condition

Subscripts

1, 2	rotor row inlet, outlet
3	stator row outlet
∞	main stream flow

REFERENCES

1 H. Wolf and H. Schulze, Theoretical investigations on the axisymmetric flow in axial flow turbomachines. Proc. 6th Conference On Fluid Machinery, Vol.2, AKADEMIAI KIADO BUDAPEST 1979.

2 H. Wolf, H. Schulze, J. Brechling, M. Hultsch, Untersuchungen zur Berechnung der Strömung in Turbomaschinen unter Berücksichtigung der Stromlinienkrümmung im Meridianschnitt. Maschinenbautechnik Berlin 30 (1981) 3, S. 110-114.

3 P. Boos, Experimentelle Untersuchungen für Axialverdichterstufen bei hohen Unterschall-Machzahlen. Dissertation Ingenieurhochschule Zittau 1979.

Wolf, Heinz
Prof. Dr.-Ing. habil.
Lehrstuhl für Strömungsmechanik
und Strömungsmaschinen
Ingenieurhochschule Zittau
DDR 88 Zittau

I N D E X   O F   A U T H O R S
(With the serial numbers of papers)